Advanced Micro & Nanosystems
Volume 8
Carbon Nanotube Devices

Related Titles

Saile, V., Wallrabe, U., Tabata, O., Korvink, J. G. (eds.)

LIGA and its Applications

2008
ISBN: 978-3-527-31698-4

Tabata, O., Tsuchiya, T. (eds.)

Reliability of MEMS

2008
ISBN: 978-3-527-31494-2

Misawa, H., Juodkazis, S. (eds.)

3D Laser Microfabrication
Principles and Applications

2006
ISBN: 978-3-527-31055-5

Klauk, H. (ed.)

Organic Electronics
Materi als, Manufacturing and Applications

2006
ISBN: 978-3-527-31264-1

Kockmann, N. (ed.)

Micro Process Engineering
Fundamentals, Devices, Fabrication, and Applications

2006
ISBN: 978-3-527-31246-7

Kumar, C. S. S. R. (ed.)

Nanosystem Characterization Tools in the Life Sciences

2006
ISBN: 978-3-527-31383-9

Baltes, H., Brand, O., Fedder, G. K., Hierold, C., Korvink, J. G., Tabata, O., Löhe, D., Haußelt, J. (eds.)

Microengineering of Metals and Ceramics
Part I: Design, Tooling, and Injection Molding

2005
ISBN: 978-3-527-31208-5

Baltes, H., Brand, O., Fedder, G. K., Hierold, C., Korvink, J. G., Tabata, O., Löhe, D., Haußelt, J. (eds.)

Microengineering of Metals and Ceramics
Part II: Special Replication Techniques, Automation, and Properties

2005
ISBN: 978-3-527-31493-5

Kickelbick, G. (ed.)

Hybrid Materials
Synthesis, Characterization, and Applications

2007
ISBN: 978-3-527-31299-3

Advanced Micro & Nanosystems
Volume 8

Carbon Nanotube Devices

Properties, Modeling, Integration and Applications

Edited by
Christofer Hierold

WILEY-VCH

WILEY-VCH Verlag GmbH & Co. KGaA

The Editor

Prof. Dr. Christofer Hierold
ETH Zürich
Department of Mechanical and
Process Engineering
Tannenstr. 3
8092 Zürich
Schweiz

AMN Series Editors

Prof. Dr. Oliver Brand
School of Electrical and Computer Engineering
Georgia Institute of Technology
777 Atlantic Drive
Atlanta, GA 30332-0250
USA

Prof. Dr. Gary K. Fedder
ECE Department & Robotics Institute
Carnegie Mellon University
Pittsburgh, PA 15213-3890
USA

Prof. Dr. Christofer Hierold
ETH Zürich
Department of Mechanical and
Process Engineering
Tannenstr. 3
8092 Zürich
Schweiz

Prof. Dr. Jan G. Korvink
Institute for Microsystem Technology (IMTEK)
Albert-Ludwigs-Universität Freiburg
Georges-Köhler-Allee 103
79110 Freiburg
Germany

Prof. Dr. Osamu Tabata
Dept. of Mechanical Engineering
Kyoto University
Yoshida Honmachi, Sakyo-ku
606-8501 Kyoto
Japan

Library of Congress Card No.:
applied for

British Library Cataloguing-in-Publication Data
A catalogue record for this book is available from the British Library.

Bibliographic information published by the Deutsche Nationalbibliothek
Die Deutsche Nationalbibliothek lists this publication in the Deutsche Nationalbibliografie; detailed bibliographic data are available on the Internet at <http://dnb.d-nb.de>.

Composition SNP Best-set Typesetter Ltd., Hong Kong
Printing Betz-Druck GmbH, Darmstadt
Bookbinding Litges & Dopf GmbH, Heooenheim

Cover Design Grafik Design Schulz, Fußgönheim

Printed in the Federal Republic of Germany
Printed on acid-free paper

ISBN: 978-3-527-31720-2
ISBN: 1865-1399

Preface

The breakthrough of microsystems in the 1990s was triggered by products, which have been fabricated in silicon mainstream or even CMOS compatible technologies and thus taking advantage of a wealth of experience in process technologies and economy of scale. Prominent examples are integrated and intelligent sensors for automotive applications and consumer products. Other applications like those in health care, life sciences, analysis, and instrumentation, which utilize the miniature size of microsystems, jumped on the bandwagon or motivated the development of new technologies, e.g. microsystems polymer technology for microfluidic devices. The technology options in micro and nanosystems are much broader than in mainstream memory and CMOS technologies, but as for every product the technology costs must pay off. Therefore a continuing demand for cost reduction by device scaling, technology optimization, integration of more functionality must be fulfilled. Therefore research is ongoing on new functional materials for novel micro- and nanosystems to maintain transducer performance even in further miniaturized devices, on modeling and simulation of device characteristics and on reproducible fabrication processes for system integration and innovations.

Carbon nanotubes (CNTs) have been identified as novel material with potential for technology entry in mainstream technologies. CNTs are also under exploration and evaluation for new functional structures in micro- and nanosystems. Single-walled carbon nanotubes (SWNTs) for example show unique mechanical, electromechanical, electrooptical, and thermal properties and they change electronic properties by interacting with the environment (for chemical and biochemical sensing). Therefore CNTs are a very promising material for active elements in future nanoscaled transducers. It is obvious that the challenges to fabricate and integrate CNTs will be the same for nanosystems and mainstream technologies. The breakthrough of CNTs as new functional elements in both domains will depend on the techniques to reproduce electronic and physical device properties. The research on new functional materials for electronic devices for mainstream applications (logic, memory) and micro- and nanosystems for medical, life science, analysis and instrumentation, automotive and consumer applications will share a high communality on the near-term and long-term perspective. Nanosystems technology however may even become the first user of CNTs for e.g. sensors, because in contrast to mainstream technologies for which ultra large scale integra-

Advanced Micro & Nanosystems Vol. 8. Carbon Nanotube Devices.
Edited by Christofer Hierold

ISBN: 978-3-527-31720-2

tion (ULSI) is the goal, transducers will require the integration of individual and "just a few" structures on wafer level, only. Yield issues coming with ULSI will be therefore of minor importance in nanosystems.

The topical volume "Carbon Nanotube Devices" of the book series "Advanced Micro & Nanosystems" is dedicated to major aspects of CNT integration and envisioned applications and it illustrates and reports on the recent and significant advances in the field. There is a strong focus on those engineering topics that are expected to provide an important impact towards the utilization of nanostructures: modeling, fabrication, integration and functional properties in "around room temperature" applications. Chapter 1 provides an easy to read introduction in electronic properties of CNTs and reviews recent progress and challenges in CNT integration for interconnects and mainly transistor devices. The chapters 2 and 3 report from research on the electromechanical or piezoresistive properties of SWNTs and on the progress in localized catalytic growth (CVD) for direct integration of nanotubes in MEMS. Process technologies, which are supposed to become production technologies, require methods for efficient process control. In chapter 4 recent advances in CNT characterization by optical spectroscopy are presented. The chapters 5 and 6 are dedicated to modelling of carbon nanotube properties. While chapter 5 focuses on the electronic structure, electronic transport and mechanical properties of SWNTs, chapter 6 emphasizes on the computational modeling of nanoscale flows interfacing with carbon nanotubes, which is of particular importance for nanodevices interacting with biomolecular structures. Last but not least in chapters 7 and 8 emerging applications of CNTs in devices are reviewed, in which the added value of the macro molecular nanostructure is exploited: CNT field emitters utilizing the nano size of emitting tips and CNT gas sensors, taking additional advantage of the high surface to volume ratio together with an option for low power operation, respectively.

In summary, the objectives of this book are to report on the recent advances in the field of carbon nanotube devices and relevant technologies. It will support the experienced reader with a quick overview of the state-of-research on a particular topic of interest, and it will introduce the less experienced reader in the basics of physics and chemistry of carbon nanotubes and their applications.

Reaching these objectives will be the accomplishments of my fellow colleagues, who spent enormous efforts in authoring the chapters and who will receive adequate compensation by your – dear reader's – appreciation. Many thanks to all of them for their diligence and dedication, and many thanks also to Wiley-VCH for supporting this project.

Christofer Hierold
January 2008
Zurich, Switzerland

Foreword (by Series Editors)

We present the eighth volume of Advanced Micro & Nanosystems (AMN), entitled Carbon Nanotube Devices – Properties, Modeling, Integration and Applications.

Why is there a need for further device miniaturization in microsystems technology or MEMS beyond the aspect of cost reduction? Scaling laws are unfavourable for many device concepts, e.g. inertial sensors, and the lack of reproducible fabrication processes beyond photolithography and dry etching for the integration of nanostructures in systems increases the effort in research and process development disproportionately. Even cost reduction by miniaturization is not as obvious as in mainstream microelectronic technologies and must be justified case by case.

Information and communication systems of the future will demand lightweight, mobile, personalized and autonomous components embedded in the environment and on or in the body. These systems will enable us, for example, to detect health risks in real time by implanted bio sensors, to reduce security risks by environmental monitoring or in smart buildings. They will help us saving energy through ambient sensing, and they may allow monitoring environmental hazards. These systems will require solutions, which allow fulfilling complex tasks with lowest power consumption at smallest size. New functional nanostructures and in particular carbon nanotubes (CNTs) promise to enable these functions, because they provide highly sensitive detection at ultra miniature size, the option for ultra low power operation and exceptional mechanical, thermal and chemical properties, which are important for robustness and functionalization. The potential of carbon nanotubes is not limited to sensor functions in the above sketched scenarios. Research is ongoing to utilize their electronic properties in micro- and nanoelectronics as material for high current density interconnects and one-dimensional electron conductors, to name only two examples. All new and maybe still unforeseen applications for CNTs however will face the same challenge: technology and system integration with a potential for a high yield and cost efficient production. The solutions will be developed by engineers; engineering science research is currently taking off to pave the ways towards the utilization of the carbon nanotubes' unique properties for future innovations.

We are very glad to present the first volume of our series on "Advanced Micro & Nanosystems", which is fully dedicated to nanotechnologies and nanosystems

Advanced Micro & Nanosystems Vol. 8. Carbon Nanotube Devices.
Edited by Christofer Hierold

ISBN: 978-3-527-31720-2

and the challenges at the crossroads between basic science and research in engineering. Twelve internationally renowned researchers from academia and industry joined their efforts for this book to report on the recent advances in carbon nanotube devices and the technologies that will be needed for product development: modeling, simulation, fabrication and characterization.

Oliver Brand, Gary K. Fedder, Christofer Hierold, Jan G. Korvink,
and Osamu Tabata
Series Editors
January 2008
Atlanta, Pittsburgh, Zurich, Freiburg, and Kyoto

Contents

Advanced Micro & Nanosystems Vol. 8. Carbon Nanotube Devices.
Edited by Christofer Hierold

ISBN: 978-3-527-31720-2

List of Contributors

Christofer Hierold
Micro and Nanosystems
Department of Mechanical and
Process Engineering
ETH Zürich
8092 Zürich
Switzerland

Alain Jungen
Micro and Nanosystems
Department of Mechanical and
Process Engineering
ETH Zürich
8092 Zürich
Switzerland

Petros Koumoutsakos
Computational Science and
Engineering Laboratory
ETH Zürich
8092 Zürich
Switzerland

Franz Kreupl
Qimonda AG
Technology Innovations
Am Campeon 1–12
85579 Neubiberg
Germany

Janina Maultzsch
Technische Universität Berlin
Institut für Festkörperphysik
Hardenbergstr. 36, Sekr. EW5–4
10623 Berlin

John Robertson
Engineering Department
Cambridge University
Cambridge CB2 1PZ
UK

Stephan Roche
Commissariat à l'Energie Atomique
DSM/DRFMC/SPSMS/GT
17 avenue des Martyrs
38054 Grenoble
France

Cosmin Roman
Mikro- und Nanosysteme
ETH Zürich
Tannenstrasse 3
8092 Zürich
Switzerland

Advanced Micro & Nanosystems Vol. 8. Carbon Nanotube Devices.
Edited by Christofer Hierold

ISBN: 978-3-527-31720-2

Angel Rubio
Universidad del País Vasco
Centro Mixto UPV–CSIC
and
European Theoretical
Spectroscopy Facility (ETSF)
Departamento de Física de
Materiales
Facultad de Ciencias Químicas
Apdo. 1072
Paseo Manuel de Lardizabal 4
20018 San Sebastián/Donostia
Spain

Christoph Stampfer
Micro and Nanosystems
Department of Mechanical and
Process Engineering
ETH Zürich
8092 Zürich
Switzerland

Christian Thomsen
Technische Universität Berlin
Institut für Festkörperphysik
Hardenbergstr. 36, Sekr. EW5–4
10623 Berlin

John T. W. Yeow
Department of Systems Design
Engineering
University of Waterloo
Waterloo
Ontario
Canada

1
Carbon Nanotubes in Microelectronic Applications

Franz Kreupl, Qimonda AG Technology Innovations, Neubiberg, Germany

1.1
Introduction

Carbon nanotubes (CNTs) are the hottest topic in physics, according to a 2006 ranking of different scientific fields in the published literature [1]. The interest in these objects has been sparked by the exceptional properties of those nano-sized objects combined with the ease of theoretical investigations due to the relatively limited number of atoms in CNTs, facilitating *ab initio* calculations [2]. The first investigations of CNT properties reveal many interesting features which are very attractive for solving the technological hurdles that the semiconductor industry is

Advanced Micro & Nanosystems Vol. 8. Carbon Nanotube Devices.
Edited by Christofer Hierold

ISBN: 978-3-527-31720-2

facing if scaling of circuits continues for another decade [3, 4]. The high current-carrying capacity, high thermal conductivity and reduced charge carrier scattering combined with the huge resilience of CNTs promise to solve challenges in the interconnect area, whereas the low effective electron and hole mass, the attractive band gap and the absence of dangling bonds address the needs of a fast, energy-efficient and high-*k* dielectric-compatible device of the future.

However, the step from a hand-crafted, proof-of-concept device example to a highly integrated, reliable technology is huge and hardly achievable within a few years. Therefore, this chapter summarizes some critical aspects of a microelectronic-compatible integration of CNTs and highlights the recent progress that has been achieved in terms of possible applications.

1.2 Carbon Nanotube Basics

Carbon nanotubes may be considered to be graphene cylinders. Graphene is a single planar sheet of sp^2-bonded carbon atoms, as shown in Figure 1.1. Graphite consists entirely of individual graphene layers, which are stacked on each other. The properties of graphite already give a first hint towards the remarkable properties of carbon nanotubes. The charge carrier densities in graphite are almost equal for electrons and holes ($n_e \approx n_h \approx 7 \times 10^{18}\,cm^{-3}$) and routinely measured mobilities are of the order of $10^4\,cm^2\,V^{-1}\,s^{-1}$ at room temperature and $10^6\,cm^2\,V^{-1}\,s^{-1}$ at 4.2 K [5]. The in-plane resistivity is as low as $50\,\mu\Omega\,cm$ and can be engineered down to $1\,\mu\Omega\,cm$, which is half of the value of copper by doping and intercalation [5]. The thermal conductivity of graphite is also very high, ranging between 24 and $470\,W\,m^{-1}\,K^{-1}$. Recent experiments have verified these remarkable properties also in individual graphene layers and even field effect modulation of the conductivity has been demonstrated in these samples, leading to a first verification of a recently proposed metallic field effect transistor [6, 7]. However, the viability of graphene-based microelectronic devices and interconnects is limited by the high temperatures of 1400–2000 °C which are required to fabricate graphite or graphene.

1.2.1 Band Structure of Carbon Nanotubes

The basic structure of CNTs is shown in Figure 1.1. A single-walled CNT (SWCNT) can be thought of as a rolled-up graphene sheet in which the edges of the sheet are joined together to form a seamless tube. By changing the direction in the roll-up, different chiralities can be created. Further, several tubes of different diameter can be fitted into each other to make a multi-walled carbon nanotube (MWCNT), as shown in Figure 1.1.

The band structure of graphene is the basis for understanding the electronic behavior of carbon nanotubes. Graphene has a honeycomb lattice structure of carbon atoms in the sp^2 hybridization state. Every lattice point of the two-

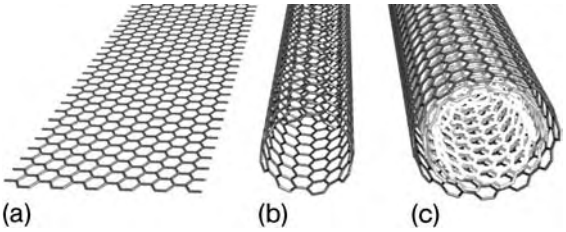

Figure 1.1 Structure of a single layer of graphite (graphene) (a), single-walled carbon nanotube (b) and a multi-walled carbon nanotube with three shells (c).

dimensional graphene point can be described by multiples (n,m) of two unit vectors a_1 and a_2, as shown in Figure 1.2a. The multiples are also used to describe the chirality of the CNT by defining the chiral vector $C_h = n \cdot a_1 + m \cdot a_2$. The length of C_h is just the circumference of the CNT. Every CNT is then characterized by the two indices (n,m). There are two carbon atoms in a unit cell and each atom contributes a free electron. The Brillouin zone of graphene is shown in Figure 1.2 and has been calculated by a simple tight-binding approach. The Brillouin zone is also hexagonal in shape and the unhybridized orbitals give rise to valence and conduction bands. The band structure of graphene is unique in the sense that at the six corners of the Brillouin zone, the valence and the conduction bands meet exactly at a point where the Fermi energy lies.

The cones in Figure 1.2b represent the electron energy dispersion of graphene close to the Fermi energy and the parallel lines indicate the allowed states of a nanotube with the periodicity around the circumference in reciprocal space. By imposing the quantization condition, $C_h \cdot k = 2\pi q$, of the wavevector k around the circumference C_h, the energy landscape is cut into slices of allowed states as indicated in Figure 1.2b by the thick solid lines. The slices are separated by $2/d$, where d is the diameter of the tube. The spacing of the lines is inversely proportional to the CNT diameter and their angle depends on the nanotube chirality or index (n,m). For specific tube diameter and chirality the lines intersect with the apex of the cones, as shown in Figure 1.2d, and the nanotubes are metallic, i.e. there is an allowed state at the Fermi energy. If, as shown in Figure 1.2c, the lines intersect elsewhere on the cones, there is a band gap around the Fermi energy and the tubes are semiconducting. For larger diameter CNTs the spacing between the lines is reduced and the maximum possible band gap decreases. The condition for achieving metallic tubes can be expressed by $n - m = 3q$, with q being an integer [8]. The electrical properties of CNTs are strongly dependent on the chirality and the tube diameter.

Every possible nanotube configuration (n,m) can be mapped by symmetry operations on the blue and red colored dots in Figure 1.2e. From a statistical point of view, one-third of the possible nanotube conformations are metallic whereas the remaining two-thirds are semiconducting. This can be deduced by analysis of the index map shown in Figure 1.2e. This has severe implications as no specific chirality can be grown to date and one always obtains a mixture of chiralities of

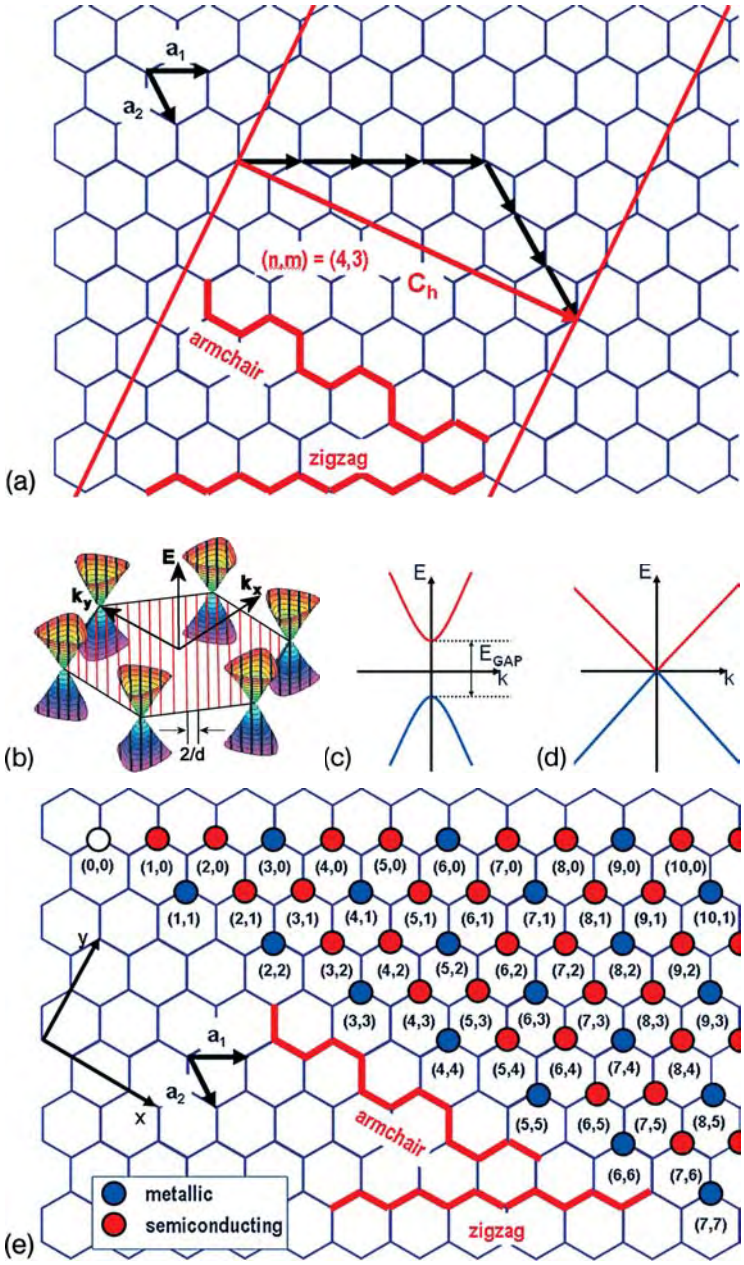

Figure 1.2 (a) The index (n,m) determines the chirality of the CNT and the circumference C_h. To make a CNT with index (4,3), the graphene layer needs to be cut out along the two parallel gray lines and rolled up to from a seamless cylinder. (b) The band structure of graphene form hexagonal cones in the vicinity of the Fermi energy. The formation of a nanotube cuts the energy landscape into slices of allowed states. The location of the conic section determines whether the resulting band structure is semiconducting (c) or metallic (d). (e) A map showing which (n,m) gives semiconducting and metallic tubes can be drawn. Only armchair CNTs ($n = m$) are strictly metallic.

predominantly semiconducting CNTs. The band gap of semiconducting SWCNTs is inversely proportional to the diameter and corresponds to 0.8 eV for a tube with a diameter of 1 nm. Single-walled tubes with diameters up to 5 nm and as small as 0.4 nm have been observed, but the diameter is typically between 0.7 and 2 nm, providing band gaps in a range that is interesting for transistor and diode applications [3, 8]. Multi-walled nanotubes with diameters up to 100 nm have been observed although their diameters are usually around 10–20 nm. The separation of the layers in an MWCNT is about the same as in graphite and corresponds to 0.34 nm. The curvature of the nanotube, especially at small diameters, leads to some modifications which are not incorporated in a simple tight-binding approximation [8]. Even CNTs which satisfy the condition $n - m = 3q$, with q being an integer, develop a small band gap due to the distortion of the bonds and are so-called small band gap CNTs. Only CNTs with $n = m$ are genuine metallic tubes due to their special symmetry. The effect is only important at very small diameters, because the distortion induced band gap scales inversely with the square of the diameter [8]. For example, while a semiconducting nanotube with a diameter of 1 nm has a band gap of 0.8 eV, a semimetallic nanotube with a comparable diameter has a band gap of only 40 meV.

1.2.2
Fabrication of Carbon Nanotubes

There are three main methods to produce CNTs: arc discharge, laser ablation and catalyst-enhanced chemical vapor deposition (CCVD). Each of these techniques has its advantages and disadvantages, which are only briefly discussed below due to the extensive literature available on this topic [3, 4, 9, 10].

Arc discharge and *laser ablation* rely on the evaporation of a graphite target to create gas-phase carbon fragments that recombine to form CNTs. The temperatures reached in these processes are in the range 2000–3000 °C, more than sufficient for the carbon atoms to rearrange into the tube structure. In order to increase the yield of nanotubes in the carbon material created, several different metals in concentrations of the order of 1% are incorporated into the target material that is evaporated. The metals evaporate with the carbon and coalesce into clusters that form a base from which the nanotubes can grow.

Under optimized conditions, both of these processes produce nanotubes with the highest achievable crystallinity due to the high temperature during formation. Unfortunately, a large amount of unwanted non-nanotube graphitic and amorphous carbon material is also produced, and a cleaning process is necessary before the nanotubes can be used. Further, the purified nanotubes are dispersed in a solvent and are typically deposited in a random manner on the substrate by dipping, spraying or spin-on. This is useful for investigations of the physical properties of CNTs in individual "hand-crafted" devices or for large-size applications, such as conductive transparent coatings or conductive plastic material, but is not suitable for the reproducible, parallel integration of CNTs into microelectronic systems. On the other hand, preparation of the nanotubes in solution allows

the application of various processes to separate the semiconducting and metallic CNTs and chemically functionalize the CNTs.

Catalyst-enhanced chemical vapor deposition utilizes small metal catalyst clusters in the gas phase or on surfaces to decompose a carbon containing feedstock gas, such as methane or acetylene. The resulting carbon dissolves in, or is adsorbed on, the catalyst particle and is released in the form of a nanotube starting with a buckyball-type cap when the concentration exceeds the maximum solubility. The nanotube continues to grow as long as carbon continues to be delivered at the right rate and the form of the catalyst does not change. The growth temperature depends on the type of nanotube to be grown and the catalyst composition and lies in the range 400–1100 °C, lower than the temperatures in the arc discharge or laser ablation processes. For this reason, it is believed that CCVD tubes have a higher density of defects.

The advantage of CCVD nanotube production is the possibility of structuring the catalyst particles and, hence, selectively growing the nanotubes where they are required. Further, under the right conditions only nanotubes are produced and no unwanted graphitic material. Using this CCVD method, SWCNTs and MWCNTs can be grown on semiconductor wafers with semiconductor production equipment without almost any equipment modifications using carbon-containing gases such as methane or acetylene.

1.2.3
Density of States, Resistance and Resistivity

The density of states (DOS) without small band gap effects can be easily calculated for different CNTs following an approach of Mintmire and White [11] or using the online simulation facilities of www.nanohub.org [12], both of which are based on the tight-binding approach. The result for two metallic CNTs with diameters of 1 and 20 nm are shown in Figure 1.3. The DOS is constant in an energy window of 2 eV for the 1-nm diameter CNT and additional van Hoove states are energetically far away from the Fermi energy. In contrast, the 20-nm thick CNT, which might constitute the outer shell of an MWCNT, has additional states available in an energy window of ~0.2 eV and can be much easier manipulated by charge transfer doping. In Figure 1.3, a small p-doping of the 20-nm diameter CNT is assumed, which shifts the Fermi level below the charge neutrality point of the undoped CNT.

The DOS of CNTs is four orders of magnitude smaller than that of metals and this would normally result in bad conductivity. However, the one-dimensional nature of the nanotubes leads to a huge mean free path of the order of 1–10 μm of the charge carriers, in contrast to that of metals, which is around 40 nm for copper. Additional states have to be available for the scattered carriers, to where the charge state can be scattered. However, additional states for small-angle scattering events are energetically far away due to the circumferential quantization. The only allowed states are in the direction along the CNT. The phase space for scattering is therefore strongly restricted, even at room temperature. At low bias voltage the only energetically allowed state to be scattered to is just backwards in the opposite direction.

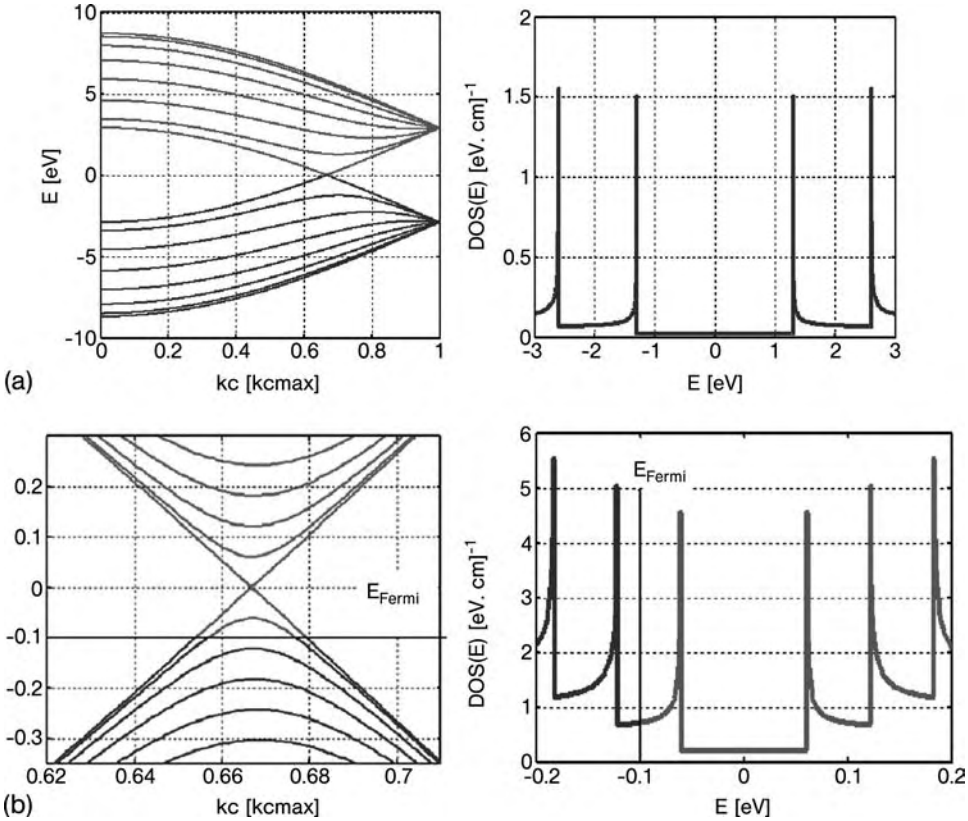

Figure 1.3 (a) The band structure of an $(n,m) = (7,7)$ metallic CNT of diameter 1 nm with the corresponding density of states. (b) The band structure of an $(n,m) = (150,150)$ metallic CNT of diameter ~20 nm with the corresponding density of states. Due to charge transfer doping the CNT is p-doped with additional density of states.

From the Landauer approach, the conductance G can be modeled by $G = 2e^2/hMT$, where M is the number of the allowed channels for the transport and T is the quantum mechanical transmission coefficient, which models the transmission probability. The factor 2 in the Landauer expression accounts for spin degeneracy and e^2/h is the fundamental Klitzing conductance of a single eigenstate. The transmission T can be influenced by defects in the CNT, nearby located trapped charges, and bending-induced strain. The transport channels are related to the k-value with which every electron is characterized in the band structure. Two bands cross at the Fermi level in the band structure of the metallic CNT, an example of which can be seen for an $(n,m) = (7,7)$ CNT in Figure 1.3.

The lowest possible resistance for an SWCNT including the contact resistance is ~6.5 kΩ because there are two bands with spin degeneracy and therefore $M = 2$. In a perfectly contacted, ballistic nanotube, half of the 6.5 kΩ resistance drops just at each of the two contacts to the nanotube. Additional contact resistance can occur

which is dependent on the nature of the contacts. The kind of metal and the way it is deposited are equally important as the size and the diameter of the contacts, but resistances close to the theoretical value can be obtained on a routine basis [8, 55].

For MWCNTs, each shell contributes according to its diameter and chirality to the density of states and therefore to the conductivity. In thicker shells, additional states may become populated by thermally activated carriers, because more energy levels are accessible, as can be seen in Figure 1.3b for the 20-nm diameter tube. The 20-nm CNT would even conduct well in the case of a semiconducting CNT because the band gap is small compared with the thermal energy.

MWCNTs almost always show metallic behavior and can be easily used in interconnect applications because of the guarantee of a metallic behavior. The number of participating channels in an MWCNT can be calculated for each case and an approximate method is discussed by Naeemi and Meindl [13].

For interconnect applications, the maximum conductivity should be achieved, which means that the number of conducting channels per unit cross-sectional area should be maximized. It is worth looking at the specific resistivity of SWCNT and MWCNTs, because this will indicate the quality of the various materials for interconnect applications. The low bias resistivity for SWCNTs and MWCNTs is depicted in Figure 1.4 and shows a peculiar dependence on the length of the nanotubes. For SWCNTs, the experimental values are plotted and calculated values are given for MWCNTs with two different diameters. The resistivity of the SWCNTs is calculated by the measured resistance at a given length for an effective area cross-section of $1\,nm^2$. The length dependence of the resistivity stems from the very large mean free path of the charge carriers, which is typically around $1\,\mu m$ for SWCNTs. Making the SWCNT shorter than $1\,\mu m$ does not reduce its overall resistance any further. Therefore, the resistivity increases sharply at short lengths of a few nanometers. SWCNTs exceeding $1\,\mu m$ have an almost one order of magnitude better resistivity than copper and an SWCNT of length 100 nm still outpaces the resistivity

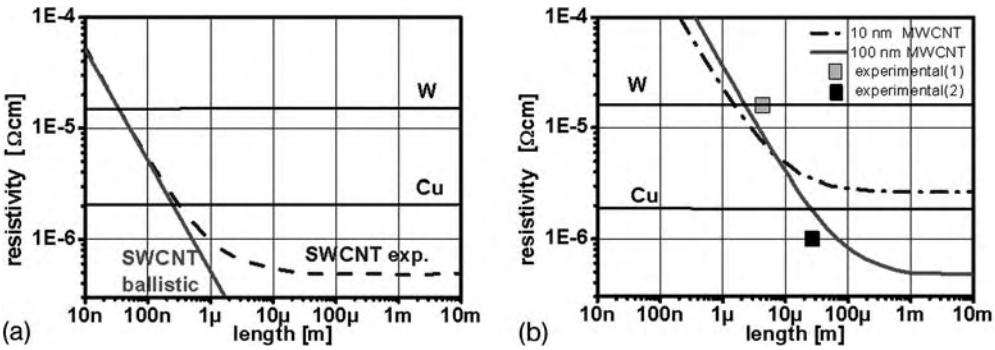

Figure 1.4 (a) The length dependent resistivity of SWCNTs based on experimental data compared with a pure ballistic SWCNT. As a reference, the values without size effects for W and Cu are indicated. (b) The resistivities of two different MWCNTs which differ in diameter are calculated according to Reference [13] for a shell filling factor of 0.5 and two experimental findings are incorporated, which demonstrate the achievable resistivities.

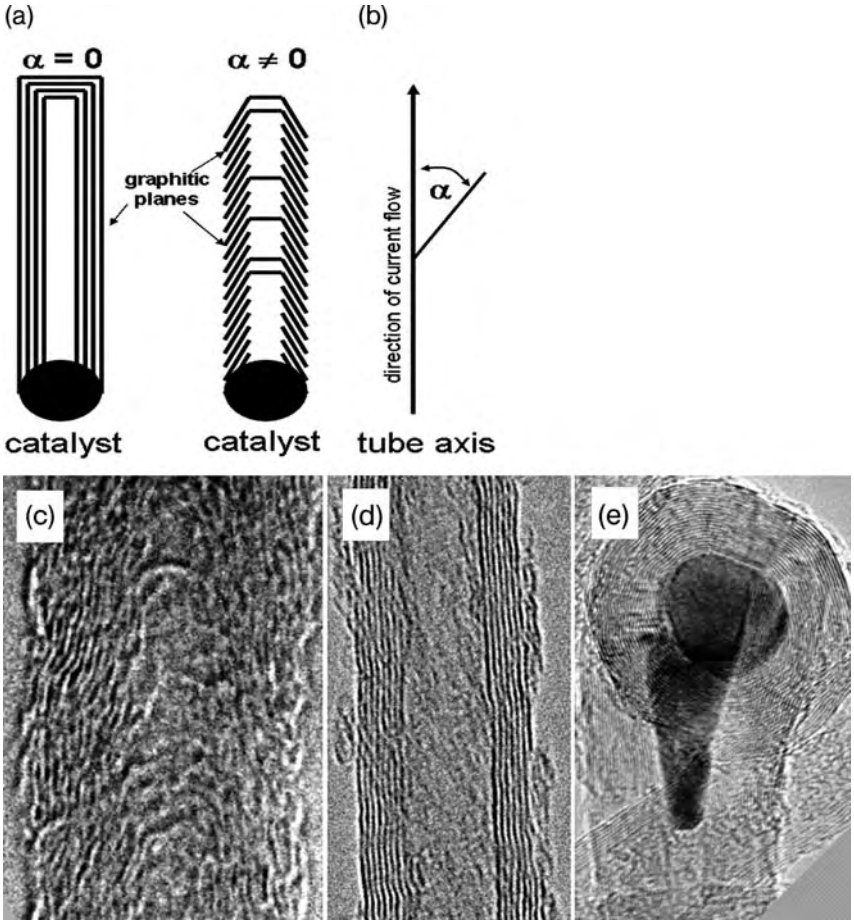

Figure 1.5 (a, b) Factors influencing the resistivity of a tube: number of shells and orientation of the graphitic planes. Ballistic transport can only occur for $\alpha = 0°$; for graphite $\rho_c = 1000\rho_a$ and the averaged resistivity can be expressed as $\rho(\alpha) = \rho_a \sin^2(90° - \alpha) + \rho_c \cos^2(90° - \alpha)$. (c–e) TEM images for CVD-grown MWCNTs. The interlayer distance is 0.34 nm. (c) A poor-quality tube grown at 450 °C with $\alpha \approx 18°$. (d) A high-quality tube with $\alpha \approx 0°$, but with only seven shells. (e) A high-quality tube with ~25 shells also showing the encapsulated catalyst particle.

of tungsten. The length-dependent resistance for SWCNTs can be approximated by ~6 kΩ μm^{-1} if the length exceeds the mean free path length. This explains the superior performance of metallic SWCNTs in interconnect applications.

The resistivity calculation of the MWCNTs in Figure 1.4 is based on a ratio of 0.5 for the inner to outer diameter of the MWCNT, because transmission electron microscopy, as shown in Figure 1.5d, demonstrates that most of the MWCNTs are not completely filled but have a hollow core, which does not contribute to the conductance. The conductivity values can vary by a factor of two for completely filled MWCNTs. A unique feature of the mean free path in metallic nanotube is

its proportionality to the diameter of the nanotube [14]. This is shown in Figure 1.4b, where a long 100-nm thick MWCNT can achieve the same resistivity as an SWCNT despite the fact that a huge portion of its diameter (~50 nm) is hollow and cannot contribute to the conductivity. The missing inner conducting shells are compensated by a larger mean free path of the thicker outer shells. Experimental data support this finding. Li et al. have contacted an MWCNT with spot welding, which almost assures contact with all shells [15]. The contacted MWCNT has a diameter of about 100 nm and a length of 25 μm with a resistance of 37 Ω. The resistivity obtain from these values is around 1 μΩ cm and close to the respective values in Figure 1.4b. A second example, also shown in Figure 1.4b, from de Pablo et al. [16], gives a value of 15 μΩ cm for a 4 μm long MWCNT of 40 nm diameter. Other experimental data often refer to situations where only the outer tube of a MWCNT is contacted and the contributions of the inner shells are not known in detail [17]. The outer shell is often corrupted by processing methods and does not perform adequately and therefore gives rise to irreproducible results. Furthermore, growth of CNTs with chemical vapor deposition (CVD), especially when supported by plasma, results often in misaligned shells, as indicated in Figure 1.5. Quasi-ballistic transport can only occur if the shells are strictly aligned in the direction of current flow. Any misalignment as shown in the TEM image of Figure 1.5c impairs the conductivity as the charge carriers have to tunnel from shell to shell. The conductance perpendicular to the shells is almost a factor of 1000 smaller than the in-graphene-plane conductance. A typical value for the resistivity of these more carbon fiber-like structures is in the region of 4 mΩ cm.

1.2.4
Doping of Multi-Walled Carbon Nanotubes

The diagram of the DOS of the CNTs in Figure 1.3 suggests the possibility of enhancing the conductivity of MWCNTs by doping the outer shell. Chemical doping of CNTs by charge transfer would shift the Fermi energy (E_F) of the nanotubes to a level with a higher DOS and, consequently, increase the conductivity. As the DOS is independent of the circumference of the CNT, it is much easier to achieve higher conductive channels for metallic MWCNTs than for metallic SWCNTs, for two reasons. First, the surface area for interaction with charge donors is larger for MWCNTs, and second, additional channels are energetically closer to the Fermi level for MWCNTs. Therefore, the doping of the MWCNTs with either an aryldiazonium salt or with an oxonium salt can reduce the resistance by 20% on average to values as low as 2.8 kΩ, as will be demonstrated below [18].

In the following, the as-deposited CNTs are compared with those doped by the deposition of various charge-transfer adsorbates. In addition, the chemical doping of two different qualities of MWCNTs, namely CNTs grown by CCVD and arc discharge fabricated MWCNTs are investigated [18].

The MWCNT samples were dispersed in a solution of 1% sodium dodecyl sulfate (SDS) and deposited on a silicon–silicon oxide substrate with cobalt microelectrodes with gap spacings ranging between several hundred nanometers and

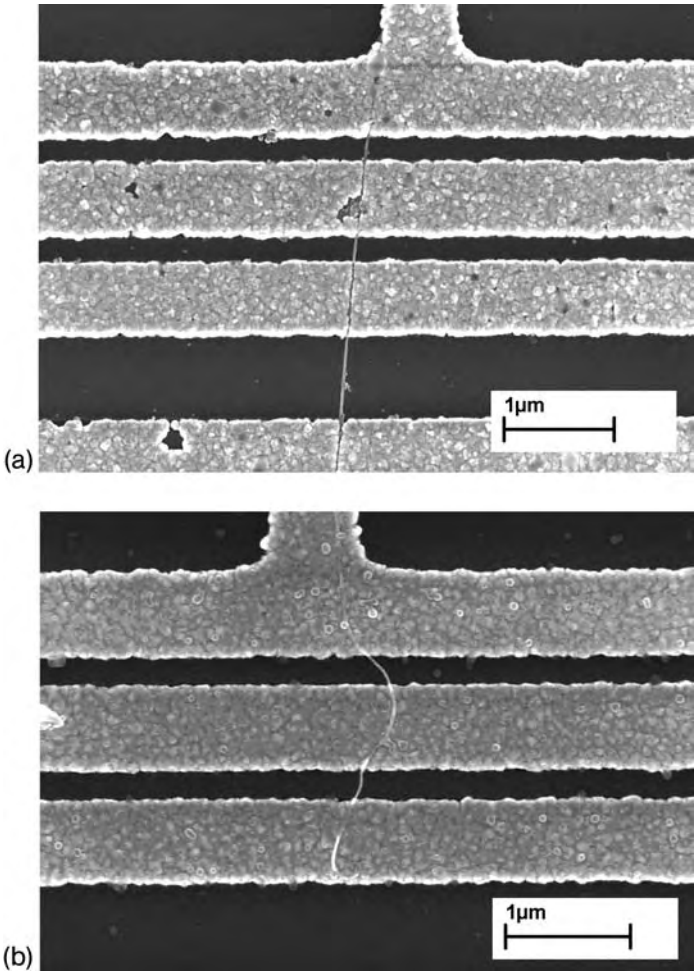

Figure 1.6 (a) Scanning electron microscope images of MWCNTs embedded in palladium contacts on a silicon oxide surface. The nanotubes shown in the images (a) were produced in an arc discharge, whereas those in the images (b) were generated using a CCVD process.

15 μm. The contact resistances were reduced by embedding the tubes in palladium using an electroless metal deposition process that has been described earlier [19, 20] and annealing at 400 °C in an argon atmosphere. Figure 1.6 shows samples of MWCNTs on cobalt electrodes made by arc discharge (a) and by CCVD (b). It can be seen that the CVD tubes have a number of kinks, whereas the arc discharge tubes appear very straight. This is ascribed to the higher density of defects in CCVD tubes and the misaligned shells as discussed in Figure 1.5. Figure 1.6 shows the contact regions between the CNTs and the metal electrodes after electroless palladium deposition.

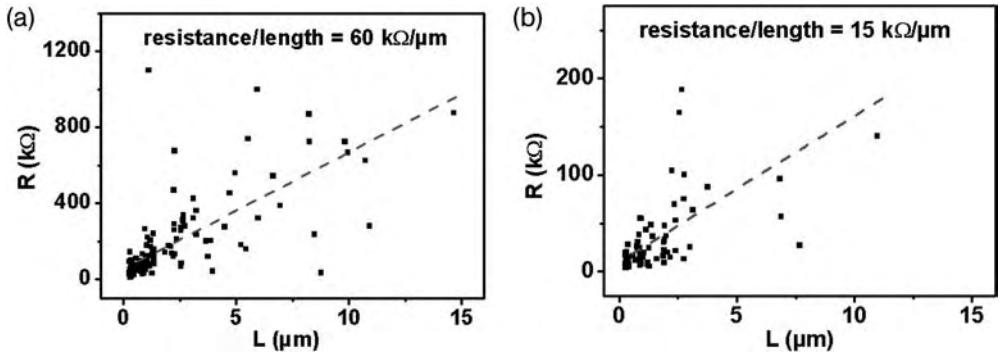

Figure 1.7 Two-point resistance measurements of (a) CCVD and (b) arc discharge CNTs of different lengths between palladium contacts. The CCVD produced CNTs display an intrinsic resistance that is four times higher than those produced by arc discharge [18].

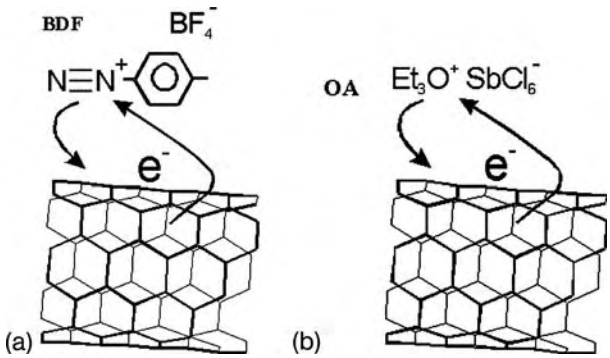

Figure 1.8 Schematic of the adsorbate doping of CNTs by electron extraction using 4-bromobenzenediazonium tetrafluoroborate (BDF) or triethyloxonium hexachloroantimonate (OA).

The two-point resistances of about 100 devices with different nanotube lengths were determined. The length dependence of the resistances is shown in Figure 1.7 for the CCVD- and arc discharge-produced tubes. As can be seen, the CCVD tubes show a significantly higher length-dependent or intrinsic resistance compared with the arc discharge tubes. This probably originates from a higher defect density due to the different growth conditions. Further, the average intrinsic resistances derived from four-point probe measurements turned out to be $60\,k\Omega\,\mu m^{-1}$ for the CCVD CNTs and $15\,k\Omega\,\mu m^{-1}$ for the CNTs produced by arc discharge. These values differ from two-point probe measurements due to scattering of electrons in the vicinity of the contacts and due to the inter-shell conductance in MWCNTs by the application of four microelectrodes [17].

The influence of chemical doping can be investigated by two approaches. One way that has been well investigated is chemical functionalization of CNTs by diazonium salts [21, 22]. As shown in Figure 1.8, 4-bromobenzenediazonium tetra-

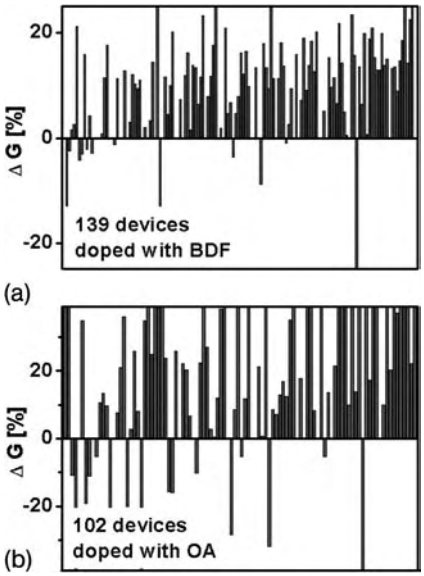

Figure 1.9 Percentage difference between the two point resistances of pristine and doped CNTs between palladium contacts after doping [18].

fluoroborate (BDF) [21, 22] extracts electrons from the CNT and releases nitrogen. The reaction is driven by the formation of a stabilized charge transfer complex and will lead to p-type doping of the CNTs. Another approach uses triethyloxonium hexachloroantimonate (OA) as a one-electron oxidant, thus leading to a similar doping state. The devices were treated with either a 5.5 mM solution of BDF in water for 10 min or with a 2.7 mM solution of OA in chlorobenzene for 12 h [23, 24]. After chemical modification, the samples were annealed at 100 °C in air. Both chemical reactions should lead to hole injection into the CNTs and will preferentially affect defects in the sidewalls of the CNTs. In addition, the conditions must be optimized so that no additional structural defects are introduced.

Two-point probe measurements of a large number of devices confirmed a statistical increase in the conductance of CNTs after chemical doping with either BDF or OA. As shown in Figure 1.9, more than 70% of the devices showed higher conductance after chemical doping than before. The conductance was found to improve by up to 20% on that of the initial state. The decrease in the conductance in some cases (less than 10% for BDF doping) is attributed to a destructive reaction with the outer shells [21]. As a result of the large diameter of the CNTs, and the corresponding separation of the states, there is no significant difference between metallic and semiconducting CNTs at room temperature. Thus, by optimization of the doping conditions it will be possible to reduce the amount of destruction. The reaction should preferentially lead to chemical adsorption and not to the formation of covalent bonds.

The highest conductivity was obtained for individual MWCNTs treated with OA, where about 20% of the tubes showed conductivity above the quantum

conductance limit ($G = 4e^2/h$) and a minimum resistance of about 3 kΩ. Finally, four-point probe measurements showed an average conduction increase of about 10%, which confirms the above results after consideration of the scattering effects and the smaller number of samples. The temperature stability has not been studied in detail, but seems to be limited to below 200 °C.

In conclusion, a chemical modification increases the conductivity of MWCNTs. The conductivity of an individual CNT can be more than twice as high as the quantum limit, indicating a shift of E_F and, thus, the activation of additional electronic states. The doping of the inner shells cannot be achieved with that method and intercalation approaches needs to be considered. However, the presented methods and results indicate a first approach to overcome the fundamental limitation of the conductivity of CNTs.

1.3 Carbon Nanotube Interconnects

The resistivity of various chip interconnects, with cross-sectional dimensions of the order of the mean free path of electrons (~40 nm in Cu at room temperature) in current and imminent technologies, is increasing rapidly under the combined effects of enhanced grain boundary scattering, surface scattering and the presence of a highly resistive diffusion barrier layers. The resistivity increases further at higher temperatures (metal interconnect temperatures are above the typical device operating temperature of ~100 °C) due to temperature-dependent bulk resistivity and electron mean free path [25].

The rising Cu resistivity also leads to a significant rise in the metal temperature due to self-heating. This rise in the metal temperature is further exacerbated by decreasing thermal conductivity of low-*k* dielectrics and increasing current density (J) demands from interconnects. Since the electromigration lifetime of metal interconnects depends quadratically on J and exponentially on the metal temperature, all these trends of interconnect scaling lead to a growing threat to the reliability of future interconnects and severely limits their current-carrying capacity to below the requirements. While interconnect delay has always been a major concern, these reliability issues have become the driving force behind the search for alternative interconnect materials [25]. Carbon nanotubes, with their many attractive properties, are emerging as frontrunners in this search if their large-scale integration can be shown. In the following, the current status and possible applications will be discussed.

1.3.1 Fabrication and Integration Challenges for Carbon Nanotube Interconnects

The current state of the art of on-chip integration of CNTs focuses on the substitution of vertical interconnects (vias) for two reasons. First, vias carry the highest current densities and are prone to failure, hence the use of more reliable materials

such as CNTs would be a distinct advantage. Second, there is no convincing approach yet for growing dense CNT bundles of varying length parallel to the chip surface in two perpendicular directions. The only demonstration of CNT bundle growth in a horizontal direction (parallel to the silicon wafer surface) uses the fact that CNT bundles always tend to grow perpendicular to a surface [26, 27]. However, it requires challenging catalyst deposition techniques and various growth steps to provide a two-dimensional mesh of CNT bundles and therefore, it has not yet been accomplished. Horizontal alignment in two dimensions up to millimeters length has been achieved for small SWCNT bundles and single SWCNTs [28, 29]. The orientation of nanotubes is directly controlled by the direction of gas flow in the CVD system. The substrate needs to be rotated to acquire a different orientation of the CNTs. Other approaches such as electric field-induced alignment [30] or fluidic methods are not suited for large-scale integration [31].

The only viable solution for large-scale integration of CNTs seems to be to grow them directly in the place of use on the chip by CVD methods. This imposes the challenge of implementing a microelectronic-compatible manufacturing approach that guarantees an array of dense catalyst particles capable of growing a dense bundle of CNTs.

Achieving a good contact resistance in addition to a fertile catalyst is a non-trivial task because at the high temperatures required for CNT growth the catalyst particles tend to alloy with the underlying substrate to form a catalyst component which does not facilitate CNT growth, or the particles agglomerate to large particles by a high surface mobility at a given material combination. The problem has been solved in most cases by the introduction of a thin oxide layer below the catalyst particle. The oxide forms also in most metal substrates (Ta, Ti, TaN, TiN, Ni, Cu) unintentionally by oxidation of the surface under ambient conditions or by residual water contamination in the CVD chamber. The oxide layer in turn is responsible for bad contact resistance because the charge carriers have to tunnel through the insulating layer. Fortunately, both the oxide layer growth and the mobility of the catalyst on the oxide become lower at lower temperatures. By tailoring the amount and size of catalyst in combination with a suitable material combination, the temperature for CNT growth can be brought down to microelectronic-compatible temperatures of 400–600 °C. Another aspect influencing the contact resistance arises from the interaction of hydrocarbon gases with the substrate material. Depending on the temperatures and gases, considerable formation of carbide on the substrate may occur, which leads to degradation of the resistivity of the underlying contact material. A decrease in the process temperature is also beneficial for lower carbide formation.

Until recently, it was not possible to grow dense bundles of SWCNTs and all of the work has focused on the implementation of MWCNTs which can also guarantee a metallic behavior.

Currently, two different approaches to integrate CNTs have been investigated by four groups. Li et al. [32] proposed a so-called bottom-up approach, shown in Figure 1.10a. Here, the CNT via is grown on the metal layer 1 before the deposition of the inter-metal dielectric (IMD). Lithographically defined nickel spots act

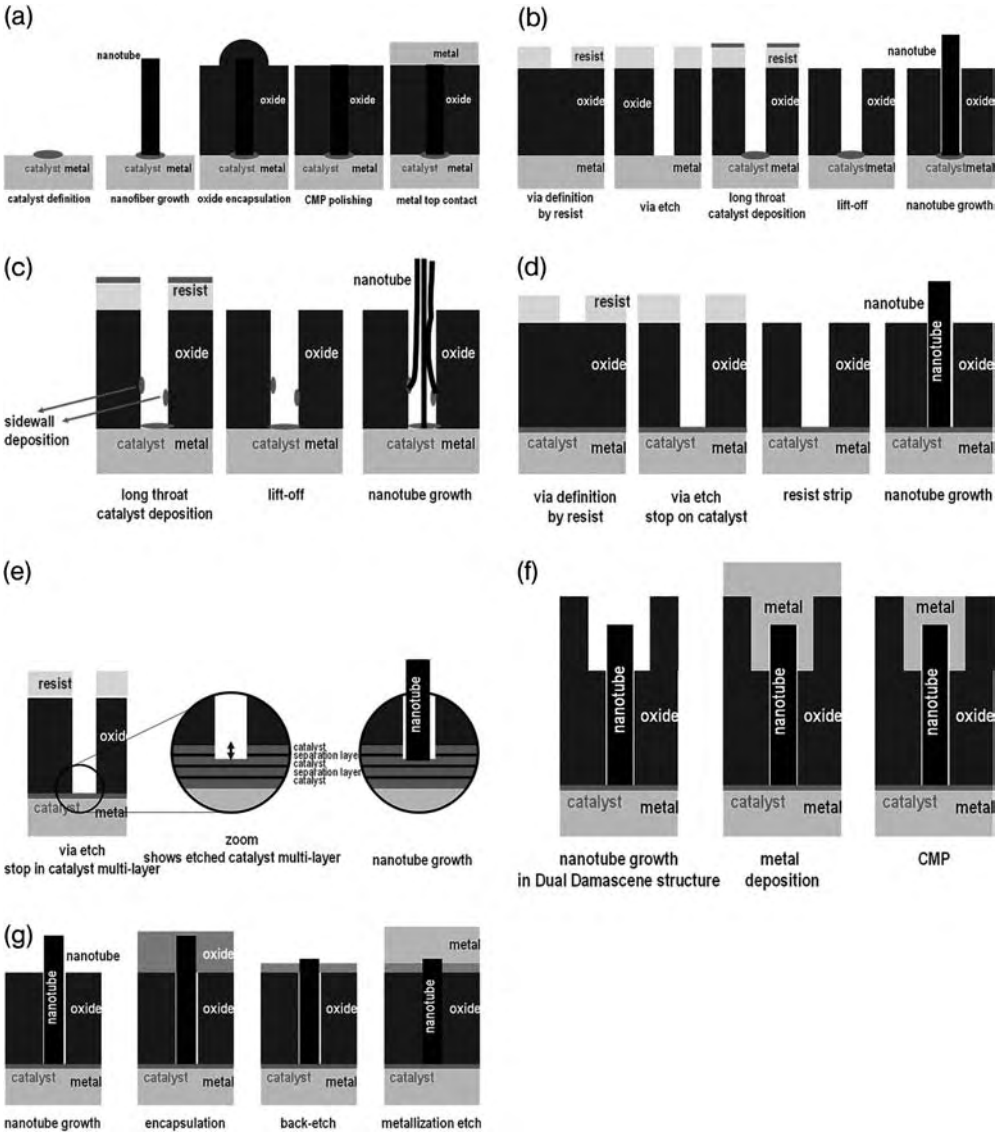

Figure 1.10 (a) Schematic of process sequence for bottom-up fabrication of CNT bundle vias [32]. (b) Schematic of process sequence for via first integration with catalyst deposition after via formation and lift-off process. (c) Problems of the lift-off approach due to sidewall deposition of the catalyst. (d) Schematic of process sequence for the buried catalyst approach. (e) The buried catalyst may consist of a multilayer to increase the yield [33]. (f) Top metallization can be employed by a conventional dual-damascene approach or with (g) conventional subtractive etching of the metallization.

as catalyst particles, from where carbon fibers are grown. As a prerequisite, the fibers need to be aligned perpendicular to the surface. This is achieved by PECVD and an applied bias voltage, which aligns the fibers almost perpendicular to the wafer. Subsequently, SiO_2 is deposited and the wafer is planarized with chemical wafer polishing (CMP). The last step also opens the nanotube ends for contacts with metal layer 2. A high resistance of ~300 kΩ per CNT interconnect has been evaluated for that approach, which may be attributed to the imperfect structure of PECVD-grown MWCNTs [34]. The approach is especially suited for single MWCNT fillings because high-density growth cannot be demonstrated. Another drawback of this approach is that the fibers do not always grow at the selected location and are sometimes shifted and tilted from the projected locations. This makes lithographic overlay at minimum pitch size for further processing a nightmare. Therefore, the more conventional approach of etching the vias down to metal layer 1 and growing the CNTs in these vias has been pursued by semiconductor companies and first results have been presented by Kreupl et al. (Infineon) [35], Nihei et al. (Fujitsu) [36] and Choi et al. (Samsung) [37]. Figure 1.10 gives an overview of the different approaches that have been realized so far.

The straightforward method shown in Figure 1.10b deposits a thin catalyst layer by physical vapor deposition or related methods into the etched via. The catalyst on top of the resist needs to be removed carefully by a lift-off process from the chip surface so that only the catalyst in the vias remains. The lift-off process is not favored in semiconductor manufacturing because it creates a lot of particles which, in turn, are considered to be yield detractors. Another disadvantage for this approach is sketched in Figure 1.10c. Sidewall deposition of the catalyst occurs and leads to CNT growth from the sidewalls. These CNTs are not directly connected to the lower electrode and do not contribute proportionally to the conductivity of the CNT-filled via. The influence of these sidewall CNTs is strongest in high aspect ratio holes and almost negligible in low aspect ratio vias. Furthermore, shadowing of the sidewall in high aspect ratio holes reduces the amount of catalyst material which reaches the bottom. The main advantage of this approach is that there are fewer process steps after the catalyst deposition and this reduces degradation of the catalyst. In Figure 1.11, one of the first realized CNT vias is shown where a $4 \times 4\,\mu m$ wide via with Ta bottom electrode has been filled with CNTs. A lift-off approach together with an iron-based catalyst has been used to enable CNT growth [35].

A buried catalyst approach has been developed in order to omit the lift-off process. Figure 1.10d shows the basic schematics of the buried catalyst approach. The catalyst layer is deposited on top of the lower bottom electrode and embedded in the inter-metal dielectric. After lithographic definition of the vias in the resist, a fluorine-based dry etch process etches the oxide and stops on the catalyst layer. The etching process impairs the fertility of the catalyst layer due to polymer residues and implanted ions from the etch chemistry. Preconditioning steps and cleaning methods have to be applied to allow successful CNT growth. The etch stop on the 1–5 nm thin catalyst is challenging. Nihei et al. used a buried catalyst approach, where the dry etching of the vias has to stop on the thin Ni or Co catalyst

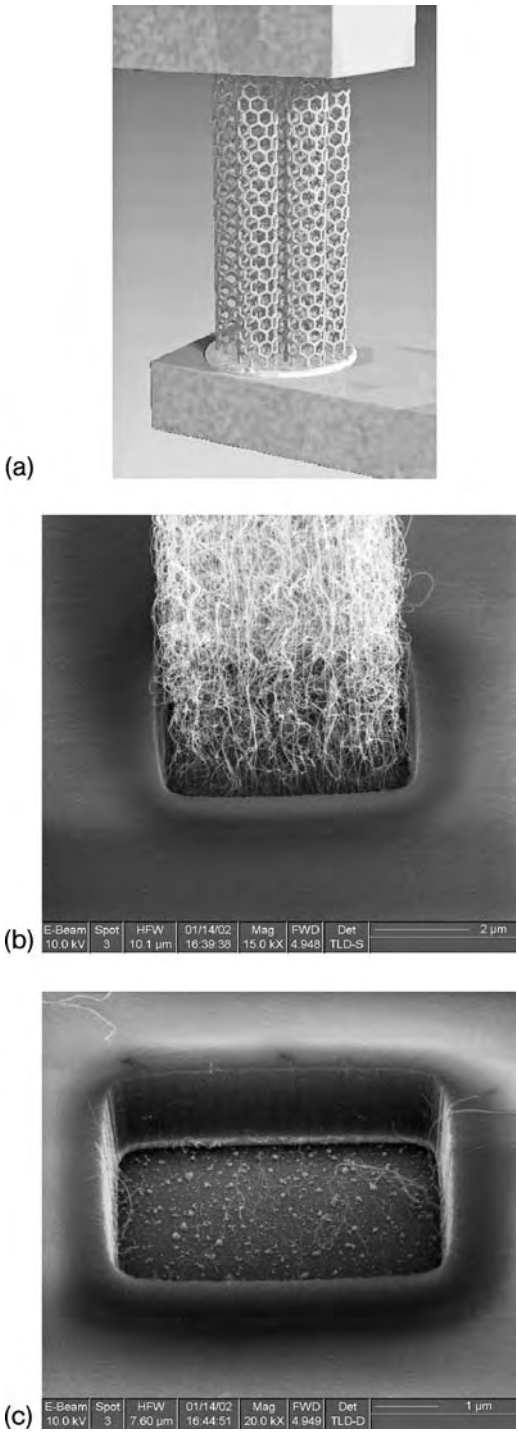

Figure 1.11 (a) Schematic view of a CNT interconnect. (b) One of the first CNT via interconnects before top electrode contacts are deposited. (c) Via with removed CNTs. Some catalyst particles can still be seen on the Ta bottom plate.

layer [36]. Arrays of MWCNTs have been grown in ~2-μm diameter vias by hot-filament CVD (HF-CVD). A resistance of ~134 kΩ per MWCNT has been achieved, a value which again can be attributed to the quality of the tubes grown by HF-CVD. The process has been improved to yield lower resistances [27], but careful interpretation of the data is needed, because the possibility of shorts induced by the top metal electrode deposition exists. Figure 1.10f and g detail how to make various top contacts in a dual-damascene or a conventional subtractive etching approach.

If the CNTs are not encapsulated after growth with oxide or spin-on-glass, the top metal deposition could lead to shorts induced by line-of-sight connections to the bottom contact during sputtering. This would yield a better resistivity because a metal–CNT composite would give a much better value than an oxide–CNT composite. In the work of Kreupl et al. [35], Li et al. [32] and Choi et al. [37], oxide encapsulation was used to ensure that only the contribution of the CNTs is evaluated.

A multilayer buried catalyst approach, as shown in Figure 1.10e, has been developed to increase the CNT growth yield after the via etch [33, 38]. The metal multilayer system includes a high-melting metal layer, a metal separating layer, a catalyst layer and a final metal separating layer. The high-melting metal layer is composed of at least one of tantalum, molybdenum and tungsten. The metal separating layer is composed of aluminum, gold or silver. The catalyst layer is composed of at least one of iron, cobalt, nickel, yttrium, titanium, platinum and palladium or a combination thereof. The final metal separating layer, which is arranged below the inter-metal dielectric (oxide), is composed of aluminum. Each of the layers is around 1 nm thick. With this approach, end-of-the-roadmap-sized CNT interconnects of diameter 20 nm have been fabricated [38]. Figure 1.12 details the results, where a lowest resistance of 8 kΩ has been achieved for a completely integrated carbon nanotube via.

Until recently, it was difficult to grow bundles of SWCNTs for interconnects because the fertility of the catalyst particles for SWCNT growth was low. Although progress has been made recently in growing bundles of SWCNTs by addition of water or oxygen to increase the fertility of the growth catalyst [39, 40], this approach has not yet been applied to the fabrication of interconnects. Moreover, the lack of control of chirality means that it is difficult to ensure that the SWCNTs forming a bundle are all metallic. As mentioned in the Introduction, more than two-thirds of all SWCNTs are semiconducting. Therefore, it will be very challenging to obtain densely packed bundles of metallic SWCNTs. One viable method would probably be to use double-walled CNTs (DWCNTs) as there are indications that the plurality of DWCNTs show metallic behavior with considerable DOS at the Fermi level [41, 42]. The orbital mixing in thin-diameter CNTs by neighboring shells leads to significant interlayer interactions and can cause semiconductor–metal transitions, which in turn can be employed for interconnect applications.

1.3.2
Application Areas for Multi-Walled Carbon Nanotubes

The useful competitive applications of MWCTs in microelectronic applications are determined by their length-dependent resistivity as shown in Figure 1.4b. The

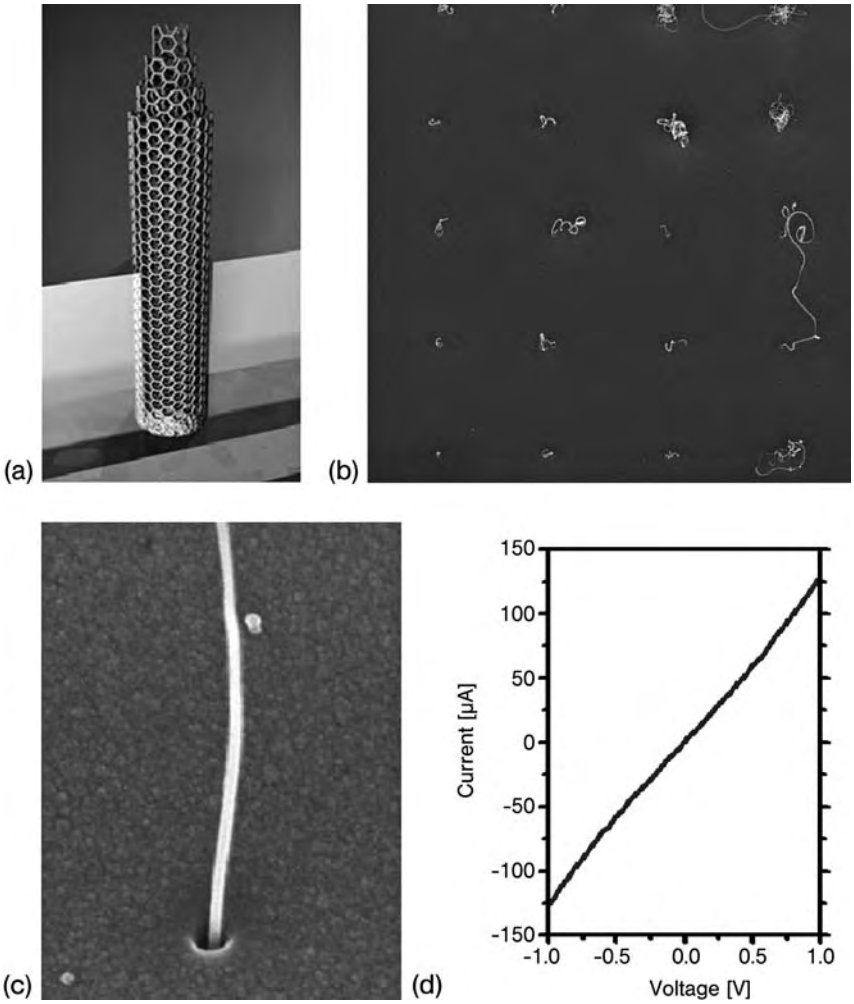

Figure 1.12 (a) Schematic view of the 20-nm diameter CNT interconnect. (b) Array of single MWCNTs protruding from the vias and demonstrating the high yield of the buried catalyst multilayer approach. (c) Single 20-nm diameter MWCNT protruding from a 100-nm deep via. (d) $I(V)$ curve of a 20-nm CNT interconnect having a resistance of 8 kΩ.

competitive range starts at a length of 1–2 μm where MWCNTs already outperform tungsten. These might be applicable in typical high aspect ratio vias and contact holes which are usually filled with polysilicon or tungsten. It is worth noting that MWCNTs can compete with highly doped silicon at length scales below 100 nm as their resistivity is usually in the range 1–5 mΩ cm. However, contact resistances of the MWCNTs to the underlying contact needs to be taken into account. Other applications may include vias in DRAMs where the typical capacitor structure

height is in the region of 8 μm and higher and deep vias needs to be filled for contacting the lower structures. In this case, MWCNTs already approach the values for copper and are therefore more competitive. Longer on-chip interconnects are usually global wires which run in-plane of the chip surface, but this is an area where no CNT technology exists in terms of integration to compete with current copper or aluminum processes.

The high thermal conductivity combined with the mechanical strength make MWCNTs applicable for flip-chip bonding. An impressive example has been given by Iwai et al. [43], who successfully developed thermal and source bumps made of CNTs for flip-chip high-power amplifiers. The developed 15-μm long MWCNT bumps exhibit a thermal conductivity of $1400\,W\,m^{-1}\,K^{-1}$. A flip-chip AlGaN/GaN HEMT amplifier utilizing CNT bumps exhibits an output power of 39 dB at a frequency of 2.1 GHz without any degradation due to heat-up. Furthermore, the MCNT bumps reduced ground inductance and maintained RF gain up to very high frequencies.

To circumvent the high growth temperature and poor adhesion with the substrates Zhu et al. proposed a MWCNT transfer technology enabled by open-ended MWCNTs [44]. The process is featured with separation of MWCNT growth and device assembly. The hollow cavity of MWCNTs will allow the wicking of solders, such as Sn/Pb and Sn/Ag/Cu, due to capillary forces. As a result, interconnects of MWCNTs with metal electrodes by solders are possible and the limited wetting of solders on CNT films is eliminated [45].

In response to environmental legislation, the lead–tin alloys commonly used for soldering of chips will be replaced with lead-free alloys and electrically conductive adhesives. Lead-free alloys usually require higher reflow temperatures than the traditional lead–tin alloys, which can impact the assembly yields. Isotropic conductive adhesives are an alternative to solder reflow processing; however, they require up to 80 wt.% metal filler to achieve minimum electrical resistivity. The high loading content degrades the mechanical properties of the polymer matrix and reduces the reliability and assembly yields compared with soldered assemblies. MWCNTs make it possible to provide electrical conductivity for the polymer matrix while maintaining or even reinforcing the mechanical properties. Replacing the metal particles with carbon nanotubes in compositions has the potential benefits of using a low process temperature, being lead free, corrosion resistant and lightweight and having high electrical conductivity and high mechanical strength. Li and Lumpp recently investigated the properties of conductive adhesives with 50-μm long MWCNTs [46]. Their findings show that MWCNT-filled epoxy retains its shear strength (in contrast to metal-filled epoxy) and can compete with the electrical performance of metal-filled epoxy up to an evaluated frequency of 3 GHz.

1.3.3
Low-*k* Dielectrics with Carbon Nanotubes

Electrically insulating layers are required for many applications in semiconductor technology, in particular when forming integrated circuits in semiconductor

substrates. With ongoing miniaturization in silicon microelectronics, i.e. as the distance between adjacent interconnects decreases, a high coupling capacitance C results in particular if the mutually adjacent surfaces of the interconnects are large, i.e. if the interconnects run parallel to one another over a considerable length in the integrated circuit. By contrast, the coupling capacitance of two lines which cross one another is lower. Problems with coupling capacitances are intensified by the ongoing miniaturization of integrated circuits. As the coupling capacitance increases, the propagation time of a signal in the electrical coupling means becomes ever longer, since this propagation time is determined by the product of resistance R and capacitance C (known as the "RC delay"). On the other hand, the energy uptake for a chip is simply proportional to the capacitances involved and can be reduced considerably if the participating capacitances are diminished.

It is possible to reduce a coupling capacitance if the relative dielectric constant k of the insulating material is reduced. It is therefore attempted to use materials with a low relative dielectric constant (known as "low-k materials") as materials for insulation layers in integrated circuits.

Amorphous silicon dioxide with a relative dielectric constant of approximately 4.0 is often used as dielectric for electrically insulating metallic interconnects from one another. It is possible to reduce further the dielectric constant of a material for an electrically insulating layer if silicon oxide material which additionally contains fluorine, hydrogen or alkyl groups (in particular CH groups) is used for this purpose. This makes it possible to reduce the relative dielectric constant to as little as 2.5. Furthermore, organic materials, in particular polymers or PBO (polybenzoxazole), are used to achieve relative dielectric constants of 2.7. It is also possible for the "low-k materials" used to be materials based on silicon, such as a silicon–oxygen–fluorine compound, a silicon–carbon–oxygen–hydrogen compound, hydrogen silsesquioxane (HSQ) or methyl silsesquioxane (MSQ).

The relative dielectric constant of electrically insulating layers can be reduced further by introducing cavities into the "low-k material". The k value of the porous material is reduced further as a function of the proportion of the volume formed by the cavities or pores.

It can be seen from Figure 1.13a that the higher the proportion of the volume formed by cavities, the greater is the extent to which the k value in a porous material is reduced compared with the k value in a homogeneous material. The dependent relationship between the effective k value and the pore cross-sectional area is shown in a semilogarithmic illustration for different pore shapes and pore geometries in Figure 1.13b. The simulation calculations demonstrate that the effective k value decreases to a greater extent with the pores oriented perpendicular to an electric field than in the case of a parallel orientation between the direction in which the pores run and the electric field vector.

If elongate and oriented pores are used, it is possible to reduce significantly the effective k value without increasing the proportion of the volume which is made up of the pores. With the same proportion of pores by volume, a reduction of 13% is achieved with a pore aspect ratio of 4 : 1 and a reduction of 20% is achieved with a pore aspect ratio of 24 : 1. If the pores are randomly oriented, there is no

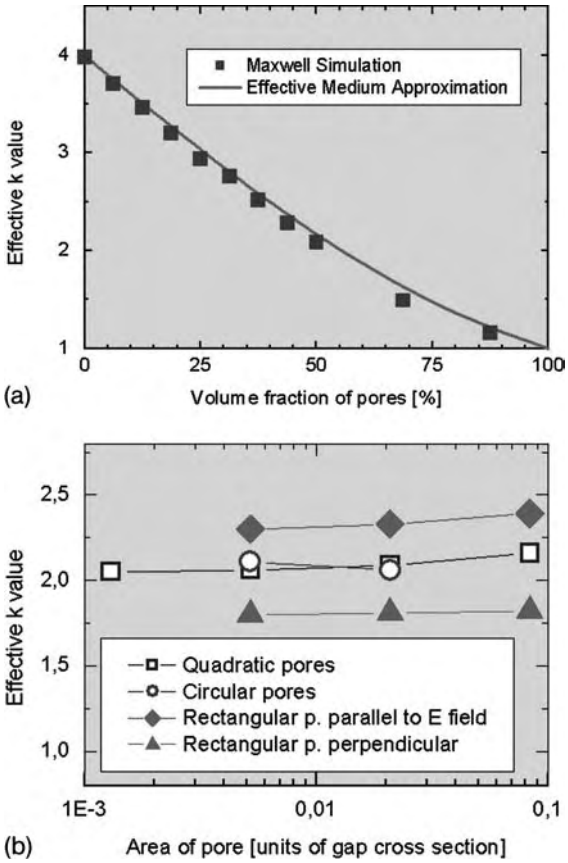

Figure 1.13 (a) Effective *k* value for silicon oxide depending on the volume fraction of the pores [47, 48]. (b) Effective *k* value with volume fraction of 50% in silicon dioxide for different pore sizes and orientations. Pores aligned perpendicular to the electric fields have the lowest effective *k* [47, 48].

advantage over round pores (aspect ratio 1 : 1). In this case, the same mean *k* value is obtained.

Nanotubes can be used to introducing elongate, oriented pores into a dielectric in order to reduce the effective *k* value of a dielectric. As shown in Figure 1.14a, a dense felt of CNTs needs to be grown on the desired surface – preferentially in the tip-growth mode. After infiltration of the CNT felt by silicon dioxide, the top oxide is removed by chemical mechanical polishing (CMP) and/or by a fluorine-based dry-etch process. This gives access to the CNTs again, which are subsequently removed by high-temperature oxidation and/or oxygen or hydrogen plasma. High-rate SiO_2 deposition by PECVD, as shown in Figure 1.14b, is not recommended, because only the outer surface becomes covered and the inner part

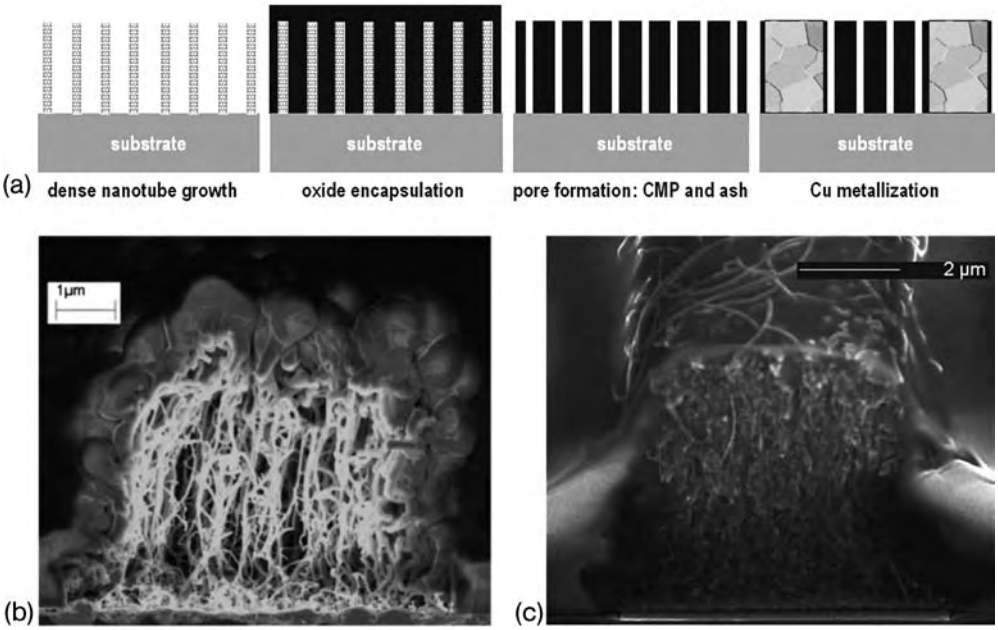

Figure 1.14 (a) Process for longitudinal pore formation with nanotubes as sacrificial structures. The CNTs are burned off with oxygen after encapsulation in oxide. This results in fine pores in the oxide and forms a low-*k* dielectric based on silicon dioxide. The metallization is then embedded in this porous oxide [48]. (b) SEM cross-section of CNT felt covered with SiO_2 deposited by high-rate PECVD deposition. (c) SEM cross-section of CNT felt infiltrated with a spin-on-glass.

is only covered at the initial deposition state. The use of spin-on-glasses (SOGs), as shown in Figure 1.14c, is most useful for achieving complete infiltration of the CNT film. In order to avoid crack formation, a combination of a thin layer of SiO_2 deposited by PECVD and subsequent SOG infiltration seems to work best. The SOG process parameters need to be optimized and the focus in the SOG process should be placed on initial oxide thickness, bake temperatures, cure temperatures and ramp rate.

Fabricating low-*k* dielectrics with CNTs as sacrificial structures is still in its infancy but holds promise to lower considerably the *k* values with aligned pores. Given the recent progress [49] in the density of grown CNTs, which yielded almost 10^{12} CNTs cm^{-2}, the approach may also be suited for advanced feature sizes.

1.3.4
Stretchable and Flexible Interconnects with Carbon Nanotubes

There are numerous potential applications where lightweight, flexible and stretchable conductors are needed. Protective packaging for electromagnetic shielding, transparent conductors for displays and photosensors, elongation and pressure

sensors, electronic textiles and skins and microelectrode arrays for brain and body signal recording would all benefit from flexible and bendable interconnects [50–52]. Normal metal interconnects fracture during deformation of the substrate by a few percent and the recently developed gold– polydimethylsiloxane (PDMS) interconnects [50] withstand unidirectional elongation of 10–15% but fail to be elongated in an arbitrary direction. In contrast, CNT-based stretchable interconnects can be elongated by 100% in an arbitrary direction.

In order to fabricate stretchable CNT interconnects, the desired structure is lithographically defined on a conventional silicon substrate as shown in Figure 1.15a. MWCTs are grown to a height of 50–500 μm perpendicular to the substrate. A liquid prepolymer is poured over the CNT structures and cured for 1 h at 60 °C to obtain a solid, flexible PDMS structure [53]. Subsequently the PDMS is peeled off the substrate, taking the lithographically defined CNT interconnect structure

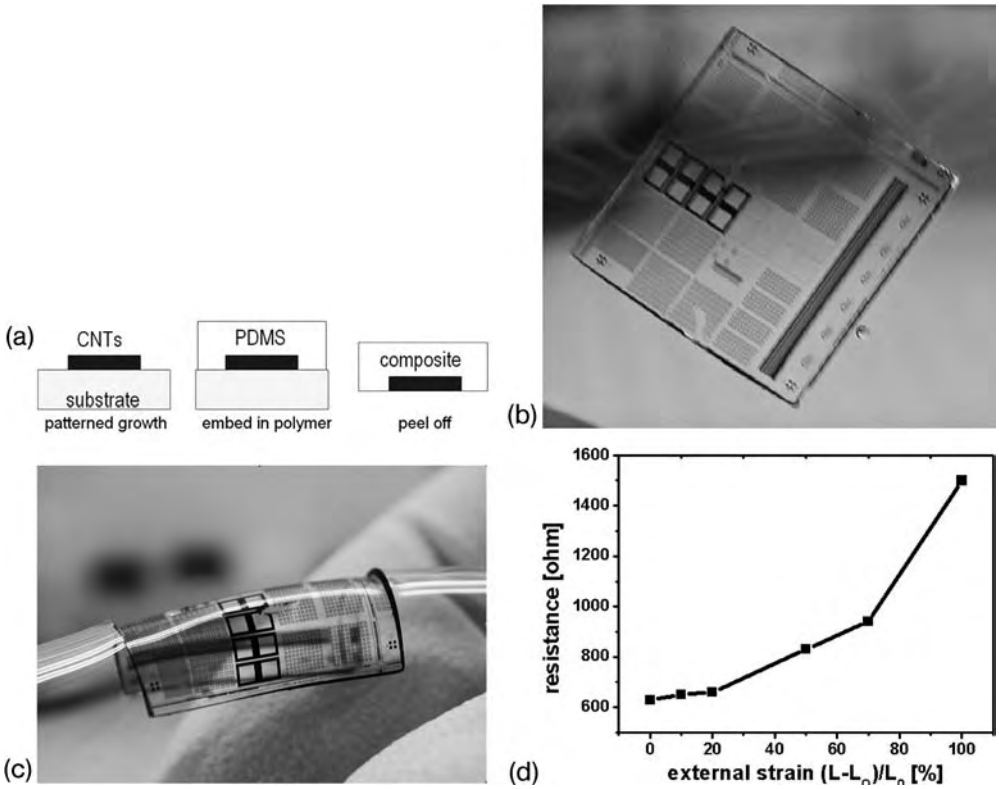

Figure 1.15 (a) Process for fabrication of stretchable integrated circuits with PMDS embedded CNTs. (b) CNT interconnect circuitry embedded in bendable PMDS. The size is roughly 2 × 2 cm (c) Picture demonstrating the flexibility of the created stretchable wiring. (d) Variation of electrical resistance of an embedded CNT stripe with applied tensile strain.

with it, as shown in Figure 1.15b and c. The structure is cured for additional 24 h at 60 °C before further investigations. PDMS is the most widely used silicon-based organic polymer and is particularly known for its elasticity. It is optically clear and is generally considered to be inert, non-toxic and non-flammable. The good wettability of PDMS on CNTs enables the PDMS to infiltrate effectively into the CNT felt and form a relatively defect-free composite film.

The electrical volume resistivity which can be achieved in these samples depends on the area density of the grown CNTs and amounts typically to 1–5 Ω cm. This is a fairly high value compared with ordinary metals (~μΩ cm) but can compete with resistances obtained for stretchable metal interconnects made of metal because the metal film needs to be as thin as 25 nm for this purpose [50]. The elongation-dependent resistance in these CNT composites is shown in Figure 1.15d. Up to an elongation of 20% the resistance increases almost linearly, which has also be confirmed by the results of Jung et al. [53]. Further elongation results in a parabolic increase in the resistance up to a maximum evaluated elongation of 100%. The composite withstands repeated elongation to 100% without major deterioration of its electrical performance. This may be related to the interwoven structure of the CNT felt in combination with the elasticity of PDMS.

The properties of CNT-based flexible interconnect outperform the unidirectional properties of metal-based stretchable interconnects in terms of resistance isotropy of the deformation direction and maximum achievable elongation.

1.4 Carbon Nanotube Devices

Many of the problems that silicon transistor technology is or will be confronted with do not exist for CNT transistors. The strictly one-dimensional transport in CNTs results in a reduced phase space, which allows almost ballistic transport and reduced scattering, especially at reduced gate length and low voltages. The direct band structure of CNTs is completely symmetric for hole and electron transport and allows for symmetrical devices and optically active elements. As there are no dangling bonds in CNTs, the use of high-*k* material as gate dielectrics is simple. In fact, the application of Ta_xO_y, Hf_xO_y and Al_xO_y as gate material has produced superior CNT transistors with low sub-threshold slopes and low hysteresis [54–58]. Both n-type and p-type conduction is possible, enabled by charge transfer doping or different work functions for gate, source or drain. CNTs are created in a "self-assembling" process and not by conventional top-down structuring methods. The scalability has been shown down to an 18-nm channel length recently [59]. CNTs are chemically inert and due to the covalent bonds mechanically very stable. Therefore, they would allow integration even in a high-temperature process. The device performance is considered to be more robust against process-induced fluctuations than their silicon counterpart [60]. Due to the extensive literature available on CNT transistors, the following discussion is focused primarily on some fundamentals and our own work.

1.4.1
Carbon Nanotube Transistors

Transistor devices made of semiconducting SWCNTs can be considered as a simple silicon CMOS field-effect transistors with the silicon material replaced by the carbon nanotube structure. The source and drain contacts in conventional silicon devices are made by highly doped silicon regions, which in turn are contacted by metals to form low-resistance contacts, as shown in Figure 1.16. Contacting a piece of silicon with metals leads to the formation of a Schottky contact and results in a Schottky barrier transistor if the source–drain areas have not been doped. The doping of the source–drain areas makes the Schottky barrier thin enough so that charge carriers can easily tunnel through the barrier and at an interface doping level of ~$2 \times 10^{21}\,cm^{-3}$, a contact resistance of the order of $10^{-7}\,\Omega\,cm^2$ should be achievable. Therefore, a low-resistance contact to a MOSFET-type transistor can be formed with metal contacts if the contact regions are highly doped.

The same approach can be applied to the contact formation of a nanotube transistor. The metal contacts can be formed on highly doped CNT regions, where the doping can also be introduced by electrostatic doping of a nearby gate voltage, or the intrinsically doped nanotube is contacted directly by the metal, as shown in Figure 1.16. In the latter case, a Schottky barrier field effect transistor (SBFET) is formed. The height of the Schottky barrier is basically determined by the differences in the work function of the CNT and the metal contact. Therefore, the Schottky barrier can be considerably reduced and a quasi-MOSFET transport behavior established if the right work function material is chosen. For a typical CNT, the mid-gap work function is 4.5 eV. High work function materials such as Au, Pt and Pd with work function values of around 5.1 eV give almost ohmic contacts to CNTs with a band gap of 0.8–0.6 eV [8]. The use of aluminum contacts leads to n-type transistors because Al has a work-function of ~4.2 eV [8, 57]. Titanium contacts lead to the formation of SBFETs despite the fact that Ti has a work

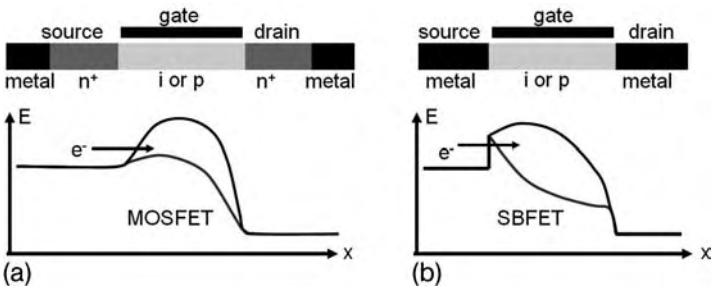

Figure 1.16 Schematic for MOSFET-type (a) and Schottky barrier-type (b) transistor. The energy diagram shows the conduction band in the off-state (black) and in the on-state (gray) of the transistors. Charge carrier conduction is by emission over the barrier for the MOSFET-type transistor. The current flow for the SBFET is controlled by the tunneling current through the Schottky barrier. The schematic is applicable to silicon and carbon nanotube transistors.

function of ~4.3 eV. The interface reaction at the contact leads almost always to the formation of TiC, which has a CNT mid-gap work function of ~4.5 eV. Interface design, cleanness, temperature treatment and the way in which the metal is deposited account for the quality of the contact [57]. Titanium contacts to nanotube transistors lead to ambipolar behavior of the transistor in the gate voltage-dependent conductance. The ambipolar behavior is characterized by hole *and* electron transport in the channel depending on the polarity of the gate voltage. The on/off ratio of the current is severely affected by the ambipolar behavior, which therefore should be avoided in logic devices. Exceptions to this are optoelectronic applications of CNTs where the injection of electrons and holes is mandatory [54] and the intentionally created carbon nanotube Schottky diodes, which are fabricated by contacting one end of a SWCNT by a high work function metal and the other by a low work-function metal.

The formation of the gate stack in CNT devices is of the utmost importance and should be discussed next. The threshold voltage and performance are influenced by the structure and choice of the gate oxide and metal gate. Two implementations of the gate can be envisioned, as indicated in Figure 1.17. The natural and first approach was the bottom-gate or back-gate approach, where an oxidized silicon substrate can be used and the CNT, source and drain contacts are formed on top of it. The whole Si substrate is then acting as a gate electrode. Another approach is the top-gate approach, also shown in Figure 1.17. Here, the nanotubes are covered with the gate dielectric prior the top metal-gate deposition. In the following, it will be shown that a combination of top and bottom gates achieves the best performance.

The capacitance of the gate is a critical issue for future high-performance transistors. A high-*k* dielectric is, therefore, unavoidable since the thickness of a silicon oxide or an oxy-nitride gate dielectric cannot be reduced below a certain value without causing an intolerable increase in the gate leakage by direct tunneling. In

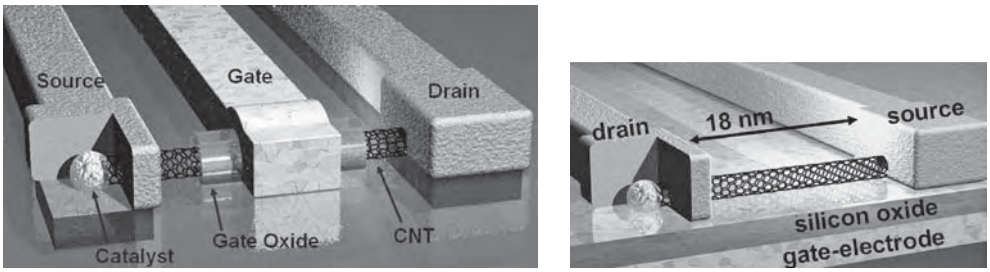

(a) (b)

Figure 1.17 Schematic of two different gate contacts for nanotube transistor. A top-gate is shown on the image in (a), where a gate dielectric needs to be deposited on the CNT before the metal gate is formed. A cross-section through a bottom-gate (back-gate) device where the CNT is grown on top of the silicon oxide and the gate-electrode is depicted on the image in (b).

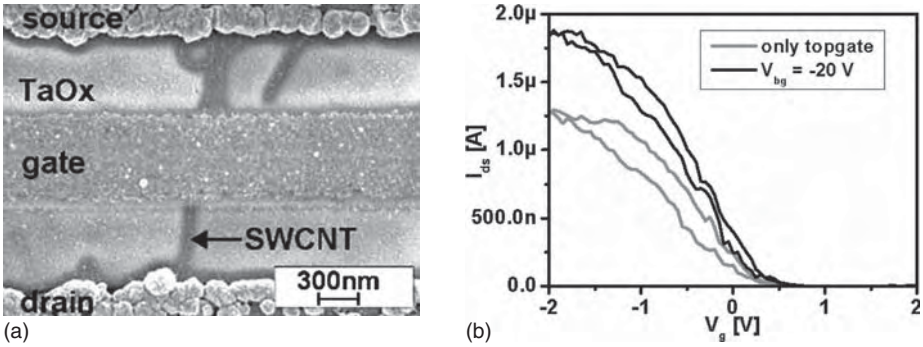

Figure 1.18 (a) SEM image showing a CNTFET with a Ta_xO_y high-*k* dielectric. The tantalum oxide gate dielectric is ~4 nm thick [55]. The gate electrode has been deposited by evaporation of Al and the source–drain contacts improved by electroless Pd deposition. The curves in (b) compare the top-gate measurements with Ta_xO_y dielectric at floating back-gate or with back-gate voltage set to –20 V [55]. The gate-voltage sweep is from +2 to –2 V and back to +2 V and induces some hysteresis due to trapped charges near the nanotube.

addition, encapsulation of nanotubes is necessary in order to protect the dopants from desorption and to allow further integration. Therefore, it is necessary to evaluate different processes and high-*k* materials for the encapsulation of nanotubes. While the application of high-*k* stacks to silicon transistors is still cumbersome due to severe mobility degradation of the Si device, the use of high-*k* dielectrics for CNT transistors is relatively easy. A "poor man's" atomic layer deposition (ALD) process has been developed to deposit high-*k* Ta_xO_y dielectric on the CNT [55]. About 3–5 nm of Ta_xO_y is deposited during each cycle of the dip-coating process. Since no high-temperature anneal was performed, it has to be assumed that instead of Ta_2O_5 a non-stoichiometric Ta_xO_y is obtained.

Figure 1.18 shows an SEM image of CNT transistor with Al top gate, Ta_xO_y dielectric and Pd source/drain contacts. The difference in the on-current, shown in Figure 1.18b, is caused by enhanced transmission through the Schottky barrier. If a negative back gate voltage is applied, the Schottky barriers at the contacts are made more transparent for the tunneling of holes. This reduces the series resistances originating from the Schottky barriers and, therefore, decreases the on-resistances.

The scaling properties of every rival technology to silicon need to be explicitly demonstrated before the new technique can be taken seriously. And although CNT transistors have already shown their superior performance at gate lengths above 100 nm, the key question of how they will perform at very short gates has not been addressed until recently. As the Schottky barriers at the contacts play a major role, as discussed above, their influence on the device scaling might become stronger when both depletion width interact at short gate lengths. Therefore, short channel nanotube transistors with gate length down to 18 nm have been fabricated successfully in a back-gate geometry, such as that shown in Figure 1.17b, with

different source-drain contact materials [59]. The SEM image in Figure 1.19 shows a top view image of an 18-nm channel length nanotube transistor contacted with Pd contacts. The highly doped silicon substrate is acting as a gate electrode and the nanotube resides on a 12-nm thick silicon dioxide gate dielectric as shown in Figure 1.17b. The diameters of the CVD-grown CNTs are in the range 0.7–1.1 nm, yielding reasonable band gaps in the range 0.8–1.3 eV, which, in turn, are able to suppress ambipolar switching. In fact, Figure 1.19b details the drain–source current of the 18-nm transistor with Pd source–drain contacts as the gate voltage is swept from –5 to +5 V.

The device delivers a record 15 μA of current at a mere 0.4 V source–drain voltage and no current saturation can be seen in the logarithmic transfer curve as the gate voltage is increased to more negative values. Apparently, no ambipolar behavior can be seen at positive gate voltages, which is in striking contrast to the logarithmic transfer curve of the device with Ti source–drain contacts, shown in Figure 1.19c.

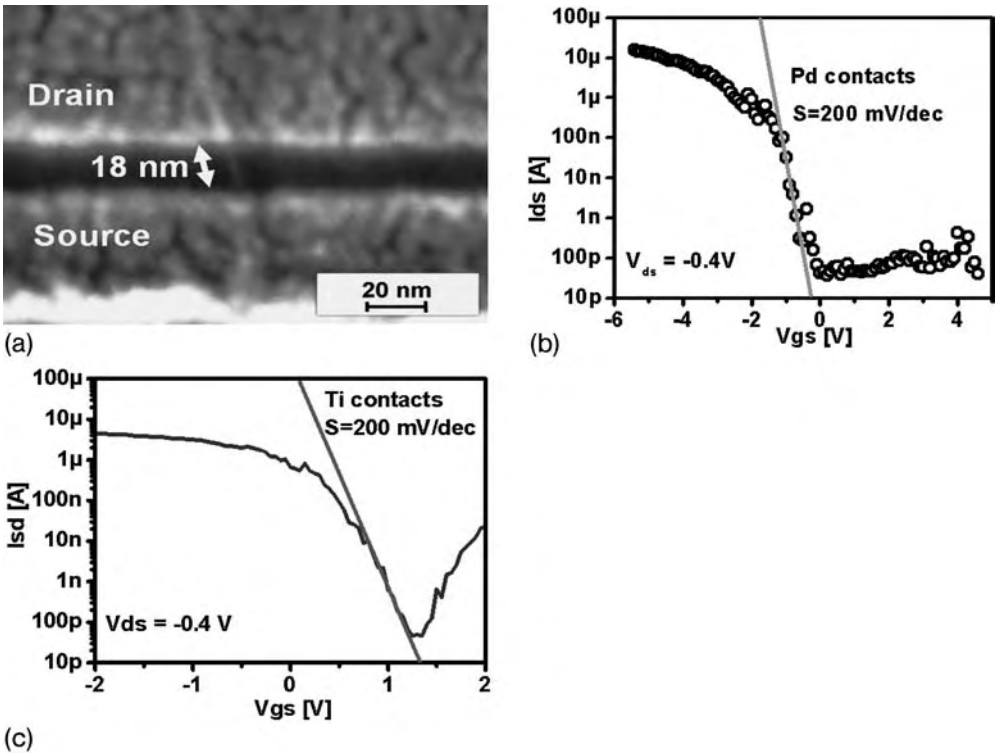

Figure 1.19 (a) SEM image showing the shortest nanotube transistor to date with a channel length of only 18 nm and Pd source–drain contacts [59]. (b) The logarithmic transfer curve of the device with Pd contacts shows no ambipolar behavior and has a record current of 15 μA. (c) The logarithmic transfer curve of a 20-nm gate length device with Ti contacts demonstrates lower on-currents due to the higher Schottky barriers for holes and ambipolar behavior due to lower Schottky barriers for electrons.

Here, a device with a slightly larger gate length of ~20 nm and with Ti drain–source contacts exhibits current saturation at a gate voltage of only 2 V and considerable ambipolar behavior, indicated by the current increase at positive gate voltages. The current amounts only to 5 μA at an applied voltage of 0.4 V – only one-third of the value of the device with Pd contacts. This is due to the different Schottky barriers for holes and electrons induced by the varying work functions of titanium and palladium. It also demonstrates that the threshold voltage of the devices can be shifted by using different metal contacts. The minimum current is achieved at $V_{gate} \approx 0$ V for Pd and at $V_{gate} \approx 1.3$ V for Ti.

The sub-threshold slope S, which is a measure of how many decades of current can be reduced by a change in gate voltage and indicates how fast a device could be switched off, is around 200 mV per decade for both devices. This is almost a factor of three higher than the theoretical limit of ~70 mV per decade. The deviation can be attributed to the "bad" electrostatic design of the device, where the gate electrode is 12 nm away from the channel and the source–drain distance of ~20 nm shields the influence of the gate. In fact, devices from this batch with 360 nm channel length exhibits a sub-threshold slope of around 80 mV per decade, which is close to the ideal value.

The tremendous progress in device performance can only be judged if a thorough benchmark, as suggested by Chau et al. [61], is performed. Although a complete benchmark is out of reach, but has been tackled theoretically [60], one can at least address one important metric of it: the intrinsic speed versus gate length is measured by the CV/I metric and is characteristic for the device speed. For the 18-nm CNT device, the insulator capacitance is 0.4 pF cm^{-1} and the quantum capacitance which accounts for the finite DOS in nanoscale systems [8] is 4 pF cm^{-1}. Given the current of 15 μA at 0.4 V, a device speed ($t = CV/I$) of 18 fs is evaluated for this short-channel CNT device. This value is almost two orders of magnitude lower than what has been achieved with silicon devices ($t \approx 1$ ps) of similar gate length. Calculations of power consumptions for various digital circuits made of scaled nanotube device suggest a similar improvement for the dynamic and static behavior [60].

1.4.2
Carbon Nanotube Diodes

Nanotube diodes can be fabricated as Schottky diodes or as pn-diodes as is the case with silicon. For state-of-the-art Schottky diodes used as detectors at frequencies above a few hundred gigahertz, the parasitic capacitances and the resistances associated with low electron mobilities limit the achievable sensitivity. The performance of such a detector falls off exponentially with frequency roughly above 400 GHz [62]. Moreover, when used as frequency multipliers, state-of-the-art solid-state Schottky diodes exhibit low efficiencies, generally putting out only microwatts of power at frequencies up to 2 THz. The shortcomings of the state-of-the-art solid-state Schottky diodes can be overcome by Schottky diodes based on carbon nanotubes. Because of the narrowness of nanotubes, Schottky diodes based on carbon

nanotubes have ultra-small junction areas and consequently junction capacitances of the order of 10^{-18} F, which translates to cutoff frequencies >5 THz, if several CNTs are paralleled to reduce the serial resistances [62, 63].

For the fabrication of pn-diodes, the nanotubes need to be doped. This can be done electrostatically by gating electrodes [64] or by charge transfer doping [65]. In classical devices, the dopants are impurity atoms in the bulk of the semiconductor. However, doping can also be achieved by an electron exchange between the semiconductor and dopants situated at its surface. For instance, the surface dopants have unoccupied molecular orbitals for electrons. If the energetically lowest of these orbitals is close to the valence band maximum of the semiconductor, an electron from the semiconductor can occupy this orbital. As a result, holes will form in the semiconductor and negative charge will be localized on the surface acceptors [66]. This happens for the usually p-doped nanotubes by oxygen absorption. UV irradiation of the CNT in an ultra-high vacuum environment results in desorption of water and oxygen and reveals mid-gap doped device properties. The absence of substitutional doping in nanotubes leads to reduced scattering rates and higher currents. Successful n-type doping has been achieved with functionalization of the SWCNTs with amine-rich polymers [65]. Figure 1.20 shows the completely altered characteristics of an SWNT transistor after doping with

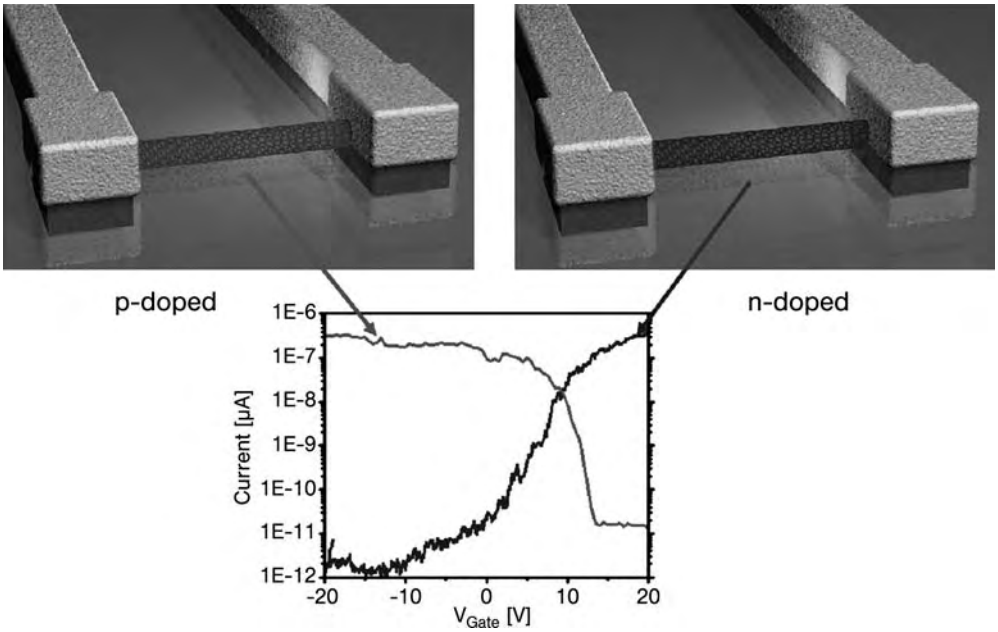

Figure 1.20 Both p- and n-doping of the same SWCNT device. The light gray curve is the current response of a p-doped device. After polymer amine doping the same device has an equally high on-current as the p-doped device indicating no additional charge scattering induced by this doping method.

polyethylenimine (PEI). The device was submerged in a 20 wt.% solution of PEI (average molecular weight 500 Da) in methanol for various times. Subsequently, the sample was rinsed with methanol and 2-propanol to remove non-specifically adsorbed PEI on the sample, leaving approximately a monolayer of PEI adsorbed on the device. A 1-min anneal at 50 °C evaporated the remaining solvent. Prior to PEI adsorption, the semiconducting SWNT exhibits p-type FET characteristics revealed by the decreasing current as a gate voltage is stepped to more positive values. The p-type behavior is due to adsorbed O_2 from the ambient. After PEI adsorption, the SWNT exhibits clear n-type FET characteristics. The current of the device increases when V_{gate} is stepped to more positive values (Figure 1.20). The current of the device is completely undisturbed, remaining at around 400 nA at 0.1 V source–drain voltage after n-doping. This is indicative of the low number of scattering centers introduced in the device by this doping scheme.

A nanotube pn-diode can be fabricated with this doping scheme by exposing only one half of a nanotube transistor channel to the polymer amine and leaving the other half p-doped, as shown in Figure 1.21. This is achieved by covering the CNT device with PMMA resist and exposing only a small area of the channel to

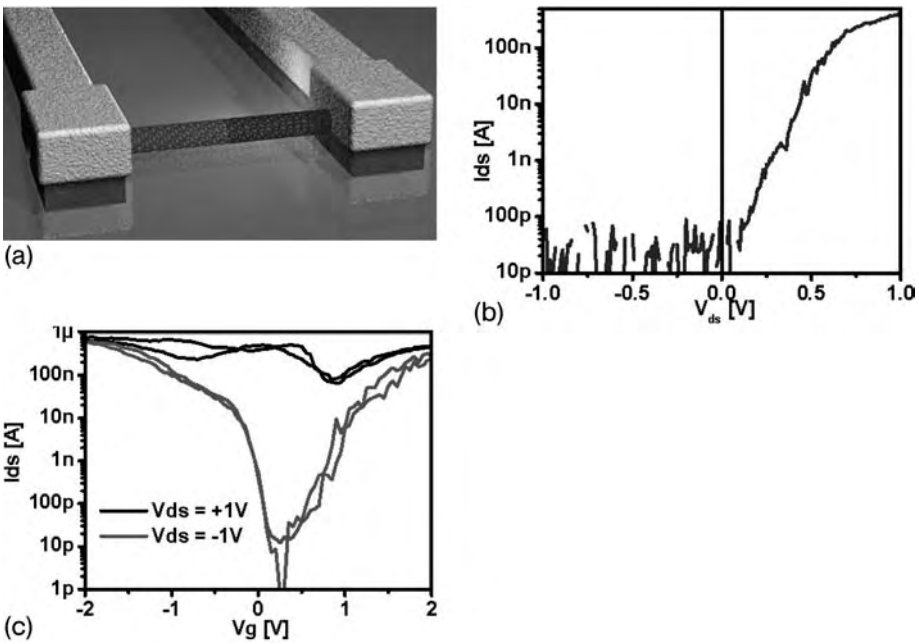

Figure 1.21 (a) Fabrication of a nanotube pn-diode by doping only half of a p-doped nanotube with polymer amine. (b) Diode characteristic of Pd-contacted ~1 μm long nanotube with one half of the channel being n-doped. (c) The gate voltage dependency of the nanotube pn-diode for forward and reverse-biased diode. A low hysteretic behavior can be observed during the gate voltage sweep.

the electron beam. After dissolution of the exposed PMMA area the device is locally n-doped with PEI. The diode-like current voltage characteristic is shown in Figure 1.21b. The off-current cannot be determined exactly and is limited by the measurement setup. However, an extrapolation from the positive exponential behavior would yield a value of ~2 pA. The forward current grows exponentially and is limited by the overall serial resistance of ~1 MΩ. If one applies the ordinary diode equation for the exponential forward current an ideality factor of the diode of $n \approx 2.1$ can be fitted to the curve. The device behaves like a gated diode if operated with the Si substrate as gate (Figure 1.21c). There is only a current modulation of one order of magnitude, if the diode is biased in the forward direction. The influence of the gate voltage is more pronounced in the reverse direction where the blocking behavior can be completely lifted by the application of a positive or negative gate voltage. The gated diode leads to new applications as it is able to detect and amplify small signals and sense amplifier circuits make use of the gated-diode unique property that allows precise distinction of small signals of low and high levels and the nonlinear boosting of only one of them [67].

1.4.3
Carbon Nanotube Power Transistors

Power switches are ubiquitous in use and need high blocking voltages and very low on-resistances. CNTs could even improve these power devices due to the following key advantages.

First, the nanotube acts as a current limiter, because the current in one single-walled CNT is limited to ~25 μA for CNT lengths exceeding 200 nm due to optical phonon emission [8]. This is in contrast to most silicon devices where overload leads to heating up and the avalanche effect, which destroy the device. Second, the specific resistivity of a long SWCNT is roughly one-tenth of that of copper wire, which means that one can in principle construct a power device with an on-resistance similar to a copper wire. The length of the nanotube should be proportional to the required operation voltage to guarantee proper operation and avoid impact ionization. A typical scaling factor would be ~200 nm V^{-1} and that includes already a safety margin for over-voltage protection. For normal Si-based devices the on-resistance is orders of magnitude higher and scales roughly with a power law of the form $V^{2.5}$ for the required blocking voltage. Third, the sustained current densities in CNTs are orders of magnitudes higher than in silicon or even copper. Therefore, CNTs would allow very compact low-loss power switches if thousands and millions could be paralleled to deliver an overall current up to some kA. Figure 1.22 gives an example of a vertical CNT power transistor and compares the obtainable values for on-resistance and maximum operating current densities with those of silicon. The on-resistance is already one order of magnitude better at a CNT density of only 100 μm^{-2}. The values in Figure 1.22b are calculated for two different CNT resistances. A 25 μm long CNT would have an on-resistance of ~200 kΩ and could sustain an operating voltage of 125 V. A 62 μm long CNT could be operated at 300 V and would have an on-resistance of ~500 kΩ. The current density

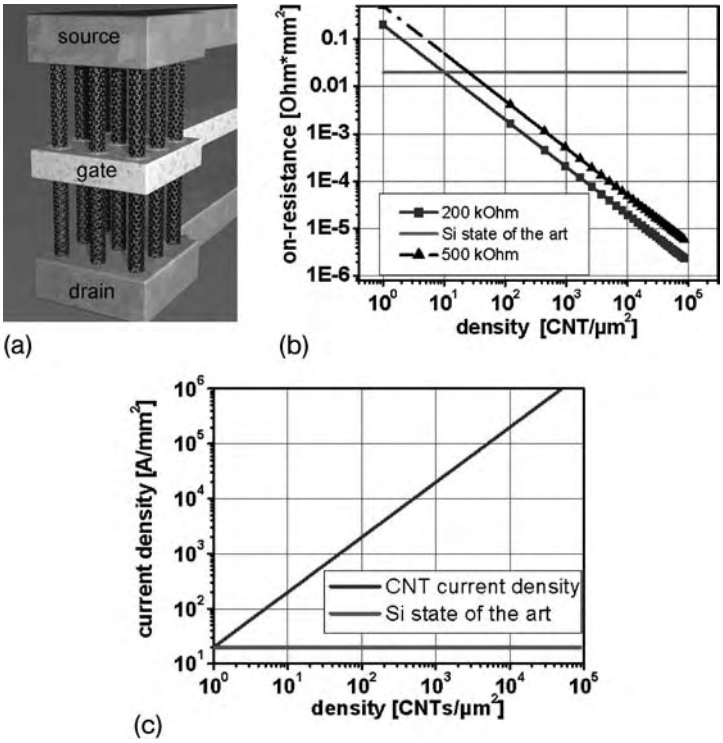

Figure 1.22 (a) Proposed vertical CNT power transistor, where many CNTs are paralleled. (b) The on-resistance of a CNT power transistor is plotted against the varying density of CNTs for two different resistances of the CNTs and compared with the silicon limit. (c) The maximum current density for varying CNT densities is compared to the silicon limit.

dependence in Figure 1.22c is calculated with a maximum current density of 20 µA for one CNT and gives the upper limit for the current. A low resistance design approach would restrict the current per nanotube to below 5 µA to ensure the operation in the linear current voltage regime.

From integration point of view, there would be the advantage that no precise control of the CNT arrangement on the nanometer scale would be required for a power switch that uses millions of paralleled CNTs. However, all metallic and small band gap CNTs need to be removed by either selective burning or functionalization.

The fabrication of a power switch which uses vertical SWCNTs, as shown in Figure 1.22a, is very challenging. Therefore, a planar prototype with horizontally aligned SWCNTs has been fabricated to support this idea [68]. The prototype with ~300 CNTs in parallel was able to deliver up to 2.4 mA at 1 V. The device, sketched in Figure 1.23, had enough power to operate small motors and LEDs. It consists of a metallic back gate layer covered with a thin layer of high dielectric constant

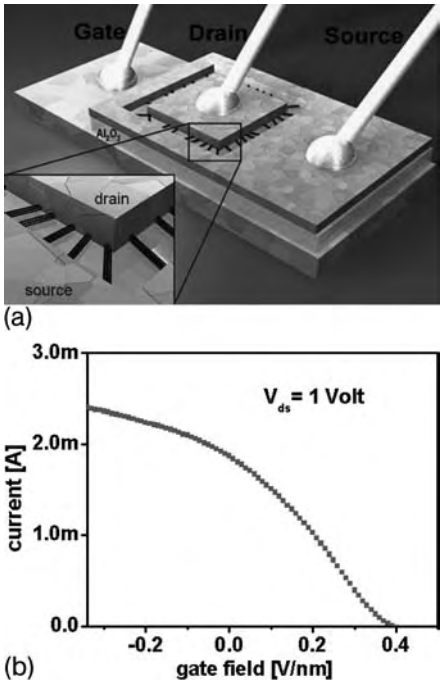

Figure 1.23 (a) Schematic of the first nanotube power transistor with 300 nanotubes operating in parallel. (b) The plot of the device current versus gate field demonstrates a current drive of 2.4 mA at 1 V source–drain bias voltage [68].

material on which a sparse layer of small diameter SWCNTs was grown. The palladium source and drain regions were defined on the SWCNT layer using electron beam lithography, metal deposition and lift-off. These transistors initially display an on/off ratio of about 3 due to the parallel connection of metallic and small band gap SWCNTs together with the semiconducting nanotubes. As progressively higher burn pulses are applied at high positive gate voltage, which turns the semiconducting CNTs off, first the metallic and then the small band gap SWCNTs are eliminated. The semiconducting tubes remain unaffected since they are switched off by the positive gate voltage. Using this method, on/off current ratios of over 1000 could be achieved. Despite the relatively modest performance of this transistor, it demonstrates that high current devices can be created by the parallel connection of many SWCNTs.

In order to investigate the possible performance of horizontally aligned nanotube power switches, an interdigital structure, as shown in Figure 1.24, can be considered. Here, the surface of a substrate is covered with aligned nanotubes and an interdigital metal contact structure is formed on the nanotubes for source and drain contacts. In this example, a distance of 1 μm is assumed, which translates to an operating voltage of 5 V. The achievable current densities (b) and on-resistances (c) are plotted in Figure 1.24 for various CNT packing densities. For a reasonable 3 μA per CNT and a packing density of 50 CNTs per micrometer, the

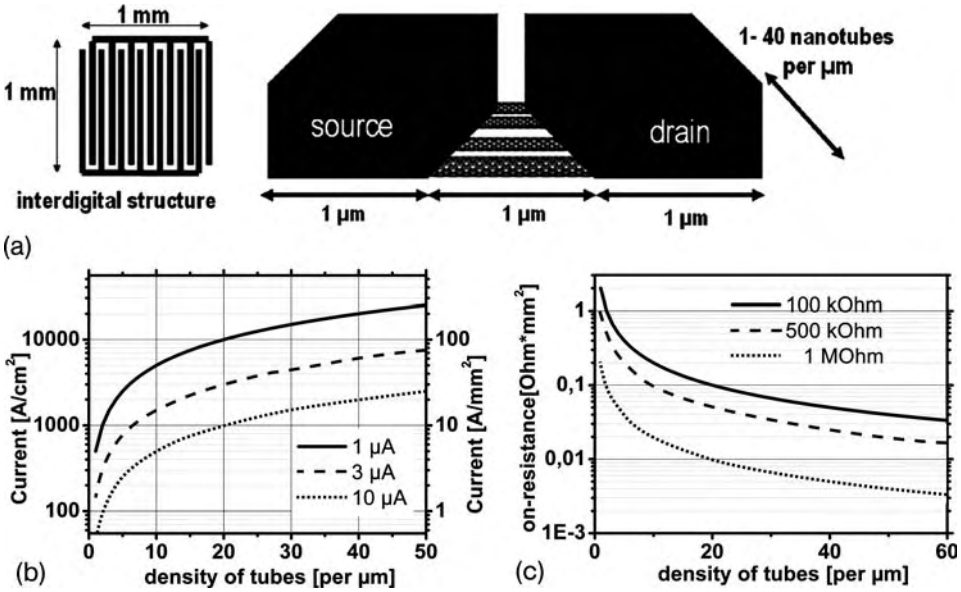

Figure 1.24 (a) Schematic of an interdigital source–drain structure for a high current switch. (b) Current density versus CNT density for the interdigital contacts at three different current levels. (c) On-resistance for varying CNT densities and three individual CNT resistances.

device can deliver 8 kA cm^{-2} at an on-resistance of only 3 mΩ mm^2. However, these optimistic values can only be obtained with challenging progress in the aligned fabrication of small-diameter semiconducting nanotubes.

1.5 Conclusions

The promising properties of carbon nanotubes have sparked a huge world-wide activity to investigate these objects in many technical areas – not only in microelectronic applications. Implementations, which rely on the statistical averaging of material properties, i.e. CNTs as additives in plastics, polymers and epoxies or as transparent conductive coatings, are closer to or already in the market. For microelectronic applications, the attractiveness has been already verified experimentally on the laboratory scale; however, a detailed strategy for large-scale integration of carbon nanotubes is still lacking. Integrated CNTs have to fulfill a whole range of requirements simultaneously – the most stringent demand being the precise placement of only one kind of CNT. The placement might be solved by localized growth of CNTs in vertical structures and the yield of semiconducting CNTs increased by special growth methods which favor the occurrence of only semiconducting CNTs. However, up to now, no-one has devised a CNT device which incorporates all needs for a scalable, reliable switch. Meanwhile, CNTs are

facing severe competition from nanowire technology [69], which benefits from clearly defined semiconducting properties of the nanowires and the lower processing temperature. However, the performance of nanotube-based devices still outperforms every other existing technology [69]. And if one looks back and recognizes the tremendous progress which has been achieved in nanotube technology during the past decade, one is certainly looking forward to what the future might bring.

1.6 Acknowledgments

The results discussed in this chapter were achieved in Infineon's research department together with the colleagues Georg S. Duesberg, Andrew P. Graham, Maik Liebau, Robert Seidel, Werner Steinhögl and Eugen Unger and diploma students Ronan Martin, Anita Neumann and Bijoy Rajasekahran and with continuous support from Wolfgang Hönlein. Werner Pamler contributed with artwork and Zvonimir Gabric with expert technical assistance. Part of the work was supported by the German Federal Ministry of Education and Research (BMBF) under contract No. 13N8402.

References

1 M. G. Banks, An extension of the Hirsch Index: indexing scientific topics and compounds, physics/0604216; http://arxiv.org/abs/physics/papernum=0604216.

2 E. Artacho, D. Sánchez-Portal, P. Ordejón, A. García, J. M. Soler, Linear-scaling ab-initio calculations for large and complex systems, *Physica Status Solidi B* **215** (1999) 809–817.

3 A. P. Graham, G. S. Duesberg, W. Hoenlein, M. Liebau, R. Martin, F. Kreupl, R. Seidel, E. Unger, W. Pamler, How do carbon nanotubes fit into the semiconductor roadmap? *Appl. Phys. A* **80** (2005) 1141.

4 J. Robertson, Growth of nanotubes for electronics, *Mater. Today* **10** (*1–2*) (2007) 36–43.

5 *Gmelin Handbook of Inorganic and Organometallic Chemistry*, 8th edn. Element C: Carbon (System Nr. 14), eds. E. Best, R. J. Meyer, F. Peters, L. Gmelin, E. H. E. Pietsch, M. Becke-Goehring, Springer-Verlag, Berlin, 1968.

6 K. S. Novoselov, A. K. Geim, S. V. Morozov, D. Jiang, Y. Zhang, S. V. Dubonos, I. V. Grigorieva, A. A. Firsov, Electric field effect in atomically thin carbon films, *Science* **306** (2004) 666.

7 F. Kreupl, Field effect transistor and method for producing a field effect transistor, *US Patent 6 809 379* (2000).

8 M. P. Anantram, F. Léonard, Physics of carbon nanotube electronic devices, *Rep. Prog. Phys.* **69** (2006) 507–561.

9 A. C. Dupuis, The catalyst in the CCVD of carbon nanotubes – a review, *Prog. Mater. Sci.* **50** (2005) 929–961.

10 R. Seidel, G. S. Duesberg, E. Unger, A. P. Graham, M. Liebau, F. Kreupl, Chemical vapor deposition growth of single-walled carbon nanotubes at 600 degrees C and a simple growth model, *J. Phys. Chem. B* **108** (2004) 1888–1893.

11 J. W. Mintmire, C. T. White, Universal density of states for carbon nanotubes, *Phys. Rev. Lett.* **81** (1998) 2506–2509.

12 Online simulation and more, http://www.nanohub.org.

13 A. Naeemi, J. D. Meindl, Compact physical models for multiwall carbon-nanotube interconnects, *IEEE Electron Device Lett.* **27** (2006) 338–340.

14 J. Jiang, J. Dong, H. T. Yang, D. Y. Xing, Universal expression for localization length in metallic carbon nanotubes, *Phys. Rev. B* **64** (2001) 045409.

15 H. J. Li, W. G. Lu, J. J. Li, X. D. Bai, C. Z. Gu, Multichannel ballistic transport in multiwall carbon nanotubes, *Phys. Rev. Lett.* **95** (2005) 86601.

16 J. de Pablo, E. Graugnard, B. Walsh, R.P. Andres, S. Datta, R. Reifenberger, A simple, reliable technique for making electrical contact to multiwalled carbon nanotubes, *Appl. Phys. Lett.* **74** (1999) 323–325.

17 B. Bourlon, C. Miko, L. Forró, D. C. Glattli, A. Bachtold, Beyond the linearity of current–voltage characteristics in multiwalled carbon nanotubes, *Semicond. Sci. Technol.* **21** (2006) S33–S37.

18 A. Neumann, Chemical optimization of carbon nanotubes for electronic devices, *Diploma Thesis*, Technical University of Ilmenau, 2005.

19 M. Liebau, E. Unger, G. S. Duesberg, A. P. Graham, R. Seidel, F. Kreupl, W. Hoenlein, Contact improvement of carbon nanotubes via electroless nickel deposition, *Appl. Phys. A* **77** (2003) 731–734.

20 R. Seidel, M. Liebau, G. S. Duesberg, F. Kreupl, E. Unger, A. P. Graham, W. Hoenlein, W. Pompe, *In-situ* contacted single-walled carbon nanotubes and contact improvement by electroless deposition, *Nano Lett.* **3** (2003) 965–968.

21 M. S. Strano, C. A. Dyke, M. L. Ursey, P. W. Barone, M. J. Allen, H. Shan, C. Kittrell, R. H. Hauge, J. M. Tour, R. E. Smalley, Electronic structure control of single-walled carbon nanotube functionalization, *Science* **301** (2003) 1519–1522.

22 L. An, Q. Fu, C. Lu, J. Liu, A simple chemical route to selectively eliminate metallic carbon nanotubes in nanotube network devices, *J. Am. Chem. Soc.* **126** (2004) 10520–10521.

23 J. Chen, C. Klinke, A. Afzali, K. Chan, P. Avouris, Self-aligned carbon nanotube transistors with novel chemical doping, *IEDM Tech. Dig.* (2004) 695–698.

24 J. K. Kochi, R. Rathore, P. Le Magueres, Stable dimeric aromatic cation-radicals, structural and spectral characterization of through-space charge delocalization, *J. Org. Chem.* **65** (2000) 6826–6836.

25 S. Im, N. Srivastava, K. Banerjee, K. E. Goodson, scaling analysis of multilevel interconnect temperatures for high performance ICs, *IEEE Trans. Electron Devices* **52** (2005) 2710–2719.

26 B. Q. Wei, R. Vajtai, Y. Jung, J. Ward, Y. Zhang, G. Ramanath, P. M. Ajayan, Organized assembly of carbon nanotubes, *Nature* **416** (2002) 495.

27 M. Nihei, D. Kondo, A. Kawabata, S. Sato, H. Shioya, M. Sakaue, T. Iwai, M. Ohfuti, Y. Awano, Low-resistance multi-walled carbon nanotube vias with parallel channel conduction of inner shells, in *IEEE Interconnect Technology Conference, 2005, San Francisco* (2005) 234–236.

28 S. Huang, X. Cai, J. Liu, Growth of millimeter-long and horizontally aligned single-walled carbon nanotubes on flat substrates, *J. Am. Chem. Soc.* **125** (2003) 5636–5637.

29 X. Huijun, A. T. Woolley, Directional orientation of carbon nanotubes on surfaces using a gas flow cell, *Nano Lett.* **4** (2004) 1481–1484.

30 A. Nojeh, A. Ural, R. F. Pease, H. Dai, Electric-field-directed growth of carbon nanotubes in two dimensions, *J. Vac. Sci. Technol. B* **22** (2004) 3421–3425.

31 Y. H. Yan, S. Li, L. Q. Chen, M. B. Chan-Park, Q. Zhang, Large-scale submicron horizontally aligned single-walled carbon nanotube surface arrays on various substrates produced by a fluidic assembly method, *Nanotechnology* **17** (2006) 5696–5701.

32 J. Li, Q. Ye, A. Cassell, H. T. Ng, R. Stevens, J. Han, M. Meyyappan, Bottom-up approach for carbon nanotube interconnects, *Appl. Phys. Lett.* **82** (2003) 2491–2493.

33 R. Seidel, F. Kreupl, A. Graham, Integrated electronic component, *US Patent Application 20060234080*, 2006.

34 M. Meyyappan, L. Delzeit, A. Cassell, D. Hash,Carbon nanotube growth by PECVD:

a review, *Plasma Sources Sci. Technol.* **12** (2003) 205–216.

35 F. Kreupl, A. P. Graham, G. S. Duesberg, W. Steinhögl, M. Liebau, E. Unger, W. Hönlein, Carbon nanotubes in interconnect applications, *Microelectron. Eng.* **64** (2002) 399–408.

36 M. Nihei, M. Horibe, A. Kawabata, Y. Awano, Simultaneous formation of multiwall carbon nanotubes and their end-bonded ohmic contacts to Ti electrodes for future ULSI interconnects, *Jpn. J. Appl. Phys.* **43** (2004) 1856–1859.

37 Y. M. Choi, S. Lee, H. S. Yoon, M. S. Lee, H. Kim, I. Han, Y. Son, I. S. Yeo, U.-I. Chung, J. T. Moon, Integration and electrical properties of carbon nanotube array for interconnect applications, in *Proceedings of the 2006 IEEE Conference on Nanotechnology, Cincinnati, USA* **1** (2006) 262–265.

38 F. Kreupl, A. P. Graham, M. Liebau, G. S. Duesberg, R. Seidel, E. Unger, Carbon nanotubes for interconnect applications, *IEDM Tech. Dig.* (2004) 683.

39 K. Hata, D.N. Futaba, K. Mizuno, T. Namai, M. Yumura, S Iijima, Water-assisted highly efficient synthesis of impurity-free single-walled carbon nanotubes, *Science* **306** (2004) 1362–1364.

40 G. Zhang, D. Mann, L. Zhang, A. Javey, Y. Li, E. Yenilmez, Q. Wang, J. P. McVittie, Y. Nishi, J. Gibbons, H. Dai, Ultra-high-yield growth of vertical single-walled carbon nanotubes: hidden roles of hydrogen and oxygen, *Proc. Natl. Acad. Sci. USA* **102** (2005) 16141–16145.

41 R. Pfeiffer, F. Simon, H. Kuzmany, V. N. Popov, V. Zólyomi, J. Kürti, Tube–tube interaction In double-wall carbon nanotubes, *Phys. Status Solidi B* **243** (2006) 3268–3272.

42 V. Zólyomi, Á. Rusznyák, J. Kürti, Á. Gali, F. Simon, H. Kuzmany, Á. Szabados, P. R. Surján, Semiconductor-to-metal transition of double walled carbon nanotubes induced by inter-shell interaction, *Phys. Status Solidi B* **243** (2006) 3476–3479.

43 T. Iwai, H. Shioya, D. Kondo, S. Hirose, A. Kawabata, S. Sato, M. Nihei, T. Kikkawa, K. Joshin, Y. Awano, N. Yokoyama, Thermal and source bumps utilizing carbon nanotubes for flip-chip high power amplifiers, *IEDM Tech. Dig.* **11** (2005) 3.

44 L. Zhu, Y. Sun, J. Xu, Z. Zhang, D. W. Hess, C. P. Wong, Aligned carbon nanotubes for electrical interconnect and thermal management, in *Proceedings of the IEEE Electronic Components and Technology Conference, Lake Buena Vista, FL* **1** (2005) pp. 44–50.

45 L.-B. Zhu, Y.-Y. Sun, D. W. Hess, C.-P. Wong, Well-aligned open-ended carbon nanotube architectures: an approach for device assembly, *Nano Lett.* **6** (2006) 243–247.

46 J. Li, J. K. Lumpp, Characterization of carbon nanotube filled conductive adhesive, in *Proceedings of 39th International Symposium on Microelectronics, IMAPS, San Diego, CA* (2006) pp. 1–5.

47 W. Steinhögl, G. Schindler, Towards minimum k values of porous dielectrics: a simulation study, presented at the *Advanced Metallization Conference, Montreal, October 9–11, 2001*, eds. A. J. McKerrow, Y. S. Diamand, S. Zaima, and T. Ohba, *Materials Research Society, Warrendale, Pennsylvania* (2002) p. 393.

48 W. Steinhögl, F. Kreupl, W. Hönlein, Method of producing layered assembly and a layered assembly, US Patent Application 20050196950, 2005.

49 D. N. Futaba, K. Hata, T. Namai, T. Yamada, K. Mizuno,Y. Hayamizu, M. Yumura, S. Iijima, 84% catalyst activity of water-assisted growth of single walled carbon nanotube forest characterization by a statistical and macroscopic approach, *J. Phys. Chem. B* **110** (2006) 8035–8038.

50 S. P. Lacour, S. Wagner, Z. Huang and Z. Suo, Stretchable gold conductors on elastomeric substrates, *Appl. Phys. Lett.* **82** (2003) 2404–2406.

51 S. P. Lacour, J. Jones, S. Wagner, T. Li, Z. Suo, Stretchable interconnects for elastic electronic surfaces, *Proc. IEEE* **93** (2005) 1479–1467.

52 S. P. Lacour, C. Tsay, S. Wagner, Z. Yu, B. Morrison III, Stretchable microelectrode arrays for dynamic neural recording of *in vitro* mechanically injured brain, in *Proceedings of the 4th IEEE Conference on Sensors, Irvine, California* (2005) pp. 617–620.

53 Y. J. Jung, S. Kar, S. Talapatra, C. Soldano, G. Viswanathan, X. Li, Z. Yao, F. Suong Ou, A. Avadhanula, R. Vajtai, S. Curran, O. Nalamasu, P. M. Ajayan, Aligned carbon nanotube-polymer hybrid architectures for diverse flexible electronic applications, *Nano Lett.* **6** (2006) 413–418.

54 P. Avouris, J. Chen, Nanotube electronics and optoelectronics, *Mater. Today* **9** (*10*) (2006) 46–54.

55 R. V. Seidel, Carbon nanotube devices, *PhD Thesis*, TU Dresden, 2004; http://deposit.ddb.de/cgi-bin/dokserv?idn=973879505.

56 A. Javey, J. Guo, Q. Wang, M. Lundstrom, H. Dai, ballistic carbon nanotube transistors, *Nature* **4** (2003) 654–657.

57 C. Chen, D. Xu, E. S. Kong, Y. Zhang, Multichannel carbon-nanotube FETs and complementary logic gates with nanowelded contacts, *IEEE Electron Device Lett.* (2006) 27852–27855.

58 A. Javey, J. Guo, D. B. Farmer, Q. Wang, D. Wang, R. G. Gordon, M. Lundstrom, H. Dai, Carbon nanotube field-effect transistors with integrated ohmic contacts and high-*k* gate dielectrics, *Nano Lett.* **3** (2004) 447–450.

59 R. V. Seidel, A. P. Graham, J. Kretz, B. Rajasekharan, G. S. Duesberg, M. Liebau, E. Unger, F. Kreupl, W. Hoenlein, Sub-20 nm short channel carbon nanotube transistors, *Nano Lett.* **5** (2005) 147–150.

60 J. Deng, N. Patil, K. Ryu, A. Badmaev, C. Zhou, S. Mitra, H-S. Wong, Carbon nanotube transistor circuits: circuit-level performance: benchmarking and design options for living with imperfections, in *Proceedings of the IEEE International Solid-State Circuits Conference, ISSCC 2007*, San Francisco, CA (2007) pp. 586–588.

61 R. Chau, S. Datta, M. Doczy, B. Doyle, B. Jin, J. Kavalieros, A. Majumdar, M. Metz and M. Radosavljevic, Benchmarking nanotechnology for high-performance and low-power logic transistor applications, *IEEE Trans. Nanotechnol.* **4** (2005) 153–158.

62 H. M. Manohara, E. W. Wong, E. Schlecht, B. D. Hunt, P. H. Siegel, Carbon nanotube Schottky diodes using Ti-Schottky and Pt-ohmic contacts for high frequency applications, *Nano Lett.* **5** (2005) 1469.

63 C. Lu, L. An, Q. Fu, J. Liu, H. Zhang, J. Murduck, Schottky diodes from asymmetric metal–nanotube contacts, *Appl. Phys. Lett.* **88** (2006) 133501.

64 J. U. Lee, P. P. Gipp and C. M. Heller, Carbon nanotube p–n junction diodes, *Appl. Phys. Lett.* **85** (2004) 146.

65 M. Shim, A. Javey, N. Wong, S. Kam, H. Dai, Polymer functionalization for air-stable n-type carbon nanotube field-effect transistors, *J. Am. Chem. Soc.* **123** (2001) 11512–11513.

66 J. Ristein, Surface transfer doping of semiconductors, *Science* **313** (2006) 1057.

67 W. K. Luk, R. H. Dennard, Gated-diode amplifiers, *IEEE Trans. Circuits Systems II: Express Briefs* **52** (2005) 266–300.

68 R. V. Seidel, A. P. Graham, E. Unger, G. S. Duesberg, M. Liebau, W. Steinhoegl, F. Kreupl, W. Hoenlein, High-current nanotube transistors, *Nano Lett.* **4** (2004) 831.

69 W. M. Weber, L. Geelhaar, A. P. Graham, E. Unger, G. S. Duesberg, M. Liebau, W. Pamler, C. Chèze, H. Riechert, P. Lugli, F. Kreupl, Silicon-nanowire transistors with intruded nickel-silicide contacts, *Nano Lett.* **6** (2006) 2660–2666.

2
Electromechanical Carbon Nanotube Transducers

Christoph Stampfer, Christofer Hierold, Mikro- und Nanosysteme, ETH Zürich, Switzerland

2.1
Introduction

The field of nanomechanics [1] and nanoelectromechanical systems (NEMS) [2, 3] is rapidly growing, mainly due to considerable potential for future ultra-fast, high-sensitivity, low-power devices [4, 5]. A number of possible new applications and

Advanced Micro & Nanosystems Vol. 8. Carbon Nanotube Devices.
Edited by Christofer Hierold

ISBN: 978-3-527-31720-2

first demonstrators at the nanoscale level have been demonstrated such as resonating charge shuttles [6], single electron spin detection [7], ultra-sensitive mass [8] and force [9] sensing, and carbon nanotube relays [10, 11]. It is shown that the inevitable development of microelectromechanical systems (MEMS) down to nanoscale (NEMS) suffers from a discontinuity in process technologies (e.g. [12]) and from a non-optimal transfer of transducer concepts from micro- to nanoscale systems [13]. Therefore, the major driving forces for the investigations of novel and alternative transducer concepts [8–10] and for the exploration of new nanomaterials for sensing and actuation at the nanoscale level, which are being considered to overcome these so-called scaling problems, are further miniaturization, low power consumption for autonomous sensor nodes and cost reduction.

Carbon nanotubes [14–16], in particular single-walled carbon nanotubes, have among other nanostructures (e.g. nanowires [17] or fullerenes [18]) outstanding potential as a new material for novel NEMS devices. Single-walled carbon nanotubes have been intensively investigated during the last decade and have attracted great interest due to their exceptional electronic, mechanical and optical properties.

Here we focus on electromechanical transducers based on carbon nanotubes and on novel NEMS device concepts where the discussed electromechanical transducer concepts are utilized. In Section 2.2 transducers and in particular (piezoresistive) electromechanical transducers are briefly reviewed. Electromechanical properties of carbon nanotubes, in particular of single-walled carbon nanotubes are discussed in Section 2.3. Transducer concepts with nanotubes as active elements and few examples of devices based on these transducers are presented in Section 2.4. Conclusions are presented in Section 2.5.

2.2 Transducers

Transducers direct information (including energy) and, by definition[1)], convert one form of energy (or *signal*) into another form. In general, there are a large number of energy (or *signal*) forms which can be transformed into each other, including the broad range of mechanical, optical, electrical, magnetic, thermal, and chemical forms. As broad as the energy and *signal* forms are, just as diverse are the applications and system technologies (ranging from macro- and microsystems down to nanosystems technologies). An extensive review on (mainly micromachined) transducers can be found in References [19–21].

Ideal transducers convert the energy (or *signal*) forms without energy dissipation and therefore the energy transformation is reversible. However, in real systems dissipation is present and, thus, the *information* (and energy) flow is clearly directed. This in combination with different ratios between transformed energy

1) Taken from *Webster's Ninth New Collegiate Dictionary*, Springfield, MA, Mass., Merriam-Webster, 1983.

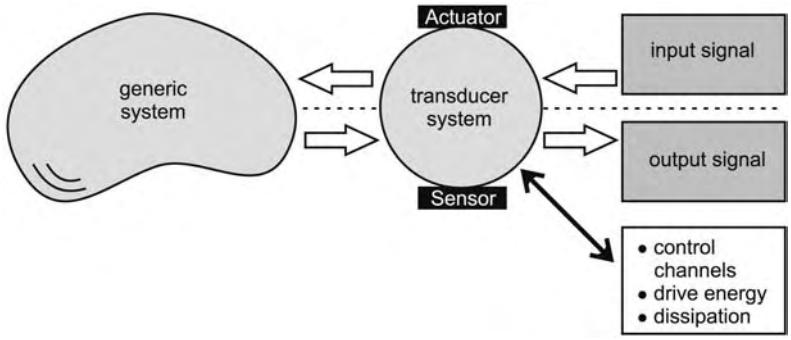

Figure 2.1 Schematic representation of a generic actuator and sensor system acting or probing on a generic system. The transducer systems forms the interface to the generic system (i.e. to the "outside world") and directs the highlighted flow of information (and mostly of energy). Here, also additional transducer control channels and drive energy channels are depicted.

and characteristic system energy scales leads to the distinction between sensor and actuator systems. Indeed, transducers are *the* key components of any sensor or actuator system. Sensor and actuator systems in general consist of (i) a transducer system acting or sensing (i.e. probing) on a generic *system* (see e.g. Figure 2.1), and (ii) of defined interfaces to this system and the control (and processing) units. In Figure 2.1 a generic actuator or sensor system is depicted, where a transducer system is coupled to a generic system. At additional control terminals, signals (and energies) could be applied and subsequently be converted by (additional) control transducers to impact the properties of the generic system.

Whether a transducer operates as an actuator or sensor strongly depends on the flow of information (and mostly of energy). *Ideal* sensor systems operate as ideal measurement systems probing most non-invasively distinct properties of the generic system. Thus in (ideal) *classical* sensor systems the transfered energy is kept at zero, whereas for (ideal) *quantum*, and consequently for a number of nanoscaled sensor systems, quantum mechanics (collapsing of quantum states when being measured) [22] limits the non-invasiveness and governs the minimum energy transfer. In contrast to sensor systems, actuator systems are built to *act* on the system, in order to modify the system's state. In summary, *ideal* nanoscaled transducers will differ qualitatively from macro- and microscaled devices due to the implications of (i) the shifted volume to surface ratio, (ii) the quantized nature of physical quantities at this scale and (iii) the quantum mechanical measurement processes.

In contrast to *normal* micro- or nanoelectronics, transducers are interfacing the so-called "outside world" (corresponding to *the* generic system in Figure 2.1), which consequently leads to different requirements and most importantly to additional motivations for further miniaturization. Among the well-known economic

and performance reasons, there are the unscalable functional reasons. There are certain novel applications (within quantum chemistry, nanobiology and medicine) which require miniaturized systems for pure functional reasons. For example, it is obvious that endoscopic techniques or novel medical applications (e.g. implants) require a sufficiently small system size in order to be successful in practice [23]. Nanomaterials (such as carbon nanotubes or nanowires) are promising for realizing this kind of novel applications.

In this chapter, we focus exclusively on electromechanical transducers based on carbon nanotubes, which indeed are an interesting natural nanomaterial. Thus we focus on systems where mechanical *signals* (mechanical stimuli; e.g. displacements or movements) are transformed into electrical *signals*, or *vice versa*. Moreover, we restrict ourselves mostly to (quasi-static) piezoresistive electromechanical transducers within a sensing scheme. The main focus is given to the physical description of the piezoresistivity and most interestingly its downscaling behavior. For a broader overview of the field of electromechanical transducers, we refer to References [20, 24] and references therein.

2.2.1 Piezoresistive Sensing

The piezoresistive[2)] sensing mechanism is based on the piezoresistive effect, which is defined as the change of the electrical resistance, R, under the influence of a mechanical tension resulting in mechanical strain, $\tilde{\varepsilon}$. To simplify the following discussion, we consider straining only in one direction, reducing the strain tensor $\tilde{\varepsilon}$, down to a single (scalar) component ε. In this case the strain-dependent resistance $R(\varepsilon)$ in the small strain regime can be simply expanded in a Taylor series around $R_0 = R(\varepsilon = 0)$, leading to

$$R(\varepsilon) = R_0 + \frac{\mathrm{d}R}{\mathrm{d}\varepsilon}\varepsilon + \sum_{n=2}^{\infty}\frac{1}{n!}\left(\frac{\mathrm{d}R}{\mathrm{d}\varepsilon}\right)^{(n)}\varepsilon^n \tag{1}$$

In the following discussion we consider the linear response term only. Thus the third term on the RHS[3)] of Equation (1) will be neglected. The piezoresistance as a function of strain ε therefore reduces to $R(\varepsilon) = R_0(1 + \beta_{\mathrm{GF}}\varepsilon)$, where $\beta_{\mathrm{GF}} \equiv \Delta R(\varepsilon)/R_0\ \varepsilon^{-1}$ is the so-called piezoresistive gauge factor being a measure for the sensitivity of the strain gauge. Piezoresistive gauge factors for different materials (in general of micro- or macroscopic size) are given in Table 2.1. In the next two subsections we will examine the physical effects, which are responsible for the piezoresistive effect in different materials and different electron transport regimes.

2) The word *piezo* is derived from the Greek *piezein*, and means to squeeze or press.
3) RHS stands for right-hand side.

Table 2.1 Comparison of piezoresistive gauge factors [$\beta_{GF} = \Delta R(\varepsilon)/R_0\ \varepsilon^{-1}$] of different types of strain gauges. This table has been partially adapted from Reference [20].

Material	*Piezoresisitve gauge factor (β_{GF})*
Metal foils [20]	1–5
Thin films [20]	~2
Doped semiconductors [20]	80–200
Doped poly-Si [25]	15–27
Single-walled carbon nanotubes [26]	600–1000

2.2.1.1 Classical Piezoresistance

The *classical* piezoresistive effect includes a wealth of electromechanical effects in classical conductors [27]. Thus we focus on resistors where the electron transport is governed by the hydrodynamic Boltzmann equation [29] (see Figure 2.2a). This is true for systems in the micro and macro regime, where the classical Ohm's law holds to describe the resistance, $R = \rho L/A$, where ρ is the specific resistance, L the length and $A = WH$ the cross-section[4)] of the conductor (see Figure 2.2b). The piezoresistive gauge factor, β_{GF}, as a function of $\varepsilon = \Delta L/L$, therefore follows as

$$\beta_{GF} = \frac{\Delta R(\varepsilon)}{R_0}\varepsilon^{-1} = \frac{\Delta\rho(\varepsilon)}{\rho_0}\varepsilon^{-1} + \left[\frac{\Delta L(\varepsilon)}{L_0}\varepsilon^{-1} - \frac{\Delta A(\varepsilon)}{A_0}\varepsilon^{-1}\right] = \frac{\Delta\rho(\varepsilon)}{\rho_0}\varepsilon^{-1} + (1+2\nu), \quad (2)$$

where $\nu = -\Delta A(\varepsilon)/(2A_0)\varepsilon^{-1}$ is Poisson's ratio. In *metallic* strain gauges the relative change in the specific resistance [first term on the RHS of Equation (2)] can be neglected and the piezoresistive effect arises only from the change of the geometry [$\Delta L(\varepsilon)$, $\Delta A(\varepsilon)$] of the strained conductor. Thus the piezoresistive gauge factor reduces for metals to $\beta_{GF,m} = 1 + 2\nu$, and lies in the range of 1–5 [20]. For *semiconductor* piezoresistors the geometric gauge effect is much smaller than the effect on the specific resistivity [$\Delta\rho(\varepsilon)/\rho_0 >> \varepsilon(1 + 2\nu)$], hence the geometric gauge effect will be neglected for further discussions on semiconductors, leading to $\beta_{GF,s} = \Delta\rho(\varepsilon)/\rho_0\ \varepsilon^{-1}$. To understand the physical nature of the strain dependency of the specific resistivity we focus on the specific conductivity, $\sigma(\varepsilon) = n(\varepsilon)\mu(\varepsilon)e = \rho(\varepsilon)^{-1}$, where n is the electron density, $\mu(\varepsilon) = e\tau(\varepsilon)/m^*(\varepsilon)$ is the mobility[5)] and e is the electron charge.

In References [30, 31] it has been shown that for many valley semiconductors (like n-type silicon[6)]) two effects predominate over all others the change in resis-

4) Here, W is the width and H the thickness.
5) Where $\tau(\varepsilon)$ is the relaxation time and $m^*(\varepsilon)$ is the effective mass of the carriers.
6) For a discussion on the piezoresistive properties of p-type silicon, see References [32, 33].

tance as a function of strain, as observed e.g. by Smith [27] for silicon (Si) and germanium (Ge). The first of these is the change in population of different valleys due to the different shifts in the energies of band edge points as a function of applied strain. This *electron transfer effect* gives a contribution to the piezoresistance, which is proportional to the anisotropy of the conductivity (due to the anisotropy of the effective mass m^*) for a single valley and is inversely proportional to the absolute temperature [31]. The second effect, which is important only when intervalley scattering is appreciable, is the effect of strain on the relaxation time $\tau(\varepsilon)$, due to increase or decrease in the energies of the valleys containing possible final states for intervalley scattering. Moreover, the absolute magnitude of the piezoresistive effect increases with decreasing temperature and decreases with heavy doping [34]. The strain independence of the piezoresistive gauge factor, however, is generally better in heavily doped *n*-type silicon strain gauges than in lightly doped ones. This is mainly due to statistical degeneracy, or more generally due to the nature of scattering mechanisms [35]. Finally, the highest strain applied within piezoresistance measurements on doped silicon[7)] to date is $\varepsilon_{max} \approx 0.1\%$ and only small non-linearties have been measured [36], knowing that the fracture strain of crystalline silicon is in the range between 0.6% and 1.8%, strongly depending on the orientation [38].

For further details on the classical piezoresistive effect in semiconductors (mainly Si or Ge), see References [25, 27, 30–37, 39–41].

2.2.1.2 Piezoconductance in Mesoscopic Systems

The conductance of large samples follows the well-known ohmic scaling law, $G = \sigma A/L$. This law needs some corrections if we go to smaller dimensions, in particular by coming close (or even crossing) the mean free path[8)], λ_{el}, and the Fermi wavelength, λ_F. We find a channel resistance, which is independent of the length L of the conductor, and second the conductance does not decrease linearly with lateral dimension W. The Landauer equation [42, 43] incorporates both of these features and describes the electron transport in the ballistic regime [44]. In Figure 2.2a, the different size-dependent electron transport regimes are depicted. The strain-dependent Landauer equation [42] at zero temperature is

$$G(\varepsilon) = \frac{2e^2}{h} \sum_{n,m}^{M(\varepsilon)} |t_{nm}(\varepsilon)|^2 , \tag{3}$$

where $t_{nm}(\varepsilon)$ are the transmission amplitudes representing the probability that an electron injected in the mth mode at one end of the conductor will transmit to the

7) For completeness, it is noteworthy that recently piezoresistance measurements on submicron diameter doped silicon fibers ($d \approx 150$ nm) have been performed up to strains of $\varepsilon_{max} \approx 1\%$, showing a non-linear piezoresistive gauge factor, which decreases for high strains [37].

8) The mean free path is the average trajectory length covered by an electron before being elastically scattered into a different wavevector direction. It has been introduced by the classical Boltzmann equation [29].

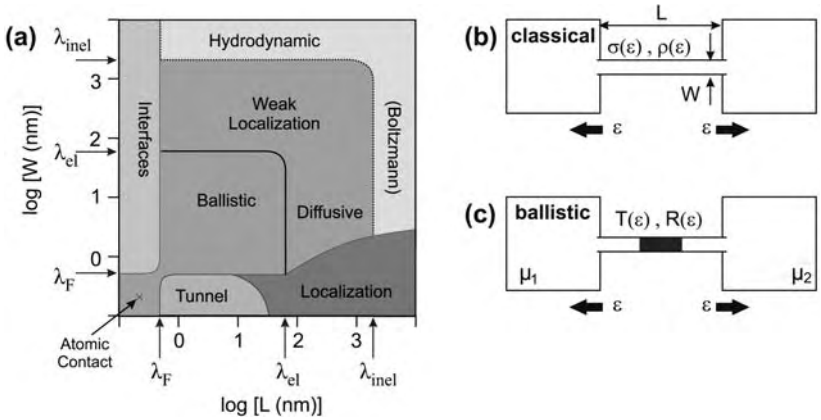

Figure 2.2 (a) Regimes of electronic transport as a function of the wire width W and length L (b). λ_F is the Fermi wavelength of the carriers in the contact electrodes (away from the constriction), λ_{el}, the elastic mean free path in the wire and λ_{inel}, the inelastic mean free path in the wire. (b, c) Schematic representation of the qualitative difference between the piezoresistivity in *classical* and ballistic conductors connected to two ideal reservoirs with chemical potentials μ_1 and μ_2, respectively. (b) Classical conductor with length L, width W and specific resistance ρ. (c) Ballistic conductor including a scattering center described by the strain-dependent transmission and reflection coefficients, $T(\varepsilon)$ and $R(\varepsilon)$, respectively. Partially adapted from Reference [28].

nth mode at the other end. Note that if the transmission probability is unity, we obtain the correct expression for the resistance of the reflection less ballistic conductor including the contact resistance [44]. $M(\varepsilon)$ is the number of open modes involved in the transport. We start the discussion by focusing on the strain dependency of the Landauer equation for a reflectionless conductor (e.g. an *ideal* nanowire or nanotube), $G(\varepsilon) = 2e^2/hM(\varepsilon)$, where $M(\varepsilon)$ is the number of propagating waves and can be written as[9)]

$$M(\varepsilon) = \left\lfloor \frac{k_F(\varepsilon)W(\varepsilon)}{\pi} \right\rfloor = \left\lfloor \frac{2W(\varepsilon)}{\lambda_F(\varepsilon)} \right\rfloor, \tag{4}$$

where $W = W_0(1 - \nu\varepsilon)$ is the width of the sample (ν is Poisson's ratio) and k_F is the Fermi wavevector. Hence the piezoresistive gauge factor for the reflectionless conductor is given by

$$\beta_{GF} = -\frac{\Delta G(\varepsilon)}{G(\varepsilon)}\varepsilon^{-1} = -\frac{\Delta M(\varepsilon)}{M(\varepsilon)}\varepsilon^{-1} = \left(\frac{\lfloor M_c \rfloor}{\lfloor M_c(1-\nu\varepsilon)\rfloor} - 1\right)\varepsilon^{-1}, \tag{5}$$

where M_c is the *continuous* mode number, $M_c = 2W_0/\lambda_F$.

9) Here $\lfloor x \rfloor$ is the integer truncation (or floor value) of x.

Note that $\Delta M(\varepsilon)$ and $M(\varepsilon)$ are integer numbers, leading to a quantized (step-like) strain dependency for narrow wires. Here, moreover, it has been assumed that the Fermi wavelength λ_F is independent of strain, $\lambda_F(\varepsilon) = \lambda_F$. This approximation should in particular hold for metals.

For a wide conductor with many open modes, the number of *continuous* modes M_c is large, $M_c >> 1$, and assuming $\nu\varepsilon$ is very small ($\nu\varepsilon << 1$), the piezoresistive gauge factor can be approximated[10] by $\beta_{GF} = \nu$. This expression corresponds to the contribution due to pure classical dimension changes corresponding to Equation (2)[11].

It is noteworthy that the threshold value at which strain ε the conductance change occurs depends sensitively on M_c, which is also a function of $\lambda_F(E_F)$. Thus one might think of tuning the Fermi wavelength by an external potential in order to sweep the threshold values. On the other hand, by setting the continuous mode number M_c e.g. to 1.001, a strain of $\varepsilon = 0.1\%/\nu$ (corresponding to $\varepsilon = 0.5\%$ for $\nu = 0.2$) is sufficient to switch off the current flow completely, by closing the last open mode. This effect might be useful for future electromechanical switches, where an applied strain controls the current running through a ballistic strain gauge.

In general, we have to consider also the strain dependence of the transmission amplitudes $t_{nm}(\varepsilon)$ and it is shown that they can be sensitive to small changes in strain. Since the ballistic electron transport (at zero temperature) is via the Landauer [Equation (3)] directly linked to the transmission amplitudes, this sensitive nature is reflected in the electron transport itself. However, the transmission coefficients, and thus their dependence on strain, are highly dependent on the system geometry itself. Therefore, it is challenging (in general impossible) to discuss the piezoconductance for generic mesoscopic systems.

Since the piezoconductance is given by $G(\varepsilon) = 2e^2/hT(\varepsilon)$, where T is the averaged transmission probability, the piezoresistive gauge factor reads $\beta_{GF} = -\Delta T(\varepsilon)/T(\varepsilon)\varepsilon^{-1}$. Note that this expression can be further approximated for the infinitesimally small strain regime[12] to $\beta_{GF} = -T(0)^{-1}\, \mathrm{d}T(0)/\mathrm{d}\varepsilon$.

Next, the connection of the strain dependent Landauer equation to the familiar Ohm's law for large dimensions[13] is discussed. As we have seen above, for a wide conductor the mode number is proportional to the width, $M \approx k_F W/\pi$, thus $G(\varepsilon) = 2e^2h^{-1}k_F W/\pi T_m$, where T_m is the averaged transmission probability per open mode. By treating the electrons as purely classical particles (hence neglecting any quantum interference), the transmission amplitude T_m through the sample of length L can be written as $T_m = L_{el}/(L + L_{el})$, where L_{el} is a characteristic length of the order of the mean free path λ_{el} (in particular it can be shown that $L_{el} = \pi\lambda_{el}/2$). For significantly large L we can neglect L_{el} (resulting in the neglect of the length-

10) Here the following approximations have been used: $\lfloor M_c \rfloor \approx M_c$, $\lfloor M_c(1 - \nu\varepsilon) \rfloor \approx M_c(1 - \nu\varepsilon)$ and $1/(1 - \nu\varepsilon) \approx 1 + \nu\varepsilon$.

11) The missing factor 2 is due to the reduction from two lateral dimensions W and H, down to one single lateral dimension, W.

12) Making use of $T(\varepsilon) \approx T(0) + (\mathrm{d}T/\mathrm{d}\varepsilon)\, \varepsilon$ and $1/(1 + x) \approx 1 - x$ for $x << 1$.

13) For more details on this connection, see Reference [44].

independent contact resistance $R_c = (2e^2k_F)^{-1}h\pi/W$), and we find the classical Ohm's law[14] $G = (en\mu)W/L$ and the corresponding classical piezoresistivity, where in the non-trivial case (e.g semiconductors) the strain dependence of the electron density $n(\varepsilon)$ and the mobility $\mu(\varepsilon)$ has to be considered.

Finally, we will have a look at the strain-dependent Landauer equation at non-zero temperature, which is given according to [44] by

$$G(\varepsilon) = \frac{2e^2}{h}\int\left[-\frac{\partial f_0(E)}{\partial E}\right]\sum_{n,m}^{M(\varepsilon)}|t_{nm}(E,\varepsilon)|^2\,\mathrm{d}E, \tag{6}$$

where $f_0(E)$ is the Fermi function. First we assume that the number of open modes M is independent of strain[15] and the averaged transmission coefficient $|t|^2$ is independent of energy, E. Therefore, we can reduce Equation (6) in the limit of thermally activated transport[16] to

$$G(\varepsilon) = \frac{4e^2M|t(\varepsilon)|^2}{h}\left[1+\mathrm{e}^{\frac{E_{\mathrm{gap}}(\varepsilon)}{k_BT}}\right]^{-1} \tag{7}$$

$$\approx \frac{2e^2M\overline{T}(\varepsilon)}{h}\left[1-\frac{E_{\mathrm{gap}}(\varepsilon)}{2k_BT}\right]+\mathcal{O}\left[\frac{E_{\mathrm{gap}}(\varepsilon)}{k_BT}\right]^3, \tag{8}$$

where $E_{\mathrm{gap}}(\varepsilon)$ is the strain-dependent band gap of the low-dimensional system and $\overline{T}(\varepsilon) = |t(\varepsilon)|^2$. Further, we focus on small strains ε for which the RHS of Equation (7) can be reduced to the linear term of the corresponding Taylor series expansion of the band gap-dependent factor, as shown in Equation (8). Note that Equation (7) will later be used to describe the conductance of suspended and strained single-walled carbon nanotubes, whereas the first term of the RHS of Equation (8) will be used to describe the conductance (within the small strain regime) of strained nanotubes mounted on ultrathin membranes. However, here we concentrate on the infinitesimally small strain regime, where the piezoresistive gauge factor can be approximated by $\beta_{\mathrm{GF}} \equiv -G_0^{-1}\mathrm{d}G(\varepsilon)/\mathrm{d}\varepsilon$. The piezoresistive gauge factor is therefore given by

$$\beta_{\mathrm{GF}} = \frac{1}{\overline{T}(0)[2k_BT - E_{\mathrm{gap}}(0)]}\left[(E_{\mathrm{gap}}(\varepsilon)-2k_B\overline{T})\frac{\mathrm{d}\overline{T}(\varepsilon)}{\mathrm{d}\varepsilon}+\overline{T}(\varepsilon)\frac{\mathrm{d}E_{\mathrm{gap}}(\varepsilon)}{\mathrm{d}\varepsilon}\right].$$

This is the general piezoconductive gauge factor for a mesoscopic system in the ballistic transport regime with fixed mode number M. Note that for zero temperature or no band gap dependence this equation reduces to $\beta_{\mathrm{GF}} = -\overline{T}(0)^{-1}\mathrm{d}\overline{T}(\varepsilon)/\mathrm{d}\varepsilon$, which corresponds to a pure change in transmission.

14) Note that the mobility is given here by $\mu = e\lambda_{\mathrm{el}}/(v_F m^*)$.
15) Note that the strain dependence could eventually be also included in an effective transmission coefficient.
16) For more details, see Reference [44].

2.2.2
Conclusion and Outlook

We have briefly reviewed transducer systems and discussed the piezoresistive effect in the classical and the ballistic transport regimes. The strain-dependent Landauer equation has been introduced and discussed in detail. There is definitely much more to explore and several effects might be very interesting from a fundamental and an applied point of view, such as piezomagnetoconductance in open quantum dots, piezoconductance within the Coulomb blockade regime, or phonon blocking of the electron transport (e.g. [45]).

2.3
Electromechanical Properties of Carbon Nanotubes

Single-walled carbon nanotubes (SWNTs) [46] have been intensively investigated over the last decade and a wealth of interesting mechanical, electrical and optical properties have been observed. For an extended review, see References [14–16]; a short summary of electromechanical properties of SWNTs (including early experiments) can be found in Reference [47]. Here we mainly focus on electromechanical (piezoresistive) properties of SWNTs[17]. However, in order to develop the strain-dependent band gap opening of nanotubes we start by briefly reviewing their electrical properties.

2.3.1
Electronic Structure of SWNTs

SWNTs, which can be either thought of an elongated buckyball or of a graphene layer which has been rolled up to form a hollow cylinder with a typical diameter of 1–2 nm, exhibit both metallic or semiconducting signatures. This striking property, which strongly depends on the chiral vector, $\vec{c}$ (or chiral indices (n_1, n_2), e.g. [14]), can be most easily explained by the zone-folding approximation applied to the semi-metallic graphene layer.

Figure 2.3a shows the hexagonal, honeycomb-like lattice of graphene and the two carbon atoms (A and B) per unit cell (spanned by $\vec{a}_1$ and $\vec{a}_2$; $a_0 \equiv |\vec{a}_{1,2}|$) are highlighted. The band structure of this material, approximated by the nearest-neighbor tight binding model, is given according to Wallace [48] by

$$E(\vec{k}) = E_0 \pm \left| \sum_{i=1}^{3} \gamma_i \exp(-i\vec{k}\cdot\vec{r}_i) \right|, \tag{9}$$

17) Note that from both experimental and theoretical points of view electromechanical properties of SWNTs are still under investigation. Moreover, we would like to explicitly mention that within this chapter we do not cover the highly interesting high-frequency regime, including nanotube-based resonators.

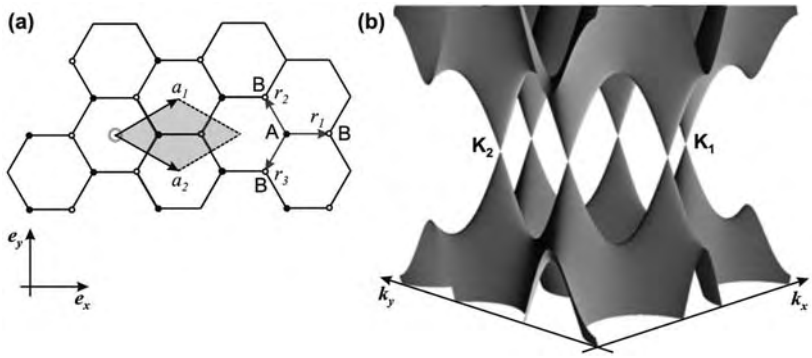

Figure 2.3 (a) Graphene honeycomb lattice with the lattice vectors $\vec{a}_1$ and $\vec{a}_2$. There are two carbon atoms (black and white dots) per unit cell, denoted A and B. (b) 2D dispersion relation of graphene. The energy of the valence and conduction bands is plotted as a function of the wavevectors k_x and k_y. Note that the high- and low-energy bands touch at the so-called Dirac points.

where γ_i are the so-called hopping integrals, E_0 is the energy of the bare p_z orbital and $i = 1$, 2 or 3 refers to the three B atoms neighboring each A atom (see Figure 2.3a). Figure 2.3b shows the high-energy conductance band and the low-energy valence band. The energy difference between these bands vanishes at the so-called Dirac points (K_{D1} and K_{D2})[18]. Near the Fermi level (E_F) the electronic states can be linearized and are best described by linear dispersion cones[19] (e.g. Figure 2.4a), which clearly highlights the semi-metallic character of graphene.

By rolling up a slice of graphene, periodic boundary conditions along the circumference are introduced. The two-dimensional (2D) dispersion relation of graphene (Figure 2.3b) reduces by the so-called zone-folding approximation to one-dimensional (1D) subbands formed by the continuum of $k_{\parallel}$ states (parallel to the tube axis) in each discrete $k_{\perp}$ wrapping mode. Since only electron eigenstates $E(\vec{k})$ with allowed $\vec{k}$ next to K_1 or K_2 are close to E_F, the exact alignment between allowed $\vec{k}$ and the K points of unstrained graphene is crucial for determining the electrical properties of SWNTs. For simplicity, we start by considering zigzag nanotubes with chiral indices of the form (n_1, 0) to discuss the different types of allowed K states to K point alignments. Zigzag nanotubes have a circumference of $d\pi = n_1 a_0$ (where d is the tube diameter) and allowed $k_{\perp,m} = 2\pi m/(n_1 a_0)$, where m is an integer ranging from $-n_c/4 + 1, \ldots, 0, 1, \ldots n_c/4$, and n_c is the number of carbon atoms in the SWNT unit cell. In the case when n_1 is a multiple of 3 there

18) For unstrained graphene the k-space positions of the Dirac points K_D coincide with the Brillouin zone symmetry points K. However, when straining graphene this coincidence is lifted.

19) The slop of these cones, which is given by $\sqrt{3}\gamma_1 a_0/2$, determines the Fermi velocity $v_F \approx 8 \times 10^5\,\mathrm{ms}^{-1}$.

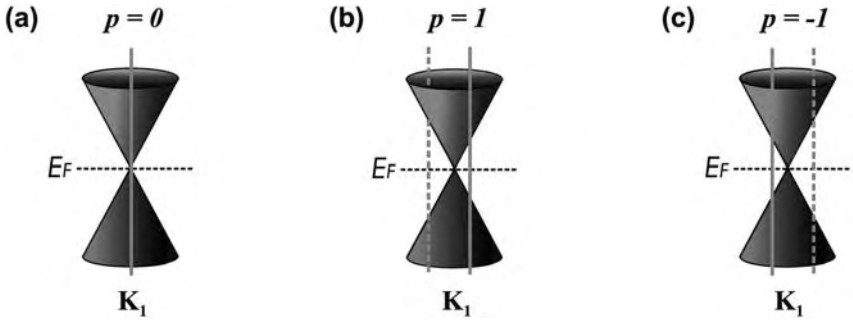

Figure 2.4 Carbon nanotube families $p = 0, +1, -1$ determined by the different alignment between the dispersion cone at K_1 and allowed k. (a) When $p = 0$ a subband (vertical solid line) intercepts the Dirac point. (b, c) When $p = \pm 1$ the misalignment between K_1 and the nearest 1D subband is $\pm 2/(3d)$ leading to a band gap of $E_{gap} = 4h\nu_F/(3d)$.

is an allowed $k_{\perp,m}$ that coincidences with K_1 (illustrated in Figure 2.4a) and K_2, where the energy difference between the 1D conductance and valance band vanishes. In general, there exist two cases when n_1 is not a multiple of 3, given by $n_1 = 3q \pm 1$, where q is an integer. We find the closest $k_{\perp,m_1}$ to K_1 by setting $m_1 = 2q \pm 1$, leading to $k_{\perp,m_1} = 4\pi/(3a_0) \pm 2/(3d)$. All three cases where the 1D subbands do and do not intersect K_1 are shown in Figure 2.4.

More generally, for a given chiral index (n_1, n_2) we determine $n_1 - n_2 = 3q + p$, where q is an integer and p is either -1, 0 or 1. The index p defines the (family) type of alignment between allowed $\vec{k}$ and the Dirac points by[20] (i) $p = 0$, where a line of allowed $\vec{k}$ intercepts K_1 (both 1D subbands are metallic, $E_{gap} = 0$), (ii) $p = 1$, where a line of allowed $\vec{k}$ misses K_1 by $\Delta k = \Delta k_\perp = +2/(3d)$, leading to a band gap of $E_{gap} = 4h\nu_F/(3d)$, and (iii) $p = -1$, where a line of allowed k misses K_1 by $\Delta k = -2/(3d)[E_{gap} = 4h\nu_F/(3d)]$. The nanotubes falling in the families of $p = \pm 1$ exhibit large band gaps ($E_{gap} \approx 0.9\,\text{eV}/d[\text{nm}]$), a property which clearly distinguishes them from $p = 0$ type (metallic) nanotubes. The physical differences between $p = +1$ and $p = -1$ type (semiconducting) nanotubes (Figure 2.4b, c) are less obvious, but will become clearer when we discuss the electromechanical properties of single-walled carbon nanotubes.

2.3.2
Tight-Binding Approximation for Strained Graphene

Now we consider the dispersion relation of graphene and subsequently of SWNTs under the influence of applied strain ε. By stretching the graphene lattice, the distances $\vec{r}_i$ (see Figure 2.3a) between neighboring carbon atoms will change and

20) The symmetry between $+k$ and $-k$ states ensures that the subbands near K_1 and K_2 are degenerate.

therefore the hopping integrals γ_i will become unequal, leading to a modified dispersion relation $E(\vec{k}, \varepsilon)$. Here we follow Minot [49] and without loss of generality we derive the strain-dependent Dirac point shifts by assuming the case that the graphene is stretched (strain ε) in the $\vec{e}_x$ direction (see Figure 2.3a). In this case the strained bond vectors $\vec{r}_i$ are given by

$$\begin{aligned}
&\vec{r}_1(\varepsilon) = r_0(1+\varepsilon)\vec{e}_x, \\
&\vec{r}_2(\varepsilon) = -r_0(1+\varepsilon)/2\vec{e}_x + r_0\sqrt{3}/2(1-\varepsilon\nu)\vec{e}_y, \text{ and} \\
&\vec{r}_3(\varepsilon) = -r_0(1+\varepsilon)/2\vec{e}_x - r_0\sqrt{3}/2(1-\varepsilon\nu)\vec{e}_y,
\end{aligned} \tag{10}$$

where $r_0 = a_0/\sqrt{3} = 1.42\,\text{Å}$ is the unstrained C–C bond length and ν is Poisson's ratio of the 2D carbon material. Moreover, the symmetries of $r_2 = r_3$ are still maintend allowing to set $\gamma_2 = \gamma_3$. Since we are mainly interested in the dispersion relation in the vicinity of the Dirac points, we focus on a cross-section of the dispersion relation Equation (9) along the line $k_x = 0$. Note that this line intercepts K_1 and K_2 at zero strain, $\varepsilon = 0$ (Figure 2.5). We find for the strain-dependent dispersion relation

$$E(k_x = 0, k_y, \varepsilon) - E_0 \equiv \Delta E(k_y, \varepsilon) = \pm 2\gamma_2 \left| \cos\left(\frac{k_y a_0(1-\varepsilon\nu)}{2}\right) + \frac{\gamma_1}{2\gamma_2} \right|. \tag{11}$$

It is obvious from Equation (11) that for $\varepsilon > 0$ there also remains a unique pair of $K_{D1} = -K_{D2}$, where we have $\Delta E(K_{D1,D2}) = 0$. Thus the special property of graphene, namely the linear dispersion relation at the Fermi energy, survives when the lattice is strained [50]. In order to quantify the shift of the K_D points with respect to ε we

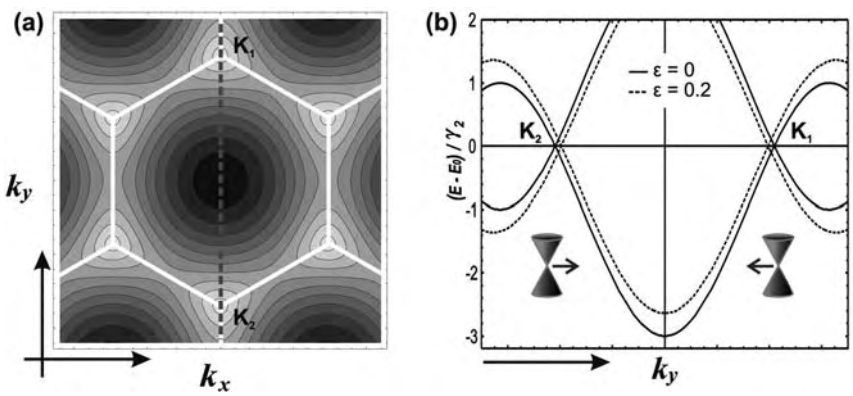

Figure 2.5 Modifications of the graphene band structure when strain is applied in the x-direction. (a) A contour plot of valence states in unstrained graphene. The vertical dashed line shows the slice $k_x = 0$, which passes through both K_1 and K_2. (b) Energy of valence and conduction states along the line $k_x = 0$ when strain $\varepsilon = 0$ and $\varepsilon = 0.2$. The Dirac points (intersection of valence and conduction states) move toward smaller k_y as strain is increased. Adapted from [49].

follow Yang et al. [51] and approximate the hopping integrals by $\gamma_i \propto |r_i|^{-2}$. For small strains ε we find from Equation (10) the relation $\gamma_1/\gamma_2 = 1 - 3/2(1 + \nu)\varepsilon$. Finally, we express the quantitative strain dependent K_D-point shift, here the cosine function has been linearized, by

$$\vec{K}_{D1}(\varepsilon) = -\vec{K}_{D2}(\varepsilon) = \left[\frac{4\pi}{3a_0}(1+\varepsilon\nu) - \frac{\sqrt{3}}{a_0}(1+\nu)\varepsilon\right]\vec{e}_{ky}. \tag{12}$$

This equation describes the strain-induced shift of the K_D points when the applied strain is parallel to one of the bond vectors $\vec{r}_i$. Note that the shift is significant even at very small strain, and it is crucial in order to understand the electromechanical properties of carbon nanotubes.

2.3.3
Mechanical Band Gap Tuning of Carbon Nanotubes

In the previous subsections we have shown that (i) the band gap of SWNTs depends strongly on the alignment of the allowed $\vec{k}$ states with the Dirac points (K_{D1} and K_{D2}), and that (ii) the dispersion cones keep (to first order) their shape but shift when an external strain is applied to the graphene lattice. This, consequently, leads to strain-sensitive SWNT band gaps due to the zone-folding approximation. Moreover, the band gap sensitivity depends, among the chiral angle θ, strongly on the family index $p = -1$, 0 or +1, which also determines the sign of the relative change of the band gap [51–53]. Considering a nanotube of type $p = 0$ with chiral angle $\theta = 0°$ (metallic zigzag tubes) as shown in Figure 2.6a. When the nanotube is unstrained, allowed k states intercepts the Dirac points. However, when the nanotube is strained both $K_{D1,D2}$ and the allowed $\vec{k}$ shift, whereas the $K_{D1,D2}$ shift due to axial strain is given by Equation (12) and the quantized $k_{\perp,m}$ values change due to changing tube diameter $d(\varepsilon)$. The diameter shrinks by a factor $(1 - \nu\varepsilon)$, and the $k_{\perp,m_{1,2}}$ nearest $K_{D1,D2}$ becomes $k_{\perp,m_{1,2}} = \pm 4\pi/(3a_0)(1-\nu\varepsilon)^{-1}$. To first order in ε, the misalignment between $K_{D1,D2}$ and the nearest allowed $\vec{k}$ is then given by $\Delta k(\varepsilon) = \sqrt{3}/a_0(1+\nu)\varepsilon$. Since, the same absolute shift occurs near K_1 and K_2, the subbands remain degenerate. From the slope of the dispersion cones around the K points, we finally obtain

$$E_{gap}(\varepsilon) = 2\frac{\sqrt{3}}{2}\gamma_1 a_0|\Delta k(\varepsilon)| = 3\gamma_1(1+\nu)\varepsilon. \tag{13}$$

Note that the band gap opening for this $p = 0$ (and $\theta = 0°$) family-type SWNT is to first order independent of diameter. More generally, we next consider $p = \pm 1$ type zigzag nanotubes ($\theta = 0°$), where the unstrained $p = \pm 1$ has $\Delta k = \pm 2/3d$, leading to a strain-induced shift expressed by $\Delta k(\varepsilon) = \pm 2/3d + \sqrt{3}/a_0(1+\nu)\varepsilon$. Because Δk depends on the energy gap, it is found that the band gap of a $p = 1$ type nanotube increases with strain, whereas the band gap of a $p = -1$ type nanotube decreases. It is clear that the chirality strongly affects the angle between $dK_{D1,D2}/d\varepsilon$ and the

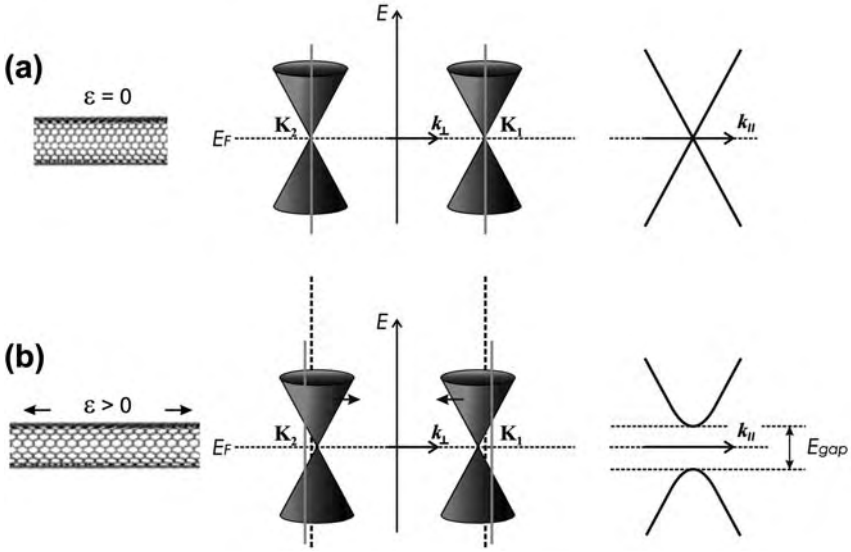

Figure 2.6 Stretching a $p = 0$ carbon nanotube. The quantized $k_\perp$ values are represented by the vertical (solid) lines intercepting the dispersion cones near K_1 and K_2. (a) For unstrained $p = 0$ nanotubes allowed k intercept the Dirac points and the 1D subbands near K_1 and K_2 have zero band gap. (b) Both the Dirac points and the quantized $k_\perp$ values shift when the nanotube is strained ($\varepsilon > 0$). Band gaps open in the 1D subbands. Note that subbands remain degenerate due to k, $-k$ symmetry.

line of allowed $\vec{k}$ states. For example, for the discussed zigzag nanotubes the lines of allowed $\vec{k}$ move perpendicular to the Dirac cones, whereas for armchair nanotubes ($\theta = 30°$) they move in parallel and no strain-dependent band gap tuning occurs.

The most general case of a chiral SWNT with an arbitrary chiral angle θ has been discussed by Yang and coworkers [51, 53]. In Figure 2.7 we show schematically the mechanical band gap tuning for a generic $p = -1, 0, +1$ SWNT with chiral angle θ. By applying strain the K_D points become shifted (see full black arrows in Figure 2.7), which leads to an increase (for $p = 0, +1$) or decrease (for $p = -1$) of Δk. This shift in k-space is most generally given by [51, 53]

$$\Delta k(\varepsilon) = \Delta k_0 + r_0^{-1}[(1+\nu)\varepsilon\cos(3\theta) + \zeta\sin(3\theta)], \tag{14}$$

where ζ is an added torsion of the nanotube. Within a first-order approximation, the torsion ζ can just be treated like a *strain* along the nanotube circumference (perpendicular to the nanotube axis). As long as Δk is smaller than the 1D subband spacing δk (Figure 2.7), a linear (strain-dependent) band gap opening ($p = 0, +1$) or closing ($p = -1$) is expected. This is illustrated in Figure 2.7a. However, if Δk exceeds δk, which can either be due to (i) substantially high strain ε or (ii) very large nanotube diameters (consequently leading to small $\delta k = 2/d$), an oscillatory

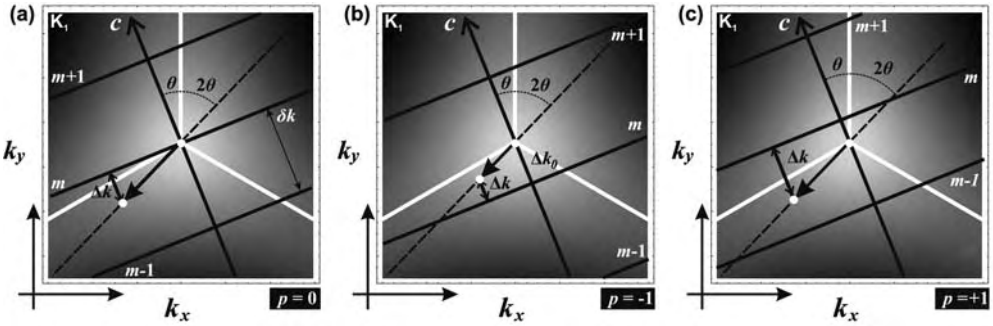

Figure 2.7 Band gap tuning in single-walled carbon nanotubes with chiral angle θ, chiral vector $\vec{c}$ and different family types p = 0, −1, +1, (a), (b) and (c) respectively. The relative strain-dependent shift between allowed k states and K points is depicted.

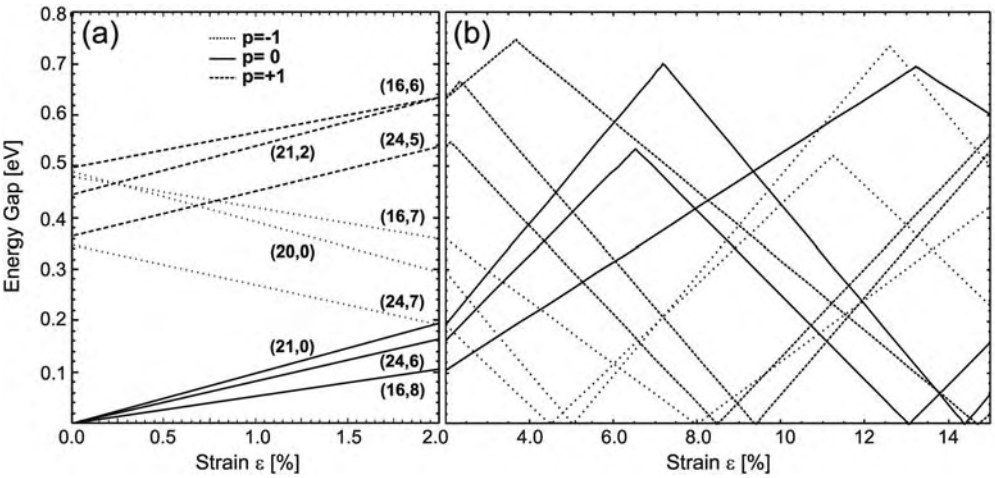

Figure 2.8 Energy band gap as a function of applied axial strain ε for different chiralities, including different nanotube family types. Part (a) shows the linear regime, whereas in (b) the non-linear regime is highlighted. Note the different strain scales.

response is found [54]. Figure 2.8 shows the mechanically induced band gap tuning of nanotubes for different chiral indices (n_1, n_2) including different families in the linear (Figure 2.8a) and "non-linear" regime (Figure 2.8b).

The full range of electromechanical behavior in nanotubes is summarized within the Yang model by

$$E_{\text{gap}}(\varepsilon, \zeta) = |p|\frac{2\gamma_1 a_0}{\sqrt{3}d} + \text{sign}(2p+1)3\gamma_1[(1+\nu)\varepsilon\cos(3\theta)+\zeta\sin(3\theta)], \tag{15}$$

where γ_1 is the tight-binding hopping integral (≈ 2.6 eV), $a_0 \approx 2.49$ Å is the graphene lattice unit vector length, and ζ is an additional torsion. Most important for the strain sensitivity is the change in band gap as a function of strain, which follows as

$$\frac{\mathrm{d}E_{\mathrm{gap}}(\varepsilon)}{\mathrm{d}\varepsilon} = \mathrm{sign}(2p+1)3\gamma_1(1+\nu)\cos(3\theta). \tag{16}$$

The maximum strain-induced band gap change in nanotubes, by assuming $\gamma_1 \approx 2.6$ eV and $\nu \approx 0.2$, is approximately 95 meV per 1% strain. It is noteworthy that Klein and Eggert [55] refined the Yang model by also including curvature effects, which are most important to describe small band gap ($E_{\mathrm{gap}} < 50$ meV) semiconducting nanotubes. They found for unperturbed small band gap nanotubes a mechanically induced band gap dependence given by

$$E_{\mathrm{gap}}(\varepsilon,\zeta) = \left|\left[\frac{\gamma_1 a_0^2}{4d^2} - \frac{\sqrt{3}\alpha_0}{2}\left(\frac{d\gamma_1}{da_0}\right)\varepsilon\right]\cos(3\theta) - \frac{\sqrt{3}a_0}{2}\left(\frac{\mathrm{d}\gamma_1}{\mathrm{d}a_0}\right)\zeta\sin(3\theta)\right|, \tag{17}$$

where $\mathrm{d}\gamma_1/\mathrm{d}a_0 \approx 3.5$ eV/Å. The dependence on strain or torsion is again linear. However, the maximum value for the strain-induced band gap change in nanotubes is shifted to approximately 75 meV per 1% strain [55].

Both theoretical models on the electromechanical properties of carbon nanotubes do not include electron–electron interaction. This has further been included by Gloor and Mila [56, 57], who finally showed that even armchair nanotubes exhibit a small band gap increase of a few meV per 1% strain when a mechanical load is applied.

2.3.4
Piezoresistance of Carbon Nanotubes

Combining the strain-dependent band gap opening [Equation (15)] with the thermal activation model for the electron transport [Equation (7)] enables the strain-dependent conductance of single-walled carbon nanotubes to be expressed. For simplicity, the series resistance R_s will be neglected in the following discussion and, moreover, it is assumed that the average transmission $|t|^2$ is independent of strain. Thus, the strain-dependent conductance can therefore be written as [51, 53, 58]

$$G(\varepsilon) = \frac{8e^2}{h}|t|^2\left[1+\exp\left(\frac{E_{\mathrm{gap}}(\varepsilon)}{k_{\mathrm{B}}T}\right)\right]^{-1} \tag{18}$$

and

$$E_{\mathrm{gap}}(\varepsilon) = |p|\frac{2\gamma_1 a_0}{\sqrt{3}d} + \mathrm{sign}(2p+1)3\gamma_1[(1+\nu)\varepsilon\cos 3\theta], \tag{19}$$

where γ_1 is the tight-binding hopping integral (≈ 2.6 eV), $a_0 \approx 2.49$ Å is the graphene lattice unit vector length, d is the nanotube diameter, θ is the chiral angle, and $p = 0, \pm 1$ labels the nanotube family. Note that here torsion has been neglected [51].

In Figure 2.9a the piezoresistive gauge factor, defined by $\beta_{GF} = \Delta R(\varepsilon)/R_0\varepsilon^{-1}$, is plotted as function of strain ε for different single-walled carbon nanotubes indicated by their chiral indices (n_1, n_2). The theoretical model has been extended by including an additional resistance (the series resistance R_s) in series leading to on effective resistance of the form $R(\varepsilon) = R_s + R_1\,[1 + \exp(\tilde{E}_{gap}\varepsilon/k_B T)]$, where $R_1 = 8e^2|t|^2/h$ and $\tilde{E}_{gap} = \mathrm{sign}(2p + 1)[3\gamma_1(1 + \nu)\cos 3\theta]$ is the band gap opening per applied strain. Here, we assumed a transmission coefficient $|t|^2 = 0.25$ and varied the series resistance between $R_s = 250$ and 350 kΩ (leading to the gray areas in Figure 2.9a). Note that (i) examples from all three nanotube families $p = 0, \pm 1$ are shown, (ii) negative and positive gauge factors are found and (iii) the highly non-linear piezoresistive gauge factors clearly exceed the values of state-of-the-art highly doped silicon ($\beta_{GF} \approx 200$).

These rather theoretical findings are very promising and recently motivated a number of experimental studies [26, 58–62] to confirm these exceptional high gauge factors.

Most recently, Grow et al. [60] studied the electromechanical response of semiconducting and small band gap semiconducting (SGS) SWNTs adhering to a silicon nitride surface. They found gauge factors of down to –400 and up to 850 for semiconducting and SGS SWNTs, respectively. In an earlier experiment, Cao et al. [26] stretched metallic, SGS and semiconducting single-walled carbon nanotubes suspended between a surface micromachined cantilever and a platform. Cao et al. observed, for all three family types, an increase in resistance under mechanical load (on the cantilever). Effective piezoresistive gauge factors between 600 and 1000 were reported.

Most of the available experimental data [26, 58–60] are plotted in Figure 2.9b. The overall non-linear characteristic of the piezoresistance of single-walled carbon nanotubes agrees well in most cases with the theoretical model and most important the measured gauge factors are also significantly higher than state-of-the-art materials, clearly confirming the theoretical expectations. However, a direct comparison between Figure 2.9a and Figure 2.9b is not yet possible since too many internal parameters of the systems (i.e. test devices) are unknown. Most prominently, the chiral indices of the investigated single-walled carbon nanotube are unknown in all presented experiments, and just very recently it has been started to design structures which allow both (i) chirality assignment and (ii) electromechanical characterization. Additionally, the series resistance R_s and the overall transmission should be better controlled in order to compare directly the theoretical model and the measurements.

2.3.4.1 **Conclusion**

We conclude that the electromechanical model to describe the piezoresistance of carbon nanotubes holds to describe the experimental data qualitatively (and

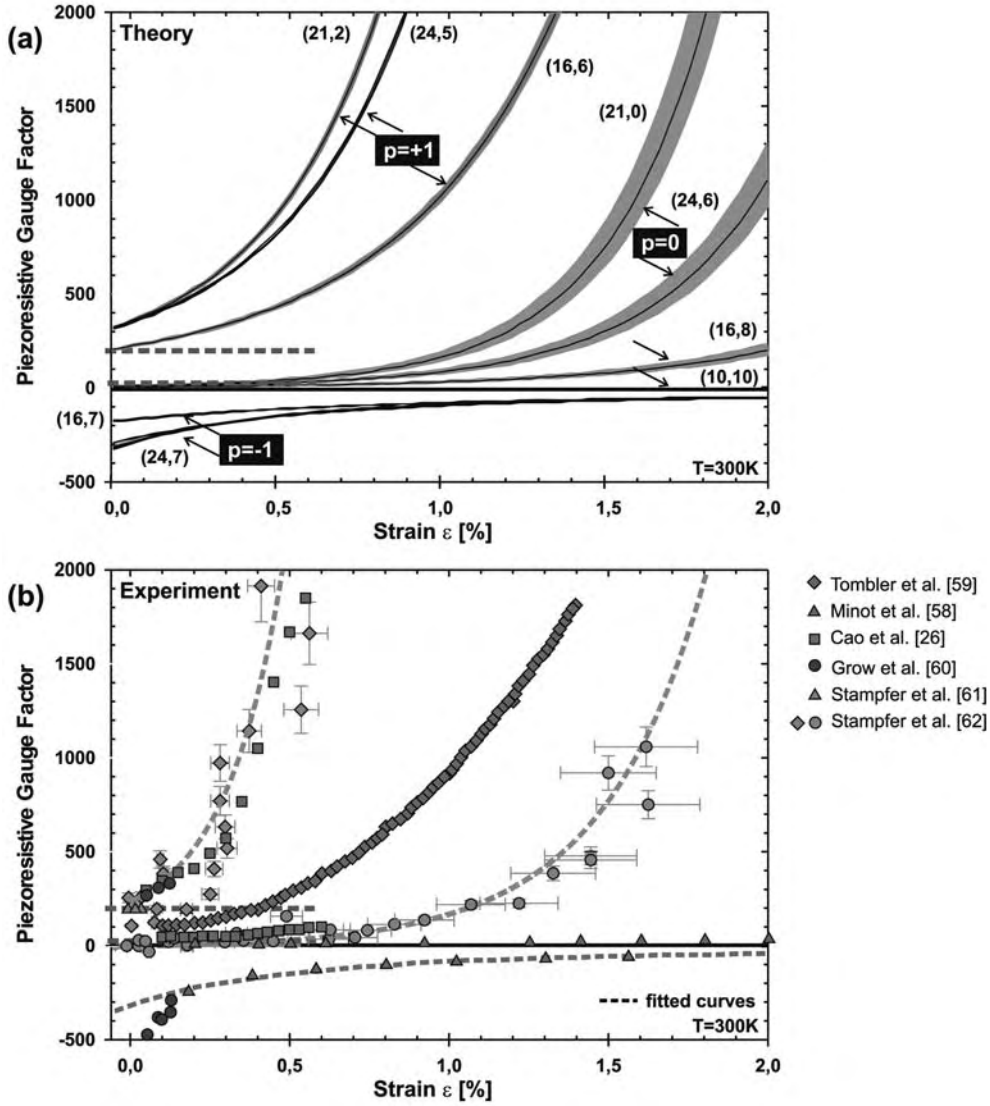

Figure 2.9 Piezoresistive gauge factors of single-walled carbon nanotubes. (a) Theoretical curves for different nanotubes labeled by their chiral indices (n_1, n_2). The dashed lines represent metal strain gauges (1–5) and state-of-the-art silicon strain gauges (≈ 200). (b) Set of experimental data which are currently available. Note that the setups used to measure the piezoresistive gauge factor are not the same for all data shown.

partially quantitatively). Moreover, it is shown that nanotubes indeed show very high piezoresistive gauge factors (up to ~2900 [62]), significantly exceeding the values of state-of-the-art materials (e.g. highly doped silicon with values of 200).

2.4 Transducers Based on Carbon Nanotubes

In Section 2.2 we have seen that transducers in general convert one form of energy or *physical information* (signal) into another form. Here, we discuss different transducer concepts where these *signal* conversion is accomplished by a carbon nanotube acting as the *active* transducer element by making use of their unique physical properties.

Before we focus exclusively on the piezoresistivity of SWNTs for electromechanical transducer concepts, we briefly discuss a matrix of possible carbon nanotube-based electrical, mechanical and optical transducers and their applications for sensing and actuation purposes. This (by no means complete) matrix is illustrated in Figure 2.10. Since optomechanical sensor and actuator systems have not yet been investigated systematically, we consequently did not fill the corresponding matrix elements. The first column labels the different input *signals* (lines) such as electrical, mechanical or optical signal, whereas the upper line labels the different output *signals*. The inset at the lower right corner illustrates schematically some of the possible physical processes, including the absorption and emission of photons, the electron (e) and hole (h) transport and applied forces and displacements to mechanically deform the nanotube. The first entry in this table (upper

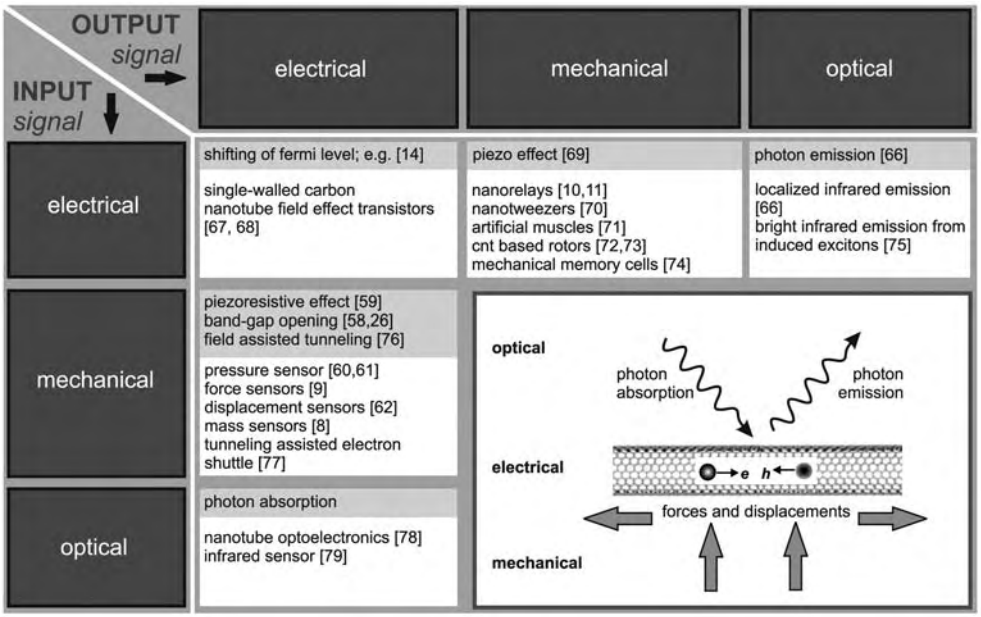

Figure 2.10 Matrix of possible carbon nanotube-based electrical, mechanical and optical transducers and their applications for sensing and actuation purposes. For more information, see the text.

left corner) is transducers converting an electrical signal into an electrical one; the most prominent example here is the nanotube-based field effect transistor [63]. The second entry (upper center) covers electromechanical actuation devices based e.g. on the so-called piezo effect [64] or on electrostatic forces (acting on suspended structures), where an electrical signal is converted to mechanical deformation or motion. Examples are nanorelays, nanotweezers, carbon nanotube-based rotors and mechanical memory cells. An example of a carbon nanotube-based switch is discussed in Section 2.4.2. Recently, optoelectronic transducers for highly localized infrared emission and absorption have attracted great interest, with considerable potential for future applications in optoelectronics [65, 66]. Finally, we will focus on electromechanical transducers for sensing purposes (center left), where a variety of different devices and concepts based on piezoresistive strain gauges or field emission have been demonstrated.

In contrast to state-of-the-art silicon-based strain gauges, SWNTs also show very interesting mechanical properties (high Young's modulus and very high elasticity). Actually, it is shown that suspended double-clamped SWNTs can be described as a piezoconducting string [58, 59]. This combination of strong piezoconductance and the string-like mechanical response of a suspended SWNT allows, among interesting test devices, new concept of electromechanical transducers[21)].

In the following we discuss basic electromechanical transducer concepts based on non-suspended and suspended SWNTs (Section 2.4.1), including concepts which are close to the concepts of state-of-the-art strain sensing and we present new devices based on SWNTs (Sections 2.4.2–5).

2.4.1
Electromechanical Transducer Concepts Based on Nanotubes

The substitution of silicon-based strain gauges by carbon nanotubes integrated in state-of-the-art MEMS device concepts is definitely most straightforward for SWNT-based nanodevices. This approach leads to the so-called transducer concept based on non-suspended SWNTs (i.e. nanotubes resting on a substrate material), which is illustrated schematically in Figure 2.11. An electrically connected mechanically fixed SWNT is placed on a membrane or any other mechanically deformable substrate in order to sense the strain on the surface of the substrate, which subsequently is (assumed to be) also present at the nanotube. By electrically measuring the conductance change, due to the significant piezoresistive gauge factor, the external strain (or deformation) can be detected. Note that in the first place this setup is used to study the electromechanical properties of carbon nanotubes adhering to a substrate in the small strain regime [60, 80]. However, if one is interested in investigating the electromechanical properties for larger strains, the configuration based on suspended carbon nanotubes is better suited.

Nanoscale devices based on suspended carbon nanotubes have attracted great interest in the last few years [45, 58, 59, 81, 82]. This is mainly due to the unique

21) Note that the broad emerging field of carbon nanotube-based resonators is not considered in this chapter.

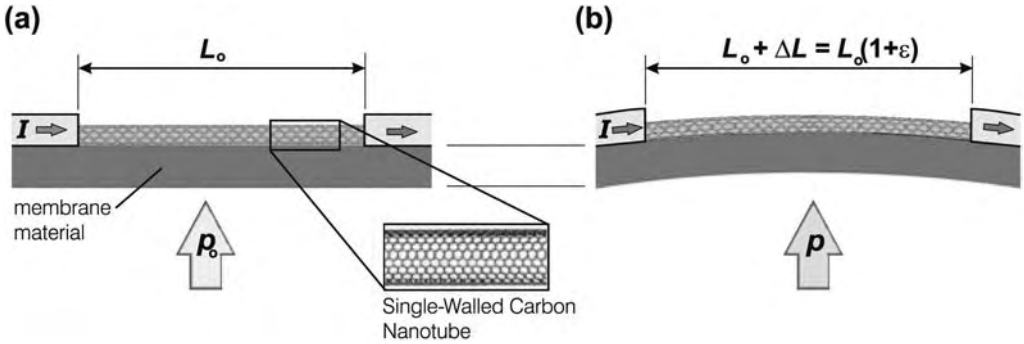

Figure 2.11 Schematic illustration of the basic transducer concept based on a non-suspended carbon nanotube; also used to investigate the electromechanical transport properties of single-walled carbon nanotubes. (a) An individual SWNT, which adheres to a membrane, is electrically connected and mechanically clamped (fixed) by two electrodes that are separated by L_0. (b) Applying a differential pressure, $\Delta p = p - p_0$, leads to a membrane deflection w_0, which results in straining the nanotube by $\varepsilon = \Delta L / L_0$.

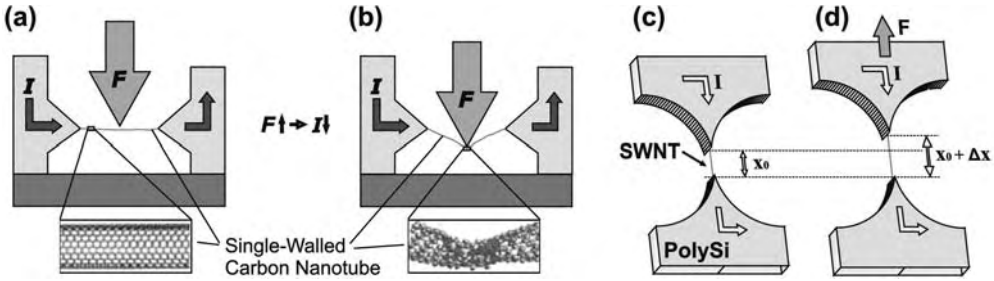

Figure 2.12 Schematic illustration of basic transducer concept based on a suspended carbon nanotube. (a, b) By applying an external force perpendicular to the suspended nanotube, the tube becomes locally deformed (see inset in b; adapted from [59]) and strained at the branches. Transducer concept based on the uniaxial straining of an SWNT. (c, d) Schematic illustration of a double-clamped SWNT, before and while uniaxially straining.

mechanical properties of nanotubes and their great potential for future high-frequency NEMS devices, such as tunable high-frequency resonators [81, 82], with potentially high mechanical quality factors. However, few studies have been performed to investigate the piezoconductance of these systems [26, 58, 59, 62]. We will show that SWNTs, combing high elasticity and pronounced piezoconductivity have an outstanding potential for future nanoscaled devices.

The basic transducer concepts based on suspended SWNTs is illustrated in Figure 2.12. In Figure 2.12a and b we show an electrically connected mechanically suspended double-clamped SWNT, which can be used to detect forces acting perpendicular to the nanotube. In this context, the carbon nanotube can be thought of as a piezoconducting string. By applying a force to the nanotube (string) the

nanotube becomes locally deformed (see inset in Figure 1.12b), which actually may result also in a local transition from sp^2 carbon-carbon bonding towards sp^3 hybridization [59]. Moreover, the strained SWNT leads to uniformly strained nanotube side branches, which finally may lead to strain-dependent band gap changes [26, 58] as discussed in Section 2.3. This transducer allows one to examine and utilize the high-strain regime (including the corresponding non-linearity of the piezoconductance) for sensing purposes. Moreover, it permits measurement areas down to the nanoscale limit since the contact point is basically just limited by the nanotube diameter (in the order of 1–3 nm). However, the major disadvantage of this setup is that kinking and local deformations are present, which may alter some physical properties and may damage the nanotube in the long run. Figure 2.13 summarizes Tombler et al.'s [59] first electromechanical experiment on an individual SWNT. An atomic force microscope (AFM) tip was used to apply locally a force on the nanotube (Figure 2.13a), leading to an effective strain in the nanotube branches. Tombler et al. showed a reproducible conductance change in the range of two orders of magnitude for approximately 3% strain. They explained this effect by a partially transition from sp^2 to sp^3 hybridization of the nanotube bonding.

In Figure 1.12c and d an alternative device concept is illustrated, which circumvents these problems of local deformations. A suspended SWNT integrated into a micro- or nanoelectromechanical structure (an example of such a fabricated structure is shown in Figure 3.17c) can be unixially strained by displacing the non-anchored structure (illustrated in Figure 1.12c and d). This concept, which is at

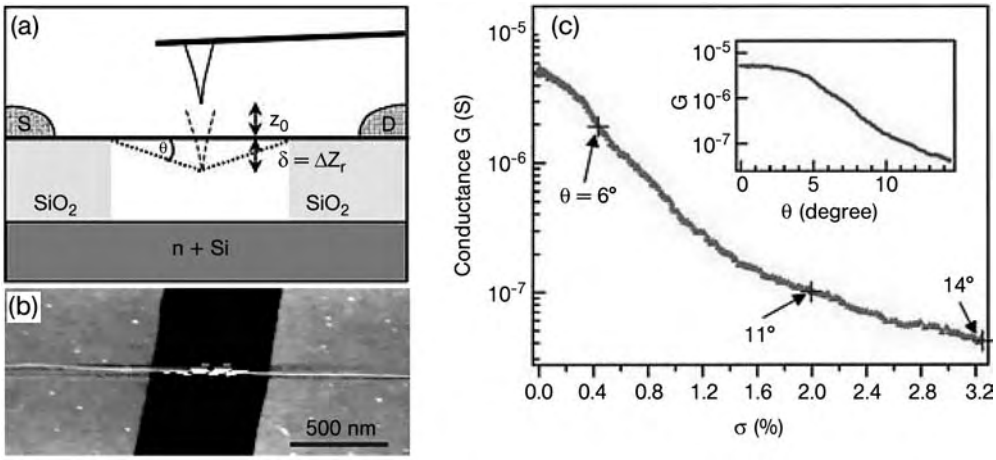

Figure 2.13 (a, b) An SWNT partly suspended over a trench for electromechanical measurements. (a) Side-view of the AFM pushing experiment. The tip is centered above the SWNT suspension by slowly zooming into the tube suspension during real-space imaging. (b) AFM image of an SWNT with suspended length $L \approx 605$ nm. (c) Electrical conductance versus mechanical deformation for a manipulated SWNT. Experimental result of conductance (G) of the SWNT sample versus strain (σ) in the suspended part of the nanotube. Inset, conductance (G) versus bending angle (θ). Images taken from Reference [59].

least from a technological point of view far more complicated, has a series of benefits: There are no local deformations (i.e. kinking) present when straining the nanotube and moreover integration into MEMS structures allows one to introduce forces or displacements via state-of-the-art MEMS concepts. Additionally, this setup permits pure uniaxial straining of nanotubes or nanowires, which further allows systematic studies on e.g. tunable nanotube-based resonators, strain-dependent Raman measurements and optoelectronic applications. This transducer system may actually open many exciting future experiments to evaluate the interaction between mechanics, electronics and optics in mesoscopic systems.

Before discussing the first realizations of nanoelectromechanical systems, which make use of strain-dependent band gap tuning, we would like to start with two examples, based on electrostatic nanotube actuation.

2.4.2
Carbon Nanotube Relay

Here we briefly review a multi-walled carbon nanotube (MWNT) three-terminal nanorelay studied and fabricated by Lee et al. [10]. A schematic illustration of the three-terminal nanorelay is shown in Figure 2.14a. A conducting MWNT is connected to a source (S) electrode and suspended above the surface of the substrate, where gate (G) and drain (D) electrodes have been patterned. A scanning electron image (top view) of a fabricated device is shown as an inset in Figure 2.14b. Charge is induced in the suspended nanotube by applying a potential between the source and the gate electrode. The resulting capacitive force between the nanotube and the gate bends the nanotube (see state b in Figure 2.14a) and finally brings the

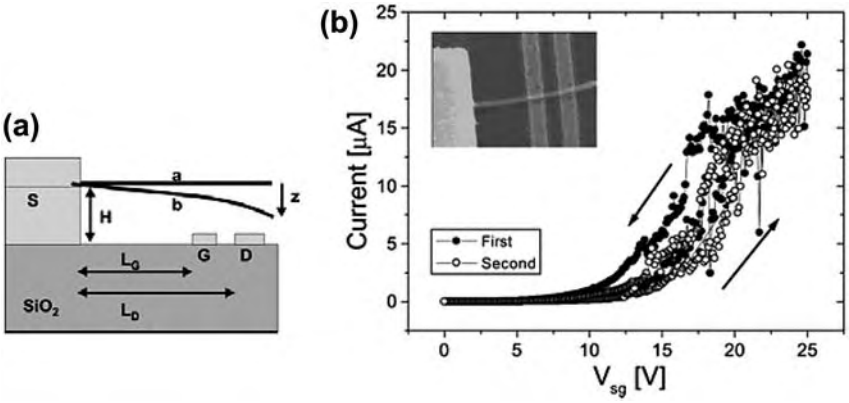

Figure 2.14 (a) Schematic diagram of a carbon nanorelay device. The device consists of a multi-walled nanotube held by a source electrode (S) and a suspended above gate (G) and drain (D) electrodes (typical geometry: $H = 150\,\text{nm}$, $L_G = 1\,\mu\text{m}$ and $L_D = 1.5\,\mu\text{m}$). (b) I–V_{sg} characteristics of a nanorelay consisting of a nanotube initially suspended approximately 80 nm above the gate and drain electrodes. The applied source–drain voltage (V_{sd}) is 0.5 V. Images taken from Reference [10].

nanotube end into electrical contact with the drain electrode, which is patterned next to the gate electrode. The electromechanical properties of the nanotube relay were investigated by measuring the current–gate voltage (I–V_{sg}) characteristics, while applying a constant source-drain voltage. Figure 2.14b shows the I–V_{sg} characteristics of a fabricated nanotube relay with an initial height difference between the CNT and drain electrode of approximately 80 nm. The drain current starts to increase non-linearly when the gate voltage reaches approximately 3 V, which clearly is a signature of electron tunneling as the distance between nanotube and drain electrode is decreased, due to the electrostatic attraction by the gate contact. The exponential increase changes to a resistance-based linear increase at a voltage of approximately 20 V. Here, it is assumed that the nanotube is in weak physical contact (contact with an adsorbed layer on the electrode surface) with the underlying drain electrode. This gate-dependent nanotube deflection is reversible (see black and white data points in Figure 2.14b).

These nanotube-based switches have considerable potential for high-frequency systems. Resonant frequencies in the range of low GHz and switching times in the sub-nanosecond regime are realistic goals for further device improvements.

2.4.3
Rotational Actuators and Sensors Based on Carbon Nanotubes

A second example of a multi-walled carbon nanotube device operated by electrostatic forces is shown in Figure 2.15. Fennimore et al. [72] demonstrated a multi-walled nanotube bearing for a small plate that can be thought of as acting as a sub-microelectromechanical mirror, shown in Figure 2.15a. By applying quasi-static DC stator voltages the metallic rotor is demonstrated to "walk" through a complete rotation as shown in Figures 2.15c–j. This device worked over repeated rotations. The authors expect their nanotube-based rotor system to be relevant also for ultra-high-density optical sweeping and switching. This nanoelectromechanical system is, moreover, expected to work up to fairly high frequencies due to high torsional force constants (intershell sliding) and the very small mass involved. Later, Meyer et al. [73] replaced the MWNT by a SWNT and proved the same functionality. Moreover, the configuration had been changed to allow diffraction transmission electron microscope studies to determine the SWNT chiral indices [73].

A very similar MWNT device (Figure 2.16) was later fabricated by Cohen-Karni et al. [54] in order to study the electromechanical sensing properties of carbon nanotubes. A suspended MWNT is clamped by the source and drain electrode and a mechanical torsion ζ is applied by an AFM tip acting on a metal paddle fixed on the suspended nanotube. The authors assume that both the torque and the electron current are predominantly carried by the outermost shell of the MWNT. Thus, within this system the clamped MWNT can be thought of as a very large diameter SWNT. In contrast to small-diameter SWNTs, where Δk is smaller than the subband spacing $\delta k = 1/r$ (see e.g. Figure 2.7a), for a large-diameter SWNT δk can be significantly smaller than Δk. Consequently, the linear band gap changes

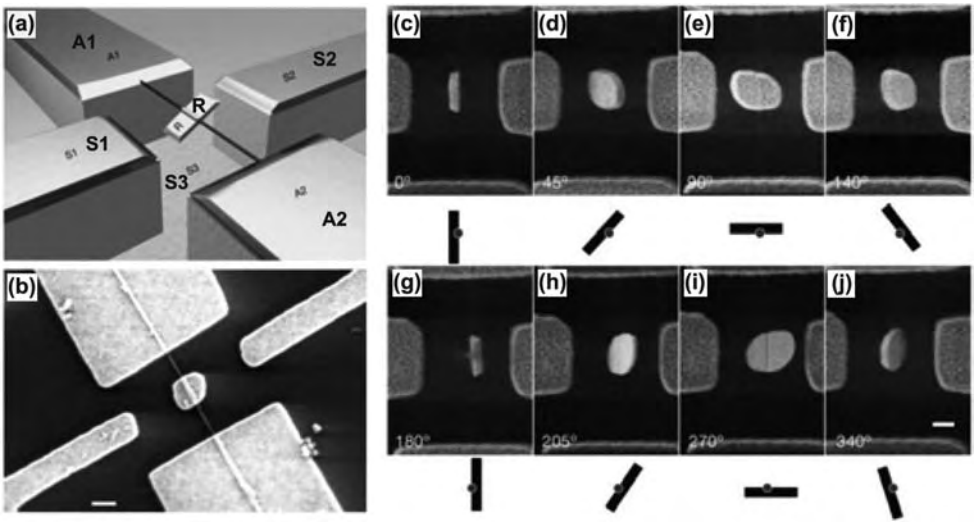

Figure 2.15 Schematic diagram of the multi-walled carbon nanotube (MWNT)-based actuator. A metal plate rotor (R) is attached to an MWNT, which is as a bearing anchored by A1 and A2. The rotation can be electrostatically driven by applying a potential via the stator electrodes S1, S2 and S3. (b) Scanning electron microscope (SEM) image of the nanodevice just before the final release. (c–j) Series of SEM images of the mirror plate at different angles induced by different stator voltages. The schematic diagrams located beneath illustrate the angular position of the mirror. Images taken from Reference [72].

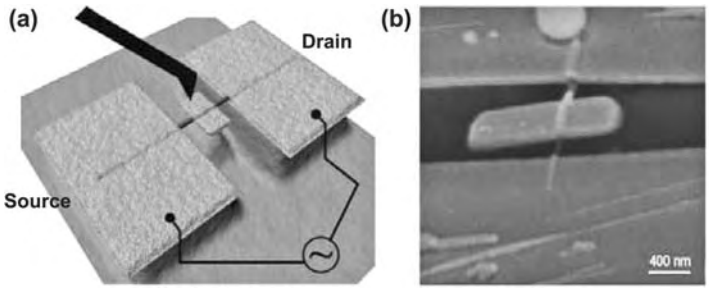

Figure 2.16 Nanotube-based torsional nanoelectromechanical system for the study of torsional electromechanical properties of carbon nanotubes. (a) Schematic illustration of the device and the measurement set-up. (b) SEM image of such a device. Images taken from Reference [54].

$\Delta E(\varepsilon, \zeta)$ with strain ε or torsion ζ break down for large diameters, where the nanotube becomes metallic at each torsion angle for which a subband intersects a K point. This finally leads to periodic metal–semiconductor transitions with a torsional angular period $\delta\phi = 4r_0L/d^2 \sin^3\theta$, where L is the nanotube length, d is the diameter and r_0 is the unstrained C–C bond length [54]. Figure 2.17 shows

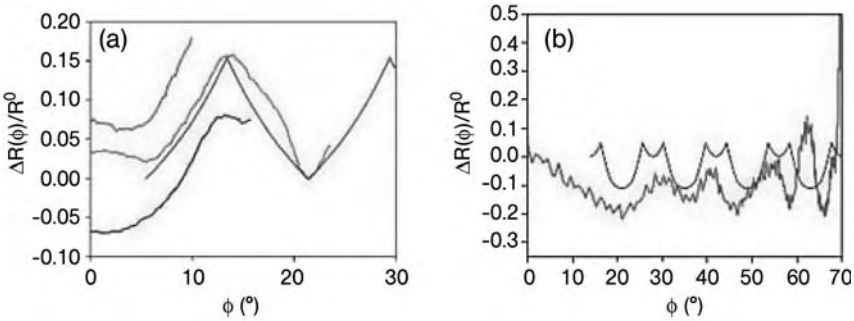

Figure 2.17 Torsional electromechanical measurements for two representative devices (a) and (b). The relative change in resistance ($\Delta R/R_0$) is plotted as a function of the torsion angle ϕ. Device (a) is assumed metallic based on the overall decrease in conductance upon torsion, whereas device (b) is assumed semiconducting based on the initial decrease and increase in conductance. The dipped peaks in the theoretical curves of device (b) arise from a phase lag of 120° between the periodic metal–semiconductor transitions expected for the two nanotube segments on either side of the pedal as they are simultaneously twisted in opposite directions. Images taken from Reference [54].

such (onsets) of periodic conductance oscillations for two different devices [(a) and (b)]. The black lines have been modeled by relating the changes in conductance with torsion to the induced change in the band gap, which affects the barrier height for the thermally activated transport [see e.g. Equation (7)].

In summary, Cohen-Karni et al. have studied the torsional electromechanical response of carbon nanotubes. The experimental results nicely confirm the theoretical model, which has been discussed in Section 2.3. Finally, it is expected that the carbon nanotubes can act as torsional transducers in nanoelectromechanical systems where oscillatory behavior could resemble the response of an interferometric sensor [54].

2.4.4
Pressure Sensors Based on SWNTs

Pressure sensors were in the early 1980s [83] the first micromachined products and the miniaturization of micromachined pressure sensors over the ensuing decades has led to successful sensor devices with better performance, improved reliability, lower cost and lower power consumption [84]. However, further downscaling becomes increasingly difficult and the use of SWNT-based strain gauges might be an interesting approach to overcome these so-called scaling problems [13]. The concept we would like to discuss is schematically illustrated in Figure 2.18. An individual SWNT is mounted on a scalable membrane acting as an active strain gauge. By applying an external differential pressure, the membrane (or diaphragm) is deflected and subsequently the nanotube becomes strained (see also Figure 2.11). Thus the pronounced piezoresistance of the nanotube leads to a change in the resistance, which can finally be measured electrically. Since the

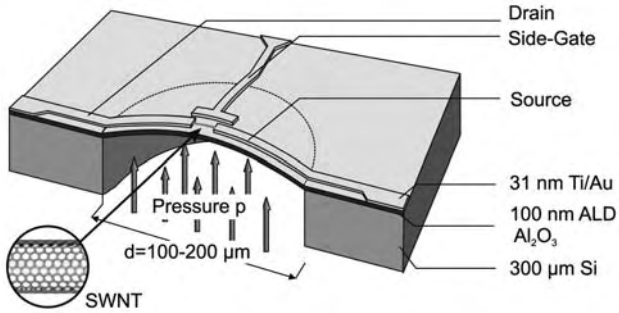

Figure 2.18 Schematic of a carbon nanotube based-pressure sensor consisting of an ultra-thin alumina membrane of diameter *d*. The single-walled carbon nanotube (SWNT) adhering to the membrane is additionally clamped by two metal electrodes and a side gate is patterned to control the electrical response of the different nanotube types. Image taken from Reference [61].

nanotube as the active sensing element has a diameter in the range of a few nm, and a length of 2–10 µm, the membrane can be potentially scaled down to the lower µm regime. This may lead to ultra-miniaturized pressure sensors based on SWNTs with a variety of promising applications ranging from low-power sensor arrays, nanoscale pressure sensors for micro- and nanobiological characterization to medical applications.

Here we briefly report on a SWNT pressures sensor device (based on membranes, in the range of a few hundred µm) to prove the feasibility and the concepts. For more details, see References [61, 80].

Figure 2.19 shows scanning electron microscope (SEM) images of a pressure sensor device based on a 100-nm thick released Al_2O_3 membrane with Ti/Au electrodes. The large gold electrodes are heading to the center area of the membrane (black disk in Figure 2.19a), where the reference alignment markers have been patterned and the individual electrodes are placed to contact individual SWNTs (e.g. Figure 2.19b). If a differential pressure (Δp) is applied the membrane becomes bulged (e.g. white light interferometer image in Figure 2.20b), leading to a membrane deflection (Figure 2.20a), which consequently leads to an isotropic strain in the inner area of the membrane (Figure 2.20b). The electromechanical response of a device based on a metallic SWNT is shown in Figure 2.21. The *I*–*V* traces in Figure 2.21a clearly show that the conductance decreases with increasing pressure. The pressure sensor characteristic is plotted in Figure 2.21b, and the strain-dependent resistance change is shown in Figure 2.21c. For the small strain regime Equation (7) can be linearized, which finally leads for metallic nanotubes to

$$R(\varepsilon) = R_0 + \frac{h}{8e^2|t|^2 k_B T}\left(\frac{\mathrm{d}E_{\mathrm{gap}}}{\mathrm{d}\varepsilon}\right)\varepsilon, \tag{20}$$

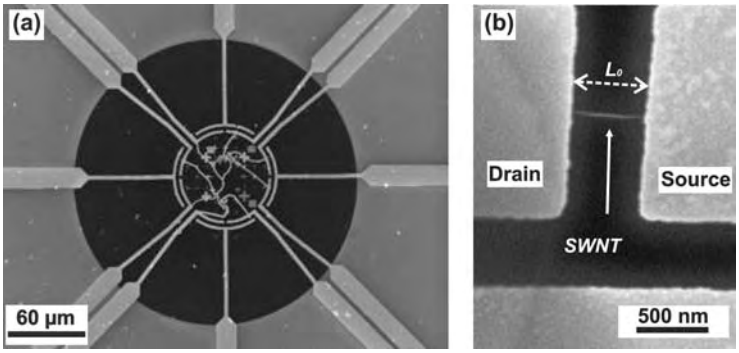

Figure 2.19 Scanning electron microscope (SEM) images of a pressure sensor device consisting of an alumina membrane [see black disc in (a)] with electrically contacted single-walled carbon nanotubes. (b) Close-up of a contacted individual single-walled carbon nanotube with an electrode separation of $L_0 \approx 500$ nm. Images taken from References [61, 80].

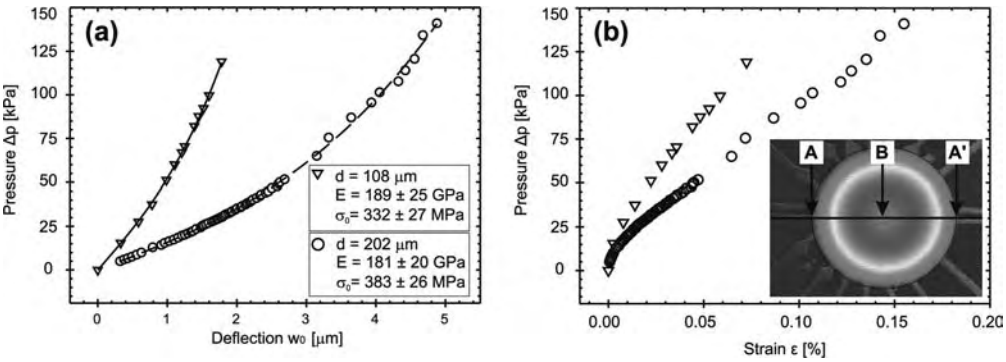

Figure 2.20 Bulge test of two alumina membranes (with different radii) to extract Young's modulus and initial in-plane stress. (a) Deflection w_0 vs. differential pressure (Δp) for 100-nm thick alumina membranes with $r_0 = 54\,\mu$m and $r_0 = 101\,\mu$m. (b) Strain vs. differential pressure relation extracted from the measurement shown in (a). The inset shows a typical white light interferometer image of the deflected membrane under load. Images taken from Reference [61].

where $R_0 = R_s + h/(4e^2|t|^2)$ and R_s is a series resistance. Thus, the strain-dependent resistance sensitivity can be extracted from a linear fit (dashed line in Figure 2.21c). The piezoresistive gauge factor of the shown SWNT given by $\beta_{GF} = \Delta R/R_0\varepsilon^{-1}$ is 210. This value is in good agreement with the theoretical considerations for low-strain SWNT operation. The value slightly exceeds the value for state-of-the-art doped-silicon strain gauges ($\beta_{GF} = 200$).

The authors expect that this concept of a nanotube-based pressure sensor can be further downscaled to allow pressure sensing on a scale of few microns, leading to a number of novel applications in the field of nanotechnology, biology and medicine.

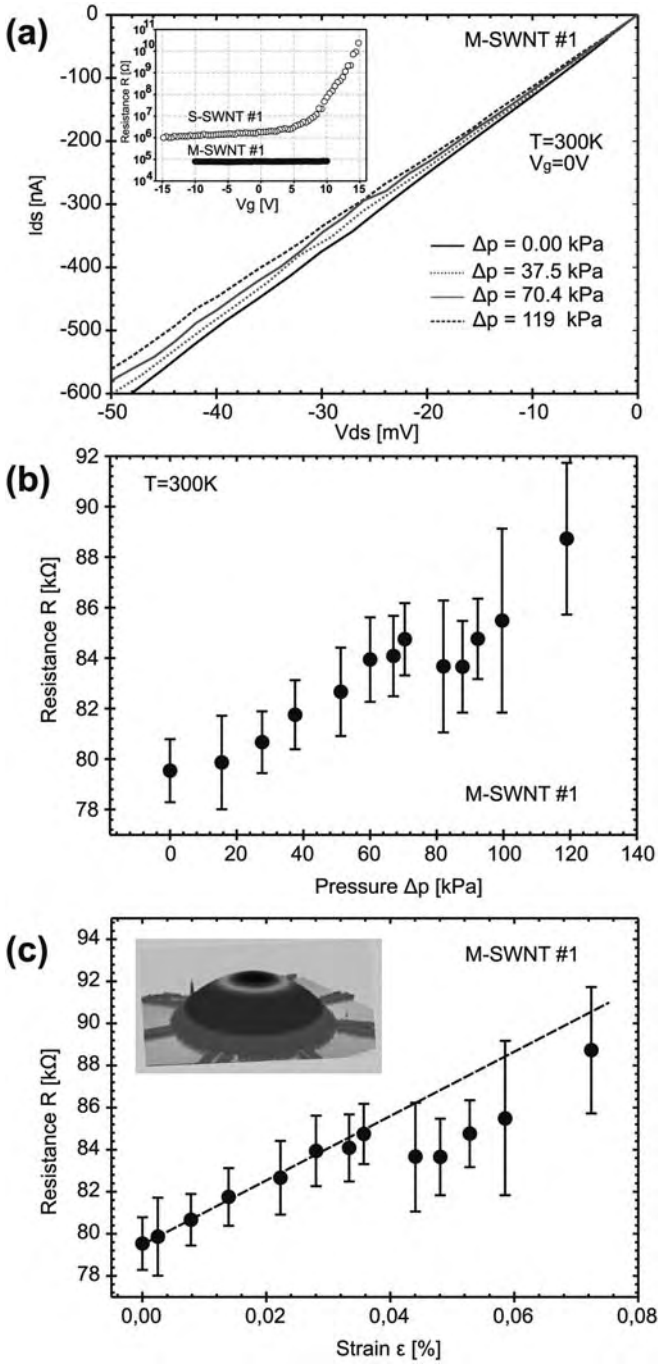

Figure 2.21 Electromechanical measurements on a metallic single-walled carbon nanotube (M-SWNT) adhering to the alumina membrane. (a) *I–V* characteristics of the metallic nanotube under different applied pressures. The inset shows a logarithmic plot of the resistance of a semiconducting (S-SWNT) and the shown M-SWNT as a function of the gate voltage. This plot proves the basic functionality of the implemented side gates (see Figure 2.19). (b) The average resistance of the M-SWNT as a function of the differential pressure, Δp, at room temperature. The inset shows the resistance change as a function of axial strain, where a linear curve is fitted (dashed line) to the measured data. Image adapted from Reference [61].

2.4.5
SWNTs for Displacement and Force Sensing

Displacement and force sensing at the nanoscale level may significantly benefit from the exceptional electrical, mechanical and electromechanical properties of SWNTs. In particular, the small dimensions of a SWNT (diameter ~1 nm and a length of up to several μm) permit a measurement area of down to approximately 1×1 nm (mainly limited by the nanotube diameter). These small dimensions are difficult to reach by most conventional methods, since the size on which deflection (or force) can be measured is (intrinsically) limited by the measurement method: (i) optical methods are limited by the wavelength; (ii) capacitive sensing is limited by area and suffers from signal loss [15]; (iii) scaling down classical piezoresistors leads to a strongly increased resistance and resistance noise at the nanoscale [86]. From this point of view, new materials (such as carbon nanotubes) and new transducer concepts for sensing deflections and local forces at the nanoscale become very interesting and promising.

Figure 2.22a and b show schematic illustrations of two examples of displacement or force sensors based on suspended SWNTs. The basic concept of the displacement sensing mechanism is illustrated in Figure 2.22c and d. A double-clamped suspended SWNT of length L_{NT} is electrically connected to two electrodes, source (S) and drain (D). Further, the SWNT is mechanically connected to the object which is measured. By deflecting the structure, e.g. a cantilever (C) (or a bridge, Figure 2.22a) by z, the SWNT is deformed and stretched (see Figure 2.22d), leading to a significant change in conductance, which is directly correlated with the deflection z. The deflection z, moreover, can be correlated to the applied force F (see Figure 2.22b). This concept has been proven by investigating test structures as shown in Figure 2.23.

For the electromechanical displacement sensing, an atomic force microscope (AFM) tip is used to apply a controlled force to the suspended metal cantilever (at the point P, as depicted in Figure 2.23b), which consequently deflects the SWNT at their center position by z. The electromechanical response and the sensor performance of a characteristic device are shown in Figure 2.24. The large non-linear resistance change is attributed to changes in the band gap of the nanotube due to the strong reproducibility of the resistance changes (see different cycles in Figure 2.24) rather than to changes in the metal-electrode contacts [51, 58]. A typical force versus displacement measurement is shown as the lower inset. By transforming the deflection z into strain $\varepsilon(z) = \sqrt{1 + (z/L_{NTB})^2} - 1$, which appears in the nanotube branches, the exponential relation between resistance change and strain [see Equation (7)] can be obtained. This is shown in the upper inset of Figure 2.24.

The authors conclude that the described sensing scheme based on suspended SWNT exhibits a relative differential resistance sensitivity of up to 27% per nm signal change. This and their small size make suspended SWNT-based sensor systems proimising for a host of new applications throuhgout the upcoming nanoworld.

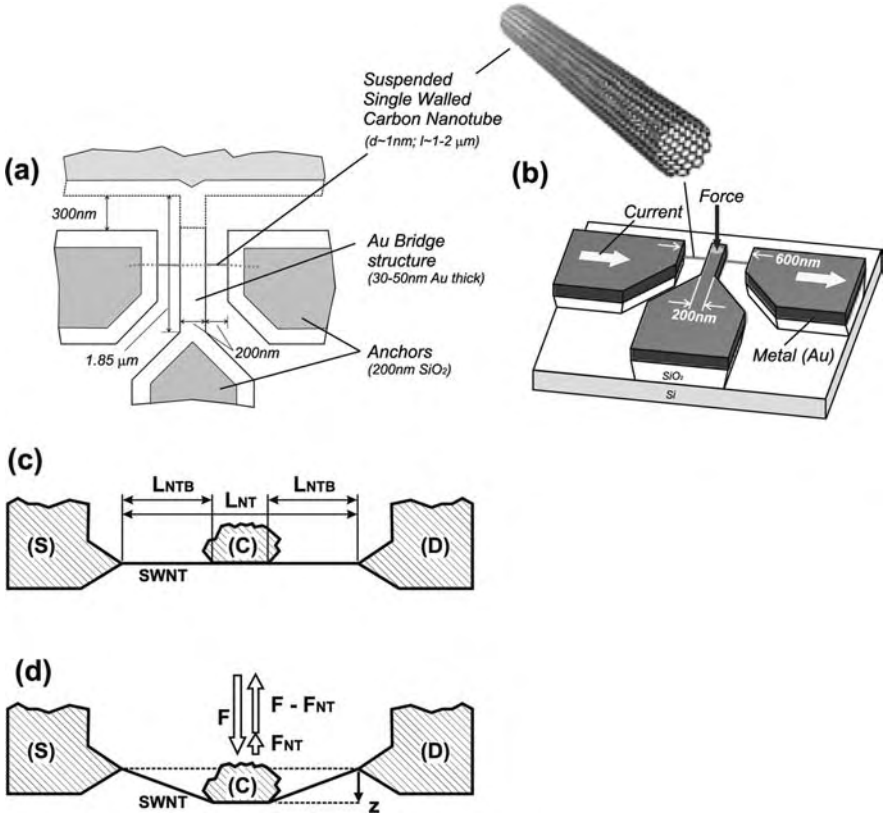

Figure 2.22 Schematic illustration of fabricated carbon nanotube-based nanoelectromechanical system: (a) bridge- and (b) cantilever-based configuration. The metal bridge or cantilever is 200 nm wide, 30–50 nm thick and 1–2 μm long. The suspended nanotubes span a trench of 600 nm. (c, d) Schematic illustrations of the proposed SWNT-based displacement sensing mechanism. (c) A double-clamped suspended SWNT of length L_{NT} and branch lengths L_{NTB} is electrically connected to source (S) and drain (D) electrodes; and the SWNT is mechanically connected to the object (C) which is measured. (d) Deflecting the structure (C) by z, including a force F, leads to stretched SWNT and a nanotube-induced back-coupling force F_{NT}. Images taken from References [62, 85].

2.5 Conclusion

Nanoelectromechanical systems based on carbon nanotubes are promising for the development of a host of novel functionalities leading to new applications in physics, engineering, biology and medicine. Electromechanical transducers, *the* key component of any electromechanical system, have been discussed. The

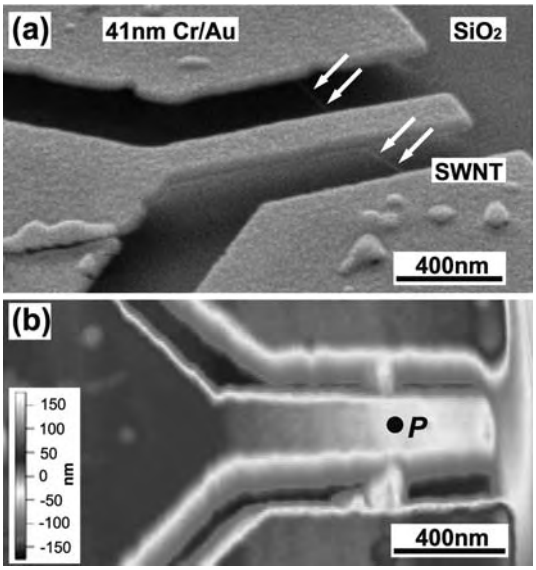

Figure 2.23 (a) SEM image of the final cantilever-SWNT based sensing device. The white arrows indicate the location of the suspended SWNT. (b) Tapping mode AFM image of the device. Note that the resolution of the AFM image is limited by the envelope of the AFM tip dimensions. Image taken from Reference [62].

information handling has been highlighted and we paid attention to the scaling down of electromechanical transducers from (macro- and) micro- to nano-dimensions, where quantum mechanical concepts may play a significant role.

The piezoresistance in classical systems has been briefly reviewed and has subsequently been extended to mesoscopic systems. Here, we introduced and discussed the strain-dependent Landauer equation to describe piezoresistance in ballistic conductors. The electromechanical properties of single-walled carbon nanotubes have been discussed in Section 2.3. Most importantly, a simple model has been shown to explain the extraordinary piezoresistance of SWNTs. The modeled piezoresistive gauge factors were compared with experimental data.

Possible carbon nanotube-based transducers are summarized in Section 2.4 and a few examples of single-walled carbon nanotube-based electromechanical transducers were presented. The implementation of a carbon nanotube relay is briefly reviewed and some rotor devices based on single- and multi-walled carbon nanotubes are discussed. Additionally, the functionality of single-walled carbon nanotube-based pressure and displacement (or force) sensors are presented.

In conclusion, single-walled carbon nanotubes, clearly one of the best studied nanostructures today, exhibit very promising properties for use as active elements

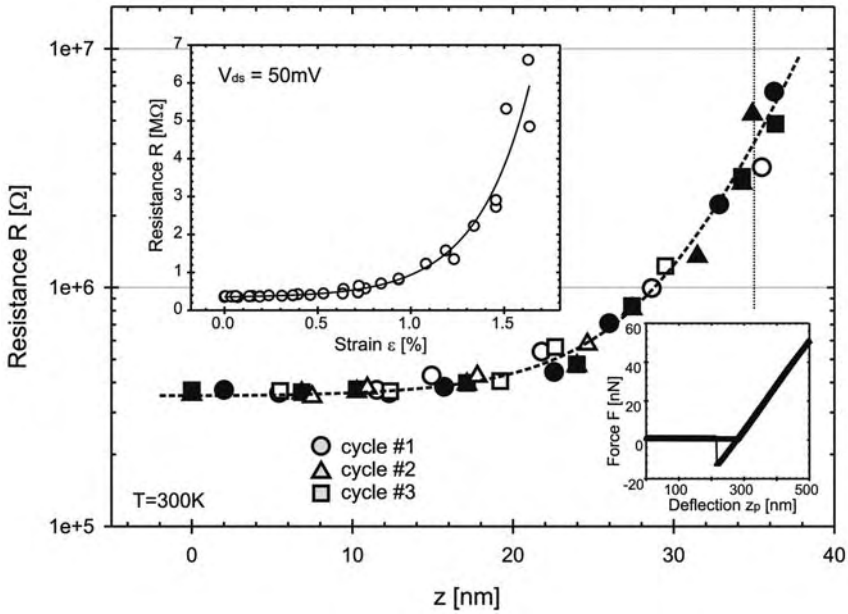

Figure 2.24 Electromechanical measurements of an electromechanical sensor device based on a metallic SWNT. The upper insert shows the resistance plotted as a function of the strain ε [see Equation (7)] in the nanotube branch. Note that all three cycles have been used for fitting (solid line). The lower insert shows a typical force versus deflection measurement performed on the cantilever-SWNT contact point (P). Image adapted from [62].

in future nanoelectromechanical systems. An increasing number of single-walled carbon nanotube-based nanoelectromechanical test devices are emerging in order to prove their functionalities. However, the shortcomings of today's fabrication and analysis methods (see Chapters 3, 4) make it very difficult to advance beyond the present level of individual demonstrators.

2.6 Acknowledgments

We are grateful to Alain Jungen, Thomas Helbling, Dirk Obergfell, Ronald Grundbacher, Ryan Linderman, Victor Bright, Marie Tripp, Sigmar Roth, Cosmin Roman, Bakir Babic, Franck Robin, Davy Graf, Paul Studerus, Renaud Leturcq, Robert Stark, David Junker, Otte Homan, Bernd Schöberle, Sybille Vuillmers and Bernhard Boser for many useful discussions and collaborations. Financial support by grant TH-18/03-1 and the Swiss National Science Foundation (20021-108059/1) is gratefully acknowledged.

2.7 List of Symbols

A	Area
$\vec{a}_i$	Unit cell vectors
$\vec{c}$	Chiral vector
d	Nanotube diameter
E_F	Fermi energy
E_{gap}	Energy band gap
e	Electron charge
$\vec{e}_i$	Unit vectors
f_0	Fermi function
G	Conductance
H	Thickness
h	Planck's constant
I, I_{sd}	Current
$K_{1,2}$	Inequivalent K points
k_B	Boltzmann constant
k_F	Fermi wavevector
$\vec{k}$	Wavevector
L	Length
M	Mode numbers
m^*	Effective mass of electrons
n	Electron density
n_1, n_2	Chiral indices
p	Nanotube family type ($p = 0, \pm 1$)
R, R_c, R_s	Resistance, contact resistance, series resistance
r_0	Membrane radius or unstrained C–C bond length
$\vec{r}_i$	Lattice vectors
T	Temperature
$\overline{T}$	Averaged transmission amplituide
t_{nm}	Transmission amplitudes
V, V_{sg}, V_{sd}	Voltage
W	Width
w_0	Membrane defelction
Y	Young's modulus
z	Cantilever deflection
β_{GF}	Piezoresistive gauge factor
δk	Subband spacing
Δp	Differential pressure
ε	Strain
ϕ	Torsion angle
γ_i	Overlap integrals
λ_{el}	Elastic mean free path
λ_F	Fermi wavelength

μ	Mobility
v_F	Fermi velocity
ρ	Resistivity
σ	Conductivity
σ_0	In-plane stress
τ	Relaxation time
θ	Chiral angle
ν	Poisson's ratio
ζ	Torsion

References

1 A. N. Cleland, *Foundations of Nanomechanics*. Springer, Berlin, 2003.
2 M. L. Roukes, *Nanoelectromechanical Systems*. In: Technical Digest of the 2000 Solid-State Sensor and Actuator Workshop, Hilton Head Island, SC, 4–8 June 2000.
3 H. G. Craighead, Nanoelectromechanical Systems, *Science*, **290** (2000) 1532–1535.
4 K. C. Schwab, M. L. Roukes, Putting Mechanics into Quantum Mechanics, *Phys. Today*, **35** (2005) 36.
5 K. L. Ekinci, M. L. Roukes, Nanoelectromechanical Systems, *Rev. Sci. Instrume.*, **76** (2005) 0611101.
6 A. Erbe, C. Weiss, W. Zwerger, R. H. Blick, Nanomechanical ResonAtor Shuttling Single Electrons At Radio Frequencies, *Phys. Rev. Lett.*, **87** (2001) 096106.
7 D. Rugar, R. Budakian, H. J. Mamin, B. W. Chui, Single spin detection by magnetic resonance force microscopy, *Nature*, **430** (2004) 329.
8 M. Nishio, S. Sawaya, S. Akita, Y. Nakayama, Carbon nanotube oscillators toward zeptogram detection, *Appl. Phys. Lett.*, **86** (2005) 133111.
9 C. Stampfer, A. Jungen, C. Hierold, Fabrication of Discrete Nano-Scaled Force Sensors Based on Single Walled Carbon Nanotubes. *IEEE Sens. J.*, **6** (2006) 613–627.
10 S. W. Lee, D. S. Lee, R. E. Morjan, S. H. Jhang, M. Sveningsson, O. A. Nerushev, Y. W. Park, E. E. B. Campbell, A Three-Terminal Carbon Nanorelay, *Nano Lett.*, **4** (2004) 2027–2030.
11 A. B. Kaul, E. W. Wong, L. Epp, B. D. Hunt, Electromechanical Carbon Nanotube Switches for High-Frequency Applications, *Nano Lett.*, **6** (2006) 942–947.
12 D. Mijatovic, J. C. T. Eijkel, A. van den Berg, Technologies for nanofluidic systems: top-down vs. bottom–up–a review, *Lab Chip*, **5** (2005) 492–500.
13 C. Hierold, From micro- to nanosystems: mechanical sensors go nano, *J. Micromech. Microeng.*, **14** (2004) 1–11.
14 S. Reich, C. Thomsen, J. Maultzsche, *Carbon Nanotubes*, Wiley-VCH, Weinheim, 2003.
15 M. S. Dresselhaus, G. Dresselhaus, P. Avouris (eds.), *Carbon Nanotubes: Synthesis, Structure, Properties and Applications*, Vol. 80, Springer, Berlin, 2001.
16 R. Saito, G. Dresselhaus, M. S. Dresselhaus, *Physical Properties of Carbon Nanotubes*, Imperial College Press, London, 2001.
17 Y. Cui, C. M. Lieber, Functional nanoscale electronic devices assembled using silicon nanowire building blocks, *Science*, **291** (2001) 851–853.
18 H. W. Kroto, J. R. Heath, S. C. O'Brien, R. F. Curl, R. E. Smalley, C60: Buckminsterfullerene, *Nature*, **331** (1985) 162–163.
19 L. Ristic, *Sensor Technology and Devices*, Artech House, Boston, London, 1994.
20 G. T. A. Kovacs, *Micromachines Transducers Sourcebook*, WCB/McGraw-Hill, New York, 1998.

21 M. Elweenspoek, R. Wiegermink, *Mechanical Microsensors*, Springer, Berlin, 2001.

22 J. A. Wheeler, W. H. Zurek, *Quantum Theory and Measurement*, Princton, NJ: Princeton Uinversity Press, 1982.

23 C. Hierold, B. Clasbrummel, D. Behrend, T. Scheiter, M. Steger, K. Opeermann, H. Kapels, E. Landgraf, D. Wenzel, D. Etzrodt, Low Power Integrated Pressure Sensor Systems for Medical Applications, *Sens. Actuators A*, **73** (1999) 58–67.

24 M.-H. Bao, *Micro Mechanical Transducers*, Handbook of Sensors and Actuators, Elsevier, Amsterdam, 2000.

25 J. Y. W. Seto, Piezoresistive properties of polycrystalline silicon, *J. Appl. Phys.*, **47** (1976) 4780.

26 J. Cao, Q. Wang, H. Dai, Electromechanical properties of metallic, quasimetallic, and semiconducting carbon nanotubes under stretching, *Phys. Rev. Lett.*, **90** (2003) 157601–157604.

27 C. S. Smith, Piezoresistance Effect in Germanium Silicon, *Phys. Rev.*, **94** (1954) 42–49.

28 C. Joachim, J. K. Gimzewski, A. Aviram, Electronics using hybrid-molecular and mono-molecular devices, *Nature*, **408** (2000) 541.

29 N. W. Ashcroft, N. D. Mermin, *Solid State Physics*, Saunders College Publishing, *New York*, 1976.

30 C. Herring, Transport properties of a many-valley semiconductor, *Bell. Syst. Tech. J.*, **34** (1955) 237–290.

31 C. Herring, E. Vogt, Transport and Deformation-Potential Theory For Many-Valley Semiconductros with Anistropic Scattering, *Phys. Rev.*, **101** (1956) 944–961.

32 P. Kleimann, B. Semmache, M. Le Berr, D. Barbier, Stress-dependent hole effective mass and piezoresistive properties of p-type monocrystalline and polycrystalline silicon, *Phys. Rev. B*, **57** (1998) 8966–8971.

33 J. C. Hensel, G. Feher, Cyclotron Resonance Experiments in Uniaxially Stressed Silicon: Valence Ban Inverse Mass Parameters and Deformation Potentials, *Phys. Rev.*, **129** (1963) 1041–1062.

34 A. R. Charbonnieras, C. R. Tellier, A kinetic formulation of piezoresistance in N-type silicon: Application to non-linear effects, *Eur. Phys. J. AP*, **7** (1999) 1–11.

35 D. Long, Stress Dependence of the Piezoresistance Effect, *J. Appl. Phys.*, **32** (1961) 2050–2051.

36 K. Matsuda, K. Suzuki, K. Yamamura, Y. Kanda, Nonlinear piezoresistance effects in silicon, *J. Appl. Phys.*, **73** (1993) 1838–1847.

37 J. M. Chen, N. C. MacDonald, Measuring the nonlinearity of silicon piezoresistance by tensila loading of a submicron diameter fiber using a microinstrument, *Rev. Sci. Instrum.*, **75** (2004) 276–278.

38 K. Sato, M. Shikida, T. Yoshioka, T. Ando, T. Kawabata, Micro Tensile Test of Silicon Film having different crystallographic orientations. In: *International Conference on Solid-State Sensors, Actuators Microsystems, Transducers 1997, Chicago*, 2D1.02, 1997, pp. 595–598.

39 K. Matsuda, Y. Kanda, K. Yamamura, K. Suzuki, Nonlinearity of Piezoresistance Effect in p- and n-Type Silicon, *Sens. Actuators A*, **21–23** (1990) 45–48.

40 G. Dorda, Piezoresistance in Quantized Conduction Bands in Silicon Inversion Layers, *J. Appl. Phys.*, **42** (1971) 2053.

41 Y. Kanda, A Graphical Representation of the Piezoresistance Coefficients in Silicon, *IEEE Trans. Electron Devices*, **ED-29** (1982) 71–77.

42 R. Landauer, Spatial Variation of Currents and Fields Due to localized Scatterers in Metallic Conduction, *IBM J. Res. Deve.*, **1** (1957) 223–231.

43 R. Landauer, Spatial Variation of Currents and Fields Due to localized Scatterers in Metallic Conduction, *IBM J. Res. Dev.*, **32** (1988) 306–316.

44 S. Datta, *Electronic Transport in Mesoscopic Systems*, Cambridge Studies in Semiconductor Physics Series, Cambridge University Press, Cambridge, 1998.

45 S. Sapmaz, P. Jarillo-Herrero, Ya. M. Blanter, C. Dekker, H. S. J. van der Zant, Tunneling In Suspended Carbon Nanotubes Assisted by Longitudinal Phonons, *Phys. Rev. Lett.*, **96** (2006) 026801.

46 S. Iijima, T. Ichihashi, Single-shell carbon nanotubes of 1-nm diameter, *Nature*, **363** (1993) 603–605.
47 M. J. O'Bonnell, *Carbon Nanotubes, Properties and Applications*, CRC Press, Taylor & Francis Group, Boca Raton, FL, 2006.
48 P. R. Wallace, The band theory of graphite, *Phys. Rev.*, **71** (1947) 622–634.
49 E. D. Minot, *Tuning the Band Structure of Carbon Nanotubes*, Dissertation, Cornell Univ., 2004.
50 C. L. Kane, E. J. Mele, Size, shape, and low energy electronic structure of carbon nanotubes, *Phys. Rev. Lett.*, **78** (1997) 1932–1935.
51 L. Yang, M. P. Anantram, J. Han, J. P. Lu, Band-gap change of carbon nanotubes: effect of small uniaxial and torsional strain, *Phys. Rev. B*, **60** (1999) 13874–13878.
52 R. Heyd, A. Charlier, E. McRae, Uniaxial-stress effects on the electronic properties of carbon nanotubes, *Phys. Rev. B*, **55** (1997) 6820–6824.
53 L. Yang, J. Han, Electronic structure of deformed carbon nanotubes, *Phys. Rev. Lett.*, **85** (2000) 154–157.
54 T. Cohen-Karni, L. Segev, O. Sur-Lavi, S. R. Cohen, E. Joselevich, Torsional electromechanical quantum oscillations in carbon nanotubes, *Nat. Nanotechnol.*, **1** (2006) 36–41.
55 A. Kleiner, S. Eggert, Band gaps of primary metallic carbon nanotubes, *Phys. Rev. B*, **63** (2001) 073408–073412.
56 T. A. Gloor, F. Mila, Correlation gap in armchair carbon nanotubes, *Europhysi. Lett.*, **61** (2003) 513–519.
57 T. A. Gloor, F. Mila, Strain induced correlation gaps in carbon nanotubes, *Eur. Physi. J. B: Condens. Matter*, **38** (2004) 9.
58 E. D. Minot, Y. Yaish, V. Sazonova, J.-Y. Park, M. Brink, P. L. McEuen, Tuning carbon nanotube band gaps with strain, *Phys. Rev. Lett.*, **90** (2003) 156401–156404.
59 T. W. Tombler, C. Zhou, L. Alexseyev, J. Kong, H. Dai, L. Liu, C. S. Jayanthi, M. Tang, S. Wu, Reversible electromechanical characteristics of carbon nanotubes under local-probe manipulation, *Nature*, **405** (2000) 769–772.
60 R. J. Grow, Q. Wang, J. Cao, D. Wang, H. Dai, Piezoresistance of carbon nanotubes on deformable thin-film membranes, *Appl. Phys. Lett.*, **86** (2005) 093104.
61 C. Stampfer, T. Helbling, D. Obergfell, B. Schöberle, M. K. Tripp, A. Jungen, S. Roth, V. M. Bright, C. Hierold, Fabrication of single-walled carbon nanotube based pressure sensors, *Nano Lett.*, **6** (2006) 233–237.
62 C. Stampfer, A. Jungen, R. Linderman, D. Obergfell, S. Roth, C. Hierold, Nano electromechanical displacement sensing based on single-walled carbon nanotubes, *Nano Lett.*, **6** (2006) 1449–1453.
63 S. J. Tans, A. R. M. Verscheren, C. Dekker, Room-temperature transistor based on a single carbon nanotube, *Nature*, **393** (1998) 49.
64 R. Waser, *Nanoelectronics and Information Technology*, Wiley-VCH, Weinheim, 2003.
65 Ph. Avouris, Jia Chen, Nanotube electronics and optoelectronics, *Materi. Today*, **9**(10) (2006) 48–54.
66 M. Freitag, J. C. Tsang, J. Kirtley, A. Carlsen, J. Chen, A. Troeman, H. Hilgenkamp, Ph. Avouris, Electrically Excited, Localized Infrared Emission from Single Carbon Nanotubes, *Nano Lett.*, **6** (2006) 1425–1433.
67 S. J. Tans, M. H. Devoret, R. J. A. Groeneveld, C. Dekker, Electron–electron correlations in carbon nanotubes, *Nature*, **394** (1998) 761–764.
68 R. Martel, T. Schmidt, H. R. Shea, T. Hertel, Ph. Avouris, Single- and Mulit-wall Carbon Nanotube Field-effect Transistors, *Appl. Phys. Lett.*, **73** (1998) 2447.
69 M. Verissimo-Alves, B. Koiller, H. Chacham, R. B. Capaz, Electromechanical effects in carbon nanotubes: *ab initio* and analytical tight-binding calculations, *Phys. Rev. B*, **67** (2003) 161401.
70 P. Kim, C. M. Lieber, Nanotube Nanotweezers, *Science*, **286** (1999) 2148.
71 R. H. Baughman, C. Cui, A. Zakhidov, Z. Iqbal, J. N. Barisci, G. M. Spinks, G. G. Wallace, A. Mazzoldi, D. de Rossi, A. G. Rinzler, O. Jaschinki, S. Roth, M. Kertesz, Carbon nanotube actuators, *Science*, **284** (1999) 1340.

72 A. M. Fennimore, T. D. Yuzvinsky, W.-Q. Han, M. S. Fuhrer, J. Cumings, A. Zettl, Rotational actuators based on carbon nanotubes, *Nature*, **424** (2003) 408.

73 J. C. Meyer, M. Paillet, S. Roth, Single-Molecule Torsional Pendulum, *Science*, **309** (2005) 1539–1541.

74 T. Rueckes, K. Kim, E. Joselevich, G. Y. Tseng, C.-L. Cheung, C. M. Lieber, Carbon Nanotube-Based Nonvolatile Random Access Memory for Molecular Computing, *Science*, **289** (2000) 94–97.

75 J. Chen, V. Perebeinos, M. Freitag, J. Tsang, Q. Fu, J. Liu, Ph. Avouris, Bright Infrared Emission from Electrically Induced Excitons in Carbon Nanotubes, *Science*, **310** (2005) 1171.

76 W. A. de Heer, A. Chatelain, D. Ugarte, A Carbon Nanotube Field-Emission Electron Source, *Science*, **270** (1995) 1179.

77 L. M. Jonsson, L. Y. Gorelik, R. I. Shekter, M. Jonson, Electromechanical Instability in Suspended Carbon Nanotubes, *Nano Lett.*, **5** (2005) 1165–1196.

78 D. A. Stewart, F. Leonard, Energy Conversion Efficiency in Nanotube Optoelectronics, *Nano Lett.*, **5** (2005) 219–222.

79 J. M. Xu, Highly Ordered Carbon Nanotubes Array and IR detection, *Infrared Phys. Technol.*, **42** (2001) 485.

80 C. Stampfer, T. Helbling, A. Jungen, C. Hierold, Micromachined pressure sensors for electromechanical characterization of carbon nanotubes, *Physi. Status Solidi B*, **243** (2006) 3537–3541.

81 V. Sazonova, Y. Yaish, J. Üstünel, D. Roundy, T. A. Arias, P. L. McEuen, A tunable carbon nanotube electromechanical oscillator, *Nature*, **431** (2004) 284.

82 H. B. Peng, C. W. Chang, S. Aloni, T. D. Yuzvinsky, A. Zettl, Ultrahigh Frequency Nanotube Resonator, *Phys. Rev. Lett.*, **97** (2006) 087203.

83 K. Petersen, Silicon as a Mechanical Material, *Proc. IEEE*, **70**, (1982) 420–457.

84 W. Eaton, J. Smith, Micromachined pressure sensors: review and recent developments, *Smart Mater. Struct.*, **6** (1997) 530–539.

85 C. Stampfer, A. Jungen, C. Hierold, Single walled carbon nanotubes as active elements in nanotransducers. In: Molecular Nanostructures: XVII InternationalWinterschool/Euroconference on Electronic Properties of Novel Materials, H. Kuzmany, J. Fink, M. Mehring, S. Roth (eds.), AIP Conference Proceedings, vol. 786 2005, p. 616 619.

86 M. Wautelet, Scaling laws in the macro, micro- and nanoworlds, *Eur. J. Phys.*, **22** (2001) 601–611.

3
Carbon Nanotube Direct Integration into Microsystems

Alain Jungen, Christofer Hierold, Micro and Nanosystems ETH Zürich, Switzerland

Advanced Micro & Nanosystems Vol. 8. Carbon Nanotube Devices.
Edited by Christofer Hierold

ISBN: 978-3-527-31720-2

3.1 Introduction

The downscaling of state-of-the-art sensors leads to major changes in functionality since the surface to volume ratio of the active elements changes dramatically and can be accompanied by reduced performance. In order to overcome this miniaturization trap, novel materials and fabrication approaches have to be found in order to access the full potential of quantum effect nanostructures as opposed to miniaturized conventional devices and, thus, allow the development of nanometer-sized semiconductor devices, probes, interconnects, sensors, displays and data storage devices, to name just a few.

Since carbon nanotubes are naturally nanometer-scale objects, they may allow one to overcome complex and expensive photolithographic nanostructures through self-assembly [1, 2]. Because of this factor and their unique mechanical and electrical properties, carbon nanotubes may be ideal candidates for use in nanoscale systems. As mechanical elements, nanotubes are among the strongest known fibers, can undergo large nonlinear deformations or even buckling without permanent damage to the atomic structure and have demonstrated exceptionally high thermal conductivity. As electrical elements, single-walled nanotubes can conduct electrons at unprecedented current densities using ballistic conduction (resistance does not increase with additional length and heat generation occurs only at the electrical interfaces) [3].

Microelectromechanical systems (MEMS), or microsystems, are microscopic mechanical systems that combine mechanical, optical, electromagnetic, thermic and fluidic elements with electronics on semiconductor substrate electronics (Figure 3.1). MEMS manufacturing uses high volume, integrated-circuit-style batch processing. Because the technology encompasses several different approaches, there are multiple ways to manufacture MEMS, including surface micromachining, bulk micromachining, electro-discharge micromachining (EDM), and high aspect ratio micromachining. Silicon surface micromachining uses the same equipment and processes as the semiconductor manufacturing industry, so it was one of the first techniques widely adopted for MEMS fabrication [4]. Typical applications for this method include actuators and electrostatic motors. In silicon bulk micromachining, the device structures are created using etch techniques on bulk silicon. Applications using this technology range from mirrors to accelerometers such as those used in airbag deployment, or complex pressure sensors such as those used in aerospace applications.

There are two routes that lead to devices in the deep submicron range covering the area of nanotechnology. The first route is based on the extension of conven-

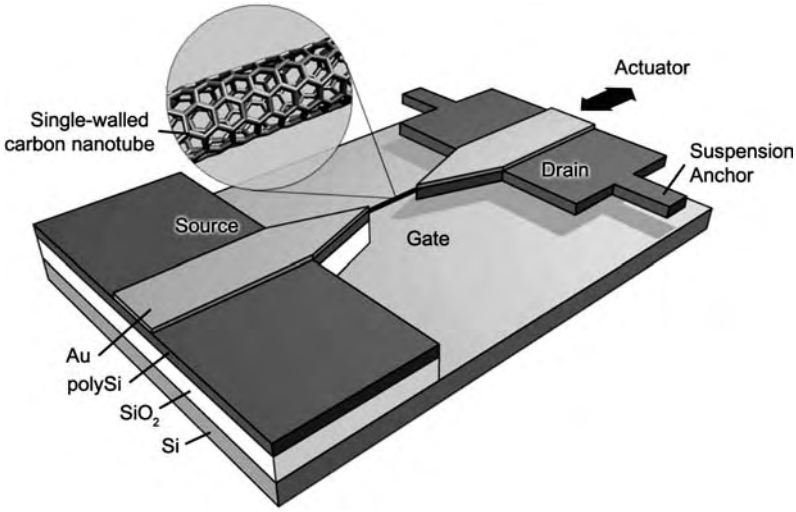

Figure 3.1 Concept of carbon nanotube-based MEMS by direct integration. A linear actuator can be operated to apply tensile loads to the nanotube.

tional micromachining. It is called the *top-down* approach (from large to small) because it starts at the wafer level and patterning proceeds by lithography and etching, to obtain features on the micron and nanometer scale. The extension of the technological capabilities towards smaller minimum feature sizes is predominantly facilitated by reducing the wavelength for photolithography, using deep UV lithography. Due to the precision required for all essential parts of the fabrication tools, the effort and the installation costs grow at an incredible pace on top-down routes.

Alternatively, the fabrication of nanosized structures can be started from individual atoms and molecules which are ordered physically or reacted chemically to obtain the desired features. This approach is referred to as the *bottom-up* technique (from small to large). This technique has attracted considerable research interest in the past decade and is still expanding. The approach utilizes physical or chemical processes to synthesize nanosized structures which are grown from individual atoms or molecules on a regular order. Bottom-up techniques are typically based on self-organization processes and, in particular, self-assembly processes. The driving forces of self-organization are, in general, based on an interplay of thermodynamics and chemical kinetics, assisted by the structure of the system to be assembled or on which the assembly takes place.

Building of new structures from the atom up is a complementary method to *top-down* nanomachining. However, because of the molecular size of the building blocks, this method is often too slow to be practicable. To attain a more acceptable building speed, self-assembly is essential. Even the self-assembly is hindered at some point of the scalable synthesis of nanosensors, so there is the need for interfacing at least at the packaging stage.

The quest for nanoscale integration is twofold: one is technology drive and market pull, and the other comes from a low-dimensional fundamental physics drive. That is, the miniaturization of microelectronics and MEMS is carried out in conjunction with physics-motivated studies of electrical and mechanical properties of mesoscopic and nanoscale devices. The motivating vision of the future for NEMS is the emergence of high-sensitivity devices which permit innovative products in life sciences, environmental control, localized energy generation, efficiency increase and storage, transportation, security and information technology in general and they will also serve as nanolabs for fundamental investigations into physics at the mesoscale.

In order to take full advantage of the small dimensions and the remarkable properties of carbon nanotubes, which may overcome fundamental physical and economic limitations of conventional silicon-based VLSI (very large-scale integration) fabrication techniques [5], nanotubes need to be assembled into hierarchical arrays over larger scales for them to be used as active components, which often need to be interfaced with other device components. How to place the nanotubes at desired locations with targeted shapes, directions and densities for fabricating functional devices has been one of the long-standing unsolved problems of nanotube-based molecular devices. In fact, the demonstrated applications of carbon nanotubes in molecular devices are still at the prototype level [6–9].

The approach employed in this chapter encompasses a combination of *top-down* and *bottom-up* strategies to built microsystems with nanoscale elements. This "hybrid" technology solution is aimed to solve the interfacing problem between extremely small and hardly manipulable nanostructures and the mature batch-compatible microsystem fabrication as shown in Figure 3.2. Indeed, the ability to synthesize nanoscale building blocks with precisely controlled size and composition and then to integrate them into larger structures with unique properties and functions is highly anticipated [10].

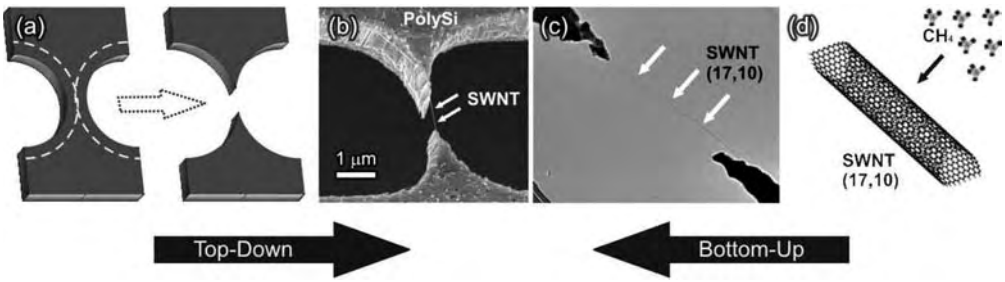

Figure 3.2 Proposed nanotube integration into microsystems. (a) Surface micromachining of sharp tips; (b) scanning electron microscope image of an individual nanotube embedded into micromachined tips; (c) transmission electron micrograph of the same structure; (d) self-assembly of a nanotube using methane as the carbon feedstock.

3.2
Chemical Vapor Deposition of Carbon Nanotubes

Figure 3.3 shows the evolution of production methods of single-walled carbon nanotubes (SWNTs) since 1993 with a focus on chemical vapor deposition (CVD). CVD allows for surface-bound SWNT growth enabling direct device integration [11, 12]. The CVD growth process involves heating a catalyst material to high temperatures in a tube furnace and flowing a hydrocarbon gas through the tube reactor for a period of time [13]. SWNTs grown over the catalyst are collected after cooling of the system to room temperature. The key parameters in CVD growth are the hydrocarbons, catalysts and growth temperature. For carbon nanotube (CNT) synthesis the following process steps are involved:

1. adsorption of the gas precursor molecule on the catalyst surface
2. dissociation of the precursor molecule on the catalyst surface
3. diffusion of the growth species in or on the catalyst particle (surface or bulk diffusion)
4. nucleation and incorporation of carbon into the growing structure (Figure 3.4).

Theoretical studies on nucleation exist, but the catalyst interaction with the carbon precursors is still not fully understood [15, 16]. Therefore, experimental optimizations can be undertaken to tune the control of the CNT properties and their abundance [17]. As far as the growth mechanism is concerned, it is

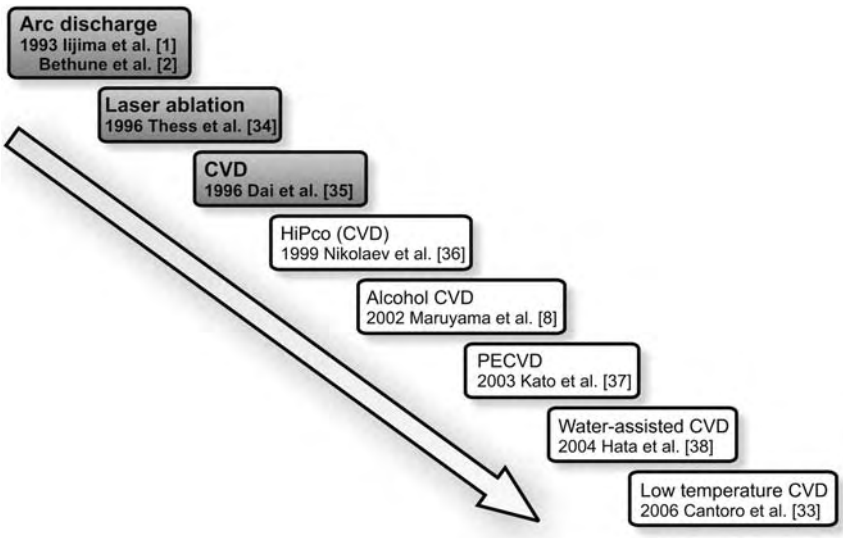

Figure 3.3 Evolution of SWNT production methods.

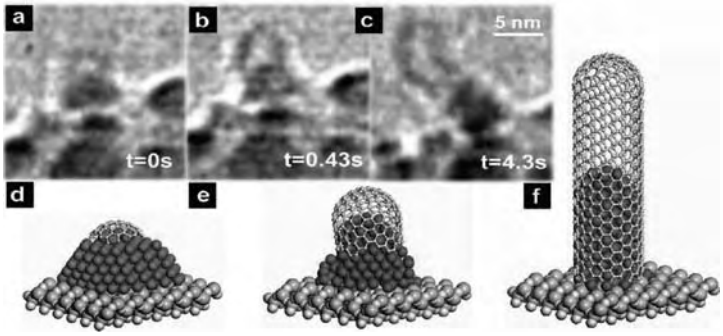

Figure 3.4 Relaxation mechanism of a strained carbon cap (a) that initiates SWNT growth (b). The growth continues by incorporation of carbon atoms at the catalyst particle combined with an extrusive force resulting from a slightly strained CNT shell. After Reference [14].

commonly accepted that carbon dissolves in the catalyst and CNTs grow by precipitation of excess carbon on the metal surface above or behind (base or tip growth) the catalyst particle [18]. This idea originates from the vapor–liquid–solid (VLS) mechanism. Here, the catalyst forms from a liquid droplet and preferentially adsorbs the growth species from the surrounding vapor and solids grow from a supersaturated eutectic liquid. In contrast, Hofmann [19] showed that the catalytic state can be solid during growth at reduced temperatures. The selective growth of nanotubes can be achieved by pre-patterning a suitable catalyst and by applying an electric field [20, 21] or plasma during growth. In surface carbon diffusion, the metal particle remains a solid, the carbon atoms diffuse around the surface and carbon nanotube nucleates on the side of the metal particle. Since carbon continually breaks down on the particle, the tube continues to grow. This is a common mechanism used to explain low-temperature growth, notably with Ni or Fe catalyst nanoparticles [22, 23]. In bulk carbon diffusion carbon atoms are cracked at the metal surface as in surface carbon diffusion. The metal dissolves the carbon until it reaches saturation, at which point a nanotube grows from the surface. Here, the metal particle can be a solid or a liquid but it is instructive to imagine the droplet dissolving carbon until it saturates. Saito et al. described this process in a vapor–liquid–solid model (hydrocarbon vapor, metal–carbon liquid, crystalline carbon) [24]. Both mechanisms have been observed indirectly via HRTEM, where the particular growth method depends on the temperature (and its ramping), the type of metal catalyst and the carbon feedstock used.

In surface-bound CVD, once the nanotube begins to grow, the tube will undergo either base growth or tip growth. Both mechanisms have been proposed and indirectly observed for growth of carbon fibers, MWNT and SWNTs depending on the catalyst type, hydrocarbon source and growth temperature. The method can be influenced by the stiction properties of the nanoparticle to the substrate [25]. Termination of the growth is due to the over-coating of the catalytic particle by

amorphous carbon or when an excessive external force is exceeding the energy for forming a nanotube and graphene may form, which coats and terminates the tube growth [26].

3.2.1 Carbon Feedstock

The first SWNT CVD used carbon monoxide as the carbon feedstock. Since then, methane, ethylene, acetylene, ethanol, methanol and benzene have been successfully used. There are many specific applications in which a gas selection is preferred as their reactivity changes considerably. Methane is the most stable at high temperatures and is much less reactive than acetylene. As a result, SWNT growth was reported at temperatures as low as 400 °C using acetylene [27], whereas the lowest temperature using methane was 680 °C [28]. Additionally, the oxygen content in the feedstock may have an effect on growth quality and yield. Amorphous carbon is effectively etched by H_2O, which preserves and stimulates catalyst activity [29]. Recently, Magrez et al. demonstrated highly efficient nanotube growth by enhancing the catalyst activity from an equimolar feedstock mixture of C_2H_2 and CO_2 [30].

3.2.2 Catalyst Material and Support

The parameter space of carbon nanotube growth is not limited to deposition characteristics, such as temperature, pressure and dissociation, but also includes catalyst and substrate composition. For surface-bound synthesis, catalyst prepatterning offers a high level of synthesis control, and therefore also processability and compatibility with high-resolution pattern transfer techniques have to be considered.

Regardless of the carbon feedstock, it has been found that Fe, Ni and Co nanoparticles are all able to from SWNTs. Recently, it was shown that any metal, even gold, silver and copper, can act as a catalyst for SWCNT synthesis in CVD [31]. The use of bi- or trimetallic mixtures with elements such as Mo, Y, Ru and Pt has led to massive increases in yield under certain conditions [32]. These results are mostly empirical and many studies analyzed the effects on yield of varying concentrations of elements using a particular growth condition [33].

3.2.2.1 Liquid-Phase Catalyst

The catalyst is generally prepared by impregnating support material such as silica, alumina or MgO by wet chemical reactions or simply by drying a stirred mixture of support material with the catalyst salt. A metal salt solution allows for electrochemical substrate deposition. The catalyst can be electroplated on non-planar geometries with current density and time as additional control parameters [34]. The catalysts can be deposited in lithographically patterned islands or via lithographic techniques, resulting in well-defined SWNT growth sites across a substrate. The current benchmark method for high-resolution patterning is electron

beam (e-beam) lithography in combination with a lift-off process. In addition to wet catalyst methods which offer good control over the catalyst concentration, additives (such as surfactants or silica/alumnia particle support) catalysts can be deposited as thin films by physical deposition techniques [35, 36].

3.2.2.2 **Solid-Phase Catalyst**

Sputtered or evaporated catalyst thin films offer control mainly through film thickness but also through parameters influencing film morphology such as deposition rate and bias. The advantage of thin-film technology is the accurate pattern transfer by masking and etching techniques based on photo- or electron beam lithography.

3.2.2.3 **Catalyst Support**

As known from general catalysis [37], the catalyst support can significantly influence the process. At high deposition temperatures, catalyst deactivation by diffusion or alloying has to be considered. Regarding silicon substrates, Ni is known to diffuse more readily than Co or Fe [38]. Therefore, insulating or conducting diffusion barriers such as SiO_2 or Al_2O_3 thin films are often used [8, 39]. Catalyst diffusion and alloying processes might, however, also be used to adjust the density of as-grown structures, i.e. the efficiency might be deliberately suppressed. Apart from a barrier function, catalyst underlayers can also play a more active role, enhancing or modifying the catalyst activity [40]. Rough and porous support is often found to be more effective [41]. A further increase in active surfce can be obtained by chemical or physics pretreatment steps, such as heat or plasma treatment in reducing or etching atmosphere, e.g. hydrogen or ammonia [42].

Reflecting on the large parameter space of carbon nanotube growth, including catalyst material, preparation, support, pretreatment and the numerous deposition parameters previously described, a direct comparision of specfic catalyst activities reported in the literature is limited.

3.2.3 **State-of-the-Art of Controlled Nanotube Growth**

3.2.3.1 **Alignment and Location Control**

Electronic applications in particular require precise alignment and orientation of the SWNTs. They can be grown in bulk, suspended in solution and then deposited on a substrate. However, for large-scale high-performance and reproducible device production, it is advantageous to grow the SWNTs in specific places, without any postsynthesis methods.

For certain applications such as interconnects or oscillators, tubes suspended between pillars or electrical contacts are practical and useful (Fig. 3.5). To that end, SWNT between SiO_2 pillars was demonstrated [43]. During growth the SWNTs formed bridges between the tops of adjacent pillars. Since the nanotube grew via the base growth mechanism, the tube grew out from the pillars and remained suspended in space until they attached to another pillar. Homma et al. [44] reported

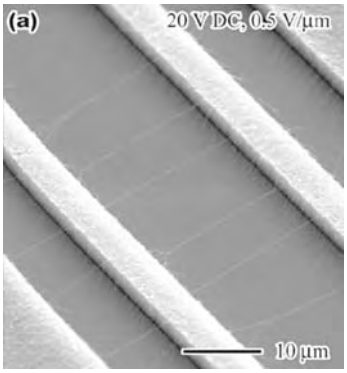

Figure 3.5 SEM images of suspended SWNTs grown in various electric fields. The spacing between the outer poly-Si electrodes is 40 μm. After Reference [20].

observation of the formation processes of suspended structures and bundles of single-walled carbon nanotubes are directly observed during chemical vapor deposition of SWNTs on a patterned specimen. SWNTs exhibit lively movements during extension from micropillar patterns, resulting in bridging, bundling, merging and debundling. Fluctuation of the extension direction of an SWNT cantilever is observed. Swing of the SWNT cantilever is the reason for the enhanced-nearest-neighbor interconnection.

Alignment of nanotubes on a substrate improves the patterned CVD growth. The electric field alignment of carbon nanotubes was demonstrated by Ural et al. [45] (among others), who produced large numbers of long and highly aligned nanotubes. A recent fast heating method allowed for alignment, wherein the substrate was plunged into a hot furnace. The suggestion was that the catalyst particles leap off the substrate and enter the laminar flow of the feedstock gas, producing SWNT as they float like kites [25].

3.2.3.2 Catalyst Patterning Techniques

Standard lithographic steps, employing either an electron beam or UV light, are used to pattern holes in the resist in which catalyst is deposited. The current benchmark method for high-resolution patterning is electron beam (e-beam) lithography in combination with a lift-off process [22]. The resist is lifted off, leaving isolated catalyst islands. Growth is then performed on the substrate, producing nanotubes only from the predefined islands. Competing state-ofthe art methods are the maskless focused ion beam (FIB) writing of Pt film nucleating preferentially nanofibers [46] and pulsed electrochemical deposition to form Ni and Fe catalyst islands of controlled size and density [47]. Nanocontact printing can be employed to deposit purified Co colloids in regular patterns for low-cost patterning over large areas [48]. These permit the fabrication of nanotube-based devices on a wafer scale.

3.2.3.3 Diameter and Chirality Control

Diameter control and chirality control are the key missing factors towards real deterministic SWNT synthesis [12]. CVD produces a comparably large diameter range from 0.4 to 5 nm. The catalyst design has been shown to improve diameter control in the sense that the range was narrowed and correlated with the diameter distribution of the catalyst nanoparticles. The former Infineon group [49] reported the synthesis of individual carbon nanotubes with controlled diameters employing conventional catalyst-mediated CVD to grow isolated CNTs out of nanoholes. The diameter of each multi-walled CNT adjusted to the hole size.

The selection of chirality is still more difficult, since several semiconducting and metallic chiralities have almost the same diameter. The chirality control research effort is also hindered by the difficulty of measuring the chirality of a nanotube sample. Paillet's group [50] used electron diffraction to characterize as-grown nanotubes by CVD from Ni nanoparticles and found an average chiral angle of as much as 25.3°. Their growth produced SWNTs with large diameters (mean diameter 1.75 nm) and with a relatively broad diameter distribution (standard deviation 0.5 nm). Chiral angle control was claimed to some extent.

Smalley et al. [51] recently proposed taking a single (n, m) nanotube sample, cutting the nanotubes in that sample into many short nanotubes, using each of those short nanotubes as a template for growing much longer nanotubes of the same type, and then repeating the process. The result would be an amplification of the original tube type. As a proof-of-concept, they used a short SWNT seed as a template for VLS amplification growth of an individual long SWNT. Analysis indicated that the templated VLS-grown long SWNT had the same diameter and surface orientation as the original short SWNT seed, although amplifying the original (n,m) type remains to be proven.

3.3 Direct Integration of Carbon Nanotubes into Microsystems

3.3.1 Polysilicon Supports

Practically all CVD growth studies using patterned catalysts were carried out on plain Si/SiO_2 chips or wafers [22]. What we start off from are triple-layered polycrystalline silicon (poly-Si) chips obtained from surface micromachining as shown in Figure 3.6. A detailed description of this process can be found in Reference [52]. In brief, alternating sequences of micron-thick silicon oxides and poly-Si layers are grown on top of a nitride-coated silicon wafer. This process has the general features of a standard surface micromachining process: (i) poly-Si is used as the structural material, (ii) deposited oxide is used as the sacrificial layer and (iii) silicon nitride (black bottom layer) is used as electrical isolation between the poly-Si and the substrate. The process is different from most customized surface micromachining processes in that it is designed to be as general as possible.

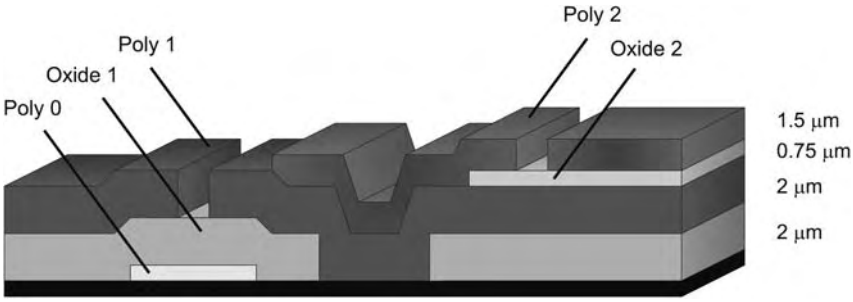

Figure 3.6 Layer composition of the surface micromachined chip used for nanotube integration.

Any layer can be structured, thus allowing the synthesis of truly movable mechanical parts such as gears or hinges. Seen from the material composition, no dramatic change is expected when going from single-crystal Si to poly-Si. However, two major drawbacks accompany the usage of surface micromachined poly-Si layers as the catalyst support:

- high chip topopgraphy
- high surface roughness.

3.3.2
Generic Process Flow

Two different methods of integration into surface micromachined chips have been carried out. They differ most significantly in the composition and method of deposition of the catalyst. Both coming with their specific advantages and drawbacks, they share several common process steps, as outlined below:

1. MEMS chip fabrication
2. catalyst deposition and patterning
3. CVD growth of carbon nanotubes
4. post-contacting[1)]
5. MEMS relase.

In the following, each process will be discussed individually.

3.3.3
Integration from Catalytic Solutions

The process flow is shown schematically in Figure 3.7. Note that the staircase in Figure 3.7 represents the topography of a multi-layer process without polishing steps. Electron beam (e-beam) lithography resist (PMMA) of 400-nm thickness is

1) This step was skipped during first investigations.

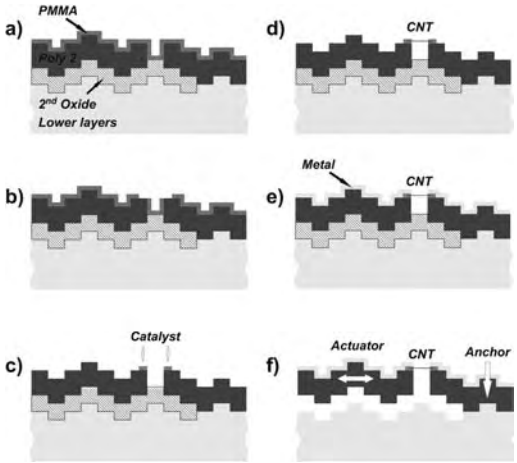

Figure 3.7 Schematic diagram of the process flow: (a) spin coating; (b) e-beam lithography; (c) catalyst deposition; (d) CNT growth (900 °C for 10 min in CH_4 at 100 mbar); (e) metallization; (f) release.

spin coated on top of the 2 × 2 mm chip (Figure 3.7a). The written structures are openings, typically 2 μm in feature size, defining place holders for the catalyst material and resulting in a locally defined spot for catalysts for spatial control of nanotube growth (Figure 3.7b). In order to spin coat a continuous resist layer that covers the chip surface, featuring a strong topography, sufficient resist thickness is required. It was found that at least a 400-nm thickness is needed. Spin coating on 2 × 2 mm chips generated a considerable waste area due to surface tension at the edges. The edge beads represented as much as 12% of the total chip area. However, this area can be used for the definition of (three) alignment markers to be used for the upcoming e-beam lithography. The latter was carried out on a Raith 150 system and a typical dose was 150 μC/cm^{-2}. After development (MIBK : IPA 1 : 3), a droplet of a catalytic solution based on iron nitride dissolved in methanol was placed on the chip and evaporated.

The catalyst ingredients were proposed by Kong et al. [13]. To 15 mL of methanol, 15 mg of alumina, 20 mg of $Fe(NO_3)_3 \cdot 9H_2O$ and 5 mg of $MoO_2(acac)_2$ are added. The suspension is sonicated for 1 h, stirred overnight and sonicated each time for at least 20 min before deposition on the substrate. A drop of the suspension is placed on a bare substrate surface or on a substrate with predefined structured areas. The solvent evaporation can be accelerated by using a hot-plate heated to 40 °C. The ultrasonic experiment did not result in a significant tendency of decreasing the diameter. However, sonication leads to a more stable suspension, which is useful for a regular deposition process. Deposition experiments have shown that usually at the borders of the catalyst stripe, increased catalyst accumulation can be seen due to capillary forces. In general, evaporation at 40 °C is recom-

mended to achieve a more regular particle distribution without large spots of catalyst accumulation. The deposited catalyst layer on top of the PMMA layer should be disconnected from the deposited layer sitting on top of the opened polysilicon support. Different methods for deposition had been investigated. Both spin coating and dip coating, however, resulted in either poor uniformity of the coating layer or increased layer thickness. The lift-off process is completed by stripping the PMMA in acetone under ultrasonic agitation (Figure 3.7c).

Chips for processing are placed horizontally on the carrier, which, in turn, is inserted into the reaction chamber. Samples are first heated to 200 °C under atmospheric pressure. The chamber is then evacuated and heated in parallel to the desired process temperature typically between 750 and 950 °C. For the case of liquid-phase catalysts, the process temperature was 900 °C. The chamber is evacuated to the base pressure and the growth sequence is enabled by opening the methane and hydrogen MFCs to the desired partial pressures. Methane, fed at 1000 sccm and kept at 100 mbar, is provided as a carbon feedstock for 10 min. During the growth time all valves are closed and the chamber temperature is regulated with a precision of ±1 °C. The residence time of the gas is equal to the growth time. The gas is evacuated and cooling to at least 250 °C finalizes the CNT synthesis. The chamber can be opened by establishing atmospheric pressure using nitrogen.

A second e-beam lithography and lift-off step is applied immediately afterwards to deposit a Cr/Au layer for electrical connectivity. Since the growth occurs on the surface of the Poly 2 layer, most of the CNTs are freestanding prior to the HF release of the MEMS. The second spin coating has been proven not to destroy the CNTs. After a standard HF release, the MEMS chip is ready for actuation (Figure 3.7f).

Crucial in this process is the successful catalyst deposition and subsequent patterning. Series of tests were performed to determine the smallest feature size and the smallest spacing between two features, i.e. two catalyst islands. An SEM image of catalytic spots of different sizes is shown in Figure 3.8. Using these periodic test structures we evaluated the process resolution for the catalyst structuring. We found that the minimum feature size and the minimum spacing depend on the concentration of the catalytic solution. Figure 3.8 shows regions from the catalyst window which remained uncoated after deposition. We performed a numerical investigation of the fill factor defined as $FF = 1 - (A_{void}/A_{total})$. Table 3.1 shows the influence of the catalyst concentration c_{cat}, minimum feature size f_{min}, minimum spacing s_{min} resulting in different fill factors FF.

The table shows that the resolution of the process can be improved by diluting the catalyst solution. This, however, is accompanied by poor surface coverage expressed by the fill factor. Note that the fill factor was evaluated from areal considerations and that the catalyst thickness control was found to be very poor.

There is a profound temperature dependence. At relatively low temperatures (750–850 °C), predominantly individual MWNTs or ropes of SWNTs are obtained with high yield. At intermediate temperatures (850–900 °C), individual SWNTs are grown with a typical diameter of 2 nm or thin bundles of SWNTs, but with less yield than at lower temperatures. At high temperatures (>950 °C), the substrate

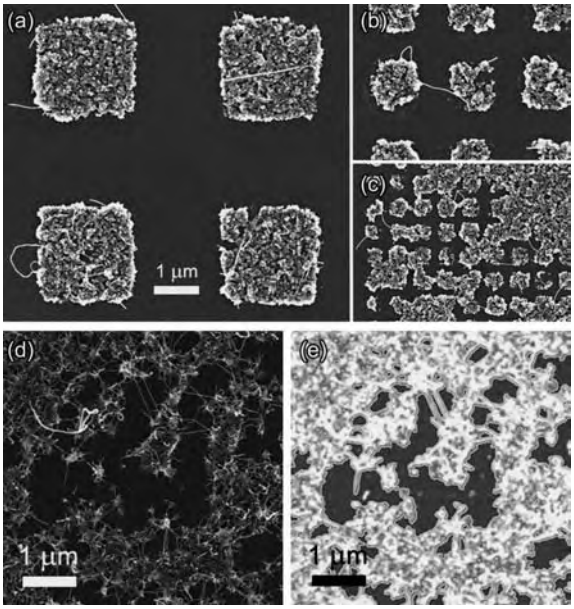

Figure 3.8 (a–c) SEM images of CNTs grown on catalytic spots of various sizes defined by e-beam lithography and lift-off. (d) SEM image of a catalyst coated surface; coated and uncoated regions appear. (e) Selected uncoated area using threshold value from filtered (smoothing and edge detection filters) histogram.

Table 3.1 Influence of catalyst catalyst concentration.

c_{cat} *(mM)*	f_{min} *(nm)*	s_{min} *(nm)*	FF *(%)*
14.75	>2000	>2000	N.A.
7.37	1000	1000	91.53
2.95	600	700	72.43
1.64	400	500	48.76
0.7	350	500	23.18

and the CNTs are often found to be covered with an additional material, which is most likely amorphous carbon.

Given that the micromachining process used in this work does not allow the definition of polysilicon trenches smaller than 2 µm, CNTs need to grow a considerable distance before the gap bridging is complete, which reduces the number of connecting tubes. There is thus no need for small catalyst island spots for the synthesis of individual CNT-based systems. In this work, the catalysts were deposited directly on polysilicon.

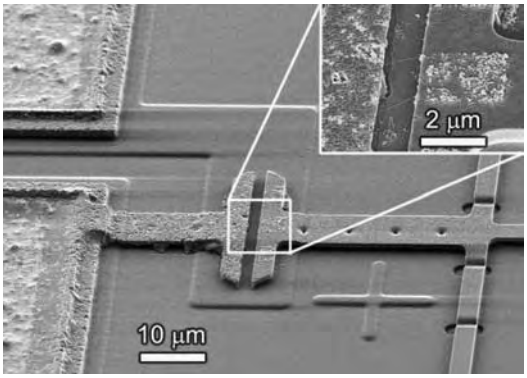

Figure 3.9 SEM image of CNTs grown on directly into the trench of a surface micromachined silicon chip. Inset shows zoomed area of nanotube region.

Although the catalyst deposition method is not well controllable in terms of layer uniformity and density, using a properly adapted CVD process as described above, SWNT growth occurred with good reproducibility. However, if tube bundling is an issue, the catalytic "cake" yields many nanotubes which, through mutual interaction, bundle during growth (Fig. 3.9). A more uniform catalytic coating can be achieved by performing a solid-phase catalyst deposition. This technique is detailed below.

3.3.4
Integration from Sputtered Metal Catalysts

Alternatively, a metal bi-layer can be sputtered or evaporated on top of the chip, replacing the catalytic solution. Typically, a 10-nm Al layer is evaporated followed by a thin 1-nm sputtered Ni layer. The Al layer, which may have been oxidized into Al_2O_3 by contact to ambient air, in this case serves as a diffusion barrier for the catalyst, which consists of Ni nanoparticles. In order to grow tubes that span a 2-µm trench, the catalyst coating should come with a high surface area presenting non-aggregated nanoparticle-sized sites.

The subsequent CVD process has two functions:

1. nanoparticle formation due to annealing of thin film
2. catalytic thermal CVD of nanotubes.

3.3.5
Surface Restructuring of Catalyst Films

The sputtered Ni thin film of about 1-nm thickness does not form a flat, continuous layer but rather a random texture of Ni particles. It is a requirement for the Ni layer to have a strong topography in order to nucleate single-walled carbon nanotubes. However, if the metal film is heated, the mobility of its atoms increases,

and islands coalesce driven by a mechanism that minimizes surface energy and/or the free energy of the substrate/metal interface [53–55]. This is strongly dependent on the type of metal, the type of substrate and the annealing environment [56]. Pisana et al. [57] reported large differences in samples annealed in hydrogen compared with the as-deposited samples. It was found that the annealing atmosphere and its pressure greatly influenced the catalytic island formation. Thicker films always result in larger cluster sizes. At the same time, varying the atmosphere leads to different surface morphologies. Annealing in vacuum leads to larger islands than annealing in hydrogen, for instance. Higher gas pressures are found to be more effective at restructuring the catalyst thin film, yielding catalyst island heights suitable for SWNT growth. Hydrogen can reduce oxidized Ni, increasing its surface mobility. Indeed, if the metal interacts strongly with an oxygen-containing substrate or it is oxidized itself, its mobility will be lowered. The reduction of an oxidized metal can also occur following the catalytic decomposition of a hydrogenated carbon precursor [58].

3.3.6
Process Parameters

CVD parameters were as follows:

- evacuation below 10^{-5} mbar and heating to 800 °C
- (pretreatment) 10 min in H_2 at 200 mbar and 800 °C
- evacuation and refill to 50 mbar H_2 and 150 mbar CH_4
- (growth) 15 min at 200 mbar and 800 °C
- evacuation and cooling under vacuum.

The influence of the metal layer thicknesses on the CNT growth is difficult to analyze. Nanotube growth conditions could be observed when the nickel layer was between 0.5 and 1.8 nm in thickness. On one sample some very thick tubes could be seen on a relatively thick nickel layer of as much as 5 nm. The particle size after the baking process grows proportionally to the nickel layer thickness. A layer of 1 nm results in comparatively uniform-shaped particles, whereas a 2-nm nickel layer evolves into irregularly shaped particles as evidenced by SEM. Good growth conditions were found for a metal stack of 10 nm Al + 1 nm Ni. Note that these nominal layer thicknesses were measured by a quartz rate monitor. The system was an Edwards coating system operated at a base pressure of 10^{-5} mbar.

If the sputtering conditions are varied in the sense that the deposition rate is changed, the results vary dramatically. Figure 3.10 shows three samples subjected to similar conditions but with varying Ni deposition rates from 0.01 (a) to 1.5 Å s^{-1} (c). Only the rate used in (b), namely 0.5 Å s^{-1}, produced SWNTs suitable for integration. It can be seen in (a) and (b) that the catalyst efficiency is low. The catalyst efficiency can be increased by optimizing the catalyst film thickness; however, a high catalyst efficiency results in vertically aligned SWNT forests due to tube–tube van der Waals interactions [27], which is detrimental here regarding the desired lateral SWNT bridging. The catalyst thickness used in Figure 3.10c has best effi-

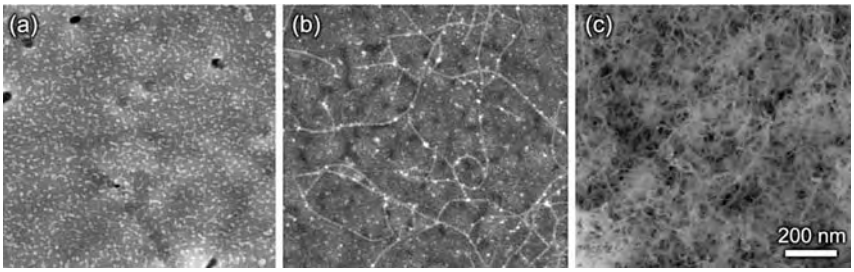

Figure 3.10 Influence of catalyst from varying nickel deposition rates. Rates were (a) 0.01, (b) 0.1 and (c) 1.5 Å s^{-1}.

ciency for SWNT nucleation; however, the nanotube density is too high to allow their horizontal placement.

The process is very temperature sensitive. At 750 °C the amount of tubes grown was very poor. Increasing it to 800 °C results in a very good tube density, but if the temperature is increased further to 900 °C, the only thing one obtains is a very dirty oven and chips which are badly contaminated with amorphous carbon. As amorphous carbon deposition often accompanies nanotube growth based on thermal CVD, a detailed study is presented below.

3.3.7
Amorphous Carbon Monitoring

Amorphous carbon (*a*-C) formation can be avoided by preventing the hydrocarbon gas from undergoing self-pyrolysis. As this self-decomposition does not require a catalytic additive and as the Raman signal from well-crystallized nanotubes correlates with the signal from *a*-C, experiments were made on catalyst-less silicon oxide chips. Figure 3.11a shows the summed D- and G-peak Raman intensities I of *a*-C-coated chips from CVD runs at varying temperatures. The summation was done as a function of the vertical z-displacement of the laser spot. This allowed for precise focusing of each sample, which is a requirement when comparing the signal intensity between the samples. The focus position $z = z(I_{max})$ of each sample was stored into the system and the summed intensity is plotted as a function of the laser displacement relative to $z = 0$. Figure 3.11b shows the Raman spectra of the samples from (a). Here, each spectrum was obtained by averaging 256 spectra from planar x-, y-scans of $4 \times 4\,\mu m$ over a portion of the *a*-C layer while z was locked to $z = 0$ to yield the maximum Raman signal. The presence of *a*-C is indicated by two spectral features at approximately 1350 and 1600 cm^{-1}. The signal intensities I(D), I(G) of both peaks increased with increasing process temperature. This is an indicator of enhanced *a*-C deposition at higher temperatures.

We considered in the following the parameters of the methane–hydrogen gas composition to study its influence on the *a*-C production [59]. Several CVD processes were performed with the partial pressure of hydrogen varying from 0 to 100 mbar at a process temperature of 900 °C. The total pressure (the sum of the

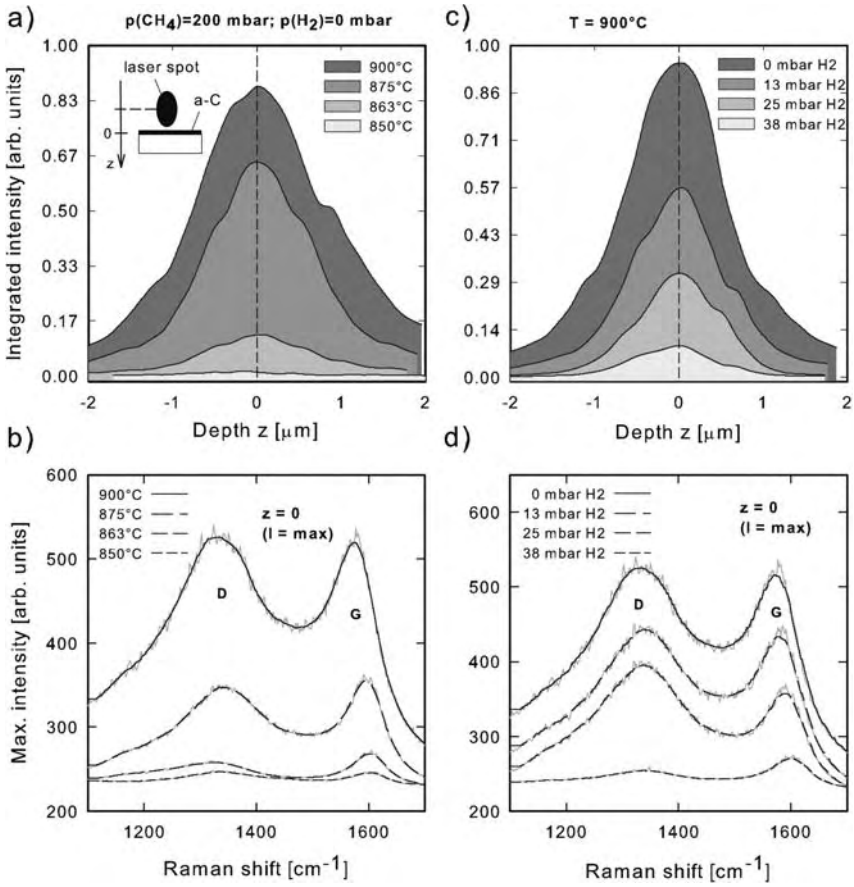

Figure 3.11 (a) Integrated D- and G-band Raman spectra for varying process temperatures. (b) Maximum Raman intensity spectra of the D- and G-bands for varying process temperatures. Methane pressure: 200 mbar; no hydrogen. (c) Integrated D- and G-band Raman spectra by depth scan for various H_2 (and CH_4) pressures. (d) Maximum Raman intensity spectra of the D- and G-bands for varying partial pressures of H_2. The methane partial pressure varied accordingly as $p(CH_4) = 200 - p(H_2)$ mbar. Process temperature: 900 °C.

partial pressures of H_2 and CH_4) was kept constant at 200 mbar. The Raman measurements shown in Figure 3.11c and d were obtained in the same way as the plots in Figure 3.11a and b. It is seen that the intensity reduces gradually with increase in hydrogen (and with the reduction of methane). Similarly, the *a*-C layer thickness increased with a reduced hydrogen amount.

Both CVD parameters (temperature and hydrogen amount) were shown to influence greatly the Raman intensity of the deposited *a*-C. As the abundance of matter

is directly proportional to the Raman intensity, one can assume that the intensity is strongly related to the deposited *a*-C amount or layer thickness. However, visible Raman spectroscopy is reported to be 50–250 times more sensitive to sp^2 (graphite) sites than to sp^3 (diamond) sites, as visible photons preferentially excite their π-states. Note that only high-energy Raman from UV sources can reach the σ-states from all types of carbon bindings. Our excitation energy of 2.33 eV is thus only probing the sp^2 content [60–62]. Changes in the Raman intensities seen in Figure 3.11 can thus be due to both structural changes in the carbon bindings and layer thickness changes. However, no trend can be seen in the development of the $I(D)/I(G)$ ratio, which remains at approximately 1. Given the weak structural changes, we assume the changes in the Raman intensity to be mainly due to the changes in the deposited layer thickness [63]. To conclude the study of the CVD parameters dependence, we found thicker *a*-C layers for increasing process temperatures and reduced amount of hydrogen in the reaction gas. At the same time, the carbon bindings showed a weak disordering with increasing temperature and reduced hydrogen amount.

Figure 3.12 shows the amount of deposited *a*-C by means of the measured maximum G-peak intensity for 5×5 process combinations between 0 and 50% hydrogen content and a temperature range between 800 and 900 °C. The plot reflects the importance of the addition of hydrogen to the methane mixture to reduce the *a*-C amount. Independently, reducing the process temperature also contributed in reducing the carbon deposit.

3.3.8
a-C Layer Leakage Currents and Chip Releasability

The presence of *a*-C on top of a device can exhibit leakage currents. For each sample the resistance on the oxide along a path of ~10 μm was measured. In the absence of an *a*-C layer a very high resistance in the order of several hundreds MΩ was measured. The samples with a detectable *a*-C layer display a considerably lower resistance, depending on the amount of *a*-C deposited. The results are shown in Table 3.2. We point to the fact that the (small) structural changes in the carbon bonds might have contributed to the measured conductances changes. However, their influence is low compared with the strong material thickness changes which provided observable changes in chip opacity.

After the resistance measurement, attempts were made to etch the SiO_2 by immersing the chips in concentrated HF (40%) for 5 min. Structures with very little or zero leakage current were found to be releasable, whereas thick *a*-C layers (with resistances below 100 kΩ) prevented the latter. These results are summarized in Table 3.2. They show a correlation between the Raman intensity of the G-peak and the electrical resistance through the same carbon layer. Layers which yielded a resistance in the kΩ range prevented the HF from dissolving the underlying SiO_2. From Figure 3.12 and Table 3.2 one can thus define regions of either *reduced* or *high* *a*-C amount/contamination.

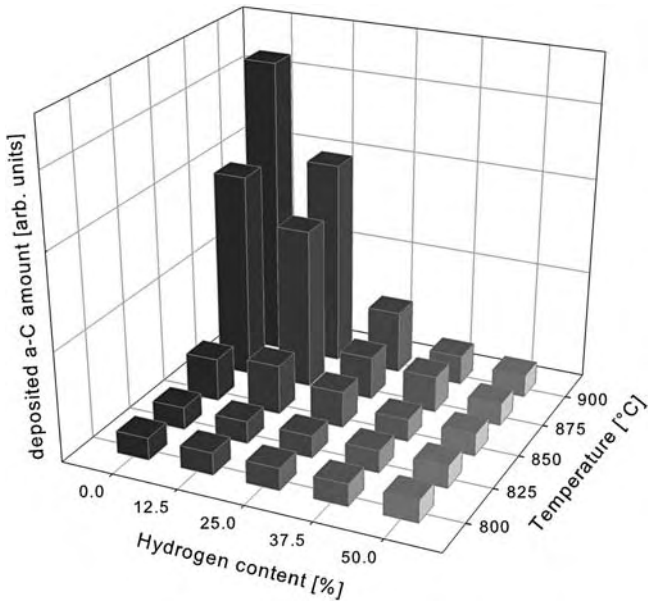

Figure 3.12 Monitored *a*-C deposit for various gas mixtures and temperature combinations by Raman scattering.

Table 3.2 LPCVD runs from varying temperature *T* and hydrogen amount $p(H_2)$ with $[p(CH_4) + p(H_2) = 200\,\text{mbar}]$, listing the G-peak intensity *I*(G), the electrical resistance *R* of the *a*-C film and HF test. "Releasable?" describes the success of the acidic HF etch of the silicon oxide.

T *(°C)*	p*(H_2) (mbar)*	I*(G) (CCD Counts)*	*Resistance (kΩ)*	*Releasable?*
800	0	230 ± 4	∞	Yes
850	0	240 ± 2	∞	Yes
863	0	270 ± 2	131 ± 11.5	Yes
875	0	360 ± 2	4.92 ± 0.53	No
900	0	530 ± 2	1.98 ± 0.12	No
900	13	488 ± 2	1.78 ± 0.10	No
900	25	390 ± 2	2.52 ± 0.17	No
900	38	272 ± 2	∞	Yes
900	50	239 ± 2	∞	Yes
900	100	230 ± 4	∞	Yes

3.3.9
Growth with Reduced Amorphous Carbon

SWNTs typically have small diameters of about 1 nm and thus require small catalyst particles and high growth temperatures [64, 65]. Note that at such high temperatures acetylene is not stable and methane must be used. Delzeit et al. reported SWNT growth using a 10-nm Al support layer below a 1-nm metal catalyst such as Fe, under a growth temperature of 900 °C and under pure methane [66]. The results from Figure 3.12 show that this process is not allowed for contamination-free SWNT integration using our system. Increasing the hydrogen amount in the gas mixture, in addition to reducing the *a*-C amount, decreases the rate of CH_4 decomposition by hydrogenating the reactive carbon species (the carbon feedstock) [67, 68]. This, together with the fact that fewer CH_4 molecules are present in the mixture, results in a strongly reduced SWNT density. At a pressure ratio of 50% hydrogen, few SWNTs were observed, decreasing the system yield of SWNT-based NEMS devices. A partial pressure ratio of 150 mbar CH_4/50 mbar H_2 has yielded a tube density which is well suited for the horizontal alignment of individually separated SWNTs.

Catalyst was deposited on the topmost layer of a surface micromachined chip [52] by sputtering a 10 nm Al/1 nm Ni bi-metal. The chips were then heated under Ar to a temperature of 850 °C. Hydrogen pretreatment was performed for 10 min at a pressure of 200 mbar. Then, thermal CVD under a 150 mbar/50 mbar mixture of CH_4 and H_2 at 850 °C for 15 min was carried out for the growth of SWNTs. Cooling was done in vacuum and nitrogen venting after cooling to at least 250 °C. After growth, the chip was subjected to a acidic HF release. The releasability is proven in the sense that the micromachined structure shown in Figure 3.13a layer became available for TEM as the MEMS was actuated off the support substrate. The TEM image shown in Figure 3.13b shows a regular, straight SWNT with few defects and *a*-C. Figure 3.13c shows the Raman spectrum from an integrated nanotube into a MEMS obtained with the aforementioned process. The spectrum shows a typical G feature splitting and a single radial breathing mode (RBM) specific for individual SWNTs [69]. The weak defect-induced D-peak indicates an SWNT with few defects. In the present Raman spectrum, the G-peak is dominated by the high-energy mode of the SWNT while the D-peak is a sum of *a*-C around the tube diameter and the defects in the tube.

3.3.10
Alignment and Location Control

3.3.10.1 Horizontal Growth and Aligned Bridges

Figure 3.14a shows that the catalytically seeded SWNTs preferentially bridge over the shorter gap (1.5 μm wide) of a rectangular hole. The majority of the SWNTs is aligned normal to the hole edge and appears taut and straight. We emphasize that no electric field was applied during growth. Also, the CVD was performed under static pressure, hence there was no gas flow. Several *in situ* thermocouples

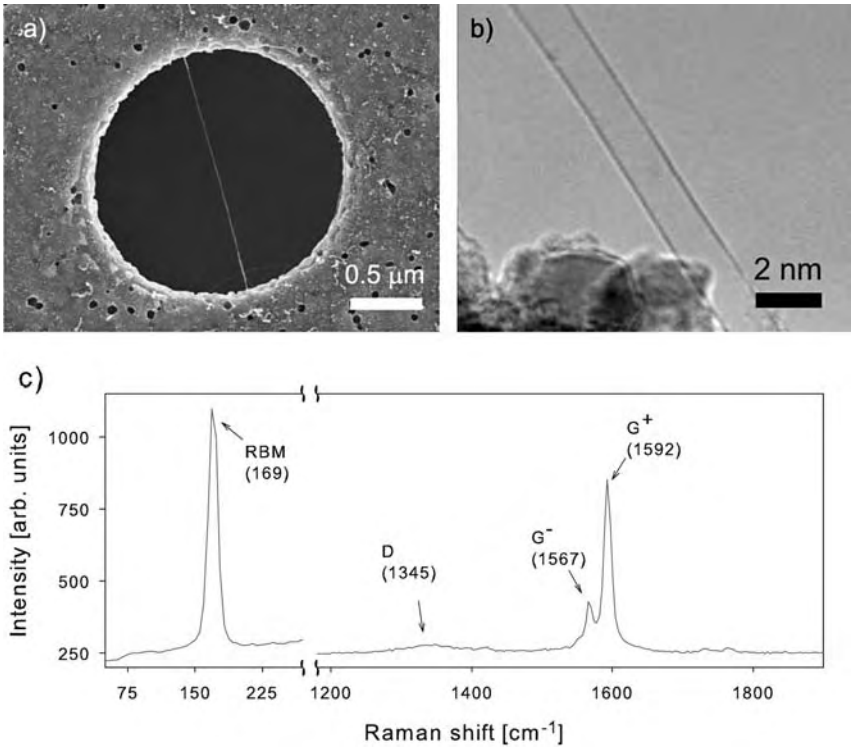

Figure 3.13 (a) Example of a MEMS device with incorporated carbon nanotubes grown at 850 °C from a 10 nm Al/1 nm Ni bi-layer under 150 mbar CH_4/50 mbar H_2 for 15 min. (b) TEM image from SWNT from the same MEMS chip. (c) Raman spectrum recorded from an integrated SWNT synthesized from the aforementioned process.

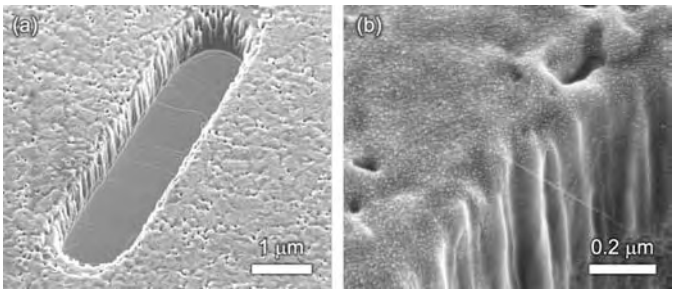

Figure 3.14 (a) SEM image of a rectangular hole from the surface micromachined grid with aligned SWNT bridges. (b) Zoomed SEM image showing catalytic Ni particles and a SWNT bridge.

and separately addressable temperature controllers ascertained an equal temperature distribution in the CVD chamber. The poly-Si grid was highly doped (n = 1019 cm^{-3}), thus charge trapping and local electric fields can be excluded. We therefore suggest that the directionality in SWNT bridging is due to a simple nearest neighbor attachment.

SWNTs nucleate on the surface of individual catalyst particles, which typically remain on the substrate (root growth) [70]. At the initial stages of growth, the SWNT body grows away from the substrate and with increasing length is subjected to thermal waving [71]. The SWNT thereby remains anchored at its nucleation point; however, the catalyst particle itself dynamically deforms during the continuous catalytic gas decomposition and carbon formation/incorporation [72]. Once the waving end of an SWNT comes close to the substrate, such as the opposing hole edge (Figure 3.14a), it is proposed that vander Waals interactions provide strong adhesion, tightening and straightening the now suspended nanotube [73].

Figure 3.14b shows a close-up SEM image of an SWNT bridge. The Ni catalyst islands are visible, uniformly covering the poly-Si surface. It can be seen that for the given CVD conditions the catalyst efficiency is low, i.e. the Ni island density is far higher that the SWNT density. The catalyst efficiency can be increased by optimizing the catalyst film thickness and pretreatment together with the carbon feedgas concentration and (reactive) dilution. However, a high catalyst efficiency results in vertically aligned SWNT forests due to van der Waals (tube–tube) interactions [27, 29], which is detrimental here regarding the desired lateral SWNT bridging.

For the given CVD conditions, Figure 3.15b shows the influence of a gapsize variation between 1.5 and 3 μm on the number of crossing SWNT. The data are based on 60 highly resolved SEM images showing one hole at a time. All holes were on the same chip and thus were exposed to identical experimental conditions. The tube density is determined by taking the number of tubes divided by the hole's perimeter. Very occasional bridging was observed for trench sizes >3 μm. There is a clear trend of increasing SWNT bridge formation with reduced gap size. The plot in Figure 3.15c shows that the SWNT density mainly relates to the catalyst efficiency and hence is not affected by the variation in gap size. We emphasize that the absolute number of suspended SWNTs depends strongly on the given CVD conditions, as gaps even larger than 20 μm can be bridged [73]. Given the relative trend in Figure 3.15, we demonstrate that by surface micromachining of the catalyst support the number of SWNT bridges can be controlled.

3.3.10.2 Towards Individual Nanotube Bridges

In this section, we discuss the possibility of localizing the growth of individual tubes between two adjacent tips. Figure 3.16 shows three suspended SWNTs across a trench defined by a tip pair at the technological limit for standard lithography. The shape has been designed based on the previous results, namely by alternating the gap spacing between 12 and 2 μm (Figure 3.15b) to force SWNT growth only between the small gaps without the need of masking the catalyst.

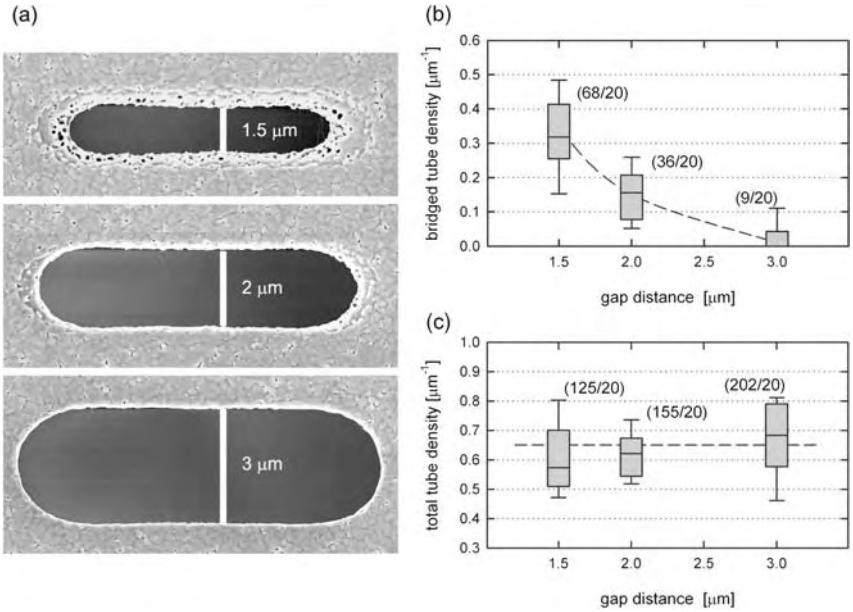

Figure 3.15 (a) SEM image of rectangular holes of different gap sizes. (b) Tube bridge density across different gap sizes. Figures in parentheses indicate number of measured tubes which successfully bridged over the gaps (*tube bridges/gaps*). (c) Total tube density in the same gaps. Figures in parentheses indicate number of measured tubes grown inside the gaps but which did not necessarily lead to a bridge (*tubes/gaps*).

Figure 3.16c shows a Raman map of the suspended SWNTs. The image was obtained by integrating the SWNT-specific Raman signatures, i.e. the radial breathing modes in the range from 80 to 350 cm^{-1} and the tangential (G) mode at around 1592 cm^{-1} as shown in Figure 3.16d. No defectinduced D-band signal at around 1350 cm^{-1} was observed, which is indicative of good SWNT crystallinity. The Raman map displayed in Figure 3.16c was obtained by integrating over the longitudinal optical phonon mode of the poly-Si material. Both images can be overlayed as they picture the same structure. There is no doubt about the origin of these Raman features as the free-standing sample geometry does not suffer from any background signal.

The minimum feature size for the structures shown in Figure 3.16 is about 2 μm. It should be noted that the lateral resolution of the MEMS technology was three orders of magnitude larger than the diameter of the SWNTs. We improved the lateral resolution of the micromachined tips by over-etching two initially circular holes to obtain two sharp adjacent tips defining a gap as shown in Figure 3.17a. Over-etching can be achieved by a controlled poly-Si oxidation and a subsequent acidic wet-etch. The distance between the two adjacent tips is below 1 μm. Crystal grains and their boundaries from the polycrystalline material influenced

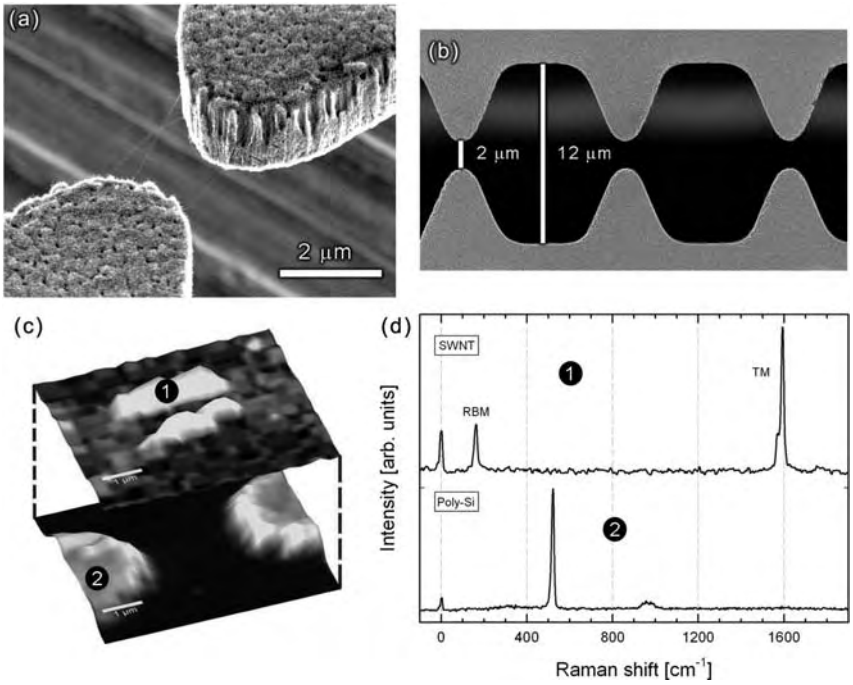

Figure 3.16 (a) SEM image of three spanned SWNTs between a pair of closely spaced poly-Si tips. (b) Demagnified SEM image from (a) to show the tip definition. (c) Raman image of the same tip-pair as shown in (a). (d) Representative snapshots showing SWNT and poly-Si specific phonon modes in the Raman shift.

the shape of the tip upon over-etching, as can be seen in Figure 3.17c. Some nanotubes can be found attached to the sidewalls of the microstructures. As these additional SWNTs do not span across the gap, the system yield defined by individual crossing SWNTs is not affected.

One good way of confirming the presence of an individual (unbundled) SWNT with good crystallinity is to combine high-resolution TEM with electron diffraction imaging. Only if straight nanotubes over a relatively short distance (~800 nm) are integrated into freestanding structures can one obtain a clear diffraction pattern. Figure 3.17c and d show a TEM image and the corresponding electron diffraction (ED) pattern of an as-grown SWNT between the tips of the microstructure. The ED analysis is described in detail in Reference [74]. Electrons scattered at the condenser aperture lead to a shadow image of the sample structure together with the pattern. The fact that we can obtain a diffraction pattern at all shows that we have a straight, well-crystallized nanotube with a constant chirality within the illuminated region. The high-pass filtered and rotated pattern is compared with

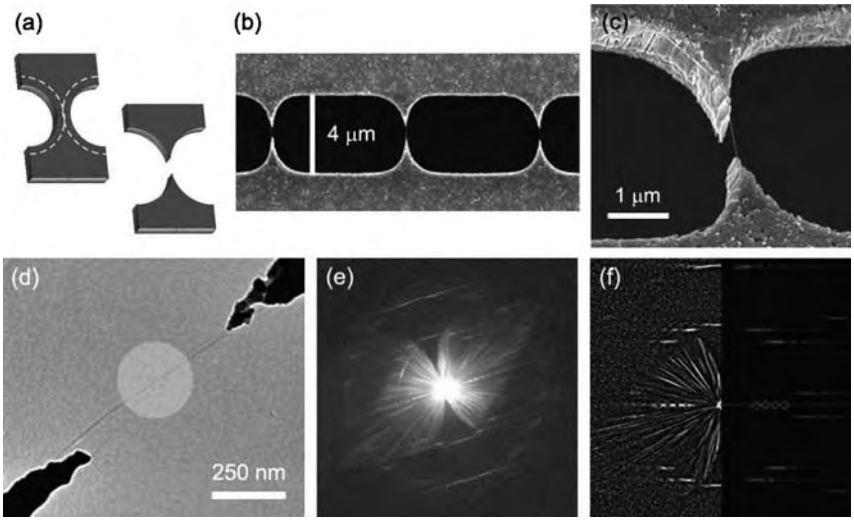

Figure 3.17 (a) Schematic of sharp tip formation from over-etching. (b) SEM image of a series of sharp tips. (c) SEM image of an SWNT which spanned over the predefined tips and (d) its corresponding TEM image. (e) ED pattern from the area indicated by the gray circle in (c). (f) High-pass filtered and rotated diffraction pattern (left) and simulated diffraction pattern of a (17,10) SWNT (right). The boxes mark streaks in the pattern, the circles mark minima in the equatorial line. By comparing all nearby indices we verify that only the (17,10) pattern matches the experimental one.

simulated diffraction pattern in order to identify the chiral indices of the SWNT (Figure 3.17d). In this example, only the pattern simulated for an individual (17,10) SWNT matches the experimental one, and all other candidates (and also bundles or multi-shell nanotubes) can be unambiguously excluded. The (17,10) SWNT has a diameter of 1.85 nm and a chiral angle of 21.5°. This particular tube has energy separations (with good Raman scattering efficiency) closest to the excitation line of $E_{33}^{S} = 1.932\,\text{eV}$ and $E_{55}^{S} = 2.928\,\text{eV}$ [75]. As these two values are off the resonant window of $2.33 \pm 0.4\,\text{eV}$, these transitions could not be observed in the Raman experiment and a Raman map of the tube shown in Figure 3.17b could not be recorded.

Figure 3.18 gives a comparison between the standard tip pairs seen in Figure 3.16 and the ultra-sharp tips investigated in Figure 3.17. For the ultra-sharp tips, in most cases only one SWNT bridged on defined sites giving a remarkable device yield (one tube per gap). The reduction in the gap size combined with the sharpening of the tip apexes also appears to give straighter SWNTs. We suggest the sharp tip apexes minimize potential SWNT bending and buckling related to the tube–support interactions [73]. Opposing sharp tips can clearly improve an SWNT alignment based on nearest-boundary attachment. Since our process does not rely on directional electric fields and gas flows, individual SWNTs can be aligned in multiple directions across 4-inch wafers in an off-the-shelf industrial LPCVD furnace. The surface micromachining can be adapted to different CVD conditions,

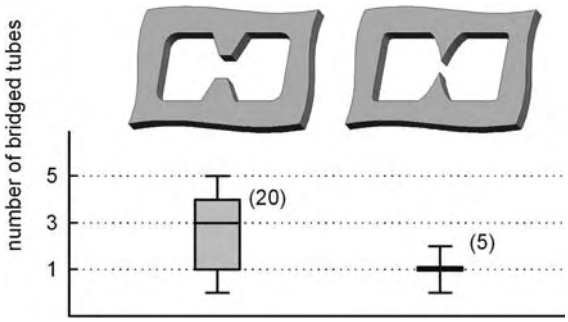

Figure 3.18 Box plot of two different tip apex geometries. Figures in parentheses indicate the number of measured tip pairs. The ultra-sharp tips have a mean number of spanned SWNT of one tube per tip pair.

thus the described method offers a simple, universal way of integrating individual SWNTs into scalable device designs.

3.3.11
Examples of Nanotube-Embedded Microsystems

3.3.11.1 Micro Sliders

A microchip containing a movable microsize grid (i.e. a drilled thin plate) is used to accommodate SWNTs. The nanotubes are integrated into the voids of the grid directly by thermal CVD. The grid is moved beneath the chip edge in order to become optically accessible from the top and the bottom directions. The as-grown nanotubes can then be investigated repeatedly by several characterization tools resulting in combined studies.

Figure 3.19a shows an SEM record of the structure realized from the surface micromachining process described earlier. SWNTs can be grown directly to span over the holes of the grid. After the completion of the CVD growth process step, the chips are subjected to an HF wet-etch step (40% HF for 3 min) to release the grid. If HF exposure of the nanotubes is not desired, the grid can be released optionally before the CVD growth allowing for *as-grown* investigation of the SWNTs. The poly-Si grid can be moved along the direction defined by the four anchored posts. The chip is therefore operated with microprobers in order to push the grid off the chip edge. The microprobe lands in the relatively large hole visible in Figure 3.19a and displaces the grid without damaging the nanostructures. Stoppers integrated into the lower poly-Si layer define the end of the grid travel. The anchors, defined in the topmost poly-Si layer, overlap with the underlying poly-Si layer (the carrier layer), allow the chip to be flipped upside down without losing the grid or hold the grid when the chip is exposed to rapid pressure changes, i.e. when venting a vacuum chamber. Additionally, nanotubes of different suspension lengths can be integrated by varying the size and shape of the drills in the silicon layer. This opens a new parameter space for the integration process.

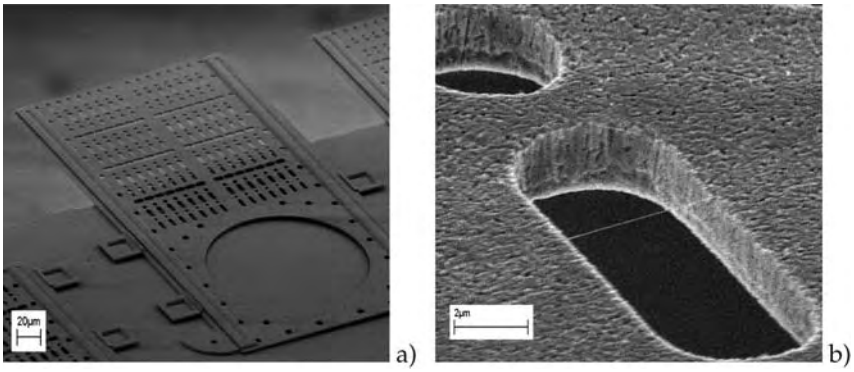

Figure 3.19 (a) SEM image of the freestanding microgrid. (b) Close-up of an area on the grid seen in (a) showing an as-grown by thermal CVD suspended SWNT (eventually bundled).

3.3.11.2 **Raman Imaging**

Analysis is performed, as an example, by combining SEM and micro-Raman scattering. Information on the location of as-grown SWNTs can be obtained quickly by SEM (see Figure 3.19). Raman spectra are acquired from a 532-nm laser line in the confocal mode by scanning grid locations which were matched with the map of the SEM recordings. Raman maps were established and were found to compare with the SEM data. Figure 3.20 shows the Raman maps of a hole from the grid by locking the LO mode of silicon, an SWNT by locking the RBM signal and a combined image of both. As Figure 3.20a and b were extracted from the same data, an overlay of both allows for spatial mapping as seen in (c). One can observe that the Raman signal enhances over the freestanding part of the nanotube. This is most likely due to reduced van der Waals interactions of the nanotube with the substrate.

3.3.11.3 **TEM Imaging and Electron Diffraction**

The same MEMS sample can be readily used for transmission electron microscopy (TEM). The die sizes are typically 2×2 or 1×1 mm. Depending on the TEM sample holder, only small dies fit to it. In this case the poly-Si grid has to be removed from the chip and attached to a TEM copper ring as shown in Figure 3.21a. The grid is attached to the metal ring by a carbon tape.

A low-resolution TEM image of the grid can be seen in Figure 3.21b. The Philips CM200 microscope operated at 120 kV is then magnified to high resolution, which allows the imaging of the shells of the nanotubes. Figure 3.21c shows that two SWNTs grew off from the edge of a rectangular slid and bundled by mutual van der Waals interaction. This image justifies the need for sharp tips to avoid tube bundling and confirms the previous Raman experiment in which an RBM signal was detected. RBM are typically only observed in SWNTs. Sharp tips inside the

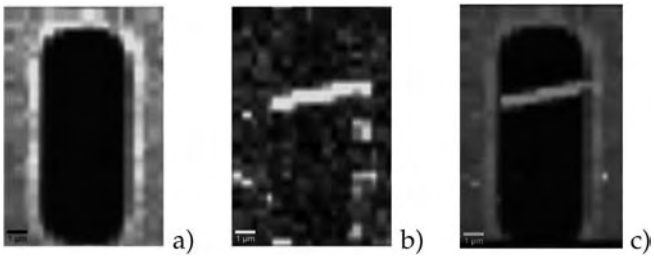

Figure 3.20 Raman images of the CNT contained poly-Si grid. (a) poly-Si map obtained by integrating the LO mode Raman spectrum of silicon (520 cm^{-1}). (b) CNT resonant Raman map of the RBM band (100–300 cm^{-1}). (c) Overlayed image of (a) and (b). Note that (a) and (b) were obtained from the same data set of spectra.

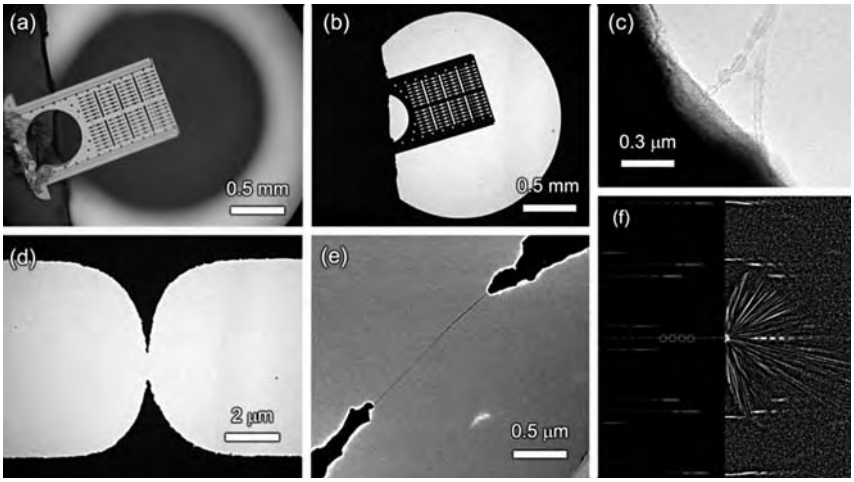

Figure 3.21 (a) Sample preparation for TEM and its corresponding low resolution TEM image. (c) HR-TEM of two SWNT which form a bundle during growth (d) TEM image of a tip pair accomodating a single SWNT and (e) its corresponding HR-TEM image and diffraction pattern (f).

same grid were imaged in Figure 3.21d and e. One can observe an individual straight nanotube aligning with the tip-pair.

The synthesis of straight nanotubes over a relatively short distance (~800 nm) integrated into freestanding thin-film microstructures allows also for electron diffraction. Diffraction patterns were recorded on a Zeiss 912 Ω microscope at 60 kV. Figure 2.21f show the corresponding electron diffraction pattern of the tube seen in (e). The electron diffraction analysis is described in detail in Reference [74].

Briefly, the electron beam is limited to an area of 250 nm in diameter by the demagnified image of the condenser aperture. The illumination angle in the Koehler illumination condition is set to 0.16 mrad, the energy filter to 25 eV and the diffraction pattern is recorded on image plates with an exposure time of 4 min. Electrons scattered at the condenser aperture lead to a shadow image of the sample structure together with the pattern. The fact that we can obtain a diffraction pattern at all shows that we have a straight, well-crystallized nanotube with a constant chirality within the illuminated region.

3.3.11.4 Tensile Loaders

MEMS actuators were fabricated [52] in such a way as to be compatible with our inhouse CNT integration process. Further, the actuator was designed to apply a maximal strain length of 800 nm in the linear range. The thermal actuator is comprised of a pair of five heater beams arranged in a bent-beam way in order to exhibit linear motion (see Figure 3.22).

Beams are angled 5° off the perpendicular position to the actuator axis, amplifying the displacement by a factor 10 and thus reducing the drive power for a given displacement. The bent-beam mechanism reduces the generated force by a factor of 11.5; however, it is still larger than 600 μN for small displacements. The choice of the beam angle comes as a trade-off between low power, low temperature (high magnification) and high resolution, high stability (low magnification). If the supplied power is very high, the structure enters a nonlinear resistivity regime and might exhibit creep due to stress at elevated temperatures [76]. The typical size of a polysilicon trench which is spanned by CNTs is about 2 μm (minimum spacing). As it is known from literature that CNTs can be strained to ~5% [77–79], the strain length of 800 nm is balancing process variations, i.e. trenches are larger than laid out and CNTs can span the trench in a curled fashion, requiring greater travel for the actuator actually to strain them.

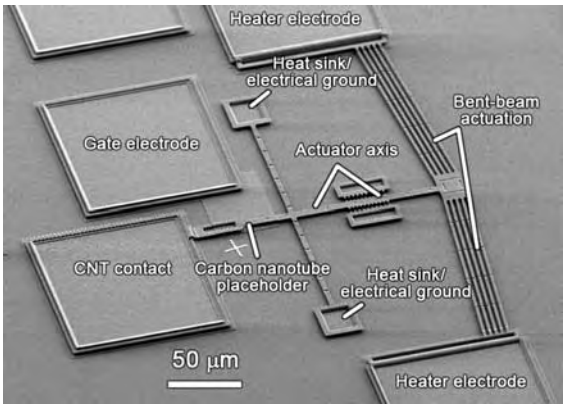

Figure 3.22 SEM of a MEMS actuator based on bent-beam electrothermal actuation.

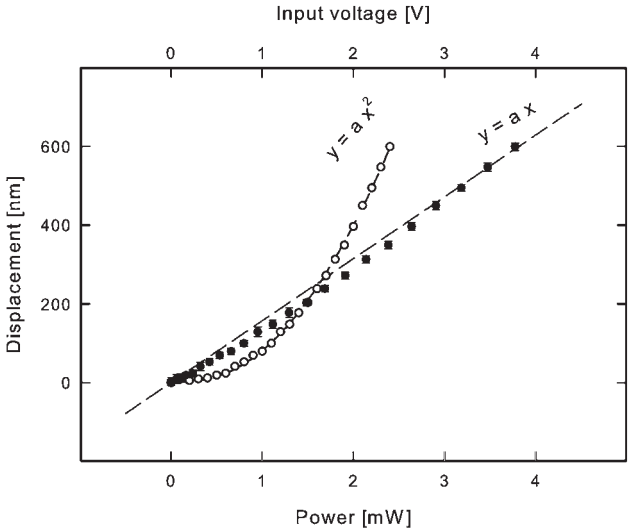

Figure 3.23 Relative displacement characteristic from DC voltage source and DC power source. The characteristic was extracted from scanning electron microscopy and image processing.

In order to obtain the voltage displacement – and the power – displacement characteristics, the actuator was fed with a power supply, and pictures were taken for a distinct number of voltages. With the help of these pictures, the displacement is determined by using the different methods of investigation. The voltage levels are applied only in the linear range of the actuator, which have been determined beforehand. Figure 3.23 shows the recorded voltage–displacement characteristics. A quadratic behavior is observed, according to the law

$$\Delta y = \alpha V^2 \tag{1}$$

In this case $\alpha = 84.2 \pm 6\,\mathrm{nm\,V^{-2}}$. Using $V_{max} = 3.0\,\mathrm{V}$, the maximum displacement is $\Delta y_{max} = 758 \pm 54\,\mathrm{nm}$. The regime was thus purely ohmic and a temperature coefficient of resistance (TCR) could not be measured, $\alpha_{TCR} \approx 0$. The power–displacement characteristic shows a linear behavior, according to the law

$$\Delta y = \beta P \tag{2}$$

where β was found to be $\beta = 157.2\,\mathrm{nm\,mW^{-1}}$ ($R^2 = 0.9905$). Although the actuator is voltage driven, because of the constant resistance in the chosen range, it can be considered to be power driven. Noticeable here is a swing in the displacement characteristic seen in Figure 3.23.

3.4 Localized Carbon Nanotube Growth from Microheaters

During the last decade, a lot of research effort has been spent on the controlled growth of carbon nanotubes. In particular, the CVD process was adjusted to specific applications. Due to high synthesis temperatures, their compatibility with microelectronic processes by means of direct integration is an issue. Market-competitive SWNT-based sensors need to be built from a CMOS factory line, hence the need for chip compliance during the growth/integration process of SWNTs [80].

In this section, we demonstrate localized and CMOS-compatible nanotube integration. It is achieved by the synthesis of carbon nanotubes utilizing a super-localized CVD method. The modified CVD method uses tiny heat sources defined by microscale resistive heaters as opposed to global furnace heating. The method has a series of advantages such as the reduced process time due to increased heating ramps or the suppression patterning step of the catalyst by costly electron beam lithography. Also, methane pyrolysis and the subsequent amorphous carbon contamination of the exposed chip are reduced. Since the synthesis is carried out globally at room temperature, the process is compatible with standard CMOS technology.

3.4.1 Growth Using Microheaters

Englander et al. [80] proposed resistive heating of microline resistors to activate the vapor-deposition synthesis of silicon nanowires and carbon nanotubes in a room temperature chamber. Their process is localized, selective and scalable. Synthesized dimensions of the nanotubes of 10–50 nm in diameter and up to 5 μm in length have been demonstrated.

In their work, two types of suspended MEMS structures were fabricated to serve as localized microresistive heaters for the synthesis processes: polysilicon microstructures using a standard surface micromachining process and single-crystal silicon microstructures based on a silicon-on-insulator (SOI) wafer (see Figure 3.24). In both cases the microstructures were heavily doped with phosphorus and suspended 2 mm, defined by the sacrificial silicon dioxide layer, above a silicon substrate for electrical and thermal isolation. The typical thickness of the bridges is 2 μm for polysilicon microstructures and 20 μm for single-crystal silicon microstructures. The wet chemical release etching process naturally creates recessed regions underneath the electrical contacts such that a maskless catalyst deposition process cannot cause an electrical short circuit.

For nanotube synthesis, a 5-nm evaporated nickel, iron or Ni–Fe (80 : 20 by weight) mixture was used used, with higher growth rates occurring when iron was present. After placement in the vacuum chamber and being electrically connected, acetylene was introduced to supply carbon. With the acetylene pressure constant at 245 mTorr, growth occurred at 0.25 mm min^{-1} at optimal temperature locations.

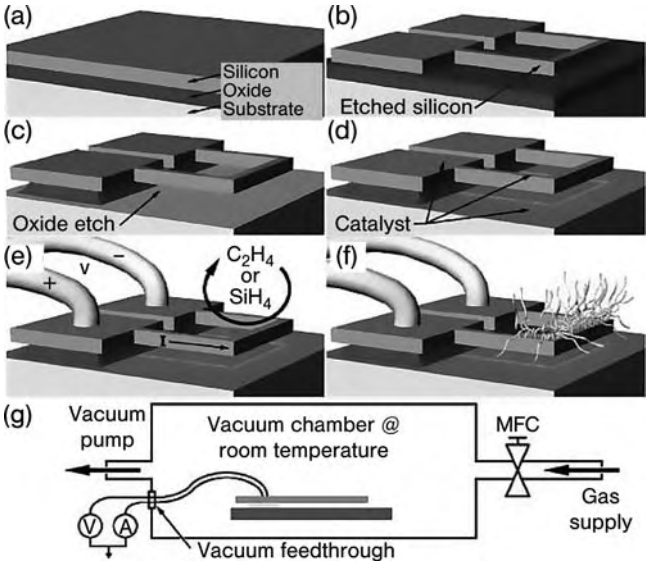

Figure 3.24 Series depicting the fabrication of microbridges, growth of nanostructures and experimental setup and process. (a) Initial threelayer wafer. (b) Microstructure layer patterning and etching. (c) Timed etch of the sacrificial oxide layer. (d) Maskless catalyst evaporation. (e) Wirebonds and electrical actuation in the desired gaseous ambient. (f) Resulting nanostructures. (g) Schematic of the experimental setup in a room temperature chamber. After Reference [80].

Carbon nanotube growth requires higher temperatures for the synthesis reaction to occur; higher voltages and currents are therefore required for similar MEMS microstructures.

Sunden et al. [81] reported on a novel method for selectively synthesizing CNTs directly on the tip of a heated atomic force microscope (AFM) cantilever via CVD, using only the heating of the probe provided. Like previous research into CNT growth on micro-heaters, this approach eliminates the need for chemical processing and ambient CVD temperatures that might otherwise damage sensitive microfabricated features. They additionally demonstrated integration of functional nanostructures into a microscale sensing device that allows *in situ* characterization of the CNTs. The experiment used a heatable AFM cantilever. Electron beam evaporation deposited a 10-nm iron catalyst film on the cantilever prior to temperature calibration. The electron beam evaporated film was sufficiently thin to form islands upon heating; each island acts as an individual growth site for CNTs (see Figure 3.25). Scanning electron microscopy was used to confirm the presence of vertically aligned nanotubes, which were highly localized on only the heater area of the cantilever. The cantilever mechanical resonance decreased on CNT growth, and then returned to its initial frequency following cantilever cleaning, indicating a CNT mass on the order of 10^{-14} kg.

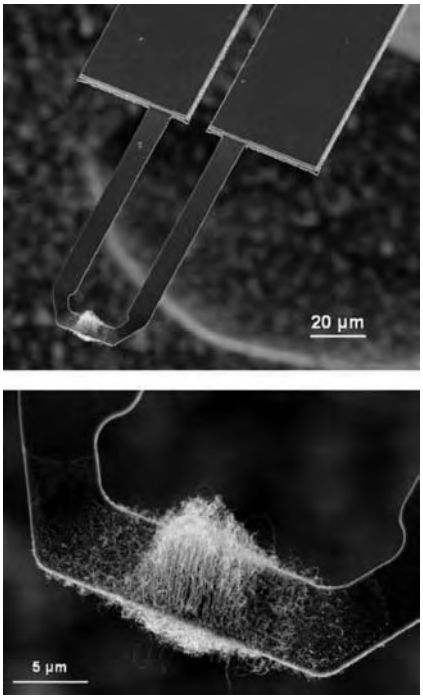

Figure 3.25 Carbon nanotubes grown only on the heated region of the cantilever. After Reference [81].

3.4.2
Localized Heat Spots

In this section, we discuss the option of constraining the heat spots to minimal sizes. Resistive heating of a microscale bar induces uniform heating along its entire length. Several mechanisms can be employed to tailor the development of heat. As the decomposition of hydrocarbon gases is catalytically activated, there is no need to preheat the gaseous atmosphere, thus justifying the use of point heat sources. Two mechanisms to favor the development of strong temperature gradients and hence constrain the maximum temperature to micron-sized spots are exploited: (i) in series resistance modulation and (ii) local anchorage to the substrate forming heat sinks.

Figure 3.26 shows an image of an uncoated released microheater array. It was powered from a single two-point connection. Their radiative spots can be clearly seen. The anchors are ideal in the sense that they remain at ambient temperature at all times. The heat conduction from the freestanding bridge through the air gap (2 μm) to the substrate can be neglected. This assumption is acceptable as the heated surface is comparably small and, what is more, the air conduction reduces in a low-pressure regime (below 100 mbar). The heat spot is constrained to approximately $3 \times 3\,\mu m$ (see also Figure 3.26 to confirm the dimensions of the square-

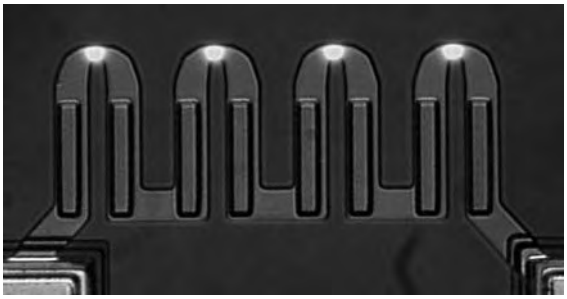

Figure 3.26 Array of four microheaters powered from a two-point connection. Hot spots show radiation. Their intensity and color code suggest equal temperatures at the hot spots.

shaped heat spot) and temperature gradients of 100 K μm^{-1} were achieved. The method of constraining heat generation to a localized spot enhances the position control of the CNT synthesis and the integration density of discrete nanotube-based devices on a chip.

The electric field and the heat flux, simplified using $\nabla \cdot j = 0$ as we assume current confinement in the material, yield

$$c_p \frac{\partial}{\partial t} T - \nabla \cdot (k_{th} \nabla T) + \Theta \nabla T \cdot j = \rho j^2 \tag{3}$$

where Θ is the Thomson coefficient, defined as

$$\Theta = T \frac{\partial \alpha_S}{\partial T} \tag{4}$$

which represents the first Kelvin relation.

If the Thomson term becomes negligible in Equation (3), the temperature profile is quadratic and $T_{\max}$ is in the middle of the heater. If currents (and the resulting temperature and temperature gradients) are high enough, the Thomson term disturbs the symmetry of the parabola, resulting in a skid of the heat spot. This dragging is due to the fact that the Thomson term depends on the temperature gradient, which has alternating sign left and right from the heater beam center. The direction of the skid depends on the current direction. As revealed by scaling, the Thomson effect is most effective when scaling the heater dimensions down [82]. Figure 3.27 shows the current dependence of the microheater used for local growth. Temperature measurement was done by confocal Raman scattering [83]. Due to the Thomson effect, the hot spot is shifted by several microns. Is is thus important to consider its influence when designing point heater sources.

The sample is coated with a catalytic solution containing iron nitride, molybdenum and alumina nanoparticles dissolved in methanol [13]. The evaporation of

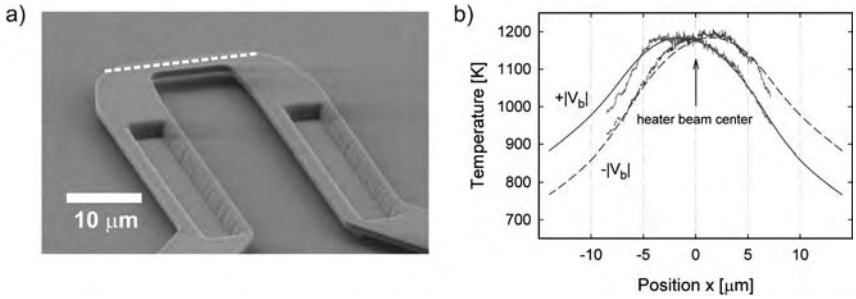

Figure 3.27 (a) SEM picture of a microheater. (b) Measured and simulated temperature profile through the heater tip (see a) for opposite bias voltages.

the solvent is enhanced in air using a hot-plate (40 °C). After evaporation, the chip is die bonded to a support chip containing large contact pads using non-permanent hot wax and wire bonded. The system is then transferred into a vacuum chamber featuring *in situ* electrical connection. The cold-wall CVD consists of a vertically placed quartz tube with a gas inlet on top and a vacuum valve at the bottom. It is operated in a low-pressure range from 10^{-2} to 100 mbar. It is first subjected to argon purge and evacuation cycles. Subsequently methane is fed at 150 and the pressure is kept at 75 mbar. Heat is produced through resistive heating by flowing electric current through polysilicon beams. A voltage-controlled power supply is used and simultaneous resistance monitoring is done. The reaction is carried out at the region of the generated heat during 15 min using increasing voltage steps. Figure 3.28 shows carbon nanotubes locally grown directly on the microheater spot. Smallest diameter tubes were observed in the vicinity of the maximum temperature. Bundles of single-walled or thick multi-walled CNTs were observed in colder regions away from the maximum heat spot.

Within the framework of a CMOS-compatible process [84], not only the maximum process temperature but also thermal budgets, taking into account both temperature and time, are considered. A typical hydrogen annealing step at 700 K for 30 min (CMOS 0.5 μm technology generation) might already affect doping profiles, but this could be considered from a total process flow point of view. Additional process steps as proposed for a compatible integration of MEMS and CNTs should perform lower thermal budgets. Typical CVD processes for nanotube growth are run at 1175 K for about 10 min. Additionally, heating and cooling ramps of 150 and 30 K min^{-1}, respectively, are achieved with industrial-grade LPCVD furnaces. The resulting thermal budget is far beyond CMOS compatibility. In microheaters, instantaneous heating ($\tau = 0.01$ ms) and very low power consumption (200 mW) are achieved.

The synthesis of carbon nanotubes utilizing local heat sources defined in microscale heaters was demonstrated. The method provides a remedy to amorphous carbon contamination of the exposed chip and most importantly a significant step towards the process integration of nanotubes into functional devices. Since the synthesis was carried out globally at room temperature, the suggested

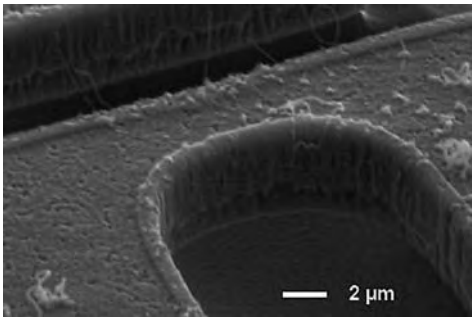

Figure 3.28 SEM of microheater containing locally synthesized carbon nanotubes.

process is compatible with standard CMOS technology. Thermal budgets can be lowered compared with classical thermal CVD.

3.5 Conclusion

While a lot of basic research effort is currently being spent on the physics of one-dimensional structures or on nanoscale materials in general, nano-based devices are at the demonstrator level at best. Hence there is a strong technology need for reproducible batch-compatible nano-integration. This chapter has provided a first revision of state-of-the-art single-walled carbon nanotube integration control. Through surface-bound CVD, CNTs were grown directly inside microsystems with good control over their location and orientation. Furthermore, advanced top-down processing producing nano-sharp tips indicated ways to integrate scalably individual single-walled carbon nanotube suspensions. Additionally, amorphous carbon contamination issues were solved.

A CMOS-compatible integration solution by room temperature local CVD has been provided. The synthesis of carbon nanotubes utilizing a localized CVD method relying on the use of local heat sources defined in microscale heaters was demonstrated. Since the synthesis was carried out globally at room temperature, the suggested process is compatible with standard CMOS technology. Results yielded the presence of strong temperature gradients throughout the microheaters, allowing high-density nanotube integration processes. Thermal budgets have been lowered compared with classical thermal CVD.

3.6 Acknowledgments

This work was supported by the ETH FIRST clean room and ETH EMEZ electron microscopy facilities and funded by the Swiss National Science Foundation (Grant

No. 200021–108059/1). Acknowledged for their support are Jannik Meyer for TEM images and electron diffraction patterns, Christoph Stampfer, Stephan Hofmann, Simone Pisana, Bakir Babic, Murray Height and Cosmin Roman for valuable discussions and Sébastien Schiesser and Lukas Durrer for laboratory support.

Microsystems featuring various functionalities with integrated single-walled carbon nanotubes are available commercially from the Micro and Nanosystems Group, ETH Zurich (Zurich, Switzerland).

References

1 S. Iijima, T. Ichihashi, Single-shell carbon nanotubes of 1-nm diameter, *Nature*, **363** (1993) 603–605.

2 D. S. Bethune, C. H. Klang, M. S. de Vries, G. Gorman, R. Savoy, J. Vazquez, R. Beyers, Cobalt-catalysed growth of carbon nanotubes with single-atomic-layer walls, *Nature*, **363** (1993) 605–607.

3 R. Martel, T. Schmidt, H. R. Shea, T. Hertel, P. Avouris, Single- and multi-wall carbon nanotube field-effect transistors, *Appl. Phys. Lett.*, **73** (1998) 2447–2449.

4 M. Madou, *Fundamentals of Microfabrication*. CRC Press, Boca Raton, FL, 2002.

5 ITRS, *Emerging Research Devices*, Technical Report, International Technology Roadmap for Semiconductors, 2005.

6 A. P. Graham, G. S. Duesberg, R. V. Seidel, M. Liebau, E. Unger, W. Pamler, F. Kreupl, W. Hoenlein, Carbon nanotubes for microelectronics? *Small*, **1** (2005) 382–390.

7 H. Sato, K. Hata, Growth of carbon nanotubes by plasma-enhanced chemical vapor deposition, *New Diamond Frontier Carbon Technol.*, **16** (2006) 163–176.

8 M. Chhowalla, K. B. K. Teo, C. Ducati, N. L. Rupesinghe, G. A. J. Amaratunga, A. C. Ferrari, D. Roy, J. Robertson, W. I. Milne, Growth process conditions of vertically aligned carbon nanotubes using plasma enhanced chemical vapor deposition, *J. Appl. Phys.*, **90** (2001) 5308.

9 S. Maruyama, R. Kojima, Y. Miyauchi, S. Chiashi, M. Kohno, Low-temperature synthesis of high-purity single-walled carbon nanotubes, *Chem. Phys. Lett.*, **360** (2002) 229–234.

10 *National Nanotechnology Initiative: Leading to the Next Industrial Revolution*, Interagency Working Group on Nanoscience, Engineering and Technology of the National Science and Technology Council's Committee on Technology, Washington, DC, 2000.

11 S. Hofmann, M. Cantoro, M. Kaempgen, D. J. Kang, V. B. Golovko, H. W. Li, Z. Yang, J. Geng, W. T. S. Huck, B. F. G. Johnson, S. Roth, J. Robertson, Catalyst patterning methods for surface-bound chemical vapor deposition of carbon nanotubes, *Appl. Phys. A*, **81** (2005) 1559–1567.

12 D. Mann, in Synthesis of carbon nanotubes, *Carbon Nanotubes: Properties and Applications*, CRC Press, Boca Raton, FL, (2006) 19–42.

13 J. Kong, H. T. Soh, A. M. Cassell, C. F. Quate, H. J. Dai, Synthesis of singlewalled carbon nanotubes on patterned silicon wafers, *Nature*, **395** (1998) 878–881.

14 S. Hofmann, R. Sharma, C. Ducati, G. Du, C. Mattevi, C. Cepek, M. Cantoro, S. Pisana, A. Parvez, F. Cervantes-Sodi, A. C. Ferrari, R. Dunin-Borkowski, S. Lizzit, L. Petaccia, A. Goldoni, J. Robertson, *In situ* observations of catalyst dynamics during surface-bound carbon nanotube nucleation, *Nano Lett.*, **7** (2007) 602–608.

15 X. Fan, R. Buczko, A. A. Puretzky, D. B. Geohegan, J. Y. Howe, S. Pantelides, S. Pennycook, Nucleation of single-walled carbon nanotubes, *Phys. Rev. Lett.*, **90** (2003) 145501.

16 J. Gavillet, A. Loiseau, C. Journet, F. Willaime, F. Ducastelle, J. C. Charlier, Root-growth mechanism for singlewall

carbon nanotubes, *Phys. Rev. Lett.*, **87** (2001) 275504.

17 R. H. Baughman, A. A. Zakhidov, W. A. de Heer, Carbon nanotubes – the route toward applications, *Science*, **297** (2002) 787–792.

18 H. Kanzow, A. Ding, Formation mechanism of single-wall carbon nanotubes on liquid-metal particles, *Phys. Rev. B*, **60** (1999) 11180–11186.

19 S. Hofmann, Low temperature growth of high aspect ratio structures. *PhD Thesis*, University of Cambridge, 2004.

20 Y. G. Zhang, A. L. Chang, J. Cao, Q. Wang, W. Kim, Y. M. Li, N. Morris, E. Yenilmez, J. Kong, H. J. Dai, Electric-field-directed growth of aligned single-walled carbon nanotubes, *Appl. Phys. Lett.*, **79** (2001) 3155–3157.

21 E. Joselevich, C. M. Lieber, Vectorial growth of metallic and semiconducting single-wall carbon nanotubes, *Nano Lett.*, **2** (2002) 1137–1141.

22 S. Hofmann, G. Csanyi, A. C. Ferrari, M. C. Payne, J. Robertson, Surface diffusion: the low activation energy path for nanotube growth, *Phys. Rev. Lett.*, **95** (2005) 036101.

23 R. Seidel, G. S. Duesberg, E. Unger, A. P. Graham, M. Liebau, F. Kreupl, Chemical vapor deposition growth of single-walled carbon nanotubes at 600 degrees C and a simple growth model, *J. Phys. Chem. B*, **108** (2004) 1888–1893.

24 Y. Saito, M. Okuda, M. Tomita, T. Hayashi, Extrusion of single-wall carbon nanotubes via formation of small particles condensed near an arc evaporation source, *Chem. Phys. Lett.*, **236** (1995) 419–426.

25 S. Huang, M. Woodson, R. Smalley, J. Liu, Growth mechanism of oriented long single walled carbon nanotubes using fast-heating chemical vapor deposition process, *Nano Lett.*, **4** (2004) 1025–1028.

26 W. Kim, H. C. Choi, M. Shim, Y. M. Li, D. W. Wang, H. J. Dai, Synthesis of ultralong and high percentage of semiconducting single-walled carbon nanotubes, *Nano Lett.*, **2** (2002) 703–708.

27 M. Cantoro, S. Hofmann, S. Pisana, V. Scardaci, A. Parvez, C. Ducati, A. C. Ferrari, A. M. Blackburn, K.-Y. Wang, J. Robertson, Catalytic chemical vapor deposition of single-wall carbon nanotubes at low temperatures, *Nano Lett.*, **6** (2006) 1107–1112.

28 A. R. Harutyunyan, B. K. Pradhan, U. J. Kim, G. G. Chen, P. C. Eklund, CVD synthesis of single wall carbon nanotubes under soft conditions, *Nano Lett.*, **2** (2002) 525–530.

29 K. Hata, D. N. Futaba, K. Mizuno, T. Namai, M. Yumura, S. Iijima, Waterassisted highly efficient synthesis of impurity-free single-waited carbon nanotubes, *Science*, **306** (2004) 1362–1364.

30 A. Magrez, J. W. Seo, V. L. Kuznetsov, L. Forro, Evidence of an equimolar c2h2- co2 reaction in the synthesis of carbon nanotubes, *Angew. Chem. Int. Ed.*, **46** (2007) 441–444.

31 D. Takagi, Y. Homma, H. Hibino, S. Suzuki, Y. Kobayashi, Single-walled carbon nanotube growth from highly activated metal nanoparticles, *Nano Lett.*, **6** (2006) 2642–2645.

32 A. M. Cassell, J. A. Raymakers, J. Kong, H. J. Dai, Large scale CVD synthesis of single-walled carbon nanotubes, *J. Phys. Chem. B*, **103** (1999) 6484–6492.

33 S. C. Lyu, B. C. Liu, S. H. Lee, C. Y. Park, H. K. Kang, C. W. Yang, C. J. Lee, Large-scale synthesis of high-quality double-walled carbon nanotubes by catalytic decomposition of n-hexane, *J. Phys. Chem. B*, **108** (2004) 2192–2194.

34 Y. Tu, Z. P. Huang, D. Z. Wang, J. G. Wen, Z. F. Ren, Growth of aligned carbon nanotubes with controlled site density, *Appl. Phys. Lett.*, **80** (2002) 4018.

35 C. L. Cheung, A. Kurtz, H. Park, C. M. Lieber, Diameter-controlled synthesis of carbon nanotubes, *J. Phys. Chem. B*, **106** (2002) 2429.

36 T. Sato, D. G. Hasko, H. Ahmed, Nanoscale colloidal particles: Monolayer organization and patterning, *J. Vac. Sci. Technol. B*, **15** (1997) 45.

37 A. B. Stiles, *Catalyst Supports and Supported Catalysts: Theoretical and Applied Concepts*. Butterworth, Boston, 1987.

38 S. M. Sze, *Physics of Semiconductor Devices*. Wiley, New York, 1981.

39 A. M. Rao, D. Jacques, R. C. Haddon, W. Zhu, C. Bower, S. Jin, *In-situ* grown carbon nanotube array with excellent field

emission characteristics, *Appl. Phys. Lett.*, **76** (2000) 3813–3815.

40 R. T. K. Baker, S. J. Tauster, J. A. Dumesic, *Strong Metal–Support Interactions*. ACS Symposium Series, American Chemical Society, Washington, DC, 1986.

41 S. S. Fan, M. G. Chapline, N. R. Franklin, T.W. Tombler, A. M. Cassell, H. J. Dai, Self-oriented regular arrays of carbon nanotubes and their field emission properties, *Science*, **283** (1999) 512.

42 Z. F. Ren, Z. P. Huang, J. W. Xu, J. H. Wang, P. Bush, M. P. Siegal, P. N. Provencio, Synthesis of large arrays of wellaligned carbon nanotubes on glass, *Science*, **282** (1998) 1105.

43 N. R. Franklin, Q. Wang, T.W. Tombler, A. Javey, M. Shim, H. Dai, Integration of suspended carbon nanotube arrays into electronic devices and electromechanical systems, *Appl. Phys. Lett.*, **81** (2002) 913–915.

44 Y. Homma, D. Takagi, Y. Kobayashi, Suspended architecture formation process of single-walled carbon nanotubes, *Appl. Phys. Lett.*, **88** (2006) 023115.

45 A. Ural, Y. M. Li, H. J. Dai, Electric-field-aligned growth of single-walled carbon nanotubes on surfaces, *Appl. Phys. Lett.*, **81** (2002) 3464–3466.

46 K. A. Telari, B. R. Rogers, H. Fang, L. Shen, R. A. Weller, D. N. Braski, Characterization of platinum films deposited by focused ion beam-assisted chemical vapor deposition, *J. Vac. Sci. Technol. B*, **20** (2002) 590–595.

47 C. Scheck, P. Evans, R. Schad, G. Zangari, L. Sorba, G. Biasiol, S. Heun, Selective metal electrodeposition through doping modulation of semiconductor surfaces, *Appl. Phys. Lett.*, **86** (2005) 133108.

48 J. P. Chen, C. M. Sorensen, K. J. Klabunde, G. C. Hadjipanayis, Magnetic properties of nanophase cobalt particles synthesized in inversed micelles, *J. Appl. Phys.*, **76** (1994) 6316–6318.

49 G. S. Duesberg, A. P. Graham, M. Liebau, R. Seidel, R. Unger, F. Kreupl, W. Hoenlein, Growth of isolated carbon nanotubes with lithographically defined diameter and location, *Nano Lett.*, **3** (2003) 257–259.

50 J. C. Meyer, M. Paillet, G. S. Duesberg, S. Roth, Electron diffraction analysis of individual single-walled carbon nanotubes, *Ultramicroscopy*, **106** (2006) 176–190.

51 R. E. Smalley, Y. Li, V. C. Moore, B. K. Price, J. R. Colorado, H. K. Schmidt, R. H. Hauge, A. R. Barron, J. M. Tour, Single wall carbon nanotube amplification: en route to a type-specific growth mechanism, *J. Am. Chem. Soc.*, **128** (2006) 15824–15829.

52 J. M. Bustillo, R. T. Howe, R. S. Muller, Surface micromachining for microelectromechanical systems, *Proc. IEEE*, **86** (1998) 1552–1574.

53 J.-M. Wen, J. W. Evans, M. C. Bartelt, J. W. Burnett, P. A. Thiel, Coarsening mechanisms in a metal film: from cluster diffusion to vacancy ripening, *Phys. Rev. Lett.*, **76** (1996) 652.

54 E. Jiran, C. V. Thompson, Capillary instabilities in thin, continuous films, *Thin Solid Films*, **208** (1992) 23.

55 P. R. Gadkari, A. P. Warren, R. M. Todi, R. V. Petrova, K. R. Coffey, Comparison of the agglomeration behavior of thin metallic films on SiO_2, *J. Vac. Sci. Technol A*, **23** (2005) 1152.

56 J. A. Moulijn, V. A. van Diepen, F. Kapteijn, The role of precursor gases on the surface restructuring of catalyst films during carbon nanotube growth, *Appl. Catal. A*, **3** (2001) 212.

57 S. Pisana, M. Cantoro, A. Parvez, S. Hofmann, A. C. Ferrari, J. Robertson, The role of precursor gases on the surface restructuring of catalyst films during carbon nanotube growth, *Physica E*, **37** (2007) 1–5.

58 T. de los Arcos, M. G. Garnier, J. W. Seo, P. Oelhafen, V. Thommen, D. Mathys, The influence of catalyst chemical state and morphology on carbon nanotube growth, *J. Phys. Chem. B*, **108** (2004) 7728.

59 Y. M. Li, W. Kim, Y. G. Zhang, M. Rolandi, D.W. Wang, H. Dai, Growth of single-walled carbon nanotubes from discrete catalytic nanoparticles of various sizes, *J. Phys. Chem. B*, **105** (2001) 11424–11431.

60 S. R. Sails, D. J. Gardiner, M. Bowden, J. Savage, D. Rodway, Monitoring the quality of diamond films using Raman spectra excited at 514.5 nm and 633 nm, *Diamond Relat. Mater.*, **5** (1996) 589–591.

61 E. Anastassakis, E. Burstein, Electric-field-induced infrared absorption and Raman scattering in diamond, *Phys. Rev. B*, **2** (1970) 1952–1965.

62 R. Loudon, The Raman effect in crystals, *Adv. Phys.*, **13** (1964) 423–482.

63 A. Jungen, Direct integration by synthesis and properties of single-walled carbon nanotubes. *PhD Thesis*, ETH Zurich, 2007.

64 A. P. Graham, G. S. Duesberg, R. Seidel, M. Liebau, E. Unger, F. Kreupl, W. Hoenlein, Towards the integration of carbon nanotubes in microelectronics, *Diamond Relat. Mater.*, **13** (2004) 1296–1300.

65 M. Paillet, V. Jourdain, P. Poncharal, J.-L. Sauvajol, A. Zahab, J. C. Meyer, S. Roth, N. Cordente, C. Amiens, B. Chaudret, Versatile synthesis of individual single-walled carbon nanotubes from nickel nanoparticles for the study of their physical properties, *J. Phys. Chem.*, **108** (2004) 17112–17118.

66 L. Delzeit, B. Chen, A. Cassell, R. Stevens, C. Nguyen, M. Meyyappan, Multilayered metal catalysts for controlling the density of single-walled carbon nanotube growth, *Chem. Phys. Lett.*, **348** (2001) 368–374.

67 N. R. Franklin, Y. Li, R. J. Chen, A. Javey, H. Dai, Patterned growth of single-walled carbon nanotubes on full 4-inch wafers, *Appl. Phys. Lett.*, **79** (2001) 4571–4573.

68 A. M. Dean, Detailed kinetic modeling of autocatalysis in methane pyrolysis, *J. Phys. Chem.*, **94** (1990) 1432–1439.

69 A. Jorio, J. H. Hafner, C. M. Lieber, M. Hunter, T. McClure, G. Dresselhaus, M. S. Dresselhaus, Structural (*n,m*) determination of isolated single-wall carbon nanotubes by resonant Raman scattering, *Phys. Rev. Lett.*, **86** (2001) 1118–1121.

70 H. W. Zhu, K. Suenaga, A. Hashimoto, K. Urita, K. Hata, S. Iijima, Atomic-resolution imaging of the nucleation points of single-walled carbon nanotubes, *Small*, **1** (2005) 1180–1183.

71 M. Lin, J. P. Y. Tan, C. Boothroyd, K. P. Loh, E. S. Tok, Y. L. Foo, Direct observation of single-walled carbon nanotube growth at the atomistic scale, *Nano Lett.*, **6** (2006) 449–452.

72 S. Helveg, C. Lopez-Cartes, J. Sehested, P. L. Hansen, B. S. Clausen, J. R.-N. F. Abild-Pedersen, J. N. Norskov, Atomic-scale imaging of carbon nanofibre growth, *Nature*, **427** (2004) 426–429.

73 Z. R. Abrams, Y. Hanein, Tube–Tube and Tube–surface interactions In straight suspended carbon nanotube structures, *J. Phys. Chem. B*, **110** (2006) 21419–21423.

74 J. C. Meyer, M. Paillet, G. S. Duesberg, S. Roth, Electron diffraction analysis of individual single-walled carbon nanotubes, *Ultramicroscopy*, **106** (2006) 176–190.

75 V. N. Popov, P. Lambin, Resonant Raman intensity of the totally symmetric phonons of single-walled carbon nanotubes, *Phys. Rev. B*, **73** (2006) 165425.

76 K. Tuck, A. Jungen, A. Geisberger, M. Ellis, G. Skidmore, A study of creep in polysilicon MEMS devices, *J. Eng. Mater. Technol.*, **127** (2005) 90–96.

77 J. P. Salvetat, G. A. D. Briggs, J. M. Bonard, R. R. Bacsa, A. J. Kulikand, T. Stockli, N. A. Burnham, L. Forro, Elastic and shear moduli of single-walled carbon nanotube ropes, *Phys. Rev. Lett.*, **82** (2004) 944–947.

78 P. A. Williams, P. J. Papadakis, A. M. Patel, M. R. Falvo, S. Washburn, R. Superfine, Torsional response and stiffening of individual multiwalled carbon nanotubes, *Phys. Rev. Lett.*, **89** (2002) 255502.

79 M. F. Yu, O. Lourie, M. J. Dyer, K. Moloni, T. F. Kelly, R. S. Ruoff, Strength and breaking mechanism of multiwalled carbon nanotubes under tensile load, *Science*, **287** (2000) 637–640.

80 O. Englander, D. Christensen, L. Lin, Local synthesis of silicon nanowires and carbon nanotubes on microbridges, *Appl. Phys. Lett.*, **82** (2003) 4797–4799.

81 E. O. Sunden, T. L. Wright, J. Lee, W. P. King, S. Graham, Room-temperature chemical vapor deposition and mass detection on a heated atomic force

microscope cantilever, *Appl. Phys. Lett.*, **88** (2006) 033107.

82 A. Jungen, M. Pfenninger, M. Tonteling, C. Stampfer, C. Hierold, Electrothermal effects at the microscale and its consequences on system design, *J. Micromech. Microeng.*, **16** (2006) 1633–1638.

83 A. Jungen, C. Stampfer, C. Hierold, Thermography on a suspended microbridge using confocal Raman scattering, *Appl. Phys. Lett.*, **88** (2006) 191901.

84 C. Hierold, A. Hildebrandt, U. Naeher, T. Scheiter, B. Mensching, M. Steger, R. Tielert, A pure CMOS surface-micromachined integrated accelerometer, *Sens. Actuators A*, **57** (1996) 111–116.

4
Characterization of Carbon Nanotubes by Optical Spectroscopy

Janina Maultzsch, Christian Thomsen, Technische Universität Berlin, Institut für Festkörperphysik, Berlin, Germany

The characterization of carbon nanotubes for applications in electronic, nanomechanical or sensing devices can be performed by various methods, including optical spectroscopy, scanning probe techniques and electron diffraction. The

Advanced Micro & Nanosystems Vol. 8. Carbon Nanotube Devices.
Edited by Christofer Hierold

ISBN: 978-3-527-31720-2

method of choice depends on the required level of characterization, for instance whether it is sufficient to distinguish metallic from semiconducting nanotubes or whether the chiral index must be determined. Furthermore, it depends on the sample conditions such as its environment, and whether the sample is a single nanotube or a nanotube ensemble. For example, an individual nanotube as part of a single-molecule electronic device might need to be characterized. On the other hand, after nanotube synthesis large quantities of nanotubes might require analysis regarding their diameter distribution and purity, or the chemical treatment of nanotube suspensions is to be monitored. Optical spectroscopy is a versatile, non-destructive method which can be applied under many different conditions and which ranges from detecting the presence of carbon nanotubes to identifying the chiral index (n,m). Here we give a review on how optical spectroscopy can be used to characterize carbon nanotubes.

The two most widely used optical methods to characterize carbon nanotubes are resonant Raman scattering and photoluminescence/absorption spectroscopy. A further optical technique is Rayleigh scattering, which, however, requires individual free-standing nanotubes, whereas the other two methods can be applied to a large variety of sample types. The determination of the chiral index of a nanotube in all optical methods relies on patterns in the so-called Kataura plot, which presents the optical transition energies of all chiral indices (n,m) as a function of the nanotube diameter.

In Section 4.1 we discuss resonant Raman spectroscopy, starting with a brief introduction to Raman scattering and the Raman response of carbon nanotubes in Section 4.1.1. Section 4.1.2 compares the Raman spectrum of a single-walled carbon nanotube with that of graphite and multi-walled nanotubes. In Section 4.1.3 we develop the (n,m) assignment procedure, starting with the nanotube diameter in Section 4.1.3.1, explaining the Kataura plot in detail in Section 4.1.3.2, and presenting the assignment results in Section 4.1.3.3. We give an instruction for (n,m) assignment based on one laser line in Section 4.1.3.4; in Section 4.1.3.5 we discuss the procedure for the case of one individual nanotube. Finally, we comment on the relative abundance of different (n,m) and on the distinction between metallic and semiconducting nanotubes in Sections 4.1.3.6 and 4.1.3.7. How to detect the presence of defects in the nanotube structure by Raman scattering is explained in Section 4.1.4; the imaging methods presented there apply to photoluminescence imaging correspondingly.

In Section 4.2 we give an overview of photoluminescence and Rayleigh scattering spectroscopy. Many of the concepts presented for Raman spectroscopy are the same as for nanotube characterization by photoluminescence and Rayleigh spectroscopy. Again we explain the (n,m) assignment procedure for nanotube ensembles by pattern matching (Section 4.2.1), discuss the relative (n,m) abundance (Section 4.2.1.1), and present photoluminescence spectroscopy on individual nanotubes and under varying environmental conditions (Section 4.2.1.2). A brief introduction to Rayleigh scattering is given in Section 4.2.2.

Finally, in Section 4.3 we briefly compare the presented optical methods with imaging techniques, including electron diffraction, scanning probe microscopy and transmission electron microscopy.

Our notation of nanotube structural properties follows the definitions in References [1, 2] with the exception that in the present work the symbol m does not denote the band index/symmetry number. The chiral index (n,m) gives the coordinates of the chiral vector defined with respect to the graphene lattice vectors. The chiral angle θ is defined such that armchair nanotubes $[(n, n)]$ have $\theta = 30°$ and zig-zag nanotubes $[(n, 0)]$ have $\theta = 0°$. Nanotubes with $(n - m)/3 =$ integer are called metallic, although chiral "metallic" nanotubes have a small gap on the order of 10 meV.

4.1 Raman Spectroscopy

Raman spectroscopy is one of the most widely used characterization tools for carbon nanotubes [1]. One advantage is its abilitity to probe both semiconducting and metallic nanotubes. Furthermore, unlike luminescence spectroscopy, Raman scattering requires virtually no special sample preparation. It can be performed on individual single tubes and also on samples consisting of nanotube bundles, nanotubes on various substrates, in solution or even on free-standing individual nanotubes. Therefore, it is frequently used to characterize nanotubes after growth and adjust growth conditions, and to monitor chemical reactions; see for instance References [3–7].

In this section, we discuss Raman scattering from carbon nanotubes as a characterization technique. Some of the concepts presented here also apply to photoluminescence and Rayleigh scattering. For details about the Raman process itself, such as symmetry and selection rules, the reader is referred to the literature; see References [1, 8].

4.1.1 Introduction to Raman Scattering

Raman spectroscopy probes the vibrational, optical and electronic properties of a material. Raman scattering is a third-order process, where the incoming light is inelastically scattered by excitations of quasi-particles, such as lattice vibrations (phonons), electronic or magnetic excitations [9, 10]. In Figure 4.1 we show a schematic illustration of the Raman process: the incoming light excites an electron–hole pair, the electron (or hole) is scattered by emitting or absorbing a phonon, and the electron–hole pair recombines. The difference in energy between the incident and the scattered light corresponds to the energy of the phonon. The phonons which are allowed to participate in this process are selected by the requirements of energy and quasi-momentum conservation:

$$\hbar\omega_{\mathrm{i}} = \hbar\omega_{\mathrm{s}} \pm \hbar\omega_{\mathrm{ph}} \tag{1}$$

$$\hbar\vec{k}_{\mathrm{i}} = \hbar\vec{k}_{\mathrm{s}} \pm \hbar\vec{q} \tag{2}$$

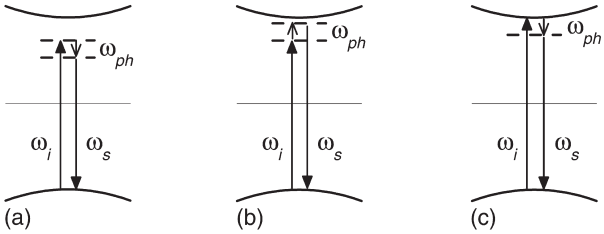

Figure 4.1 Schematic view of a Raman process, where the incoming light with frequency ω_i excites an electron–hole pair, and the electron (or hole, not shown here) is scattered by a phonon. (a) The phonon is emitted (Stokes scattering); (b) the phonon is absorbed (anti-Stokes). In non-resonant scattering, the intermediate states (dashed lines) correspond to virtual transitions. (c) Resonant Raman scattering: if the incoming or outgoing light matches a real transition, the Raman signal is enhanced by several orders of magnitude. From the resonance profile, the energy of the resonant optical transition is determined.

where $\omega_{i,s}$ are the angular frequencies of the incident and scattered light, respectively, ω_{ph} is the phonon frequency, $\hbar = h/2\pi$ with Planck's constant h, $\hbar\vec{k}_{i,s}$ are the photon momenta and $\hbar\vec{q}$ is the phonon quasi-momentum. The plus and minus signs correspond to Stokes (phonon emission, Figure 4.1a) and anti-Stokes scattering (phonon absorption, Figure 4.1b), respectively.

The maximum momentum transferred from the incident photons to the phonon in the scattering process is $\hbar q \approx 2\hbar\vec{k}_i$ (backscattering). Since in the visible range the photon wavevector is much smaller than the extension of the Brillouin zone in a crystal structure with a lattice constant of a few Ångstroms, only phonons close to the zone center ($q \approx 0$) can be probed in first-order Raman scattering. Higher-order Raman scattering may be used to probe phonons in the entire Brillouin zone. Alternatively, inelastic X-ray scattering with much larger photon energy and momentum can probe all phonon branches in solids [11–14]. Selection rules based on the symmetry of the system and the scattering geometry further restrict the phonon modes that can be observed in a Raman experiment [9, 10].

Since in Raman scattering just the difference between incoming and outgoing photon energies is measured, one can usually choose the excitation energy independently of the properties of the sample, in particular, independently of the vibrational energies. However, if the energy of the incoming or outgoing light matches a real transition in the electronic structure, the Raman signal is resonantly enhanced (Figure 4.1c). By recording the Raman intensity as a function of excitation energy (resonance profile), the optical transition energies can be determined. This resonance effect is used to assign the chiral index (n,m) of carbon nanotubes and is explained in more detail in Section 4.1.3.3.

A typical Raman spectrum of an ensemble of single-walled carbon nanotubes is shown in Figure 4.2; see also References [1, 8, 15, 16]. The first-order spectrum is dominated by three main bands: the radial breathing mode (RBM) in the low-frequency region corresponds to an in-phase, mainly radial vibration of the carbon atoms. Its frequency scales approximately inversely with the nanotube diameter d

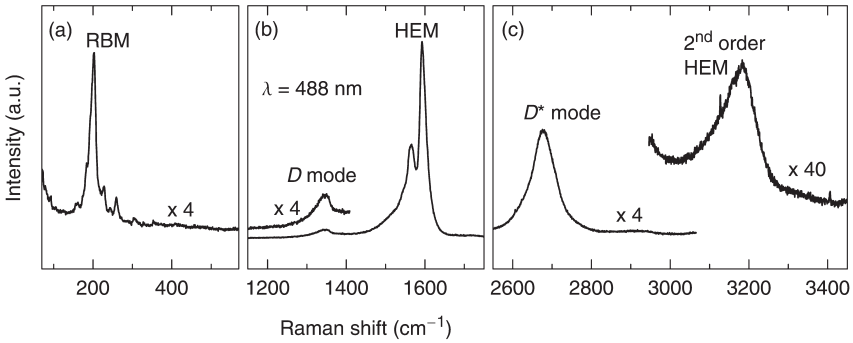

Figure 4.2 Raman spectrum of an ensemble sample of single-walled carbon nanotubes. (a) Radial breathing modes. Each of the peaks corresponds to a different nanotube (*n*,*m*). (b) Defect-induced *D* mode and high-energy modes (HEM, *G* mode). In SWNT, the high-energy modes show a double (or multiple) peak structure. (c) Second-order spectrum with the overtones of the *D* mode (*D**, *G*′) and of the HEM. After Reference [23].

[1, 17]; see Section 4.1.3.1. Therefore, each of the RBM peaks in Figure 4.2a is from a different nanotube. The RBM is characteristic of single-walled carbon nanotubes and will be used for the chiral index assignment; see Section 4.1.3.3. The *D* mode at around 1350 cm^{-1} is disorder induced; it comes from a phonon with non-zero wavevector, corresponding to the *K* point in the graphite Brillouin zone [18–20]. It is observed because its intensity is enhanced in a double-resonant process; as a consequence, its Raman frequency shifts with the excitation energy [21]. The *D*-mode intensity increases if the concentration of defects in the nanotube increases; see also Section 4.1.4. Defects can be, for instance, structural disorder such as vacancies, kinks or bends, the ends of the nanotube or chemical groups attached to the nanotube wall. The high-energy modes at 1600 cm^{-1} (HEM, *G* mode) correspond to tangential vibrations, where two neighboring atoms move out-of-phase along the tube axis or along the circumference of the tube. The second-order Raman spectrum is shown in Figure 4.2c. The two most prominent peaks are the overtones of the *D* mode (named *D** or *G*′ in the literature) and of the HEM. In second-order Raman scattering, two phonons with opposite wavevector are scattered simultaneously, either as an overtone, i.e., two phonons with the same energy giving a Raman peak at twice the frequency of the first-order peak, or as a combination of two different phonon modes. Usually, the second-order modes are weaker than the first-order spectrum; the *D** mode is exceptionally strong because of its double-resonant origin. As the *D** mode results from scattering by two phonons, it is always present and often stronger than the *D* mode, whereas the *D* mode requires a defect and can therefore be vanishingly small. All of the Raman peaks in Figure 4.2 are observed if the incident and the detected light are polarized parallel to the nanotube axis [2, 22]. For a detailed description of symmetry and selection rules in carbon nanotubes, see References [1, 2].

In general, Raman scattering can be performed on nanotubes in any sample environment, on bundled tubes, ensembles of nanotubes and single individual

tubes. Raman measurements have been reported from bulk samples (see, e.g., References [24–27]), from individual tubes or thin bundles on an SiO_2 substrate [22, 28–32], individual suspended tubes [33–37], and from surfactant-wrapped nanotubes in aqueous solutions [38–41].

4.1.2
Detection of Carbon Nanotubes

The Raman spectrum shown in Figure 4.2 is typical for single-walled carbon nanotubes. In particular, the presence of one or more RBM peaks and the clearly double-peaked structure of the HEM make it unique compared with the Raman spectrum of graphite or multi-walled nanotubes. To a first approximation, the two peaks in the nanotube HEM (*G* mode) below and above the graphite *G* mode result from a splitting of the doubly-degenerate *G* mode in graphite (E_{2g} symmetry) due to the nanotube-wall curvature. They are typically at ~1595 and ~1550–1570 cm^{-1} for nanotubes with diameters below 2 nm. The separation between the peaks (often referred to as G^+ and G^-) increases with decreasing nanotube diameter [30, 35, 42] and vanishes if the diameter goes to infinity. In semiconducting nanotubes, the higher-frequency peak G^+ is usually attributed to the vibration along the tube axis and G^- to the vibration perpendicular to the tube axis, in accordance with calculations of the phonon frequencies [42–45]. The phonon eigenvectors are shown schematically in Figure 4.3. For convenience, we call the vibration along the nanotube axis longitudinal optical (LO) phonon and that perpendicular to the axis transverse optical (TO) phonon, although in chiral nanotubes the atomic displacements are not purely longitudinal or transverse, but of mixed character [46]. In addition, the tangential modes can have a small radial component and *vice versa*

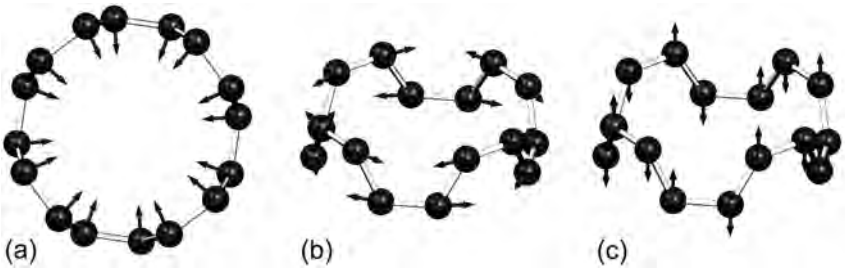

Figure 4.3 Phonon eigenvectors in the (4,4) nanotube; one unit cell is shown. (a) Radial breathing mode; the nanotube axis is perpendicular to the plane of the paper. (b) Transverse optical (TO) phonon. (c) Longitudinal optical (LO) phonon. The nanotube axis in (b) and (c) is vertical. In armchair (zigzag) nanotubes, the LO (TO) mode is Raman forbidden. The Raman HEM (*G* mode) is usually attributed to the phonon modes corresponding to (b) and (c) in chiral tubes. The atomic displacement in chiral tubes is not restricted to the purely longitudinal or transverse direction; the phonons are, however, often assumed to be predominantly "LO" and "TO". From Reference [23].

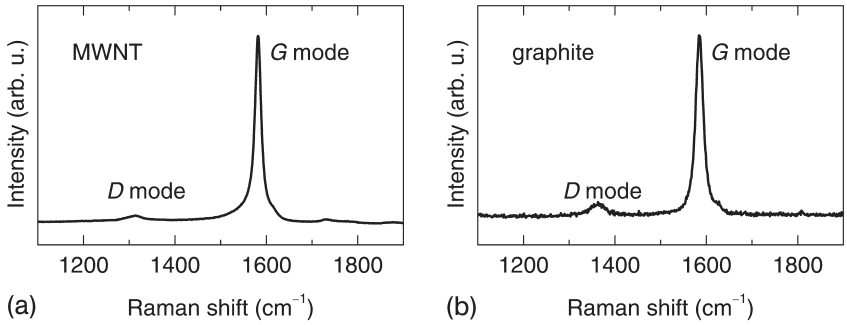

Figure 4.4 Raman spectra of multi-walled carbon nanotubes (a) and of graphite (b). In contrast to single-walled carbon nanotubes, the *G* mode in MWNT and graphite consists of a single peak. If the sample contains defects, i.e. if the *D* mode is present, the *G* mode typically shows a small shoulder on the high-energy side above 1600 cm^{-1}. This peak results from double-resonant scattering with near-Γ-point, $q \neq 0$ phonons and is higher in frequency than the Γ-point phonon because of the overbending in the phonon dispersion of graphite.

[42, 47]. Regarding metallic carbon nanotubes, the assignment of the higher- and lower-frequency peaks to LO and TO phonons, respectively, is currently under debate [29, 48–50]; see also Section 4.1.3.7. Calculations predict an interchange of the frequencies at the Γ point, and recent experiments are in accordance with this interpretation. Furthermore, in the presence of defects, contributions from double-resonant scattering to the HEM have been predicted to be significant away from the resonance [29]. These questions will, however, not affect the (n,m) assignment procedure described below.

In graphite, the *G* mode is a single peak at around 1582 cm^{-1} with a full width at half-maximum (fwhm) of ~20 cm^{-1} at room temperature [51]; see Figure 4.4. Multi-walled nanotubes (MWNT) are often composed of more than ten nanotubes with diameters in the range of 10 nm. Therefore, the MWNT spectrum resembles the graphite spectrum rather than that of single-walled carbon nanotubes. Because of the large diameters of the constituent tubes, RBM-like modes of MWNT are usually too small in intensity and frequency to be detected. In Reference [52], it was shown that Raman modes in the RBM region can be observed in high-purity MWNT samples if the diameter of the inner tube is smaller than 2 nm. Also, the high-energy mode in MWNT is very similar to the graphite *G* mode, mainly because of the large nanotube diameters. In contrast, double-walled carbon nanotubes typically consist of smaller-diameter tubes and have a Raman spectrum similar to that of single-walled nanotubes [53–55].

Double-walled nanotubes can be synthesized from so-called peapods, i.e. single-walled carbon nanotubes filled with C_{60} or C_{70} fullerenes [55, 56]. In this case, the diameter of the outer tube ranges between 1.3 and 1.5 nm, and correspondingly the inner tubes have diameters around 0.7 nm. Double-walled carbon nanotubes produced by chemical vapor deposition can also have inner-tube diameters smaller

than 1 nm [53]. In such double-walled structures with small inner diameters it has been attempted to identify the chiral index of both the inner and outer tubes [53, 57]. One has to take into account, however, that due to the interaction between the tube walls the radial breathing modes of the isolated inner and outer tubes are no longer present; instead, in double-walled nanotubes two breathing-like modes exist, where the two tubes move in-phase and out-of-phase [58]. These breathing-like modes are both upshifted compared with the RBM frequencies of the corresponding single-walled nanotubes.

In summary, the double-peak HEM shape in combination with RBM Raman peaks is a unique signature of single- and double-walled carbon nanotubes compared with multi-walled nanotubes and graphite.

4.1.3
Chiral Index (*n*,*m*) Assignment

For a range of applications of carbon nanotubes, it might be sufficient just to distinguish between certain categories of their properties such as whether the tubes are metallic or semiconducting, to estimate their diameter range or to determine whether they are bundled or unbundled. Very often, however, knowledge of the chiral index (n,m) is desired, in particular in experiments on individual nanotubes or if the properties of individual tubes are determined in ensemble measurements. The (n,m) assignment is also important if the experimental results are to be compared with numerical calculations, which usually provide predictions for distinct (n,m) tubes. Another example are metallic nanotubes, where it can be required to distinguish between truly metallic armchair nanotubes [(n, n)] and chiral quasi-metallic tubes that exhibit a small gap in the electronic band structure.

In this section we explain the procedure for (n,m) assignment by (resonant) Raman spectrocscopy, including the determination of the nanotube diameter and the metallic or semiconducting character. The concepts of the (n,m) assignment procedure by resonant Raman scattering are very similar to the ones used in photoluminescence and Rayleigh scattering (Section 4.2), in particular, the systematics and structure of the so-called Kataura plot described in Section 4.1.3.2.

4.1.3.1 **Diameter Dependence of the Radial Breathing Mode**

The frequency of the radial breathing mode is approximately linear with the inverse nanotube diameter $1/d$ [17]. This can be understood from a simple geometric consideration: a given atomic displacement in the radial direction produces a smaller component of restoring force along the carbon–carbon bonds the larger the tube diameter. In the limit of infinite diameter, the atomic displacement is perpendicular to the carbon bonds, and the RBM displacement becomes the out-of-plane acoustic phonon of graphite.

The geometric diameter d of a nanotube with chiral index (n,m) with an ideal cylinder shape is given by [1]

$$d = \frac{a_0}{\pi}\sqrt{n^2 + nm + m^2} \tag{3}$$

where a_0 = 2.461 Å is the in-plane lattice constant of graphite[1]. The relation between the RBM frequency ω_{RBM} and the tube diameter d can be modeled by

$$\omega_{RBM} = \frac{c_1}{d} + c_2 \tag{4}$$

where the coefficients c_1 and c_2 reported in the literature range from c_1 = 215 to 260 cm^{-1} nm and c_2 = 0 to 20 cm^{-1}, both from theory and experiment [1]. For example, (n,m) assignments in samples of surfactant-wrapped nanotubes with diameters between 6.5 and 13.5 Å yielded coefficients $c_1 = 219 \pm 5$ cm^{-1} nm and $c_2 = 15 \pm 5$ cm^{-1} [39, 40, 59]. Different c_1 and c_2 values or deviations from the linear behavior in Equation (4) have been reported for very large-diameter tubes [34], for nanotubes on substrates [28] and for nanotubes with very small diameters [60]. The empirically obtained coefficients c_1 and c_2 depend also on the value of the graphite lattice constant a_0 used in Equation (3) and on whether d refers to the theoretical diameter after numerical relaxation of the nanotube structure, as for instance in References [42, 61]. However, we would like to point out that although Equation (4) is important for estimating the diameter of nanotubes, it is not the most relevant part of an (n,m) assignment; in particular, an (n,m) assignment does not necessarily improve with "better" c_1 and c_2 parameters.

In nanotubes with diameters smaller than ~1.3 nm, the frequency of the radial breathing mode varies strongly with the tube diameter: the difference in ω_{RBM} between two nanotubes with similar diameter and transition energy (i.e. appearing in the same Raman spectrum) is in the range 4–10 cm^{-1} for $d < 1$ nm and still more than 2 cm^{-1} up to d = 1.3 nm with a few exceptions including zigzag nanotubes [62]. A spectral resolution of 2 cm^{-1} can be achieved with standard spectrometers. Therefore, it might seem straightforward to deduce the chiral index (n,m) directly from the RBM frequency using Equation (3). On the other hand, considering the uncertainties resulting from the wide variation of the coefficients c_1 and c_2 in the empirical relation Equation (4), the RBM frequency alone will not give unambiguous (n,m) assignments. In particular, such an assignment is not a matter of improving the accuracy of the ω_{RBM} measurement or of improving numerical calculations of the RBM frequency. Instead, by combining the experimental RBM frequency with a second piece of information, we have to assign this *experimental* value of ω_{RBM} to a particular (n,m)[2].

4.1.3.2 **Optical Transition Energies: Kataura Plot**

If we aim at a reliable (n,m) assignment, we need a second piece of information in addition to the nanotube diameter obtained from the RBM frequency. This will

1) Often $a_0 = a_{C\text{–}C}\sqrt{3}$ is used in the literature with a carbon–carbon distance $a_{C\text{–}C}$ = 1.44 Å. This has to be taken into account when using empirical relations of the diameter dependence of the RBM frequency or the optical energies.

2) If instead we correlated ω_{RBM} to the diameter first, based on Equation (4), we would assign a given experimental RBM peak to different (n,m) each time we change the empirical

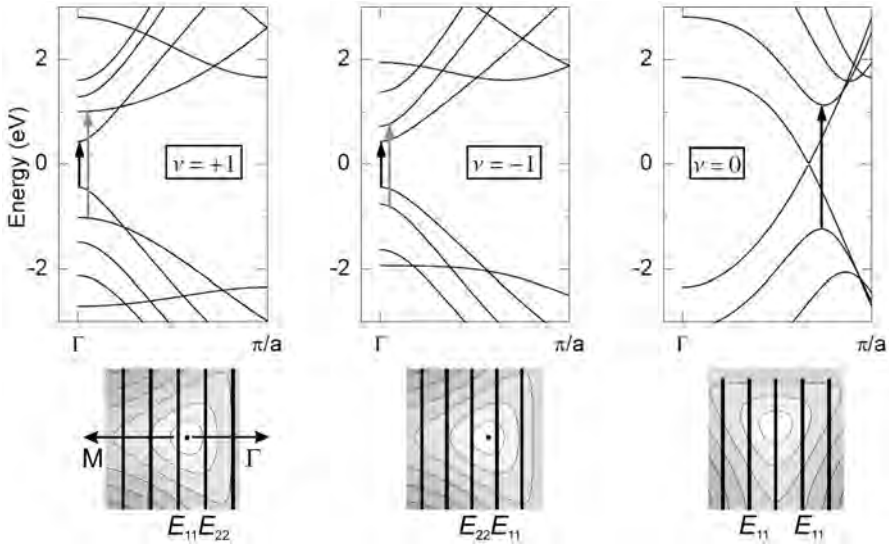

Figure 4.5 Top: electronic band structure of the (10,0) tube ($\nu = +1$), the (11,0) tube ($\nu = -1$), and the (6,6) tube ($\nu = 0$), calculated from a third-nearest neighbor tight-binding model [64]. The first and second transitions are indicated by black and gray arrows, respectively. Bottom: corresponding bands (thick black lines) in the graphite Brillouin zone around the *K* point (dot). The background is a contour plot of the graphite conduction band; the energy increases from white to dark gray.

be provided by the optical transition energies of the nanotube under consideration, which are accessible by resonant Raman spectroscopy; see also Section 4.1.3.3. We first present an overview of the electronic structure in carbon nanotubes and their transition energies. In Section 4.1.3.3,we give a detailed description of the assignment procedure. The so-called Kataura plot [63], which shows the transition energies as a function of nanotube diameter, will be the basis for (n,m) assignments by photoluminescence and Rayleigh scattering spectroscopy as well.

In Figure 4.5, we show the electronic band structure of the (10,0), (11,0), and (6,6) nanotubes. They belong to the three families $\nu = (n - m) \bmod 3$, where nanotubes with $\nu = +1$ and $\nu = -1$ are semiconducting, and tubes with $\nu = 0$ are metallic. The (10,0) tube has $\nu = +1$; for the (11,0) tube $\nu = -1$[3]. The (6,6) tube with $\nu = 0$ is metallic. The arrows indicate the first and second transitions allowed for light polarized along the tube axis, i.e. transitions E_{ii} between valence and conduction bands with the same index i [1]. In semiconducting tubes, the first transition energy E_{11} is slightly smaller in the $\nu = +1$ nanotube than in the $\nu = -1$ tube. In contrast, the second transition E_{22} is larger in the $\nu = +1$ nanotube. This pattern between the two families of semiconducting tubes is valid for all nanotubes. It can be explained

3) Note that $\nu = -1$ is equivalent to $\nu = 2$, sometimes used in the literature; the notation "type I" and

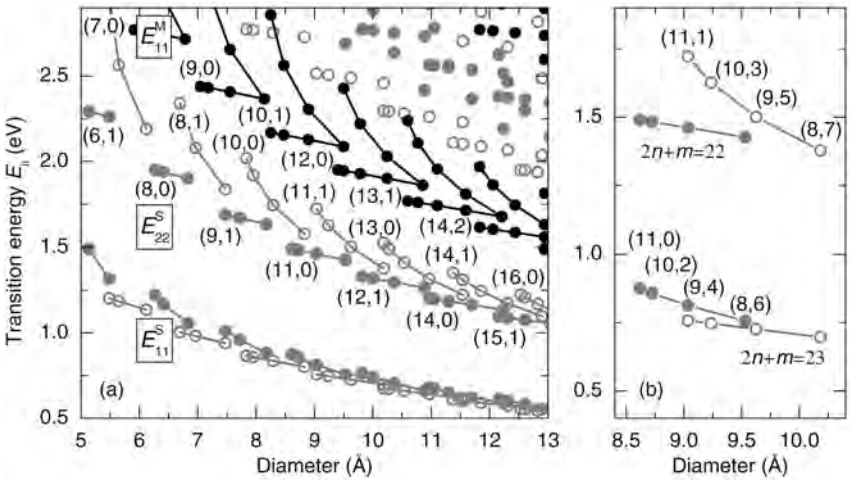

Figure 4.6 (a) Theoretical Kataura plot from a third-nearest neighbor tight-binding calculation [64]. The gray symbols indicate semiconducting tubes with $\nu = -1$ (closed circles) and $\nu = +1$ (open circles). The E_{11}^{M} transitions of metallic tubes are shown by black circles. The lines connect the nanotubes forming a branch with $2n + m$ = constant. The chiral index of the outermost (smallest diameter) tubes of the V-shaped branches is given. (b) Zoom into the E_{11}^{S} and E_{22}^{S} region of the (11,0) and (11,1) branches; the chiral index is indicated for each nanotube. Within a branch, neighboring tubes from left to right are given by $(n - 1, m + 2)$.

within the zone-folding picture: the bottom row in Figure 4.5 shows the lines forming the nanotube Brillouin zone close to the graphite K point. In $\nu = +1$ tubes, the lowest transition comes from the left side of the K point, and the second from the right side. In $\nu = -1$ tubes, this is reversed, i.e. the first transition E_{11} is to the right and the second transition E_{22} to the left. As the transition energies to the right of the K point (i.e. in the K–Γ direction) are larger than those at the same distance to the left (i.e. in the K–M direction), the magnitude of the transition energies in $\nu = -1$ and $\nu = +1$ tubes alternates when going from E_{11}^{S} to E_{22}^{S}.

By plotting the transition energies E_{ii} for all nanotubes as a function of diameter, we obtain a Kataura plot [63]. Figure 4.6 shows a Kataura plot for all tubes in the diameter range from $d = 5$ to 13 Å. The energy range covers the first and second transitions of semiconducting tubes (gray symbols, E_{11}^{S} and E_{22}^{S}), and the first transition of metallic tubes (black symbols, E_{11}^{M}). Except for armchair tubes, the metallic E_{11}^{M} is split into a lower-energy and a higher-energy transition, which corresponds in the zone-folding picture to transitions from opposite sides of the graphite K point [1, 67]. Although there is an overall $1/d$ dependence, the transition energies show systematic deviations, forming V-shaped patterns (lines in Figure 4.6). Each of these branches is defined by a constant value $2n + m$ of its constituent nanotubes. For E_{11}^{M}, the upper and lower V branches are the split transitions and belong to the same (n,m) tubes; the innermost tube is always an armchair nanotube (no splitting).

The outermost tube is a zigzag (n, 0) or an (n, 1) tube. The V-shaped patterns in the semiconducting transitions are formed each by a $\nu = +1$ and a $\nu = -1$ branch, where in the first transitions E_{11}^{S} the $\nu = -1$ branch is higher in energy than the $\nu = +1$ branch, and *vice versa* in E_{22}^{S}; see also Figure 4.5. Again, at the outermost positions are zigzag or close-to-zigzag tubes, and at the inner positions are close-to-armchair tubes. The chiral indices of neighboring tubes in a branch are given by

$$(n',m') = (n-1, m+2) \tag{5}$$

for $n' > m'$; see Figure 4.6b.

So far, we have treated the transitions E_{ii} as band-to-band transitions, where an uncorrelated electron–hole pair is excited. It is known from theory and experiment, however, that the optically excited electron–hole pairs form excitons with binding energies on the order of a few hundred meV [68–74]. Although the strength of the exciton binding energy and of other many-body effects depends on the tube diameter and might be different for different transitions E_{ii}, there has been no evidence so far for any fundamental change in the *patterns* of the Kataura plot or in the order of the optical transitions compared to the single-particle picture shown in Figure 4.6. Therefore, we will mostly use calculations neglecting excitonic effects, although all experimental data E_{ii} from optical spectroscopy correspond to exciton states.

The (n,m) assignment by any optical method involves a comparison between experimentally obtained E_{ii} and a calculated Kataura plot. Therefore, we summarize in the following different methods of obtaining a Kataura plot and discuss their usability.

1. *Zone folding from tight-binding models.* Zone folding from a tight-binding calculation of the structure of the electronic π bands in a graphite sheet is probably the simplest method to derive a Kataura plot [63]. If the tight-binding model includes only first neighbors of carbon atoms, it contains one adjustable parameter [63, 75]. Including up to third-nearest neighbors (see Figure 4.6), however, has been shown to give qualitatively better agreement with density functional theory calculations [64]. The advantage of the zone-folding approach is that it can be applied to any nanotube structure, independent of the number of atoms in the nanotube unit cell. On the other hand, the tight-binding models are single–electron models, neglecting electron–electron and electron-hole interactions that have been shown to be important [68–74, 76]. Moreover, the zone-folding approach neglects the curvature of the nanotube wall and makes incorrect predictions for very small diameter tubes. Therefore, we cannot directly compare the absolute E_{ii} energies from experiment with those from zone-folding tight-binding calculations.

However, as we show below, the systematics and the V-shaped patterns in the tight-binding Kataura plot (Figure 4.6), agree well with experiment and have been successfully used for (n,m) assignments by photoluminescence and Raman spectroscopy [39, 59].

2. *Non-orthogonal tight-binding model.* The non-orthogonal tight-binding model presented in Reference [61] is based on a structural optimization of the nanotube atomic positions and includes both the 2s and the 2p electrons. Therefore, curvature effects and σ–π rehybridization for small-diameter nanotubes are taken into account by this model. It has been shown that the calculated E_{11} and E_{22} for nanotubes in the diameter range from $d = 6$ to 12 Å agree well with experimental data after a uniform upshift of the calculated values by 300 meV [77]. However, at larger diameters the 300 meV upshifted values from the non-orthogonal thight-binding model seem to be slightly higher than empirical relations based on experimental data would predict, as shown in Figure 4.7b. For the higher transitions of semiconducting tubes, an empirically determined upshift of 400 meV has been reported [78].

   A table containing all E_{ii} from this model up to 3.5 eV for nanotubes with diameters $d = 4 - 24$ Å can be found in Reference [79]. Empirically determined corrections that take into account many-body effects are discussed in References [65, 78].
3. *First-principles calculations.* First-principles calculations of the electronic band structure in carbon nanotubes first revealed the σ–π rehybridization due to the curvature of the nanotube wall [80, 81] and the failure of zone-folding predictions for very small diameters [82, 83]. Electron–electron and electron–hole interactions have been included in some of the *ab initio*-based calculations, predicting a large range of exciton binding energies for different nanotube diameters and dielectric environments [68, 70–72]. However, *ab initio* calculations even within the single-electron picture require a large amount of computational time. Therefore, they are mostly restricted to achiral (armchair and zigzag) tubes or to selected chiral tubes with relatively small unit cells. To our knowledge, no complete Kataura plot has been reported so far based on *ab initio* calculations.
4. *Empirical relations.* In addition to theoretical Kataura plots, available experimental data or empirical relations provide an excellent basis for (n,m) assignment. Experimental

values of E_{11}^{S}, E_{22}^{S}, E_{33}^{S} and E_{44}^{S} from photoluminescence excitation spectroscopy are listed in, e.g., References [84, 85] and those for E_{22}^{S}, E_{33}^{S}, E_{44}^{S}, and E_{11}^{M} from resonant Raman spectroscopy in, e.g., References [62, 78].

From the resonant Raman experiments discussed in Section 4.1.3.3, the following empirical relations have been found for E_{22}^{S} in semiconducting tubes and E_{11}^{M} in metallic tubes [62]:

$$E_{22}^{S} = \gamma_0 \left(\frac{4a_{C-C}}{d} + \gamma_1 \frac{a_{C-C}^2}{d^2} \right) + \nu\gamma_2 \cos(3\theta) \frac{a_{C-C}^2}{d^2} \tag{6}$$

where θ is the chiral angle of the nanotube [1], d is the geometric diameter, a_{C-C} is the carbon–carbon bnond length and $\nu = (n - m)\text{mod}3$. The fitting parameters are $\gamma_0 = 3.53\,\text{eV}$, $\gamma_1 = -4.32$ and $\gamma_2 = 8.81\,\text{eV}$. The first transition in metallic tubes is fitted by

$$E_{11}^{M} = \gamma_0 \left(\frac{6a_{C-C}}{d} + \gamma_1 \frac{a_{C-C}^2}{d^2} \right) - \gamma_2 \cos(3\theta) \frac{a_{C-C}^2}{d^2} \tag{7}$$

with the parameters $\gamma_0 = 3.60\,\text{eV}$, $\gamma_1 = -9.65$ and $\gamma_2 = 11.69\,\text{eV}$ [62]. These results have been obtained on HiPco-produced nanotubes [87] in D_2O solution with diameters between 6.3 and 13.6 Å; the tubes were unbundled and wrapped in micelles [85]. Similar empirical relations for semiconducting nanotubes were found from photoluminescence experiments on the same type of sample [84]. We give here the empirical relations from Reference [84] for the first transitions in semiconducting nanotubes, E_{11}^{S}:

$$E_{11}^{S}(\nu = +1) = \frac{\alpha_0}{\alpha_1 + \alpha_2 d} + \alpha_3 \frac{\cos(3\theta)^{1.374}}{d^{2.272}} \tag{8}$$

with the parameters $\alpha_0 = 0.124 \times 10^4\,\text{eV}$, $\alpha_1 = 157.5$, $\alpha_2 = 1066.9\,\text{nm}^{-1}$ and $\alpha_3 = -0.0956\,\text{eV}$; for $\nu = -1$ tubes:

$$E_{11}^{S}(\nu = -1) = \frac{\alpha_0}{\alpha_1 + \alpha_2 d} + \alpha_3 \frac{\cos(3\theta)^{0.886}}{d^{2.129}} \tag{9}$$

with the same parameters as above, but $\alpha_3 = 0.043\,\text{eV}$.

In Figure 4.7a and b we show experimentally and empirically obtained Kataura plots, respectively. The gray dots are calculated values from Reference [79], upshifted by 0.3 eV. The experimental data in Figure 4.7a are from photoluminescence, resonant Raman and Rayleigh scattering experiments [78, 84–86]. For claritiy, similar data from other references have been omitted. Within the diameter range of the measurements, the experimental data for E_{11}^{S}, E_{22}^{S} and E_{11}^{M} agree well with the upshifted theoretical data [79]; for higher transitions the calculated values

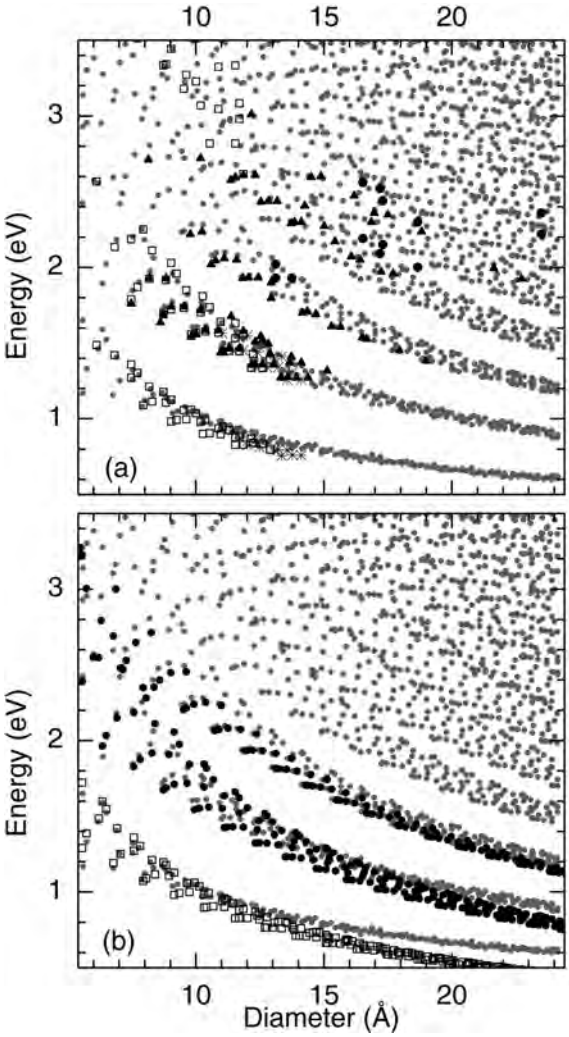

Figure 4.7 Kataura plots. (a) Experimental data from photoluminescence excitation spectroscopy (open squares, from References [59, 84], and stars, from Reference [85]), resonant Raman scattering (triangles, from Reference [78]), and Rayleigh scattering (full circles, from Reference [86]). (b) Empirical data from Eqs. (6) and (7) (full circles, Reference [62]), and from Reference [84] (open squares). Gray dots in (a) and (b) indicate the non-orthogonal tight-binding calculation from Reference [79] after a uniform upshift by 0.3 eV.

are slightly red shifted compared with the experimental ones, as discussed in Reference [78]. The empirical E_{ii} values in Figure 4.7b were fitted to photoluminescence (E_{11}^{S}, open squares) and resonant Raman data [E_{22}^{S} and E_{11}^{M}, full circles: Eqs. (6) and (7)]. For diameters above 15 Å, the calculation seems to slightly overestimate the empirical transition energies.

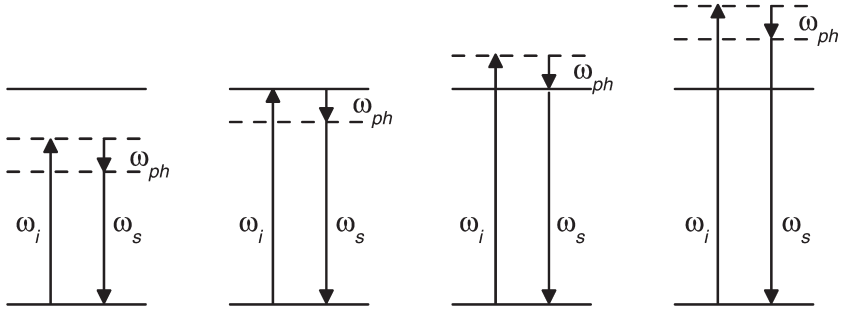

Figure 4.8 Resonant Raman scattering scheme. Arrows to solid and dashed lines indicate real and virtual transitions, respectively. From left to right: non-resonant scattering (incoming photon energy smaller than the real transition energy), incoming resonance, outgoing resonance, non-resonant scattering above the real transition.

The transition energies depend on the sample type, in particular on the nanotube environment; see also Section 4.2.1.2. For example, bundled nanotubes have been reported to show E_{ii} values red shifted by ~70 meV compared with individual, surfactant-wrapped nanotubes in solution [40, 88]. In nanotubes suspended in air, a blue shift in E_{11}^{S} and E_{22}^{S} of a few tens of meV has been observed for most nanotubes; in addition, the shifts depend on the chiral angle [66, 89].

4.1.3.3 (*n*,*m*) Assignment: Experimental Kataura Plot

After having discussed the relevant properties of the Kataura plot, we now show how to obtain the Kataura plot experimentally by resonant Raman scattering, and how to assign the chiral indices (*n*,*m*) from it.

Resonant Raman Scattering The concept of resonant Raman scattering is depicted in Figure 4.8. The energy of the incoming laser light is tuned across a real electronic transition (solid line). The intensity of the Raman signal as a function of excitation energy first increases and then decreases again, giving a so-called resonance (or excitation) profile. For single resonant states, such as the optically active excitons in carbon nanotubes, the Raman intensity shows the following proportionality [10]:

$$I \propto \left| \frac{\mathcal{M}^{b}_{\mathrm{e-r}} \mathcal{M}_{\mathrm{e-ph}} \mathcal{M}^{a}_{\mathrm{e-r}}}{(E_{\mathrm{l}} - E^{a}_{ii} - i\gamma^{a}/2)(E_{\mathrm{l}} - E^{b}_{ii} \mp \hbar\omega_{\mathrm{ph}} - i\gamma^{b}/2)} \right|^{2}$$
$$\propto \frac{|\mathcal{M}^{b}_{\mathrm{e-r}} \mathcal{M}_{\mathrm{e-ph}} \mathcal{M}^{a}_{\mathrm{e-r}}|^{2}}{[(E_{\mathrm{l}} - E_{ii})^{2} + \gamma^{2}/4][(E_{\mathrm{l}} - E_{ii} \mp \hbar\omega_{\mathrm{ph}})^{2} + \gamma^{2}/4]} \tag{10}$$

where E_{l} is the laser energy, $E^{a,b}_{ii}$ the real transition to the intermediate states *a* and *b*, $\hbar\omega_{\mathrm{ph}}$ the phonon energy and $\gamma^{a,b}$ the lifetime broadening of state $E^{a,b}_{ii}$. $\mathcal{M}^{a,b}_{\mathrm{e-r}}$

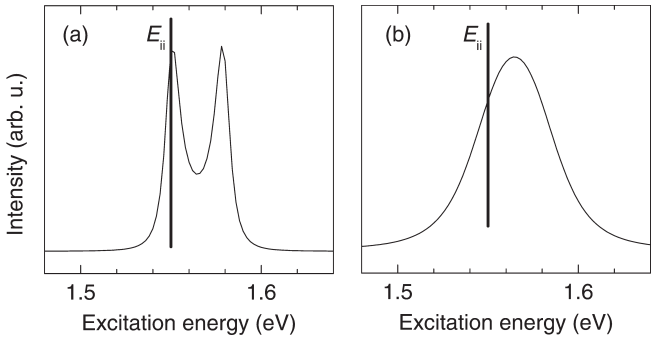

Figure 4.9 Model resonance profiles [Equation (10)] with E_{ii} = 1.55 eV, ω_{RBM} = 237 cm^{-1} = 0.03 eV. The vertical lines indicate the real transition E_{ii}. (a) γ = 0.01 eV; the two peaks correspond to incoming and outgoing resonance. (b) The broadening is increased, γ = 0.056 eV, and incoming and outgoing resonance are not resolved.

and $\mathcal{M}_{e-ph}$ are the matrix elements for exciton–radiation coupling and exciton–phonon coupling, respectively. If we observe only fully symmetric phonons, as is the case in carbon nanotubes (with polarization of the light parallel to the tube axis), the intermediate electronic states are the same, $E_{ii}^a = E_{ii}^b = E_{ii}$. The minus and plus signs in the second term in the denominator correspond to Stokes and anti-Stokes scattering, respectively.

If the energy of the incoming light, E_l, or of the outgoing light, $E_l \mp \omega_{ph}$, matches the real transition E_{ii}, the intensity is at a maximum. In this case, one term in the denominator in Equation (10) becomes very small. In Figure 4.9 (a) we show a resonance profile [Equation (10)] with E_{ii} = 1.55 eV, ω_{RBM} = 237 cm^{-1} and γ = 0.01 eV. The two peaks correspond to incoming and outgoing resonance, respectively, i.e. $E_l = E_{ii}$ (first peak) and $E_l = E_{ii} + \hbar\omega_{ph}$ (second peak). The separation between the two peaks is equal to the phonon energy. For larger broadening γ, however, the two peaks are not resolved (Figure 4.9b), and the maximum of the resonance profile is at $E_{ii} + \hbar\omega_{ph}/2$. A resonance profile as in Figure 4.9b is typically observed in the higher-lying transitions; only in E_{11}^S are incoming and outgoing resonance resolved. By fitting an experimental resonance profile to Equation (10), we can determine E_{ii} and γ.

Experimental Kataura Plot In the case of carbon nanotubes we obtain, in addition to the transition energy E_{ii}, the approximate nanotube diameter from the RBM frequency ω_{RBM}. As mentioned above, the coefficients in the empirical RBM-diameter relation Equation (4) vary widely in the literature and depend on, among others, the nanotube environment. On the other hand, even if we do not want to assume any specific value for the coefficients c_1 and c_2 in Equation (4), we can turn the RBM frequencies into $1/\omega_{RBM}$, being approximately proportional to the diameter. By doing this we obtain an experimental Kataura plot of E_{ii} vs. $1/\omega_{RBM}$.

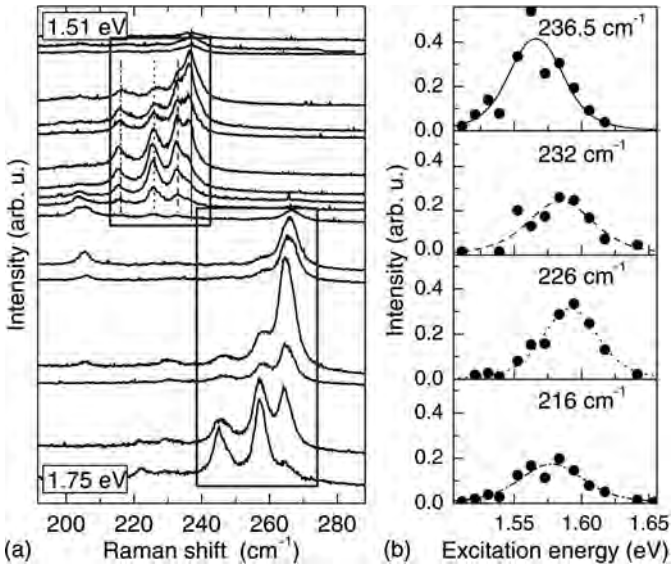

Figure 4.10 (a) RBM Raman spectra of single-walled carbon nanotubes at different laser energies. The tubes are wrapped in SDS (sodium dodecyl sulfate) and suspended in D_2O. The gray rectangles indicate the RBM peaks of nanotubes forming a branch in the Kataura plot. (b) Resonance profiles from the RBMs in the first group indicated by vertical lines in (a). After Reference [62].

In Figure 4.10a we show a typical set of Raman spectra with varying laser energy. Each RBM has a certain energy range over which it is present, being at a maximum at a particular excitation energy. In addition, the RBM peaks appear in groups, in which the peaks reach their maximum one after the other within a rather small energy range. We will later identify these groups with the branches in the Kataura plot. By analyzing the RBM intensity as a function of laser energy, we obtain for each RBM a resonance profile; see Figure 4.10b. The E_{ii} from fitting Equation (10) are shown in the Kataura plot in Figure 4.11 as a function of $1/\omega_{\mathrm{RBM}}$ (black symbols). We can immediately recognize the patterns of the theoretical Kataura plot. To assign the chiral index (n,m) to each data point in this experimental Kataura plot, we have to match it to a theoretical one, as shown by gray symbols.

The (n,m) assignment is solely based on matching the patterns between the branches of the experimental and theoretical Kataura plots. We do not use the absolute E_{ii} values from theory and we do not make any assumptions about the coefficients c_1 and c_2. Instead, we stretch and shift both axes of the theoretical Kataura plot. On the energy axis, this accounts for the many-body and curvature effects not included in the calculation; on the diameter axis, stretching and shifting corresponds to changing c_1 and c_2, respectively. The match in Figure 4.11 is the final assignment, i.e. for each nanotube we assigned the pair $(\omega_{\mathrm{RBM}}, E_{ii})$ of experimentally determined quantities to the chiral index (n,m). The measured transition energies and RBM frequencies with their assigned (n,m) are listed in Reference

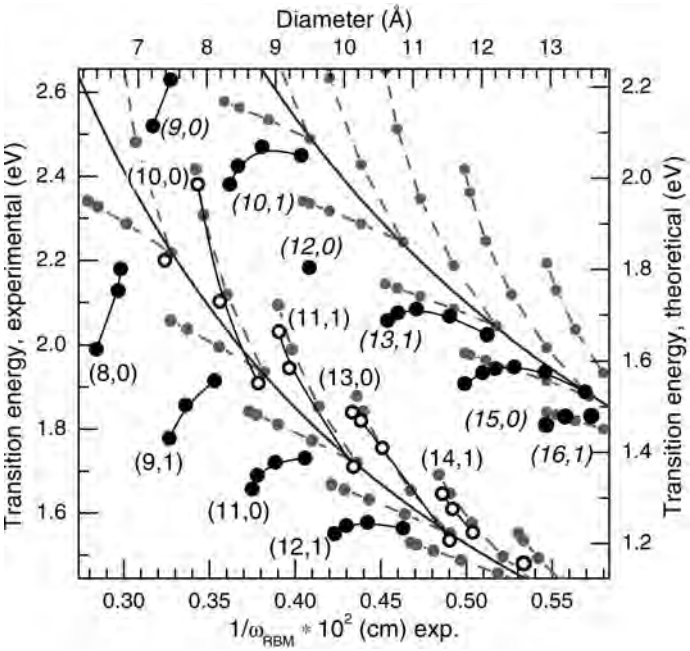

Figure 4.11 Transition energies from resonant Raman scattering as a function of $1/\omega_{RBM}$ (black symbols, left and bottom axes). For semiconducting tubes, open and closed symbols indicate tubes with $\nu = +1$ and $\nu = -1$, respectively. Gray symbols (right and top axes) are theoretical values from Figure 4.6. The final (n,m) assignment is given. After References [39, 62].

[62]. This assignment agrees with others based on photoluminescence data combined with RBM Raman spectra [59].

To show that the (n,m) assignment in Figure 4.11 is indeed unambiguous, we present two alternative choices in Figure 4.12 and explain how they can be ruled out. At first sight it might seem possible to shift the experimental and theoretical Kataura plots "up" or "down" against each other by one or more entire branches. This is shown in Figure 4.12a and b. However, shifting the experimental data up [(a)] leads to a discrepancy in the number of tubes belonging to the same branch: the experimental branch highlighted by the circle contains four different nanotubes (plus one from the opposite branch), whereas only three chiral indices exist for this branch. In (b), the relative distances along the diameter axis do not match simultaneously for all nanotubes. Even if the positions of the inner tubes are matched, the outer tubes follow a pattern that is violated in Figure 4.12b. Because only every other branch starts with a zigzag nanotube, the distances between the first two tubes alternate between very small [see the (11,0) branch] and slightly larger [see the (9,1) branch]. In Figure 4.12b, an experimental branch with two close-lying outer tubes would be assigned to a theoretical branch with two separated outer tubes, and *vice versa*. Thus none of the assignments proposed in Figure 4.12 is correct.

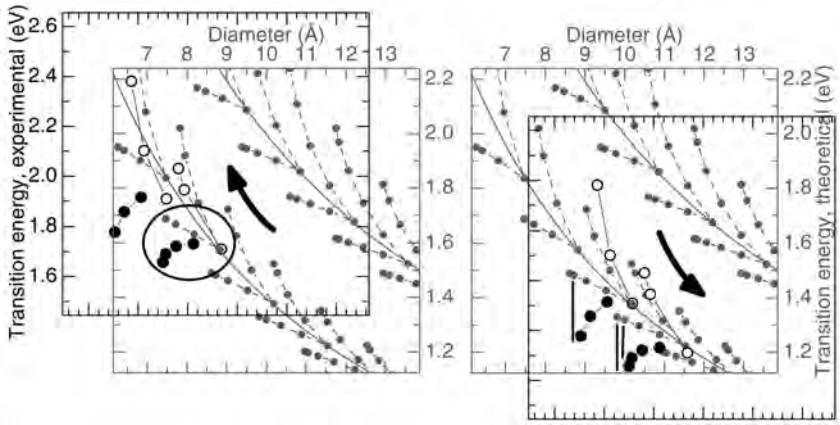

Figure 4.12 Two alternative (incorrect) assignments, where the experimental Kataura plot (black) is shifted up by one branch in (a) and down by one branch in (b). Gray symbols indicate the theoretical Kataura plot. Only part of the experimental data are shown for clarity. In (a), the highlighted branch from experiment contains more RBM peaks than nanotubes (*n*,*m*) exist in this branch. In (b), the vertical lines indicate a mismatch in the relative distances between the theoretical and experimental branches. After Reference [62].

4.1.3.4 (*n*,*m*) Assignment Using a Single Laser Line

Although resonant Raman scattering as discussed above yields comprehensive information about the system under investigation, it is also laborious. For example, each experimental point in the Kataura plot in Figure 4.11 represents approximately 10–15 Raman spectra which constitute a resonance profile, measured with a tunable laser. The RBM intensities must be carefully analyzed and normalized to a non-resonant reference sample. On the other hand, once the experimental Kataura plot for a given type of sample has been obtained, one can easily assign the RBM peaks observed from a similar sample using only one single excitation energy. For convenience, we show in Figure 4.13 the experimental Kataura plot from Figure 4.11 as a function of the measured RBM frequency. It can be directly used to compare a single Raman spectrum of a similar sample (i.e. HiPco-grown nanotubes wrapped by SDS/SDBS in solution) and assign the chiral index to the measured RBM peaks, as we explain below. In this case, Equation (4) is not needed for the assignment.

The procedure to assign the chiral indices to the RBM peaks at a given laser energy for a sample type with a known Kataura plot is the following:

1. Record the Raman spectrum at excitation energy E_l.
2. Draw a horizontal line in the experimental Kataura plot at E_l.
3. Find the range of RBM frequencies observed in the experiment. If a Kataura plot with a diameter axis is used, the RBM range can be converted into an *approximate* diameter range by Equation (4).

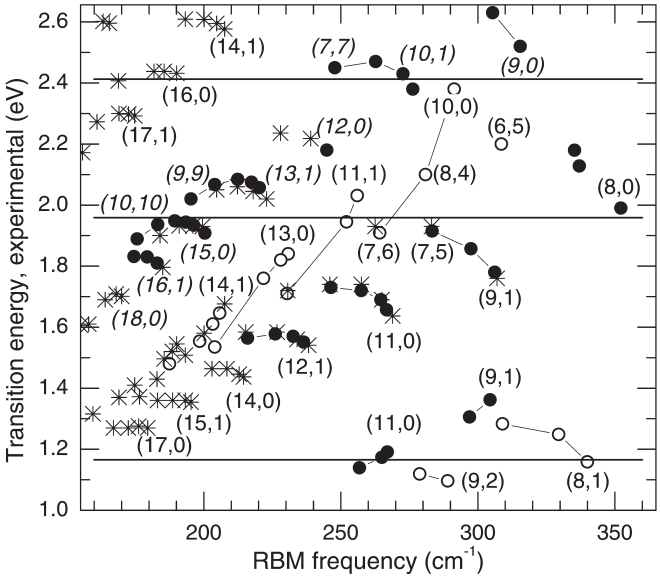

Figure 4.13 Experimental Kataura plot as a function of experimental RBM frequency, showing E_{11}^{S}, E_{22}^{S} and E_{11}^{M} from resonant Raman scattering on surfactant-wrapped nanotubes in solution. The chiral index (n,m) for each tube at the outer position of a branch is given; in addition, the observed armchair tubes are indicated. The horizontal lines indicate typical laser wavelengths: 514, 633 and 1064 nm. After References [62] and [90]. Stars are Raman data taken from Reference [78].

4. Find the nanotubes in a range of approximately 100–200 meV around the E_l line in the Kataura plot. (Note that the transition energies are, in the case of Stokes-scattering, on the low-energy side of the resonance profile, i.e. the strongest signal is observed at $E_{ii} + \hbar\omega/2$; see Figure 1.9b.)
5. Identify complete branches close to the E_l line and possibly correlate them with groups of RBM peaks in the Raman spectrum.
6. Match all remaining peaks in the spectrum to the Kataura plot data.
7. If some ambiguities remain, such as two tubes above and below the E_l line with very similar RBM frequencies, take a spectrum at a second laser line, if possible.

If the Kataura plot for a given sample type is not known, one has to determine it once from full Raman resonance profiles. This Kataura plot can again be used for similar samples.

In Figure 4.14, we show for reference the RBM Raman spectra from HiP coproduced, surfactant-wrapped nanotubes [39, 62] at three typical laser wavelenghts,

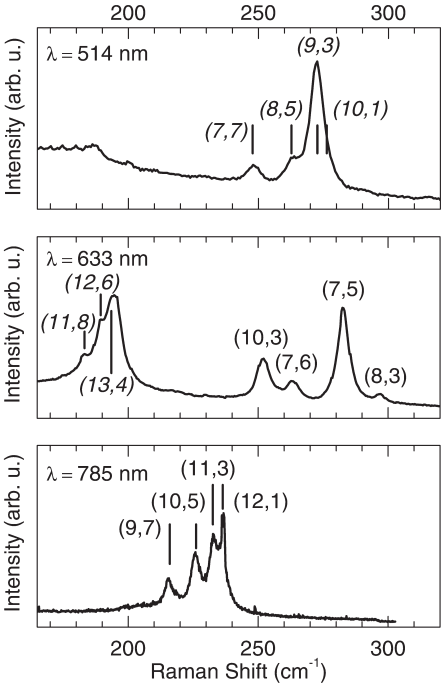

Figure 4.14 Raman spectra from HiPCo-produced, surfactant-wrapped carbon nanotubes in D_2O solution at three typical laser wavelengths λ. The strongest peaks are assigned by their chiral index, where italic numbers indicate metallic tubes. After Reference [62].

514, 633 and 785 nm, together with the (n,m) assignment of the most intense peaks. At 514 nm, the metallic (10,1) branch is observed. At 633 nm, we observe larger-diameter metallic tubes mainly from the (15,0) branch and smaller-diameter semiconducting tubes from several different branches. At 785 nm, only semiconducting tubes are probed; the entire (12,1) branch is visible. At all three wavelengths, the RBM peaks belonging to the same branch form a group of close-lying peaks.

In general, the relevant information about the chiral index is already obtained if the correct *branch* is identified. Many properties are very similar for nanotubes of the same branch; within a branch they depend mainly on the chiral angle. For example, the electron–phonon coupling has a strong dependence on the nanotube family $\nu = \pm 1$ [79, 91, 92]. As a result, nanotubes with similar diameter and transition energy but different ν can have very different strength in their RBM Raman signal. Therefore, it is more important to distinguish between, e.g., the (11,0) and the (11,1) tubes with $\nu = -1$ and $\nu = +1$, respectively, than between the (11,0) and (10,2) tubes from the same branch.

Table 4.1 Resonant Raman scattering: summary of nanotubes and diameter ranges observable under typical experimental conditions. Note that the values given in this table are based on the data from unbundled nanotubes, References [39, 59, 78], and on the non-orthogonal tightbinding calculation upshifted by 0.3 eV from Reference [79]. Those (*n*,*m*) branches are named that are almost complete within the given energy range.

laser (nm)	*Diameter range (Å)*	*(n,m)*	E_{ii}
514–488, green/ blue Ar lines	8–11	Metallic, (10,1) branch	E_{11}^{M}
	>11	Semiconducting	E_{33}^{S}, E_{44}^{S}
560–690, dye lasers	6–11	Semiconducting, (9,1), (8,0), (11,1) branch	E_{22}^{S}
	10.5–14	Metallic, (15,0), (13,1) branch	E_{11}^{M}
	15–20	Semiconducting	E_{33}^{S}, E_{44}^{S}
700–1000, Ti: sapphire	≤8.5	Semiconducting	E_{11}^{S}
	8.5–14.5	Semiconducting, (11,0), (12,1), (13,0), (14,0), (15,1), (14,1), (16,0) branch	E_{22}^{S}
	14.5–21	Metallic	E_{11}^{M}
	≥21	Semiconducting	E_{33}^{S}

In Table 4.1, we summarize the nanotubes (*n*,*m*) that are observed for different diameter ranges at typical laser energies. The values given are based on resonance Raman [39, 62], photoluminescence [59] and Rayleigh scattering [86] experiments on unbundled nanotubes, and also on predictions by the calculation from Reference [79]. When working with nanotubes in different environments (e.g. nanotube bundles, chemically functionalized nanotubes, nanotubes suspended in air), possible shifts of the resonance energies must be taken into account.

4.1.3.5 (*n*,*m*) Assignment of a Single Nanotube

The advantage of the assignment procedure described above was to use an ensemble of nanotubes, thereby obtaining the full Kataura plot branches and patterns: even if the resonance energies or RBM frequencies vary slightly from one sample to another, the patterns will persist; thus small shifts of the Kataura plot branches can be recognized. On the other hand, it is often required to determine the chiral index (*n*,*m*) of an individual nanotube such as a single tube on a substrate [28] or a single tube suspended over trenches [36]. There are two approaches to determine the chiral index of a single, individual nanotube from one or two laser lines. First, the experimental Kataura plot for a given type of sample, say individual nanotubes on a silicon substrate, can be established by recording Raman resonance profiles of a large number of these tubes. Once this has been achieved, a single Raman spectrum (if close to resonance) will be sufficient to determine the chiral index as

described in Section 4.1.3.4. To the best of our knowledge, however, such an experimental Kataura plot from single, individual nanotubes has not been reported so far. The second approach, therefore, might not always lead to a definite (n,m) assignment: if at a given excitation energy E_l the RBM of a single nanotube is detected at all, E_l is probably close to the resonance energy E_{ii}. This argument has been used, e.g., for (n,m) determination of individual nanotubes on a substrate [28, 93] and for E_{ii} determination of single suspended tubes [35]. How close the excitation energy is to the resonance energy can vary widely, depending on the Raman scattering cross-section of the particular nanotube, but also on the sensitivity of the experimental setup and on the integration time. "Close" to the resonance energy would mean that the excitation energy is within the width (at half-maximum) of the resonance profile. As explained in Section 4.1.3.3, the resonance profile width is mainly given by the difference in energy between the incoming and the outgoing resonance, i.e. the phonon energy, see also Figure 4.9. In addition, the broadening γ in Equation (10) plays a role. Values for γ found in the literature range from 13 to 38 meV for E_{22}^{S} in individual suspended nanotubes [36, 37] and from 60 to 120 meV for E_{22}^{S} in nanotube ensembles [40]. In addition, the broadening has been found to depend on the transition E_{ii}; it is smaller for the lowest transition E_{11}^{S} than for higher transitions [94].

From the RBM position and the approximate transition energy ($\approx E_l \pm \omega_{ph}/2$) one can *approximately* define the tube's position in the Kataura plot, distinguish between semiconducting and metallic nanotubes and possibly determine the branch to which the nanotube belongs. However, this approach must be applied with special care, in particular because usually the intensity maximum is at $\sim\omega_{ph}/2$ above the transition energy; see Figure 4.9b. If a second laser line is available, it should be used for cross-checking the result. We would like to point out that from only a single Raman measurement on a single nanotube without a reference Kataura plot one cannot determine E_{ii}.

Using tunable lasers and recording an entire resonance profile of the RBM of a single nanotube yields a reliable (n,m) assignment as described above for nanotube ensembles.

4.1.3.6 Raman Scattering: Relative Abundance of Different (n,m)

In Figures 4.13 and 4.14 we saw that the (7,5) and the (7,6) tubes are both very close to the laser wavelength of 633 nm, but the RBM of the (7,5) tube is much stronger in the Raman spectrum (Figure 4.14) than that of the (7,6) tube. At first sight, one might conclude that the sample contains more nanotubes with chiral index (7,5) and fewer (7,6) tubes. On the other hand, the matrix elements entering the Raman cross-section in Equation (10) might be different for both nanotubes. Indeed, the electron–phonon coupling is in general larger for nanotubes with $\nu = -1$ [i.e. the (7,5) tube] than for $\nu = +1$ tubes, if the second transition E_{22}^{S} is considered [79, 91, 92]. In contrast, in resonance with the first transition E_{11}^{S}, the ν dependence of the electron–phonon coupling strength is reversed. This prediction is in agreement with resonant Raman scattering experiments [90, 95], as seen in

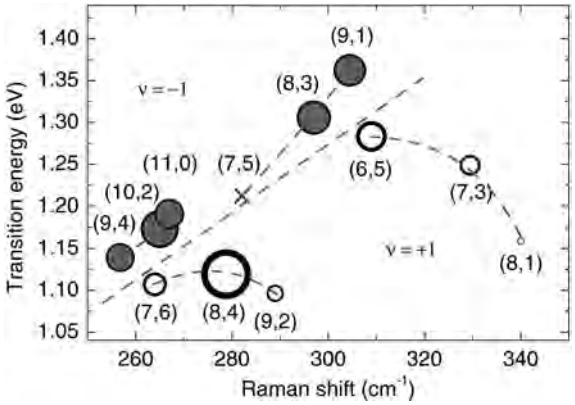

Figure 4.15 Experimental Kataura plot from Raman scattering on surfactant-wrapped, HiPco-produced nanotubes in resonance with E_{11}^{S}. Full gray and open black circles indicate $\nu = -1$ and $\nu = +1$ tubes, respectively; the cross shows the expected position of the not detected (7,5) nanotube. After Reference [90].

Figure 4.15. In Figure 4.15 the E_{11}^{S} region of the experimental Kataura plot (see Figure 4.13) is shown, where the size of the symbols indicates the Raman intensity. In contrast to the E_{22}^{S} resonance, the (7,5) tube was not observed at all (indicated by the cross), whereas the (7,6) nanotube shows a Raman signal comparable to several other nanotubes in this region. Therefore, if we did not take the (n,m) dependence of the Raman cross-section into account, we would – for the same sample – arrive at opposite conclusions about the relative abundance of the (7,5) and (7,6) nanotubes, depending on the resonant transition E_{11}^{S} or E_{22}^{S}. The (n,m) dependence of the electron–phonon coupling with alternating strength for $\nu = +1$ and $\nu = -1$ nanotubes holds in general; in addition, the RBM intensity decreases with increasing nanotube diameter [79, 91, 92].

Also in different environments the RBM signal strength of a given nanotube might vary. One reason is a possible shift ΔE in resonance energy, i.e. the Raman spectrum at excitation energy E_l in one environment would correspond to the Raman spectrum at $E_l + \Delta E$ in the other environment [62]. For example, in Figure 4.16a the Raman spectra of carbon nanotubes in two different surfactants, SDS and SDBS, are shown. Although the spectra are taken at the same excitation energy, the relative intensities of the RBM peaks are different. In SDS, the (8,3) nanotube shows a stronger RBM signal than the (7,5) tube, whereas in SDBS it is weaker than the (7,5) tube. This intensity variation is mainly due to a shift in E_{22}^{S} of the (8,3) nanotube. We show in Figure 4.16b the SDBS spectrum at E_l = 1.908 eV. The relative RBM intensities are again similar to the SDS spectrum at E_l = 1.916 eV, indicating a shift in resonance energy.

In addition, the electron–phonon coupling and the strength of the optical transition can depend on the nanotube environment. Therefore, the relative abundance

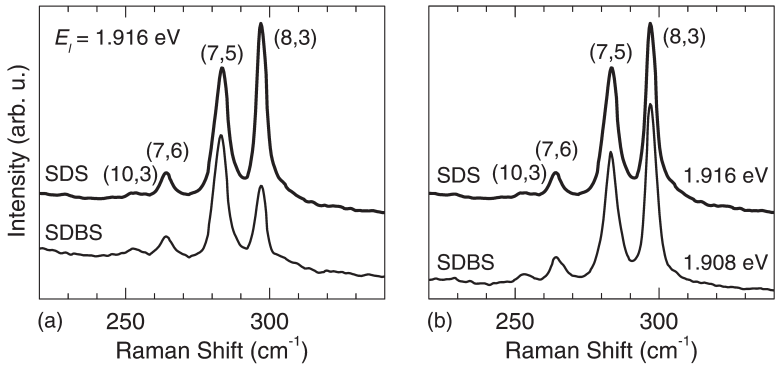

Figure 4.16 Raman spectra of carbon nanotubes in different surfactants: SDS (sodium dodecyl sulfate; gray line) and SDBS (sodium dodecylbenzene sulfonate; black line). (a) The excitation energy is 1.916 eV; the spectra are normalized to the amplitude of the (7,5) tube. (b) The SDBS spectrum at 1.908 eV corresponds to the SDS spectrum at 1.916 eV. After Reference [62].

of different (n,m) tubes in a given sample can only be determined if the chiral index dependence of the Raman cross-section is taken into account. For each (n,m) nanotube which is compared with nanotubes with different (n,m), the Raman spectrum has to be in resonance and must be normalized to the theoretical Raman cross-section. In general, it is difficult to obtain numerical results on the matrix elements in Equation (10) for any arbitrary chiral index. Extensive theoretical data of the RBM Raman cross-section for many (n,m) have been presented in References [79, 91, 92, 96, 97].

4.1.3.7 Metallic vs. Semiconducting Nanotubes

For some applications of carbon nanotubes, such as in electronic circuits, it is important to determine whether a given nanotube is metallic or semiconducting, or whether nanotube raw material is enriched in one type of tubes. In this section we briefly discuss detecting the metallic or semiconducting character of a nanotube by Raman scattering without determining the chiral index.

The RBM spectra discussed above represent in most cases a simple tool to determine whether a nanotube is metallic or semiconducting. If the diameter range of the nanotubes in the sample is sufficiently small, the RBM spectra at a given laser energy will either show predominantly one type of nanotubes, or, if both types of nanotubes are in resonance at the same laser energy, their RBM frequencies will be clearly separated; see also Figure 4.14 and Table 4.1. Therefore, in order to determine the metallic or semiconducting character of a nanotube, it is often not neccessary to determine (n,m). Possible shifts in resonance energies E_{ii} that result from different nanotube environments, however, have to be taken into account. At a laser energy where both metallic and semiconducting nanotubes

are observed, the evolution of RBM intensities has been used to monitor selective chemical functionalization of metallic nanotubes as the optical transition of metallic nanotubes became very weak [98]. This example shows again that a vanishing RBM intensity does not imply that the corresponding (n,m) nanotube is missing in the sample; see Section 4.1.3.6.

Another method to determine whether a nanotube is metallic or whether metallic nanotubes are affected by chemical treatment relies on the high-energy mode (G mode) in the Raman spectrum. When nanotube bundles are excited in resonance with the transition of metallic nanotubes, the low-energy side of HEM line is significantly broadened and downshifted [25, 26], often being fit by a Fano lineshape [27, 99]. In isolated single metallic nanotubes, however, there has been some debate whether the HEM lineshape is similar to that observed in bundles. In Raman experiments on isolated metallic nanotubes, a broadened lineshape is sometimes observed, whereas in other experiments semiconducting-like HEM spectra are reported; see for instance References [29, 30, 100–104]. Therefore, a possible extrinsic origin of the large broadening of the HEM has been discussed. On the other hand, a broadened HEM lineshape has been observed from single nanotubes in some experiments. As an intrinsic origin of this broadening, a strong coupling between the phonon and the electrons near the Fermi level has been predicted [48, 50], where the phonon decays via excitation of an electron–hole pair in the metallic band structure. Indeed, gate-dependent Raman experiments showed that this coupling can be tuned by changing the Fermi level [104]. The HEM linewidth in metallic nanotubes appears to depend on the chiral index, ranging between ~20 and ~100 cm^{-1}, explaining the large variety in experimental results. Therefore, *if* the HEM Raman lineshape of single nanotube is very broad and downshifted, the nanotube is most likely metallic. However, if a narrow line is observed, the nanotube can be metallic or semiconducting.

4.1.4
Deviations from the Ideal Nanotube Structure

As long as the nanotubes under investigation are "ideal", for example free of defects and structural variations, we do not expect any dependence of the Raman spectra on the segment of the tube that is probed. Usually, the size of the laser focus area is in the range of one to several micrometer, although ~200 nm can be achieved with blue laser light and high numerical aperture optics. Therefore, in ensemble samples or in individual nanotube bundles, the laser excites many nanotubes at the same time. Also for an isolated single nanotube, the size of the laser focus exceeds that of the tube, if the nanotube is not longer than a few micrometers, and the entire nanotube is probed. On the other hand, if the nanotube is not ideal, the Raman signal (and any other optical response) might vary over the length of the nanotube. In this section we present two approaches to observe perturbations of the nanotube structure by Raman scattering. First, the nanotube sample (a single tube or an ensemble) is probed globally, where the Raman spectrum indicates the *presence* of defects. Second, a single nanotube is

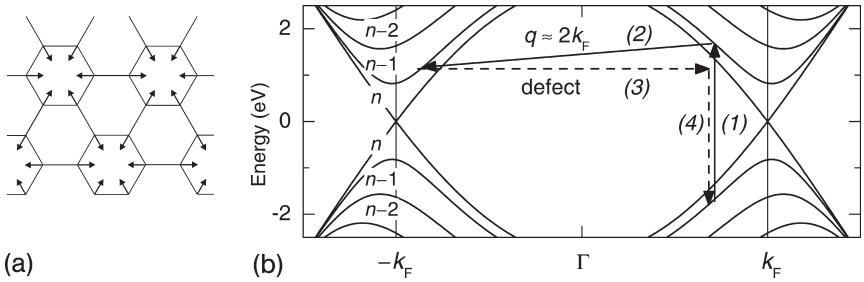

Figure 4.17 (a) Displacement pattern in the graphene lattice of the *K*-point phonon that gives rise to the *D* mode in graphite and carbon nanotubes. (b) Double-resonant Raman process resulting in the *D* mode. Schematic view of the band structure of an (*n*, *n*) armchair nanotube; k_F indicates the Fermi wavevector. After Reference [23].

locally excited, giving information on the positions and the distribution of defects within the same nanotube.

Raman scattering is particularly suited to determine the presence of structural defects in both individual nanotubes and also in nanotube ensembles. In the first-order Raman spectrum of carbon nanotubes (see Figure 4.2), the *D* mode at around 1350 cm^{-1} appears if structural defects are present. These defects can be constituted by vacancies, other atoms or molecules attached to the nanotube wall, chiral index changes within the tube, kinks or bends of the tube or the nanotube ends.

The presence of defects breaks the translational symmetry of the nanotube and therefore relaxes the $q \approx 0$ rule; see Section 4.1.1. As a result, phonons from throughout the Brillouin zone can contribute to the Raman spectrum. Among those phonon modes, the *D* mode is selected, i.e. particularly strong, because it is enhanced in a double-resonant scattering process [21]. This is shown schematically in Figure 4.17. The resonantly excited electron–hole pair *(1)* is scattered in a second resonant step *(2)* by a phonon with large wavevector $q \approx 2\,k_F$ [18]. The defect elastically scatters the electron (or hole) back *(3)* such that the electron–hole pair can recombine *(4)*. In Figure 4.17a, the phonon eigenvector of the *D* mode in graphene is shown. It is formed by breathing-like motions of the carbon hexagons, and its wavelength corresponds to the *K* point in the graphene Brillouin zone [105]. In graphite, it belongs to the phonon branch derived from the transverse optical phonon at the Γ point [13, 105, 106].

The intensity of the *D* mode scales with the relative number of defects in the nanotubes. Therefore, the *D* mode is often used to monitor the introduction of defects into a nanotube sample [107, 108] and to determine the sample purity during or after synthesis; see for instance [6, 109]. The second-order overtone of the *D* mode at ~2700 cm^{-1} (named *D** or *G*′), does not require defects. Instead, two "*D*-mode" phonons with opposite wavevector participate in the double-

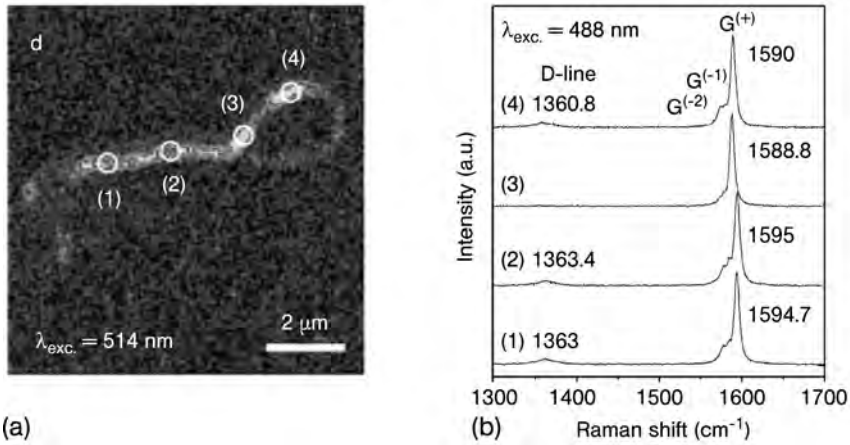

Figure 4.18 (a) Confocal Raman image of an individual single-walled carbon nanotube directly grown on an Si substrate. The gray scale indicates the intensity of the Raman HEM. (b) Raman spectra from different locations on the nanotube as given by the numbered circles in (a). From Reference [31].

resonance process. Therefore, the D^* mode is present and relatively strong even in a perfect nanotube. To analyze the relative defect concentration, the intensity of the D mode should be normalized to the D^* intensity [108].

An additional effect of the double-resonant Raman process shown in Figure 4.17 is that the frequency of the D mode in the Raman spectrum shifts with the excitation energy. This unusual behavior can be understood in the following way: if the excitation energy is, e.g., smaller than the one indicated by the arrow in Figure 4.17, the resonant optical transition *(1)* would occur closer to k_F. As a result, the phonon wavevector in the resonant second step *(2)* would be larger, and the phonon with this larger wavevector – and with a different energy – would be enhanced. Therefore, at each excitation energy a different phonon from near the K point is observed in the Raman spectrum. In graphite and in carbon nanotubes, the D mode position shifts by $\sim 50\,\mathrm{cm^{-1}\,eV^{-1}}$ [18, 21, 110, 111]. The double-resonance Raman effect in graphite and carbon nanotubes can *vice versa* be used to probe the phonon dispersion relation; for details see References [8, 112, 113].

If one is interested in a specific single nanotube, e.g., to be integrated into an electronic device, a useful method is spatial Raman mapping of the nanotube [31, 115]. With a confocal Raman microscope setup, the nanotube can be imaged by scanning the laser focus with respect to the sample and detecting its Raman signal; see Figure 4.18 [31]. The spatial resolution is given by the diffraction limit of the laser wavelength, i.e. it is on the order of a few hundred nanometers. The scattered light is either recorded within a given spectral window, or at each point the entire Raman spectrum is taken. Figure 4.18a shows the Raman image of a single nanotube on a substrate forming a loop. The image maps the intensity of the HEM in the spectral range $1590 \pm 15\,\mathrm{cm^{-1}}$. Another form of a Raman image of individual

nanotubes can be obtained by "global" imaging, where, instead of scanning the laser spot with respect to the sample, the laser spot is defocused to ~20 μm [116]. By recording the Raman signal in a narrow spectral range around one of the Raman modes, the entire image can be obtained by a single measurement.

In addition to information from the *D* mode intensity about defects, Raman imaging also gives information about the homogeneity of the properties along the nanotube. In Figure 4.18b the Raman spectra taken at four different positions of the tube are shown. Small changes in the intensity of the *D* mode and in the position of the HEM (*G* mode) are observed; the latter were attributed to changes in the structure along the nanotube axis [31]. In general, variation in the intensity of the RBM or the high-energy Raman modes would indicate a change in the resonance energy or quenching of the optical transition; a shift in the RBM frequency would indicate a change of chiral index within the same nanotube. Possible reasons for slight changes in the resonance energy can be local interaction with the substrate or interaction with attached particles.

A novel technique to observe the Raman signal from a single nanotube with high spatial resolution is tip-enhanced (or near-field) Raman scattering [114]. In this method, the electric field of the exciting laser is enhanced by a sharp metal tip, which is positioned in the center of the laser focus area and held at a distance of ~1 nm to the nanotube. The spatial resolution in this optical near-field regime is in the range 10–30 nm [114, 117]. In Figure 4.19a a near-field Raman image of single nanotubes on a glass substrate is shown, where the intensity of the *D** mode is mapped [114]. Local variations in the Raman intensity within tens of nanometers

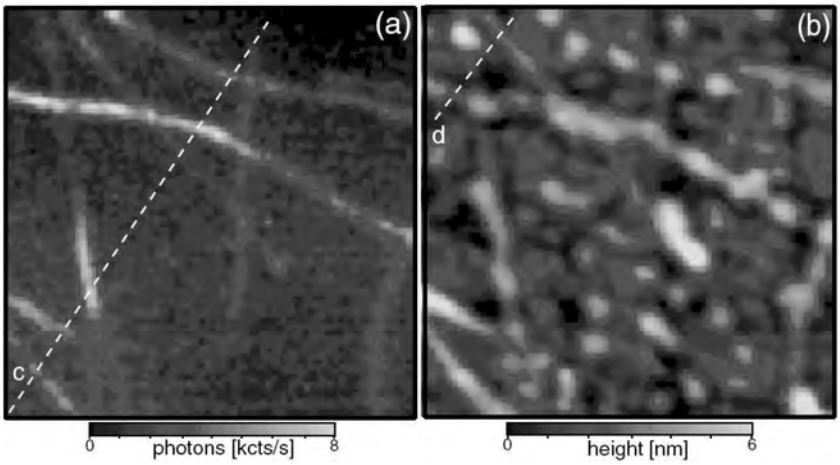

Figure 4.19 (a) Near-field Raman image of single-walled carbon nanotubes on a glass substrate. The gray scale shows the intensity of the *D** mode. (b) Corresponding topographical image. The scanning area in (a) and (b) is 1 × 1 μm. For the cross-sections along the dashed lines, see Reference [114]. Taken from Reference [114].

are observed. During the Raman measurement, a topographic image is recorded simultaneously by the metal tip; see Figure 4.19b. Therefore, near-field Raman imaging allows local variations in the Raman signal to be correlated directly with the nanotube structure on a nanometer scale. For a review on tip-enhanced Raman scattering in carbon nanotubes, see also References [118, 119].

4.2 Photoluminescence and Rayleigh Scattering

In semiconducting materials, luminescence spectroscopy is among the most widely used optical methods. It gives information on, e.g., the band gap or the structure of excited states. Although two-thirds of all possible carbon nanotube structures are semiconducting, it has taken almost 10 years after their discovery until photoluminescence from semiconducting single-walled carbon nanotubes was observed [59, 120]. The main challenge to be overcome was the bundling of carbon nanotubes: bundles of more than a few nanotubes almost certainly contain both semiconducting and metallic tubes, and the luminescence of semiconducting nanotubes is assumed to be quenched by nearby metallic nanotubes. In Reference [120], the originally bundled nanotubes were for the first time not just separated from each other, but in addition stabilized in micelles and thus prevented from re-bundling; see also Figure 4.20. Since then, photoluminescence (PL) and photoluminescence excitation (PLE) spectroscopy have become a standard tool in carbon

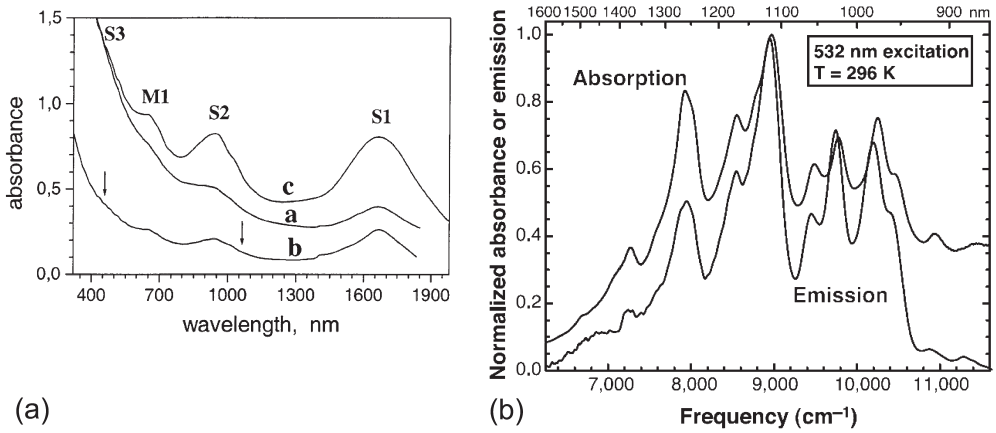

Figure 4.20 (a) Absorption spectra of single-walled carbon nanotubes. Lines a and b indicate the nanotubes in solution before and after centrifugation, respectively; c is from a freestanding nanotube film. The semiconducting transitions E_{11}^{S} and E_{22}^{S} (S1 and S2) and the first metallic transition E_{11}^{M} (M1) are clearly seen. Taken from Reference [85]. (b) Absorption and emission spectra of individual, SDS-wrapped nanotubes in solution in the range of E_{11}^{S}. The peaks corresponding to different nanotube (n,m) are resolved. Taken from Reference [120].

nanotube characterization; luminescence has been reported even from single, isolated nanotubes [32, 121, 122] and also from 4 Å diameter nanotubes grown in zeolite channels [123]. Electroluminescence has been observed in field-effect transistors, indicating ambipolar transport domains in these devices [124]. From large multi-walled carbon nanotubes no strong luminescence is expected, because they are likely to contain metallic tubes. Double-walled carbon nanotubes, on the other hand, show photoluminescence similar to single-walled nanotubes [125, 126].

Already before the discovery of photoluminescence, optical absorption in carbon nanotubes was used to characterize bundled nanotubes. Absorption spectra of carbon nanotube bundles show inhomogeneously broadened peaks corresponding to the first, second and third transitions of semiconducting tubes and the first transition of metallic tubes; see Figure 4.20a. Only if the nanotubes are unbundled are the absorption peaks of different (n,m) tubes resolved (Figure 4.20b). The questions addressed by optical absorption range from the determination of transition energies [127] and the dependence of the transition energies on pressure [128] to the interaction of nanotubes with polymers [129] and to the analysis of sample purity [130, 131].

Similarly to resonant Raman scattering, photoluminescence spectroscopy permits the determination of the chiral index, as will be explained in Section 4.2.1. Furthermore, as the photoluminescence intensity decreases for large bundles, the dissociation of nanotube bundles can monitored by changes in PL intensity [132, 133]. Other examples of nanotube characterization without the neccessity for (n,m) determination include monitoring of sample purification by photoluminescence [134] and determination of nanotube film thickness by its optical absorbance [135].

As mentioned in Section 4.1.3.2, all optical excitations in carbon nanotubes are excitons, i.e. bound electron–hole pairs with binding energies on the order of a few hundred meV for nanotubes with diameters smaller than 1 nm [73, 74, 136]. Therefore, all E_{ii} measured in optical absorption or emission are exciton energies, even if they are compared with Kataura plot calculations regarding them as band-to-band transitions for simplicity. The exciton binding energies have been determined by experiment so far only for the lowest exciton state, E_{11}^{S}.

4.2.1
Photoluminescence Excitation Spectroscopy

The first (n,m) assignment based on the pattern matching described in Section 4.1.3.3 was performed on data from photoluminescence excitation (PLE) spectroscopy [59].

In photoluminescence excitation spectroscopy, the optical emission is measured as a function of excitation energy. If the incoming light resonantly excites a higher transition in the nanotubes, say E_{22}^{S}, and relaxation to the emitting state E_{11}^{S} is efficient, the intensity shows a maximum. This is shown schematically in Figure 4.21a and b. The incoming light excites E_{22}^{S} and the E_{22}^{S} exciton relaxes to E_{11}^{S}, which decays radiatively to the ground state. By recording the emission spectra as a

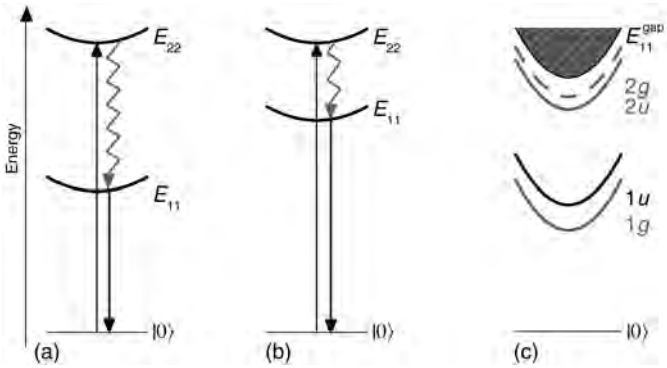

Figure 4.21 Schematic view of a PLE process with resonant excitation into the E_{22}^{S} state and emission from the E_{11}^{S} lowest exciton. The zigzag arrow symbolizes any relaxation path from E_{22}^{S} to E_{11}^{S}. $|0\rangle$ denotes the ground state. (a) In small-chiral angle $\nu = +1$ tubes, $E_{22}^{S} > 2E_{11}^{S}$. (b) In small-chiral angle $\nu = -1$ tubes, $E_{22}^{S} < 2E_{11}^{S}$. (c) Ordering of the four lowest non-degenerate bound exciton states with their symmetry labels; u and g refer to odd and even states under two-fold rotation of the nanotube, respectively; the rotational axis is perpendicular to the tube axis [2]; 1 and 2 denote even and odd under inversion of the relative coordinate between the electron and the hole. The $1u$ state (black line) is the only optically active state and is the same as E_{11}^{S}. The $2g$ state is two-photon active (dashed gray line). E_{11}^{gap} denotes the band-to-band transition energy. For details see Reference [74].

function of excitation energy, one obtains a modified Kataura plot showing the higher-lying transitions as a function of emission energy E_{11}^{S}. Such a PLE map can be compared and matched with a calculated one similarly to the procedure explained in Section 4.1.3.3.

Figure 4.21a and b indicates only the optically active excitons belonging to the E_{11} and E_{22} band-to-band transitions. In Figure 4.21c we show the four lowest bound singlet excition states with their symmetry given. Only the $1u$ state is optically active; it is the same as E_{11}^{S}. The $2g$ state is two-photon allowed [74, 137]. For details, see also References [76, 138, 139].

In Figure 4.22a we show a PLE intensity map from Reference [59]. The data were recorded on surfactant-wrapped, HiPco-produced nanotubes, i.e. the same type of sample as in the Raman experiments discussed in Section 4.1.3.3. Cutting a vertical line in the PLE map gives a photoluminescence excitation spectrum; a horizontal line corresponds to a photoluminescence (emission) spectrum. Each intensity maximum (highlighted by a full/open circle) corresponds to an emission peak E_{11}^{S} after resonant excitation into E_{22}^{S}. In Figure 4.22b the corresponding calculated PLE map is shown. Again, we observe the pattern of V-shaped branches, where the tubes with $\nu = -1$ are at larger excitation wavelength (full symbols) and $\nu = +1$ tubes at smaller excitation wavelength (open symbols). The assignment is found by matching the patterns from the experiment (a) and the calculation (b). As in the case of resonant Raman scattering, we do not consider the absolute values of the wavelength in the calculation, and we keep in mind that we observe excitonic transitions whereas the calculation is based on band-to-band transitions.

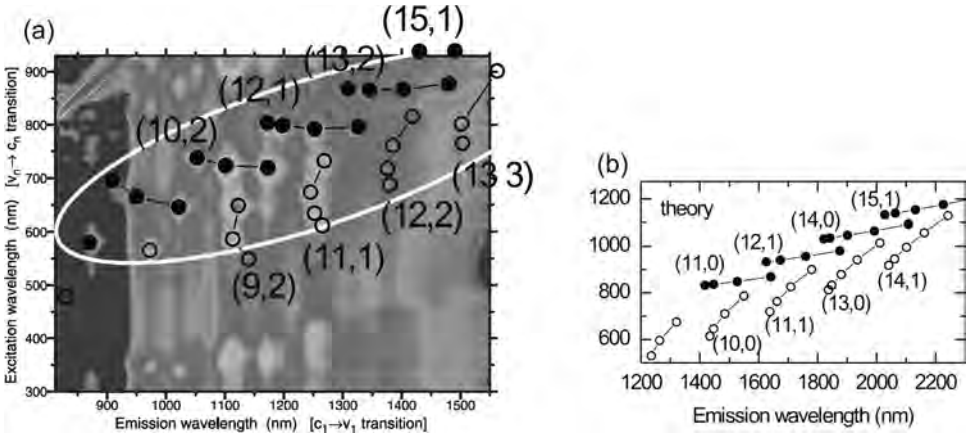

Figure 4.22 (a) PLE data showing the luminescence intensity as a function of excitation wavelength and emission wavelength. After Reference [59]. Full and open circles indicate $\nu - 1$ and $\nu = +1$ nanotubes, respectively. The lines connect tubes belonging to the same branch, where the chiral index of the outer tube is given. (b) PLE map from a third-nearest-neighbor tight-binding calculation [64].

However, the relative "distances" between the tubes within a given branch and the number of tubes belonging to the same branch are again the criterion on which the pattern matching is based. For example, the larger the diameter of the nanotubes, i.e. the higher the emission wavelength, the more tubes (*n,m*) form a branch.

In contrast to the resonant Raman scattering experiments (Section 4.1.3.3), the pattern matching based on photoluminescence experiments alone still had some ambiguity [59]. From several possible assignments one was chosen based on additional RBM measurements and the requirement that the relation between the RBM frequency and the diameter of the assigned tubes showed minimum deviation from linearity. The final (*n,m*) assignment in Reference [59] is the same as that found from resonant Raman scattering. The difference between the resonant Raman data and the PLE data is that in PLE in many branches the outer tube was not observed. This is clearly seen in Figure 4.22; for instance, the zigzag tubes (10,0), (11,0), (13,0) and (14,0) are missing in the experimental plot, as well as the (14,1) tube. The latter effect has been suggested to come from a resonance of the E_{22}^{S} exciton with the excitation of two E_{11}^{S} excitons [68, 140]. In nanotubes with small chiral angle, the ratio between the second and first transition energies is greater or smaller than two, depending on the family index ν; see Figure 4.21a and b. Therefore, in $\nu = +1$ tubes with $E_{22}^{S} > 2E_{11}^{S}$, the E_{22}^{S} exciton can excite two E_{11}^{S} excitons, whereas this decay channel does not exist in $\nu = -1$ tubes [68, 140].

In addition to the maxima corresponding to E_{22}^{S} excitation, the PLE map shows additional peaks corresponding to resonant excitation of other states, among them

Table 4.2 Photoluminescene excitation spectroscopy: summary of nanotubes and diameter ranges observable under typical experimental conditions. The given energy ranges are based on PLE data and empirical extrapolations from References [59] and [84], i.e. experiments on surfactant-wrapped, HiPco-produced single-walled carbon nanotubes in D_2O.

Detector limit (nm)	*excitation (nm)*	*(n,m)*	*Diameter (Å)*	*emission (nm)*
1100	E_{22}: 480–730	(5,4), (6,4), (9,1), (8,3), (6,5), (7,5), (10,2), (9,4)	6.1–9	830–1100
1700	E_{22}: ≤900	Up to (10,9)	≤13	≤1560 [**a**]
	E_{33}: 330–475	(6,5)–(12,5)	7.5–12	≤1500 [**a**]
	E_{44}: 290–400	(6,5)–(12,5)	7.5–12	≤1500 [**a**]
	E_{22}: ≤1050		≤14.7	≤1700 [**b**]

a Observed [59].
b Empirical extrapolation [84].

the higher-lying transitions E_{33}^{S} and E_{44}^{S} [84]. In Reference [141], some of the weaker peaks were identified as arising from transitions of light with perpendicular polarization to the tube axis. Furthermore, the Raman HEM and D^* modes have been observed in PLE maps, in addition to phonon sidebands that result from coupling of the optically inactive degenerate exciton to the *K*-point phonons. For details, the reader is referred to the literature [138, 142–144].

As in the case of resonant Raman scattering, all available experimental and empirical Kataura plot data can be used to assign (*n*,*m*) in a similar sample; see Section 4.1.3.2. If the nanotube environment is changed, a measurement on a nanotube ensemble helps to determine a possible shift in the energies E_{ii}. The small-diameter nanotubes, such as the (6,4), (9,1), (8,3), (6,5) and (7,5), give very well separated peaks in the PLE map (Figure 4.22) and can therefore be unambiguously identified even in luminescence from a single nanotube.

The advantage of photoluminescence excitation spectroscopy compared with Raman scattering is that it can be very fast and does not require the laborious analysis necessary for extracting Raman resonance profiles. Furthermore, a broadband white light source is usually sufficient for excitation, in contrast to tunable lasers required for resonance Raman spectroscopy. On the other hand, photoluminescence probes only semiconducting nanotubes, in contrast to Raman and Rayleigh scattering. In particular, if growth conditions are adjusted to enrich the samples in distinct chiral indices (*n*,*m*) [145, 146], it might be interesting also to analyze whether there is an effect on metallic nanotubes. Furthermore, the luminescence is quenched in nanotube bundles containing metallic tubes; therefore, PLE cannot be used to characterize carbon nanotubes in large bundles.

Table 4.2 summarizes the diameters of nanotubes from which emission can be observed at the two typical long-wavelength detector limits (Si, 1100 nm; InGaAs, 1700 nm).

4.2.1.1 PLE: Relative Abundance of Different (*n*,*m*)

The small or vanishing intensity of luminescence from the zigzag or close-to-zigzag nanotubes can result from two effects: first, the relative abundance of those tubes in the sample might be smaller than that of nanotubes with large chiral angle (at the inner positions of the branches) [59]. Second, it reflects the varying absorption cross-section for different chiral angles [97, 140, 147].

Again, as in resonant Raman scattering, the determination of the relative (*n*,*m*) abundance must take into account the (*n*,*m*) dependence of the optical matrix elements and also a possible dependence on the nanotube environment. In particular, if a certain (*n*,*m*) tube is not observed, this does not mean that this chiral index does not exist in the sample; instead, its signal might be too weak. Such a situation occurs for the zigzag and (*n*, 1) nanotubes missing in the PLE map in Figure 4.22: those missing nanotubes were clearly observed by resonant Raman scattering in the same type of sample (Figure 4.11). On the other hand, comparing PLE intensity maps for different samples of nanotube ensembles can provide qualitative differences of relative (*n*,*m*) abundance [146, 148, 149]. In Figure 4.23 we show PLE intensity maps from surfactant-wrapped carbon nanotubes in aqueous solution, where the nanotube material was synthesized under different conditions [146]. We clearly observe differences in the relative intensities of the PLE peaks from different nanotubes, e.g. in Figure 4.23b the larger-diameter tubes (at higher emission wavelength) appear very weak compared with (a) and (c). Unless there is an indication that the growth condition selectively changes the optical transition strengths of some (*n*,*m*), it seems safe to assume that the *relative* abundance of nanotubes (*n*,*m*) with very strong intensity in (b) is increased compared with their relative abundance in (a). However, without further analysis and normalization to the cross-section of the optical transitions, we cannot determine whether the abundance of nanotubes with strong PLE peaks is higher on an absolute scale than that of tubes with weak PLE signals in the same plot.

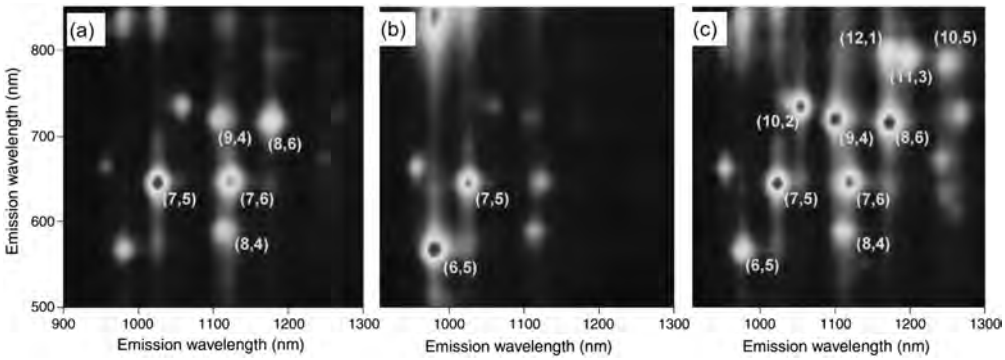

Figure 4.23 PLE intensity maps from surfactant-wrapped carbon nanotubes in D_2O at different growth conditions. (a) Alcohol–catalytic chemical vapor deposition (ACCVD) at 850 °C reaction temperature; (b) ACCVD at 650 °C; (c) HiPco nanotubes. After Reference [146].

4.2.1.2 Photoluminescence from Carbon Nanotubes Under Different Conditions

As mentioned above, the optical transition energies are sensitive to the nanotube environment. So far, we have considered mainly photoluminescence from surfactant-wrapped nanotubes in solution. Alternatively, photoluminescence can be observed from individual nanotubes directly grown across pillars, slits or grooves on a substrate; see Figure 4.24a. These nanotubes are usually suspended in air and, depending on the density of tubes per area, are either probed as an ensemble [66, 89, 150, 151] or individually [122, 152–155]. The photoluminescence signal from individual single nanotubes can be mapped spatially to probe the homogeneity of the nanotube's structural and electronic properties and possible (n,m) changes within the same tube [122]. As mentioned in Section 4.1.4, optical near-field spectroscopy can in addition correlate the topographic structure of the nanotube with its optical properties on a ~10-nm scale [156].

Comparison between nanotubes suspended in air and surfactant-wrapped nanotubes has shown blue shifts of the excitation and emission energies in air-suspended tubes between 10 and 30 meV [66, 89]. The shift of the excitation energy E_{22}^{S} was found to be slightly smaller on average than that of E_{11}^{S} [89]. In addition, a chiral angle and $\nu = \pm 1$ dependence of the energy shifts was reported in Reference [66]. This is shown in Figure 4.24b: tubes with $\nu = -1$ ("type I") exhibit a blue shift, whereas the excitation energy in some of the tubes with $\nu = +1$ ("type II") even shifts to lower energies [66]. The energy shifts of E_{11}^{S} decrease with increasing chiral angle in $\nu = +1$ nanotubes and increase in $\nu = -1$ nanotubes, and *vice versa* for E_{22}^{S}. The energy shift is attributed to the change of the dielectric environment of the nanotube, affecting both the electron–electron and the electron–hole interactions. The chiral angle dependence of the effective electron and hole masses has been suggested as the origin of the chiral angle dependence of the energy shifts [66].

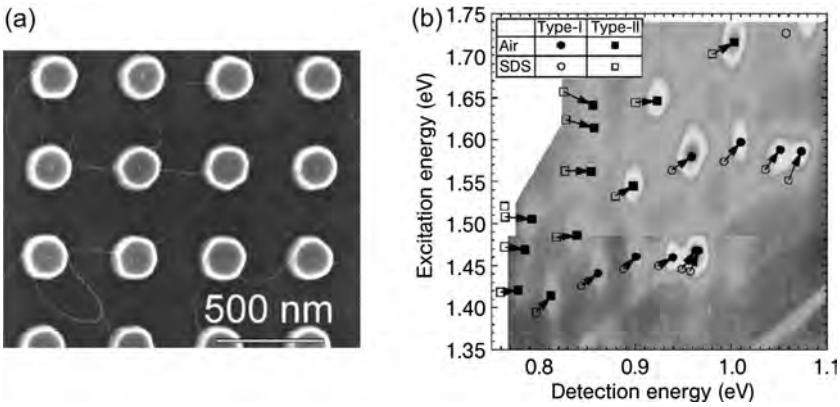

Figure 4.24 (a) Scanning electron microscopy image of individual suspended nanotubes grown directly on pillars. From Reference [89]. (b) PLE map of air-suspended nanotubes. Open symbols represent the PLE data from surfactant-wrapped nanotubes [59] for comparison. Taken from Reference [66].

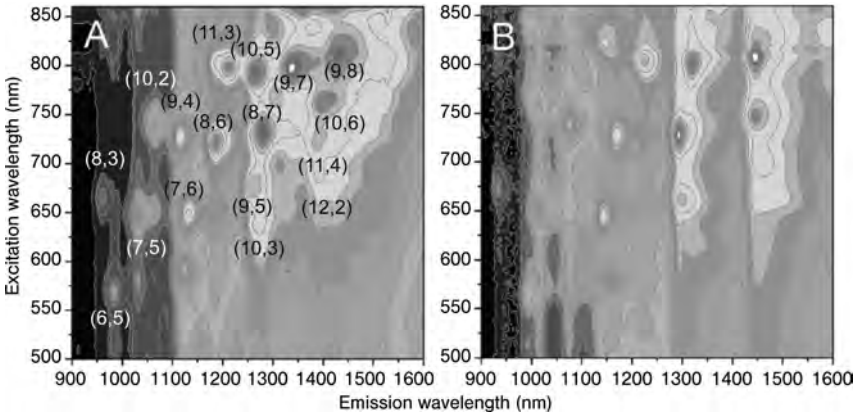

Figure 4.25 PLE intensity maps from HiPco-produced surfactant-wrapped carbon nanotubes in D_2O. (A) Room temperature; (B) at 16 K. The shifts of the excitation and emission energies can be explained as resulting from the strain induced by freezing of the water. After Reference [157].

Differences between the photoluminescence spectra from nanotube ensembles and from a single tube appear only at low temperatures [151, 152]. Below 20 K, the PL linewidth decreases to a few meV in a single nanotube, whereas the linewidth in a nanotube ensemble remains almost unaffected at ~25 meV [151]. In nanotube ensembles and in single tubes, the PL peak positions depend slightly on temperature; the emission from E_{11}^{S} shows a blue shift on the order of ~10 meV at 5 K [151]. An additional effect on the transition energies is observed, if the temperature in surfactant-wrapped nanotubes in solution is varied [157, 158]: below the freezing temperature, the nanotubes are exposed to strain from the surrounding medium. Since the transition energies have a chiral angle and family ν dependence on strain [159], some of the energies shift even to lower energies with decreasing temperature. This is seen in Figure 4.25: in tubes with $\nu = -1$, the E_{11}^{S} energies shift up, whereas they shift down in tubes with $\nu = +1$. The family behavior is reversed in the second transition E_{22}^{S}.

4.2.2
Rayleigh Scattering

Rayleigh scattering is the elastic light scattering from an object that is small in diameter compared with the wavelength of the light. Rayleigh scattering is commonly known as the origin of the blue appearance of the sky, as its cross-section increases strongly with the frequency of the light. If the frequency of the light is in resonance with an electronic transition of the object, the scattering intensity is enhanced. Therefore, it can probe the transition energies of a nanotube independent of the tube's metallic or semiconducting character, combining in principle some advantages from PLE and Raman spectroscopy, i.e. a rather fast experiment

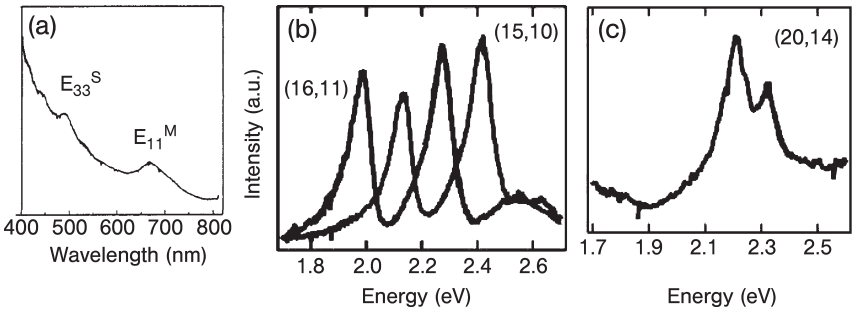

Figure 4.26 (a) Rayleigh spectrum from a small bundle, where the peaks are assigned to E_{33}^{S} and E_{11}^{M}. After Reference [160]. (b), (c) Rayleigh spectra from different individual nanotubes, identified by their chiral index. In (b) the Rayleigh spectra of semiconducting tubes are shown, where the peaks correspond to the E_{33}^{S} and E_{44}^{S} transitions; (c) shows a typical spectrum of the two close-by transitions of a metallic tube, E_{22}^{M-} and E_{22}^{M+}. After Reference [86].

and the access to the transitions in metallic nanotubes. On the other hand, the signal strength is typically very low, requiring a bright light source and a sample geometry in which possible scattering background from nearby scatterers is almost entirely supressed.

Rayleigh scattering from small individual nanotube bundles on a glass substrate in dark-field geometry has been reported in Reference [160]. A Rayleigh spectrum from Reference [160] is shown in Figure 4.26a. The contributions from individual nanotubes within the bundle are not resolved, but the peaks were assigned to the first transition E_{11}^{M} in metallic tubes (at 650–700 nm) and to the E_{33}^{S} transition in semiconducting tubes (at 450–500 nm).

In Reference [33], Rayleigh scattering from individual single nanotubes was presented; see Figure 4.26b and c. The ability to observe Rayleigh scattering from a single nanotube is based on two experimental conditions: first, a bright white light source, and second, a sample with freestanding nanotubes to prevent scattering from a nearby substrate. The bright white light source was realized by passing femtosecond pulses from a Ti:sapphire laser through a microstructured optical fiber, resulting in a white-light continuum in the wavelength range ~450–1550 nm [33, 161]. The nanotube sample was fabricated by CVD growth of long single-walled carbon nanotubes across 20–100 μm wide slits in a silicon substrate [162]. In Figure 4.27, a scanning electron microscope image of nanotubes grown across a slit is shown. As the focus size of the white light is on the order of 2 μm, each of the tubes can be probed separately; also different positions along the same nanotube can be studied.

In Figure 4.26b and c, Rayleigh spectra typical for individual semiconducting and metallic tubes are shown, respectively [86]. The indicated chiral index had been assigned by electron diffraction. The Rayleigh spectrum of metallic nanotubes usually displays pairs of close-by peaks corresponding to the upper and lower

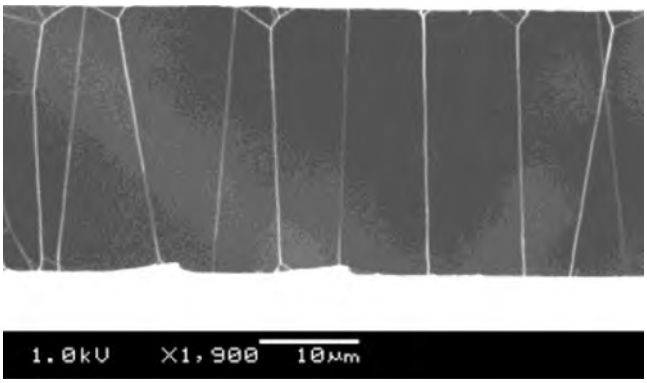

Figure 4.27 Scanning electron microscopy image of single nanotubes grown across a 26-μm wide slit in a silicon substrate. At the edges of the slit, some tubes form Y-junctions. Taken from Reference [162].

branch in a given set of metallic transitions in the Kataura plot. In Figure 4.26c, the E_{22}^{M-} and E_{22}^{M+} transitions are seen [86]. Only in armchair nanotubes, which are at the inner positions of the V-shaped branches in the Kataura plot, are the transitions not split, and only one peak is expected.

If a small nanotube bundle consists of only two or three tubes, their Rayleigh peaks are still resolved; see Reference [163]. The Rayleigh spectrum of such small bundles seems to be mainly a superposition of the individual Rayleigh responses. However, bundling results in a red shift of a few tens of meV, as observed also by Raman scattering and PLE spectroscopy.

The Rayleigh spectra are fit to the scattering cross-section, which contains the dielectric function of the nanotube. The Rayleigh scattering cross-section per unit length, if the nanotube is regarded as an infinite cylinder with diameter d, is given by [163]

$$\sigma(\omega) \propto \left(\frac{d}{2}\right)^4 \frac{\omega^3}{c^3} |\varepsilon(\omega) - 1|^2 \tag{11}$$

where ω is the frequency of the light, c is the velocity of light and $\varepsilon(\omega)$ is the complex dielectric function. From the transition energies E_{ii}, the chiral index can be assigned in the same way as in Raman scattering or PLE spectroscopy (Sections 4.1.3.3 and 4.2.1), if an additional piece of information is available. This can be an estimation of the nanotube diameter from, e.g., the growth conditions, or a Raman measurement of the radial breathing mode. If the nanotubes have a large diameter, usually two resonances are observed in the visible range of the Rayleigh-scattered light.

The advantage of Rayleigh scattering spectroscopy is that it is a very fast probe of optical transitions in a nanotube over a large spectral range. It is not restricted

to semiconducting nanotubes, but can also be applied to metallic tubes. Furthermore, metallic nanotubes can often be distinguished easily from semiconducting ones by the lineshape, as shown in Figure 4.26b and c. In addition to an (*n*,*m*) assignment, the freestanding nanotubes permit studies of possible chiral index changes along the nanotube [33], and also direct optical imaging of the nanotube shape such as *Y*-junctions or variation in thickness of small bundles [163]. On the other hand, freely suspended nanotubes and a specially bright white light source seem to be neccessary for a sufficiently strong Rayleigh signal. Single nanotubes or very thin bundles are required in order to resolve the Rayleigh signal from individual nanotubes.

4.3 Comparison with Other Characterization Techniques

In this section, we briefly summarize other characterization methods for carbon nanotubes, mainly imaging techniques, and compare them with the optical methods described above.

In order to determine the chiral index of a nanotube, we probe by optical spectroscopy certain properties of the tube such as its RBM frequency and its optical excitation energies. From these properties, possibly together with theoretical predictions, the chiral index is deduced. On the other hand, one might directly "visualize" the nanotube structure either by scanning probe microscopy or by electron diffraction.

All the following methods are mainly for *imaging* purposes rather than characterization of optical or electronic properties. Even imaging with optical spectroscopy (e.g. confocal Raman spectroscopy) aims at imaging the properties of the tube, not the tube structure itself. For example, the homogeneity of the Raman or luminescence signal is analyzed.

4.3.1 Electron Diffraction

Electron diffraction has become a well-established tool for (*n*,*m*) determination [86, 164–168]. The diffraction pattern of a single-walled carbon nanotube consists of two structures with hexagonal symmetry, which are rotated against each other. They arise from the front and back wall of the nanotube; from the angle between them the chiral angle of the nanotube can be derived. The diffraction peaks are elongated in the direction of the nanotube diameter, since due to the curvature the lattice constant perpendicular to the nanotube axis appears to be decreasing [166].

In Figure 4.28a a typical electron diffraction image is shown from a nanotube assigned to a (24,11) tube [164]. The two six-fold patterns and the streaks along the horizontal direction are clearly seen. Figure 4.28b shows a simulation of the electron diffraction image of the same nanotube. Usually, comparison with a

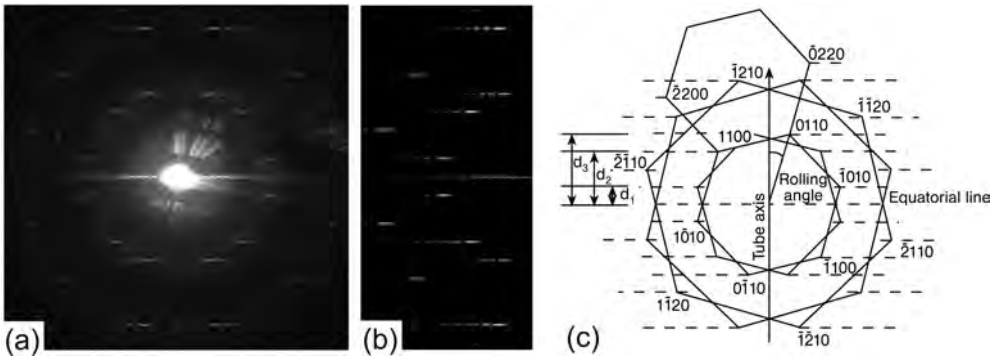

Figure 4.28 (a) Electron diffraction image of a single carbon nanotube and (b) simulation of the electron diffraction image. The nanotube is identified as a (24,11) tube. (c) Schematic view of the geometry of the diffraction pattern. After Reference [164].

simulated image is required in order to obtain an unambiguous (n,m) assignment.

The advantage of electron diffraction is its reliability, in particular, the chiral indices of large-diameter tubes are identified. This appears to be difficult in Raman scattering and PLE, as the RBM frequencies and optical energies are too close within the same Kataura branch for diameters above 2 nm. On the other hand, to the best of our knowledge, only very few independent (n,m) assignments of the same nanotube by optical methods and by electron diffraction have been reported so far [86]. Compared with optical measurements, electron diffraction requires special sample preparation: the nanotube must be straight over the probed tube segment and freestanding or placed on a TEM grid. Furthermore, only one nanotube can be probed at a time, i.e. electron diffraction cannot be applied to nanotube ensembles. Finally, the nanotube might be damaged or even destroyed by the electron beam.

4.3.2
High-Resolution Transmission Electron Microscopy

High-resolution transmission electron microscopy (HRTEM) is suited to measure quickly the diameter of a nanotube. Due to the curvature of the nanotube wall, the tube walls appear as dark lines in the HRTEM image. This is shown in Figure 4.29a: several single-walled carbon nanotubes are clearly seen [169]. Figure 4.29b and c show double- and multi-walled nanotubes, as recognized by the number of equally spaced dark lines corresponding to the nanotube walls. From the distance between the dark lines, the tube diameter is measured. However, it has been shown [170] that the diameter is usually underestimated in HRTEM and changes with the focus condition, the error depending on the tilt angle between the nano-

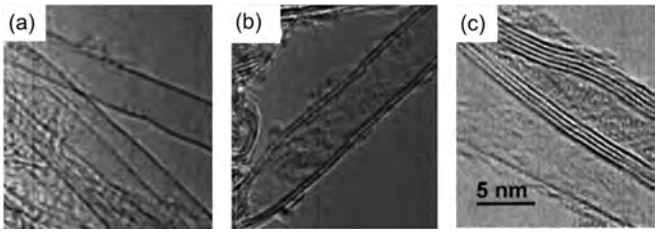

Figure 4.29 High-resolution TEM images of (a) single-walled nanotubes, (b) double-walled tubes and (c) multi-walled carbon nanotubes. The scale bars in (a) and (b) are roughly the same as in (c). After Reference [169].

tube axis and the plane perpendicular to the electron beam. HRTEM analysis aiming at precise determination of the diameter or even of the chiral index, is frequently combined with electron diffraction; see, for instance, Reference [168]. HRTEM images of the hexagonal pattern of the nanotube wall have been observed recently due to increased phase contrast in a special TEM instrument with decreased spherical aberration [171].

In addition, HRTEM is used to determine whether single- or multi-walled nanotubes are predominant in a sample and to analyze the diameter distribution. Furthermore, the shape (e.g. kinks, Y-junctions) and the purity of nanotubes can be imaged, and also molecules inside the nanotubes can be observed, such as C_{60} in so-called peapod structures [172].

As in electron diffraction, high-resolution TEM can be applied only to a limited number of nanotubes at a time, and the tube might be damaged by the electron beam. Therefore, statistics have to be performed in order to characterize sample purity or diameter distribution after growth.

4.3.3
Scanning Tunneling Microscopy

Scanning tunneling microscopy (STM) probes the surface structure of carbon nanotubes with atomic resolution, which in principle permits determination of the chiral index [173, 175–177]. In Figure 4.30a the STM image of a nanotube wall is shown; the dark spots represent the inner area of the carbon hexagons. The chiral angle of the nanotube is determined from the angle between the zigzag direction and the direction of the nanotube axis. Together with the diameter, the chiral index (n,m) of the nanotube can be derived. Several corrections to the image have to be taken into account. First, the diameter is usually overestimated, because the image is formed by a convolution of the STM tip and the investigated object. Second, as the nanotube appears flattened, the angle between the armchair and zigzag direction is larger than 30° in the STM image; see Figure 4.30 (a), upper panel. In the lower panel, these corrections have been applied; the image of the tube is now narrower, and the angle between the zigzag and armchair directions

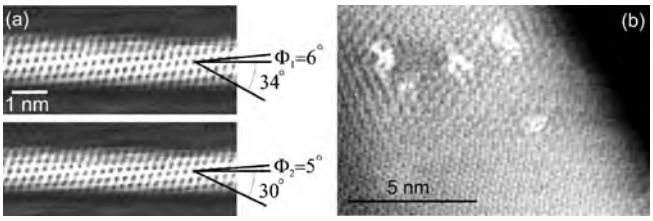

Figure 4.30 STM images of carbon nanotubes with atomic resolution. (a) Single-walled carbon nanotube on a gold substrate. The image appears distorted along the direction perpendicular to the nanotube axis (top); the corrected image (bottom) shows an angle of 30° between the armchair and zigzag directions. The chiral angle for this tube is 5°. From Reference [173]. (b) Multi-walled nanotube with defects (white areas) created by Ar^+ irradiation. After Reference [174].

is 30°. As the STM image also depends on the applied bias [178], the (n,m) assignment can be assisted by simulations of the image [179, 180]. In Figure 4.30b we show an STM image of the outer wall of a multi-walled nanotube, where defects have been introduced by Ar^+ irradiation [174]. The damaged areas of the tube wall are clearly seen.

In scanning tunneling spectroscopy (STS), the electronic structure of the nanotube is determined [181, 182]. The tunneling current is measured as a function of applied bias, mapping the electronic density of states around the Fermi level. Therefore, metallic and semiconducting nanotubes can be easily distinguished, and an (n,m) assignment based on an STM image can be verified by an STS measurement.

Scanning tunneling microscopy provides information about the nanotube properties on an atomic length scale. It is therefore not suited to characterize large quantities of nanotubes or bulk samples.

4.3.4
Atomic Force Microscopy and Scanning Electron Microscopy

Atomic force microscopy (AFM) and scanning electron microscopy (SEM) are both standard methods to characterize nanotubes on a substrate with respect to their shape and location. They are fast and usually image larger sample areas than STM.

In AFM, the topography of a nanotube is measured. As in STM, the nanotube diameter in lateral direction is overestimated by the convolution with the tip, but the measured height can provide a reliable determination of the nanotube diameter. AFM imaging can be applied to single nanotubes and bundles on a substrate; however, it cannot easily image freely suspended nanotubes. Instead of imaging, AFM can also be used to mechanically manipulate the nanotube; see for instance Reference [183].

Scanning electron microscopy, on the other hand, does not provide the spatial resolution to determine the nanotube diameter, but shows the location and shape

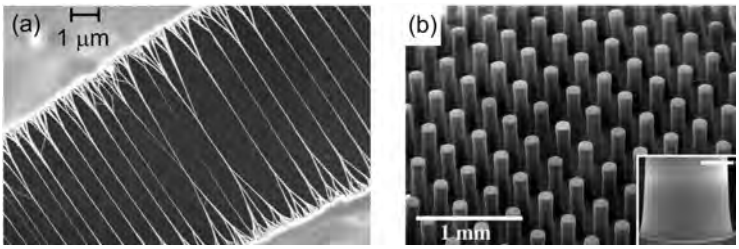

Figure 4.31 (a) SEM image of single-walled carbon nanotube bundles bridging a crack in a free-standing single-walled nanotube film of ~300 nm thickness. After Reference [184]. (b) SEM image of vertical pillar-like structures formed by aligned single-walled carbon nanotubes from synthesis by water-assisted chemical vapor deposition. The inset shows a zoom into one of the pillars; the scale bar is 50 μm. Taken from Reference [185].

of nanotubes. Unlike AFM, it also images freely suspended nanotubes; furthermore, the accessible scanning area is typically larger (in the mm^2 range). In Figure 4.31, two typical SEM images are shown. In (a), single nanotubes are crossing a crack in a substrate [184]; the image size is in the range of a few micrometers, and individual nanotubes are observed. Figure 4.31b, in contrast, shows an overview on the millimeter scale of a sample of pillars formed by vertically aligned nanotubes [185]. Again, a single nanotube might sometimes be damaged in an SEM measurement.

4.4 Conclusion

In summary, optical spectroscopy provides versatile characterization tools for carbon nanotubes. It is non-destructive and can be applied to many different sample types, ranging from one individual nanotube, probing even different segments of the same tube, to bulk samples of nanotube bundles. Furthermore, the optical methods presented here do not require low temperatures; in Raman scattering, not even special sample environments are neccessary.

The Raman spectrum of carbon nanotubes, showing the radial breathing mode and the high-energy modes, unambiguously identifies the presence of single-walled carbon nanotubes in the sample. The diameter of the nanotube can be estimated from the RBM frequency, and the resonance of the laser energy with optical transitions permits finally identification of the chiral index (n,m). Structural defects in the nanotube structure are reflected in an increased intensity of the Raman *D* mode.

Whereas Raman spectroscopy probes both semiconducting and metallic nanotubes, photoluminescence is restricted to semiconducting tubes. Also, individual (unbundled) nanotubes are required for photoluminescence measurements. As in Raman scattering, the chiral index can be determined by PLE. If the optical transition energies are to be analyzed under several different conditions, PLE intensity

maps are typically much faster obtained than complete Raman resonance profiles.

From Rayleigh scattering, the chiral index of carbon nanotubes can also be determined, but this requires freely suspended nanotubes. Rayleigh scattering combines the ability to probe the optical transitions in metallic and semiconducting tubes with a very fast measurement.

The above-presented methods have in common that they require at least two pieces of information in order to arrive at a reliable (n,m) determination. These can be two optical transition energies, as in PLE and Rayleigh scattering, or the RBM frequency and one transition energy, as in resonant Raman scattering. On the other hand, in many applications of carbon nanotubes the relevant information about the nanotubes in a sample might be their metallic or semiconducting character, or their family index ν. The pattern of an alternating $\nu = \pm 1$ dependence exists in many of the nanotube properties, such as luminescence intensities, electron–phonon coupling and dependence of electronic energies on strain or temperature.

Imaging techniques, which probe the structure of nanotubes spatially, are complementary to the optical techniques, which probe the structure via the electronic, optical and vibrational properties, and ideally both of these techniques would be combined.

4.5 List of Symbols

a_0	Graphite in-plane lattice constant
a_{C-C}	Carbon–carbon bond length in graphite
d	Nanotube diameter
E_{ii}	Optical transition between valence and conduction band with same index i
E_l	Photon energy
$\hbar$	Planck's constant, $h/2\pi$
k_F	Fermi wavevector
$k_{i,s}$	Wavevector of incoming, scattered photon
$M_{e-r,\ e-ph}$	Exciton–radiation and exciton–phonon coupling matrix elements
(n,m)	Chiral index
q	Wavevector of phonon
ν	Nanotube family index, $\nu = (n - m) \bmod 3 = 0,-1,+1$
$\varepsilon(\omega)$	Complex dielectric function
γ	Broadening of the electronic states
$\sigma(\omega)$	Rayleigh scattering cross-section
θ	Chiral angle
$\omega_{i,s}$	Angular frequency of incoming, scattered light
ω_{ph}	Angular frequency of phonon
ω_{RBM}	Angular frequency of the radial breathing mode

4.6 Acknowledgments

We are grateful to Hagen Telg, Stephanie Reich and María Machón for many useful discussions and collaborations. J.M. would like to thank Tony F. Heinz and the NSEC at Columbia University for their hospitality and for many helpful discussions. J.M. acknowledges support from the Alexander von Humboldt Foundation.

References

1 S. Reich, C. Thomsen, and J. Maultzsch, *Carbon Nanotubes: Basic Concepts and Physical Properties*. Wiley-VCH, Berlin, 2004.
2 M. Damnjanović, I. Milošević, T. Vuković, R. Sredanović, Full symmetry, optical activity, and potentials of single-wall and multiwall nanotubes. *Phys. Rev. B*, **60** (1999) 2728.
3 M. S. Strano, Probing chiral selective reactions using a revised Kataura plot for the interpretation of single-walled carbon nanotube spectroscopy. *J. Am. Chem. Soc.*, **125** (2003) 16148.
4 Y. Wang, M. J. Kim, H. Shan, C. Kittrell, H. Fan, L.M. Ericson, W.-F. Hwang, S. Arepalli, R. H. Hauge, R. E. Smalley, Continued growth of single-walled carbon nanotubes. *Nano Lett.*, **5** (2005) 997.
5 R. Graupner, J. Abraham, D. Wunderlich, A. Vecelová, P. Lauffer, J. Rörl, M. Hundhausen, L. Ley, A. Hirsch, Nucleophilic-alkylation-reoxidation: a functionalization sequence for single-wall carbon nanotubes. *J. Am. Chem. Soc.*, **128** (2006) 6683.
6 M. Cantoro, S. Hofmann, S. Pisana, V. Scardaci, A. Parvez, C. Ducati, A. C. Ferrari, A. M. Blackburn, K.-Y. Wang, J. Robertson, Catalytic chemical vapor deposition of single-wall carbon nanotubes at low temperatures. *Nano Lett.*, **6** (2006) 1107.
7 K. Kaminska, J. Lefebvre, D. G. Austing, P. Finnie, Real-time *in situ* Raman imaging of carbon nanotube growth. *Nanotechnology*, **18** (2007) 165707.
8 C. Thomsen, S. Reich, Raman scattering in carbon nanotubes. *Top. Appl. Phys.* **108** (2007) 115.
9 M. Cardona, Resonance phenomena. *Top. Appl. Phys.* **50** (1982) 19.
10 R. M. Martin, L. M. Falicov, Resonant Raman scattering. *Top. Appl. Phys., 2nd ed.* **8** (1983) 79.
11 T. Ruf, J. Serrano, M. Cardona, P. Pavone, M. Pabst, M. Krisch, M. D'Astuto, T. Suski, I. Grzegory, M. Leszczynski, Phonon dispersion curves in wurtzite structure GaN determined by inelastic X-ray scattering. *Phys. Rev. Lett.*, **86** (2001) 906.
12 J. Kulda, H. Kainzmaier, D. Strauch, B. Dorner, M. Lorenzen, M. Krisch, Overbending of the longitudinal optical phonon branch in diamond as evidenced by inelastic neutron and X-ray scattering. *Phys. Rev. B*, **66** (2002) 241202.
13 J. Maultzsch, S. Reich, C. Thomsen, H. Requardt, P. Ordejón, Phonon dispersion of graphite. *Phys. Rev. Lett.*, **92** (2004) 075501.
14 M. Krisch, F. Sette, Inelastic X-ray scattering from phonons. *Top. Appl. Phys.* **108** (2007) 317.
15 C. Thomsen, S. Reich, J. Maultzsch, Resonant Raman spectroscopy of nanotubes. *Philos. Trans. R. Soc. London, Ser. A*, **362** (2004) 2337.
16 M. S. Dresselhaus, G. Dresselhaus, R. Saito, A. Jorio, Raman spectroscopy of carbon nanotubes. *Phys. Rep.*, **409** (2005) 47.
17 J. Kürti, G. Kresse, H. Kuzmany, First-principles calculations of the radial breathing mode of single-wall carbon

nanotubes. *Phys. Rev. B*, **58** (1998) 8869(R).

18 J. Maultzsch, S. Reich, C. Thomsen, Chirality selective Raman scattering of the D-mode in carbon nanotubes. *Phys. Rev. B*, **64** (2001) 121407(R).

19 A. G. Souza Filho, A. Jorio, G. Dresselhaus, M. S. Dresselhaus, R. Saito, A. K. Swan, M. S. Ünlü, B. B. Goldberg, J. H. Hafner, C. M. Lieber, M. A. Pimenta, Effect of quantized electronic states on the dispersive Raman features in individual single-wall carbon nanotubes. *Phys. Rev. B*, **65** (2001) 035404.

20 J. Kürti, V. Zólyomi, A. Grüneis, H. Kuzmany, Double resonant Raman phenomena enhanced by van Hove singularities in single-wall carbon nanotubes. *Phys. Rev. B*, **65** (2002) 165433.

21 C. Thomsen, S. Reich, Double-resonant Raman scattering in graphite. *Phys. Rev. Lett.*, **85** (2000) 5214.

22 G. S. Duesberg, I. Loa, M. Burghard, K. Syassen, S. Roth, Polarized Raman spectroscopy of individual single-wall carbon nanotubes. *Phys. Rev. Lett.*, **85** (2000) 5436.

23 J. Maultzsch, Vibrational properties of carbon nanotubes and graphite. *PhD Thesis*, Technische Universität Berlin, 2004.

24 A. M. Rao, E. Richter, S. Bandow, B. Chase, P. C. Eklund, K. A. Williams, S. Fang, K. R. Subbaswamy, M. Menon, A. Thess, R. E. Smalley, G. Dresselhaus, M. S. Dresselhaus, Diameter-selective Raman scattering from vibrational modes in carbon nanotubes. *Science*, **275** (1997) 187.

25 M. A. Pimenta, A. Marucci, S. A. Empedocles, M. G. Bawendi, E. B. Hanlon, A. M. Rao, P. C. Eklund, R. E. Smalley, G. Dresselhaus, M. S. Dresselhaus, Raman modes of metallic carbon nanotubes. *Phys. Rev. B*, **58** (1998) R16016.

26 P. M. Rafailov, H. Jantoljak, C. Thomsen, Electronic transitions in single-walled carbon nanotubes: a resonance Raman study. *Phys. Rev. B*, **61** (2000) 16179.

27 S. D. M. Brown, A. Jorio, P. Corio, M. S. Dresselhaus, G. Dresselhaus, R. Saito, K. Kneipp, Origin of the Breit–Wigner–Fano lineshape of the tangential *G*-band feature of metallic carbon nanotubes. *Phys. Rev. B*, **63** (2001) 155414.

28 A. Jorio, R. Saito, J. H. Hafner, C. M. Lieber, M. Hunter, T. McClure, G. Dresselhaus, M. S. Dresselhaus, Structural (*n*,*m*) determination of isolated single-wall carbon nanotubes by resonant Raman scattering. *Phys. Rev. Lett.*, **86** (2001) 1118.

29 J. Maultzsch, S. Reich, U. Schlecht, C. Thomsen, High-energy phonon branches of an individual metallic carbon nanotube. *Phys. Rev. Lett.*, **91** (2003) 087402.

30 A. Jorio, A. G. Souza Filho, G. Dresselhaus, M. S. Dresselhaus, A. K. Swan, M. S. Ünlü, B. B. Goldberg, M. A. Pimenta, J. H. Hafner, C. M. Lieber, R. Saito, G band resonant Raman study of 62 isolated single-wall carbon nanotubes. *Phys. Rev. B*, **65** (2002) 155412.

31 C. Jiang, J. Zhao, H. A. Therese, M. Friedrich, A. Mews, Raman imaging and spectroscopy of heterogeneous individual carbon nanotubes. *J. Phys. Chem. B*, **107** (2003) 8742.

32 A. Hartschuh, H. N. Pedrosa, L. Novotny, T. D. Krauss, Simultaneous fluorescence and Raman scattering from single carbon nanotubes. *Science*, **301** (2003) 1354.

33 M. Y. Sfeir, F. Wang, L. Huang, C.-C. Chuang, J. Hone, S. P. O'Brien, T. F. Heinz, L. E. Brus, Probing electronic transitions in individual carbon nanotubes by Rayleigh scattering. *Science*, **306** (2004) 1540.

34 J. C. Meyer, M. Paillet, T. Michel, A. Moréac, A. Neumann, G. S. Duesberg, S. Roth, J.-L. Sauvajol, Raman modes of index-identified freestanding carbon nanotubes. *Phys. Rev. Lett.*, **95** (2005) 217401.

35 M. Paillet, T. Michel, J. C. Meyer, V. N. Popov, L. Henrard, S. Roth, J.-L. Sauvajol, Raman active phonons of identified semiconducting single-walled carbon nanotubes. *Phys. Rev. Lett.*, **96** (2006) 257401.

36 S. B. Cronin, Y. Yin, A. Walsh, Rodrigo B. Capaz, A. Stolyarov, P. Tangney, Marvin L. Cohen, Steven G. Louie, A. K. Swan, M. S. Ünlü, B. B. Goldberg, M. Tinkham, Temperature dependence of the optical transition energies of carbon nanotubes: the role of electron–phonon coupling and thermal expansion. *Phys. Rev. Lett.*, **96** (2006) 127403.

37 Y. Yin, A. N. Vamivakas, A. G. Walsh, S. B. Cronin, M. S. Ünlü, B. B. Goldberg, A. K. Swan, Optical determination of electron–phonon coupling in carbon nanotubes. *Phys. Rev. Lett.*, **98** (2007) 037404.

38 S. K. Doorn, D. A. Heller, P. W. Barone, M. L. Usrey, M. S. Strano, Resonant Raman excitation profiles of individually dispersed single walled carbon nanotubes in solution. *Appl. Phys. A*, **78** (2004) 1147.

39 H. Telg, J. Maultzsch, S. Reich, F. Hennrich, C. Thomsen, Chirality distribution and transition energies of carbon nanotubes. *Phys. Rev. Lett.*, **93** (2004) 177401.

40 C. Fantini, A. Jorio, M. Souza, M. S. Strano, M. S. Dresselhaus, M. A. Pimenta, Optical transition energies for carbon nanotubes from resonant Raman spectroscopy: environment and temperature effects. *Phys. Rev. Lett.*, **93** (2004) 147406.

41 F. Hennrich, R. Krupke, S. Lebedkin, K. Arnold, R. Fischer, D. E. Resasco, M. M. Kappes, Raman spectroscopy of individual single-walled carbon nanotubes from various sources. *J. Phys. Chem. B*, **109** (2005) 10567.

42 E. Dobardžić, I. Milošević, B. Nikolić, T. Vuković, M. Damnjanović, Single-wall carbon nanotubes phonon spectra: symmetry-based calculations. *Phys. Rev. B*, **68** (2003) 045408.

43 D. Sánchez-Portal, E. Artacho, J. M. Soler, A. Rubio, P. Ordejón, *Ab initio* structural, elastic, and vibrational properties of carbon nanotubes. *Phys. Rev. B*, **59** (1999) 12678.

44 R. Saito, A. Jorio, J. H. Hafner, C. M. Lieber, M. Hunter, T. McClure, G. Dresselhaus, M. S. Dresselhaus, Chirality-dependent *G*-band Raman intensity of carbon nanotubes. *Phys. Rev. B*, **64** (2001) 085312.

45 O. Dubay, G. Kresse, Accurate density functional calculations for the phonon dispersion relations of graphite layer and carbon nanotubes. *Phys. Rev. B*, **67** (2003) 035401.

46 S. Reich, C. Thomsen, P. Ordejón, Eigenvectors of chiral nanotubes. *Phys. Rev. B*, **64** (2001) 195416.

47 M. Mohr, M. Machón, C. Thomsen, I. Milosević, M. Damnjanović, Mixing of the fully symmetric vibrational modes in carbon nanotubes. *Phys. Rev. B*, **75** (2007) 195401.

48 M. Lazzeri, S. Piscanec, F. Mauri, A. C. Ferrari, J. Robertson, Phonon linewidths and electron–phonon coupling in graphite and nanotubes. *Phys. Rev. B*, **73** (2006) 155426.

49 O. Dubay, G. Kresse, H. Kuzmany, Phonon softening in metallic nanotubes by a Peierls-like mechanism. *Phys. Rev. Lett.*, **88** (2002) 235506.

50 S. Piscanec, M. Lazzeri, J. Robertson, A. C. Ferrari, F. Mauri, Optical phonons in carbon nanotubes: Kohn anomalies, Peierls distortions, and dynamic effects. *Phys. Rev. B*, **75** (2007) 035427.

51 R. J. Nemanich, S. A. Solin, First- and second-order Raman scattering from finite-size crystals of graphite. *Phys. Rev. B*, **20** (1979) 392.

52 J. M. Benoit, J. P. Buisson, O. Chauvet, C. Godon, S. Lefrant, Low-frequency Raman studies of multiwalled carbon nanotubes: experiments and theory. *Phys. Rev. B*, **66** (2002) 073417.

53 R. R. Bacsa, A. Peigney, Ch. Laurent, P. Puech, W. S. Bacsa, Chirality of internal metallic and semiconducting carbon nanotubes. *Phys. Rev. B*, **65** (2002) 161404(R).

54 S. Bandow, C. Chen, G. U. Sumanasekera, R. Gupta, M. Yudasaka, S. Iijima, P. C. Eklund, Diameter-selective resonant Raman scattering in double-wall carbon nanotubes. *Phys. Rev. B*, **66** (2002) 075416.

55 F. Simon, Ch. Kramberger, R. Pfeiffer, H. Kuzmany, V. Zólyomi, J. Kürti, P. M. Singer, H. Alloul, Isotope engineering of

carbon nanotube systems. *Phys. Rev. Lett.*, **95** (2005) 017401.

56 S. Bandow, M. Takizawa, K. Hirahara, M. Yudasaka, S. Iijima, Raman scattering study of double-wall carbon nanotubes derived from the chains of fullerenes in single-wall carbon nanotubes. *Chem. Phys. Lett.*, **337** (2001) 48.

57 Ch. Kramberger, R. Pfeiffer, H. Kuzmany, V. Zólyomi, J. Kürti, Assignment of chiral vectors in carbon nanotubes. *Phys. Rev. B*, **68** (2003) 235404.

58 E. Dobardžić, J. Maultzsch, I. Milošević, C. Thomsen, M. Damnjanović, The radial breathing mode frequency in double-walled carbon nanotubes: an analytical approximation. *Phys. Status Solidi B*, **237** (2003) R7.

59 S. M. Bachilo, M. S. Strano, C. Kittrell, R. H. Hauge, R. E. Smalley, R. B. Weisman, Structure-assigned optical spectra of single-walled carbon nanotubes. *Science*, **298** (2002) 2361.

60 J. Kürti, V. Zólyomi, M. Kertesz, G. Sun, The geometry and the radial breathing mode of carbon nanotubes: beyond the ideal behaviour. *New J. Phys.*, **5** (2003) 125.1.

61 V. N. Popov, Curvature effects on the structural, electronic and optical properties of isolated single-walled carbon nanotubes within a symmetry-adapted non-orthogonal tight-binding model. *New J. Phys.*, **6** (2004) 17.

62 J. Maultzsch, H. Telg, S. Reich, C. Thomsen, Radial breathing mode of single-walled carbon nanotubes: optical transition energies and chiral-index assignment. *Phys. Rev. B*, **72** (2005a) 205438.

63 H. Kataura, Y. Kumazawa, Y. Maniwa, I. Umezu, S. Suzuki, Y. Ohtsuka, Y. Achiba, Optical properties of single-wall carbon nanotubes. *Synth. Met.*, **103** (1999) 2555.

64 S. Reich, J. Maultzsch, C. Thomsen, P. Ordejón, Tight-binding description of graphene. *Phys. Rev. B*, **66** (2002a) 035412.

65 A. Jorio, C. Fantini, R. B. Capaz, G. G. Samsonidze, G. Dresselhaus, M. S. Dresselhaus, J. Jiang, N. Kobayashi, A. Grüneis, R. Saito, Resonance Raman spectroscopy (n,m)-dependent effects in small-diameter single-wall carbon nanotubes. *Phys. Rev. B*, **71** (2005) 075401.

66 Y. Ohno, S. Iwasaki, Y. Murakami, S. Kishimoto, S. Maruyama, T. Mizutani, Chirality-dependent environmental effects in photoluminescence of single-walled carbon nanotubes. *Phys. Rev. B*, **73** (2006) 235427.

67 S. Reich, C. Thomsen, Chirality dependence of the density-of-states singularities in carbon nanotubes. *Phys. Rev. B*, **62** (2000) 4273.

68 C. L. Kane, E. J. Mele, Ratio problem in single carbon nanotube fluorescence spectroscopy. *Phys. Rev. Lett.*, **90** (2003) 207401.

69 C. L. Kane, E. J. Mele, Electron interactions and scaling relations for optical excitations in carbon nanotubes. *Phys. Rev. Lett.*, **93** (2004) 197402.

70 E. Chang, G. Bussi, A. Ruini, E. Molinari, Excitons in carbon nanotubes: an *ab-initio* symmetry-based approach. *Phys. Rev. Lett.*, **92** (2004) 196401.

71 V. Perebeinos, J. Tersoff, P. Avouris, Scaling of excitons in carbon nanotubes. *Phys. Rev. Lett.*, **92** (2004) 257402.

72 C. D. Spataru, S. Ismail-Beigi, L. X. Benedict, S. G. Louie, Excitonic effects and optical spectra of single-walled carbon nanotubes. *Phys. Rev. Lett.*, **92** (2004) 077402.

73 F. Wang, G. Dukovic, L. E. Brus, T. Heinz, The optical resonances in carbon nanotubes arise from excitons. *Science*, **308** (2005b) 838.

74 J. Maultzsch, R. Pomraenke, S. Reich, E. Chang, D. Prezzi, A. Ruini, E. Molinari, M. S. Strano, C. Thomsen, C. Lienau, Exciton binding energies in carbon nanotubes from two-photon photoluminescence. *Phys. Rev. B*, **72** (2005) 241402(R).

75 R. Saito, M. Fujita, G. Dresselhaus, M. S. Dresselhaus, Electronic structure of chiral graphene tubules. *Appl. Phys. Lett.*, **60** (1992) 2204.

76 H. Zhao, S. Mazumdar, Electron–electron Interaction effects on the optical

excitations of semiconducting single-walled carbon nanotubes. *Phys. Rev. Lett.*, **93** (2004) 157402.

77 V. N. Popov, L. Henrard, Comparative study of the optical properties of single-walled carbon nanotubes within orthogonal and nonorthogonal tight-binding models. *Phys. Rev. B*, **70** (2004) 115407.

78 P. T. Araujo, S. K Doorn, S. Kilina, S. Tretiak, E. Einarsson, S. Maruyama, H. Chacham, M. A. Pimenta, A. Jorio, Third and fourth optical transitions in semiconducting carbon nanotubes. *Phys. Rev. Lett.*, **98** (2007) 067401.

79 V. N. Popov, L. Henrard, P. Lambin, Electron–phonon and Electron–photon interactions and resonant Raman scattering from the radial-breathing mode of single-walled carbon nanotubes. *Phys. Rev. B*, **72** (2005) 035436.

80 X. Blase, L. X. Benedict, E. L. Shirley, S. G. Louie, Hybridization effects and metallicity in small radius carbon nanotubes. *Phys. Rev. Lett.*, **72** (1994) 1878.

81 S. Reich, C. Thomsen, P. Ordejón, Electronic band structure of isolated and bundled carbon nanotubes. *Phys. Rev. B*, **65** (2002) 155411.

82 M. Machón, S. Reich, C. Thomsen, D. Sánchez-Portal, P. Ordejón, *Ab initio* calculations of the optical properties of 4-Å-diameter single-walled nanotubes. *Phys. Rev. B*, **66** (2002) 155410.

83 H. J. Liu, C. T. Chan, Properties of 4 Å carbon nanotubes from first-principles calculations. *Phys. Rev. B*, **66** (2002) 115416.

84 R. B. Weisman, S. M. Bachilo, Dependence of optical transition energies on structure for single-walled carbon nanotubes in aqueous suspension: an empirical Kataura plot. *Nano Lett.*, **3** (2003) 1235.

85 S. Lebedkin, F. Hennrich, T. Skipa, M. M. Kappes, Near-infrared photoluminescence of single-walled carbon nanotubes prepared by the laser vaporization method. *J. Phys. Chem. B*, **107** (2003) 1949.

86 M. Y. Sfeir, T. Beetz, F. Wang, L. Huang, X. M. H. Huang, M. Huang, J. Hone, S. O'Brien, J. A. Misewich, T. F. Heinz, L. Wu, Y. Zhu, L. E. Brus, Optical spectroscopy of individual single-walled carbon nanotubes of defined chiral structure. *Science*, **312** (2006) 554.

87 P. Nikolaev, M. J. Bronikowski, R. K. Bradley, F. Rohmund, D. T. Colbert, K. A. Smith, R. E. Smalley, Gas-phase catalytic growth of single-walled carbon nanotubes from carbon monoxide. *Chem. Phys. Lett.*, **313** (1999) 91.

88 M. J. O'Connell, S. Sivaram, S. K. Doorn, Near-infrared resonance Raman excitation profile studies of single-walled carbon nanotubes intertube interactions: a direct comparison of bundled and individually dispersed HiPco nanotubes. *Phys. Rev. B*, **69** (2004) 235415.

89 J. Lefebvre, J. M. Fraser, Y. Homma, P. Finnie, Photoluminescence from single-walled carbon nanotubes: a comparison between suspended and micelle-encapsulated nanotubes. *Appl. Phys. A*, **78** (2004) 1107.

90 H. Telg, J. Maultzsch, S. Reich, C. Thomsen, Resonant-Raman intensities and transition energies of the E_{11} transition in carbon nanotubes. *Phys. Rev. B*, **74** (2006) 115415.

91 M. Machón, S. Reich, H. Telg, J. Maultzsch, P. Ordejón, C. Thomsen, Strength of radial breathing mode in single-walled carbon nanotubes. *Phys. Rev. B*, **71** (2005) 035416.

92 S. V. Goupalov, Chirality dependence of the Raman cross section of carbon nanotubes. *Phys. Rev. B*, **71** (2005) 153404.

93 A. Jungen, V. N. Popov, C. Stampfer, L. Durrer, S. Stoll, C. Hierold, Raman intensity mapping of single-walled carbon nanotubes. *Phys. Rev. B*, **75** (2007) 041405(R).

94 B. C. Satishkumar, S. V. Goupalov, E. H. Haroz, S. K. Doorn, Transition level dependence of Raman intensities in carbon nanotubes: role of exciton decay. *Phys. Rev. B*, **74** (2006) 155409.

95 S. V. Goupalov, B. C. Satishkumar, S. K. Doorn, Excitation and chirality dependence of the exciton–phonon

coupling in carbon nanotubes. *Phys. Rev. B*, **73** (2006) 115401.

96 A. P. Shreve, E. H. Haroz, S. M. Bachilo, R. B. Weisman, S. Tretiak, S. Kilina, S. K. Doorn, Determination of exciton–phonon coupling elements in single-walled carbon nanotubes by Raman overtone analysis. *Phys. Rev. Lett.*, **98** (2007) 037405.

97 J. Jiang, R. Saito, K. Sato, J. S. Park, G. G. Samsonidze, A. Jorio, G. Dresselhaus, M. S. Dresselhaus, Exciton–photon, Exciton–phonon matrix elements, and resonant Raman intensity of single-wall carbon nanotubes. *Phys. Rev. B*, **75** (2007) 035405.

98 M. S. Strano, C. A. Dyke, M. L. Usrey, P. W. Barone, M. J. Allen, H. Shan, C. Kittrell, R. H. Hauge, J. M. Tour, R. E. Smalley, Electronic structure control of single-walled carbon nanotube functionalization. *Science*, **301** (2003) 1519.

99 Z. Yu, L. E. Brus, (*n*,*m*) structural assignments and chirality dependence in single-wall carbon nanotube Raman scattering. *J. Phys. Chem. B*, **105** (2001a) 6831.

100 C. Jiang, K. Kempa, J. Zhao, U. Schlecht, U. Kolb, T. Basché, M. Burghard, A. Mews, Strong enhancement of the Breit–Wigner–Fano Raman line in carbon nanotube bundles caused by plasmon band formation. *Phys. Rev. B*, **66** (2002) 161404(R).

101 R. Krupke, F. Hennrich, H. v. Löhneysen, M. M. Kappes, Separation of metallic from semiconducting single-walled carbon nanotubes. *Science*, **301** (2003) 344.

102 M. Paillet, Ph. Poncharal, A. Zahab, J.-L. Sauvajol, Vanishing of the Breit–Wigner–Fano component in individual single-wall carbon nanotubes. *Phys. Rev. Lett.*, **94** (2005) 237401.

103 M. Oron-Carl, F. Hennrich, M. M. Kappes, H. v. Löhneisen, R. Krupke, On the electron–phonon coupling of individual single-walled carbon nanotubes. *Nano Lett.*, **5** (2005) 1761.

104 Y. Wu, J. Maultzsch, E. Knoesel, B. Chandra, M. Huang, M. Sfeir, L. Brus, J. Hone, T. F. Heinz, Variable electron–phonon coupling in isolated metallic carbon nanotubes observed by Raman scattering. *Phys. Rev. Lett.*, **99** (2007) 027402.

105 C. Mapelli, C. Castiglioni, G. Zerbi, K. Müllen, Common force field for graphite and polycyclic aromatic hydrocarbons. *Phys. Rev. B*, **60** (1999) 12710.

106 S. Piscanec, M. Lazzeri, F. Mauri, A. C. Ferrari, J. Robertson, Kohn anomalies and electron–phonon interactions in graphite. *Phys. Rev. Lett.*, **93** (2004) 185503.

107 M. Hulman, V. Skákalová, S. Roth, H. Kuzmany, Raman spectroscopy of single-wall carbon nanotubes and graphite irradiated by γ rays. *J. Appl. Phys.*, **98** (2005) 024311.

108 J. Maultzsch, S. Reich, C. Thomsen, S. Webster, R. Czerw, D. L. Carroll, S. M. C. Vieira, P. R. Birkett, C. A. Rego, Raman characterization of boron doped multiwalled carbon nanotubes. *Appl. Phys. Lett.*, **81** (2002) 2647.

109 T. Sugai, H. Yoshida, T. Shimada, T. Okazaki, H. Shinohara, S. Bandow, New synthesis of high-quality double-walled carbon nanotubes by high-temperature pulsed arc discharge. *Nano Lett.*, **3** (2003) 769.

110 R. P. Vidano, D. B. Fischbach, L. J. Willis, T. M. Loehr, Observation of Raman band shifting with excitation wavelength for carbons and graphites. *Solid State Commun.*, **39** (1981) 341.

111 J. Kastner, T. Pichler, H. Kuzmany, S. Curran, W. Blaus, D. N. Weldon, M. Delamesiere, S. Draper, H. Zanderbergen, Resonance Raman and infrared spectroscopy of carbon nanotubes. *Chem. Phys. Lett.*, **221** (1994) 53.

112 R. Saito, A. Jorio, A. G. Souza-Filho, G. Dresselhaus, M. S. Dresselhaus, M. A. Pimenta, Probing phonon dispersion relations of graphite by double resonance Raman scattering. *Phys. Rev. Lett.*, **88** (2002) 027401.

113 S. Reich, C. Thomsen, Raman spectroscopy of graphite. *Philos. Trans. R. Soc. London, Ser. A*, **362** (2004) 2271.

114 A. Hartschuh, E. J. Sánchez, X. S. Xie, L. Novotny, High-resolution near-field

Raman microscopy of single-walled carbon nanotubes. *Phys. Rev. Lett.*, **90** (2003) 095503.

115 S. K. Doorn, M. J. O'Connell, L. Zheng, Y. T. Zhu, S. Huang, J. Liu, Raman spectral imaging of a carbon nanotube intramolecular junction. *Phys. Rev. Lett.*, **94** (2005) 016802.

116 K. Kaminska, J. Lefebvre, D. G. Austing, P. Finnie, Real-time global Raman imaging and optical manipulation of suspended carbon nanotubes. *Phys. Rev. B*, **73** (2006) 235410.

117 N. Anderson, A. Hartschuh, S. Cronin, L. Novotny, Nanoscale vibrational analysis of single-walled carbon nanotubes. *J. Am. Chem. Soc.*, **127** (2005) 2533.

118 A. Hartschuh, M. R. Beversluis, A. Bouhelier, L. Novotny, Tip-enhanced optical spectroscopy. *Philos. Trans. R. Soc. London Ser. A*, **362** (2004) 807.

119 A. Hartschuh, H. Qian, A. J. Meixner, N. Anderson, L. Novotny, Tip-enhanced optical spectroscopy of single-walled carbon nanotubes. In S. Kawata, V. Shalaev, editors, *Tip Enhancement*, Advances in Nano-optics and Nano-photonics. Elsevier, Amsterdam, 2006.

120 M. J. O'Connell, S. M. Bachilo, C. B. Huffman, V. C. Moore, M. S. Strano, E. H. Haroz, K. L. Rialon, P. J. Boul, W. H. Noon, C. Kittrell, J. Ma, R. H. Hauge, R. B. Weisman, R. E. Smalley, Band gap fluorescence from individual single-walled carbon nanotubes. *Science*, **297** (2002) 593.

121 A. Hagen, M. Steiner, M. B. Raschke, C. Lienau, T. Hertel, H. Qian, A. J. Meixner, A. Hartschuh, Exponential decay lifetimes of excitons in individual single-walled carbon nanotubes. *Phys. Rev. Lett.*, **95** (2005) 197401.

122 J. Lefebvre, D. G. Austing, J. Bond, P. Finnie, Photoluminescence imaging of suspended single-walled carbon nanotubes. *Nano Lett.*, **6** (2006) 1603.

123 J. Guo, C. Yang, Z. M. Li, M. Bai, H. J. Liu, G. D. Li, E. G. Wang, C. T. Chan, Z. K. Tang, W. K. Ge, X. Xiao, Efficient visible photoluminescence from carbon nanotubes in zeolite templates. *Phys. Rev. Lett.*, **93** (2004) 017402.

124 M. Freitag, J. Chen, J. Tersoff, J. C. Tsang, Q. Fu, J. Lie, Ph. Avouris, Mobile ambipolar domain in carbon-nanotube infrared emitters. *Phys. Rev. Lett.*, **93** (2004) 076803.

125 T. Hertel, A. Hagen, V. Talalaev, K. Arnold, F. Hennrich, M. Kappes, S. Rosenthal, J. McBride, H. Ulbricht, E. Flahaut, Spectroscopy of single- and double-wall carbon nanotubes in different environments. *Nano Lett.*, **5** (2005) 511.

126 N. Kishi, S. Kikuchi, P. Ramesh, T. Sugai, Y. Watanabe, H. Shinohara, Enhanced photoluminescence from very thin double-wall carbon nanotubes synthesized by the zeolite-CCVD method. *J. Phys. Chem. B*, **110** (2006) 24816.

127 Z. M. Li, Z. K. Tang, H. J. Liu, N. Wang, C. T. Chan, R. Saito, S. Okada, G. D. Li, J. S. Chen, N. Nagasawa, S. Tsuda, Polarized absorption spectra of single-walled 4Å carbon nanotubes aligned in channels of an $AlPO_4$-5 single crystal. *Phys. Rev. Lett.*, **87** (2001) 127401.

128 S. Kazaoui, N. Minami, H. Yamawaki, K. Aoki, H. Kataura, Y. Achiba, Pressure dependence of the optical absorption spectra of single-walled carbon nanotube films. *Phys. Rev. B*, **62** (2000) 1643.

129 A. B. Dalton, C. Stephan, J. N. Coleman, B. McCarthy, P. M. Ajayan, S. Lefrant, P. Bernier, W. J. Blau, H. J. Byrne, Selective interaction of a semiconjugated organic polymer with single-wall nanotubes. *J. Phys. Chem. B*, **104** (2000) 10012.

130 I. W. Chiang, B. E. Brinson, A. Y. Huang, P. A. Willis, M. J. Bronikowski, J. L. Margrave, R. E. Smalley, R. H. Hauge, Purification and characterization of single-wall carbon nanotubes (SWNTs) obtained from the gas-phase decomposition of CO (HiPco process). *J. Phys. Chem. B*, **105** (2001) 8297.

131 B. J. Landi, H. J. Ruf, C. M. Evans, C. D. Cress, R. P. Raffaelle, Purity assessment of single-wall carbon nanotubes, using optical absorption spectroscopy. *J. Phys. Chem. B*, **109** (2005) 9952.

132 J. N. Coleman, A. Fleming, S. Maier, S. O'Flaherty, A. I. Minett, M. S. Ferreira, S. Hutzler, W. J. Blau, Binding kinetics

and SWNT bundle dissociation in low concentration polymer-nanotube dispersions. *J. Phys. Chem. B*, **108** (2004) 3446.

133 S. Giordani, S. D. Bergin, V. Nicolosi, S. Lebedkin, M. M. Kappes, W. J. Blau, J. N. Coleman, Debundling of single-walled nanotubes by dilution: observation of large populations of individual nanotubes in amide solvent dispersions. *J. Phys. Chem. B*, **110** (2006) 15708.

134 Y.-Q. Xu, H. Peng, R. H. Hauge, R. E. Smalley, Controlled multistep purification of single-walled carbon nanotubes. *Nano Lett.*, **5** (2005) 163.

135 S. Maruyama, E. Einarsson, Y. Murakami, T. Edamura, Growth process of vertically aligned single-walled carbon nanotubes. *Chem. Phys. Lett.*, **403** (2005) 320.

136 G. Dukovic, F. Wang, D. Song, M. Y. Sfeir, T. F. Heinz, L. E. Brus, Structural dependence of excitonic optical transitions and band-gap energies in carbon nanotubes. *Nano Lett.*, **5** (2005) 2314.

137 J. Maultzsch, R. Pomraenke, S. Reich, E. Chang, D. Prezzi, A. Ruini, E. Molinari, M. S. Strano, C. Thomsen, C. Lienau, Excitons in carbon nanotubes. *Phys. Status Solidi. B*, **243** (2006) 3204.

138 V. Perebeinos, J. Tersoff, P. Avouris, Effect of exciton–phonon coupling in the calculated optical absorption of carbon nanotubes. *Phys. Rev. Lett.*, **94** (2005) 027402.

139 G. D. Scholes, G. Rumbles, Excitons in nanoscale systems. *Nat. Mater.* **5** (2006) 683.

140 S. Reich, C. Thomsen, J. Robertson, Exciton resonances quench the photoluminescence of zigzag carbon nanotubes. *Phys. Rev. Lett.*, **95** (2005) 077402.

141 Y. Miyauchi, M. Oba, S. Maruyama, Cross-polarized absorption of single-walled nanotubes by polarized photoluminescence excitation spectroscopy. *Phys. Rev. B*, **74** (2006) 205440.

142 F. Plentz, H. B. Ribeiro, A. Jorio, M. S. Strano, M. A. Pimenta, Direct experimental evidence of exciton–phonon bound states in carbon nanotubes. *Phys. Rev. Lett.*, **95** (2005) 247401.

143 X. Qiu, M. Freitag, V. Perebeinos, P. Avouris, Photoconductivity spectra of single-carbon nanotubes: implications on the nature of their excited states. *Nano Lett.*, **5** (2005) 749.

144 Y. Miyauchi, S. Maruyama, Identification of an excitonic phonon sideband by photoluminescence spectroscopy of single-walled carbon-13 nanotubes. *Phys. Rev. B*, **74** (2006) 035415.

145 B. Kitiyanan, W. E. Alvarez, J. H. Harwell, D. E. Resasco, Controlled production of single-wall carbon nanotubes by catalytic decomposition of CO on bimetallic Co–Mo catalysts. *Chem. Phys. Lett.*, **317** (2000) 497.

146 Y. Miyauchi, S. Chiashi, Y. Murakami, Y. Hayashida, S. Maruyama, Fluorescence spectroscopy of single-walled carbon nanotubes synthesized from alcohol. *Chem. Phys. Lett.*, **387** (2004) 198.

147 E. Malić, M. Hirtschulz, F. Milde, A. Knorr, S. Reich, Analytical approach to optical absorption in carbon nanotubes. *Phys. Rev. B*, **74** (2006) 195431.

148 S. M. Bachilo, L. Balzano, J. E. Herrera, F. Pompeo, D. E. Resasco, R. B. Weisman, Narrow (*n*,*m*) distribution of single-walled carbon nanotubes grown using a solid supported catalyst. *J. Am. Chem. Soc.*, **125** (2003) 11186.

149 F. Hennrich, R. Krupke, K. Arnold, J. A. Rojas Stütz, S. Lebedkin, T. Koch, T. Schimmel, M. M. Kappes, The mechanism of cavitation-induced scission of single-walled carbon nanotubes. *J. Phys. Chem. B*, **111** (2007) 1932.

150 J. Lefebvre, Y. Homma, P. Finnie, Bright band gap photoluminescence from unprocessed single-walled carbon nanotubes. *Phys. Rev. Lett.*, **90** (2003) 217401.

151 J. Lefebvre, P. Finnie, Y. Homma, Temperature-dependent photoluminescence from single-walled carbon nanotubes. *Phys. Rev. B*, **70** (2004) 045419.

152 H. Htoon, M. J. O'Connell, P. J. Cox, S. K. Doorn, V. I. Klimov, Low temperature emission spectra of individual single-

walled carbon nanotubes: multiplicity of subspecies within single-species nanotube ensembles. *Phys. Rev. Lett.*, **93** (2004) 027401.

153 Y. Ohno, S. Kishimoto, T. Mizutani, Photoluminescence of single-walled carbon nanotubes in field-effect transistors. *Nanotechnology*, **17** (2006) 549.

154 T. Inoue, K. Matsuda, Y. Murakami, S. Maruyama, Y. Kanemitsu, Diameter dependence of exciton–phonon interaction in individual single-walled carbon nanotubes studied by microphotoluminescence spectroscopy. *Phys. Rev. B*, **73** (2006) 233401.

155 D. E. Milkie, C. Staii, S. Paulson, E. Hindman, A. T. Johnson, J. M. Kikkawa, Controlled switching of optical emission energies in semiconducting single-walled carbon nanotubes. *Nano Lett.*, **5** (2005) 1135.

156 A. Hartschuh, H. Qian, A. J. Meixner, N. Anderson, L. Novotny, Nanoscale optical imaging of excitons in single-walled carbon nanotubes. *Nano Lett.*, **5** (2005) 2310.

157 K. Arnold, S. Lebedkin, O. Kiowski, F. Hennrich, M. M. Kappes, Matrix-imposed stress-induced shifts in the photoluminescence of single-walled carbon nanotubes at low temperatures. *Nano Lett.*, **4** (2004) 2349.

158 D. Karaiskaj, C. Engtrakul, T. McDonald, M. J. Heben, A. Mascarenhas, Intrinsic and extrinsic effects in the temperature-dependent photoluminescence of semiconducting carbon nanotubes. *Phys. Rev. Lett.*, **96** (2006) 106805.

159 L. Yang, M. P. Anantram, J. Han, J. P. Lu, Band-gap change of carbon nanotubes: effect of small uniaxial and torsional strain. *Phys. Rev. B*, **60** (1999) 13874.

160 Z. Yu, L. E. Brus, Rayleigh and Raman scattering from individual carbon nanotube bundles. *J. Phys. Chem. B*, **105** (2001) 1123.

161 J. C. Knight, T. A. Birks, P. St. J. Russell, D. M. Atkin, All-silica single-mode optical fiber with photonic crystal cladding. *Opt. Lett.*, **21** (1996) 1547.

162 L. Huang, X. Cui, B. White, S. P. O'Brien, Long and oriented single-walled carbon nanotubes grown by ethanol chemical vapor deposition. *J. Phys. Chem. B*, **108** (2004) 16451.

163 F. Wang, M. Y. Sfeir, L. Huang, X. M. Henry Huang, Y. Wu, J. Kim, J. Hone, S. O'Brien, L. E. Brus, T. Heinz, Interactions between individual carbon nanotubes studied by Rayleigh scattering spectroscopy. *Phys. Rev. Lett.*, **96** (2006) 167401.

164 J. C. Meyer, M. Paillet, G. S. Duesberg, S. Roth, Electron diffraction analysis of individual single-walled carbon nanotubes. *Ultramicroscopy*, **106** (2006) 176.

165 Ph. Lambin, A. A. Lucas, Quantitative theory of diffraction by carbon nanotubes. *Phys. Rev. B*, **56** (1997) 3571.

166 A. A. Lucas, F. Moreau, Ph. Lambin. Optical simulations of electron diffraction by carbon nanotubes. *Rev. Mod. Phys.*, **74** (2002) 1.

167 M. Gao, J. M. Zuo, R. D. Twesten, I. Petrov, L. A. Nagahara, R. Zhang, Structure determination of individual single-wall carbon nanotubes by nanoarea electron diffraction. *Appl. Phys. Lett.*, **82** (2003) 2703.

168 K. Hirahara, M. Kociak, S. Bandow, T. Nakahira, K. Itoh, Y. Saito, S. Iijima, Chirality correlation in double-wall carbon nanotubes as studied by electron diffraction. *Phys. Rev. B*, **73** (2006) 195420.

169 S. Chakrabarti, H. Kume, L. Pan, T. Nagasaka, Y. Nakayama, Number of walls controlled synthesis of millimeter long vertically aligned brushlike carbon nanotubes. *J. Phys. Chem.*, **111** (2007) 1929.

170 C. Qin, L.-M. Peng, Measurement accuracy of the diameter of a carbon nanotube from TEM images. *Phys. Rev. B*, **65** (2002) 155431.

171 K. Hirahara, K. Saitoh, J. Yamasaki, N. Tanaka, Direct observation of sixmembered rings in the upper and lower walls of a single-wall carbon nanotube by spherical aberration-corrected HRTEM. *Nano Lett.*, **6** (2006) 1778.

172 B.-Y. Sun, Y. Sato, K. Suenaga, T. Okazaki, N. Kishi, T. Sugai, S. Bandow, S. Iijima, H. Shinohara, Entrapping of exohedral metallofullerenes in carbon nanotubes: $(CsC_{60})n$@SWNT nanopeapods. *J. Am. Chem. Soc.*, **127** (2005) 17972.

173 L. C. Venema, V. Meunier, Ph. Lambin, C. Dekker, Atomic structure of carbon nanotubes from scanning tunneling microscopy. *Phys. Rev. B*, **61** (2000) 2991.

174 Z. Osváth, G. Vértesy, L. Tapasztó, F. Wéber, Z. E. Horváth, J. Gyulai, L. P. Biró, Atomically resolved STM images of carbon nanotube defects produced by Ar^+ irradiation. *Phys. Rev. B*, **72** (2005) 045429.

175 M. Ge, K. Sattler, Vapor-condensation generation and STM analysis of fullerene tubes. *Science*, **260** (1993) 515.

176 T. W. Odom, J. L. Huang, P. Kim, C. M. Lieber, Atomic structure and electronic properties of single-walled carbon nanotubes. *Nature*, **391** (1998) 62.

177 T. W. Odom, J. H. Hafner, C. M. Lieber, Scanning probe microscopy studies of carbon nanotubes. *Top. Appl. Phys.*, **80** (2001) 173.

178 L. P. Biró, P. A. Thiry, Ph. Lambin, C. Journet, P. Bernier, A. A. Lucas, Influence of tunneling voltage on the imaging of carbon nanotube rafts by scanning tunneling microscopy. *Appl. Phys. Lett.*, **73** (1998) 3680.

179 V. Meunier, Ph. Lambin, Tight-binding computation of the STM image of carbon nanotubes. *Phys. Rev. Lett.*, **81** (1998) 5588.

180 Ph. Lambin, V. Meunier, Interpretation of the STM images of carbon nanotubes. In L. P. Biró, C. A. Bernardo, G. G. Tibbetts, and Ph. Lambin (eds.), *Carbon Filaments and Nanotubes: Common Origins, Differing Applications*? Vol. 372 of *NATO Science Series E: Applied Sciences*, Kluwer, Dordrecht, 2001, p. 233.

181 L. C. Venema, J.W. Janssen, M. R. Buitelaar, J. W. G. Wildöer, S. G. Lemay, L. P. Kouwenhoven, C. Dekker, Spatially resolved scanning tunneling spectroscopy on single-walled carbon nanotubes. *Phys. Rev. B*, **62** (2000) 5238.

182 M. Ouyang, J.-L. Huang, C. L. Cheung, C. M. Lieber, Energy gaps in "metallic" single-walled carbon nanotubes. *Science*, **292** (2001) 702.

183 E. D. Minot, Y. Yaish, V. Sazonova, J.-Y. Park, M. Brink, P. L. McEuen, Tuning carbon nanotube band gaps with strain. *Phys. Rev. Lett.*, **90** (2003) 156401.

184 S. Malik, H. Rösner, F. Hennrich, A. Böttcher, M. M. Kappes, T. Beck, M. Auhorn, Failure mechanism of free standing single-walled carbon nanotube thin films under tensile load. *Phys. Chem. Chem. Phys.*, **6** (2004) 3540.

185 K. Hata, D. N. Futaba, K. Mizuno, T. Namai, M. Yumura, S. Iijima, Water-assisted highly efficient synthesis of impurity-free single-walled carbon nanotubes. *Science*, **306** (2004) 1362.

5
Modeling the Properties of Carbon Nanotubes for Sensor-Based Devices

Cosmin Roman, Mikro- und Nanosysteme, ETH Zürich, Switzerland
Stephan Roche, Commissariat à l'Energie Atomique, Grenoble, France
Angel Rubio, Universidad del País Vasco, Centro Mixto, San Sebastián/Donostia, Spain

Advanced Micro & Nanosystems Vol. 8. Carbon Nanotube Devices.
Edited by Christofer Hierold

ISBN: 978-3-527-31720-2

5.1 Introduction

At only 16 years since the discovery of carbon nanotubes (CNTs) by Sumio Iijima [1], we are witnessing an explosive development of nanotube science and technology. Considering the rapid progress made in the fabrication, manipulation, characterization and modeling of nanostructures based on nanotubes, it is reasonable to expect that CNTs will, in the next few years, spread to key application areas such as energy, materials and devices. Several structural varieties of nanotubes have been identified and classified based on criteria such as helicity (also known as chirality), number of walls and inclusion of pentagons–heptagons. The simplest form is the single-walled carbon nanotube (SWNT), which resembles a honeycomb graphite layer rolled into a monoatomic-thick cylinder. Several concentrically embedded SWNTs form a multi-walled carbon nanotube (MWNT). Other nanotube varieties include nanotube bundles or ropes, inter-tube junctions, nanotori and coiled nanotubes [2–5].

A brief analysis of the patent activity on carbon nanotube-based applications reveals that the major slots in the pie chart are occupied (in decreasing percentage order) by field emission, energy storage, composites, nanoelectronics, sensors and actuators. Judging by the exponential increase in the number of journal papers and patent applications per year [6], the technological potential of nanotubes is still far from being fully explored. Moreover, other applications are appended to this list every day. The fifth place of sensors and actuators can be explained by their relative later invention [7, 8]. CNT-based sensors will undoubtedly climb into the top of the applications list.

In this dynamic context, the discovery and subsequent understanding of elementary physical mechanisms, supported by modeling and simulation, will be the key for custom-designed CNT-based devices for the next decade. In order to bridge micro-, meso- and macro-scales, as typically dictated by nanotube physics, it is desirable to find a hierarchy of models, for both ease of computation and conceptual understanding. Once models bridging different scales have been worked out, it will become possible to analyze and optimize materials properties at different levels of approximation, eventually leading to the theoretical understanding of materials or even design of novel forms. A further step will consist in constructing predictive models, going beyond the simulation of fundamental properties, that will assist the innovation and design of CNT-based devices.

Investigating nanotube properties through modeling and simulation is preferable in a context in which nanotube manipulation and characterization are still limited, time consuming and expensive. This does not automatically mean that one has to accept blindly the validity of any calculations, at least within the gross approximations sometimes employed. It is precisely at this point that theoretical models and measurements have to be brought together and re-aligned. Higher order corrections, validity ranges and hints for model improvements are obtained in this way.

Due to their relative simplicity and atomically precise morphology, SWNTs offer the opportunity of assessing the validity of different macro- and microscopic

models. For this reason, SWNTs will receive special attention in this chapter. Encouragingly, for SWNTs, the agreement between theoretical predictions and experimental data is constantly improving. As a side note, it is actually via simple theoretical calculations that the metallic/semiconducting nature of nanotubes, their Young's moduli and optical transitions were predicted in the first place.

The aim of this chapter is to give a brief introduction to CNT-based sensing from a modeling and simulation perspective. The remainder of this chapter is split into four main sections. Section 5.2 gives a quick overview of the basic properties of CNTs, with emphasis on the tight-binding band structure and density of states. A condensed state-of-the-art of experimental measurements on CNT sensor demonstrators is given in Section 5.3. In Section 5.4, we list the common modeling methods for calculations of the electronic structure, transport and mechanical properties calculations of the CNT-based devices. A number of illustrative modeling case studies are presented in Section 5.5, with the goal of showing how the often difficult task of modeling CNT systems should be tackled.

5.2
Properties of Carbon Nanotubes: Reminder

The purpose of this section is to provide a brief survey of the properties of carbon nanotubes necessary to understand the different sensing mechanisms analyzed in the next section. A review of the tools available for modeling the properties of CNTs will be developed later in Section 5.4. For a thorough analysis of the properties of nanotubes we refer the reader to any of the many excellent books and review articles available on this subject [2, 3, 9].

Broadly speaking, the properties of carbon nanotubes ca be grouped in three categories: structural, mechanical and electronic. From the structural point of view, in most situations CNTs can be considered one-dimensional (1D) objects, with typical diameters (d_t) in the nanometer range and lengths (L) reaching several micrometers. This one-dimensionality of tubes impacts on and is visible mostly through the mechanical and electronic properties. However, the structure of nanotubes can be exploited in itself such as for instance by field emitters or gas breakdown sensors, which are based on the "sharpness" of CNTs giving rise to huge local electric fields.

The mechanical properties class encompasses the elastic, thermal, vibrational or any other properties related to the motion of the tube's atoms. In nanotubes, carbon is sp^2-hybridized, resulting in strong σ-bonds weakly reinforced by π-bonds. Considering the hybridization, it is natural to assume a certain overlap between nanotube and graphite (graphene) elastic properties, such as Young's modulus, bending, tensile and torsional stiffness and yield strength. SWNTs have tensile moduli close to 1 TPa (stiff as diamond) and strengths of ~50 GPa (corresponding to 5–10% maximal strain), which earned them the title of ultimate fibers. Despite their stiffness, CNTs retain a high bending flexibility due to their high aspect ratios (L/d_t). With some exceptions, the thermal and vibrational properties

of nanotubes also show similarities with graphite. Since the in-plane thermal conductivity of pyrolytic graphite is very high, it is expected that the on-axis thermal conductivity of defect-free tubes would be even higher. At low temperatures the phonon mean free path is controlled mainly by boundary scattering and the coherence length (micrometer scale) is larger in tubules than in high oriented pyrolytic graphite (<0.1 μm). Another difference between CNTs and graphite is the Raman spectra, exhibiting new signal features in tubes, particularly the radial breathing mode (RBM), specific to a cylindrical geometry (see Chapter 4).

Since it refers to the response of the fermion system to different excitations, the class of electronic properties practically encompasses all remaining properties. Therefore, it contains transport and electric properties (classical, spin-dependent and superconductivity, dielectric permittivity), optical properties (absorption, scattering, luminescence), magnetic properties (susceptibility, Zeeman splitting, Aharonov–Bohm effect), chemical properties (covalent and noncovalent binding), in addition to hybrid properties and correlated many-body effects (thermopower, piezoresistivity, piezoelectricity, Coulomb blockade, Kondo effect, Tomonaga–Luttinger liquid behavior).

In this chapter, we touch on only basic properties and include, whenever possible, references to texts treating more advanced topics. We indicate that a simple zone folding of the graphitic tight-binding (TB) band structure is able to explain most of these basic electronic properties, provided that the diameter of the tube d_t is large enough. For small nanotubes ($d_t < 12$ Å) curvature induces hybridization between the π and σ bands of graphite changing the electronic band structure. Henceforth, we exploit the TB description, and return later to more refined models such as *ab initio* density functional theory (see Section 5.4).

The electronic properties of nanotubes are strongly modulated by small structural variations; in particular, their metallic or semiconducting character is determined by the diameter and helicity (chirality) of the carbon atoms in the tube. To understand this dependence, one has to start from the energy dispersion relations of graphene in the vicinity of the Fermi level. A major simplification is achieved by noting that only π–π^* bands populate this spectral region, and σ-bands can therefore be removed with almost no influence. Subsequently, in going from the graphene to a nanotube, periodic boundary conditions for the wavefunctions along the circumference are imposed (zone folding), resulting in the quantization of the wavevector component along this direction. The derivation details of the tight-binding graphene dispersion relations and the subsequent zone folding procedure can be found in Reference [2]. As an example, for armchair metallic tubes of chirality (n, n), the analytically derived bands are given by

$$E_q^{\pm}(k) = \pm\gamma_0\sqrt{1 \pm 4\cos\frac{ka}{2}\cos\frac{q\pi}{N} + 4\cos^2\frac{ka}{2}} \tag{1}$$

where $q(\in \overline{1,2N})$ specifies the discrete part of the wavevector perpendicular to the tube axis (i.e. the band index), k is the continuous component that describes eigenstates in a given subband ($-\pi < ka < \pi$), $a = 2.46$ Å is the graphene lattice

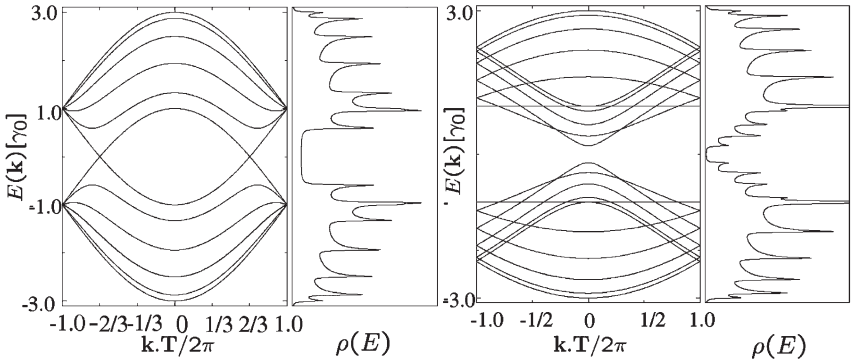

Figure 5.1 Dispersion relations and density of states for the metallic (5,5) and semiconducting (10,0) nanotubes.

constant and $\gamma_0 \approx 2.9\,\mathrm{eV}$[1)] is the hopping integral matrix element between nearest-neighbor atoms.

As a matter of illustration, the band structures and densities of states (DoS) for the metallic (5,5) armchair tube and the semiconducting (10,0) zigzag tube are shown in Figure 5.1. Densities of states are calculated by tracing the spectral measure operator $\delta(E - \hat{\mathrm{H}})$ over the band index and first Brillouin zone, i.e.

$$\rho(E) = \sum_q \int \mathrm{d}k |\partial E_q(k)/\partial k|^{-1} \delta(E - E_q(k)) \tag{2}$$

The intrinsic one-dimensionality of the CNTs gives rise to a number of sharp features ($\rightarrow \infty$) in the DoS (see Figure 5.1) called van Hove singularities (vHS). The vHS positions are derived from the condition $\partial E_q(k)/\partial k = 0$, which yields the solutions $\varepsilon_q = \pm\gamma_0 \sin(q\pi/N)$. Because of these singularities, optical transitions are resonantly enhanced at energies corresponding to $2\gamma_0 \sin(q\pi/N)$.

For metallic SWNTs, the development of the dispersion relations to first order at the Fermi level yields a Fermi velocity $v_F \approx 10^6\,\mathrm{m\,s^{-1}}$, independent of chirality. Thus, in the absence of electron scattering, the intrinsic conductance of a metallic tube should be $2G_0$, where $G_0 = 2e^2/h = (1/12.906)\,\mathrm{k\Omega^{-1}}$ is the conductance quantum, because there are two open channels at the Fermi level, each with a conductance G_0. On the other hand, semiconducting SWNTs have a bandgap $E_g \approx 0.9/d_t[\mathrm{eV}]$[2)], with d_t the nanotube diameter in nanometers. The next section will review how these remarkable properties have resulted in experimental breakthrough sensor demonstrators.

1) The actual value of the γ_0 parameter depends on the property to be analyzed; e.g. the value for STM is ~2.5 eV whereas that used in Raman spectroscopy ∈ 2.9–3.1 eV.

2) Here the gap refers to the quasi-particle gap, which is different from the optical gap relevant for Raman spectroscopy (see Reference [47] and references therein). Also the dispersion becomes nonlinear for large tubes, known as the trigonal wrapping effect. Although important for excitations, these effects do not affect too much the transport properties close to E_F.

5.3 Carbon Nanotube-Based Sensor Demonstrators: State-of-the-Art

Continuously expanding, the field of CNT-based sensors includes an already impressive list of demonstrators, encompassing (bio)chemical, strain, stress, pressure, mass, flow, thermal and optical sensors. The field is too vast to be surveyed exhaustively here and is also not the focus of this chapter dealing with modeling CNT sensing devices[3]. Rather, the goal of this concise state-of-the-art is to present to the reader a survey of possible sensing mechanisms involved so far in CNT sensors. After this section, it should become clear what kind of modeling tools are necessary to investigate nanotube devices. In analogy with the classification made in the previous section, we group sensing mechanisms in three categories, centered around the electronic and the mechanical properties, plus other mechanisms.

5.3.1 Modulation of Electronic Properties

In terms of number of publications, sensors involving the modulation of a CNT's electronic properties lead the competition by far. This can be easily understood by a brief examination of the structure of a nanotube. A CNT is hollow, meaning that only "surface" electronic states are present, making a tube extremely sensitive to any perturbations.

It is precisely this observation that led Kong et al. [7] and Collins et al. [8] to propose CNTs as sensitive materials for **chemical sensors**. Kong et al. [7] found the electrical conductance of a nanotube to increase when the tube was exposed to NO_2, and to decrease when exposed to NH_3. Electron charge transfer (doping) was proposed as the mechanism dictating the change in conductivity (ΔG) by shifting the Fermi level of the channel. Collins et al. showned [8] that exposure to air or oxygen dramatically influences the nanotubes' electrical resistance, thermoelectric power and local density of states, as determined by transport measurements and scanning tunneling spectroscopy. These electronic parameters can be reversibly "tuned" by surprisingly small concentrations of adsorbed gases, and semiconducting nanotubes can apparently be converted into metallic tubes through such exposure. Since these initial two reports, the list of chemFET-like gas and biological sensors has increased considerably[4]. Innovations have also been brought, such as nanotube functionalization, which has yielded highly sensitive and selective sensors [12, 13]. Also, Goldsmith et al. [14] have recently demonstrated that it is possible to control the functionalization density by monitoring in real time the conductance of a nanotube in an electrochemical setup.

Carbon nanotube-based chemFETs deserve special attention. Although they were the first type of sensors proposed, the understanding of their operation is still hindered by the multitude of potential effects stemming from the interaction

3) See References [9–11] and Chapter 8 (anthor John Yeow) of this book for a thorough review.
4) See Table 1 in Reference [10] for a list of detected agents so far.

of chemical molecules with this system. Among these, molecules interacting with chemFETs can: (i) if charged and isolated from nanotube, gate the transistor (field effect), (ii) if polar, modify the gate capacitance, (iii) regardless of charge, dope the nanotube or modify the work function of the contacting metal resulting in a Schottky barrier modulation, or (iv) increase carrier scattering. All these mechanisms overlap, rendering it very difficult experimentally to tell which one is responsible for the I–V characteristic. This motivates the development of modeling tools capable, in principle, of identifying the correct mechanism.

Another emergent sub-family of chemical sensors exploit subtle changes in the polarizability of nanotubes subject to gas exposure, which can result in either capacitance modulation ΔC, as shown by Snow et al. [15], or in a shift of the electrical resonant frequency of a microwave circuit Δf_0, as demonstrated by Chopra et al. [16]. As suggested by Snow et al. [11], future generation chemical SWNT sensors could exploit simultaneously ΔG (charge transfer) and ΔC (dipole moments and polarizability), increasing the information gathered from a single device with potential improvements in resolution, sensitivity and selectivity.

It is also worth mentioning that reading out the modulation of the electronic properties in chemical sensors needs not be confined to electrical measurements. For example, Sumanasekera et al. [17] have utilized thermopower measurements (see also Reference [8]) to evidence the sensitivity of CNTs to C_6H_6. An even more promising approach is using light to probe either the photo-absorption or the fluorescence spectra [18, 19]. Cao et al. [18] have studied band-gap photo-absorption in SWNTs, previously exposed to air, in different organic solvents. The observed bleach and recovery of optical spectra are due to the charge transfer between nanotubes and adsorbates (e.g. H_2O), in their process of (ad)/(de)sorption from the nanotube surface. Heller et al. [19] have shown that DNA-wrapped SWNTs can be placed inside living cells to detect trace amounts of harmful contaminants using near-infrared light. When the ensemble is exposed to certain ions (Hg^{2+}, Co^{2+}, Ca^{2+}, Mg^{2+}) the wrapping DNA changes shape from the B form to Z form, reducing the surface area covered by the DNA, which further perturbs the electronic structure and shifts the nanotube's natural, near-IR fluorescence to a lower energy. These results open the door to new types of optical sensors and biomarkers inside living systems (*in vivo*).

The second best known family of CNT-based sensors is the one exploiting the huge *piezoresistive* gauge factors reported for nanotubes. We do not insist on this family, since Chapter 2 is dedicated entirely to this subject. We only mention that piezoresistive pressure, force (stress) and strain sensors utilize the band-gap modulation of nanotubes subject to torsional or tensile strain. The effect should be visible either via transport or via Raman spectra (see Chapter 4).

5.3.2
Shifting of Mechanical Resonances

There are not many reports of sensors in this category, but we discuss resonant CNT devices, motivated by their potential in sensing applications. Due to the huge

stiffness and extremely low mass density – carbon is one of the lightest atoms, and SWNTs are one atom thick – nanotubes hold the promise of unequaled high resonating frequencies and mass sensitivities.

The first to propose CNT as nanobalances were Poncharal et al. [20], demonstrating femtogram-resolution mass detection with large MWNT cantilevers. A transmission electron microscope (TEM) was utilized in tracking the resonant frequency. Later, by moving the setup inside a scanning electron microscope (SEM), and analyzing secondary electron intensities, Nishio et al. [21] achieved zeptogram sensitivities. The measuring schemes in these references are obviously not suitable for large-scale integration. Nevertheless, recently, tunable CNT resonators have been reported [22–24], opening the way to integrated nanobalances for minute mass detection.

5.3.3
Other Transduction Mechanisms

The list of CNT-based sensors is far from being closed, with exotic, new sensor mechanisms frequently being proposed. Here we provide a brief selection of promising devices that do not necessarily conform to the previous two subsections.

Ghosh et al. reported [25] flow sensors in which the conductance of carbon nanotubes, disposed parallel to the flow lines, is clearly changed at different flow rates. The suggested mechanism for this nonlinear effect is forcing of the electrons in the nanotubes by the fluctuating Coulombic field of the liquid, or, briefly, Coulomb drag. Another CNT flow meter demonstrated recently by Bourlon et al. [26] operates differently from the previous device. A CN-FET is placed within the electrical double layer of an SiO_2 channel (i.e. almost tangentially with one of the internal surface of the channel), being gated by the flow rate-dependent ζ-potential.

An ionization CNT sensor has been demonstrated by Modi et al. [27], based on the ionization fingerprint which is characteristic to each analyte gas. This device simply exploits the geometry of the nanotubes, since their sharp tips generate very high electric fields at relatively low voltages, lowering gas breakdown voltages. Another category of sensor demonstrators that make use of CNTs as electrodes are the amperometric biosensors utilizing nanotubes as electrode material in electrochemical setups. This type of sensor is exhaustively reviewed in Reference [28], and will not be analyzed here.

Still other CNT sensing devices could be mentioned here, such as low-temperature quantum electrometers [29] and superconducting quantum interference device (SQUID) magnetometers [30]. Nevertheless, understanding the physics of these devices is beyond the scope of this chapter. We therefore end this section here, and reassert that CNT sensors are based on a huge variety of sensing mechanisms. Although unifying principles exist, which have allowed us, for instance, to group the sensors in three major classes, the spectrum of phenomena is still too broad to be addressed by a single modeling methodology. The following section

will attempt to display the tool available for the modeling of nanotubes, trying at the same time to identify their context-dependent usefulness and limitations.

5.4
Modeling: Reviewing Methods and Tools

Because of their nanometric diameters, carbon nanotubes are quantum objects, and are therefore governed by the many-body Schrödinger equation. The Schrödinger equation is still unsolved for systems more complex than the hydrogen atom, forcing series of approximations followed by numerical simulation. The most frequent approximations utilized in solid-state physics and quantum chemistry include mean-field (or effective) electronic structure theories (tight binding, Hartree-Fock, density functional theory), within the Born–Oppenheimer approximation that decouples the motion of atoms from the electronic structure problem. This is also the dominant workbench in nanotube science.

Even within the simplest framework, the large number of atoms involved in a typical CNT-based nanodevice is a major bottleneck. The recurrent problem in nanotube modeling is a certain square (Hamiltonian diagonalization or Green's functions calculations) or cubic scaling (inter-atomic force calculation for molecular dynamics) in the number of atoms, which drives simulation into the intractable realm. Sometimes, when translational symmetry is lost, simulations might involve 10^5 atoms or even more, particularly in the modeling of transport within chemically perturbed tubes or vibrational properties of long nanotube cantilevers (see Section 5.5). Storing a matrix with $10^5 \times 10^5 = 10^{10}$ elements is costly but this is nothing compared with the time it would take to invert or diagonalize such a matrix, requiring in the order of $(10^5)^3$ operations.

In the light of computational challenges engendered by modeling CNT-based devices, we start with a brief review of the different approaches and methods available for the task of modeling both properties and devices based on carbon nanotubes.

5.4.1
Electronic Structure Calculations

The strong similarity of the short-range chemical order of carbon nanotubes to that of graphite [31, 32] allows theoretical analyses based on empirical methodologies imported from graphite. The methodology spectrum is wide and ranges from the direct zone folding of the graphite results to the quantum-mechanical tight-binding Hamiltonians fitted to graphite properties. The performance of the different techniques varies, from the qualitative picture offered by zone folding, with intrinsic deficiencies at low frequencies, to the almost quantitative results of tight-binding approaches.

Zone folding and tight binding are at the base of the very first electronic structure predictions for carbon nanotubes, partly discussed in Section 5.2. Electronic

properties in the vicinity of the Fermi level have been successfully captured for single- and multi-walled nanotubes, bundles and even topological defects [3, 33, 34], with the simplest π-band nearest-neighbor tight-binding Hamiltonian[5)]

$$\hat{H} = \sum_{\nu} \varepsilon_0 |\nu\rangle\langle\nu| + \sum_{\nu} \sum_{\mu \in \mathrm{nb}(\nu)} \gamma_0 |\nu\rangle\langle\mu| \tag{3}$$

where ε_0 is the on-site energy (typical value 0, that shifts the Fermi level to E_F = 0), $\gamma 0$ the hopping integral (typical value –2.7 eV[1)], $|\nu\rangle$ and $|\mu\rangle$ are p_z orbitals located at different atomic positions and nb(ν) is a function giving the nearest topological neighbors of $|\nu\rangle$[6)]. The first limitation of this model is revealed by systems involving charge transfer, such as charge redistribution at the interface between a CNT and a metallic contact in a solid-state device, or the interaction of a tube with a molecule. Although attempts in developing charge self-consistency to tight-binding calculations have been made [35], in a situation involving strong transfer (or re-hybridization) one has to be cautious in employing these schemes. The only solution to this is *ab initio* electronic structure methods.

First principles (*ab initio*) total energy calculations are one of the most accurate methods available to the study of nanotubes. These calculations provide the bonding, electronic structure and atomic arrangement, and are nowadays based on density functional theory (DFT) [36]. For a general description of DFT and its applications, see Reference [37]. This allows the calculation of the ground-state and dynamic properties of a many-electron system from a simple one-electron, effective Schrödinger equation (a mean-field approximation). In this theory, the total energy, expressed as a functional of the total electron density $\rho(\mathbf{r})$, is decomposed into three contributions. These are the well-known kinetic energy term of non-interacting particles, the Coulomb energy due to classical electrostatic interactions and a part that takes care of the many-electron interactions, so-called exchange-correlation energy. The effective one-electron eigenfunctions and eigenvalues allow for a formulation of bonding and structure in terms of molecular orbitals and band structure of solids. The fact that the problem has been reformulated in terms of independent electrons does not mean that correlations are ignored. This formulation is based on a self-consistent procedure in which the effective potential depends on the electron density that also depends on the one-electron eigenfunctions. The achievement of self-consistency is one of the main technical problems in first-principles calculations [38], raising the complexity to $\mathcal{O}(N^3)$, with N the number of atoms.

When still more accurate results, or non-ground-state properties (e.g. electronic excitations) are required, many-body electronic correlations are explicitly included. Depending on the origin field, correlations are added as in quantum chemistry via

5) This Hamiltonian can only describe single tube properties. Intertube coupling terms are necessary to model multi-walled or tube bundles. Examples of such Hamiltonians are given in Section 5.5.2.4 and Section 5.5.2.5.

6) Hereafter, the summation limit $\mu \in$ nb(ν) will be replaced by $\mu \neq \nu$.

so-called post-Hartree–Fock methods such as configuration interaction (CI), Møller–Plesset (MP) or coupled-cluster (CC) [39], or as in condensed-matter physics via perturbation theory supported by diagrammatic techniques [40–42]. Regardless of the choice, the numerical complexity is boosted to at least $\mathcal{O}(N^6)$. An example of where these methods are required is the accurate calculation of optical spectra in carbon nanotubes, known to be modified from the simple vHS as obtained via tight binding (see Section 5.2) by excitonic effects. The optics of nanotubes is of outmost importance as it offers one of the few reliable frameworks for CNT characterization (e.g. Raman spectroscopy, Chapter 4). The most widely used methods to include excitonic effects are time-dependent density functional theory (TDDFT) [43] and the GW scheme followed by the Bethe–Salpeter equation (BSE) solution [44]. Also applied to carbon nanotubes [45] (TDDFT [46]; GW+BSE [47]), these many-body corrections have shown a major deviation from the simple tight-binding picture, with optical transitions modified by as much as ~0.5 eV. We do not continue detailing many-body methods hereafter and refer the reader to the previous citations for thorough treatments. We do mention, however, that other electron-correlation effects might be present in CNTs, especially at low temperature, including Tomonaga–Luttinger liquid behavior, Coulomb blockade, the Kondo effect and superconducting contacts [3]. Another important effect not treated in this chapter is the electron–phonon interaction that leads to a mean-free-path reduction, and therefore plays a major role in quantum transport in nanotubes.

5.4.2
Transport Formalisms

The electronic transport properties of nanostructures are governed by the quantum conductance scaling features, that range from ballistic to diffusive or localized regimes, depending on the strength of quantum interference effects and decoherence phenomena. As device geometries are downsized to the ultimate limits of miniaturization, and become comparable to the elastic mean free path for the electrons, the transport enters the ballistic regime, which is characterized by vanishingly low intrinsic dissipation.

In Section 5.3.1 we gave a brief glimpse of a number of ways in which a molecule, for instance, can interact with a chemFET device. This example is very appropriate since it allows us to assess the typical challenges encountered in modeling CNT-based sensors. To determine to what extent the observed current–voltage (I–V) device characteristic can be attributed to the adsorption of analyte molecules, several tasks have to be tackled. First, the interaction between CNT and attached molecules, and resulting chemical binding energies, charge transfer and polarizability need to be precisely described from first principles approaches. The role of topological defects along the SWNT sidewall should be analyzed owing to their particular chemical reactivity level, which might severely affect the sorption properties of other chemical vapors. The consequent impact of this functionaliza-

tion on the resulting intrinsic charge transport properties need then to be assessed initially for quantum coherent regimes, but also for out-of equilibrium situations, in which electrostatics and intrinsic dissipation (e.g. electron–phonon interaction) might play a substantial role. Finally, the changes in the dipole properties at the metal/CNT interfaces must be investigated to explore the potential modulations of charge injection through the resulting modified Schottky barrier.

Anantram and Léonard [48] reviewed the physics and modeling of carbon nanotubebased field-effect transistors (CNFETs), focusing on issues related to electrostatics and Schottky barriers. There is, however, no straightforward prescription on how to extend the presented methods to chemical sensors.

Tools developed for modeling molecular electronics devices can in principle also be applied to nanotubes. The main approach nowadays is a methodology combining non-equilibrium Green's functions (NEGF) with density functional theory (DFT) [49]. Several surveys and books are available for molecular transport [50, 51]. It is also noteworthy that NEGF can be combined with more advanced electronic properties schemes for a more accurate description of correlations, such as the NEGF-GW approach detailed in Reference [52]. However, CNTs are far bigger than common molecular electronics devices. A *self-consistent*, linearly scaling (order-*N*) transport method for nanotube device simulation is still missing[7]. Therefore, both in the past and currently, one has to rely on assumptions about the CNT–metal contacts, electrostatics and charge transfer with chemical species. The utilized model Hamiltonian becomes the central object, crucially influencing the results obtained. Hamiltonian choices and/or parameterizations are a recurrent theme in Section 5.5.2.

Once a Hamiltonian model has been obtained, investigating coherent quantum transport in a nanotube segment of length L with reflectionless contacts to external reservoirs is achieved in practice mainly via two complementary transport formalisms[8]. First, following linear response theory, the Kubo conductance is computed as $\mathcal{G}(E) = (2e^2/L)\lim_{t\to\infty} \mathrm{Tr}\,[\hat{D}(t)\delta(E-\hat{H})]$, where $\delta(E-\hat{H})$ is the spectral measure operator, whose trace gives the total density of states (DoS). $\hat{D}(t)$ is the diffusivity operator defined as $\hat{D}(t) = (\hat{X}(t) - \hat{X}(0)^2)/t$ with the help of $\hat{X}(t)$, the Heisenberg representation of the position operator [53]. Much information about the propagation of electrons can be gained from the energy-dependent diffusion coefficient, the ensemble average of $\hat{D}(t)$:

$$D(E,t) = \frac{\mathrm{Tr}\left[\left(\hat{X}(t)-\hat{X}(0)\right)^2 \delta\left(E-\hat{H}\right)\right]}{t\,\mathrm{Tr}\left[\delta\left(E-\hat{H}\right)\right]} \tag{4}$$

In the presence of static disorder, the time-dependent diffusivity for a given wave packet always reaches a saturation regime, whose value will be related to the

7) Self-consistency is highlighted because this affirmation is valid only for this case. Once the charge transfer problem has been solved, with a self-consistent charge and potential distribution along the device, transmission or diffusion coefficients can be calculated using order-*N* methods (see below).

8) Unless explicitly specified, the temperature is assumed to be 0 K in all transport calculations.

elastic mean free path $\ell_e(E)$ through $D(E) \propto v(E)\ell_e(E)$, with $v(E)$ the velocity of a wave packet of energy E. Such an approach, implemented using order-N [$\mathcal{O}(N)$] computational techniques, has been successfully compared to analytical results derived from the Fermi Golden Rule (FGR), but for uniform disorder [53–55] (see Section 5.5.2.1). It has also been extended to more realistic disorder models such as chemical substitutions (Section 5.5.2.2) and physisorbed molecules (Section 5.5.2.4).

In another approach, the Landauer–Büttiker conductance is evaluated from the transmission coefficient $G(E) = (2e^2/h)T(E)$. In a multi-terminal setup in which the leads are labeled by λ, the transmission coefficients between any two contacts[9)] is given by

$$T_{\lambda\lambda'}(E) = \mathrm{Tr}[\Gamma_\lambda(E)G^{(r)}(E)\Gamma_{\lambda'}(E)G^{(a)}(E)] \tag{5}$$

in terms of the retarded Green's function $\hat{G}^{(r)}(E) = [E\hat{I} - \hat{H} - \Sigma_\lambda\hat{\Sigma}_\lambda(E)]^{-1}$ where $[\hat{G}^{(a)}(E) = \hat{G}^{(r)\dagger}(E)]$ and level broadening functions (escape rates) $\hat{\Gamma}_\lambda(E)$ given by $i\left[\hat{\Sigma}_\lambda(E) - \hat{\Sigma}_\lambda(E)\right]$. $\hat{\Sigma}_\lambda(E)$ stands for the self-energy accounting for the coupling with the lead-λ [50]. In general, order-N methods to evaluate these quantities are facilitated by the 1D character of CNTs. For instance, $\hat{\Sigma}_\lambda(E)$ are typically obtained through the decimation technique [56, 57], while $\hat{G}^{(r)}(E)$ can be obtained either by tube slicing and fast elimination methods [57, 58], or by two-sided Lanczos recursion [59]. At times, it is also useful to calculate the current through lead-λ, which is achieved by integrating in energy and summing over $\lambda' \neq \lambda$:

$$I_\lambda = \sum_{\lambda' \neq \lambda} \frac{2e}{h}\int_{-\infty}^{\infty} T_{\lambda\lambda'}(E)[f(E,\mu_\lambda) - f(E,\mu_{\lambda'})]\mathrm{d}E \tag{6}$$

in which $f(E,\mu_\lambda) = 1/[1 + e^{(E-\mu_\lambda)/k_B T}]$ is simply the Fermi–Dirac distribution of states in lead-λ, considered in thermal equilibrium and having the chemical potential μ_λ.

A connection between the Landauer and Kubo conductances is made possible through the ergodic assumption [60], i.e. $\bar{T} = T = N_\perp(E)\ell_e(E)/L$, where $\bar{T}$ is the averaged transmission coefficient. To ensure convergence of $\bar{T}$, averaging over a few hundred configurations of disorder is performed in practice.

5.4.3
Mechanical Models

The classical continuum beam theory, although questionable for nanometric objects, has produced the first predictions of nanotube elastic properties, and is still employed nowadays with relatively good results [2, 61]. This theory contains

9) Assuming reflectionless contacts, the terms leads, terminals and contacts can be used interchangeably (see Reference [50] for a thorough discussion).

a parameter, the Young's modulus, which still proves to be extremely hard to measure experimentally. Therefore, simplified analytical models with periodic boundary conditions were initially used for evaluating the Young's modulus of nanotubes and graphene, utilizing for instance the Tersoff–Brenner potential [62]. Later, molecular dynamics (MD) imposed itself as the common choice allowing the simulation of finite systems composed of nanotubes in a variety of configurations.

There is currently a large variety of force-fields to drive MD simulations. For carbon-based systems, analytic many-body force-fields such as Tersoff-Brenner and Stillinger–Weber have long been available [62]. The Tersoff-Brenner potential works particularly well for crystalline, amorphous and molecular phases of carbon, such as diamond, graphite, fullerenes and nanotubes and has been thoroughly tested in a variety of settings. An important bonus for the Tersoff–Brenner potential is that it is reactive, i.e. chemical bonds can form and break during the simulation. Consequently, the neighbor list of each atom is dynamic that slows the simulation to a certain extent. Therefore, for larger systems it is often convenient to turn to simpler, fixed-topology force-fields such as CHARMM or Amber [63].

More realistic models including electronic effects are obtained through tight-binding methods [64] using a minimum sp-basis. The TB approximation captures part of the chemical strain through the geometry dependence of its electronic matrix elements. However, when still higher accuracy is desired, *ab initio* methods can be used.

Ab initio molecular dynamics simulations based on DFT can be performed by minimizing the total energy with respect to the eigenfunctions for a given ionic configuration, then computing the forces and moving the ions [65]. A different and very elegant scheme was proposed by Carr and Parrinello [66]. The idea is to introduce a fictitious electronic dynamics, which keeps, during the ionic motion, the electronic wavefunction adiabatically close to the instantaneous eigenstates of the quantum Hamiltonian. In this approach, both the ions and the eigenfunctions are treated as classical fields following the Newtonian dynamics, with the orbitals subject to the constraint of orthonormality. The trade-off in the simulations is between having smaller electronic masses, thus keeping the system close to the Born–Oppenheimer minimum, and the necessity of keeping the integration time step as large as possible, in order to simulate the dynamics for a time adequate for the atomic scales (typically from a fraction of a picosecond up to several picoseconds). This technique can be used both for molecular dynamics simulations and for energy minimization of the DFT functional.

Finally, we draw attention to a promising use of model potentials; hybrid modeling. In situations where a large system contains a site of specific interest, one may succeed by treating the region of interest quantum mechanically and the rest with a model potential, accelerating significantly the computation time. The same technique can be generalized in replacing mildly bent nanotube segments by continuum beams (see Chapter 6 and references therein for details about hybrid modeling).

5.5
Modeling Case Studies: Highlighting Physical Mechanisms

In the previous section we have briefly reviewed some of the most utilized modeling methods for carbon nanotubes. This final section will bring to attention a few modeling examples with the goal of illustrating the challenges but also the achievements of CNT-based systems simulation.

Some results coming from scanning tunneling microscopy simulations of nanotubes are first presented in the following subsection. Spectra for pristine CNTs are compared with spectra for nanotube ropes, CNT on Au substrates and CNTs with topologic Stone–Wales defects. This comparison will give an indication of the influence of different coupling on the electronic properties of nanotubes, and suits as a preparation for the following subsection, that will deal in detail with the interactions of CNTs with different molecules from a transport perspective. Section 5.5.2 will therefore dive into the transport phenomena in CNT and the effect of functionalization, doping, adsorption and other types of chemical disorder on these properties. From modeling properties, we move to a final example of a device-level modeling in Section 5.5.3. Both the mechanical and transport properties of an electromechanical deflection transducer are treated in this subsection with the goal of validating the device operation, and showing the usefulness of modeling tools in the design of future generation CNT-based devices.

5.5.1
Scanning Tunneling Microscopy of Nanotubes

Scanning tunneling microscopy (STM) and scanning tunneling spectroscopy (STS) are two extremely useful techniques in the study of the role of the local environment on the electronic properties of nanotubes. Therefore, this topic is relevant for sensors, in particular for those involving modulation of electronic properties (see Section 5.3.1). For a basic introduction into the simulation of STM images, see Reference [34] and references therein. Here we only discuss a selection of simulation results for CNTs in several configurations.

In the simplest approximation, STM topographic images can be obtained through the Tersoff–Hamann theory [67]. In this model, the tip is not taken into account explicitly, therefore convolution effects due to the tip shape are neglected. The STM current, for an external applied bias voltage V, is proportional to the local density of states (LDoS) integrated between the Fermi levels of the tip and sample:

$$I(\mathbf{r},V) = \int_{E_F-V}^{E_F} \mathrm{d}E\rho(\mathbf{r},E) = \int_{E_F-V}^{E_F} \mathrm{d}E \sum_i |\psi_i(\mathbf{r})|^2 \delta(E-E_i) \tag{7}$$

where $\{\psi_i, E_i\}_i$ are electronic eigenfunctions and their corresponding eigenenergies. Formally, LDoS is nothing more than the diagonal matrix element of the

spectral measure operator in real-space representation, $\rho(\mathbf{r}, E) = \langle \mathbf{r}|\delta(E - \hat{H})|\mathbf{r}\rangle$. The summation over i can stand for summation over the band index q and integration over the k points of the first Brillouin zone of the tube in the infinite case (see Section 5.2), or a summation over the discrete energy level indices in the finite tube case. Both DFT Kohn–Sham or tight-binding (TB) Hamiltonian models can be used to obtain the electronic eigenfunctions and eigenenergies. Topographic images are subsequently approximated by iso-surfaces of $I(\mathbf{r}, V)$. On the other hand, in STS experiments, the accessed quantity is the differential conductance $\mathrm{d}I/\mathrm{d}V$, which within the above assumptions can be shown to be proportional to the nanotube density of states (DoS).

The first observation made from STM simulations is that the interaction with a substrate or with other tubes does not alter the STM patterns with respect to isolated tubes [68, 69]. Finite length nanotubes exhibit standing wave patterns. In the case of armchair CNTs, the standing waves can be completely characterized by a set of four different three-dimensional shapes as catalogued in Figure 5.2. On a (111) gold substrate, even if the tubes are fairly strongly bond by charge transfer, the interaction with the substrate does not alter the main images of the isolated tubes (see Figure 5.3). The computed images are in very good agrement with the experiments in both wavelength of the standing wave (0.75 nm) and inner details (pairing). Surface states related to the boundary of the tubes are observed to appear within 1 eV above the Fermi level.

We now focus on the modification of the scanning tunneling spectra by the tube-tube interactions. In Figure 5.4, calculated STM/STS images obtained for an external voltage of +0.5 eV for a bundle made of three (8,8) nanotubes are compared with the isolated (8,8) tube. Changing the polarity of the applied voltage does not introduce appreciable changes in the STM topographic image. However, the inter-tube interaction clearly modifies the spectra seen in the DoS. A "pseudo-gap" close to the Fermi level is opened, as predicted for random oriented nanotube ropes [70] (pseudo-gap ≈ 0.1 eV). The bundle remains metallic, however[10]. Also, the electron–hole asymmetry in the DoS is accentuated and the spike structure of the van Hove singularities is smoothed out. The fact that the position in energy of the peaks is not strongly modified explains the success of using isolated SWNT spectra to describe the experimental data [71]. Nevertheless, the shape of the spectra (relative intensities) is strongly affected by tube–tube interactions, as is clearly seen in Figure 5.4.

The role of topological defects, in particular the pentagon–heptagon pair and the Stone–Wales (SW) defect has also been investigated [34]. Typical results on a (10,10) carbon nanotube for an applied bias potential of ±1.5 eV are presented in Figure 5.5. It can be observed that the SW defect creates a very localized modification of the image as compared with a perfect tube, although the decay length of the perturbation is very short (~1.5 nm). The symmetry of the image corresponding to occupied/unoccupied states is completely different. Therefore,

10) These conclusions have been confirmed experimentally [72] for metallic tubes and ropes such as that shown here.

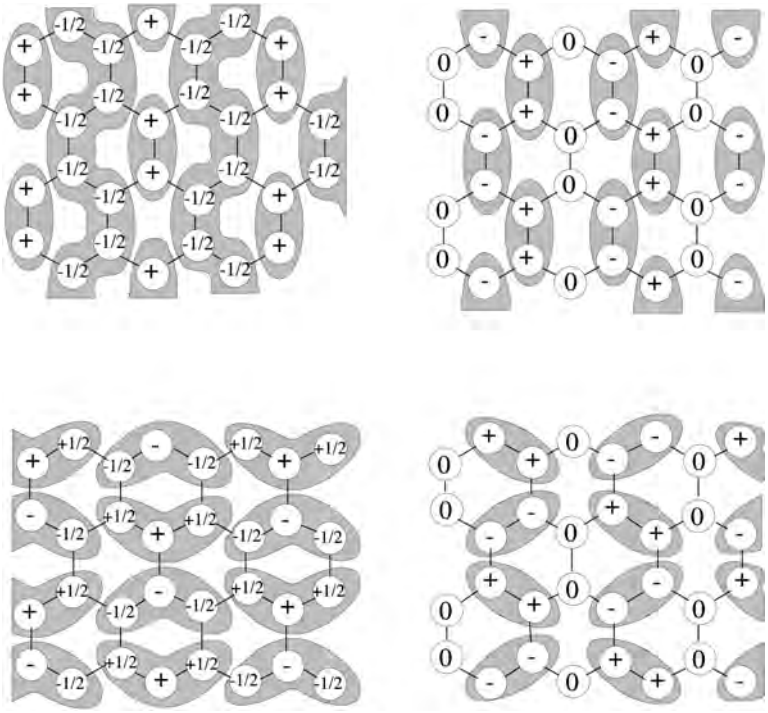

Figure 5.2 Schematic tight-binding catalog of STS images for an armchair nanotube close to the Fermi level, corresponding to the bonding and antibonding solutions in a 1D confinement box model (the wave-function values are indicated by the ± symbols). The same scheme holds for supported tubes on a Au(111) substrate. Adapted from Reference [68].

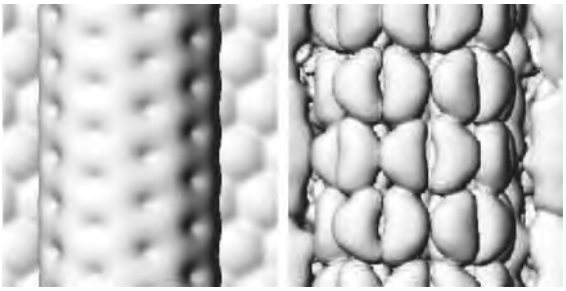

Figure 5.3 *Ab initio* calculation for a (5,5) carbon nanotube supported on Au(111). Left: STM-topographic image for an applied voltage of 2 eV. Right: standing wave pattern of the highest occupied molecular orbital (HOMO). The latter pattern fits one of the catalog of STS images in Figure 5.2. Adapted from Reference [69].

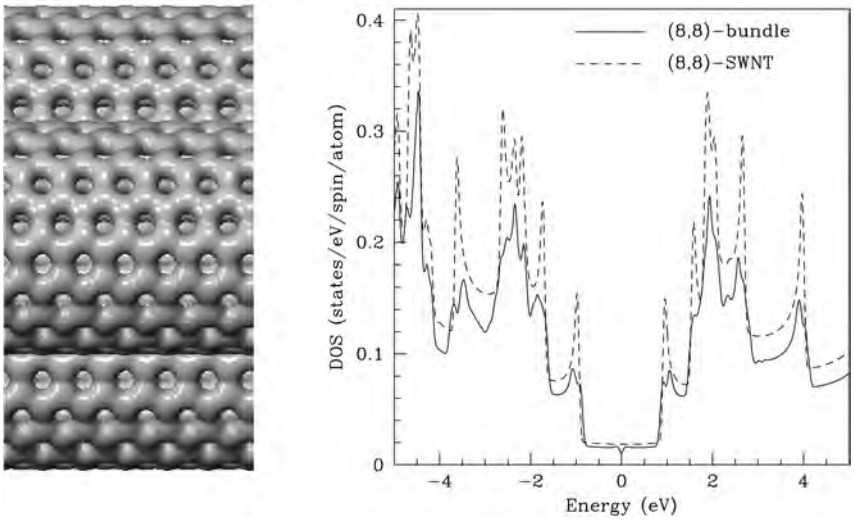

Figure 5.4 STM (a) and DoS (b) for a small CNT rope containing three (8,8) SWNTs (d_t = 1.09 nm) close-packed with an inter-tube distance of 0.345 nm. The opening of a "pseudo-gap" of about 0.1 eV around the Fermi level is clearly visible, by comparing the results for the bundle with the DoS of an isolated (8,8) SWNT (dashed line). Adapted from Reference [69].

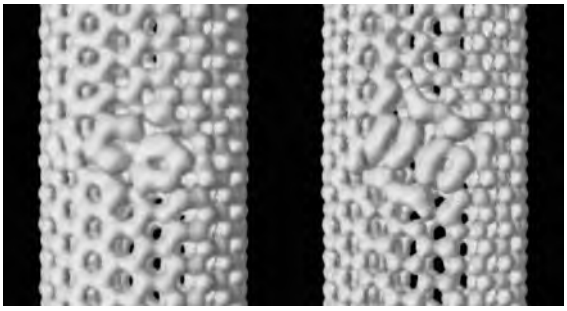

Figure 5.5 Simulated constant current STM images for a (10,10) CNT with a single Stone-Wales (SW) defect for an applied external tip-sample bias of ±1.5 eV. The orientation of the centered bond joining the two pentagons of the SW defect is set to $\pi/4$ degrees to the tube axis.

these calculations indicate that SW defects could be experimentally accessible via STM measurements. Later in this section we will show that topological defects play a major role in influencing the conductance and chemical sensitivity of a carbon nanotube channel, and have to be addressed explicitly in CNT-based sensors.

5.5.2
Transport Phenomena in Carbon Nanotubes

The peculiar geometry of carbon nanotubes yields particularly strong quantum confinement, low-dimensional physics, but also enhanced sensitivity to any disruption of the sp^2 network [2, 3, 73]. As emphasized in Section 5.3.1, this mechanism has fueled many experimental breakthroughs [7, 15, 74]. In this context, the development of efficient and predictive computational transport methodologies is fundamental in enabling in-depth exploration of complex hybrid nanotubes, with random distribution of functionalizing entities that will alter or modify the underlying carbon-based conducting channel properties [3].

Functional groups can specifically be attached to the carbon nanotube surface either by physisorption or by covalent bonding. Conventional covalent functionalization has been experimentally demonstrated to perturb severely the atomic structure of the CNT and its corresponding electronic properties. In contrast, the physisorption of organic molecules on the nanotube sidewalls is an example of noncovalent functionalization involving π-stacking interactions and corresponding to a much weaker binding energy. The main interest in noncovalent functionalization also stems from the negligible charge transfer involved within the π-stacking interactions. The induced scattering is thus mostly expected to be low and molecular dependent, in contrast to the electrochemical covalent functionalization.

In the remainder of this subsection we present a series of numerical studies on the influence of different disorder models on the transport properties of carbon nanotubes. Random uniform disorder is first approached, allowing analytic derivation of the mean free path scaling with the disorder strength. Then, semi-empirical methods are employed in assessing mean free paths or conductance functions in variously functionalized CNT from simple doping to defects and molecular chemi- and physisorption. The final paragraph is dedicated to the problem of selective detection of molecules in CNT chem-FETs.

5.5.2.1 Model Disorder: Basics of Elastic Mean-Free-Path Scaling

For a better understanding of disorder effects, including inter-band scattering in the presence of short-range disorder [75], the evaluation of the elastic mean free path ℓ_e is fundamental. For sufficiently weak disorder, a perturbative treatment can be performed within the Fermi golden rule (FGR). The FGR gives access to the elastic mean free path $\ell_e = v_F \tau$, with v_F the Fermi velocity and τ the mean free time. This was first derived by White and Todorov [54, 76] by reducing the band structure to a two-band approximation, as an effective model of the two degenerate bands at the charge neutrality point (CNP) for armchair nanotubes. By further considering an on-site Anderson-type disorder (see below), an analytical formula for ℓ_e was derived; ℓ_e was found to scale linearly with diameter for a fixed disorder strength W, whereas at a fixed diameter, the expected disorder scaling $\ell_e \propto 1/W^2$ was shown. Considering the overall Hamiltonian as composed of the pristine CNT tight-binding Hamiltonian plus a small on-site perturbation $\hat{H} = \hat{H}_0 + \hat{V}$, the application of the FGR yields

$$\frac{1}{2\tau(E_F)} = \frac{2\pi}{\hbar}\left|\langle\psi_+(k_F)|\hat{V}|\psi_-(-k_F)\rangle\right|^2 \rho(E_F)\times N_c N_R \tag{8}$$

with N_c and N_R number of pair atoms along the circumference and the total number of rings taken in the unit cell used for diagonalization, respectively. The eigenstates of $\hat{H}_0$ at the Fermi level can be written as[11)]

$$|\psi_\pm(k_F)\rangle = \frac{1}{\sqrt{N_R}}\sum_{m=1}^{N_R} e^{imk_F}\,|\alpha_\pm(m)\rangle$$

with

$$|\alpha_\pm(m)\rangle = \frac{1}{\sqrt{2N_c}}\sum_{n=1}^{N_c} e^{2\pi i n/N_c}\left(|p_z^A(mn)\rangle \pm |p_z^B(mn)\rangle\right) \tag{9}$$

The disorder considered here is an uncorrelated white noise (Anderson type) distribution given by

$$\left\langle p_z^\sigma(mn)\middle|\hat{V}\middle|p_z^{\sigma'}(m'n')\right\rangle = \varepsilon_\sigma(mn)\delta_{\sigma\sigma'}\delta_{mm'}\delta_{nn'} \tag{10}$$

with σ, σ' in $\{A, B\}$, where $\varepsilon_\sigma(mn)$ are the on-site energies of electron at atoms A and B in position (m, n)[12)], having a random uniform distribution within the energy interval $[-W/2, W/2]$, and $|p_z^\sigma(mn)\rangle$ is a π-orbital centered on either A or B at (m, n). By substituting Equation (9) in Equation (8), and using Equation (10), a straightforward calculation gives

$$\frac{1}{\tau(E_F)} = \frac{\pi\rho(E_F)}{\hbar}\left(\frac{1}{\sqrt{N_c N_R}}\sum_{N_c N_R}\varepsilon_A^2 + \frac{1}{\sqrt{N_c N_R}}\sum_{N_c N_R}\varepsilon_B^2\right) \tag{11}$$

Hence, if the disorder is described by random fluctuations of on-site energies with uniform probability $1/W$ the mean free path can be finally analytically [54, 76] derived as

$$\ell_e = \frac{18 a_{cc}\gamma_0^2}{W^2}\sqrt{n^2+m^2+nm} \tag{12}$$

with $a_{cc} = 1.42$ Å the C—C bond length and $\gamma_0 = 2.7$ V the typical TB hopping integral. For the armchair $m = n = 5$ nanotube, with disorder $W = 0.2\gamma_0$, applying Equation (12)[13)], one finds $\ell_e \approx 560$ nm, which is much larger than the circumfer-

11) The same eigenstates have been used to obtain the STS image catalog in Figure 5.2.

12) Here (m, n) refers to integer translations along graphene lattice vectors $\mathbf{a}_{1,2}$. A and B are the labels of the two inequivalent atoms in the graphene unit cell.

13) In Equation (12), (m, n) play again the role of the nanotube chiral index as opposed to Equation (10).

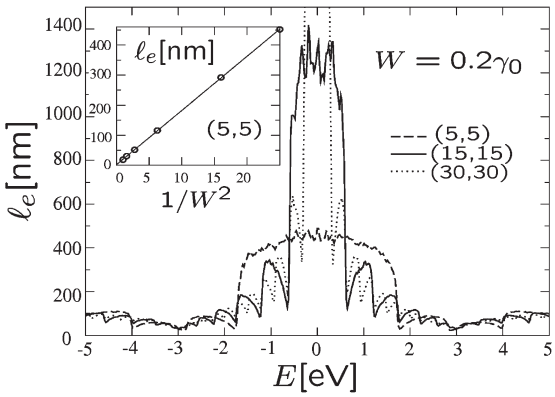

Figure 5.6 Energy-dependent mean free path as a function of diameter for different armchair carbon nanotubes. Inset: $1/W^2$ scaling in agreement with Fermi golden rule. Adapted from Reference [55].

ence length. As shown in Figure 5.6, numerical studies [55] confirm the scaling law of the mean free path with the nanotube diameter close to the charge neutrality point. For semiconducting bands, the $1/W^2$ is still satisfied, but mean free paths are seen to be much smaller and do not scale with diameter. With this information in mind, we move below to realistic disorders as created by dopants and adsorbed chemical species.

5.5.2.2 Chemical Disorder or Doping: Conduction Mechanisms and Basic Length Scales

The possibility to incorporate chemical impurities as substitutions of carbon atoms has been demonstrated experimentally [77] and offers novel possibilities to investigate coherent charge transport, and magneto-resistance phenomena in chemically modified carbon nanotubes. Substitutional doping by nitrogen or boron impurities has been a very intense research topic at the theoretical level during recent years [78, 79]. Initial work was focused on the effect of a single isolated defect on electronic and transport properties, while further studies have addressed the issue of mesoscopic transport in micrometer-long nanotubes with random distributions of impurities. These transport methods are mainly based on Kubo or Landauer–Büttiker frameworks, and mostly employed *ab initio* calculations combined with semi-empirical π–π^* Hamiltonians [80–82]. Such studies have allowed one to explore the fundamental elastic transport length scales [elastic mean free path $\ell_e(E)$] and to investigate quantum interferences phenomena bringing the system from the weak to the strong localization regime.

To elaborate an effective tight-binding model able to describe the physics around the Fermi level, it is sufficient to describe properly the long-range scattering poten-

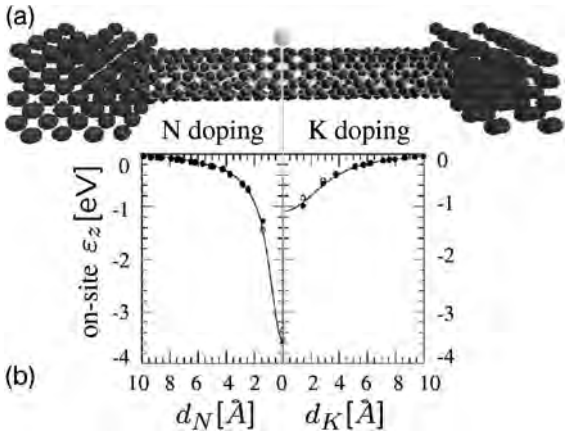

Figure 5.7 (a) Representation of a single adsorbed K atom on a CNT connected in between two metal contacts. (b) Long-range variations of the on-site and hopping parameters around K and N impurities derived from *ab initio* calculations. Adapted from Reference [81].

tial due to the chemical impurities (assuming a low-density approximation, i.e. no possible interferences between tails of individual impurity potentials). The long-range variations of the on-site and hopping parameters around impurities can be directly derived from *ab initio* calculations performed using atomic-like bases [81]. The tight-binding parameters obtained reproduce the position of the quasi-bound states in perfect agreement with the *ab initio* calculation [78]. For illustration, in Figure 5.7 the dependence of the *ab initio* on-site Hamiltonian matrix elements associated with the p_z orbitals as a function of the distance to the impurity in a doped (12×12) graphene sheet is plotted [81]. The potential well created by N in substitution is clearly much deeper that the one associated with the partially screened K^+ ion. In particular, the ability of adsorbed K^+ ions to trap electrons is significantly reduced as compared with N impurities.

In Figure 5.8, the Landauer conductance computed from the *ab initio* method (a) and the tight-binding model for a single nitrogen doped (10,10) armchair nanotube are shown (b). At selected energies ((b) inset-arrows), the conductance scaling properties are shown for a fixed impurity density $n_{\text{doping}} = 0.1\%$ (main plot). The extraction of the elastic mean free path ℓ_e is achieved by adding the contribution of the ballistic term to the diffusive one, i.e. $R = 1/G = R_0/N_\perp + R_0(N_\perp L/\ell_e)$, where $R_0 = h/2e^2$ is the resistance quantum and $N_\perp$ the number of available transverse modes at a given energy. When $\ell_e/L >> 1$, the statistical distribution of T is found to be narrowed and centered around $N_\perp$, in agreement with a ballistic limit $G = G_0 N_\perp$, with $G_0 = 1/R_0$ the conductance quantum. The other asymptotic case is found when $\ell_e/L << 1$, where the distribution of T becomes wider with a mean value downscaling with the tube length as $\overline{T}(E) = N_\perp(E)\ell_e(E)/L$. The conductance downscaling at a given energy exhibits a crossover from a ballistic to a diffusive regime.

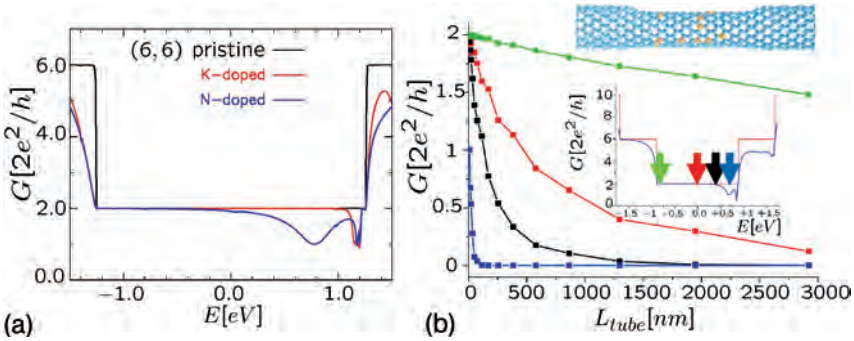

Figure 5.8 (a) *Ab initio* calculation of the conductance for a single nitrogen impurity in substitution of one carbon atom in the (6,6) metallic nanotube [81]. (b) Length dependence of the Landauer conductance for the disordered (10,10) N-doped nanotube at several energies (doping is fixed at 0.1%). Inset: conductance versus energy for the perfect (dashed line) and single-impurity (solid line) cases for a single defect. Arrows show the considered energies for the scaling analysis (main frame). Adapted from Reference [82].

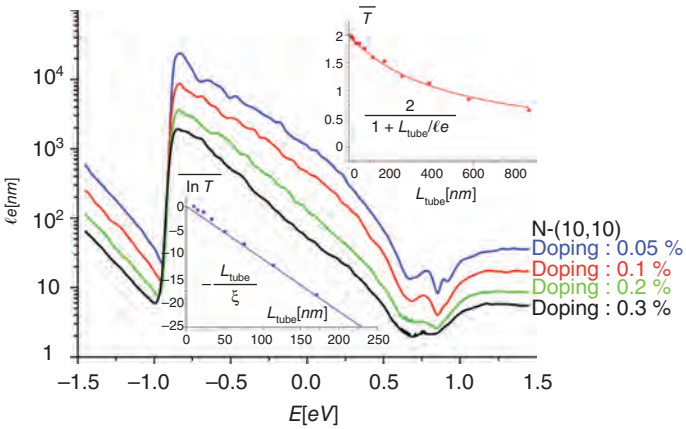

Figure 5.9 ℓ_e for several values of the doping density. Inset (top): $\overline{T}$ at CNP, for an average over 200 configurations. The linear fit (dashed) directly gives ℓ_e. Inset (bottom): $\overline{\ln T}$ at E = 0.69 eV, with linear fit (dashed) giving access to $\tilde{\zeta}$ Both insets correspond to n_{doping} = 0.1%. Adapted from Reference [82].

Figure 5.9 shows the full energy dependence of the elastic mean free path (ℓ_e), evaluated from the Kubo formula, for several values of the doping density. It is readily shown that over the whole spectral window, $\ell_e \propto 1/n_{\text{doping}}$, which is expected from the FGR. At the charge neutrality point, the scaling of ℓ_e shows a linear increase with the radius of the tube $d_t/2$ as found in a simpler Anderson model of disorder (not shown here). The comparison between ℓ_e extracted from both the

Kubo and the Landauer formalisms are in very good agreement over the full spectrum at a quantitative level [82]. For instance, the top inset in Figure 5.9b shows the averaged transmission and the fitting curve $2/[1 + L/\ell_e(E)]$, that yields $\ell_e(E = 0.00) = 495.5 \pm 17.4$ nm, in excellent agreement with the Kubo calculation that gives ~460 nm. For an energy at the frontier of the first sub-band below the CNP, i.e. $E = -0.78$ eV, the conductance slowly decays with length, and the regime remains quasi-ballistic. This is consistent with the calculated mean free path $\ell_e(E = -0.78) = 8371.6 \pm 69.4$ nm, which is much larger than the maximum length ($L = 3000$ nm) of the tube in between contact probes.

For energies close to the nitrogen quasi-bound states (Figure 5.8), the impurityinduced backscattering becomes very strong, yielding a very small mean free path (see also Figure 5.9). On the "*s* wave" resonance, one actually finds that $\ell_e(E = 0.69) = 8.2 \pm 0.8$ nm. For lengths larger than the mean free path, the conductance becomes exponentially reduced with length (Figure 5.8(b), blue and black curves), defining a localized regime with $\tilde{\zeta}$ the length scale that quantifies the exponential decay of exp $(\overline{\ln T})$ [83]. Accordingly, one obtains $\overline{\ln T}(E) = -L/\tilde{\zeta}(E)$ [82]. The next paragraph will go into more details concerning localization as expected in the presence of topological defects and covalent bonding of molecules on nanotubes.

5.5.2.3 **Defects, Covalent Functionalization and Anderson Localization**

The influence of defects is of fundamental relevance in the performance of electronic and sensing devices based on carbon nanotubes. Switching from a ballistic to either a weak or strong localization transport regime is possible above a certain density of defects. Moreover, as mentioned previously, defect sites augment the chemical reactivity of nanotube walls, rendering them sensitive to certain chemical species. Defects are most likely to be seen in nanotubes in different forms: topological defects, re-hybridization and incomplete bonding due to dislocations. Topological defects, distinguished by the presence of rings other than hexagons in the structure[14)] (e.g. the pentagon–heptagon pair or azulene structure), produces no net disclination but may slightly change the diameter and chirality of the tube, depending of its orientation relative to the tube axis. Knowing that a single sheet made of azulene as basic unit cell is metallic, as compared with the semi-metallic graphene, the introduction of pentagon–heptagon pair defects could close the band-gap of a nanotube and increase the metallic behavior [84].

Quantum transport theory [51] reveals that for a 1D conductor with defects, localization emerges whenever the "phase coherence length" ℓ_φ exceeds the localization length $\tilde{\zeta}$ For very long wires ($L \gg \tilde{\zeta}$), the electron transport is a diffusive process controlled by localization, with the electrons hopping between neighboring localized states. However, if L is not too large ($L \approx 3-10\tilde{\zeta}$) and the inelastic interaction is weak, the wire resistance is controlled by the phase-coherent electron propagation. This is the strong localization regime, in which the resistance increases exponentially with the length of the wire, $R \propto \exp(L/\tilde{\zeta})$ Depending on

14) Nanotube caps (closures) made of six pentagons according to Euler's theorem are not considered defects.

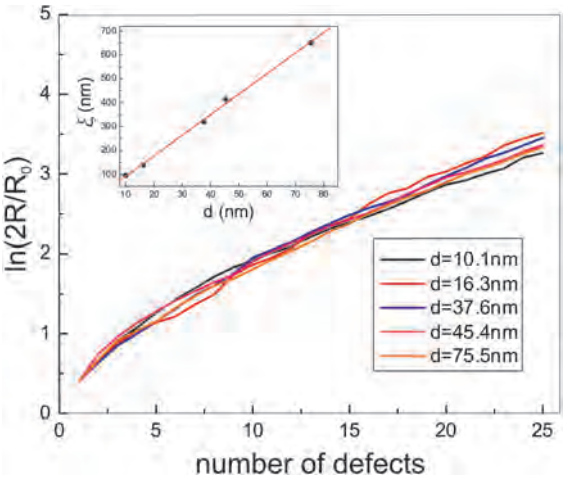

Figure 5.10 Calculated room temperature resistance for different average distances between di-vacancies (*d*) as a function of number of defects. Inset: localization length $\tilde{\zeta}$, extracted from the fitting $R = R_0 \exp(L/\tilde{\zeta})$ as a function of *d*. Adapted from Reference [86].

the defect density, in carbon nanotubes ℓ_φ can become longer than $\tilde{\zeta}$ driving the system into Anderson localization.

As an illustration, we show the extreme importance of defects (in particular di-vacancies) on the low-bias conducting properties of SWNTs irradiated with an Ar^+ ion beam [85]. Only 0.03% of di-vacancies produce an increment of three orders of magnitude in the resistance of a 400-nm long CNT segment. Theoretical *ab initio* calculations support this conclusion [86]. Indeed, for a (10,10) carbon nanotube some of the findings are as follows: (i) the transition between the ballistic and the localization regimes installs for a small number of di-vacancies (about 3–5); (ii) for a higher number of defects the system shows localization, and the number of effective channels is reduced from two (ballistic) to one; (iii) at zero temperature, the nanotube conductance is strongly fluctuating, whereas the effect of finite T is to wash out the fluctuations. The exponential scaling behavior, captured in Figure 5.10, is still preserved at room temperature. It is not clear whether electron correlation effects (e.g. Tomonaga–Luttinger liquid behavior) play a role and has to be resolved by future investigations.

We now focus on the covalent functionalization effects [87–90]. Starting from the occupied Bloch wavefunctions as obtained by *ab initio* DFT calculations on reference periodic systems, Marzari and coworkers [87, 88] extracted maximally localized Wannier functions (MLWF) to serve as basis sets for subsequent electronic structure and transport studies[15)]. The MLWF representation results in

15) Experience in parameterization of semi-empirical tight-binding-like models reveals that *real-space localized* basis sets are transferable (portable) between systems of local atomic configuration similarity.

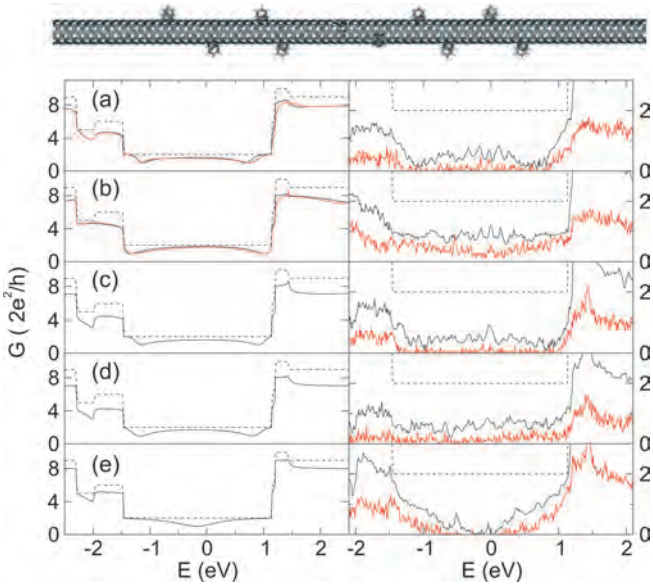

Figure 5.11 Top: Infinite metallic (5,5) CNT functionalized by an array of phenyl pairs. Left: quantum conductance of an infinite (5,5) CNT with one isolated pair of ligands in different positions (a–d), or with a single ligand attached (e) (red line in a and b, hydrogen; solid line, model calculation; dashed line, pristine CNT). Right: random distributions of pairs of ligands of of single ligands for the case of 10 defects per 1000 carbons (solid line) or 30/3000 (red line), averaged over five random configurations. Adapted from Reference [87].

sparse Hamiltonians which permit efficient implementations of the Landauer conductance calculation [see Equation (5)] and also the band dispersion everywhere in the Brillouin zone. The approach has been applied first to the study of covalent functionalization with electronegative or electropositive ligands such as nitrophenyls or aminophenyls in metallic SWNTs [87]. The band structure in the vicinity of the Fermi level is much less dependent on the chemical nature of the ligands (aminophenyl, nitrophenyl, phenyl and hydrogen), and seems rather affected by the sp^3 functionalization pattern disrupting the conjugated sp^2 network. Figure 5.11 displays several transport calculations. The ligands act as strong scatterers, reducing the conductance at the Fermi level by up to 42%. As for the dispersion relations, the dominant factor is rather topological with almost identical results for hydrogen (see Figure 5.11a and b, red line) or the removal of p_z MLWFs from the CNT sidewall (solid line).

On the other hand, cycloadditions of carbenes and nitrenes offer a radically different avenue towards chemical control of the ballistic channels. Employing the same MLWF procedure, cycloadditions have been studied [88]. Figure 5.12, which compares the quantum conductance of the two stable open and closed configurations for the (10,10) SWNT functionalized with $C(CN)_2$, captures one of the central findings. The scattering induced by a single group is negligible (Figure 5.12a).

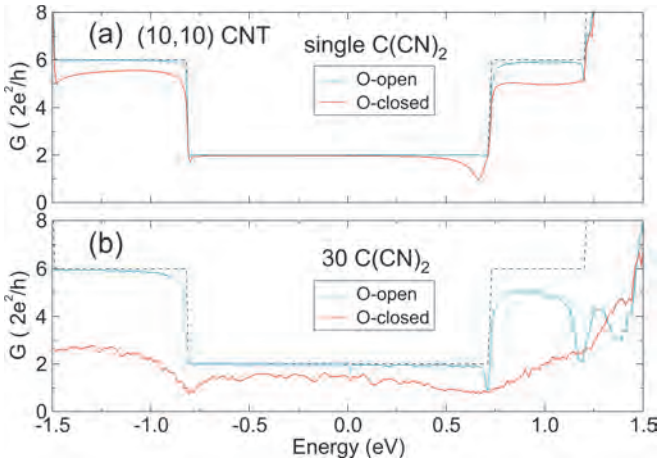

Figure 5.12 Quantum conductance for a (10,10) CNT functionalized with $C(CN)_2$, in the O-open and O-closed configurations (see [88] for details) [dashed line: pristine (10,10) CNT]. (a) Single group. (b) 30 functional groups randomly positioned on the central 32-nm segment of an infinite tube (the conductance is averaged over 10 configurations). Adapted from Reference [88].

However, as the number of functional groups is increased, the difference between the two configuration increases considerably (Figure 5.12b). Therefore, one addition configuration (i.e. the O-open) allows for reversible cleaving of the sidewall bonds, and induces direct sp^2 rehybridization, restoring the metallic conduction manifold. This observation allows a functionalization path preserving the electronic properties of CNTs around the Fermi level. A second strategy for minimally intrusive functionalization is physisorption, and constitutes the subject of the following section.

5.5.2.4 Signatures of Physisorbed Molecules on Transport

The effect of physisorption of small six-membered ring molecules C_6H_{2n} with n = 3, 4, 6, adsorbed on the CNTs has been investigated experimentally, through thermopower measurements. Sumanasekera et al. [17] reported on giant thermopower fluctuations due to the sorption of benzene molecules and attributed this effect to a strong π–π overlap between orbitals. Such an approach addresses the intrinsic effect of molecular physisorption on quantum transport since the thermopower S is related to the conductance modulations close to the Fermi level within the Mott equation. The validity of the Mott equation was further confirmed by Small et al. [91], even in the case of a Schottky-like injection regime.

Few theoretical studies have addressed the issue of molecular physisorption on the electronic properties of CNTs [92, 93]. To adjust the parameters of the semiempirical Hamiltonian operators, and since the interaction between the CNT and each molecule is geometry dependent, an *ab initio* study of the adsorption needs

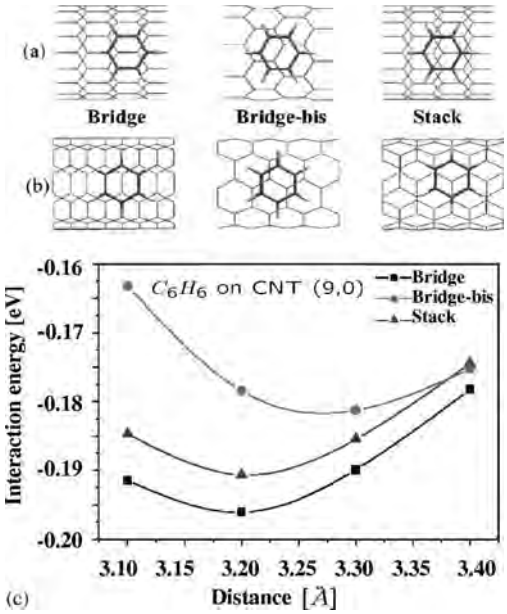

Figure 5.13 (a), (b) Different configurations considered for the adsorption of a benzene molecule on a (9,0) zigzag CNT (a) and on a (5,5) armchair. CNT (b). (c) Calculated interaction energy between a benzene molecule and a (9,0) zigzag CNT. Adsorption curves corresponding to the "bridge" (squares), "bridge-bis" (circles), and "stack" (triangles) configurations. Adapted from Reference [92].

to be carried out prior to the TB analysis. Figure 5.13 shows the adsorption energy curves computed for a benzene molecule over a (9,0) CNT in the configurations depicted in Figure 5.13a and b [92]. The two kinds of inequivalent C—C bonds of the CNT lead to the two configurations named "bridge" and "bridge-bis" depending if the center of the benzene lies over the center of a bond parallel or not to the tube axis, respectively. In the "stack" configuration, the center of the molecule is just over an atom of the CNT. The most favorable structure is the "bridge" one, with the benzene molecule over a C—C bond.

Electronic calculations have been performed on such a system using the DFT within its local density approximation (LDA) to predict the optimal geometry, and extract its electronic structure [94]. Calculations have been done using the *aimpro* code [95], with standard normconserving pseudo-potentials [96] and a $3 \times 3 \times 1$ k-points sampling for the Brillouin zone integrations [92]. From the optimized geometries, the LDA band structures are plotted for the interactive system. The interaction acts as a mixing of the molecular single states with the underlying band structure, resulting in hybrid eigenstates, with low group velocity. However, due to the relatively large gaps of the isolated molecules (5.217 and 2.089 eV for benzene and azulene, respectively), no strong modification is induced around the Fermi energy, and the linear band dispersion is maintained.

The electronic properties of CNTs are described by the zone folding model, whereas the π-conjugated molecules are treated by the usual Hückel model [97]. The tight-binding Hamiltonian of the complete system, containing the interaction between CNT and N_M molecules, reads

$$\hat{H} = \hat{H}_C + \sum_{m=1}^{N_M} [\hat{H}_m + \hat{V}_{Cm}] \tag{13}$$

where $\hat{H}_C$ is the CNT zone-folding Hamiltonian, and $\hat{H}_m$ is the Hückel Hamiltonian of the mth molecule. The remaining $\hat{V}_{Cm}$ term corresponds to the coupling between the mth molecule and the CNT, and has the expression [94]

$$\hat{V}_{Cm} = \sum_{\nu \in C} \sum_{\mu \in m} \beta \cos(\varphi_{\nu\mu}) \exp\left(\frac{-a_{gg} - r_{\mu\nu}}{\delta} \right) |\nu\rangle\langle\mu| \tag{14}$$

The parameters of the coupling term were optimized to reproduce accurately the interaction between shells in multi-walled CNTs [33]. In Equation (14), $r_{\nu\mu}$ corresponds to the distance between sites and $\varphi_{\nu\mu}$ is the angle between the axes of two $|\nu\rangle$ and $|\mu\rangle$ π-orbitals[16]. The parameters related to the interaction are a_{gg} = 3.34 Å, δ = 0.45 Å and β = –0.36 eV. The tight-binding parameters (on-sites energies ε and hopping integrals γ) are adjusted to reproduce the band structure of the graphene sheet and the energy levels of isolated benzene and azulene molecules, calculated within LDA. A standard procedure has been used to set the parameters for the graphene or the CNT, ε_C = 0 eV and γ_C = –2.56 eV, and also for the benzene molecule, ε_b = +0.411 eV and γ_b = –2.61 eV. Owing to an inhomogeneous charge distribution along the azulene molecule, the TB model should be refined by adding an electrostatic correction. New on-site energies for the azulene molecule, proportional to the net charge on each carbon atom (calculated with LDA), have been calculated. With this approach, the TB value of the azulene HOMO–LUMO gap is 2.198 eV. Finally, the band structure computed with this modified TB model is compared with the previous *ab initio* results. As presented in Figure 5.14, this re-parameterized semi-empirical model gives an excellent description of the electronic states for both benzene and azulene adsorption cases.

The next step is the implementation of these parameters into an $O(N)$ TB calculation in order to study both the electronic structure [density of states (DoS)] and the transport (diffusion properties) in a CNT with a random coverage of non-covalently attached molecules. The computation of the quantum transport properties has been performed by computing the energy dependent diffusion coefficients of propagating electrons $D(E, t)$ {see definition in Equation (4) [53]}, whose time dependence determines the conduction mechanism and the elastic mean free path ℓ_e.

The DoS of a (10,10) carbon nanotube with random coverage of adsorbed molecules are computed within this tight-binding framework. The density of grafted

16) For brevity in notation, $|\nu\rangle$ stand for $|p_z(mn)\rangle$ atomic orbitals as defined in Section 5.5.2.1.

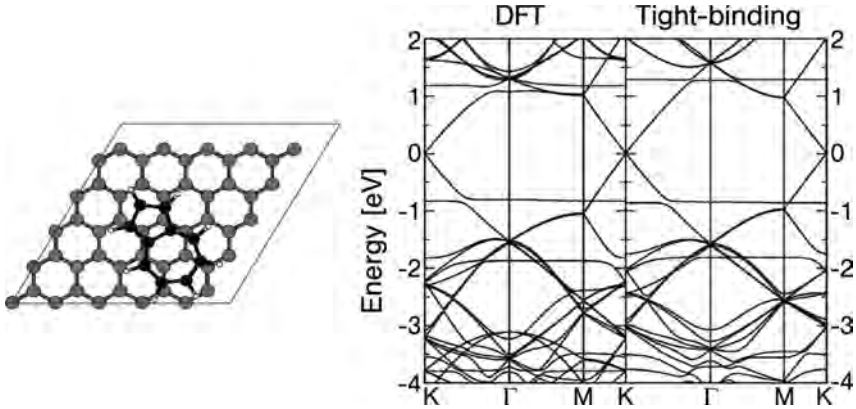

Figure 5.14 Right: The electronic structures of a graphene 5×5 supercell with one adsorbed π-conjugated molecule. Comparison between *ab initio* and TB model. Left: picture of an azulene molecule physisorbed on the graphene sheet. Adapted from [94].

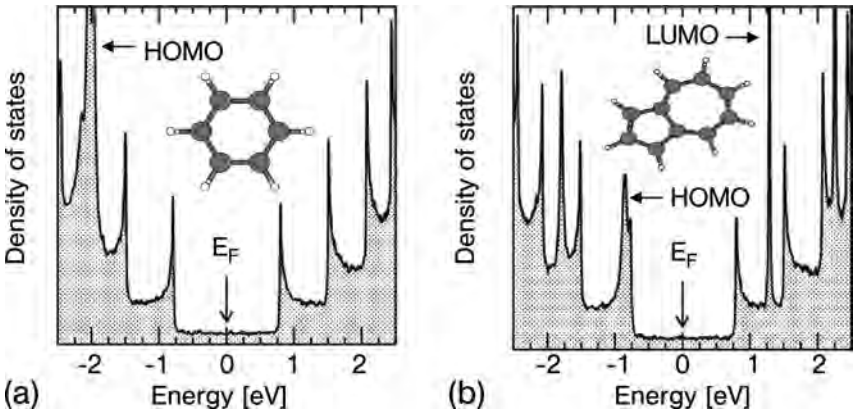

Figure 5.15 (a) DOS of the (10,10) CNT with a benzene density coverage of 16.3%. The HOMO molecular state is located by an arrow. (b) Same, but for an azulene density coverage of 11.5%. HOMO and LUMO levels are identified by arrows. Adapted from Reference [94].

molecules is chosen to be 16.3% for benzene and 11.5% for azulene[17]. Since the coupling intensity is weak, the DoS plotted in Figure 5.15 show the reminiscent discrete molecular levels, slightly enlarged by the mixing with the underlying continuum of π–π^* bands. Peaks arising from molecular HOMO and LUMO levels are indicated. In the case of benzene adsorption, the DoS is weakly affected at charge neutrality point, and the computed diffusion coefficient does not depart

17) These densities correspond to the ratio of the mass of the adsorbed molecule and to the CNT mass.

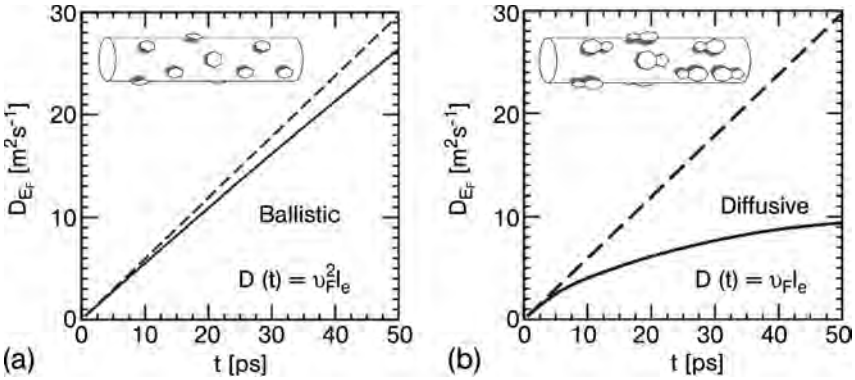

Figure 5.16 (a) Time-dependent diffusion coefficient (at the Fermi level) for the benzene/CNT system, showing quasi-ballistic behavior (solid line). Ballistic conduction for pristine CNT case is also reported (dashed line). (b) Time-dependent diffusion coefficient for the azulene/CNT structure, showing saturation at large times (diffusive regime). Adapted from Reference [94].

from a linear scaling in time (ballistic regime). Elastic backscattering induced by benzene molecules is thus extremely weak at Fermi level (Figure 5.16a), which means that ℓ_e is larger than several hundreds of microns (the considered limited tube lengths).

In contrast, in the case of azulene molecules, the HOMO level is located in the close vicinity of the last occupied Van Hove singularity of the CNT. Although the total DoS remains unchanged around the Fermi energy, the azulene adsorption impacts significantly on the intrinsic electronic conduction. In Figure 5.16b, the wave packet diffusivity at Fermi level is seen deviates more significantly from the ballistic regime. The saturation of $D(E, t)$ at long times allows one to extract the elastic mean free path ℓ_e, since $D(E, t \geq \tau) \approx v_F \ell_e$ (with v_F the Fermi velocity and τ the elastic mean free time).

Figure 5.17 gives the elastic mean free path scaling as a function of the azulene coverage density; ℓ_e is roughly divided by a factor of 6 for a density increase of ~30%. One notes that in contrast to the substitutional chemical doping of carbon nanotubes, for which ℓ_e is inversely proportional to the impurity density [80], ℓ_e associated with the azulene physisorption shows a weaker dependence on the density of attached molecules. The origin of the obtained scaling law $\ell_e \propto 1/\rho_{mol}^2$ which deviates from the conventional Fermi golden rule remains unclear. These results have shown vanishing modulations of physisorption of aromatic molecules on the intrinsic conductance close to the Fermi level. The application of the Mott equation that gives the thermopower as $S \approx (k_B^2 T / eG(E_F))(\mathrm{d}G(E_F)/\mathrm{d}E)$ has been demonstrated to be more general, however, including the effects of charge injection from external contacts [91]. In consequence, the strong modulations of thermopower in experiments [17] can hardly be attributed to physisorption effects provided that the Fermi level remains close to the undoped charge neutrality point.

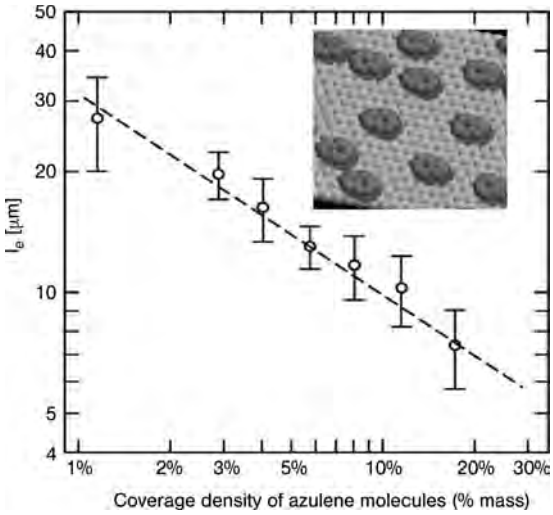

Figure 5.17 Mean-free-path of an azulene/CNT system versus the density of physisorbed molecules ρ_{mol}. The dashed line shows $\ell_e \propto 1/\rho_{mol}^2$ Adapted from [94].

Possible modulations of the Schottky barrier at the metal/nanotube interface, or inter-tube coupling modulations, driven by benzene adsorption could be the possible origin of thermopower fluctuations.

On the other hand, the physisorption of azulene molecules demonstrates that such a weak interaction may produce substantial backscattering in the nanotube, modifying its electronic mean free path and its conductance, which will downscale with the coverage density. Although the present study has been restricted to azulene molecules, other small gap π-conjugated hydrocarbon molecules such as fulvene should act in a similar way. Such a possibility of creating/removing a reversible elastic disorder by a simple adsorption/desorption of molecules covering the nanotube surface presents interesting perspectives for experimental studies and potential applications in nanotechnology.

5.5.2.5 **Sensor Specificity**

All examples treated so far, from the beginning of Section 5.5, show that carbon nanotubes are sensitive to many types of perturbations. In particular, several calculations showed that various chemical species could greatly influence the conductance of CNTs. With the huge advantage of sensitivity also comes the main challenge of CNT-based sensors, namely achieving selectivity, i.e. being able to distinguish the target in a sea of unwanted, perturbing signals. One possibility to improve selectivity is sensor functionalization such as with polymers [12] or single-stranded DNA [13]. In this subsection we investigate a second selective sensing strategy based on spectroscopic gate sweeps in CNT chemFET-like sensors giving access to the resonant molecular levels. A short first-principles discussion of zwitterion aromatic histidine (HIS), phenylalanine (PHE), tryptophan (TRP) and tyrosine (TYR) amino acids, bound through π-stacking on to a graphene sheet, is given below.

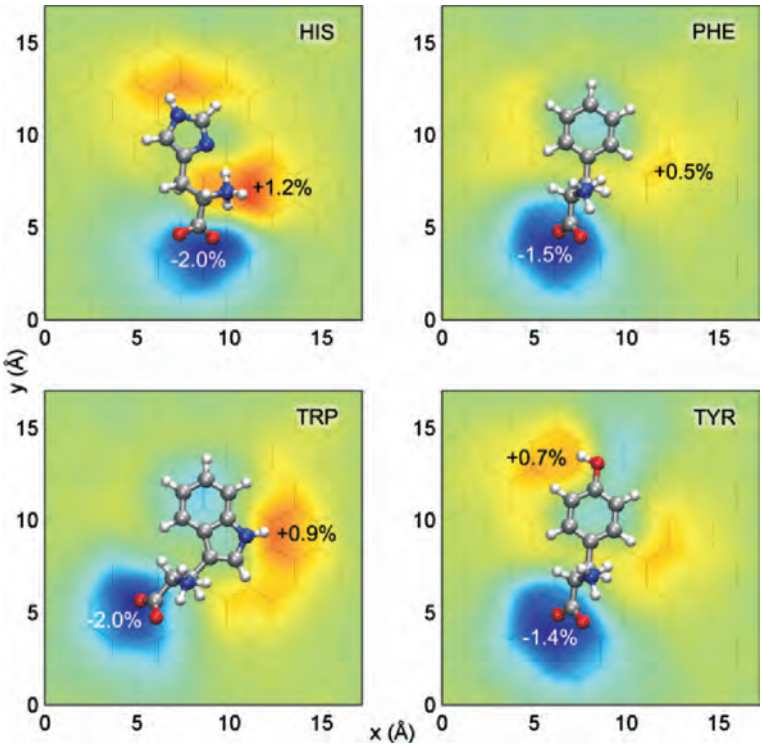

Figure 5.18 Mulliken charge transfer from/to $2p_z$ orbitals of graphene. The figure also shows the underlying graphene lattice as an indication of the stacking configuration of the amino acids. Atomic charges are represented in real space by convolution with Gaussian kernels of 2.85 Å effective cutoff centered at the atoms.

First, relaxation of the amino acids' atomic coordinates on graphene subject to weak π–π interactions is achieved. Mean field theories such as Hartree–Fock (HF) and DFT are known to have difficulties in predicting binding energies in the case of weak dispersion (London) forces. In fact, π-stacking is a benchmark for *ab initio* electronic structure methods [98–101]. Improvements can be obtained in this case either through wavefunction correlation methods such as Møller–Plesset or coupled cluster [99, 101] or through DFT plus van derWaals corrections [102]. As mentioned in Section 5.4.1, all these methods involve a significant computational effort, further complicated by the basis set superposition error (BSSE) [103] issues, inherent in finite basis set calculations. Also, *ab initio* relaxation is costly for asymmetric molecules such as amino acids because of the large number of degrees of freedom. In this light, a classical force-field CHARMM as implemented in the code NAMD [104] along with MacKerell et al.'s [105] set of amino acid parameters is preferred. van derWaals parameters for graphitic carbon are borrowed from benzene. The geometries obtained after conjugate gradient minimization, are displayed in Figure 5.18. Except for tryptophan, which relaxed into a "stack"

configuration because of the two aromatic rings, the other three amino acids relaxed into a "bridge" configuration. This together with a mean ring–graphene distance of approximately 3.3 Å, confirms the validity of the molecular mechanics relaxation method.

For each ad-system consisting of one aromatic amino acid on to a graphene layer, *ab initio* self-consistent calculations were performed with the DFT code SIESTA [106]. Since the systems are slabs (2D), an $8 \times 8 \times 1$ Monkhorst–Pack *k*-grid is chosen for sampling the rectangular first Brillouin zone with 32 *k* points. In Figure 5.18, Mulliken charges as computed with SIESTA are displayed. It is well known that Mulliken charges are strongly dependent on the basis set. Moreover, since relaxation at the *ab initio* level and counterpoise correction have been ignored, the charge analysis might further suffer from BSSE. Nevertheless, the charge maps presented in Figure 5.18 can be accepted qualitatively as they correlate well with the expected amino acid charges. The magnitude of the transferred charges[18)] places the system in the physisorption regime. The charge is mostly transferred from/to the $2p_z$ orbitals, whereas for the other orbitals the transfer is typically five times lower. A Fermi level shift (~150 meV up-shift or electron doping) together with the charge transfer from the $2p_z$ orbitals and the localized states close to E_F are mechanisms that can result in important conductance changes. Therefore, we suggest that carbon nanotubes might be suitable for aromatic amino acid detection.

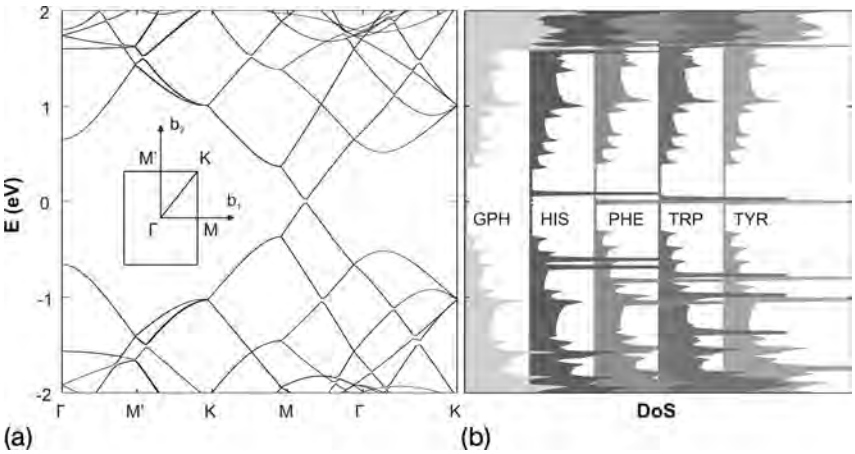

Figure 5.19 (a) DFT band structures of a graphene rectangular super-cell, along the symmetry lines defined in the first Brillouin zone sketched in the inset. (b) Total density of states for pristine graphene and the four adsystems emphasizing the amino aciddependent spectral peaks close to the Fermi level. van Hove singularities are apparent due to integration of DoS only along the symmetry lines.

18) The peak charge transferred is about 2% electrons distributed over 3–4 carbon atoms (see Figure 5.18).

Total density of states (DoS) are displayed in Figure 5.19. The presence of localized amino acid-dependent states close to the Fermi level is evident. These states are found to populate the α-carboxyl group orbitals of the amino acids and not the aromatic ring orbitals. The latter are populated significantly only by states found 3 eV away from the Fermi level and cannot, at least in theory, influence the intrinsic conductance of a carbon nanotube (see also Section 5.5.2.4 for a discussion of C_6H_6 physisorption on graphene). Hence it can be concluded that although responsible for the binding mechanism, it is not the aromatic rings of the amino acids that could change a nanotube's conductance but rather the carboxyl or amino ions. However, the most important feature is that the spectral position of the localized states is dependent on the amino acid type. These individualized signatures could prove extremely useful in the context of amino acid identification by CNT chemFETs. In sweeping the gate voltage, whenever E_F would cross these localized state resonant energies, a peak in the low bias conductance could be detected. This spectroscopic information can be used to infer the analyte, alleviating one of the known weaknesses of carbon nanotube-based sensors.

5.5.3
An Electromechanical Displacement Transducer

In this final case study, we present some modeling efforts aimed at validating the operation of a CNT-based electromechanical transducer. The analyses performed are different from the previous ones, in that device characteristics are targeted instead of intrinsic nanotube properties. This transducer, consisting of a CNT cross junction, has the principal function of measuring nanometric displacements. Relying on this basic function, both weak forces (pN) and small mass (kDa[19]) detection can be implemented, based on measurement principles detailed below.

The transducer studied is sketched in Figure 5.20 and consists of two perpendicular carbon nanotubes in a cross configuration. One nanotube is a doubly clamped linear bearing and the second is a singly clamped cantilever beam. The bearing is placed underneath the cantilever to prevent its collapse and stiction to the substrate by van der Waals attraction. The three metallic contacts, to which the tubes are clamped, serve also to bias the device electrically. For this study, a simple DC biasing scheme has been adopted, with the two terminals of the bearing set to $+V$ (where V is some potential) and the single terminal of the cantilever set to $-V$. In the steady state, when no external force is applied on the cantilever, the currents flowing through the two branches of the bearing should be approximately equal[20]. Whenever the cantilever bends, the length and consequently the current ratio of the two branches change. It is this branch current imbalance which is "measured" in order to obtain the deformation of the cantilever. A note is, however, important here. As seen in Section 5.5.2, for a

19) 1 kDa = 1.65×10^{-21} g.

20) In practice there will always be an offset owing to unequal branch lengths or differences in the doping or structural imperfections of the branches.

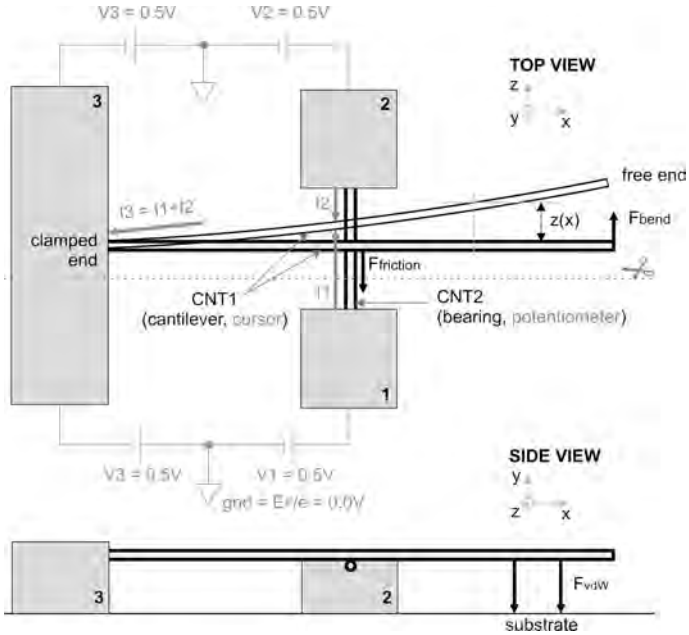

Figure 5.20 Schematic representation of the operation principle of a carbon nanotube-based displacement transducer. Top view: the bearing is biased to $+V$ and the cantilever to $-V$. In blue lines the electrical part is plotted, whereas mechanics are plotted in black lines. Bottom view: cross-sectional side view along the dashed line. Adapted from Reference [107].

ballistic tube the conductance does not scale with length so regardless of the cantilever's deflection no substantial branch current difference should be recorded. Therefore, some scattering should be present in the bearing to force length scaling, achievable in practice by doping or inducing structural defects (e.g. by ion bombardment; see Section 5.5.2.3).

Measuring forces with this transducer is straightforward. The cantilever's deflection Δz is transformed into a differential current $\Delta I = I_1 - I_2$, which is captured by readout electronics. Both the magnitude and the sign of the external force F can be obtained by multiplying the spring constant of the system with the previously determined deflection Δz, i.e. $F = k\Delta z = (3YI)/L^3\Delta z$, where Y is Young's modulus, I the moment of inertia and L the length of the cantilever tube. Regarding the second application, i.e. minute mass weighting or molecular detection, the transduction of a molecular binding event into an electrical signal is based on the oscillating frequency difference between the fundamental mode of the free cantilever versus the cantilever with a body attached. Measuring this frequency shift yields information about the mass of the attached body, which could be a macromolecule, virus or any other small particle. This device configuration is named

hereafter nanobalance. In the following, we concentrate on the modeling approach taken in order to obtain the different device characteristics. The modeling tasks are split in two, one set being related to the mechanical response and the other to charge transport.

5.5.3.1 Mechanical Transducer Behavior

Section 5.4.3 reviews some of the available choices for modeling the mechanical properties of SWNTs. As an illustration, here we discuss the model choice made, in view of the particularities of the system studied. The continuum Euler–Bernoulli beam theory [109] has been validated in moderate strain regimes for nanotube-based AFM tips [110, 111], nanotweezers [112], electromechanical resonators [20] and nanoswitches [113]. However, atomic-scale fluctuations of the van der-Waals potential coupled with the position-dependent shape of the cross junction yield pseudo-random friction forces. An atomistic description of the system in the framework of molecular dynamics (MD) is therefore imposed, which results in a new decision, namely choosing the appropriate force field (FF). Carbon nanotubes were studied using various FFs ranging from *ab initio* [114], tight-binding [115], Tersoff–Brenner [116] and even classical force fields such as CHARMM [117] (see Section 5.4.3). Nevertheless, only the last two FFs can deal with more than 10^6 atoms for a few nanoseconds of simulations. Compared with the Brenner potential, successful in describing carbon–carbon interactions, the CHARMM FF is additionally parameterized for a large spectrum of organic molecules, notably amino acids and phospholipids [105]. This advantage is exploited in the simulation the transducer in contact with a protein (streptavidin) later in this section. CHARMM is also considerably faster.

Since force fields in CHARMM's class have been used mostly for modeling CNT hydrophobic–hydrophilic effects [117], a new set of carbon parameters are derived that reproduce mechanical properties within a reasonable strain. The parametrization procedure, detailed elsewhere [107], relies on DFT *ab initio* calculations as performed with SIESTA [106]. Briefly, from the relaxed atomic coordinates in the unit cell of a (5,5) armchair CNT, the equilibrium bond length, bond angle and second neighbor distance (or Urey–Bradley term), i.e. r_0, θ_0 and $r_{0\mathrm{UB}}$, respectively, are obtained. Subsequently, the unit cell has been subjected to tensile strains in the [–10, 10]% range with a 1% step, and the total energy was calculated with SIESTA after relaxation at each strain. The rest of the CHARMM force-field parameters, namely the spring constants k, k_θ, k_{UB} and the Lennard–Jones well-depth $\varepsilon_{\mathrm{vdW}}$, were fitted by matching the total energy vs. strain curve as calculated with CHARMM against the *ab initio* one. Figure 5.21 shows the good agreement between the two curves with the final, optimized CHARMM parameters [107]. The Young's modulus extracted from the DFT curve[21)] corresponds to 1.04 TPa, which is a realistic value for this type of nanotube.

21) The Young's modulus is defined as the second derivative of total energy with respect to tensile strain, divided by the volume of the unit cell, $Y = (1/V)\mathrm{d}E/\mathrm{d}\varepsilon$.

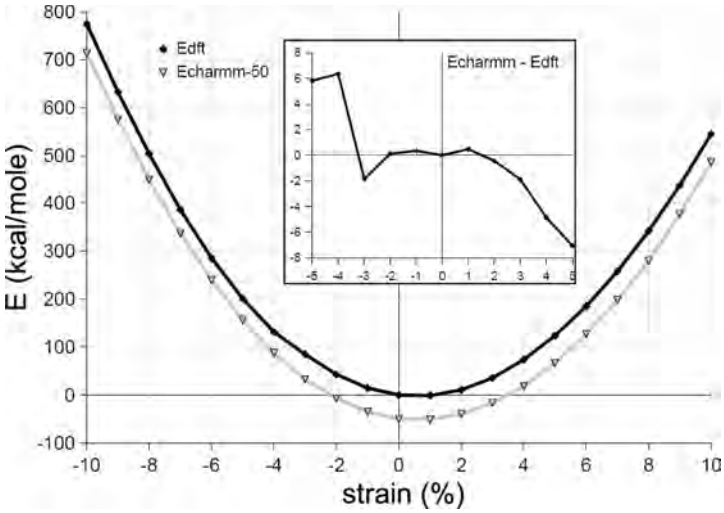

Figure 5.21 Energy-strain characteristics as obtained with DFT and the molecular dynamics CHARMM force field. The inset details the error around origin. Curves have been shifted vertically by 50 kcal/mol^{-1} for better visualization. Adapted from Reference [107].

With the parameterized CHARMM force field, several MD simulations have been performed to assess the dynamic behavior of the transducer. In the first MD simulation, a cantilever measuring 36 nm was pushed with a constant force of 10 pN evenly distributed between its 10 terminal atoms while clamping the other end of the tube. Turning on the force at the initial simulation step is equivalent to applying a unit-step stimulus, that excites simultaneously all the modes of the cantilever. For instance, the continuous component of the spectrum gives the final displacement as would be obtained in the presence of dissipation. Subsequently, three different positions of the (5,5) bearing tube, measuring 20 nm, were chosen to study the influence of the friction: at one-third half and two-thirds of the distance from either edge of the cantilever. The simulation step of the molecular dynamics was set to 1 fs and the total simulation time was limited to 0.5 ns (corresponding to 2 GHz). This time interval proved to be sufficient for capturing at least one period of the cantilever's fundamental mode (see Figure 5.22) in all four situations, but not long enough to allow the extraction of the superior modes via Fourier analysis, or the quality factor. The fundamental's mode frequency of the free cantilever agrees well with the classical Euler cantilevered beam value of 2.17 GHz. As opposed to the free cantilever case, the bearing adds friction. The mechanical work done to move the cantilever against friction, transforms to heat, as can be observed in Figure 5.22a. Although the magnitude of the friction forces is difficult to obtain from these data, it is obvious that friction is well below 10 pN, and does not influence the dynamics of the cantilever too much. Therefore, the presence of the bearing can be ignored from a mechanical point of view, which

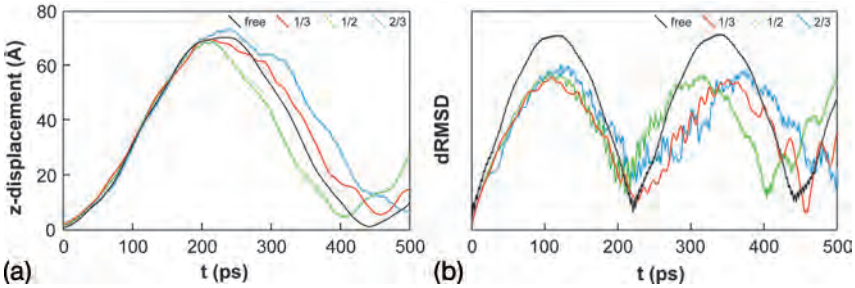

Figure 5.22 Different curves relevant to the mechanical response of the strain transducer. (a) Cantilever's deflection along the *z*-axis (the coordinate of one atom found on the tip). (b) Time derivative of the root mean square displacement (RMSD) of all atoms of the cantilever. Adapted from Reference [107].

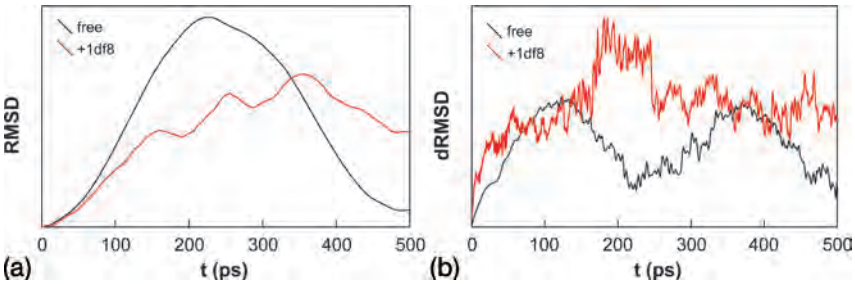

Figure 5.23 Normalized root mean square displacement (a) and its time derivative (b) for the free transducer and a single streptavidin molecule (1df8) attached at the tip of the cantilever. Adapted from Reference [108].

simplifies things considerably, and allows a simple Euler beam or other continuum theory to be used for the transducer mechanics.

We now turn our attention to the nanobalance configuration of the transducer. To demonstrate that this device is in principle capable of detecting minute masses, resonant frequency shifts are evidenced whenever an external body (typically a molecule) binds to the cantilever tube. The system under study is the biotin–streptavidin complex. Biotin can be modified to accommodate non-covalent binding on the surface of the nanotube. As before, MD is used for simulation to probe the frequency response of the system, with and without attached streptavidin. The bearing was placed at one-third of the distance from the cantilever's tip, whereas one streptavidin molecule was attached to the tip. Figure 5.23 shows that the cantilever's deflection in the molecule-attached case is retarded with respect to the free cantilever. This proves that the transducer is sensitive enough to detect a

single molecule of streptavidin, which weighs only a few kDa. The relative frequency drop $\Delta f / f_0$ estimated from Figure 5.23 is approximately 35%, which is rather important. Already seen in the RMSD (a), but highlighted in the dRMSD (b), is the abundance of additional modes introduced by the protein appearing noise-like, reducing the quality factor of the system.

5.5.3.2 Transport Strain–Current Characteristic

The molecular mechanics simulations described in the previous section focused on the operation of the transducer from the mechanical point of view. Here we switch to the investigation of the transport characteristics of the transducer, which tries to demonstrate that a deflection of the cantilever transforms into a branch current difference as explained in Figure 5.20.

The physics of CNT cross junctions is rich. The tunneling current through the junction depends strongly on the inter-tube distance, which fluctuates considerably at room temperature. Since the tunneling current is relatively weak, electrons tend to accumulate on the cantilever where they dwell for a while before disappearing into the bearing contacts. Charge shuttling and phonon-assisted tunneling may therefore be relevant, together with other potential many-body effects (e.g. correlated electron dynamics). Modeling transport through CNT cross junctions is rendered difficult – apart the complex physics – by the large number of atoms involved (a few thousand in this case). Achieving charge self-consistency is therefore too difficult, imposing a simplified tight-binding description. Due to the short lengths of the nanotube segments[22)], it is safe to assume that the intra-tube transport is ballistic. At the junction, phonon-assisted tunneling is neglected. Finite temperature effects are, however, taken into account by averaging over the ensemble of nuclear positions when computing branch currents from the transmission spectra.

The scheme used in transport calculations is similar to Reference [58], with some extensions, such as including multiple leads and taking into account the non-covalent tunnel junction. The Hamiltonian model is basically a π-only nearest-neighbor tight-binding model for intra-tube interactions plus a Slater–Koster-type cosine factor to account for the anisotropic inter-tube coupling (see also the model in Section 5.5.2.1):

$$\hat{H} = \sum_{\nu \in \mathrm{T}_{1,2}} \varepsilon_{0\nu} |\nu\rangle\langle\nu| + \sum_{\nu \in \mathrm{T}_2} \delta\varepsilon_{0\nu} |\nu\rangle\langle\nu| + \sum_{\nu,\mu \in \mathrm{T}_{1,2}} \gamma_0 \exp\left(\frac{-a_{\mathrm{CC}} - r_{\mu\nu}}{d}\right) |\nu\rangle\langle\mu| + \sum_{\nu \in \mathrm{T}_1} \sum_{\mu \in \mathrm{T}_2} \beta \cos(\varphi_{\nu\mu}) \exp\left(\frac{-a_{\mathrm{gg}} - r_{\mu\nu}}{\delta}\right) |\nu\rangle\langle\mu| \tag{15}$$

The first term is a sum over the on-site energies $\varepsilon_{0\nu} = \varepsilon_0 - |e| V(\nu)$ of all atoms in the tubes $\mathrm{T}_{1,2}$. Electrostatics is included via $|e| V(\nu)$, the field created by the leads.

22) The longest nanotube segment measures 36 nm.

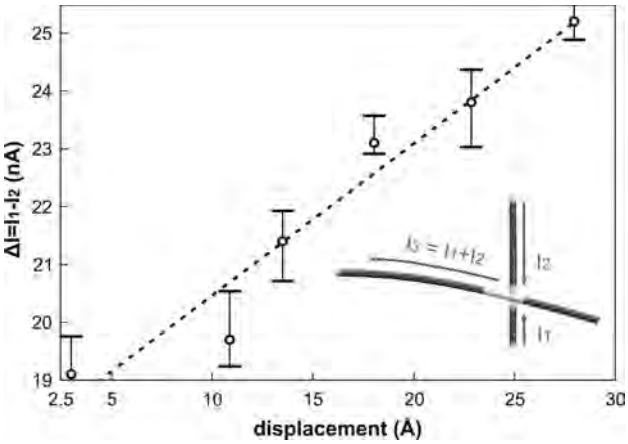

Figure 5.24 Overall current-deflection characteristic of the sensor showing a monotonic trend. Each point is obtained by averaging over thermally randomized configurations (error bars displayed). Inset: atomistic structure of the sensor and real-space partition used for quantum transport calculations. Adapted from Reference [107].

Both nanotubes are assumed to be in equilibrium with their metallic contacts, and therefore $V(\nu)$ is set constant along each tube. The second term contains a uniform disorder of on-site atom energies $\delta\varepsilon_{0\nu}$, sampled from the interval [–1, 1] eV, and applies only to the bearing atoms (T_2). This disorder is added to induce conductance length scaling in the bearing by localization. Strain in the cantilever is taken into account via the exponential modulation with a $d = 2$ Å decay length, where $r_{\nu\mu}$ represents the distance between atoms μ and ν and a_{CC} is the equilibrium C—C bond length (1.42 Å). The last sum describes inter-tube coupling, and includes the effect of non-parallel π-orbital axes via the cosine term, and finite interaction range via the second exponential factor with δ decay length[23)].

Contact currents have been calculated from Green's functions with the multi-terminal Landauer–Büttiker equation. The methodology utilized is explained elsewhere [107]. To avoid a direct inversion of the system's Hamiltonian, nanotube segments outside the junction region have been cut into thin rings, resulting in a block–chain matrix, for which fast, order-N elimination techniques work well [57]. The only matrix inversion remaining is the calculation of the junction-region Green's function, which is small enough not to penalize the simulation time. In order to take into account the atomic fluctuations at room temperature, 25 closely located junction configurations were sampled from the molecular mechanics

23) The values of the different parameters are the same as, and the Hamiltonian model is almost identical with, the model described by Equation (14).

simulation. The length of the distribution interval was of ~2 Å, consistent with thermal displacement fluctuation amplitudes as given by the equipartition theorem applied to the modes of a classical cantilever. The currents computed for each configuration were subsequently averaged and yielded Figure 5.24. An overall monotonic increase is clearly visible in Figure 5.24, which plots the current difference between the two branches of the bearing at different cantilever deflections. Although this characteristic can be used in validating the operation principle of the transducer, the model described thus far should not be interpreted quantitatively but rather qualitatively.

5.6 Conclusions and Perspectives

There is a great variety of applications for which nanotubes represent a disruptive potential, ranging from energy storage, composites, nanoelectronics and other solid-state devices, to sensors and actuators. This chapter has attempted to highlight the importance of bringing together theoretical modeling and experimental studies in the highly dynamic and complex field of CNT-based sensors. In the bio and medical fields, where target drug delivery and monitoring of specific enzymatic reactions are very important, the advantages of CNTs over traditional technologies could lead to genuine scientific and technological breakthroughs.

Under a brief examination, nanotube transducers have revealed a wide palette of sensing mechanisms, exploiting the exceptional structural, electronic and mechanical properties of CNTs. To be able to cope with the different timescales, feature sizes and phenomena present in nanotube systems, theory has often to rely on hybrid or multi-scale modeling. By producing reliable multiscale models, with real predictive value for device design, theory could assist decisively the technological efforts to overcome the remaining challenges, and promote carbon nanotubes as the material of the future in industrial applications.

5.7 Acknowledgments

We are grateful for fruitful discussions with V. Crespi, M. Cohen, S. G. Louie, P. M. Ajayan, R. Avriller, X. Blase, J. C. Charlier, S. Latil and F. Triozon and acknowledge funding from the European Community through NoE Nanoquanta (NMP4-CT-2004-500198), SANES (NMP4-CT-2006-017310), DNA-NANODEVICES (IST-2006-029192) and NANO-ERA Chemistry projects, UPV/EHU (SGIker Arina) and the Basque Governement. The work published here by C.R. was done during his thesis studies at Tima Laboratory, Grenoble, France. A.R. gratefully acknowledges the computer resources, technical expertise and assistance provided by the Barcelona Supercomputing Center – Centro Nacional de Supercomputación.

5.8 List of Symbols

$D(E, t)$	Energy-dependent diffusion coefficient
$\hat{D}(t)$	Diffusivity operator
d_t	Carbon nanotube diameter
E_F	Fermi energy, Fermi level
E_g	Semiconductor band gap
$E_q(k)$	Energy dispersion relation, band or subband
$f(E)$	Fermi–Dirac distribution
G_0	Conductance quantum
$\hat{G}(E)$	Green's function operator
$\mathcal{G}(E)$	Energy-dependent conductance
$\hat{H}$	Hamiltonian operator
I	Moment of inertia/electric current (context dependent)
k	Bending stiffness, spring constant/wavevector, wavenumber (context dependent)
L	Carbon nanotube length
$\ell_e(E)$	Energy-dependent elastic mean free path
ℓ_φ	Phase coherence length
(n, m)	Carbon nanotube chiral indices
S	Thermopower
$T(E)$	Transmission coefficient
$\hat{V}$	Coupling Hamiltonian operator
v_F	Electronic Fermi velocity
$\hat{X}(t)$	Position operator in Heisenberg representation
Y	Young's modulus
$\hat{\Sigma}_\lambda(E)$	Self-energy operator for a contact
ε_0	Tight binding on-site energy parameter
$\hat{\Gamma}_\lambda(E)$	Level broadening function, escape rate into a contact
γ_0	Tight binding hopping integral parameter
$\rho(E)$	Density of states
$\rho(\mathbf{r})$	Electron charge density
$\rho(\mathbf{r}, E)$	Spectral measure operator in real-space representation
σ, π	Atomic orbital hybrids or bonds
τ	Mean free time
$\tilde{\zeta}$	Localization length

References

1 S. Iijima, *Nature* **354** (1991) 56.

2 R. Saito, G. Dresselhaus, M. Dresselhaus, *Physical Properties of Carbon Nanotubes*, Imperial College Press, London, 1998.

3 A. Loiseau, P. Launois, P. Petit, S. Roche, J.-P. Salvetat (eds.), *Understanding Carbon Nanotubes From Basics to Applications*, Lecture Notes in Physics, Springer Berlin, **677** (2006).

4 P. J. F. Harris, *Carbon Nanotubes and Related Structures*, Cambridge University Press, Cambridge, 2002.

5 H. Terrones, M. Terrones, *New J. Phys.* **5** (2003) 126.1.

6 R. H. Baughman, A. A. Zakhidov,W. A. de Heer, *Science*, **297** (2002) 787.

7 J. Kong, N. R. Franklin, C. Zhou, M. G. Chapline, S. Peng, K. Cho, H. Dai, *Science*, **287** (2000) 622.

8 P. G. Collins, K. Bradley, M. Ishigami, A. Zettl, *Science*, **287** (2000) 1801.

9 M. Burghard, *Surf. Sci. Rep.* **58** (2005) 1.

10 N. Sinha, J. Ma, J. T. W. Yeow, *J. Nanosci. Nanotechnol.* **6** (2006) 573.

11 E. S. Snow, F. K. Perkins, J. A. Robinson, *Chem. Soc. Rev.* **35** (2006) 790.

12 P. Qi, O. Vermesh, M. Grecu, A. Javey, Q. Wang, H. Dai, S. Peng, K. J. Cho, *Nano Lett.* **3** (2003) 347.

13 C. Staii, A. T. Johnson, *Nano Lett.* **5** (2005) 1774.

14 B. R. Goldsmith, J. G. Coroneus, V. R. Khalap, A. A. Kane, G. A. Weiss, P. G. Collins, *Science*, **315** (2007) 77.

15 E. Snow, F. Perkins, E. Houser, S. Badescu, T. Reinecke, *Science*, **307** (2005) 1942; E. Snow, F. Perkins, *Nano Lett.* **5** (2005) 2414.

16 S. Chopra, A. Pham, J. Gaillard, A. Parker, A. M. Rao, *Appl. Phys. Lett.* **80** (2002) 4632.

17 G. U. Sumanasekera, B. K. Pradhan, H. E. Romeo, K. W. Adu, P. C. Eklund, *Phys. Rev. Lett.* **89** (2004) 166801.

18 A. Cao, S. Talapatra, Y. Choi, R. Vajtai, P. M. Ajayan, A. Filin, P. Persans, A. Rubio, *Adv. Mater.* **17** (2005) 147.

19 D. A. Heller, E. S. Jeng, T. K. Yeung, B. M. Martinez, A. E. Moll, J. B. Gastala, M. S. Strano, *Science*, **311** (2006) 508.

20 P. Poncharal, Z. L. Wang, D. Ugarte, W. A. de Heer, *Science*, **83** (1999) 1513.

21 M. Nishio, S. Sawaya, S. Akita, Y. Nakayama, *Appl. Phys. Lett.* **86** (2005) 133111.

22 V. Sazonova, Y. Yaish, H. Üstünel, D. Roundy, T. A. Arias, P. L. McEuen, *Nature*, **431** (2004) 284.

23 B. Witkamp, M. Poot, H. S. J. van der Zant, *Nano Lett.* **6** (2006) 2904.

24 H. B. Peng, C. W. Chang, S. Aloni, T. D. Yuzvinsky, A. Zettl, *Phys. Rev. Lett.* **97** (2006) 087203.

25 S. Ghosh, A. K. Sood, N. Kumar, *Science*, **299** (2003) 1042.

26 B. Bourlon, J. Wong, C. Mikó, L. Forró, M. Bockrath, *Nat. Nanotechnol.* **2** (2007) 104.

27 A. Modi, N. Koratkar, E. Lass, B. Wei, P. M. Ajayan, *Nature*, **424** (2003) 171.

28 J. Wang, *Electroanalysis*, **17** (2005) 7.

29 L. Roschier, R. Tarkiainen, M. Ahlskog, M. Paalanen, P. Hakonen, *Appl. Phys. Lett.* **78** (2001) 3295.

30 J.-P. Cleuziou, W. Wernsdorfer, V. Bouchiat, T. Ondarçuhu M. Monthioux, *Nat. Nanotechnol.* **1** (2006) 53.

31 M. S. Dresselhaus, G. Dresselhaus, P. C. Eklund, *Science of Fullerenes and Carbon Nanotubes*, Academic Press, San Diego, (1996).

32 T. W. Ebbesen (ed.), *Carbon Nanotubes: Preparation and Properties*, CRC Press, Tokyo, (1997).

33 P. Lambin, V. Meunier, A. Rubio, *Phys. Rev. B* **62** (2000) 5129.

34 Ph. Lambin, V. Meunier, A. Rubio, in: *Science and Application of Nanotubes*, Fundamental Materials Research, M. F. Thorpe, D. Tománek, R. J. Enbody (eds.), Springer, Berlin, 2002.

35 J. A. Majewski, P. Vogl, *Phys. Rev. B* **35** (1987) 9666.

36 W. Kohn, L. J. Sham, *Phys. Rev.* **140** (1965) A1133; P. Hohenberg, W. Kohn, *Phys. Rev. B* **136** (1964) B864.

37 S. Lunqvist, N. H. March (eds.), *Theory of the Inhomogeneous Electron Gas*, Plenum Press, New York, 1983; R. M. Dreizler, E. K. U. Gross, Density Functional Theory, an Approach to the Quantum Many Body Problem, Springer, Berlin, 1990; J. M. Seminario (ed.), *Recent Developments and Applications of Modern Density Functional Theory*, Elsevier, Amsterdam, 1996.

38 W. E. Pickett, *Comput. Phys. Rep.* **9** (1989) 115.

39 A. Szabo, N. S. Ostlund, *Modern Quantum Chemistry. Introduction to Advanced Electronic Structure Theory*, Dover, Mineola, NY, 1996.

40 L. Hedin, S. Lundqvist, in: *Solid State Physics*, H. Ehrenreich, F. Seitz,

D. Turnbull (eds.), Academic Press, New York, 1969.
41 F. Aryasetiawan, O. Gunnarsson, *Rep. Prog. Phys.* **61** (1998) 237.
42 B. Farid, in: *Electron Correlation in the Solid State*, N. H. March (ed.), Imperial College Press, London, 1999.
43 M. A. L. Marques, C. A. Ullrich, F. Nogueira, A. Rubio, K. Burke, E. K. U. Gross (Eds.), *Time Dependent Density Functional Theory (TDDFT)*, Lecture Notes in Physics, Springer, Belin, **706**, (2006).
44 G. Onida, L. Reinig, A. Rubio, *Rev. Mod. Phys.* **74** (2002) 601; F. Aryasetiawan, and O. Gunnarsson, *Rep. Prog. Phys.* **61** (1998) 237; W. G. Aulbur, L. Jönsson, J. W. Wilkins, *Solid State Phys.* **54** (1999) 1.
45 D. Prezzi, E. Molinari, *Phys. Status Solidi A* **203** (2006) 3602.
46 A. G. Marinopoulos, L. Reining, A. Rubio, and N. Vast, *Phys. Rev. Lett.* **91** (2003) 046402.
47 C. D. Spataru, S. Ismail-Beigi, L. X. Benedict, S. G. Louie, *Phys. Rev. Lett.* **92** (2004) 077402; E. Chang, G. Bussi, A. Ruini, E. Molinari, *Phys. Rev. Lett.* **92** (2004) 196401; E. Chang, G. Bussi, A. Ruini, E. Molinari, *Phys. Rev. B* **72** (2005) 195423.
48 M. P. Anantram, F. Léonard, *Rep. Prog. Phys.* **69** (2006) 507.
49 Y. Xue, S. Datta, M. A. Ratner, *Chem. Phys.* **281** (2002) 151; A. Nitzan, M. A. Ratner, *Science* **300** (2003) 1384; S. Kurth, G. Stefanucci, C. O. Almbladh, A. Rubio, E. K. U. Gross, *Phys. Rev. B* **72** (2005) 035308–1; B. G. Stefanucci, C.-O. Almbladh, S. Kurth, E. K. U. Gross, A. Rubio, R. van Leeuwen, N. E. Dahlen, U. von Barth, *Time-Dependent Transport Through Single Molecules: Nonequilibrium Greens Functions and TDDFT*, Lecture Notes in Physics, Springer, Berlin, 2006.
50 S. Datta, *Electronic Transport in Mesoscopic Systems*, Cambridge University Press, Cambridge, 1995.
51 G. Cuniberti, G. Fagas, K. Richter (eds.), *Introducing Molecular Electronics*, Lecture Notes in Physics, Springer, Berlin, 680 (2005); H. Haug, A.-P. Jauho, *Quantum Kinetics in Transport and Optics of Semiconductors*, Springer, Berlin, 1998.
52 K. S. Thygesen, A. Rubio, *J. Chem. Phys.* **126** (2007) 091101.
53 S. Roche and D. Mayou, *Phys. Rev. Lett.* **79** (1997) 2518; S. Roche, *Phys. Rev. B* **59** (1999) 2284; S. Roche, F. Triozon, A. Rubio and D. Mayou, *Phys. Rev. B* **64** (2001) 121401; S. Roche and R. Saito, *Phys. Rev. Lett.* **87** (2001) 246803; S. Roche, J. Jiang, F. Triozon, R. Saito, *Phys. Rev. Lett.* **95** (2005) 076803.
54 C. T. White, T. N. Todorov, *Nature*, **393** (1998) 240.
55 F. Triozon, S. Roche, A. Rubio, D. Mayou, *Phys. Rev. B* **69** (2004) 121410.
56 M. P. López Sancho, J. M. López Sancho, J. Rubio, J. Phys. *F: Met. Phys.* **15** (1985) 851.
57 F. Triozon, Ph. Lambin, S. Roche, *Nanotechnology*, **16** (2005) 230.
58 M. P. Anantram, T. R. Govindan, *Phys. Rev. B* **58** (1998) 4882.
59 F. Triozon, S. Roche, *Eur. Phys. J. B* **46** (2005) 427.
60 E. Akkermans, G. Montambaux, *Physique Mésoscopique des Électrons et des Photons, EDP Sciences*, Les Ulis, 2004.
61 B. I. Yakobson, C. J. Brabec, J. Bernholc, *Phys. Rev. Lett.* **76** (1996) 2511.
62 J. Tersoff, *Phys. Rev. B* **37** (1998) 6991; J. Tersoff, R. S. Ruoff, *Phys. Rev. Lett.* **73** (1994) 676; D. W. Brenner, *Phys. Rev. B* **42** (1990) 9458.
63 M. J. Field, P. A. Bash, M. Karplus, *J. Comp. Chem.* **11** (1990) 700; B. R. Brooks, R. E. Bruccoleri, B. D. Olafson, D. J. States, S. Swaminathan, M. Karplus, *J. Comput. Chem.* **4** (1983) 187.
64 C. M. Goringe, D. R. Bowler, E. Hernández, *Rep. Prog. Phys.* **60** (1997) 1447.
65 M. C. Payne, M. P. Teter, D. C. Allan, T. A. Arias, J. D. Joannopoulos, *Rev. Mod. Phys.* **64** (1992) 1045.
66 R. Carr, M. Parrinello, *Phys. Rev. Lett.* **55** (1985) 2471.
67 J. Tersoff, D. R. Hamann, *Phys. Rev. Lett.* **50** (1983) 1998.
68 A. Rubio, D. Sánchez-Portal, E. Artacho, P. Ordejón, J. M. Soler, *Phys. Rev. Lett.* **82** (1999) 3520.

69 A. Rubio, *Appl. Phys. A* **68** (1999) 275.
70 P. Delaney, H. J. Choi, J. Ihm, S. G. Louie, M. L. Cohen, *Nature*, **391** (1998) 466.
71 J. W. G. Wildöer, L. C. Venema, A. G. Rinzler, R. E. Smalley, C. Dekker, *Nature*, **391** (1998) 59; T. W. Odom, J.-L. Huang, P. Kim, C. M. Lieber, *Nature*, **391** (1998) 62.
72 M. Ouyang, J.-L. Huang, C. L. Cheung, C. M. Lieber, *Science*, **292** (2001) 702.
73 J. C. Charlier, X. Blase, S. Roche, *Rev. Mod. Phys.* **79** (2007) 677.
74 A. Star, T.-R. Han, J.-C. P. Gabriel, K. Bradley, G. Grüner, *Nano Lett.* **3** (2003) 1421; A. Star, Y. Liu, K. Grant, L. Ridvan, J. F. Stoddart, D. W. Steuerman, M. R. Diehl, A. Boukai, J. R. Heath, *Macromolecules* **36** (2003) 553; K. Balasubramanian, R. Sordan, M. Burghard, K. Kern, *Nano Lett.* **4** (2004) 827.
75 T. Ando, T. Nakanishi, R. Saito, *J. Phys. Soc. Jpn.* **67** (1998) 2857–2862; P. L. McEuen, M. Bockrath, D. H. Cobden, Y.-G. Yoon, S. G. Louie, *Phys. Rev. Lett.* **83** (1999) 5098.
76 S. Roche, G. Dresselhaus, M. S. Dresselhaus, R. Saito, *Phys. Rev. B* **62** (2000) 16092.
77 Ch. Ewels, M. Glerup, *J. Nanosci. Nanotechnol.* **5** (2005) 1354.
78 H. J. Choi, J. Ihm, S. G. Louie, M. L. Cohen, *Phys. Rev. Lett.* **84** (2000) 2917.
79 C.-C. Kaun, B. Larade, H. Mehrez, J. Taylor, H. Guo, *Phys. Rev. B* **65** (2002) 205416; A. H. Nevidomskyy, G. Csanyi, M. C. Payne, *Phys. Rev. Lett.* **91** (2003) 105502; H.-F. Song, J.-L. Zhu, J.-J. Xiong, *Phys. Rev. B* **95** (2005) 216602.
80 S. Latil, S. Roche, D. Mayou, J. C. Charlier, *Phys. Rev. Lett.* **92** (2004) 256805.
81 Ch. Adessi, S. Roche, X. Blase, *Phys. Rev. B* **73** (2006) 125414.
82 R. Avriller, S. Latil, F. Triozon, X. Blase, S. Roche, *Phys. Rev. B* **74** (2006) 121406.
83 D. J. Thouless, *Phys. Rev. Lett.* **39** (1977) 1167; E. Abrahams, P. W. Anderson, D. C. Licciardello, T. V. Ramakrishnan, *Phys. Rev. Lett.* **42** (1979) 673.
84 V. H. Crespi, L. X. Benedict, M. L. Cohen, S. G. Louie, *Phys. Rev. B* **53** (1996) 13303; V. H. Crespi, M. L. Cohen, A. Rubio, *Phys. Rev. Lett.* **79** (1997) 2093.
85 C. Gómez-Navarro, P. J. De Pablo, J. Gómez-Herrero, B. Biel, F.-J. Garcia-Vidal, A. Rubio, F. Flores, *Nat. Mater.* **4** (2005) 534.
86 B. Biel, F. J. García-Vidal, A. Rubio, F. Flores, *Phys. Rev. Lett.* **95** (2005) 266801.
87 Y.-S. Lee, M. Buongiorno-Nardelli, N. Marzari, *Phys. Rev. Lett.* **95** (2005) 076804.
88 Y.-S. Lee, N. Marzari, *Phys. Rev. Lett.* **97** (2006) 116801.
89 D. Grimm, A. Latgé, R. B. Muniz, M. S. Ferreira, *Phys Rev. B* **71** (2005) 113408.
90 N. Ranjan, G. Seifert, *Phys. Rev. B* **73** (2006) 153408.
91 J. P. Small, K. M. Perez, P. Kim, *Phys. Rev. Lett.* **91** (2003) 256801.
92 F. Tournus, J. C. Charlier, *Phys Rev. B* **71** (2005) 165421. F. Tournus, S. Latil, M. Heggie, J. C. Charlier, *Phys Rev. B* **72** (2005) 075431.
93 J. Zhao, J. P. Lu, J. Han, C.-K. Yang, *Appl. Phys. Lett.* **82** (2003) 3746; P. Gianozzi, *Appl. Phys. Lett.* **84** (2003) 3936; M. Arab, F. Picaud, M. Devel, C. Ramseyer, C. Girardet, *Phys. Rev. B* **69** (2004) 165401.
94 S. Latil, S. Roche, J.-Ch. Charlier, *Nano Lett.* **5** (2005) 2216.
95 P. R. Briddon, R. Jones, *Phys. Status Solidi B* **217** (2003) 131.
96 G. B. Bachelet, D. R Haman, M. Schlüter, *Phys. Rev. B* **26** (1982) 4199.
97 L. Salem, *The Molecular-Orbital Theory of π-Conjugated Systems*, Benjamin, Reading, MA, 1966.
98 A. V. Morozov, K. M. S. Misura, K. Tsemekhman, D. Baker, *J. Phys. Chem. B* **108** (2004) 8489.
99 F. L. Gervasio, P. Procacci, G. Cardini, A. Guarna, A. Giolitti, *J. Phys. Chem. B* **104** (2000) 1108.
100 K. M. S. Misura, A. V. Morozov, D. Baker, *J. Mol. Biol.* **342** (2004) 651.
101 M. O. Sinnokrot, E. F. Valeev, C. D. Sherrill, *J. Am. Chem. Soc.* **124** (2002) 10887.
102 F. Ortmann, W. G. Schmidt, F. Bechstedt, *Phys. Rev. Lett* **95** (2005) 186101.
103 S. F. Boys, F. Bernardi, *Mol. Phys.* **19** (1970) 553.

104 L. Kalé, R. Skeel, M. Bhandarkar, R. Brunner, A. Gursoy, N. Krawetz, J. Phillips, A. Shinozaki, K. Varadarajan, K. Schulten, *J. Comp. Phys.* **151** (1999) 283.

105 A. D. MacKerell Jr., D, Bashford, M. Bellott, R. L. Dunbrack Jr., J. D. Evanseck, M. J. Field, S. Fischer, J. Gao, H. Guo, S. Ha, D. Joseph-McCarthy, L. Kuchnir, K. Kuczera, F. T. K. Lau, C. Mattos, S. Michnick, T. Ngo, D. T. Nguyen, B. Brodhom, W. E. Reiher III, B. Roux, M. Schlenkrich, J. C. Smith, R. Stote, J. Straub, M. Watanabe, J. Wiórkiewicz-Kuczera, D. Yin, M. Karplus, *J. Phys. Chem. B* **102** (1998) 3586.

106 J. M. Soler, E. Artacho, J. D. Gale, A. García, J. Junquera, P. Ordejón, D. Sánchez-Portal, *J. Phys.: Condens Matter* **14** (2002) 2745.

107 C. Roman, F. Ciontu, B. Courtois, *Mol. Simul.* **31** (2005) 123.

108 C. Roman, F. Ciontu, B. Courtois, *4th IEEE Conference on Nanotechnology*, **263** (2004) 16–19.

109 S. Timoshenko, J. N. Goodier, *Theory of Elasticity*, McGraw-Hill, New York, 1983.

110 H. Dai, J. H. Hafner, A. G. Rinzler, D. T. Colbert, R. E. Smalley, *Nature*, **384** (1996) 147.

111 C. L. Cheung, J. H. Hafner, C. M. Lieber, *Proc. Natl. Acad. Sci. USA* **97** (2000) 3809.

112 P. Kim, C. M. Lieber, *Science*, **286** (1999) 2148.

113 M. Dequesnes, S. V. Rotkin, N. R. Aluru, *Nanotechnology*, **13** (2003) 120.

114 D. Sanchez-Portal, E. Artacho, J. M. Soler, A. Rubio, P. Ordejon, *Phys. Rev. B* **59** (1999) 12678.

115 E. Hernandez, C. Goze, P. Bernier, A. Rubio, *Appl. Phys. A* **68** (1999) 287.

116 T. Belytschko, S. P. Xiao, G. C. Schatz, R. S. Ruoff, *Phys. Rev. B* **65** (2002) 235430.

117 W. H. Noon, K. D. Ausman, R. E. Smalley, J. P. Ma, *Chem. Phys. Lett.* **355** (2002) 445.

6
Multiscale Modeling and Simulation for Fluid Mechanics at the Nanoscale

P. Koumoutsakos, Computational Science and Engineering Laboratory, ETH Zürich, Switzerland

Advanced Micro & Nanosystems Vol. 8. Carbon Nanotube Devices.
Edited by Christofer Hierold

ISBN: 978-3-527-31720-2

6.1 Introduction

One of the most important promises of nanotechnology is the capability to interact with materials and life forms at the molecular level. Along with advances in materials science and biology, nanotechnology can provides us with unprecedented insights into the natural world and the possibility for engineering innovations ranging from molecularly designed materials to personalized medicine at the cellular level. At the same time, nanotechnology and life sciences are two of the key beneficiaries from recent advances in computational science. Computational science integrates computer hardware with software development and computational methods and permits predictive modeling of complex physical phenomena and the quantitative analysis of large amounts of data while it has revolutionized our experimental capabilities. In nanotechnology, experimental techniques at present lack the capabilities to provide us with detailed temporal and spatial insight into this nanoscale world. The difficulty of carrying out controlled experiments on nanoscale systems makes computational studies potent alternatives for characterizing their properties. This realisation has led to numerous computational studies to study nanoscale phenomena and several advances to date in nanotechnology have come from theoretical or computational predictions that were later confirmed by experiments (e.g. the metallic and semiconducting nature of carbon nanotubes [101]). At the same time, we need to emphasize that the predictive capabilities of computational models depend critically on their validation by suitable experimental studies. A close collaboration between experiments and computations is expected to bring advances that will greatly enhance our understanding and will enable us to develop better engineering devices.

This chapter reviews a convergence point of nanotechnology, biology and computational science, namely the computational modeling of nanoscale fluid mechanics. Nanoscale fluid mechanics (NFM) is the study of fluid flows around and inside nanoscale configurations. It is a prototypical case of nanoscale transport as it pertains to biological systems ranging from the transport of proteins in the cytoplasm, to the transport of drug molecules and to the flow around biological sensing devices such as cilia. Nanoscale flow phenomena are ubiquitous! Where is the water? From the words of Alberts et al. [4]: “Water accounts for about 70% of a cell’s weight, and most intracellular reactions occur in an aqueous environment. Life on Earth began in the ocean, and the conditions in that primeval environment put a permanent stamp on the chemistry of living things. Life therefore hinges on the properties of water”.

The understanding of NFM is becoming critical as scientists and engineers develop nanoscale sensor and actuator devices for the study of biomolecular systems. Several key biomolecular processes such as the transport of DNA and proteins are carried out in aqueous environments, and aerobic organisms depend on gas exchange for survival. The development of envisioned nanoscale biomedical devices such as imaging nanoparticles, nanoexplorers and cell manipulators requires understanding of natural and forced transport processes of flows at the nanoscale. In addition, it is important to understand transport processes around biomolecular sensing devices for the detection of target molecules and the identification of key biological processes at the cellular and subcellular level in isolated or high background noise environments.

The goal of computational studies in NFM is to characterize prototypical nanofluidic systems and to explore specific nanoscale flow phenomena that may facilitate the development of nanoscale flow sensors and actuators and nanodevices capable of manipulating, for example, biomolecules in the form of molecular sieves. While there can be a large variety of nanoscale systems, it would be a formidable task to try to understand the essential physics of these systems by peering at every known device. Fundamental understandings can be obtained by studying the flow physics of prototypical configurations.

In this chapter, we discuss recent advances in nanoscale fluid mechanics with particular emphasis on the computational modeling of nanoscale flows interfacing with carbon nanotubes. These advances are discussed in the context of case studies, including the modeling of liquid–solid interfaces at the nanoscale, the development of multiscale computational methods for NFM, the behavior of fluids at the nanoscale and the interface of nanodevices with biomolecular structures.

Several comprehensive review articles have appeared in the area of nanoscale fluid mechanics, a non-exhaustive list of which is given here. Koplik and Banavar [139] presented one of the first reviews discussing the study of macroscale systems from atomistic simulations while Micci et al. [176] reviewed research nanoscale phenomena related to atomization and sprays. Flow in carbon nanotubes and nanopipes has been reviewed by Whitby and Quirke [277]. Maruyama [167] and Poulikakos et al. [198] have reviewed molecular dynamics simulations of micro- and nanoscale thermodynamic phenomena. Moving up to mesoscales, Gad-el Hak [79] and Ho and Tai [107, 108] presented reviews of the flow inmicro and MEMS devices. Vinogradova [262] and Churaev [47] reviewed the slippage of water over hydrophobic surfaces, including general properties of thin liquid layers. In addition, we note the emergence of interdisciplinary research communities enabled by internet advances. Projects such as the Nanohub platform (www.nanohub.org) and molecular modeling software such as NAMD (http://www.ks.uiuc.edu/Research/namd) provide researchers today with a wealth of resources for nano- and microfluidics modeling and simulation and present the start of a new kind of sharing of knowledge and computational expertise.

We emphasize that nanotechnology is a very dynamic field and new information is becoming constantly available from improved computational models and

experimental diagnostics. These words of caution must be kept in mind also when assessing the works discussed in this chapter as well as the chapter itself.

The chapter is structured as follows. In Section 6.2 we discuss computational aspects of NFM.We emphasize that practitioners must understand the ramifications of seemingly benign tasks such as the choice of the molecular interaction potentials and simulation boundary conditions. Recent advances on the multiscale modeling and simulation of NFM are presented. Section 6.3 discusses the flow phenomena at the interface of fluids and solids from the NFM perspective, and in Section 6.4 the effects of fluid confinement are discussed. Finally, Section 6.5 exemplifies some of the applications of NFM at the interface of biology and nanotechnology.

6.2
Computational Modeling: from Quantum to Atomistic and Continuum Descriptions

One of the great challenges in computational NFM is the development of efficient computational methods capable of tackling the complexity of the underlying physics. At present, there is no single computational approach that can model all length and temporal scales of nanoscale phenomena associated with NFM. The size of the system usually dictates the possible level of description and in turn the corresponding computational techniques. Quantum mechanics computations have benefitted in recent years from advances in numerical linear algebra and its application to massively parallel computers, providing us with "exact" simulations for thousands of atoms. Developments such as density functional theory and techniques such as Carr–Parrinello molecular dynamics and quantum mechanics/molcular mechanics techniques have extended the reach of quantum calculations into biomolecules in solvents and start to consider their interface with nanodevices. For larger systems the method of Molecular Dynamics (MD) is used to simulate systems that can be described with up to billions of atoms. The state of the art in the field of molecular dynamics can be found in a recent volume edited by Grubmuller and Schulten [93]. However, as nanoscale devices are often embedded in micro- and macroscale systems the computation of such flows requires proper integration of atomistic simulations with computational methods suitable for larger scales. The development of multiscaling techniques bridging quantum/atomistic/mesoscale/continuum descriptions of nano- and micro/macroscale flow phenomena will be a very fruitful area of research in the foreseeable future.

We wish to note here that the modeling and simulation of molecular systems have matured to the level where a number of software packages are readily available to researchers. Such software packages include the Carr–Parrinello MD (www.cpmd.org) and the NAMD (http://www.ks.uiuc.edu/Research/namd/) package from Schulten's group. The development of software packages for the simulation of complete molecular systems is the subject of several efforts and we envision that modeling and simulation of complex designs will become routine in the near future.

6.2.1
Quantum Mechanical Calculations

Quantum mechanical descriptions provide full detail of the dynamics of the systems under consideration, but the computational cost of solving the governing equations has been limiting these descriptions to small systems involving only a few molecules.

Quantum mechanics phenomena are described by the wavefunction Ψ, which describes the time evolution of electrons and nuclei of particles and by the solution of the equations that was developed in 1925 by Schrödinger:

$$i\hbar \frac{\partial}{\partial t}\Psi = \hat{E}\Psi = \hat{H}\Psi = -\frac{\hbar^2}{2m}\nabla^2\Psi + V(r,t)\Psi \tag{1}$$

where i is the imaginary unit, $\hbar$ is Planck's constant divided by 2π, time is represented by t and the energy operator by $\hat{E}$ and m denotes the mass of the particle. Schrödinger's equation is the quantum mechanical analog of Netwon's laws of classical mechanics. Both descriptions may be unified through the use of a Hamiltonian operator $\hat{H}$, which in this case is the sum of the potential energy operator $V(r, t)$ and the kinetic energy operator. The Schrödinger equation [Equation (1)] used in its time-independent form amounts to an eigenvalue problem that describes the spatial probability distributions corresponding to the energy states in a quantum system. The solution of this equation enables studies of atomistic systems that:

- involve the determining of structure problems, for example questions regarding conformation and configuration of molecular systems as well as geometry optimizations;
- require finding energies under given conditions, for example heat of formation, conformational stability, chemical reactivity and spectral properties.

Analytic solutions of the Schrödinger equations are known only for special cases, where the potential energy contribution to the Hamilton operator is particularly simple as in the case of no potential energy contribution (free particle) or in the case of a single electron in the field of a nucleus (hydrogen atom). In more complex situations, the Schrödinger equation has to be solved by using the Born–Oppenheimer approximation [28]. The Born–Oppenheimer approximation dictates that the nuclei remain fixed in the time scales required for the description of the motion of the electrons. *Ab initio* or *semi-empirical* methods rely on this approximation with different degrees, offering a compromise between accuracy and computational efficiency. *Ab initio* calculations tackle the full form of the equations, whereas *semi-empirical methods* replace some of the time consuming expressions and terms by empirical approximations. The parameters for semi-empirical methods are usually derived either from experimental measurements or from *ab initio* calculations on model systems. *Ab initio* calculations today are

limited to hundreds of atoms whereas methods permit simulations of thousands of atoms. For a detailed description of different methods and the associated approximations the reader is referred to quantum chemistry text books (e.g. [233]).

In the context of our focus on nanoscale fluid mechanics, we focus on the use of *ab initio* methods in studying interactions of water with aromatic systems and the extrapolation of these results to water–graphite interactions.The water–graphite interaction is of particular interest in the field of hydrophobic interactions, which are in turn important in various areas of NFM such as flow in nanopores and protein folding in aqueous environments.

In *ab initio* calculations, molecular orbitals are constructed as linear combinations of atomic orbitals with coefficients obtained via the minimization of the electronic energy of the molecular system. Feller and Jordan [72] used an approach based on second-order Møller–Plesset perturbation theory [184] to calculate the interaction energy between a water molecule and a sequence of centrosymmetric, aromatic systems, consisting of up to 37 aromatic rings. An extrapolation of the results yields an estimated electronic binding energy of $-24.3\,\mathrm{kJ\,mol^{-1}}$ for a single water molecule interacting with a monolayer of graphite. In these calculations, the largest sources of uncertainty are the basis set superposition error, the incompleteness of the basis set and the assumptions regarding the extrapolation from the clusters to the graphite sheet [72]. Note that this estimate of the binding energy of a water molecule to a graphite sheet is appreciably larger than an experimentally determined estimate of $-15\,\mathrm{kJ\,mol^{-1}}$ [72]. Size effects may very well be the reason for this discrepancy. The estimate of the water–graphite binding energy from Feller and Jordan [72] is slightly larger than the interaction between two water molecules but still significantly lower than the average electronic binding energy of a fully solvated water molecule, where hydrogen bonding provides a network leading to high binding energies. High-order QM calculations, such as the second-order Møller–Plesset [184] approach, reproduce the interaction energy of weakly bound molecular systems reasonably well but the systems that can be investigated with these methods are limited in size due to the high computational cost.

More recent *ab initio* calculations rely on the formulation of density functional theory (DFT) [132]. DFT provides an intermediate accuracy at lower computational cost by basing the calculation of system properties on the electron density. This approximation relies on the fact that the ground-state total electronic energy is a function of the density of the system. DFT methods ignore the electron correlations and take advantage of advances in linear algebra in order to provide computations that scale linearly with the number of electron orbitals. DFT simulations describe hydrogen bonds with reasonable accuracy [223]. However, weak interactions, generally denoted dispersion interactions, are not correctly reproduced. The dispersion energy results from correlated fluctuations in the charge density, which contribute to the interaction energy even at distances where electron density overlap is negligible. Since all current DFT energy functionals are approximations based on expressions for local electron density, its gradient and the local kinetic-energy density [195], they fail to reproduce the dispersion contribution to the interaction energy. Andersson and Rydberg [12] and Hult et al. [114, 115] presented

an approach to extend DFT calculations with local or semilocal approximations to include the dispersion contribution, and Rydberg et al. applied it to graphite [211]. Although their model depends on a cutoff to ensure finite polarizabilities at all electron densities [11, 115], their approach is promising with regard to a unified treatement within DFT. Wu et al. [278] concentrated on the interaction between small molecules and presented a systematic search for a possible simplified representation of the weak interaction in DFT. This approach was subsequently extended [284] to deal with the interaction between a flat semiconductor surface and a small molecule. Two distinct models are discussed which serve to calculate lower and upper bounds to the interaction energy. The model assumptions are then validated for a water–benzene system and the method is applied to the water–graphite case, to obtain the lower and upper bound to the wate–graphite interaction.

Wu et al. [278] proposed a correction term ΔE_{disp} to account for the contribution of dispersion energy in the total interaction energy as a damped correction term based on the first term of the dispersion energy expansion [62]. The dispersion energy expansion has the following form:

$$\Delta E_{\text{disp}} = \frac{C_n}{r^n} g_n(r) \tag{2}$$

where C_n denotes the dispersion coefficient, r is the distance between the two centers of mass and n is a geometry-specific integer resulting from theoretical considerations [172, 281]. In the asymptotic limit, at long distances, it can be shown that the coefficents for different geometries map on to each other [120]. Additionally, the dispersion energy correction has to be damped by a geometry-specific damping function $g_n(r)$ which is necessary as the dispersion correction diverges at short range, instead of reaching saturation [62, 234]. The definition of the interaction energy between water and graphite has been described [288]. The minimum interaction energy is computed by considering graphite as a collection of isolated molecules [172], while an upper bound is computed when considering the graphite sheet as an ideal metal [31] where the electrons are free to move, subject only to a homogeneous background charge.

6.2.2
Atomistic Computations

The computational cost of quantum mechanics calculations does not permit simulations of systems containing more than a few hundred atoms. The behavior of larger systems is modeled using molecular dynamics (MD) simulations. MD relies on the description of the molecular system as a set of bonded/nonbonded interacting masses/charges centered at the nuclei of the atoms. The motions of the atoms is determined by solving approximately the equations of Newtonian mechanics that govern the atoms of the system using model interaction force fields. MD simulations involve a large degree of *ad hoc* parameters, they do not readily handle breaking or forming bonds, while the approximate integration of the classical

Newtonian mechanics is susceptible to the well-known Lyapunov instability. At the same time, MD have made remarkable contributions in the accurate prediction of molecular systems in areas ranging from protein folding to the physics of ion channels and the modeling of structural and dynamic properties of complex fluids.

The first MD simulations date back to the mid-1950s in the work of Fermi et al. [73] and Alder and Wainwright [5], where the phase diagram of a hard sphere system was investigated. A few years later, Rahman at Argonne National Laboratory published his seminal work on correlations in the motion of atoms in liquid argon [201]. In 1967, Verlet calculated the phase diagram of argon using the Lennard–Jones potential and computed correlation functions to test theories of the liquid state [259, 260] and 2 years later phase transitions in the same system were investigated by Hansen and Verlet [99]. In 1971, Rahman and Stillinger reported the first simulations of liquid water [202]. Since then, MD simulations have provided a key computational element in physical chemistry, material science and nanofluidics for the study of pure bulk liquids [7], solutions, polymer melts [239] and multiphase and thermal transport [40, 126, 168, 269]. The motion of an ensemble of atoms in MD simulations is governed by interatomic forces obtained from the gradient of a potential energy function. This so-called force field is an approximation of the true interatomic forces arising from the interaction of electrons and nuclei. Thus, the qualitative and quantitative result of MD simulations is intimately related to the ability of the potential energy function to represent the underlying system.

Several "generic" force fields have been developled, ranging from general-purpose force fields capable of describing a wide range of molecules such as the universal force field [203], to specialized force fields designed for graphitic and diamond forms of carbon [32], for covalent systems [237] and models for liquid water [19, 123, 162, 235]. Several classes of force fields have been developed to account for specific types of molecules or chemical systems, e.g. for zeolites [39], for biomolecules such as AMBER [51] and GROMOS [257] and CHARMM for proteins [36] or for organic molecules [174].

With an abundance of potentials and parameters to account for interatomic forces, the user must consider the following criteria for choosing a potential: (i) *accuracy*: the simulation should reproduce as closely as possible the properties of interest; (ii) *generalisation*: the force field expressions should be applicable to situations for which it was not explicitely fitted; (iii) *efficiency*: force calculations are generally the most time-consuming part of a simulation and they should be as efficient as possible.

The proper balance between these criteria depends to a large extent on the system to be investigated. Thus, for NFM studies that involve chemical reactions, the classical representation is usually not sufficient and a quantum or a hybrid quantum-classical technique is required [81, 94] to capture the breaking and formation of chemical bonds. On the other hand, in large-scale simulations of non-reactive systems, computational efficiency is essential and simple expressions for the forces will suffice.

Force fields are generally empirical in the sense that a specific mathematical form is chosen and parameters are adjusted to reproduce available experimental data such as bond lengths, energies, vibrational frequencies and density [84, 162]. Generic force fields are developed in order to be suitable for a wide range of molecules. One should be aware of this fact when considering these generic force fields for the study of a specific system. In this case, it is not uncommon to conduct QM calculations for a small system in order to calibrate MD potentials for the system under consideration as in the case of water–graphite interactions [72, 274]. This can be seen as a model problem for more complex water–carbon interactions such as those involved when considering carbon nanotubes as biosensors and fullerenes as chemical reaction chambers or nanoreactors [137]. Note, however, the added complexity to this problem due to the fact that behavior of water in confined geometries is drastically different to that in bulk systems [116]. Using MD simulations to understand and analyze such systems reliably, it is important to develop suitable models for the simulation of water in such environments.

Whereas water–water potentials are well established in the literature [19, 123, 202, 235], there are no reliable water–nanotube potentials at the moment. In addition, one may need to reconsider the water–water potentials when considering its drastic change in behavior in confined geometries. The starting point for the development of such potentials is the quantification of the interaction of a single water molecule with a single layer of graphite. The reliablity of existing estimates for the interaction energy is questionable as they exhibit large variations, ranging from –5.07 [273] to –24.3 kJ mol^{-1} [72], leaving great uncertainty about predicted behavior. Furthermore, there exist surprisingly few experimental data, with an experimentally determined interaction energy of 15 kJ mol^{-1} [72]. Werder et al. [274] presented a review of recently used interaction potentials for the water–graphite interaction and a relationship between the interaction energy and the contact angle of water on graphite could be determined. There are, however, contradictory measurements of water–graphite contact angles [274], and the actual interaction still remains an open question. The use of experimental results for contact angles of liquids with surfaces for the calibration of MD potentials presents a promising approach for validating MD simulations. The work of Werder et al. [274] in developing water–carbon interaction potentials has been extended to water–silica potentials [52].

6.2.2.1 Molecular Dynamics: Force Fields and Potentials

Molecular dynamics amount to tracking the locations $\boldsymbol{r}_i$, $i = 1, \ldots, N$, of N model particles by solving numerically Newton's equations of motion:

$$m_i \frac{\mathrm{d}^2 r_i}{\mathrm{d}t^2} = \mathbf{F}(r_i, r_j, m_i, m_j, \ldots) \tag{3}$$

$$= -\nabla U(r_i, r_j, m_i, m_j, \ldots) \tag{4}$$

where **F** denotes the force field that can be derived as the gradient of a potential energy U. It is important to note that the approximate integration of these equations makes the trajectories sensitive to perturbations in the initial conditions. MD trajectories should not be viewed as exact representations of the trajectories of the systems that they aim to model, but rather as their statistical representations. The more reliable diagnostics that can be gleaned from MD trajectories are those obtained by suitable spatial and temporal averages.

The potential energy function (U) or force field (**F**) provide a description of the relative energy or forces of the ensemble for any geometric arrangement of its constituent atoms. This description includes energy for bending, stretching and vibrations of the molecules and interaction energies between the molecules. Classical force fields are usually built up as composite potentials, i.e. as sums over many rather simple potential energy expressions. Mostly pair potentials $V(r_{ij})$ are used, but in the case of systems where bonds are determining the structure, multibody contributions $V(r_{ij}, r_{ik})$, and $V(r_{ij}, r_{ik}, r_{il})$ may also enter the expression, thus

$$U = \sum_{i,j} V(r_{ij}) + \sum_{i,j,k} V(r_{ij}, r_{ik}) + \sum_{i,j,k,l} V(r_{ij}, r_{ik}, r_{i,l}) \tag{5}$$

where $r_{ij} = |\boldsymbol{r}_i - \boldsymbol{r}_j|$ is the distance between ith and jth atoms. The contribution to the interaction potential can be ordered in two classes: intramolecular and intermolecular contributions. Whereas the former describe interactions which arise in bonded systems, the latter are usually pair terms between distant atoms.

6.2.2.2 Intramolecular Forces

Various intramolecular potentials are used to described the dynamics of chemical bonds and their interactions. The potential

$$V(r_{ij}) = \frac{1}{2} K_{\mathrm{h}} (r_{ij} - r_0)^2 \tag{6}$$

is developed from consideration of simple harmonic oscillators [73], where r_{ij} and r_0 denote the bond length and the equilibrium bond distance, respectively. The force constant of the bond is given by K_{h}. Alternatively, the Morse potential [185]

$$V(r_{ij}) = K_{\mathrm{M}} (e^{-\beta(r_{ij} - r_0)} - 1)^2 \tag{7}$$

is used, allowing for bond breaking, where K_{M} and β are the strength- and distance-related parameters of the potential, respectively.

For coordination centers, i.e. atoms where several bonds come together, usually bond angle terms are applied, including harmonic bending via

$$V(\theta_{ijk}) = \frac{1}{2} K_{\theta} (\theta_{ijk} - \theta_c)^2 \tag{8}$$

or the harmonic cosine bending via

$$V(\theta_{ijk}) = \frac{1}{2} K_\theta (\cos\theta_{ijk} - \cos\theta_c)^2 \tag{9}$$

where θ_{ijk} is the angle formed by the bonds extending between the ith, jth and kth atoms and θ_c is the equilibrium angle. Dihedral bond potentials are often employed for systems involving chains of bonded atoms, to ensure a consistent representation over several centers [165, 208]:

$$V(\phi_{ijkl}) = \frac{1}{2} \sum_{m=0}^{n} K_m \cos(m\phi_{ijkl}) \tag{10}$$

where the sum can contain up to 12 terms.

As an example, a single-walled carbon nanotube (SWNT) immersed in water was described using the Morse, harmonic cosine and torsion potentials by Walther et al. [268]. The torsion potential was fitted to quantum chemistry calculations of tetracene ($C_{18}H_{12}$) using density functional theory [78].

An alternative to the direct modeling of bonded interactions and intramolecular forces is to constrain the bond length or bond angle [210]. As an example, most water models consider rigid molecules [124]. The high-frequency oscillation of the O–H bonds in water formally requires a quantum mechanical description, and removing these intramolecular degrees of freedom alleviates the problem. The computational efficiency is furthermore significantly improved by allowing a 5–10 times larger time step than the flexible models [235]. The constraints are imposed using iterative procedures such as SHAKE [76, 144, 256], SETTLE [181] or direct methods [280].

6.2.2.3 Intermolecular Forces

Commonly applied intermolecular forces terms are van der Waals forces described through a Lennard-Jones 12–6 potential [152]:

$$V(r_{ij}) = 4\varepsilon \left[\left(\frac{\sigma}{r_{ij}}\right)^{12} - \left(\frac{\sigma}{r_{ij}}\right)^{6} \right] \tag{11}$$

where ε is the depth of the potential well and σ is related to the equilibrium distance between the atoms. The parameters are usually obtained through fitting to experimental data and/or theoretical considerations For multiatomic fluids such as gaseous fluids, the Lorentz–Berthelot mixing rules are often used [7]:

$$\varepsilon_{IJ} = \sqrt{\varepsilon_I \varepsilon_J}, \quad \sigma_{IJ} = \frac{1}{2}(\sigma_I + \sigma_J) \tag{12}$$

where I and J denote the Ith and Jth atomic species. However this approach has been shown to be inadequate for accurate liquid simulations [226], as quantities such as liquid mass density are sensitive to the choice of parameters.

For large surfaces, an average 10–4 Lennard-Jones potential may be obtained by integration of the 12–6 Lennard-Jones over the surface as

$$V(z) = 4\varepsilon\sigma^2\left[\left(\frac{\sigma\pi}{z}\right)^{10} - \left(\frac{\sigma\pi}{z}\right)^{4}\right] \tag{13}$$

where z is the wall normal distance (e.g. [88]). The fast decay of the Lennard–Jones potential usually allows a spherical truncation of the potential at a cutoff distance r_c. Typical cutoff values are 1.5σ for purely repulsive interactions and 2.5σ and 10σ for homogeneous and inhomogeneous systems, respectively.

The long-range electrostatic interactions are described through the Coulomb potential:

$$V(r_{ij}) = \frac{q_i q_j}{4\pi\varepsilon_0 r_{ij}} \tag{14}$$

where q_i and q_j refer to the electric charges of the ith and jth atoms and ε_0 is the permittivity of vacuum. Fractional charges are used for polar molecules and integral values for monatomic ions. The long-range interaction implied by the electrostatics requires fast summation techniques (see Section 6.2.2.4). In order to accelerate the algorithmic development and computational time for homogeneous systems, the Coulomb potential may be truncated using a smoothly tapering of the potential energy function [230]:

$$V(r_{ij}) \approx \frac{q_i q_j}{4\pi\varepsilon_0 r_{ij}} S(r_{ij}) \tag{15}$$

where $S(r)$ is a smoothing function, e.g.

$$S(r_{ij}) = \begin{cases} [1-(r_{ij}/r_c)^2]^2 & r_{ij} < r_c \\ 0 & r_{ij} \geq r_c \end{cases} \tag{16}$$

Note, however, that the results obtained from MD simulations using a truncation may be significantly different from results using Ewald summation, in particular for systems with inhomogeneous charge distributions and for ionic solutions [261]. On the other hand, fast summation techniques may introduce artifically strong correlations in small systems [117] and, when employed with potentials calibrated with truncation, the results using Ewald summation techniques may be less accurate than using truncation [153, 162].

6.2.2.4 **Computational Issues in MD**

Molecular dynamics simulations of heterogeneous nanoscale flows may involve the computation of the interation of several millions of atoms [258]. For example, a cube of water with an edge length of 20 nm contains approximately one million atoms. The most time-consuming aspect of MD simulations of large systems is

the accurate evaluation of the long-range interactions, which include electrostatic and dispersion interactions. Without an explicit cutoff, the computational cost scales as $\mathcal{O}(N^2)$ for N particles. Efficient algorithms have been devised to reduce the computational cost, ranging from simple sorting already provided by Verlet [260] to accurate fast summation techniques such as Ewald summation [70, 197, 213], particle–mesh Ewald (PME) method [54, 69] and the particle–particle particle–mesh technique (P^3M) by Hockney and Eastwood [109, 110, 161, 267]. Whereas Ewald summation requires $\mathcal{O}(N^{1.5})$ operations, the PME and P^3M techniques scale as $\mathcal{O}(N \log N)$.

To achive this computational efficiency, the P^3M method utilizes a grid to solve for the potential field (Φ):

$$\nabla^2 \Phi = -\frac{\rho}{\varepsilon_0} \tag{17}$$

where ρ is the charge density field reconstructed from the charges on to a regular mesh ($\boldsymbol{x}_\mathrm{m}$) by a smooth projection:

$$\rho(\boldsymbol{x}_\mathrm{m}) = \frac{1}{h^3} \sum_i W(\boldsymbol{r}_i - \boldsymbol{x}_\mathrm{m}) q_i \tag{18}$$

and h denotes the mesh spacing. The Poisson equation [Equation (17)] is solved on the mesh using Fast Fourier transforms or efficient multigrid methods with an effective computational cost that scale as $\mathcal{O}(N \log N)$ or $\mathcal{O}(N)$, depending on the specific Poisson solver. The electrostatic field is computed from the potential on the mesh ($\boldsymbol{E} = -\nabla\Phi$) and interpolated on to the particles to allow the calculaton of the electrostatic field:

$$\boldsymbol{f}_i \approx q_i \sum_m W(\boldsymbol{r}_m - \boldsymbol{x}_i) \boldsymbol{E}_m \tag{19}$$

The P^3M algorithm furthermore involves a particle–particle correction term for particles in close proximity (in terms of the grid spacing) to resolve sub-grid scales.

Computations of potential forces employing a grid often involve simulations of periodic systems in order to take advantage of fast potential calculation algorithms such as fast Fourier transforms and multigrid methods. In addition, special care needs to be exercised in grid–particle interpolations so as not to induce spurious dissipation.

In the last 25 years, a number of mesh-free techniques, based on the concept of multipole expansions, have been developed that circumvent the need for simulating periodic systems and have minimal numerical dissipation. Examples of such methods involve the Barnes–Hut algorithm [14], the fast multipole method (FMM) [91, 216] and the Poisson integral method (PIM) [10, 113]. The method employs clustering of particles and uses expansions of the potentials around the cluster

centers with a limited number of terms to calculate their far field influence on to other particles. The savings are proportional to the ration of the number of terms used in the expansions versus the number of particles in the cluster and scales nominally as $\mathcal{O}(N \log N)$. By allowing groups of particles to interact with each other by translating the multipole expansion into a local Taylor expansion, the algorithm achieves an $\mathcal{O}(N)$ scaling. It has been argued that the 3D version of the Greengard–Rokhlin algorithm is not efficient, as it adds nominally a computational cost of $\mathcal{O}(N \times P^4)$, where P is the number of terms retained in the truncated multipole expansion representation of the potential field. However, this issue has been resolved by suitable implementation of fast Fourier transforms [66]. These techniques rely on tree data structures to achieve computational efficiency. The tree allows a spatial grouping of the particles and the interactions of well-separated particles is computed using their center of mass or multipole expansions for the Barnes–Hut and FMM algorithm, respectively.

Another advantage in using tree-data structures is that it allows one to incorporate variable time steps and techniques. For example, in hierarchical internal coordinates [170], some regions may be treated as rigid whereas for others only a subset or all degrees of freedom are considered. The Newton–Euler inverse mass operator method was developed for fast internal coordinate dynamics on a million atoms [170, 254]. For a review of the treatment of long-range electrostatics in molecular dynamics simulations, see [212].

6.2.2.5 **Boundary Conditions for MD**

For situations involving the simulation of a solvent, the small volume of the computational box in which solvent and other molecules of interest are contained can introduce undesirable boundary effects, if the boundaries are modeled as simple walls. To circumvent this problem, either the system may be placed in vacuum [7] or a periodic system may be assumed. In this approach, the original computational box containing the molecular system subject to investigation is surrounded with identical images of itself. Commonly, a cubic or rectangular parallelepiped box is used, but generally all space-filling shapes (e.g. truncated octahedron) are possible [7]. However, periodic boundary conditions imposed on small systems may introduce artifacts in systems that are not inherently periodic [117].

Stochastic boundary conditions allow one to reduce the size of the system by partitioning the system into two zones with different functionality: a reaction zone and a reservoir zone. The reaction zone is the zone intended to be investigated whereas the reservoir zone contains the portion which is of minor interest to the current study. The reservoir zone is excluded from MD calculations and is replaced by random forces whose mean corresponds to the temperature and pressure in the system. The reaction zone is further subdivided into a reaction zone and a buffer zone. The stochastic forces are only applied to atoms of the buffer zone. The application of stochastic boundary conditions to a water model has been described [37] and the method derived [20].

6.2.2.6 Nonequilibrium Molecular Dynamics

To study nonequilibrium processes or dynamic problems, such as flows in capillaries and confined geometries, nonequilibrium MD (NEMD) is found to be a very efficient tool. It is based on the introduction of a flux in thermodynamic properties of the system [7, 49]. NEMD has been reviewed with regard to the computation of transport coefficients of fluids from the knowledge of pair interactions between molecules [53]. Rheological issues have been addressed, focusing on shear thinning and the ordering transition [154]. Ryckaert et al. [209] compared the performance of NEMD with Green–Kubo approaches in order to evaluate the shear viscosity of simple fluids. A modified NEMD approach has been presented to ensure energy conservation [249], and an elongated flow has been studied [245] with both spatial and temporal periodic boundary conditions. For detailed background about the underlying statistical mechanics of nonequilibrium systems, see [61].

Another form of NEMD is steered molecular dynamics (SMD), applied by Grubmüller et al. [92] to determine the rupture force of proteins. The principle of SMD is to superimpose a time-dependent force on selected atoms or molecules such that the molecules or the system are driven along certain degrees of freedom in order to investigate rare events. A short review is provided by Isralewitz et al. [121].

6.2.3 Multiscaling I: Hybrid Quantum/Atomistic Simulations

Multiscale modeling is critical for the development of effective computational tools capable of handling diverse, interacting physical phenomena. In this effort, key advances include the development of suitable interaction potentials for molecular dynamics simulations based on experiments and *ab initio* calculations and the development of multiscale computational methods linking quantum, atomistic and continuum descriptions and the development of efficient multiscaling techniques.

Carr–Parrinello molecular dynamics (CPMD) constitutes one of the archetypal simulations in multiscale modeling. It relies on the Born–Oppenheimer approximation and is based on the classical propagation of the nuclei and the solution of Schrödinger equation in order to obtain the orbitals. Unlike Born–Oppenheimer MD, however, where the atoms do not move during the calculation of the wavefunctions, in CPMD the key concept is to include in the equations of motion the simultaneous evolution of the electrons and the nuclei. Hence this approach does not require that the energy associated with the electronic degrees of freedom is computed at each time step in order to obtain the new orbitals. Nuclei and electrons evolve at the same time-scale, allowing the trajectories to progress above the Born–Oppenheimer potential energy. The CPMD approach allows that the wavefunctions of the Schrödinger equations are calculated once at each state, resulting in tremendous computational savings that are bound to become

even more important as the method is being successfully implemented in massively parallel computer architectures (see http://www.cpmd.org and references therein).

CPMD techniques have become the method of choice in several investigations of biomolecules, partly due to their capability to simulate accurately spontaneous events such as proton transfer and the formation and breaking of bonds. We expect that the interface of biomolecules with nanodevices will provide a fertile ground for the applications of these methods. We note, however, that in the case where the nanodevices and biomolecules are embedded in solvents that are important for the dynamics of the systems, CPMD techniques may still be computationally intensive.

Alternatively, hybrid techniques that separate the quantum and molecular descriptions in different regions of the molecular system have been developed following the pioneering work of Warshel and Levitt in 1976 [272] on the simulation of enzymic reactions. These so-called quantum mechanics/molecular mechanics (QM/MM) calculations aim to bridge the gap between accurate, but expensive, quantum mechanical and computationally efficient, yet largely approximate, atomistic descriptions of molecular systems. Simulations using QM/MM approaches have found numerous applications, in particular for the simulation of biomolecular systems.

In the QM/MM approach, a certain core region of the molecular system is treated quantum mechanically using the Born–Oppenheimer approximation, thus allowing changes at the electronic level. The dynamic motion of the of the surrounding regions is treated classically, usually by employing MD. The potential energy of the whole system is decomposed into the following terms:

$$U = U_{\mathrm{QM}} + U_{\mathrm{QM/MM}} + U_{\mathrm{MM}} \tag{20}$$

where the quantum contribution U_{QM} can be identified with the Hamiltonian of the time-independent Schrödinger equations [Equation (1)], U_{MM} is a classical MD potential energy and $U_{\mathrm{QM/MM}}$ is the potential of the quantum/classical description coupling. The crucial point in $Q_{\mathrm{M/MM}}$ calculations is the treatment of the interface between the classical and quantum mechanical regions as it is handled by the $U_{\mathrm{QM/MM}}$ potential. Employing the nomenclature of MD, different coupling potentials can be distinguished by the treatment of the bonded and non-bonded molecular interactions. Following [60], we distinguish three types of coupling schemes:

- *Mechanical embedding*. The coupling does not involve any bonded molecular interactions and the interactions consist of classical van der Waals interactions as described by a Lennard–Jones potential:

$$U^{\mathrm{vdW}}_{\mathrm{QM/MM}} = \sum_{i\in \mathrm{MM}\,\&\, j\in \mathrm{QM}} 4\varepsilon_{ij}\left[\left(\frac{\sigma_{ij}}{r_i - r_j}\right)^{12} - \left(\frac{\sigma_{ij}}{r_i - r_j}\right)^{6}\right] \tag{21}$$

where QM and MM indicate the atoms in the QM and MM domains, respectively. The Lennard–Jones parameters are usually adopted from the MD potentials.

- *Electrostatic embedding*. In this coupling, electrostatic interactions are taken into account in addition to the van der Waals steric forces. The electrostatic potential can be expressed as

$$U^{\mathrm{el}}_{\mathrm{QM/MM}} = \sum_{i \in \mathrm{MM}} q_i \int \frac{\rho(r)}{r - r_i} \mathrm{d}r \tag{22}$$

where q_i indicates the charge located at r_i in the MM region and $\rho(r)$ denotes the charge density in the QM part of the domain. The Lennard-Jones parameters are usually adopted from the MD potentials. A number of different implementations (see [60, 238] and references therein) address modifications of the MM potential in the vicinity of the QM region so that the potential remains finite for $r - r_i \to 0$.

- *Covalent embedding*. This is the most sophisticated coupling, where covalent bonds between atoms in the QM and MM regions, in addition to steric and electrostatic electrostatic interactions, are taken into account. A number of approaches exist in order to tackle the presence of bonds across the QM/MM boundaries. The reader is referred to the excellent recent review by Senn and Thiel [220] for a survey of current approaches.

The use of QM/MM techniques in the simulations of molecular systems is rapidly expending. In computational nanotechnology, simulations using QM/MM approaches are not widespread. We expect that these types of simulations will become more important in the simulation of the interactions of biomolecular systems with nanodevices.

6.2.4
Multiscaling II: Hybrid Atomistic–Continuum Simulations

Multiscale computational modeling is required in order to describe effectively nanoscale phenomena that influence the behaviour of micro- and macroscale flows. Examples include drag reduction phenomena for flows over nanopatterned surfaces and the motion of droplets as influenced by the structure of the contact line. The simulation of such flows is challenging as one needs to couple the nanoscale systems suitably with larger spatial and time-scales. The macroscale flows determine the external conditions that influence the nanoscale system, which in turn influences the larger scales by modifying its boundary conditions.

The conservation of the system's mass, momentum and energy together with the continuum assumption lead to the compressible Navier–Stokes equations. The last 50 years has seen extensive research on the numerical simulation of these flows and a review is beyond the scope of the present chapter. These equations inherently involve the computation of averaged quantities of the flow field. Hence as in micro- and nanoscale flows the continuum assumption and/or the associated constitutive relations eventually break down, along with them breaks down the validity of the Navier–Stokes equations. Atomistic descriptions, such as MD, are suitable for simulating the behavior of nanoscale systems while computational solutions of the Navier–Stokes equations account effectively for continuum hydrodynamics. One may always consider modeling atomisticaly a fluid at these scales, with a description such as direct simulation Monte Carlo (DSMC) for dilute gases or MD for liquids. Both methods are, however, subject to enormous CPU time requirements. An example of a recent MD study involving long simulation times (400 ns, 512 water molecules) is that by Matsumoto et al. [171], where they studied the formation of ice.

To illustrate these limitations of MD, consider that the time step δt in an MD simulation is dictated by the fastest frequency one needs to resolve. For a simulation of pure water, $\delta t = 2$ fs when models with fixed O—H bonds and H—O—H angles are used; in other words, 500 million time steps are required for 1 μs of simulation time. With the optimistic assumption that the execution of single time step takes 0.1 s, a total of some 19 months of CPU time is required. Computational requirements for the simulation of transport across nanoscale channels has been identified as a challenging multiscale problem due to the disparate scales that are present. In their review article, Aluru et al. [8] proposed the use of continum simulation techniques for handling the complex geometries to resolve the drift–diffusion equation for charge flow. At the same time ion travesal can be a rather rare event. Continuum models can then be parameterized to match current–voltage characteristics by specifying a suitable space- and/or energy-dependent diffusion coefficient which accounts for the ions' interactions with the local environment. Particle methods can be implemented for the solution of such flows. A Brownian dynamics approach can be used for the description of the ion flow, in which ion trajectories evolve according to the Langevin equation. An *N*-body solver can be used to account for all the pairwise ion interactions while external forces induced by the potential can be computed from solving the potential equation for the externally computed potential fields. A frictional term is included to account for ion–water scattering, while a short-range repulsion term is used in order to account for ionic core repulsion. MD and Monte Carlo methods can be used to model water–ion interactions while Monte Carlo methods offer an interesting alternative as water and protein are treated as background dielectric media and only the individual ion trajectories are resolved [9].

The need for efficient computations dictates a hybrid approach to integrate atomistic simulations with finite volume approximations and lattice Boltzmann models of the Navier–Stokes equations, for simulations of flows at larger scales

[143]. A number of hybrid models [75, 96, 187] coupling atomistic to continuum descriptions of dense fluids have been proposed.

An early attempt to extend the length scales accessible in MD simulations of fluids was undertaken by O'Connell and Thompson [192]. In their simulations, the particle (P) and continuum (C) regions were connected through an overlap region (X). The overlap region was used to ensure continuity of the momentum flux – or, equivalently, of the stress – across the interface between the P and the C regions. The average momentum of the overlap particles was adjusted through the application of constrained dynamics. The continuum boundary conditions at C were taken to be the spatially and temporally averaged particle velocities. O'Connell and Thompson [192] applied this algorithm to an impulsively started Couette flow where the P–C interface was chosen to be parallel to the walls. This ensured that there was no net mass flux across the MD–continuum interface. As pointed out by Hadjiconstantinou and Patera [96], the scheme proposed by O'Connell and Thompson decouples length-scales, but not time-scales. Hadjiconstantinou and Patera [95, 96] therefore suggested using the Schwarz alternating method for hybrid atomistic–continuum models. The continuum solution in C provides boundary conditions for a subsequent atomistic solution in P, which in turn results in boundary conditions for the continuum solution. The iteration is terminated when the solution in the overlap region X is identical for both the particle and the continuum descriptions. The use of the Schwarz method avoids the imposition of fluxes in the overlap region, since flux continuity is automatically ensured if the transport coefficients in the two regions are consistent. The Schwarz method is inherently bound to steady-state problems. However, for cases in which the hydrodynamic time-scales are much larger than the molecular time-scales, a series of quasi-steady Schwarz iterations can be used to treat transient problems [96].

Flekkøy et al. [75] presented a hybrid model, which, in contrast to earlier hybrid schemes [95, 192], is explicitly based on direct flux exchange between the particle region and the continuum region. This scheme is robust in the sense that it does not rely on the use of the exact constitutive relations and equations of state to maintain mass, momentum and energy conservation laws. The main difficulty in the approach of Flekkøy et al. [75] arises in the imposition of the flux boundary condition from the continuum region on the particle region. The scheme was tested for a two-dimensional Lennard-Jones fluid coupled to a continuum region described by the compressible Navier–Stokes (NS) equations. To ensure consistency and to complement the NS equations, the viscosity ν and the equation of state $p = p(\rho, T)$ were measured in separate particle simulations. The first test was a Couette shear flow parallel to the P–C interface, and the second test involved a Poiseuille flow where the flow direction was perpendicular to the P–C interface. In both cases, good agreement between the observed and the expected velocity profiles was achieved. Wagner et al. [266] extended this work to include the energy equation and applied the technique to flow in a channel.

The issue of the sense in which the continuum description plays the role of a statistical mechanical reservoir for the particle region in a hybrid computation was studied by Flekkøy et al. [74] and Alexander et al. [6]. Both studies employed the

example of a one-dimensional diffusion process. Flekkøy et al. [74] used a finite difference (FD) discretization of the one-dimensional (deterministic) diffusion equation coupled to a system of random walkers moving on a lattice. They found that the size of the particle fluctuations interpolates between those of an open system and those of a closed system, depending on the ratio between the grid spacing of the FD discretization and the particle lattice constant. Alexander et al. [6] showed that a coupling of the deterministic diffusion equation to a system of random walkers does capture the mean of the density fluctuations across the particle–continuum interface but that it fails in capturing the correct variance close to the interface. With a stochastic hybrid algorithm, where the fluctuating diffusion equation is solved in the continuum region, both the expected mean and variance of the density fluctuations are recovered.

Finally, Garcia et al. [82] proposed a coupling of a direct simulation Monte Carlo (DSMC) solver embedded within an adaptive compressible Navier–Stokes solver. They successfully tested their scheme on systems such as an impulsively started piston and flow past a sphere. The DSMC method is, however, restricted to dilute particle systems. In order to maximize the effectivity of any hybrid scheme, the interface location must be chosen such that both schemes are valid around it, and such that the extent of the more expensive scheme is minimized. To locate this interface automatically, a variety of Navier–Stokes breakdown parameters have appeared in the literature [21, 30, 82, 244]. These parameters are based on the coefficients of the higher order terms of the Chapman–Enskog expansion of the solution of the Boltzmann equation. However, the validity and the cutoff value of these parameters are not very well understood yet.

Werder et al. [275] identified several computational difficulties in coupling atomistic and continuum descriptions. These difficulties are mostly attributed to the elimination of periodicity in the MD description and the resulting disturbance of the material properties on the atomistic regime (density, pressure fluctuations, etc.). A boundary force, based on the physics of the fluid being simulated [275], has been proposed in order to compensate for the density variations often observed in these couplings. This technique was initially developed for coupling MD and finite volume discretizations of the incompressible Navier–Stokes equations. The technique has been extended by coupling the MD simulations with a lattice Boltzmann (LB) method [65] of the incompressible NS equations, enhancing the exchange between atomistic and continuum domains by communicating velocity gradients in addition to velocities.

The simulations involved flow of a liquid past a carbon nanotube (CNT). An MD model describes the flow in the vicinity of a CNT whereas an LB approach is used to simulate the behaviour of the continuum system away from the CNT. The continuum hydrodynamics are described by the incompressible Navier–Stokes equations:

$$\frac{\partial \mathbf{u}}{\partial t} + (\mathbf{u}\cdot\nabla)\mathbf{u} = -\nabla p/\rho + \nu\nabla^2\mathbf{u} + \mathbf{g} \tag{23}$$

$$\nabla\cdot\mathbf{u} = 0 \tag{24}$$

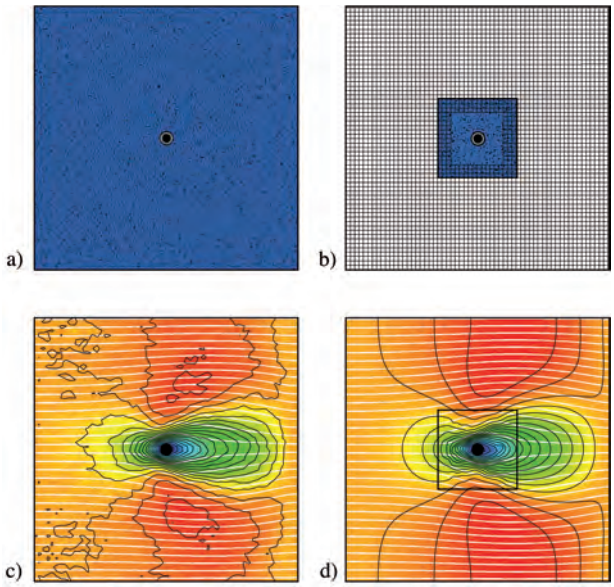

Figure 6.1 a) Computational domain for the reference solution of the flow of argon around a carbon nanotube using a purely atomistic description. b) Hybrid atomistic/continuum computational domain. Both computational domains have an extent of 30×30 nm. c) Velocity field for the reference solution averaged over 4 ns. The white lines are streamlines, and the black lines are contours of the speed ($|u|$). d) Velocity field of the hybrid solution after 50 iterations. The black square denotes the location of Γ_A. The solution in Ω_A is averaged over 10 iterations.

where $\mathbf{u}$ is the fluid velocity, p the pressure, ρ the density and $\mathbf{g}$ a body force. The body force is used in order to take into account boundary conditions at the interface of the continuum domain with the atomistic regime.

The atomistic and continuum descriptions are coupled in a hybrid approach based on a Schwarz domain decomposition technique, originally proposed in [96]. The key assumption of this hybrid approach is that the decomposition of the system is valid and that the two descriptions match in the overlap domain (see Figure 6.1).

A Schwarz iteration t_c consists of computing the continuum velocity field $\mathbf{u}_c(t_c)$ with boundary conditions set by the previous atomistic cycle $\mathbf{u}_a(t_c - 1)$ and an external boundary condition that depends on the system considered. Then, $\mathbf{u}_c(t_c)$ is used to set the boundary condition for computing $\mathbf{u}_a(t_c)$. MD velocities are sampled in cells of the same size as in the LB domain and are enforced on the continuum according to two coupling methods. The first approach corresponds to the one used by Werder et al. [275] and is to impose MD velocities within a one cell wide strip located at a distance δ_s of the MD subdomain (see Figure 6.2). This velocity coupling (VC) approach does not enforce velocity gradients implying that the geometry of the system and the external boundary conditions dictate whether

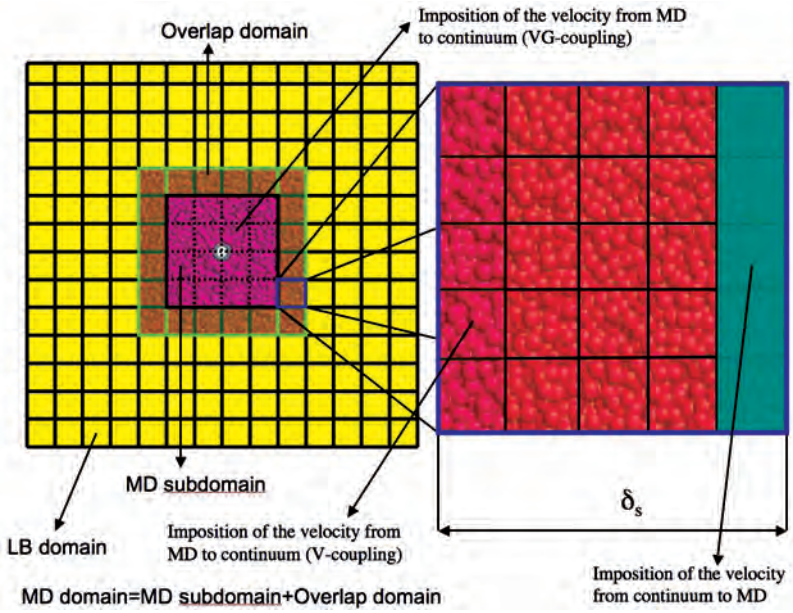

Figure 6.2 Domain decomposition. The converged solution is obtained by alternating iterations in the LB and MD domains. We consider two ways for imposing the velocity boundary condition from the MD to the continuum. In the case of V-coupling we pass the velocities within a one-cell wide strip located at distance δ_s from the end of the MD domain. In the case of the VG-coupling we impose MD velocities on every common cell except within a strip of width δ_s close to the boundary.

the hybrid solution evolves into a good approximation of the reference solution. To alleviate this issue, an enriched coupling method was proposed which enforces velocities, and implicitly velocity gradients (VGC) by imposing MD velocities on every common cell except within a strip of width δ_s close to the boundary (see Figure 6.2).

Dupuis et al. [65] compared hybrid simulations of the flow past a CNT embedded normal to the flow direction with the results of Werder et al. [275]. The results indicate that the VGC approach leads to a closer match with MD reference solutions than the VC method.

Werder et al. [275] combined a hard wall with boundary potentials based on the radial distribution function of the system that is being simulated in order to impose the local system pressure. This scheme was found to reduce significantly the density perturbations in the molecular system compared with existing algorithms at the supercritical state point ($T^* = 1.8$, $\rho^* = 0.6$). Kotsalis et al. [142] demonstrated that even this approach cannot fully eliminate density oscillations whose amplitude depends on the state point of the liquid. The validity of this method was examined in an additional state point in the liquid regime ($T^* = 0.7$, $\rho^* = 0.89$). The method was found to encounter difficulties when lowering the temperature, while increasing the density, at constant pressure, leading to density

oscillations close to the boundary. The amplitude of these oscillations amounts to 15% and is well below previously reported values in hybrid simulations [275] but they may still cause unnecessary disturbances to the atomistic system. A novel mean external boundary force using a control algorithm was developed [142] in order to minimize the density perturbations in the MD system. During each iteration the algorithm starts by applying the external boundary force as proposed [275]. Then the MD simulation is conducted for sufficiently long times to sample the density with an uncertainty of less than 2%. The error is then evaluated according to

$$e(r_w) = \rho^{\mathrm{t}} - \rho^{\mathrm{m}}(r_w) \tag{25}$$

where r_w is the distance to the boundary, ρ^{t} the desired constant target density and ρ^{m} the measured value. We compute the gradient of this error as $\varepsilon(r_w) = \nabla e(r_w) = -\nabla\rho^{\mathrm{m}}(r_w)$ and amplify this with a factor K_P . We filter the resulting signal to avoid spurious oscillations during the iteration process to obtain the changes ΔF in the boundary force. The boundary force is finally computed as

$$F_i^{\mathrm{new}} = F_i^{\mathrm{old}} + \Delta F_i \tag{26}$$

This approach was tested for the state point ($T^* = 0.7$, $\rho^* = 0.89$) where the mean force algorithm of Werder et al. [275] failed to eliminate fluctuations. The results demonstrate that the method converges and eliminates the density oscillations.

6.2.4.1 Mesoscopic Models: Dissipative Particle Dynamics

Coarse-grained models attempt to find a mesoscale description that allows for the simulation of complex fluids such as colloidal suspensions, emulsions, polymers and multiphase flows. The initial formulation of the dissipative particle dynamics (DPD) model was given by Hoogerbrugge and Koelman [112]. It is based on the notion of *fluid particles* representing a collection of atoms or molecules that constitute the fluid. These fluid particles interact pairwise through three types of forces i.e. the force on particle i is given by

$$\boldsymbol{f}_i = \sum_{j \neq i} [\boldsymbol{F}^{\mathrm{C}}(r_{ij}) + \boldsymbol{F}^{\mathrm{D}}(\boldsymbol{r}_{ij}, \boldsymbol{u}_{ij}) + \boldsymbol{F}^{\mathrm{R}}(\boldsymbol{r}_{ij})] \tag{27}$$

where

- $\boldsymbol{F}^{\mathrm{C}}$ represents a conservative force which is derived from a soft repulsive potential, allowing for large time steps.
- The dissipative force $\boldsymbol{F}^{\mathrm{D}}$ depends on the relative velocity $\boldsymbol{u}_{ij}$ of the particles with respect to model friction:

$$\boldsymbol{F}_{ij}^{\mathrm{D}} = -\gamma\omega^{\mathrm{D}}(r_{ij})(\boldsymbol{u}_{ij} \cdot \hat{\boldsymbol{r}}_{ij})\hat{\boldsymbol{r}}_{ij} \tag{28}$$

  where $\hat{\boldsymbol{r}}_{ij}$ is a unit vector and γ a scalar.

- Finally, a stochastic force $\boldsymbol{F}_{ij}^{\mathrm{R}}$ models the effect of the suppressed degrees of freedom in the form of thermal fluctuations of amplitude σ:

$$\boldsymbol{F}_{ij}^{\mathrm{R}} = \sigma\omega^{\mathrm{R}}(r_{ij})\xi_{ij}\boldsymbol{r}_{ij} \tag{29}$$

  where ξ is a random variable.

Both $\boldsymbol{F}_{ij}^{\mathrm{D}}$, and $\boldsymbol{F}_{ij}^{\mathrm{R}}$ include r-dependent weight functions ω^{D} and ω^{R}, respectively. These weight functions and amplitudes σ and γ must satisfy

$$w^{\mathrm{D}}(r) = [w^{\mathrm{R}}(r)]^2, \quad \sigma^2 = 2\gamma k_{\mathrm{B}}T \tag{30}$$

in order to simulate a canonical ensemble [68]. A review of DPD applied to complex fluids was given by Warren [271]. Although DPD has had considerable success in simulations of flows with polymers, its formulation has a conceptual difficulty [67, 221]. First, its thermodynamic behavior is determined by the conservative forces and is therefore an output of the model and not (as desirable) an input. In addition, the physical scales that are simulated are not clearly defined. Reviews on mesoscale simulations of polymer materials have been published by Glotzer and Paul [85] and Kremer and Müller-Plathe [145].

Español and Revenga [67] recently introduced the smoothed Dissipative Particle Dynamics method (SDPD), which combines elements of Smoothed Particle Hydrodynamics (SPH) with DPD. SDPD emerges from a top-down approach, i.e. from a particle discretization of the Navier–Stokes equations in Lagrangian form similar to the SPH formulation. Every particle has an associated position, velocity, constant mass and entropy. Two additional extensive variables, a volume and an internal energy, are associated with every particle. The particle volume allows one to give the conservative forces of the original DPD model in terms of pressure forces. Most importantly, the interpolant used in the SDPD formulation fulfills the second law of thermodynamics explicitly and thus allows for the consistent introduction of thermal fluctuations through the use of the dissipation–fluctuation theorem. This will allow one to study, for example, the influence of thermal effects on the formation of bubbles.

6.3 Fluid–Solid Interfaces at the Nanoscale

Hydrophobic effects and wetting phenomena have a long-standing history and open questions remain for both areas. The emphasis in this section is on the computational efforts to understand the molecular nature of wetting and hydrophobicity. Recent reviews on the general molecular theory of hydrophobic effects have been published by Pratt [199] and Pratt and Pohorille [200].

6.3.1
Hydrophobicity and Wetting

The attribute *hydrophobic* (water-fearing) is commonly used to characterize substances such as oil that do not mix with water. The classical interpretation of this phenomenon is that the interaction between the water molecules is so strong that it results in an effective oil–oil attraction. Interestingly, oil and water do in fact attract each other, but not nearly as much as water attracts itself. Lazaridis [149] performed a series of MD simulations with hypothetical solvents to identify the solvent characteristics that are necessary conditions for general solvophobic behavior. His findings support the classical view that solvophobicity is observed when the solvent–solvent interaction strength clearly exceeds the solvent–solute interaction. In the case of water, the large cohesive energy is mainly due to the strong hydrogen bond network. The importance of the hydrophobic effect as a source of protein stability was first identified by Kauzmann [129] and a review on dominant forces in protein folding was given by Dill [59]. At a certain solute size (around 1 nm), it becomes energetically more favorable to assemble hydrophobic units than to keep them apart by thermal agitation [44, 159].

The spreading and wetting of water on hydrophobic/hydrophilic surfaces are a related subject of great practical interest where substantial insight has been gained through the help of computation. The wetting behavior of a surface could be characterized through the contact angle that a liquid forms on it. One can distinguish at least two different states, namely the wetting state, where a liquid spreads over the substrate to form a uniform film, and the partial wetting state, where the contact angle lies in between 0° and 90°. The microscopic contact angle θ for a droplet with base radius r is given by the modified Young's equation [29]:

$$\gamma_{SV} = \gamma_{SL} + \gamma_{LV} \cos\theta + \frac{\tau}{r} \tag{31}$$

where the γs denote the surface tensions between the solid (S), liquid (L) and vapor (V) phases and τ is the tension associated with the three-phase contact line. In the limit of macroscopic droplets, the effect of the line tension τ becomes insignificant, i.e. for $r \to \infty$, Equation (31) reduces to the well-known Young's equation [274]. In the following, we review computational studies that aim at studying the validity of macroscopic concepts such as Young's or Laplace's equations at the nanoscale and at the molecular characterization (ordering, orientation, etc.) of a liquid at a hydrophobic–hydrophilic interface.

The wetting and drying of a liquid and a vapor phase enclosed between parallel walls were studied by Saville [214], Sikkenk et al. [222] and Nijmeijer et al. [188, 189]. The main difference in their simulations was the representation of the confining wall. The introduction of an "inert" wall [189] leads to good agreement between visually observed contact angles and those deduced from the surface tensions through Young's equation.

Hautman and Klein [102] performed one of the first MD studies to investigate a liquid droplet on different solid substrates. They observed the equilibrium contact angle of water droplets containing merely 90 molecules on hydrophobic and hydrophilic surfaces which were formed by monolayers of long-chain molecules with terminal $-CH_3$ and $-OH$ groups, respectively.

Thompson et al. [243] tested and confirmed the validity of Young's and of Laplace's equation at microscopic scales for a fluid–fluid interface in a channel. The wetting properties of the fluids were controlled by setting different interaction strengths between the fluids and the wall; all interactions were modeled using the Lennard–Jones potential. Fan and Cağin [71] simulated the wetting of crystalline polymer surfaces by water droplets containing 216 water molecules. Furthermore, they introduced a different way to measure the contact angle between a liquid and a solid surface using the volume and contact area of the droplet instead of the droplet center-of-mass height above the surface. The dynamics of spreading at the molecular level were first studied by de Ruijter et al. [57, 58]. They monitored the relaxation of the contact angle for a fluid modeled by linear chain molecules and obtained good agreement with a molecular kinetic theory of wetting. MD studies of heat transfer at solid liquid interfaces has been reported [168]. Reviews of the dynamics of wetting have appeared [55, 264].

Bresme and Quirke [33, 34] investigated by means of MD simulations the wetting and drying transitions of spherical particulates at a liquid–vapor interface as a function of the fluid–particulate interaction strengths and of the particulate size. They showed that the wetting transition for a small particulate occurs at a weaker interaction strength than for a large one. This suggests that a change in geometry of the particulate enhances its solubility. In a subsequent study, Bresme and Quirke [35] analyzed the dependence of the spreading of a lens in a liquid–liquid interface in terms of the liquid–lens surface tension. It was found that this dependence is well described by Neumann's construction, which is the analog to Young's equation when the three phases in contact are deformable. Werder et al. [273] studied the behavior of water droplets confined in pristine carbon nanotubes using molecular dynamics simulations. (Figure 6.3). They found contact angles of 110°, indicating a nonwetting behavior. Lundgren et al. [160] studied the wetting of water and water–ethanol droplets on graphite. For pure water droplets they found contact angles that were in good agreement with the experimentally observed values. Upon addition of ethanol, the contact angle decreased as expected and the ethanol molecules were concentrated close to the hydrophobic surface and at the water–vapor interface. Werder et al. [274] used the known wetting behavior of water on graphite to calibrate the water–graphite interaction in MD simulations (Figure 6.4). They found that water monomer binding energies of –6.33 and –9.37 $kJ\,mol^{-1}$ are required to recover, in the macroscopic limit, contact angles of 86° [77] and 42° [219], respectively. These binding energies include a correction to account for the line tension which, through MD simulations of droplets of different sizes, is estimated to be positive and in the order of $2 \times 10^{-10}\,J\,m^{-1}$. For a simple Lennard–Jones interaction potential acting between the oxygen atoms of the water and the carbon atom sites, the corresponding interaction parameters to obtain the desired binding

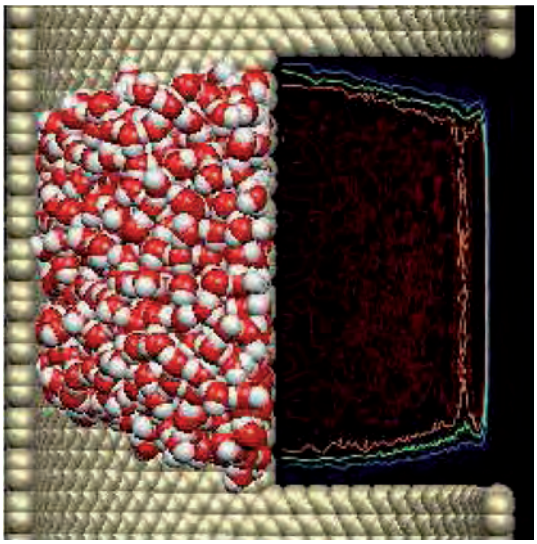

Figure 6.3 Molecular dynamics simulation of the contact angle of water droplets in single walled carbon nanotubes [273]. The molecular structure (left) and the time averaged isochor profiles (right) indicate a non-wetting behaviour of the 5 nm diameter water droplet.

energies are $\sigma_{CO} = 3.19$ Å, $\varepsilon_{CO} = 0.392\,\mathrm{kJ\,mol^{-1}}$and $\varepsilon_{CO} = 0.5643\,\mathrm{kJ\,mol^{-1}}$. This technique of using the contact angle to estimate the parameters of interacting molecules has been recently extended to the interactions of water and silica [52].

The addition of doping such as —OH terminals on graphite surfaces can be responsible for increased wetting as it has been shown in MD simulations [14]. These simulations may help to explain increased wetting inside carbon nanotubes that have been observed experimentally [86] (see Figure 6.5).

6.3.2
Slip at Fluid–Solid Interfaces

The conditions at a fluid–solid interface are of paramount interest in order to develop suitable computational models and to understand the governing physical mechanisms in order to design effective nanodevices. On the nanoscale, the fluid–solid interfaces assume greater importance because the surface-to-volume ratio is larger than in macroscale flows and the flow length scale approaches the fluid molecule size. When solids are immersed in fluids, the boundary condition usually adopted in the modeling equations of the macroscale systems is a vanishing relative velocity between the fluid and the solid surface – the *no-slip* condition [186, 231].

One of the fundamental questions in the context of micro- and nanofluidics is the range of validity of the Navier–Stokes equations and of the associated no-slip boundary condition. This range can be parametrized by the Knudsen number *Kn*,

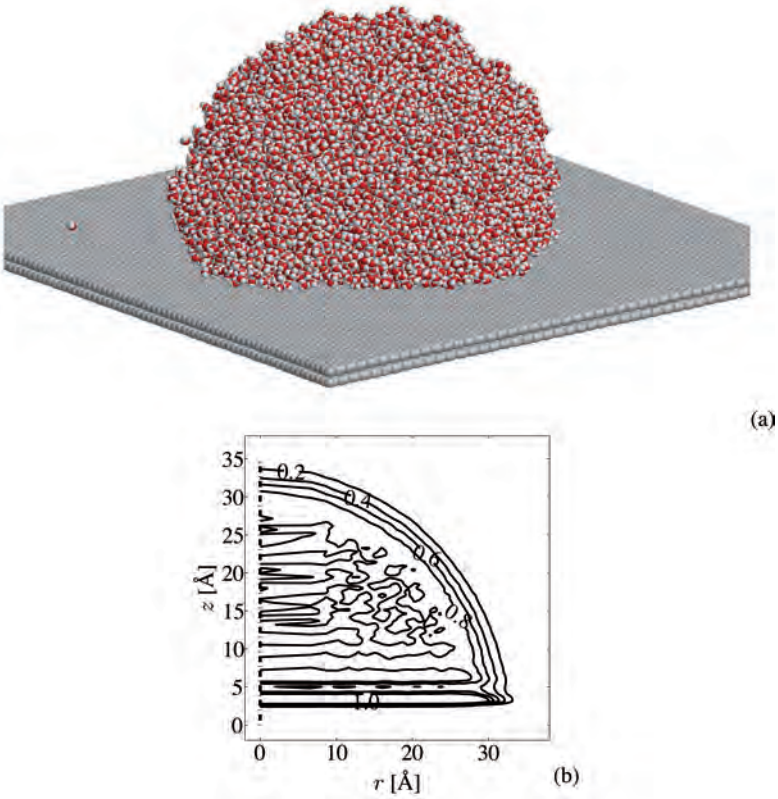

Figure 6.4 Side view of a 5 nm large water droplet on graphite (a). From molecular dynamics simulations by Werder et al. [273]. The contact angle is extracted from the time averaged water isochore profile (b). The isochore levels are 0.2, 0.4, 0.6, 0.8, and 1.0 g cm^{-3}.

which is defined as the ratio between the mean free path and a characteristic length L of the system under consideration. The value of the Knudsen number determines the degree of *rarefaction* of the fluid and therefore the validity of the continuum flow assumption. Note that a *local* Knudsen number can be defined when L is taken to be the scale L of the macroscopic gradients [22]: $L = \rho/(\mathrm{d}\rho/\mathrm{d}x)$. Until recently, noncontinuum (rarefied) gas flows were only encountered in low-density applications such as in the simulation of space shuttle re-entries. However, in micro- and even more in nanofluidic applications, such as flows in nanopores or around nanoparticles, rarefaction effects are important at much higher pressures, due to the small characteristic length scales and the large gradients [128]. An empirical classification of gas flows is the following [22]: For $Kn < 0.01$, the flow is in the *continuum regime* and can be well described by the Navier–Stokes

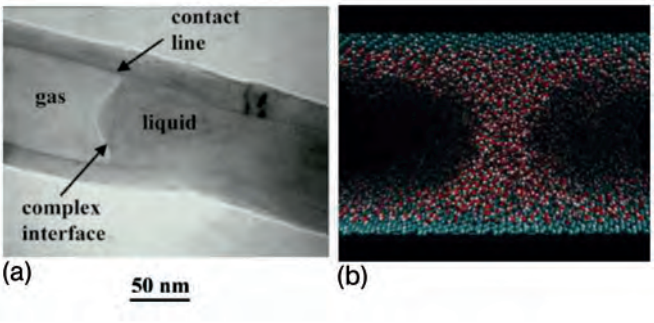

Figure 6.5 Experiments and simulations of demonstrating wetting of the interior of doped carbon nanotubes. Left image shows TEM microgrpahis of an aqueous solution trapped in a closed multi walled carbon nanotube [86]. Right image shows enhanced wetting of a carbon nanotubes with a 10% doping of its surface by —OH radicals [141].

equations with no-slip boundary conditions. For $0.01 < Kn < 0.1$, the Navier–Stokes equations can still be used to describe the flow, provided that tangential slip-velocity boundary conditions are implemented along the walls of the flow domain. This is usually referred to as the *slip-flow* regime. In the *transition regime*, for $0.1 < Kn < 10$, the constitutive equation for the stress tensor of a Newtonian fluid starts to lose its validity. In this case, higher order corrections to the constitutive equations are needed, such as the Burnett or Woods equations, along with higher order slip models at the boundary. At even larger Knudsen numbers ($Kn > 10$), the continuum assumption fails completely and atomistic descriptions of the gas flow are needed [22].

6.3.2.1 Experimental Evidence of No-Slip

Experimental evidence of the no-slip condition at wetting surfaces was provided by Whetham [276] and Bulkley [38]. On the other hand, slip is found to exist in narrow, hydrophobic capillaries, as demonstrated by Helmholtz and von Piotrowski [104] and later confirmed by Schnell [217], Churaev et al. [48] and Baudry et al. [16]. A thorough review of earlier work concerning the manifestation of slip can be consulted [262]. The existence of no-slip conditions for liquid flows in confined spaces is further complicated by the unusual behavior of the fluid properties associated with phase changes of the fluid. For water, strong density fluctuations are observed within 1 nm of the solid surface [150], and the water orientation and hydrogen bonding are perturbed [215]. Granick [90] found that the viscosity attains a significantly higher value when the fluid is confined leading to a stick–slip behaviour [25, 43], or solidification when the film thickness becomes sufficiently small [131].

One important and as yet unresolved question in NFM is the amount of slip occurring at hydrophilic surfaces. Bonaccurso et al. [27] observed a persistent slip

in measurements of water on mica and glass, whereas Vinogradova and Yakubov [263] found a no-slip condition in drainage experiments of thin films between silica surface.

The question remains if the transition from no-slip to slip follows the limit of zero to nonzero contact angle of the fluid solid interface, or if (weakly) hydrophobic surfaces can support a no-slip condition. The experimental evidence is strongly affected by uncertainties such as surface roughness, entrapped gas or vapor bubbles [13, 252], chemical impurities [262] and the purity of the fluid [204]. Alternatively, molecular dynamics simulations free of such impurities may provide valuable insight into the nature of the no-slip condition. At the same time, such conjectures rely on the existence of accurate interaction potentials that describe the fluid–solid interface.

In order to extend continuum fluid dynamics modeling to nanoscale flow systems, the liquid–solid boundary conditions must be determined and parameterized [138], and the length scale where molecular-size effects become important should be known. In contrast to traditional continuum modeling, taking into account nanoscale flow phenomena implies that the conditions will depend on the specific molecular nature of the fluid and the surface.

The slip velocity Δu at a surface may be modeled according to Maxwell [173] as

$$\Delta u = b\frac{\partial u}{\partial y} \tag{32}$$

where b is the slip length, $\alpha = 1/b$ is the slip coefficient and $\partial u/\partial y$ denotes the shear stress at the interface as shown in Figure 6.6. The slip length is a function of the properties of the fluid–solid interface. At hydrophobic surfaces, Churaev et al. [48] and Baudry et al. [16] found slip lengths of the order of 30–40 nm. The slip observed by Bonaccurso et al. [27] at hydrophilic surfaces amounted to 8–9 nm.

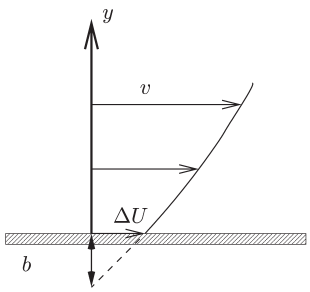

Figure 6.6 Slip at a fluid-solid interface is characterized by a finite velocity (ΔU) at the interface. This slip velocity is related to the slip length (b) through the shear rate at the interface: $\Delta U = b\partial u/\partial y$.

A closed formula for the slip length was derived for dilute systems by Bocquet [26], and an approximate formula for dense Lennard-Jones fluids was given by Barrat and Bocquet [15]. However, Richardson [205] showed that the dissipation of energy caused by the surface roughness (ε), and irrespective of the boundary condition imposed at the microscale (a no-slip or a zero shear boundary condition) results in an effective no-slip condition $b = \mathcal{O}(\varepsilon)$. Measurements by Zhu et al. [283] confirmed that the effect of surface roughness dominates the local intermolecular interaction. The analysis of Richardson [205] is based on the separation of length scales; thus $l << \varepsilon << L$, where l denotes the size of the molecules and L the bulk fluid length scales. This separation is not present in many nanoscale flows, such as the flow of water ($l \approx 0.4\,\text{nm}$) passing a single-walled carbon nanotubes ($L \approx 1\,\text{nm}$ and $\varepsilon \approx 0\,\text{nm}$). As a consequence, the amount of slip found in nanoscale flows is expected to depend not only of the wetting properties of the fluid–solid interface, but also on the particular geometry. We note here that recent studies [111, 163] have found very large slip sizes for water flow across nanotube membranes. The reported slip length values, however, need to be carefully evaluated as they were extracted by applying the concept of slip length to a flow that may amount to single-file water transport.

6.3.2.2 MD Simulations of Slip

Molecular dynamics simulations provide a controlled environment for the study of slip in nanoscale systems free from impurities and surface roughness, but limited to studies of small systems, currently of the order of tens of nanometers and tens of nanoseconds. Also, most studies have been conducted for idealized systems such as Lennard-Jones fluids in simple geometries, often confined between smooth (Lennard-Jones type) solids. However, these studies have provided valuable insight into the fundamental mechanisms of slip.

Koplik et al. [140] performed MD simulations of *Poiseuille flow* and moving contact lines. The no-slip condition was found to be satisfied for Lennard-Jones fluids confined between Lennard-Jones solids, and slip at the contact line. Bitsanis et al. [24] found velocity profiles with slip, but also a flatness of the velocity profile close to the reservoir walls used in their study.

In MD simulations of Poiseuille and Couette flows, Barrat and Bocquet [15] found the no-slip boundary condition to depend on the wetting properties of the fluid–solid interface. Both the fluid and solids were modeled as Lennard-Jones molecules using a modified Lennard-Jones potential:

$$V_{ij}(r) = 4\varepsilon\left[\left(\frac{\sigma}{r}\right)^{12} - c_{ij}\left(\frac{\sigma}{r}\right)^{6}\right] \tag{34}$$

where the parameter c_{ij} was used to adjust the relative strength of the interactions. Thus, the cohesion of the fluid was increased from the usual Lennard-Jones fluid using a value of $c_{\text{FF}} = 1.2$, and the fluid–solid interaction was varied between

0.5 and 1.0, corresponding to contact angles of 140° and 90°, respectively. The Poiseuille flow was driven by imposing an external (gravity) force, and the slip length was found to vary between 40σ and $\mathcal{O}(\sigma)$ for for contact angles of 90° and 140°, respectively. The slip length was found to decrease as a function of the pressure in the channel.

In a series of simulations of flows in narrow pores, Todd et al. [246] and Travis et al. [247, 248] found the velocity profile to deviate significantly from the quadratic form predicted by the Navier–Stokes formalism. Both the solid and fluid atoms were modeled using a purely repulsive Lennard-Jones-type (Weeks–Chander–Andersen) potential, or the full 12–6 Lennard-Jones potential. The density of the solid surface was approximately 80% of the fluid density, resulting in a high surface corrugation, and a no-slip condition at the fluid–solid interface.

Mo and Rosenberger [182] modeled the surface corrugation explicitly in two-dimensional simulations of a Lennard-Jones system. Both sinoidally and randomly roughened walls were considered with various amplitudes. The no-slip condition was found to hold when the molecular mean free path is comparable to the surface roughness. In *planar Couette flow*, the fluid is confined between two solid planar walls. The flow is generated by moving the one or both walls with constant (opposite) velocity and the imposed shear diffuses into the flow developing a linear velocity profile. Thompson and Robins [241] studied a Lennard-Jones fluid in a planar Couette flow and found slip, no-slip and locking depending on the amount of structure (corrugation) induced by the solid walls. Highly corrugated walls would result in a no-slip condition, whereas a weak fluid–wall interaction would result in slip. At strong interactions, epitaxial ordering was induced in the first fluid layers, effectively locking these to the wall. Thus the slip would occur within the fluid. For Couette flows driven by a constant force, this locking results in a stick–slip motion involving a periodic shear–melting transition and recrystallization of the film [206, 240].

The importance of the surface corrugation was later emphasized by Thompson and Troian [242], who found that the slip length diverges at a critical shear rate ($\dot{\gamma}_c$) as

$$b = \frac{b^0}{\sqrt{1 - \dot{\gamma}/\dot{\gamma}_c}} \tag{33}$$

where b^0 is the slip length in the limit of low-shear rate. The critical shear rate is reached while the fluid is still Newtonian, and depends on the corrugation of the surface energy. The importance of the corrugation of the surface was later confirmed by Cieplak et al. [50] for simple and chain-molecule fluids, and by Jabbarzadeh et al. [122] for alkenes confined between rough atomic sinusoidal walls. They found that the amount of slip is governed by the relative size of the molecular length to the wall roughness.

Sokhan et al. [227] considered methane modeled as spherical Lennard-Jones molecules confined between (high-density) graphite surfaces. They found signifi-

cant slip even in the strongly wetting case, and recovered the no-slip condition by artificially reducing the density of the wall. The constant gravity force imposed to drive the flow resulted in low-frequency oscillations of the mean flow with a time-scale ranging from 10 ps to 2 ns. Both flexible and rigid walls were considered but the dynamics of the wall was found to have little influence of the slip length.

Other confined flows include the *Hagen–Poiseuille (pipe) flow* as considered by Heinbuch and Fischer [103], who found that two layers of molecules would stick to the wall for a sufficiently strong fluid–wall interaction. Similar studies involve the flows of monoatomic fluids [250] and methane [228] through single-walled carbon nanotubes. Similar to their study of methane flowing in a slit carbon nanotube pore, Sokhan et al. [228] found a large slip in the range 5.4–7.8 nm, but significantly less that the values found for a planar graphite surface, due to the high curvature and increased friction in the carbon nanotube.

Hirshfeld and Rapaport [106] conducted MD simulations of the Taylor–Couette flow. Using a purely repulsive Lennard-Jones potential and hard walls, they found good agreement with experiments and theory. In a recent study, Walther et al. [270] performed nonequilibrium molecular dynamics simulations of water flowing past an array of single-walled carbon nanotubes. For diameters of the carbon nanotube of 1.25 and 2.50 nm and onset flow speeds in the range 50–200 ms^{-1}, they found the no-slip condition to hold, as demonstrated in Figure 6.7. Application of the same model to the Couette flow resulted in significant slip, indicating an influence of the geometry on the slip.

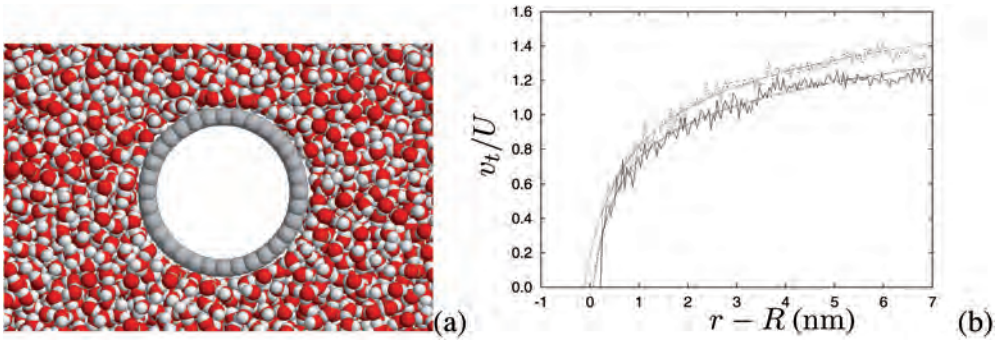

Figure 6.7 NEMD simulation for the study of hydrodynamic properties of carbon nanotubes [270]. The simulations involve water flowing past an array of 1.25 and 2.50 nm diameter carbon nanotubes. A closeup of the systems is shown in (a), and the timeaveraged tangential component of the velocity is shown in (b). The profiles are obtained for a 1.25 nm tube: —: measured; – –: fit and 2.50 nm tube: - -: measured; · · · : fit, and compared with the Stokes-Oseen solution. The slip length extracted from these simulation indicate that the continuum no-slip condition is valid.

6.4 Fluids in Confined Geometries

An understanding of the interaction of water-based liquids with carbon in confined nanoscale geometries is very important for exploring the potential of devices such as carbon nanotubes (CNTs) in nanofluidic chips, probes and capsules for drug delivery. The hollow interior of carbon nanotubes can serve as a nanometer-sized capillary. The nanotube cavities react weakly with a large number of substances and hence may serve as nanosize test-tubes. The small diameter of CNTs points to using their filled cavities as a mold or template in material fabrication. Ugarte et al. [253] filled open CNTs with molten silver nitrate by capillary forces, producing chains of silver nanobeads separated by high-pressure gas pockets.

Finally, the ability to encapsulate a material in a nanotube also offers new possibilities for investigating dimensionally confined phase transitions. In particular, water molecules in confinement exhibit several phase transitions as their network of hydrogen bonds is disrupted.

The prospect of controlled transport of picoliter volumes of fluid and single molecules requires addressing phenomena such as local density increase of several orders of magnitude and layering of transported elements in confined nanoscale geometries [119]. This presents a unique set of concerns for transport and lubrication of films on the nanometer scale. Whitby and Quirke [277] recently published a comprehensive review of experimental and computational research on this active area of research.

6.4.1 Flow Motion in Nanoscale Channels

Nanoscale channels such as ion channels are one of the most important natural devices for the transport of molecules into and out of biological cells. The behavior of confined fluids in nanoscale geometries is an area that has been under study for some time in zeolites and ideal nanoporous systems. The understanding of such processes is of great interest for nanotechnology applications in biotechnology.

Experiments have demonstrated that fluid properties become drastically altered when the separation between solid surfaces approaches the atomic scale [43, 83]. In the case of water, so-called drying transitions occur on this scale as a result of strong hydrogen bonding between water molecules, which can cause the liquid to recede from nonpolar surfaces and form distinct layers separating the bulk phase from the surface. In addition, changes such as increased effective shear viscosity as compared with the bulk, prolonged relaxation times and nonlinear responses set in at lower shear rates [90]. Computational studies of the behavior of molecules in nanoporous structures have played an important role in understanding the behaviour of fluids on the nanometer scale, complementing experimental work. A detailed study regarding the behavior of a fluid in close confinment was reported

by Thompson and Robbins [241], who used molecular dynamics simulations of Lennard-Jones liquids sheared between two solid walls. A broad spectrum of boundary conditions was observed including slip no-slip and locking. It was shown that the degree of slip is directly related to the amount of structure induced in the fluid by wall–fluid interaction potential. For weak wall–fluid interactions there is little ordering and slip was observed. At large interactions, substantial epitaxial ordering was induced and the first one or two fluid layers became locked to the wall. The liquid density oscillations also induced oscillations in other microscopic quantities normal to the wall, such as the fluid velocity in the flow direction and the in-plane microscopic stress tensor, that are contrary to the predictions of the continuum Navier–Stokes equations. However, averaging the quantities over length scales that are larger than the molecular lengths produced smooth quantities that satisfied the Navier–Stokes equations.

Molecular dynamics and Monte Carlo simulations have been used in order to simulate systems that include films of spherical molecules, straight-chain alkanes and branched alkanes [23, 24, 218, 229]. Bitsanis et al. [24] reported on the flow of fluids confined in molecularly narrow pores. They observed departure from the continuum as strong density variations across the pore render the usual dependence of the local viscosity on local density inappropriate. At separations greater than four molecular diameters, flow can be described by a simple redefinition of local viscosity. In narrower pores, a dramatic increase in effective viscosities is observed, which is due to the inability of fluid layers to undergo the gliding motion of planar flow. This effect is partially responsible for the strong viscosity increases observed experimentally in thin films that still maintain their fluidity. The simulations for Couette and Poiseulle types of flow yielded wall parallel velocity profiles that deviated from the shape predicted by continuous assumptions. Confinement also affects the electronic properties of the enclosed substances. Intermolecular dipole–dipole interactions were once thought to average to zero in gases and liquids as a result of rapid molecular motion that leads to sharp nuclear magnetic resonance lines. It has been shown [17] that a much larger, qualitatively different intermolecular dipolar interaction remains in nanogases and nanoliquids. The dipolar coupling that characterizes such interactions is identical for all spin pairs and depends on the shape, orientation (with respect to the external magnetic field) and volume of the gas/liquid container. This nanoscale effect is useful in the determination of nanostructures and could have unique applications in the exploration of quantum space.

Flows of argon, helium and a buckyball and helium fluid inside carbon nanotubes have been reported using molecular dynamics simulations [250, 251]. The fluid was started at some initial velocity; fluid particles were allowed to recycle axially through the tube via minimum image boundary conditions. Argon slowed more quickly than helium. In addition, the behavior of the fluid depended strongly on the rigidity of the tube; a dynamic tube slowed the fluid far more quickly than one in which the tube was held frozen. Han et al. [98] reported molecular dynamics simulation to investigate the properties and design space of molecular gears fashioned from carbon nanotubes with teeth added via a benzyne reaction. A number

of gear and gear/shaft configurations were simulated on parallel computers. One gear was powered by forcing the atoms near the end of the nanotube to rotate, and a second gear was allowed to rotate by keeping the atoms near the end of its nanotube constrained to a cylinder. The meshing aromatic gear teeth transferred angular momentum from the powered gear to the driven gear. The results suggest that these gears can operate at up to 50–100 GHz in a vacuum at room temperature. The failure mode involves tooth slip, not bond breaking, so failed gears can be returned to operation by lowering the temperature and/or rotation rate.

Manipulation of the geometry at the nanoscale may be readily utilized for controlled fluid transport. This was demonstrated [127] by fluidic control in lipid nanotubes 50–150 nm in radius, conjugated with surface-immobilized unilamellar lipid bilayer vesicles. Transport in nanotubes was induced by continuously increasing the surface tension of one of the conjugated vesicles, for example, by ellipsoidal shape deformation using a pair of carbon microfibers controlled by micromanipulators as tweezers. The shape deformation resulted in a flow of membrane lipids toward the vesicle with the higher membrane tension; this lipid flow in turn moved the liquid column inside the nanotube through viscous coupling. By control of the membrane tension difference between interconnected vesicle containers, fast and reversible membrane flow (moving walls) with coupled liquid flow in the connecting lipid nanotubes was achieved.

6.4.2
Nanofluidic Networks, Sieves and Arrays

Networks of nanofluidic tubes have been manufactured by using a heat-depolymerizable polycarbonate (HDP) for use as a sacrificial layer [100]. A patterned HDP film is used as a temporary support for another filmwhich is stable at the depolymerization temperature. Heating the structure removes the HDP, leaving a network of nanofluidic tubes without the use of solvents or other chemicals as required in most other sacrificial layer processes. Tube dimensions of 140 nm height, 1 μm width and 1 mm length are reported, and fabrication of other structures is discussed. Nanoimprint lithography has been used to manufacture channels with a cross-section as small as 10×50 nm [42], which can be of great importance for confining biological molecules in ultrasmall spaces. In order to avoid entropic traps in introducing biological molecules such as DNA in fluidic channels directly from the macroscale, diffraction gradient lithography techniques have been used to fabricate continuous spatial gradient structures which smoothly narrow the cross section of a volume from the micrometer to the nanometer length scale [41].

Nanofluidic devices are gaining popularity as DNA separation devices, thus replacing the standard electrophoresis tecniques. When passing throgh such nanoscale sieves ordinarily, a long-chain DNA molecule in liquid will clump into a roughly spherical shape, and to move through a sieve it must uncoil and slide in lengthwise. This movement involves an entropic force which causes DNA molecules that are only partially within a sieve to withdraw when the force pulling

them in is removed. The effect results from the motion of segments in the chain molecule as they interact with the beginning of the barrier. The force is called "entropic" because the molecule moves out of the restricted space of the sieve into an open area where it can be more disordered. A nanofluidic channel device [97], consisting of many *entropic traps*, was designed and fabricated for the separation of long DNA molecules. The channel comprises narrow constrictions and wider regions that cause size-dependent trapping of DNA at the onset of a constriction. This process creates electrophoretic mobility differences, thus allowing efficient separation without the use of a gel matrix or pulsed electric fields. Samples of long DNA molecules (5000 to ~160 000 base pairs) were efficiently separated into bands in 15-mm long channels. Multiple-channel devices operating in parallel were demonstrated. The efficiency, compactness and ease of fabrication of the device suggest the possibility of more practical integrated DNA analysis systems.

An alternative device involves nanosphere arrays [191] prepared by colloidal templating that trap the macromolecules within a two-dimensional array of spherical cavities interconnected by circular holes. Across a broad DNA size range, diffusion does not proceed by the familiar mechanisms of reptation or sieving. Rather, because of their inherent flexibility, DNA molecules strongly localize in cavities and only sporadically jump through holes. By reducing DNA's configurational freedom, the holes act as molecular weight dependent entropic barriers.

Fluidic control in nanometer-sized channels using a moving wall provides plug-like liquid flows, offers a means for efficient routing and trapping of small molecules, polymers, and colloids and offers new opportunities to study chemistry in confined spaces. Networks of nanotubes and vesicles might serve as a platform to build nanofluidic devices operating with single molecules and nanoparticles. Soft microfabrication technologies for processing of fluid-state liquid crystalline bilayer membranes have been reported by Karlsson et al. [127]. They developed a microelectrofusion method for the construction of fluid-state lipid bilayer networks of high geometric complexity up to fully connected networks. Within networks, self-organizing branching nanotube architectures could be produced where intersections spontaneously arrange themselves into three-way junctions. It is also demonstrated that materials can be injected into specific containers within a network by nanotube-mediated transport of satellite vesicles having defined contents. Using a combination of microelectrofusion, spontaneous nanotube pattern formation and satellite–vesicle injection, complex networks of containers and nanotubes can be produced for a range of applications in, for example, nanofluidics and artificial cell design. In addition, this electrofusion method allows integration of biological cells into lipid nanotube–vesicle networks.

6.4.3
Phase Transitions of Water in Confined Geometries

Encapsulation of a second phase inside carbon nanotubes offers a new avenue to investigate dimensionally confined phase transitions. When pure liquid water is encapsulated inside narrow carbon nanotubes, water molecules would be expected

to line up into some quasi-one-dimensional structures, and on freezing may exhibit completely different crystalline structures from bulk ice. Confinement may change not only resulting crystalline structures but also the way in which liquids freeze [134].

Supercooled water and amorphous ice have a rich metastable phase behavior. In addition to transitions between high- and low-density amorphous solids and between high- and low-density liquids, a fragile-to-strong liquid transition has been proposed and supported by evidence from the behavior of deeply supercooled bilayer water confined in hydrophilic slit pores [180]. Evidence from molecular dynamics simulations suggests another type of first-order phase transition – a liquid-to-bilayer amorphous transition – above the freezing temperature of bulk water at atmospheric pressure [135]. This transition occurs only when water is confined in a hydrophobic slit pore [136] with a width of less than 1 nm. On cooling, the confined water, which has an imperfect random hydrogen-bonded network, transforms into a bilayer amorphous phase with a perfect network (owing to the formation of various hydrogen-bonded polygons) but no long-range order.

Molecular dynamics simulations have been performed [190] under physiological conditions (300 K and 1 atm) using nanotube segments of various diameters submerged in water. The results show that water molecules can exist inside the nanotube segments and that the water molecules inside the tubes tend to organize themselves into a highly hydrogenbonded network, i.e. solid-like wrapped-around ice sheets. The disorder-to-order transition of these ice sheets can be achieved purely by tuning the size of the tubes.

Particularly intriguing is the conjecture [1, 64, 133] that matter within the narrow confines of a carbon nanotube might exhibit a solid–liquid critical point beyond which the distinction between solid and liquid phases disappears. This unusual feature, which cannot occur in bulk material, would allow for the direct and continuous transformation of liquid matter into a solid. Simulations by Koga et al. [133] of the behavior of water encapsulated in carbon nanotubes suggest the existence of a variety of new ice phases not seen in bulk ice, and of a solid–liquid critical point. Using carbon nanotubes with diameters ranging from 1.1 to 1.4 nm and applied axial pressures of 50–500 MPa, they found that water can exhibit a first-order freezing transition to hexagonal and heptagonal ice nanotubes, and a continuous phase transformation into solid-like square or pentagonal ice nanotubes (Figure 6.8).

Slovák et al. [225] performed a series of MD simulations in order to examine in more detail the results of a water simulation which shows that a thin film of water, when confined in a hydrophobic nanopore, freezes into a bilayer ice crystal composed of two layers of hexagonal rings. They found that only in one case did the confined water completely freeze into perfect bilayer ice, whereas in the other two cases an imperfect crystalline structure consisting of hexagons of slightly different shapes was observed. This imperfection apparently hinders the growth of a perfect bilayer crystal. After adjusting the area density to match the spatial arrangements of molecules, the latter two systems are able to crystallize completely. As a result,

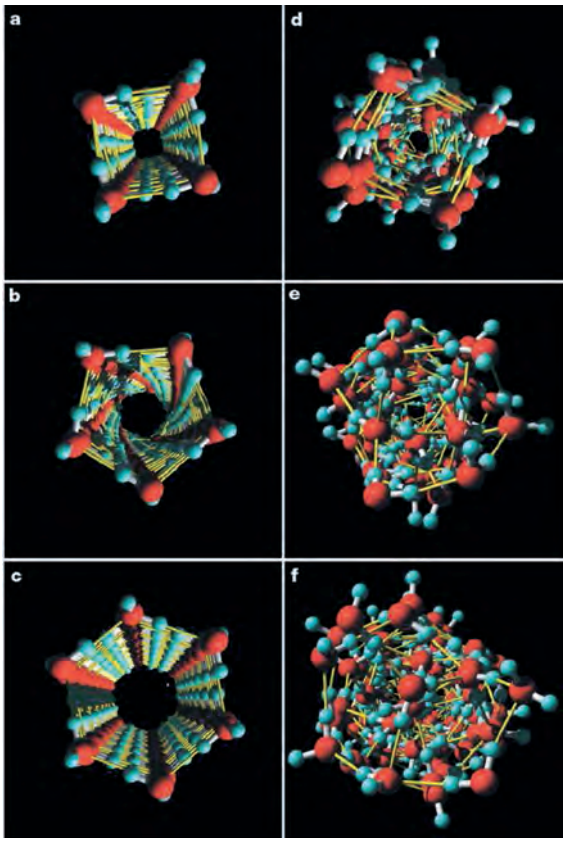

Figure 6.8 Snapshots of quenched molecular coordinates. a, Square; b, pentagonal; c, hexagonal ice nanotubes in (14,14), (15,15) and (16,16) SWCNs; d to f, the corresponding liquid phases. The ice nanotubes were formed on cooling under an axial pressure of 50 MPa in molecular dynamics simulations. The nearest-neighbour distances in both ice nanotube and encapsulated liquid water are fairly constant, about 2.7 to 2.8 Å, and this is in part responsible for the novel phase behaviour.

we obtain three forms of bilayer crystal differing in the area density and alignment of hexagonal rings.

The same group in a later study [134] considered simulations of the phase behavior of quasi-one-dimensional water confined inside a carbon nanotube, in the thermodynamic space of temperature, pressure and diameter of the cylindrical container. Four kinds of solid-like ordered structures – ice nanotubes – form spontaneously from liquid-like disordered phases at low temperatures. In the model system the phase change occurs either discontinuously or continuously, depending on the path in the thermodynamic space.

Confinement of liquids such as water on the nanoscale can also induce that correspond to water properties in *supercritical conditions*. At room temperature, water forms tetrahedral units of five molecules linked by hydrogen bonds. When

temperature is raised and/or the density is reduced, some of the hydrogen bonds are broken. Most of the dominant order is then lost and the remaining structures are linear and bifurcated chains of H-bonded water molecules which can be regarded as parts of broken tetrahedral. The destruction of the hydrogen bonds affects the water such that its compressibility and transport properties are intermediate between those of liquid and gas. However, increasing the temperature and/or decreasing the density are not the only means of achieving this effect. MD simulations indicate that when water is introduced inside carbon nanotubes, its hydrogen bonding structure is also compromised [87, 88] with an important decrease in the average number of hydrogen bonds with respect to bulk supercritical water. This reduction is greater than for water in standard conditions. The atomic density profiles are slightly smoother, but with the same general features as for water at lower temperatures.

6.5 Fluid Mechanics at the Nano–Bio Interface

The transport of liquids through lab-on-a-chip devices is one of the first applications spanning the areas of fluid mechanics, nano/microtechnology and biology. Beyond micro/nanofluidics application for analysis, however, NFM extends to a number of applications ranging from nanoscale syringes to novel gating devices.

Almost a decade after the first miniaturized gas chromatography system was successfully fabricated on a silicon wafer [236], the first liquid-phase separation was demonstrated, thereby catalyzing the development of micro total analysis systems. Since that time, there has been an enormous amount of research devoted to developing miniaturized systems for separations and chemical and biological sensing [97]. Simultaneously, a number of technological factors have driven the development of fluidic architectures towards the nanometer length scale. However, nanostructures proposed to date for chemical and biological applications rely on self-assembly and self-organizational processes [46]. A technical challenge is to construct such units into integrated three-dimensional systems. The ultimate nanofluidic device is one that can handle single molecules and colloid particles. Such devices require unprecedented control over transport and mixing behaviors, and to advance current fluidics into the single-molecule regime we have to develop systems having physical dimensions on the nanometer scale. To create such devices, we can draw much knowledge from biological systems. For example, the Golgi–endoplasmic reticulum network in eukaryotic cells has many attractive features for sorting and routing of single molecules, such as ultra-small-scale dimensions, transport control and capability to recognize different molecular species, and for performing chemical transformations in nanometer-sized compartments with minimal dilution. It is, however, extremely difficult to mimic these biological systems by using traditional microfabrication technologies and materials because of their small scale, complex geometries and advanced topologies. Advanced nanofabrication techniques are necessary in order to construct such devices and a

number of devices such as nanochannels and nanomembranes are currently being implemented.

The key characteristic feature of nanofluidic channels is that fluid flow occurs in structures of the same size as the physical parameters that govern the flow. Another factor that favors the development of nanoscale interconnects is the enhanced surface area-to-volume ratio characteristic of the nanochannels in these membranes. The ability to interface nanochannels with conventional microfluidics alleviates the need for nanofabrication techniques, and yet still allows a number of important applications that use the unique characteristics of the nanopores. For instance, the small pore size system can be used to concentrate dilute analytes or clean up analyte solutions. This latter point is especially important for biological separations where often the major components (whether salts or proteins) in a mixture obscure the ability to separate and collect the desired trace level components. While a simple transfer of a band is demonstrated here from one microfluidic channel to the other, this concept can be extended to chemical manipulation in the receiving channel with derivatizing reagents. In addition to the chemical manipulations possible between isolated microchannels, the high surface-to-volume ratio of the nanochannels offers additional opportunities. For example, by including molecular recognition elements on the interior of the nanopores, it should be possible to effect intelligent fluidic switching in which certain elements of the fluidic stream being transported through the nanopores are retained, reacted, degraded or otherwise chemically processed before being released into the next microfluidic channel.

6.5.1
Biological Nanochannels

Ion channels consist of a particular natural form of nanochannels with particular importance to biological systems. They belong to a class of proteins that form nanoscopic aqueous tunnels acting as route of communication between intra- and extracellualr compartments. Each ion channel consists of a chain of amino acids carrying a strong and rapidly varying electric charge. Ion channels regulate cell internal ion composition, control electrical signaling in the nervous system and in muscle contraction and are important for the delivery of many clinical drugs. Channels are usually "gated", i.e. they contain a region that can interrupt the flow of molecules (water, ions) that is often coupled to a sensor that controls the gate allosterically [18]. They exhibit selectivity on the types of ions that get transmitted and may exhibit switching properties similar to other electronic devices. At the same time, channels or pores for uncharged molecules mediate transport through the membrane by diffusion driven by the gradient of this substance. Pores or channels are known to exist for water, small molecules such as urea and glycerol and others. One particular non-gated channel of interest is water channels that are called aquaporins. In aquaporins, the general belief was that water diffuses through the lipids of biological membranes. On the other hand, it has been known for many years that a large portion of water transport is protein mediated. The

question of how gating works at an atomic level is one of considerable complexity. A pattern is emerging for some channels in which the most constricted region of the pore (which is usually identified with the gate) is ringed by hydrophobic amino acid side-chains, e.g. leucine or valine. So, is an effect other than steric occlusion able to close a channel, i.e. hydrophobic gating? Experimental evidence in favor of such a mechanism comes from studies of pores in modified Vycor glass, which showed that water failed to penetrate these pores once a threshold hydrophobicity of the pore walls was exceeded [18].

Molecular dynamics simulations through atomistic models of nanopores embedded within a membrane mimetic have been used in order to identify whether a hydrophobic pore can act as a gate of the passage of water. Both the geometry of a nanopore and the hydrophilicity vs. hydrophobicity of its lining determine whether water enters the channel. For purely hydrophobic pores there is an abrupt transition from a closed state (no water in the pore cavity) to an open state (cavity water at approximately bulk density) once a critical pore radius is exceeded. This critical radius depends on the length of the pore and the radius of the mouth region. Furthermore, a closed hydrophobic nanopore can be opened by adding dipoles to its lining.

The prospect of employing structures such as pure and doped carbon nanotubes for molecular transport has not been unnoticed. As a step in understanding the governing physical phenomena, in long (>50 ns) simulations of a carbon nanotube submerged in water, Hummer et al. [116] (Figure 6.9) observed water flux through the pore to occur in a pulsatory fashion, with fluctuations in flux on a time-scale

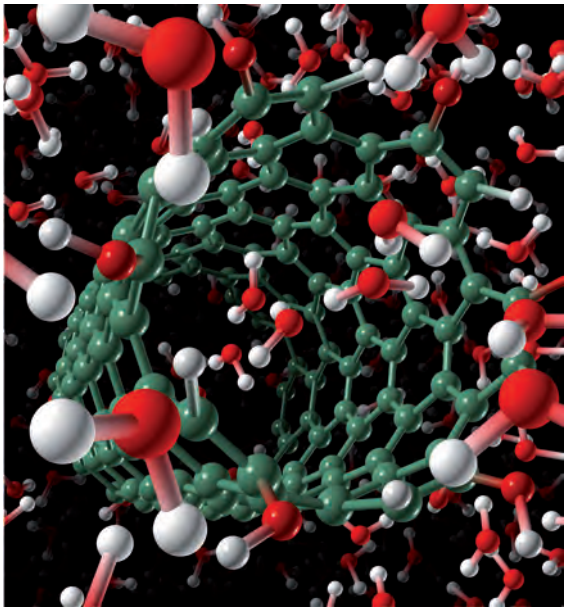

Figure 6.9 Singe file transport of water molecules inside doped carbon nanotubes [286].

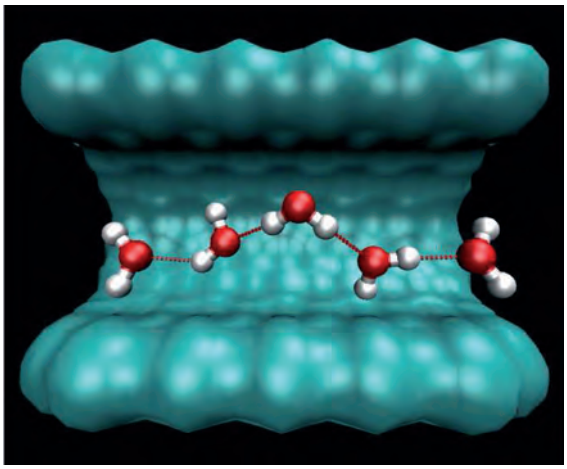

Figure 6.10 L-deffects form on chain of single-file transport of water molecules inside a carbon nanotube. L-deffects appear in short carbon nanotubes due to the interaction of the dipole on the walls of the carbon nanotubes with the water [286].

of 4 ns. In related work, L-deffects have been observed (Figure 6.10) in transport of water through naked and doped carbon nanotubes [286]. In addition, we note that without including the modeling of the dipole term in short nanotubes with a length of 2.5 nm transport rates of about 22 molecules per nanosecond were observed along with intermittent filling of the nanotubes. Including the dipole term resulted in continuous filling of the nanotube, albeit reducing the transport rate by half.

Waghe et al. [265] studied the kinetics of water filling and emptying the interior channel of carbon nanotubes using molecular dynamics simulations. Filling and emptying occur predominantly by sequential addition/removal of water to/from a single-file chain inside the nanotube. Advancing and receding water chains are orientationally ordered. This precludes simultaneous filling from both tube ends, and forces chain rupture to occur at the tube end where a water molecule donates a hydrogen bond to the bulk fluid. They used transition path concepts and a Bayesian approach to identify a transition state ensemble that was characterize by its commitment probability distribution. At the transition state, the tube is filled with all but one water molecule. One important observation is that filling thermodynamics and kinetics depend on the strength of the attractive nanotube–water interactions that increase with the length of the tubes.

Beckstein et al. [18] presented simulations of a model comprised of a membrane-spanning channel of finite length allowing water molecules within the pore to equilibrate with those in the bulk phase, thus avoiding any prior assumptions about water density. They probed entry/exit of water to/from an atomistic model of a nanopore, while retaining control over its geometry and the charge pattern of its pore lining. In summary, hydrophobicity *per se* can close a sterically open

channel to penetration by water and hence, by simple extension, to ions and small polar solutes. Such a channel can be opened by adding a relatively small number of dipoles to the lining of the pore or by a modest increase in radius. The critical gating radius depends on the geometry of the mouth region of the pore. Simulation studies of gramicidin suggested that 87% of overall channel resistance to water permeation comes from the energetic cost for a bulk water to enter the mouth. Thus, both overall dimensions and the extents of hydrophobic and hydrophilic regions in the lining provide a key to gating of nanopores.

Water plays a critical role in the dynamics of biomolecules. The simultaneous presence of nanodevices brings a new enabling component for innovative designs. Examples of recent applications include nanopore sequencing by driving DNA through the pores of an SWNT [45] which is inserted in a lipid bilayer an the use of CNTs as "nanosyringes" [155] for the molecular delivery of drugs. A number of recent studies (see [156] and references therein) have demonstrated the capabilities of molecular modeling in investigating such novel configurations. Examples include the use of SWNTs as biomedical sensors based on the modification of their electronic properties by the transport of biomolecules and the use of nanopores as electronic nanodevices for the sequencing of DNA [89].

6.5.2
Nanoporous Membranes

Nanoporous membranes containing monodisperse distributions of nanometer diameter channels have been proposed as an effective medium for controlled molecular transport [130]. The facility with which molecular manipulations may be accomplished at the nanometer scale suggests their use for integrating multilevel microfluidic systems. The use of commercially available nanoporous membranes allows quick and economical fabrication of nanochannel architectures to provide fluidic communication between microfluidic layers. By incorporating these nanoporous membranes into microfluidic systems, a variety of novel flow control concepts may be implemented. The cylindrical nanochannels ($10\,\text{nm} < d < 200\,\text{nm}$) of the membranes can be used as nanofluidic interconnects to establish controllable fluidic communication between micrometer-scale channels operating in different planes. Kuo et al. initially investigated the ability to manipulate macroscopic transport using these nanochannels [148], and also reported on interfacing the nanoporous membranes with microfluidic channels [147]. More importantly, these nanoporous membranes add functionality to the system as gateable interconnects. These nanofluidic interconnects allow control of net fluid flow based on a number of different physical characteristics of the sample stream, the microfluidic channels and the nanochannels, leading to hybrid fluidic architectures of considerable versatility. Because the nanofluidic membrane can have surfaces with excess charge of either polarity, the net flow direction inside the microdevices is principally controlled by two factors: the magnitude of the electrical and physical flow impedance of the nanoporous membrane relative to that of the microchannels and the surface chemical functionalities which determine the polarity of the excess

charge in the nanochannels. The nanochannel impedance may be manipulated by varying membrane pore size. Flow control is investigated by monitoring electrokinetic transport of both neutral and negatively charged fluorescent probes, by means of laser-induced fluorescence and fluorescence microscopy, while varying solution and nanochannel properties. When the pore size of the PCTE membrane is small, the impedance is large and the polarity of the nanochannel surface charge determines the overall direction of the net electroosmotic flow. When the combined impedance of the upper and lower microchannels exceeds 30 times the impedance of the nanochannel membrane, the direction of the flow is based on the negative surface charge of the PDMS microchannels [146].

Sun and Crooks [232] used multi-walled carbon nanotubes as templates to fabricate single-pore membranes. These membranes are better experimental models for testing specific predictions of mass transport theories than arrays of nanopores because they require fewer adjustable parameters and they have well-defined geometry and chemical structures. Using polystyrene particles as probes, they demonstrated that quantitative information about fundamental modes of transport, such as hydrodynamic and electrophoretic flow, can be obtained using these single-pore membranes.

Miller et al. [178, 179] prepared carbon nanotube membranes using chemical vapor deposition of graphitic carbon into the pores of microporous alumina template membranes. This approach yields a freestanding membrane containing a parallel array of carbon nanotubes (outside diameter ~200 nm, wall thickness ~40 nm) that spans the complete thickness of the membrane (60 μm). The electroosmotic flow (EOF) can be driven across these CNMs by allowing the membrane to separate two electrolyte solutions and using an electrode in each solution to pass a constant ionic current through the nanotubes. Lee et al. [151] developed synthetic bio-nanotube membranes and used them to separate two enantiomers of a chiral drug. These membranes are based on alumina films that have cylindrical pores with monodisperse nanoscopic diameters (for example, 20 nm). Silica nanotubes were chemically synthesized within the pores of these films, and an antibody that selectively binds one of the enantiomers of the drug was attached to the inner walls of the silica nanotubes. These membranes selectively transport the enantiomer that specifically binds to the antibody, relative to the enantiomer that has lower affinity for the antibody. Melechko et al. [175] reported a method to fabricate nanoscale pipes ("nanopipes") suitable for fluidic transport. Vertically aligned carbon nanofibers grown by plasma-enhanced chemical vapor deposition were used as sacrificial templates for nanopipes with internal diameters as small as 30 nm and lengths up to several micrometers that are oriented perpendicular to the substrate. This method provides a high level of control over the nanopipe location, number, length and diameter, permitting them to be deterministically positioned on a substrate and arranged into arrays. The use of membranes in microfluidics is a topic that has been attracting increasing interest in the recent years (for a review, see [56] and references therein) due to their versatility and the large internal surface that can be used effectively for adsorption in catalysis-based applications. The application of a voltage across a nanotube-based membrane [177]

has been used to control EOF. This new method entails coating the inside walls of the carbon nanotubes within the CNM with redox-active polymer films. The redox polymer, polyvinylferrocene, can be reversibly electrochemically switched between an electrical neutral and a polycationic form. In a study by Majumder et al. [164], membranes consisted of aligned multiwalled carbon nanotubes crossing a solid polysterene film. Ionic flux through the membrane structure was studied as a function of chemical end groups at the entrance to the CNT cores. The relative selectivity of the permeates varied from 1.7 to 3.6 as a function of tip-functionalization chemistry. Molecular dynamics simulations [255, 285] of water molecules in the narrow cylindrical pores of a (6,6) carbon nanotube exhibited single-file chains that can be modulated by an electric field.

6.5.2.1 **Electrophoretic RNA Transport through Transmembrane Carbon Nanotubes**

Transport across cellular membranes is the key to many biological processes [63, 224]. The transport may be regulated by the structure and dynamics of membrane-embedded proteins or it may be initiated externally, e.g. by a virus that punctures a cell membrane [166].

The understanding of transmembrane transport processes is crucial to the rational design of devices such as nanosyringes and molecular channels [2, 183]. Although these devices are envisioned as engineered replacements of natural transmembarne pores, it is not possible to replicate today the complex structure of biological nanopores. In turn, well-chracterized nanostructures such as CNTs when properly embedded in membranes may serve as effective components for artificial channels. CNTs have unique physical properties and a structure [118, 157, 207] that suggests their use as a canonical model of nanosyringes or stabilizing pores in biological membranes during electroporation. Pores stabilized by CNTs can persist over a broad range of voltages and they are inert to a large number of chemicals. These properties of CNTs make them suitable candidates for DNA gene delivery [194] and DNA storage [193]. Several studies have assessed the interaction of small CNTs and CNT arrays with water [116, 265, 282, 285], ions [125, 196] and RNA/DNA [80, 158, 279] and Aksimentiev and cowokers [2, 3, 105, 169] reported on the electrophoretically driven transport of DNA in nanometer-size silica pores.

A functionalized CNT was embedded in a DMPC membrane and the electrophoretic transport of RNA through the tube was studied using MD simulations [287]. These studies demonstrate the importance of quantifying the interplay of the membrane lipids with the CNT and we report on the electrostatic potential maps of the CNT in the DMPC lipid bilayer. The RNA fragment consisted of a single strand of 20 adenosine nucleotides, through a CNT embedded in a DMPC lipid bilayer using using the MD package FASTTUBE [274]. The system is illustrated in Figure 6.12 with a snapshot from one of the simulations. The electrostatic potential map [3] of the system reveals the role of the membrane components on the evolution of this system. In Figure 6.11 we show the electrostatic potential map for a CNT with hydrophilic rims embedded in a DMPC lipid bilayer subject to an electrostatic potential difference of 1.05 V. We observe a constant electrostatic

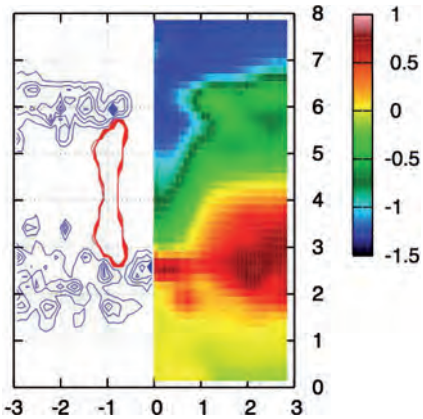

Figure 6.11 Electrostatic potential map in Volts for a carbon nanotube with hydrophilic rims in a DPMC bilayer. The system is subject to a electrostatic potential difference of 1.05 V. On the left contour lines of radially averaged density profiles are shown for the DMPC nitrogen (blue) and the CNT carbon atoms (red). The x-axis shows the in-plane distance [nm] from the tube center. The y-axis depicts the dimension perpendicular to the membrane [nm].

potential on both sides of the membrane. On the side of high electrostatic potential, we observe a barrier in the electrostatic potential that spans the tube opening. On the side of low electrostatic potential a similar barrier is absent and the pore opening is reflected in a bay of low electrostatic potential extending into the pore. A strong correlation exists between the electrostatic potential map and the corresponding radially averaged density profiles of lipid atom groups. The electrostatic potential difference across the membrane in conjunction with the geometric restriction of the whole lipid molecules causes an asymmetric reorientation of the head groups, which in turn results in the electrostatic potential described above. The head groups are pushed into the area of the tube opening on the side of high electrostatic potential and they are pulled out of the area of the tube opening on the other side.

The system was then subjected to a potential difference of 1.6 V. The translocation of the RNA across the pore takes approximately 12 ns, which corresponds to a speed of translocation of approximately 1.5 nucleotides per nanosecond. During translocation the lipid head groups of the DMPC membrane extend over the CNT and interact with the RNA (Figure 6.12). This slows the motion of the RNA and results in steric hindrance of the RNA translocation, as the lipid heads partially obstruct the pore opening. Before entering the CNT the nucleotide bases of the RNA are stacked. When a base enters the CNT the spatial restriction inside the tube forces the hydrophobic contact to its neighboring base to be broken and the interfacial area is hydrated. Simultaneously water is expelled from in between the base and the CNT wall and the base attaches to the tube wall. During this process the RNA bases are folding backwards with respect to the direction of transport (Figure 6.12).

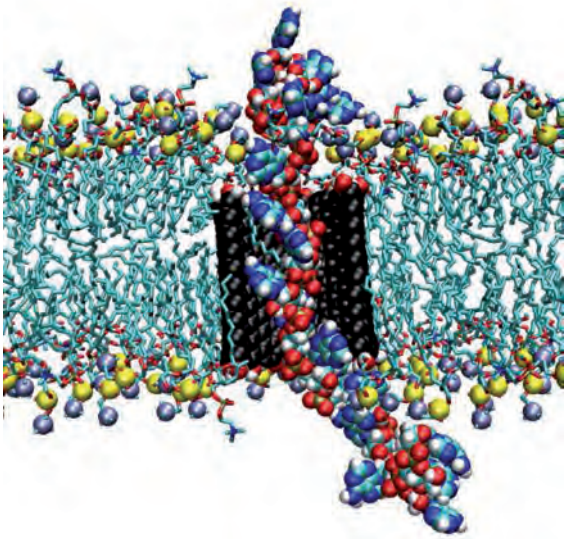

Figure 6.12 A CNT with hydrophilic rims is embedded in a lipid bilayer. A single stranded RNA fragment consisting of 20 adenosine nucleotides is translocating through the tube. The translocation direction is from top downwards. Outside the CNT the nucleotides are stacked. Inside the CNT they are folded backwards with regards to the direction of translocation and they are attached flat on the CNT wall. The lipid heads (ammonium groups indicated in blue and phosphate in yellow) protrude into the tube opening hindering translocation. The solvent (water and potassium chloride) is not shown for clarity.

When a nucleotide base enters the CNT, an energy barrier has to be overcome, which leads to temporal trapping of the RNA. The overall motion of RNA exhibits periods of fast displacement and periods of trapping. The transport of RNA within the CNT transmembrane pore shows several characteristics which were previously reported on synthetic silica nanopores [105], i.e. the nucleotide bases are attached flat on the pore wall and folded backwards with respect to the direction of translocation. Upon leaving the exit area of the CNT, the RNA protrudes into solution, and it is not adsorbed on the membrane surface. After translocation, the terminal nucleotides remain hydrophobically attached to the CNT and do not detach for the duration of the present simulations.

6.6 Outlook – *τα παντα ρυι* – Even at the Nanoscale

As the promise of nanotechnology is beginning to become realized, the new scientific frontiers for this field are outlined. In particular, the triple interface of

nanotechnology with biology and computational science seems to emerge as a rich ground for fundamental scientific research and engineering applications.

The interface of nanotechnology with computational science was the main topic of this chapter. The development of computational science tools integrating advances in hardware, software and computational methods provides us today with unprecedented capabilities in using powerful computational tools for the study of fundamental nanoscale configurations. Several software packages are readily available for quantum, atomistic, mesocale and continuum descriptions and several communities are using the Internet to exchange ideas freely and create depositories of advanced software. At the same time, significant work is necessary in order for simulations to reach the temporal and spatial scales necessary for the efficient predictive design of nanodevices. Multiscale modeling and simulations are an active field of research that is expected to have a significant impact on this field and which needs to be integrated with efficient software tools in order to exploit the available computing architectures.

The interface and the inherent close link between life and aqueous environments will continue to be explored. While visions of nanomedicine may continue to be controversial, understanding of NFM will continue to offer tools for the exploration of molecular level drug delivery and on-site interfacing with biological cells. Fluid mechanics at the nanoscale is an emerging field in need of powerful computational tools and innovative experimental diagnostic techniques aimed at a better understanding of these phenomena. In computation there is much need for the development of multiscale computational techniques linking the atomistic to the nano, meso and continuum scales. In parallel, the development of new techniques for experimental diagnosis and manipulation of fluids at the nanoscale will have a significant impact in the coming decades. These experiments and simulations will certainly allow new understandings and findings for the underlying flow physics. The exploitation of these findings in areas ranging from new computer architectures to disease-fighting methods will be a breeding ground for further fluid mechanics research at the nanoscale in the near future.

6.7 Acknowledgments

Our research in NFM has benefited tremendously by direct and indirect contacts with several research groups working in the area of nanotechnology. The references include a partial list of people whose work has served us as guidance and motivation. I wish in particular to acknowledge many inspirational discussions and fruitful collaborations with Dr. Jens Walther (ETHZ and TU Denmark), Dr. Richard Jaffe (NASA, Ames, IA, USA) and Dr. Flavio Noca (EPFL, Switzerland). The work discussed in this chapter would not have been possible without the work and motivation I have received from my students Dr. Thomas Werder and Dr. Evangelos Kotsalis.

6.8 List of Symbols

b	Slip length
b^0	Slip length in the low shear rate limit
C_n	Dispersion coefficient of order n
$c_{i,j}$	Adjustment parameter for Lennard–Jones potential
d	Diameter
E	Energy
K_h	Force constant for a harmonic oscillator
K_M	Parameter for the Morse bond potential
K_Θ	Force constant for a bond angle potential
q_i	Charge associated with atom i
r	Droplet radius
r_0	Equilibrium distance between two centers
r_c	Cutoff radius
$r_{i,j}$	Distance between two centers i and j
U	Internal energy
V	Potential function
z	Distance from a plane
α	Slip coefficient
β	Parameter for the Morse bond potential
Δu	Slip velocity
ε	Surface roughness
ε_0	Free space permittivity
$\varepsilon_{I,J}$	Lennard-Jones energy parameter for interaction between atoms I and J
$\Phi_{i,j,k,l}$	Dihedral bond angle over four centers i, j, k and l
γ	Surface tension
$\dot{\gamma}$	Shear rate
$\dot{\gamma}_\mathrm{c}$	Critical shear rate
λ	Wavelength
$\sigma_{I,J}$	Lennard-Jones distance parameter for interaction between atoms I and J
τ	Line tension
Θ	Contact angle
Θ_c	Equilibrium bond angle
$\Theta_{i,j,k}$	Bond angle between three centers i, j and k

References

1 P. M. Ajayan, S. Iijima, Capillarity-induced filling of carbon nanotubes. *Nature*, **361** (1993) 333–334.

2 A. Aksimentiev, J. B. Heng, G. Timp, K. Schulten, Microscopic kinetics of DNA translocation through synthetic nanopores. *Biophys. J.*, **87** (2004) 2086–2097.

3 A. Aksimentiev, K. Schulten, Imaging α-hemolysin with molecular dynamics: ionic conductance, osmotic permeability, and the electrostatic potential map.

Biophys. J., **88** (2005) 3745–3761.

4 B. Alberts, D. Bray, A. Johnson, J. Lewis, M. Raff, K. Roberts, P. Walter, *Essential Cell Biology*. Garland, New York, 1997.

5 B. J. Alder, T. E. Wainwright, Phase transition for a hard sphere system. *J. Chem. Phys.*, **27** (1957) 1208–1209.

6 F. J. Alexander, A. L. Garcia, D. M. Tartakovsky, Algorithm refinement for stochastic partial differential equations. I. Linear diffusion. *J. Comput. Phys.*, **182** (2002) 47–66.

7 M. P. Allen, D. J. Tildesley, *Computer Simulation of Liquids*. Clarendon Press, Oxford, 1987.

8 N. R. Aluru, J.-P. Leburton, W. McMahon, U. Ravaioli, S. Rotkin, M. Stedele, T. van der Straaten, B. R. Tuttle, K. Hess, Modeling electronics at the nanoscale, in: *Handbook of Nanoscience, Engineering and Technology*, W. A. I. Goddard, D. W. Brenner, S. E. Lyshevski, G. J. Iafrate (eds.), CRC Press, Boca Raton, FL, 2003, pp. 11.1–11.32.

9 M. Amini, S. K. Mitra, R. W. Hockney, Molecular dynamics study of boron trioxide glass. *J. Phys. C*, **14** (1981) 3689–3700.

10 C. R. Anderson, An implementation of the fast multipole method without multipoles. *SIAM J. Sci. Stat. Comput.*, **13** (1992) 923–947.

11 Y. Andersson, D. C. Langreth, B. I. Lundqvist, van der Waals interactions in density-functional teory. *Phys. Rev. Lett.*, **76** (1996) 102–105.

12 Y. Andersson, H. Rydberg, Dispersion coefficients for van der Waals complexes, including C_{60}–C_{60}. *Phy. Scr.*, **60** (1999) 211–216.

13 P. Attard, Bridging bubbles between hydrophobic surfaces. *Langmuir*, **12** (1996) 1693–1695.

14 J. Barnes, P. Hut, A hierarchical $O(N \log N)$ force-calculation algorithm. *Nature*, **324** (1986) 446–449.

15 J.-L. Barrat, L. Bocquet, Large slip effect at a nonwetting fluid–solid interface. *Phys. Rev. Lett.*, **82** (1999) 4671–4674.

16 J. Baudry, E. Charlaix, A. Tonck, D. Mazuyer, Experimental evidence for a large slip effect at a nonwetting fluid-solid interface. *Langmuir*, **17** (2001) 5232–5236.

17 J. Baugh, A. Kleinhammes, D. X. Han, Q. Wang, Y. Wu, Confinement effect on dipole-dipole interactions in nanofluids. *Science*, **294** (2001) 1505–1507.

18 O. Beckstein, P. C. Biggin, M. S. P. Sansom, A hydrophobic gating mechanism for nanopores. *J. Phys. Chem. B*, **105** (2001) 12902–12905.

19 H. J. C. Berendsen, J. R. Grigera, T. P. Straatsma, Themissing term in effective pair potentials. *J. Phys. Chem.*, **91** (1987) 6269–6271.

20 M. Berkowitz, J. A. McCammon, Molecular-dynamics with stochastic boundary-conditions. *Chem. Phys. Lett.*, **90** (1982) 215–217.

21 G. A. Bird, Breakdown of translational and rotational equilibrium in gaseous expansions. *AIAA J.*, **8** (1970) 1998–2003.

22 G. A. Bird, *Molecular Gas Dynamics and the Direct Simulation of Gas Flows*. Clarendon Press, Oxford, 1994.

23 I. Bitsanis, J. J. Magda, M. Tirrell, H. T. Davis, Molecular dynamics of flow in micropores. *J. Chem. Phys.*, **87** (1987) 1733–1750.

24 I. Bitsanis, S. A. Somers, H. T. Davis, M. Tirrell, Microscopic dynamics of flow in molecularly narrow pores. *J. Chem. Phys.*, **93** (1990) 3427–3431.

25 T. D. Blake, Slip between a liquid and a solid: D. M. Tolstoi's (1952) theory reconsidered. *Colloids Surf.*, **47** (1990) 135–145.

26 L. Bocquet, Glissement d'un fluide sur une surface de rugosité modèle. *C. R. Acad. Sci. II*, **316** (1993) 7–12.

27 E. Bonaccurso, M. Kappl, H.-J. Butt, Hydrodynamic force measurements: boundary slip of water on hydrophilic surfaces and electrokinetic effects. *Phys. Rev. Lett.*, **88** (2002) 076103.

28 M. Born, R. Oppenheimer, Zur Quantentheorie der Molekeln. *Ann. Phys.*, **84** (1927) 457–484.

29 L. Boruvka, A. W. Neumann, Generalization of the classical theory of capillarity. *J. Chem. Phys.*, **66** (1977) 5464–5476.

30 I. D. Boyd, G. Chen, G. V. Candler, Predicting failure of the continuum fluid

equations in transitional hypersonic flows. *Phys. Fluids*, **7** (1995) 210–219.

31 T. H. Boyer, Unretarded London–van der Waals forces derived from classical electrodynamics with classical electromagnetic zero-point radiation. *Phys. Rev. A*, **6** (1972) 314–319.

32 D. W. Brenner, Empirical potential for hydrocarbons for use in simulating the chemical vapor deposition of diamond films. *Phys. Rev. B*, **42** (1990) 9458–9471.

33 F. Bresme, N. Quirke, Computer simulation study of the wetting behaviour and line tensions of nanometer size particulates at a liquid–vapor interface. *Phys. Rev. Lett.*, **80** (1998) 3791–3794.

34 F. Bresme, N. Quirke, Computer simulation of wetting and drying of spherical particulates at a liquid–vapor interface. *J. Chem. Phys.*, **110** (1999) 3536–3547.

35 F. Bresme, N. Quirke, Computer simulation studies of liquid lenses at a liquidliquid interface. *J. Chem. Phys.*, **112** (2000) 5985–5990.

36 B. R. Brooks, R. E. Bruccoleri, B. D. Olafson, D. J. States, S. Swaminathan, M. Karplus, CHARMM – a program for macromolecular energy, minimization, and dynamics calculations. *J. Comput. Chem.*, **4** (1983) 187–217.

37 A. Brünger, C. L. Brooks, M. Karplus, Stochastic boundary conditions for molecular dynamics simulations of ST2 water. *Chem. Phys. Lett.*, **105** (1984) 495–500.

38 R. Bulkley, Viscous flow and surface films. *Natl. Bur. Stand. J. Res.*, **6** (1931) 89–112.

39 E. D. Burchart, V. A. Verheij, H. van Bekkum, B. de Graaf, A consistent molecular mechanics force-field for all-silica zeolites. *Zeolites*, **12** (1992) 183–189.

40 D. G. Cahill, K. E. Ford, G. D. Mahan, A. Majumdar, H. J. Maris, R. Merlin, S. R. Phillpot, Nanoscale thermal transport. *J. Appl. Phys.*, **93** (2003) 793–818.

41 H. Cao, J. O. Tegenfeldt, R. H. Austin, S. Y. Chou, Gradient nanostructures for interfacing microfluidics and nanofluidics. *Appl. Phys. Lett.*, **81** (2002) 3058–3060.

42 H. Cao, Z. N. Yu, J. Wang, J. O. Tegenfeldt, R. H. Austin, E. Chen, W. Wu, S. Y. Chou, Fabrication of 10-nm enclosed nanofluidic channels. *Appl. Phys. Lett.*, **81** (2002) 174–176.

43 D. Y. C. Chan, R. G. Horn, The drainage of thin liquid films between solid surfaces. *J. Chem. Phys.*, **83** (1985) 5311–5324.

44 D. Chandler, Two faces of water. *Nature*, **417** (2002) 491–491.

45 R. J. Chen, S. Bangsaruntip, K. A. Drouvalakis, N. W. S. Kam, M. Shim, Y. M. Li, W. Kim, P. J. Utz, H. J. Dai, Noncovalent functionalization of carbon nanotubes for highly specific electronic biosensors. *Proc. Natl. Acad. Sci. USA*, **100** (2003) 4984–4989.

46 Y. Chen, J.-G. Weng, J. R. Lukes, A. Majumdar, C.-L. Tien, Molecular dynamics simulation of the meniscus formation between two surfaces. *Appl. Phys. Lett.*, **79** (2001) 1267–1269.

47 N. V. Churaev, Thin liquid layers. *Colloid J.*, **58** (1996) 681–693.

48 N. V. Churaev, V. D. Sobolev, A. N. Somov, Slippage of liquids over lyophobic solid surfaces. *J. Colloid Interface Sci.*, **97** (1984) 574–581.

49 G. Ciccotti, G. J. Martyna, S. Melchionna, M. E. Tuckerman, Constrained isothermal–isobaric molecular dynamics with full atomic virial. *J. Phys. Chem. B*, **105** (2001) 6710–6715.

50 M. Cieplak, J. Koplik, J. R. Banavar, Boundary conditions at a fluid–solid interface. *Phys. Rev. Lett.*, **86** (2001) 803–806.

51 W. D. Cornell, P. Cieplak, C. I. Bayly, I. R. Gould, K. M. Merz, Jr., D. M. Ferguson, D. C. Spellmeyer, T. Fox, J. W. Caldwell, P. A. Kollman, A second generation force field for the simulation of proteins, nucleic acids, and organic molecules. *J. Am. Chem. Soc.*, **117** (1995) 5179–5197.

52 E. R. Cruz-Chu, A. Aksimentiev, K. Schulten, Water–silica force field for simulating nanodevices. *J. Phys. Chem. B*, **110** (2006) 21497–21508.

53 P. T. Cummings, D. J. Evans, Nonequilibrium molecular dynamics

approaches to transport properties and non-Newtonian fluidy rheology. *Ind. Eng. Chem. Res.*, **31** (1992) 1237–1252.

54 T. Darden, D. York, L. Pedersen, Particle mesh Ewald: an $N \cdot \log N$ method for Ewald sums in large systems. *J. Chem. Phys.*, **98** (1993) 10089–10092.

55 J. De Coninck, M. J. de Ruijter, M. Voué, Dynamics of wetting. *Curr. Opin. Colloid Interface Sci.*, **6** (2001) 49–53.

56 J. de Jong, R. G. H. Lammertink, M. Wessling, Membranes and microfluidics: a review. *Lab Chip*, **6** (2006) 1125–1139.

57 M. J. de Ruijter, T. D. Blake, J. De Coninck, Dynamic wetting studies by molecular modeling simulations of droplet spreading. *Langmuir*, **15** (1999) 7836–7847.

58 M. J. de Ruijter, J. De Coninck, Contact angle relaxation during the spreading of partially wetting drops. *Langmuir*, **13** (1997) 7293–7298.

59 K. A. Dill, Dominant forces in protein folding. *Biochemistry*, **29** (1990) 7133–7155.

60 M. Dittrich, J. Yu, K. Schulten, PcrA helicase, a molecular motor studied from the electronic to the functional level. Markus Dittrich, Jin Yu, and Klaus Schulten. *Topics in Current Chemistry*, **268** (2006) 319–347.

61 J. R. Dorfman, *An Introduction to Chaos in Nonequilibrium Statistical Mechanics*, Vol. 1. Cambridge University Press, Cambridge, 1999.

62 C. Douketis, G. Scoles, S. Marchetti, M. Zen, A. J. Thakkar, Intermolecular forces via hybrid Hartree–Fock–SCF plus damped dispersion (HFD) energy calculations. An improved spherical model. *J. Chem. Phys.*, **76** (1982) 3057–3063.

63 B. Dreiseikelmann, Translocation of DNA across bacterial membranes. *Microbiol. Rev.*, **58** (1994) 293–316.

64 E. Dujardin, T. W. Ebbesen, H. Hiura, K. Tanigaki, Capillarity and wetting of carbon nanotubes. *Science*, **265** (1994) 1850–1852.

65 A. Dupuis, E. M. Kotsalis, P. Koumoutsakos, Coupling lattice Boltzmann and molecular dynamics models for dense fluids. *Phys. Rev. E*, **75** (2007) 046704-2.

66 W. D. Elliott, J. A. Board, Jr, Fast Fourier transform accelerated fast multipole algorithm. *SIAM J. Sci. Stat. Comput.*, **17** (1996) 398–415.

67 P. Español, M. Revenga, Smoothed dissipative particle dynamics. *Phys. Rev. E*, **67** (2003) 026705-1–026705-12.

68 P. Espanol, P. Warren, Statistical-mechanics of dissipative particle dynamics. *Europhys. Lett.*, **30** (1995) 191–196.

69 U. Essmann, L. Perera, M. L. Berkowitz, T. Darden, H. Lee, L. G. Pedersen, A smooth particle mesh Ewald method. *J. Chem. Phys.*, **103** (1995) 8577–8593.

70 P. P. Ewald, Die Berechnung optischer und elektrostatische Gitterpotentiale. *Ann. Phys.*, **64** (1921) 253–287.

71 C. F. Fan, T. Cağin, Wetting of crystalline polymer surfaces: a molecular dynamics simulation. *J. Chem. Phys.*, **103** (1995) 9053–9061.

72 D. Feller, K. D. Jordan, Estimating the strength of the water/single-layer graphite interaction. *J. Phys. Chem. A*, **104** (2000) 9971–9975.

73 E. Fermi, J. Pasta, S. Ulam, Studies in nonlinear problems. *Los Alamos Report LA-1940*, 1955.

74 E. G. Flekkøy, J. Feder, G. Wagner, Coupling particles and fields in a diffusive hybrid model. *Phys. Rev. E*, **64** (2001) 066302-1–066302-7.

75 E. G. Flekkøy, G. Wagner, J. Feder, Hybrid model for combined particle and continuum dynamics. *Europhys. Lett.*, **52** (2000) 271–276.

76 T. R. Forester, W. Smith, SHAKE, rattle, roll: efficient constaint algorithms for linked rigid bodies. *J. Comput. Chem.*, **19** (1998) 102–111.

77 F. M. Fowkes, W. D. Harkins, The state of monolayers adsorbed at the interface solid-aqueous solution. *J. Am. Chem. Soc.*, **62** (1940) 3377–3377.

78 M. J. Frisch, G. W. Trucks, H. B. Schlegel, G. E. Scuseria, M. A. Robb, J. R. Cheeseman, V. G. Zakrzewski, J. A. Montgomery Jr., R. E. Stratmann, J. C. Burant, S. Dapprich, J. M. Millam, A. D. Daniels, K. N. Kudin, M. C. Strain, O. Farkas, J. Tomasi, V. Barone, M. Cossi,

R. Cammi, B. Mennucci, C. Pomelli, C. Adamo, S. Clifford, J. Ochterski, G. A. Petersson, P. Y. Ayala, Q. Cui, K. Morokuma, D. K. Malick, A. D. Rabuck, K. Raghavachari, J. B. Foresman, J. Cioslowski, J. V. Ortiz, A. G. Baboul, B. B. Stefanov, G. Liu, A. Liashenko, P. Piskorz, I. Komaromi, R. Gomperts, R. L. Martin, D. J. Fox, T. Keith, M. A. Al-Laham, C. Y. Peng, A. Nanayakkara, C. Gonzalez, M. Challacombe, P. M. W. Gill, B. Johnson, W. Chen, M. W. Wong, J. L. Andres, C. Gonzalez, M. Head-Gordon, E. S. Replogle, J. A. Pople, *Gaussian 98, Revision A.7. Technical Report*. Gaussian, Pittsburgh, PA, 1998.

79 M. Gad-el Hak, The fluid mechanics of microdevices – the Freeman Scolar lecture. *J. Fluids Eng.*, **121** (1999) 5–33.

80 H. Gao, Y. Kong, D. Cui, Spontaneous insertion of DNA oligonucleotides into carbon nanotubes. *Nano Lett.*, **3** (2003) 471–473.

81 J. Gao, M. A. Thompson, *Combined Quantum Mechanical and Molecular Mechanical Methods*, ACS Symposium Series, Vol. 712. American Chemical Society, Washington, DC, 1998.

82 A. L. Garcia, J. B. Bell, W. Y. Crutchfield, B. J. Alder, Adaptive mesh and algorithm refinement using direct simulation Monte Carlo. *J. Comput. Phys.*, **154** (1999) 134–155.

83 M. L. Gee, P. M. McGuiggan, J. N. Israelachvili, A. M. Homola, Liquid to solid-like transitions of molecularly thin films under shear. *J. Chem. Phys.*, **93** (1990) 1895–1906.

84 A. Glättli, X. Daura, W. F. van Gunsteren, Derivation of an improved simple point charge model for liquid water: SPC/A and SPC/L. *J. Chem. Phys.*, **116** (2002) 9811–9828.

85 S. C. Glotzer, W. Paul, Molecular and mesoscale simulation methods for polymer materials. *Annu. Rev. Mater. Res.*, **32** (2002) 401–436.

86 Y. Gogotsi, N. Naguib, J. A. Libera, *In situ* chemical experiments in carbon nanotubes. *Chem. Phys. Lett.*, **365** (2002) 354–360.

87 M. C. Gordillo, J. Martí, Hydrogen bonding in supercritical water confined in carbon nanotubes. *Chem. Phys. Lett.*, **341** (2001) 250–254.

88 M. C. Gordillo, J. Martí, Molecular dynamics description of a layer of water molecules on a hydrophobic surface. *J. Chem. Phys.*, **117** (2002) 3425–3430.

89 M. E. Gracheva, A. L. Xiong, A. Aksimentiev, K. Schulten, G. Timp, J. P. Leburton, Simulation of the electric response of dna translocation through a semiconductor nanopore-capacitor. *Nanotechnology*, **17** (2006) 622–633.

90 S. Granick, Motion and relaxations of confined liquids. *Science*, **253** (1991) 1374–1379.

91 L. Greengard, V. Rokhlin, The rapid evaluation of potential fields in three dimensions. *Lect. Notes Math.*, **1360** (1988) 121–141.

92 H. Grubmüller, B. Heymann, P. Tavan, Ligand binding: molecular mechanics calculation of the streptavidin–biotin rupture force. *Science*, **271** (1996) 997–999.

93 H. Grubmuller, K. Schulten (eds.), Special issue: Advances in molecular dynamics simulations. *J. Struct. Biol.*, **157** (2007) 443–443.

94 L. Guidoni, P. Maurer, S. Piana, U. Röthlisberger, Hybrid Carr–Parrinello/molecular mechanics modelling of transition metal complexes: structure, dynamics and reactivity. *Quant. Struct.–Act. Relat.*, **21** (2002) 119–127.

95 N. G. Hadjiconstantinou, Hybrid atomistic-continuum formulations and the moving contact-line problem. *J. Comput. Phys.*, **154** (1999) 245–265.

96 N. G. Hadjiconstantinou, A. T. Patera, Heterogeneous atomistic-continuum representations for dense fluid systems. *Int. J. Mod. Phys. C*, **8** (1997) 967–976.

97 J. Han, H. G. Craighead, Separation of long DNA molecules in a microfabricated entropic trap array. *Science*, **288** (2000) 1026–1029.

98 J. Han, A. Globus, R. Jaffe, G. Deardorff, Molecular dynamics simulations of carbon nanotube-based gears. *Nanotechnology*, **8** (1997) 95–102.

99 J.-P. Hansen, L. Verlet, Phase transitions of the Lennard-Jones system. *Phys. Rev.*, **184** (1969) 151–162.

100 C. K. Harnett, G. W. Coates, H. G. Craighead, Heat-depolymerizable polycarbonates as electron beam patternable sacrificial layers for nanofluidics. *J. Vac. Sci. Technol. B*, **19** (2001) 2842–2845.

101 P. Harris, *Carbon Nanotubes and Related Structures*. Cambridge University Press, Cambridge, 1999.

102 J. Hautman, M. L. Klein, Microscopic wetting phenomena. *Phys. Rev. Lett.*, **67** (1991) 1763–1766.

103 U. Heinbuch, J. Fischer, Liquid flow in pores: slip, no-slip or multilayer sticking. *Phys. Rev. A*, **40** (1989) 1144–1146.

104 H. Helmholtz, G. von Piotrowski, Über Reibung tropfbarer Flüssigkeiten. *Sitzungsber. Kaiserl. Akad. Wisse.*, **40** (1860) 607–658.

105 J. B. Heng, A. Aksimentiev, C. Ho, P. Marks, Y. V. Grinkova, S. Sligar, K. Schulten, G. Timp, Stretching DNA using the electric field in a synthetic nanopore. *Nano Lett.*, **5** (2005) 1883–1888.

106 D. Hirshfeld, D. C. Rapaport, Molecular dynamics simulation of Taylor–Couette vortex formation. *Phys. Rev. Lett.*, **80** (1998) 5337–5340.

107 C.-M. Ho, Y.-C. Tai, Review: MEMS and its application for flow control. *J. Fluids Eng.*, **118** (1996) 437–447.

108 C.-M. Ho, Y.-C. Tai, Micro-electro-mechanical-systems (MEMS) and fluid flow. *Annu. Rev. Fluid Mech.*, **30** (1998) 579–612.

109 R. W. Hockney, J. W. Eastwood, *Computer Simulation Using Particles*, 2nd edn. Institute of Physics Publishing, Bristol, 1988.

110 R. W. Hockney, S. P. Goel, J. W. Eastwood, A 10 000 particle molecular dynamics model with long-range forces. *Chem. Phys. Lett.*, **21** (1973) 589–591.

111 J. K. Holt, H. G. Park, Y. M. Wang, M. Stadermann, A. B. Artyukhin, C. P. Grigoropoulos, A. Noy, O. Bakajin, Fast mass transport through sub-2-nanometer carbon nanotubes. *Science*, **312** (2006) 1034–1037.

112 P. J. Hoogerbrugge, J. M. V. A. Koelman, Simulating microscopic hydrodynamics phenomena with dissipative particle dynamics. *Europhys. Lett.*, **19** (1992) 155–160.

113 Y. Hu, S. L. Johnsson, A data-parallel implementation of hierarchical N-body methods. *Int. J. Supercomput. Appl.*, **10** (1996) 3–40.

114 E. Hult, Y. Andersson, B. I. Lundqvist, D. C. Langreth, Density functional for van der Waals forces at surfaces. *Phys. Rev. Lett.*, **77** (1996) 2029–2032.

115 E. Hult, H. Rydberg, B. I. Lundqvist, D. C. Langreth, Unified treatment of asymptotic van der Waals forces. *Phys. Rev. B*, **59** (1999) 4708–4713.

116 G. Hummer, J. C. Rasaiah, J. P. Noworyta, Water conduction through the hydrophobic channel of a carbon nanotube. *Nature*, **414** (2001) 188–190.

117 P. Hünenberger, J. A. McCammon, Ewald artifacts in computer simulations of ionic solvation and ion–ion interaction: a continuum electrostatic study. *J. Chem. Phys.*, **110** (1999) 1856–1872.

118 S. Iijima, Helical microtubules of graphitic carbon. *Nature*, **354** (1991) 56–58.

119 J. Israelachvili, M. Gee, P. McGuiggan, A. Homola, Dynamic properties of molecularly thin liquid-films. *Abstr. Pap. Am. Chem. Soc.*, **196** (1988) 277.

120 J. N. Israelachvili, *Intermolecular and Surface Forces. With Applications to Colloidal and Biological Systems*, 2nd edn. Academic Press, New York, 1992.

121 B. Isralewitz, M. Gao, K. Schulten, Steered molecular dynamics and mechanical functions of proteins. *Curr. Opin. Struct. Biol.*, **11** (2001) 224–230.

122 A. Jabbarzadeh, J. D. Atkinson, R. I. Tanner, Effect of the wall roughness on slip and rheological properties of hexadecane in molecular dynamics simulation of Couette shear flow between two sinusoidal walls. *Phys. Rev. E*, **61** (2000) 690–699.

123 W. L. Jorgensen, Revised TiPS for simulations of liquid water and aqueous solutions. *J. Comput. Phys.*, **77** (1982) 4156–4163.

124 W. L. Jorgensen, J. Chandrasekhar, J. D. Madura, R. W. Impey, M. L. Klein, Comparison of simple potential functions for simulating liquid water. *J. Chem. Phys.*, **79** (1983) 926–935.

125 A. Kalra, S. Garde, G. Hummer, Osmotic water transport through carbon nanotube membranes. *Proc. Natl. Acad. Sci. USA*, **100** (2003) 10175–10180.

126 T. L. Kaltz, L. N. Long, M. M. Micci, J. K. Little, Supercritical vaporization of liquid oxygen droplets using molecular dynamics. *Combust. Sci. Technol.*, **136** (1998) 279–301.

127 R. Karlsson, M. Karlsson, A. Karlsson, A.-S. Cans, J. Bergenholtz, B. Åkerman, A. G. Ewing, M. Voinova, O. Orwar, Moving-wall-driven flows in nanofluidic systems. *Langmuir*, **18** (2002) 4186–4190.

128 G. E. Karniadakis, A. Beskok, *Micro Flows. Fundamentals and Simulation*. Springer, New York, 2002.

129 W. Kauzmann, Some factors in the interpretation of protein denaturation. *Adv. Protein Chem.*, **14** (1959) 1–63.

130 P. J. Kemery, J. K. Steehler, P. W. Bohn, Electric field mediated transport in nanometer diameter channels. *Langmuir*, **14** (1998) 2884–2889.

131 J. Klein, E. Kumacheva, Simple liquids confined to molecularly thin layers. I. confinement-induced liquid-to-solid phase transitions. *J. Chem. Phys.*, **108** (1998) 6996–7009.

132 W. Koch, M. C. Holthausen, *A Chemist's Guide to Density Functional Theory*, 2nd edn. Wiley-VCH, Weinheim, 2001.

133 K. Koga, G. T. Gao, H. Tanaka, X. C. Zeng, Formation of ordered ice nanotubes inside carbon nanotubes. *Nature*, **412** (2001) 802–805.

134 K. Koga, G. T. Gao, H. Tanaka, X. C. Zeng, How does water freeze inside carbon nanotubes? *Physica A*, **314** (2002) 462–469.

135 K. Koga, H. Tanaka, X. C. Zeng, First-order transition in confined water between high-density liquid and low-density amorphous phases. *Nature*, **408** (2000) 564–567.

136 K. Koga, X. C. Zeng, H. Tanaka, Freezing of confined water: a bilayer ice phase in hydrophobic nanopores. *Phys. Rev. Lett.*, **79** (1997) 5262–5265.

137 J. Kong, N. R. Franklin, C. Zhou, M. G. Chapline, S. Peng, C. Kyeongjae, H. Dai, Nanotube molecular wires as chemical sensors. *Science*, **287** (2000) 622–625.

138 J. Koplik, J. R. Banavar, Continuum deductions from molecular hydrodynamics. *Annu. Rev. Fluid Mech.*, **27** (1995) 257–292.

139 J. Koplik, J. R. Banavar, Corner flow in the sliding plate problem. *Phys. Fluids*, **7** (1995) 3118–3125.

140 J. Koplik, J. R. Banavar, J. F. Willemsen, Molecular dynamics of Poiseuille flow and moving contact lines. *Phys. Rev. Lett.*, **60** (1988) 1282–1285.

141 E. M. Kotsalis, E. Demosthenous, J. H. Walther, S. C. Kassinos, P. Koumoutsakos, Wetting of doped carbon nanotubes by water droplets. *Chem. Phys. Lett.*, **412** (2005) 250–254.

142 E. M. Kotsalis, J. H. Walther, P. Koumoutsakos, Control of density density fluctuations in atomistic-continuum simulations of dense liquids. *Phys. Rev. E*, **76** (2007) 016709-2.

143 P. Koumoutsakos, Multiscale flow simulations using particles. *Annu. Rev. Fluid Mech.*, **37** (2005) 457–487.

144 V. Kräutler, W. F. van Gunsteren, P. H. Hünenberger, A fast SHAKE algorithm to solve distance constraint equations for small molecules in molecular dynamics simulations. *J. Comput. Chem.*, **22** (2001) 501–508.

145 K. Kremer, F. Müller-Plathe, Multiscale simulation in polymer science. *Mol. Simul.*, **28** (2002) 729–750.

146 T. C. Kuo, D. M. Cannon, M. A. Shannon, P. W. Bohn, J. Sweedler, Hybrid three-dimensional nanofluidic/microfluidic devices using molecular gates. *Sens. Actuators A*, **102** (2003) 223–233.

147 T.-C. Kuo, D. M. Cannon, Jr., W. Feng, M. A. Shannon, J. V. Sweedler, P. W. Bohn, Three-dimensional fluidic architectures using nanofluidic diodes to control transport between microfluidic channels in microelectromechanical devices. *Proceedings of mTAS Symposium, Monterey*, 2001, pp. 60–62.

148 T.-C. Kuo, L. A. Sloan, J. V. Sweedler, P. W. Bohn, Manipulating molecular transport through nanoporous membranes by control of electrokinetic

flow: effect of surface charge density and Debye length. *Langmuir*, **17** (2001) 6298–6303.

149 T. Lazaridis, Solvent size vs cohesive energy as the origin of hydrophobicity. *Acc. Chem. Res.*, **34** (2001) 931–937.

150 C. Y. Lee, J. A. McCammon, P. J. Rossky, The structure of liquid water at an extended hydrophobic surface. *J. Chem. Phys.*, **80** (1984) 4448–4455.

151 S. B. Lee, D. T. Mitchell, L. Trofin, T. K. Nevanen, H. Soderlund, C. R. Martin, Antibody-based bio-nanotube membranes for enantiomeric drug separations. *Science*, **296** (2002) 2198–2200.

152 J. E. Lennard-Jones, J. Corner, The calculation of surface tension from intermolecular forces. *Trans. Faraday Soc.*, **36** (1940) 1156–1162.

153 M. Lísal, J. Kolafa, I. Nezbeda, An examination of the five-site potential (TIP5P) for water. *J. Chem. Phys.*, **117** (2002) 8892–8897.

154 W. Loose, S. Hess, Rheology of dense model fluids via nonequilibrium molecular dynamics: shear thinning and ordering transition. *Rheol. Acta*, **28** (1989) 91–101.

155 C. F. Lopez, S. O. Nielsen, P. B. Moore, M. L. Klein, Understanding nature's design for a nanosyringe. *Proc. Natl. Acad. Sci. USA*, **101** (2004) 4431–4434.

156 D. Y. Lu, A. Aksimentiev, A. Y. Shih, E. Cruz-Chu, P. L. Freddolino, A. Arkhipov, K. Schulten, The role of molecular modeling in bionanotechnology. *Phys. Biol.*, **3** (2006) S40–S53.

157 D. Y. Lu, Y. Li, S. V. Rotkin, U. Ravaioli, K. Schulten, Modeling the polarizability of carbon nanotube molecular channels. *Biophys. J.*, **88** (2005) 182A.

158 G. Lu, P. Maragakis, E. Kaxiras, Carbon nanotube interaction with DNA. *Nano Lett.*, **5** (2005) 897–900.

159 K. Lum, D. Chandler, J. D. Weeks, Hydrophobicity at small and large length scales. *J. Phys. Chem. B*, **103** (1999) 4570–4577.

160 M. Lundgren, N. L. Allan, T. Cosgrove, N. George, Wetting of water and water/ethanol droplets on a non-polar surface: a molecular dynamics study. *Langmuir*, **18** (2002) 10462–10466.

161 B. A. Luty, M. E. Davis, I. G. Tironi, W. F. van Gunsteren, A comparison of particle–particle, particle–mesh and Ewald methods for calculating electrostatic interactions in periodic molecular systems. *Mol. Simul.*, **14** (1994) 11–20.

162 M. W. Mahoney, W. L. Jorgensen, A five-site model for liquid water and the reproduction of the density anomaly by rigid, nonpolarizable potential functions. *J. Chem. Phys.*, **112** (2000) 8910–8922.

163 M. Majumder, N. Chopra, R. Andrews, B. J. Hinds, Nanoscale hydrodynamics – enhanced flow in carbon nanotubes. *Nature*, **438** (2005) 44–44.

164 M. Majumder, N. Chopra, B. J. Hinds, Effect of tip functionalization on transport through vertically oriented carbon nanotube membranes. *J. Am. Chem. Soc.*, **127** (2005) 9062–9070.

165 G. Marechal, J.-P. Ryckaert, Atomic versus molecular description of transport properties in polyatomic fluids. n-butane as an illustration. *Chem. Phys. Lett.*, **101** (1983) 548–554.

166 M. Marsh, A. Helenius, Virus entry: open sesame. *Cell*, **124** (2006) 729–740.

167 S. Maruyama, Molecular dynamics methods for microscale heat transfer, in: *Advances in Numerical Heat Transfer*, W. J. Minkowycz, E. M. Sparrow (eds.), Vol. II, Institute of Physics Publishing, Taylor and Francis, 2001, pp. 189–226.

168 S. Maruyama, T. Kimura, A study of thermal resistance over a solid-liquid interface by the molecular dynamics method. *Thermal Sci. Eng.*, **7** (1999) 63–68.

169 J. Mathé, A. Aksimentiev, D. R. Nelson, K. Schulten, A. Meller, Orientation discrimination of single-stranded DNA inside the α-hemolysin membrane channel. *Proc. Natl. Acad. Sci. USA*, **102** (2005) 12377–12382.

170 A. M. Mathiowetz, A. Jain, N. Karasawa, W. A. Goddard, III, Protein simulations using techniques for very large systems – the cell multipole method for nonbond interactions and the Newton–Euler inverse mass operator method for

internal coordinate dynamics. *Proteins*, **20** (1994) 227–247.

171 M. Matsumoto, S. Saito, I. Ohmine, Molecular dynamics simulation of the ice nucleation and growth process leading to water freezing. *Nature*, **416** (2002) 409–413.

172 C. Mavroyannis, M. J. Stephen, Dispersion forces. *Mol. Phys.*, **5** (1962) 629–638.

173 J. C. Maxwell, On stress in rarefied gases arising from inqualities of temperature. *Philos. Trans. R. Soc. London*, **170** (1879) 231–256.

174 S. L. Mayo, B. D. Olafson, W. A. Goddard, III, DREIDING – a generic forcefield For molecular simulations. *J. Phys. Chem.*, **94** (1990) 8897–8909.

175 A. V. Melechko, T. E. McKnight, M. A. Guillorn, V. I. Merkulov, B. Ilic, M. J. Doktycz, D. H. Lowndes, M. L. Simpson, Vertically aligned carbon nanofibers as sacrificial templates for nanofluidic structures. *Appl. Phys. Lett.*, **82** (2003) 976–978.

176 M. M. Micci, T. L. Kaltz, L. N. Long, Molecular dynamics simulations of atomization and spray phenomena. *Atomization Sprays*, **11** (2001) 351–363.

177 S. A. Miller, C. R. Martin, Redoxmodulation of electroosmotic flowin a carbon nanotube membrane. *J. Am. Chem. Soc.*, **126** (2004) 6226–6227.

178 S. A. Miller, V. Y. Young, C. R. Martin, Electroosmotic flow in template-prepared carbon nanotube membranes. *J. Am. Chem. Soc.*, **123** (2001) 12335–12342.

179 T. F. Miller III, M. Eleftheriou, P. Pattnaik, A. Ndirango, D. Newns, G. J. Martyna, Symplectic quaternion scheme for biophysical molecular dynamics. *J. Chem. Phys.*, **116** (2002) 8649–8659.

180 O. Mishima, H. E. Stanley, The relationship between liquid, supercooled and glassy water. *Nature*, **396** (1998) 329–335.

181 S. Miyamoto, P. A. Kollman, SETTLE: an analytical version of the SHAKE and RATTLE algorithm for rigid water models. *J. Comput. Chem.*, **13** (1992) 952–962.

182 G. Mo, F. Rosenberger, Molecular-dynamics simulation of flow in a two-dimensional channel with atomically rough walls. *Phys. Rev. A*, **42** (1990) 4688–4692.

183 S. M. Moghimi, A. C. Hunter, J. C. Murray, Nanomedicine: current status and future prospects. *FASEB J.*, **19** (2005) 311–330.

184 C. Møller, M. S. Plesset, Note on an approximation treatment for many-electron systems. *Phys. Rev.*, **46** (1934) 618–622.

185 P. M. Morse, Diatomic molecules according to the wave mechanics. II. vibrational levels. *Phys. Rev.*, **34** (1929) 57–64.

186 C. L. M. H. Navier, Memoire sur les lois du mouvement des fluides. *Mem. Acad. R. Sci. Inst. Fr.*, **6** (1827) 389–440.

187 X. B. Nie, S. Y. Chen, W. N. E, M. O. Robbins, A continuum and molecular dynamics hybrid method for micro- and nano-fluid flow. *J. Fluid Mech.*, **500** (2004) 55–64.

188 M. Nijmeijer, C. Bruin, A. Bakker, A visual measurement of contact angles in a molecular-dynamics simulation. *Physica A*, **160** (1989) 166–180.

189 M. J. P. Nijmeijer, C. Bruin, A. F. Bakker, J. M. J. van Leeuwen, Wetting and drying on an inert wall by a fluid in a molecular dynamics simulation. *Phys. Rev. A*, **42** (1990) 6052–6059.

190 W. H. Noon, K. D. Ausman, R. E. Smalley, J. Ma, Helical ice-sheets inside carbon nanotubes in the physiological condition. *Chem. Phys. Lett.*, **355** (2002) 445–448.

191 D. Nykypanchuk, H. H. Strey, D. A. Hoagland, Brownian motion of DNA confined within a two-dimensional array. *Science*, **297** (2002) 987–990.

192 S. T. O'Connell, P. A. Thompson, Molecular dynamics-continuum hybrid computations: a tool for studying complex fluid flow. *Phys. Rev. E*, **52** (1995) R5792–R5795.

193 T. Okada, T. Keneko, R. Hatakeyama, K. Tohji, Electrically triggered insertion of single-stranded DNA into single-walled carbon nanotubes. *Chem. Phys. Lett.*, **417** (2006) 288–292.

194 D. Pantarotto, R. Singh, D. McCarthy, M. Erhardt, J.-P. Briand, M. Prato, K. Kostarelos, A. Bianco, Functionalized

carbon nanotubes for plasmid DNA gene delivery. *Angew. Chem. Int. Ed.*, **43** (2004) 5242–5246.

195 J. P. Perdew, S. Kurth, A. Zupan, P. Blaha, Accurate density functional with correct formal properties: a step beyond the generalized gradient approximation. *Phys. Rev. Lett.*, **82** (1999) 2544–2547.

196 C. Peter, G. Hummer, Ion transport through membrane-spanning nanopores studied by molecular dynamics simulations and continuum electrostatics calculations. *Biophys. J.*, **89** (2005) 2222–2234.

197 H. G. Petersen, Accuracy and efficiency of the particle mesh Ewald method. *J. Chem. Phys.*, **103** (1995) 3668–3679.

198 D. Poulikakos, S. Arcidiacono, S. Maruyama, Molecular dynamics simulation in nanoscale heat transfer: a review. *Micro. Therm. Eng.*, **7** (2003) 181–206.

199 L. R. Pratt, Molecular theory of hydrophobic effects: "She is too mean to have her name repeated". *Annu. Rev. Phys. Chem.*, **53** (2002) 409–436.

200 L. R. Pratt, A. Pohorille, Hydrophobic effects and modeling of biophysical aqueous solution interfaces. *Chem. Rev.*, **102** (2002) 2671–2692.

201 A. Rahman, Correlations in the motion of atoms in liquid argon. *Phys. Rev.*, **136** (1964) 405–411.

202 A. Rahman, F. H. Stillinger, Molecular dynamics study of liquid water. *J. Chem. Phys.*, **55** (1971) 3336–3359.

203 A. K. Rappé, C. J. Casewit, K. S. Colwell, W. A. Goddard, III, W. M. Skiff, UFF, a full periodic table force field for molecular mechanics and molecular dynamics simulations. *J. Am. Chem. Soc.*, **114** (1992) 10024–10035.

204 U. Raviv, J. Klein, Fluidity of bound hydration layers. *Science*, **297** (2002) 1540–1543.

205 S. Richardson, On the no-slip boundary condition. *J. Fluid Mech.*, **59** (1973) 707–719.

206 M. O. Robbins, P. A. Thompson, Critical velocity of stick-slip motion. *Science*, **253** (1991) 916.

207 S. Roy, H. Vedala, W. Choi, Vertically aligned carbon nanotube probes for monitoring blood cholesterol. *Nanotechnology*, **17** (2006) 14–18.

208 J.-P. Ryckaert, A. Bellemans, Molecular dynamics of liquid n-butane near its boiling point. *Chem. Phys. Lett.*, **30** (1975) 123–125.

209 J.-P. Ryckaert, A. Bellemans, G. Ciccotti, G. V. Paolini, Evaluation of transport coefficients of simple fluids by molecular dynamics: comparison of Green–Kubo and nonequilibrium approaches for shear viscosity. *Phys. Rev. A*, **39** (1989) 259–267.

210 J.-P. Ryckaert, G. Ciccotti, H. J. C. Berendsen, Numerical integration of the cartesian equations of motion of a system with constraints: molecular dynamics of *n*-alkanes. *J. Comput. Phys.*, **23** (1977) 327–341.

211 H. Rydberg, N. Jacobson, P. Hyldgaard, S. Simak, B. I. Lundqvist, D. C. Langreth, Hard numbers on soft matter. *Surf. Sci.*, **532** (2003) 606–610.

212 C. Sagui, T. D. Darden, Molecular dynamics simulations of biomolecules: Long-range electrostatic effects. *Annu. Rev. Biophys. Biomol. Struct.*, **28** (1999) 155–179.

213 M. J. L. Sangster, M. Dixon, Interionic potentials in alkali halides and their use in simulations of the molten salts. *Adv. Phys.*, **25** (1976) 247–342.

214 G. Saville, Computer simulation of the liquid–solid–vapour contact angle. *J. Chem. Soc., Faraday Trans.*, **5** (1977) 1122–1132.

215 L. F. Scatena, M. G. Brown, G. L. Richmond, Water at hydrophobic surfaces: Weak hydrogen bonding and strong orientation effects. *Science*, **292** (2001) 908–912.

216 K. E. Schmidt, M. A. Lee, Implementing the fast multipole method in three dimensions. *J. Stat. Phys.*, **63** (1991) 1223–1235.

217 E. Schnell, Slippage of water over nonwettable surfaces. *J. Appl. Phys.*, **27** (1956) 1149–1152.

218 M. Schoen, C. L. Rhykerd, D. J. Diestler, J. H. Cushman, Fluids in micropores: I. Structure of a simple classical fluid in a slit pore. *J. Chem. Phys.*, **87** (1987) 5464–5476.

219 M. E. Schrader, Ultrahigh-vacuum techniques in the measurement of

contact angles. 5. LEED study of the effect of structure on the wettability of graphite. *J. Phys. Chem.*, **84** (1980) 2774–2779.

220 H. M. Senn, W. Thiel, *QM/MM Methods for Biological Systems*, Vol. 268, Springer, Berlin, 2007, pp. 173–290.

221 M. Serrano, P. Espanol, Thermodynamically consistent mesoscopic fluid particle model. *Phys. Rev. E*, **64** (2001) 046115-1–046115-18.

222 J. H. Sikkenk, J. O. Indekeu, J. M. J. van Leeuwen, E. O. Vossnack, A. F. Bakker, Simulation of wetting and drying at solid fluid interfaces on the Delft molecular-dynamics processor. *J. Stat. Phys.*, **52** (1988) 23–44.

223 F. Sim, A. St-Amant, I. Papai, D. R. Salahub, Gaussian density functional calculations on hydrogen-bonded systems. *J. Am. Chem. Soc.*, **114** (1992) 4391–4400.

224 S. M. Simon, C. S. Peskin, G. F. Oster, What drives the translocation of proteins. *Proc. Natl. Acad. Sci. USA*, **89** (1992) 3770–3774.

225 J. Slovák, H. Tanaka, K. Koga, X. C. Zeng, Computer simulation of water–ice transition in hydrophobic nanopores. *Physica A*, **292** (2001) 87–101.

226 G. D. Smith, R. L. Jaffe, Comparative study of force fields for benzene. *J. Phys. Chem.*, **100** (1996) 9624–9630.

227 V. P. Sokhan, D. Nicholson, N. Quirke, Fluid flow in nanopores: an examination of hydrodynamic boundary conditions. *J. Chem. Phys.*, **115** (2001) 3878–3887.

228 V. P. Sokhan, D. Nicholson, N. Quirke, Fluid flow in nanopores: accurate boundary conditions for carbon nanotubes. *J. Chem. Phys.*, **117** (2002) 8531–8539.

229 P. E. Sokol, W. J. Ma, K. W. Herwig, W. M. Snow, Y. Wang, J. Koplik, J. R. Banavar, Freezing in confined geometries. *Appl. Phys. Lett.*, **61** (1992) 777–779.

230 P. J. Steinbach, B. R. Brooks, New spherical-cutoff methods for long-range forces in macromolecular simulations. *J. Comput. Chem.*, **15** (1994) 667–683.

231 G. C. Stokes, On the effect of the internal friction of fluids on the motion of pendulums. *Trans. Cambridge Philos. Soc.*, **9** (1851) 8–106.

232 L. Sun, R. M. Crooks, Single carbon nanotube membranes: a well-defined model for studying mass transport through nanoporous materials. *J. Am. Chem. Soc.*, **122** (2000) 12340–12345.

233 A. Szabo, N. S. Ostlund, *Modern Quantum Chemistry*. McGraw-Hill, New York, 1989.

234 K. T. Tang, J. P. Toennies, An improved simple model for the van der Waals potential based on universal damping functions for the dispersion coefficients. *J. Chem. Phys.*, **80** (1984) 3726–3741.

235 O. Teleman, B. Jönsson, S. Engström, A molecular dynamics simulation of a water model with intramolecular degrees of freedom. *Mol. Phys.*, **60** (1987) 193–203.

236 S. C. Terry, J. H. Jerman, J. B. Angell, A gas chromatographic air analyzer fabricated on a silicon wafer. *IEEE Trans. Electron Devices*, **26** (1979) 1880–1886.

237 J. Tersoff, New empirical approach for the structure and energy of covalent systems. *Phys. Rev. B*, **37** (1988) 6991–7000.

238 J. Thar, W. Reckien, B. Kirchner, *Carr–Parrinello Molecular Dynamics Simulations and Biological Systems*, Vol. 268, Springer, Berlin, 2007, pp. 133–171.

239 D. N. Theodorou, U. W. Suter, Atomistic modeling of mechanical properties of polymeric glasses. *Macromolecules*, **19** (1986) 139–154.

240 P. A. Thompson, M. O. Robbins, Origin of stick–slip motion in boundary lubrication. *Science*, **250** (1990) 792–794.

241 P. A. Thompson, M. O. Robbins, Shear flow near solids: epitaxial order and flow boundary conditions. *Phys. Rev. A*, **41** (1990) 6830–6841.

242 P. A. Thompson, S. M. Troian, A general boundary condition for liquid flow at solid surfaces. *Nature*, **389** (1997) 360–362.

243 P. A. Thompson, W. B. Brinckerhoff, M. O. Robbins, Microscopic studies of static and dynamic contact angles. *J. Adhes. Sci. Technol.*, **7** (1993) 535–554.

244 S. Tiwari, Coupling of the Boltzmann and Euler equations with automatic domain decomposition. *J. Comput. Phys.*, **144** (1998) 710–726.

245 B. D. Todd, P. J. Daivis, Nonequilibrium molecular dynamics simulations of planar elongational flow with spatially and temporally periodic boundary conditions. *Phys. Rev. Lett.*, **81** (1998) 1118–1120.

246 B. D. Todd, P. J. Daivis, D. J. Evans, Pressure tensor for inhomogeneous fluids. *Phys. Rev. E*, **52** (1995) 1627–1638.

247 K. P. Travis, K. E. Gubbins, Poiseuille flow of Lennard-Jones fluids in narrow slit pores. *J. Chem. Phys.*, **112** (2000) 1984–1994.

248 K. P. Travis, B. D. Todd, D. J. Evans, Departure from Navier–Stokes hydrodynamics in confined liquids. *Phys. Rev. E*, **55** (1997) 4288–4295.

249 M. E. Tuckerman, C. J. Mundy, S. Balasubramanian, M. L. Klein, Modified nonequilibrium molecular dynamics for fluid flows with energy conservation. *J. Chem. Phys.*, **106** (1997) 5615–5621.

250 R. E. Tuzun, D. W. Noid, B. G. Sumpter, R. C. Merkle, Dynamics of fluid flow inside carbon nanotubes. *Nanotechnology*, **7** (1996) 241–248.

251 R. E. Tuzun, D. W. Noid, B. G. Sumpter, R. C. Merkle, Dynamics of He/C_{66} flow inside carbon nanotubes. *Nanotechnology*, **8** (1997) 112–118.

252 J. W. G. Tyrrell, P. Attard, Images of nanobubbles on hydrophobic surfaces and their interaction. *Phys. Rev. Lett.*, **87** (2001) 176104.

253 D. Ugarte, A. Châtelain, W. A. de Heer, Nanocapillarity and chemistry in carbon nanotubes. *Science*, **274** (1996) 1897–1899.

254 N. Vaidehi, A. Jain, W. A. Goddard, III, Constant temperature constrained molecular dynamics: the Newton–Euler inverse mass operator method. *J. Phys. Chem.*, **100** (1996) 10508–10517.

255 S. Vaitheeswaran, J. C. Rasaiah, G. Hummer, Electric field and temperature effects on water in the narrow nonpolar pores of carbon nanotubes. *J. Chem. Phys.*, **121** (2004) 7955–7965.

256 W. F. van Gunsteren, H. J. C. Berendsen, Algorithms for macromolecular dynamics and constraint dynamics. *Mol. Phys.*, **37** (1977) 1311–1327.

257 W. F. van Gunsteren, S. R. Billeter, S. R. Eising, P. H. Hünenberger, P. Krüger, A. E. Mark, W. R. P. Scott, I. G. Tironi, *Biomolecular Simulation: the GROMOS96 Manual and User Guide*. Vdf Hochschulverlag, Zürich, 1996.

258 P. Vashishta, R. K. Kalia, A. Nakano, Multimillion atom simulations of dynamics of oxidation of an aluminum nanoparticle and nanoindentation on ceramics. *J. Phys. Chem. B*, **110** (2006) 3727–3733.

259 L. Verlet, Computer experiments on classical fluids. I. Thermodynamical properties of Lennard-Jones molecules. *Phys. Rev.*, **159** (1967) 98–103.

260 L. Verlet, Computer experiments on classical fluids. II. Equilibrium correlation functions. *Phys. Rev.*, **165** (1968) 201–214.

261 D. S. Vieira, L. Degrève, Molecular simulation of a concentrated aqueous KCl solution. *J. Mol. Struct.*, **580** (2002) 127–135.

262 O. I. Vinogradova, Slippage of water over hydrophobic surfaces. *Int. J. Miner. Process.*, **56** (1999) 31–60.

263 O. I. Vinogradova, G. E. Yakubov, Dynamic effects on force measurements. 2. Lubrication and the atomic force microscope. *Langmuir*, **19** (2003) 1227–1234.

264 M. Voué, J. De Coninck, Spreading and wetting at the microscopic scale: recent developments and perspectives. *Acta Mater.*, **48** (2000) 4405–4417.

265 A. Waghe, J. C. Rasaiah, G. Hummer, Filling and emptying kinetics of carbon nanotubes in water. *J. Chem. Phys.*, **117** (2002) 10789–10795.

266 G. Wagner, E. Flekkøy, J. Feder, T. Jossang, Coupling molecular dynamics and continuum dynamics. *Comput. Phys. Commun.*, **147** (2002) 670–673.

267 J. H. Walther, An influence matrix particle–particle particle–mesh algorithm with exact particle–particle correction. *J. Comput. Phys.*, **184** (2003) 670–678.

268 J. H. Walther, R. Jaffe, T. Halicioglu, P. Koumoutsakos, Carbon nanotubes in

water: structural characteristics and energetics. *J. Phys. Chem. B*, **105** (2001) 9980–9987.

269 J. H. Walther, P. Koumoutsakos, Molecular dynamics simulation of nanodroplet evaporation. *J. Heat Transfer*, **123** (2001) 741–748.

270 J. H. Walther, T. Werder, R. L. Jaffe, P. Koumoutsakos, Hydrodynamic properties of carbon nanotubes. *Phys. Rev. E*, **69** (2004) 062201.

271 P. B. Warren, Dissipative particle dynamics. *Curr. Opin. Colloid Interface Sci.*, **3** (1998) 620–629.

272 A. Warshel, M. Levitt, Theoretical studies of enzymic reactions – dielectric, electrostatic and steric stabilization of carbonium-ion in reaction of lysozyme. *J. Mol. Biol.*, **103**, 1976.

273 T. Werder, J. H. Walther, R. Jaffe, T. Halicioglu, F. Noca, P. Koumoutsakos, Molecular dynamics simulations of contact angles of water droplets in carbon nanotubes. *Nano Lett.*, **1** (2001) 697–702.

274 T. Werder, J. H. Walther, R. L. Jaffe, T. Halicioglu, P. Koumoutsakos, On the water–graphite interaction for use in MD simulations of graphite and carbon nanotubes. *J. Phys. Chem. B*, **107** (2003) 1345–1352.

275 T. Werder, J. H. Walther, P. Koumoutsakos, Hybrid atomistic–continuum method for the simulation of dense fluid flows. *J. Comput. Phys.*, **205** (2005) 373–390.

276 W. C. D. Whetham, On the alleged slipping at the boundary of a liquid in motion. *Philos. Trans. R. Soc. London, Ser. A*, **181** (1890) 559–582.

277 M. Whitby, N. Quirke, Fluid flow in carbon nanotubes and nanopipes. *Nat. Nanotechnol.*, **2** (2007) 87–94.

278 X. Wu, M. C. Vargas, S. Nayak, V. Lotrich, G. Scoles, Towards extending the applicability of density functional theory to weakly bound systems. *J. Chem. Phys.*, **115** (2001) 8748–8757.

279 I.-C. Yeh, G. Hummer, Nucleic acid transport through carbon nanotube membranes. *Proc. Natl. Acad. Sci. USA*, **101** (2004) 12177–12182.

280 M. Yoneya, A generalized non-iterative matrix method for constraint molecular dynamics simulations. *J. Comput. Phys.*, **172** (2001) 188–197.

281 E. Zaremba, W. Kohn, Van der Waals interaction between an atom and a solid surface. *Phys. Rev. B*, **13** (1976) 2270–2285.

282 F. Zhu, K. Schulten, Water and proton conduction through carbon nanotubes as models for biological channels. *Biophys. J.*, **85** (2003) 236–244.

283 H. W. Zhu, C. L. Xu, B. Q. Wu, D. H. Wei, R. Vajtai, P. M. Ajayan, Direct synthesis of long single-walled carbon nanotube strands. *Science*, **296** (2002) 884–886.

284 U. Zimmerli, *On the Water–Graphite interaction*. Internal Report, Institute of Computational Science, ETH Zürich, Zürich, 2003.

285 U. Zimmerli, P. Gonnet, J. H. Walther, P. Koumoutsakos, Curvature induced L-defects in water conduction in carbon nanotubes. *Nano Lett.*, **5** (2005) 1017–1022.

286 U. Zimmerli, P. G. Gonnet, J. H. Walther, P. Koumoutsakos, Curvature induced l-defects in water conduction in carbon nanotubes. *Nano Lett.*, **5** (2005) 1017–1022.

287 U. Zimmerli, P. Koumoutsakos, Simulations of electrophoretic RNA transport through transmembrane carbon nanotubes. *Biophys. J.*, To appear, 2008.

288 U. Zimmerli, M. Parrinello, P. Koumoutsakos, Dispersion corrections to density functionals for water aromatic interactions. *J. Chem. Phys.*, **120** (2004) 2693–2699.

7
Carbon Nanotube Field Emission Devices

John Robertson, Engineering Department, Cambridge University, Cambridge, UK

7.1
Introduction

Field emission (FE) is the emission of electrons from a solid under an intense electric field, of the order of $10^9\,\mathrm{V\,m^{-1}}$. Emission occurs by the quantum mechanical tunneling of electrons through a potential barrier. The simplest way to produce a high field is by field enhancement at the tip of a sharp object. Originally, Si or W tips were used ("Spindt tips") and were made by etching or anisotropic etching [1]. Carbon nanotubes (CNTs) have a number of advantages over such tips [2, 3]. First, they have a much higher aspect ratio, the ratio of height to radius. Their strong covalent bonding makes them chemically inert to poisoning and physically inert to sputtering during field emission. They can also carry a very high current density of order $10^9\,\mathrm{A\,cm^{-2}}$ before electromigration. In addition, when driven at high currents and heated up, their resistivity decreases, so that they do not suffer for field-induced tip sharpening like metallic tips.

With these advantages, CNTs have been developed for a number of field emission applications, which we review here. First, we review how CNTs came to be

Advanced Micro & Nanosystems Vol. 8. Carbon Nanotube Devices.
Edited by Christofer Hierold

ISBN: 978-3-527-31720-2

chosen from other carbon systems, then consider some experimental parameters of importance, and finally describe applications.

7.2 Carbon-Based Field Emitters

Field emission has been studied in three forms of carbon, diamond, diamond-like carbon and carbon nanotubes. The first interest was in diamond. This is because diamond is a wide band gap semiconductor and, when its surface is hydrogenated, its conduction band lies above the vacuum level, giving a negative electron affinity [4, 5]. This means that electrons can be emitted from its conduction band without any energy barrier. This is superficially attractive; however, the problem is how to get electrons into the conduction band in the first place. There are no shallow donors in diamond and it turns out that there is just a large Schottky barrier at the back contact [6], so there is still a problem. For these reasons, diamond is not so good for field emission. Nevertheless, diamond is inert and does not poison. Nano-diamond is often used [7]. The groups of Sakai [8] and Davidson [9] have produced working, robust diamond field emission devices. Sakai's group [8] is developing FE backlights for liquid crystal displays.

The second material considered was diamond-like carbon (DLC). The advantage of DLC is that it has many of the advantages of diamond, but it is produced by low-cost room temperature deposition, in contrast to the high-temperature deposition needed for diamond itself [10–13]. The problem with DLC is that it is basically an insulator. Eventually, the emitter must conduct electrons. The electrons could be injected into its conduction band but they are fairly immobile. It turns out that field emission from DLC occurs by a localized electrical breakdown, which creates nanometer-scale conducting tracks across the film to the back electrode [14–16] (Figure 7.1). The conducting track acts to focus the electrical field and thereby enhance the field emission process. However, the whole process is uncontrollable

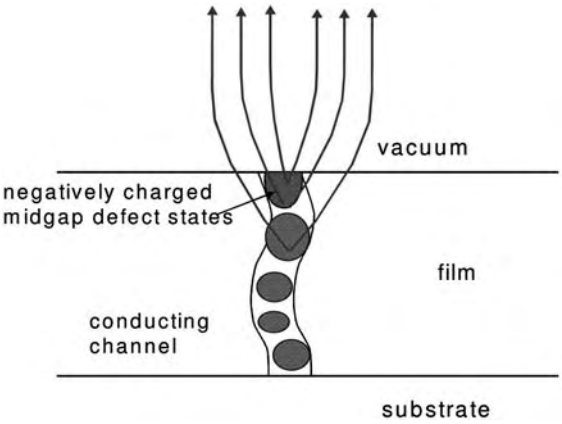

Figure 7.1 Schematic of the emission mechanism for diamond-like carbon films, with a conducting track.

and gives rise to only a few emission sites. Hence DLC is ultimately not favored for field emission.

7.3 Carbon Nanotube Field Emitters

This comparison led to the interest in field emission from carbon nanotubes [17, 18]. CNTs are rolled up sheets of graphite. They are useful for field emission because the local field F_{loc} is the applied field F_{app} multiplied by the field enhancement factor β:

$$F_{loc} = (h/r)F_{app} \tag{1}$$

where the field enhancement factor equals the aspect ratio, given by the ratio of height to radius of a tip [1],

$$\beta = h/r \tag{2}$$

β can be large, 200–1000. This allows emission at applied fields of order $1\,\mathrm{V\,\mu m^{-1}}$, a typical aim. The emission current density obeys the Fowler–Nordheim equation [1]:

$$J = a\frac{(\beta F)^2}{\phi}\exp\left(-\frac{b\phi^{\frac{3}{2}}}{\beta F}\right) \tag{3}$$

where ϕ (eV) is the barrier height, F is the applied field, β is the dimensionless geometric field enhancement factor and a and b are constants. The work function of nanotubes is essentially that of graphite, 4.7 eV. Groning et al. [19] found a barrier height of 4.8 eV.

Another important aspect of multi-walled nanotubes (MWNTs) is that they are metallic. Further, MWNTs can carry a very high current density, up to 50 μA per tube before failure. They also have a negative temperature coefficient of resistance so they do not undergo spontaneous field sharpening [20], a problem with metallic tips. They can operate at local temperatures of up to 2000 K fairly easily because the melting point of carbon is so high, 4000 K.

Emission is often tested in a parallel plate arrangement, with the cathode separated from the anode by a thin spacer. The anode can be a metal or often it is a conducting phosphor screen, as this enables the emission sites to be visualized. For many applications, a high emission site density (ESD) is important; typically $10^6\,\mathrm{cm^{-2}}$ is desirable. Another way to measure emission is using a scanning probe anode tip, which rasters the tip over the emitting sample and builds up an electrical image of the emitting area [21, 22]. A third case is emission from a single nanotube which is fixed to a cathode support.

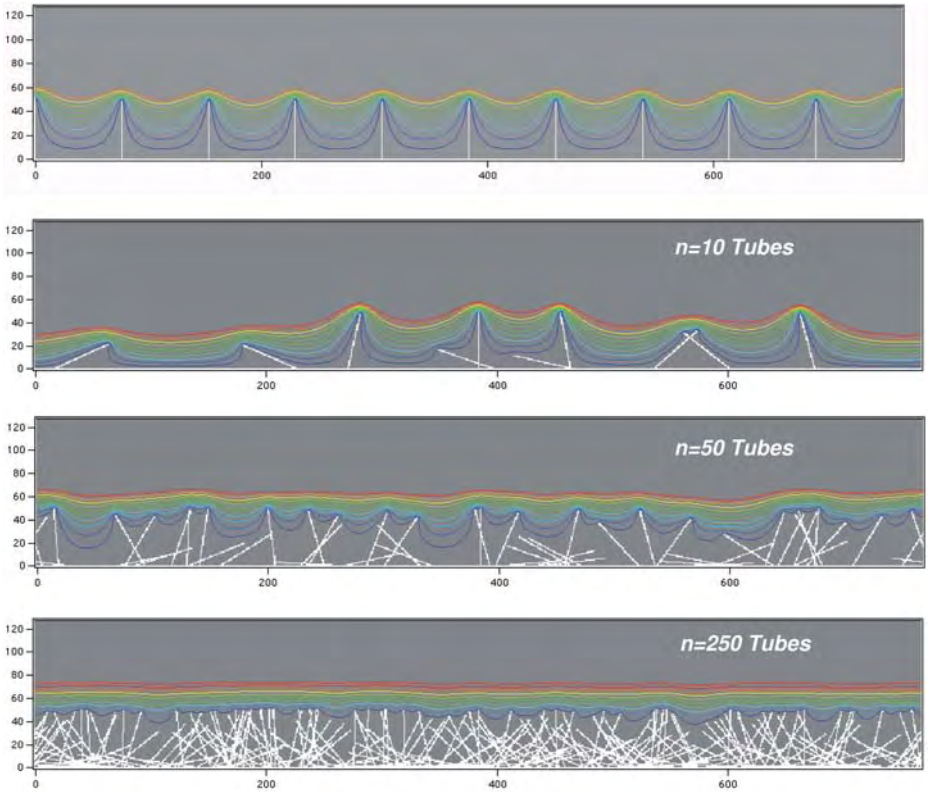

Figure 7.2 Illustrating field screening by adjacent tubes. (a) A regular well-spaced array of emitting nanotubes; (b–d) increase in density of irregularly spaced and oriented nanotubes. The irregular arrangement gives rise to wide range of reduced local fields (O. Groning, personal communication).

Often, the emitting object is a layer of nanotubes, rather than a single nanotube. It is then critical to avoid the reduction of field enhancement factor due to field screening by adjacent tubes. This is illustrated in Figure 7.2. The equipotentials of an isolated tube bend around its tip. This pattern is also found if adjacent tubes are well spaced. However, if the tube spacing becomes less than about twice their height h, $d < 2h$, then there is a progressive reduction in enhancement factor [21]. Hence nanotube arrays should have a spacing of twice the height or greater.

A second, practical problem with field emission is that the exponential dependence on the local field is so strong. There is always a distribution in enhancement factors, so this leads to a distribution of emission sites [23]. If the distribution of enhancement factors is written as

$$N(F) = N_0 \exp\left[-\frac{(\beta - \beta_0)^2}{2\sigma^2}\right] \tag{4}$$

then the overall emission current becomes

$$J \sim \int a' \exp\left(-\frac{b\phi^{\frac{3}{2}}}{\beta F}\right) \exp\left[\frac{(\beta-\beta_0)^2}{2\sigma^2}\right] \mathrm{d}\beta \tag{5}$$

The net result is that only a small fraction of tubes with particularly large β values emit.

This has led to a number of misconceptions about field emission from CNTs. The first is that a low emission field is the most important factor. The emission field or threshold field is defined as the applied field where the current density reaches some value such as $1\,\mu\mathrm{A\,cm^{-2}}$. The emission field is only one factor; a more important factor is the emission site density at a reasonable field [23].

Second, are single- or multi-walled nanotubes better? Multi-walled nanotubes are better generally, because they are stiff and if they are grown and aligned vertically, they will lead to constant and more reproducible emission currents.

Third, emission from open nanotube tips is larger than from closed tips. An open tip will have a larger enhancement factor because of local sharpness [24]. However, this is irrelevant for real applications, because it is irreproducible and not useful for any functional device.

Fourth, doped are better than undoped nanotubes. The idea here is that doped nanotubes may be more metallic and thus have higher emission currents. In practice, MWNTs are always metallic, because some of the walls will be metallic, in which case, do not bother with doping.

Field emission is usually desired from thin films and the first performance indicators to look for are turn-on field and emission site density.

A useful innovation was the ballast resistor in series with each emitter [25]. Its role is to share emission current between the different emitters, increase emission site density and try to mitigate the exponential dependence on local field.

7.4 Some Field Emission Applications

Field emission is useful for a number of applications, such as field emission displays, electron guns for scanning electron microscopes, microwave amplifiers, ionization gauges and X-ray imagers. These will be considered in turn.

7.4.1 Field Emission Displays

Field emission displays (FEDs) would be the largest application of field emission, if successful, because the display market is so large [1]. An FED is a flat panel display in which the image is assembled from pixels each of which is illuminated by its own field emission source (or sources) (Figures 7.3 and 7.4). Each field emission cathode consists of a CNT and a gate electrode spaced above the cathode

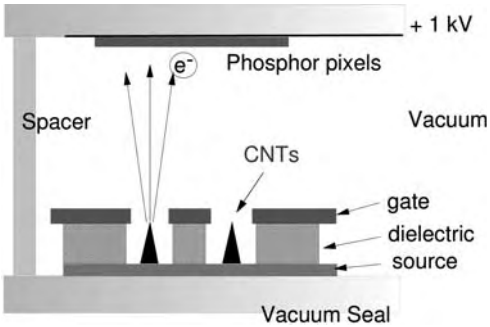

Figure 7.3 Schematic diagram of a field emission display with CNT emitters.

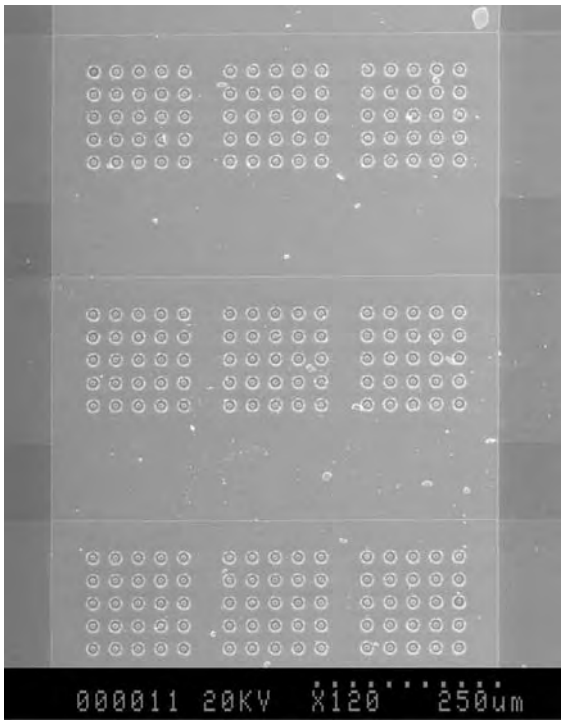

Figure 7.4 Top view of a gate array of emitters. Each group of emitters feeds a single pixel.

by an oxide insulator layer. The electrons are extracted from the CNTs by the gate field and then they are accelerated towards a high-voltage anode to form the image on the pixellated phosphor screen. The design will have a gate voltage of 50 V of less, so this sets the source dimensions.

The first FED designs envisioned one or more CNTs at the base of a gated array [26]. Typically, a cathode electrode is deposited, then a gate insulator layer and

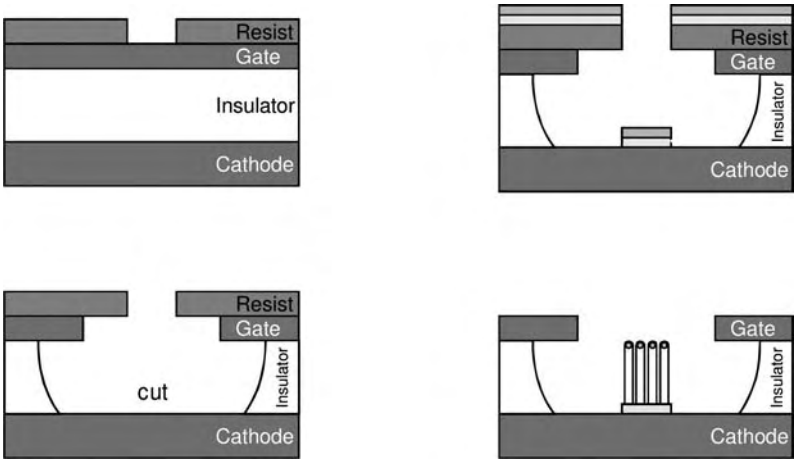

Figure 7.5 Process flow for the fabrication of a gates array of carbon nanotubes.

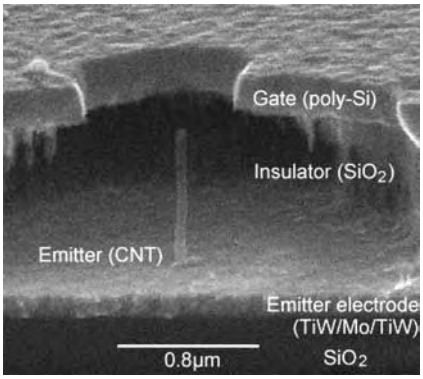

Figure 7.6 Cross-section of a gated nanotube emitter, with a single nanotube (K. Teo, personal communication).

then the gate metal (Figure 7.5). A hole pattern is etched in the gate and insulator, with under-cutting, and then CNT catalyst is placed on the cathode electrode. The CNTs are then grown by plasma-enhanced chemical vapor deposition (PECVD) [27]. A typical final cathode-gate assembly is shown in Figure 7.6. However, this is a relatively expensive process.

A lower cost method is to screen print a paste of CNTs and a binder on to the cathode plane [26]. A gate mesh is then held over the cathode. Another method is to deposit previously grown CNTs by electrophoresis [28], a process flow more comparable to that used for plasma displays.

A third arrangement of FED developed by Samsung is the back gate array [29, 30]. This low-cost solution uses a back gate to switch off the emission current. It avoids the cost of an etched array and also the problems associated with hanging a mesh gate above the cathode.

A typical gate design has a rather large ratio of the gate–hole to gate–cathode spacing. This means that the electron beam will be divergent. An extra focusing electrode will then be needed to converge the beam [31]. Otherwise, phosphor pixels receive current from adjacent pixels, causing white-out of the image.

The emission performance required for an FED is not high. The average emission current is only of order 1 mA cm^{-2}, much less than in most other applications. The more important requirement is emission uniformity. Emission endurance and lifetime in a relatively poor vacuum are also important considerations. Processing to enhance emission is carried out [32]. Tests have been made of emission failure [33].

The performance of FEDs can be compared with that of other flat panel displays (FPDs) (Table 7.1). The most successful display is the active matrix liquid crystal display (LCD). The advantage of FED over LCD is that it is an emissive display with lower power consumption, so that each pixel only consumes power when it is on, whereas the LCD is a light valve, consuming power continuously. FEDs can have a very high brightness (Table 7.1). They also have a wide viewing angle and a high frequency response. These were previously problems for LCD but they have now been largely corrected.

The organic light emitting diode (OLED) has perhaps the lowest cost base, having no vacuum, no liquid crystal and a simple manufacturing route in principle. It needs to prove its lifetime against degradation.

Another type of FPD is the plasma display (PDP). This is the standard for very large areas. Its pixel size is large and its power consumption is fairly high. The PDP also has a rapid response time and no viewing angle limitations.

A planned advantage of the FED was originally that it has a lower base cost, if everything is successful. It practice, the FED has suffered from a range of problems. The cathode technology is only one part of the overall device; it is also necessary to make a good low-voltage phosphor in red, green and blue, vacuum spacers which do not attract electrons, getters to maintain a high vacuum without pumping in the final device, beam focusing and generally a high-yield manufacturing route. The whole sandwich vacuum device must be pumped out and sealed with glass frit material.

Table 7.1 Comparative advantages and disadvantages of various flat panel display technologies.

	LCD	*Plasma*	*OLED*	*FED*
Cost	Low		Potentially lowest	–
Power	–	High	–	Low
Brightness	–	High	–	High
Response time	Originally slow	–	–	Fast
Viewing angle	Originally poor	–	–	–
Temperature range	Restricted	–		Large
Lifetime	–	–	Weakness	–

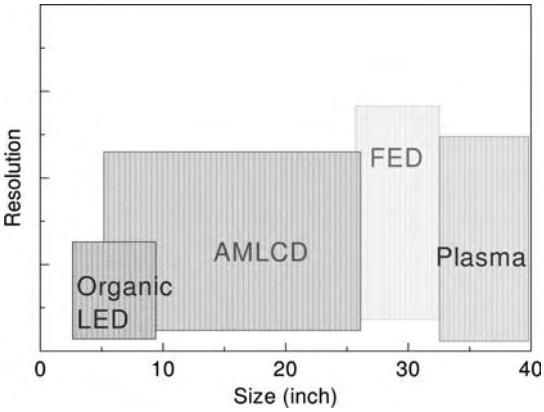

Figure 7.7 Size versus resolution plot for different flat panel display technologies, showing the likely entry point of FEDs.

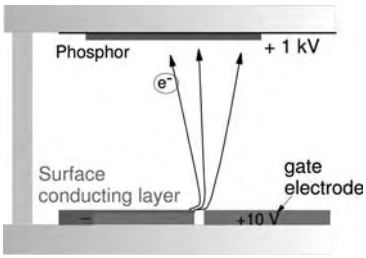

Figure 7.8 Schematic of the surface conductor emitting display (SED).

It has proved difficult to achieve all these goals, while the LCD has continuously lowered its costs. Originally, the FED was envisioned as a small area display for applications such as GPS displays in cars, where image brightness is needed, but the LCD can now do this. Now, the FED is aimed at the medium size market, at around 30 inches, between the LCD and PDP (Figure 7.7).

A number of firms have commercialized FEDs and shown production examples at conferences (Samsung, Motorola, etc.) [26, 34, 35]. The first fully available FED may be that from the Canon–Toshiba joint venture (now Canon) known as the surface conductor emitting display (SED) [36]. This device has cathode which emit electrons from a corner of a cathode (Figure 7.8).

7.4.2
Electron Guns for Scanning Electron Microscopes

The problem for FEDs is that it directly attacks a well-established display technology, the LCD, which is able to respond by cutting prices. There are a number of other high added value, niche opportunities where CNTs have unique advantages. The first is in electron guns for scanning electron microscopes (SEMs). This is

Table 7.2 Comparison of the performances of cold FE, Schottky emitters and CNT emitters for electron guns for scanning g electron microscopes.

	Brightness,* B *(A Sr^{-1} m^{-2} eV^{-1})	***Energy spread (eV)***
Cold FE	10^7	0.3
Schottky	10^8	0.7
CNT field emitter	3×10^9	0.3

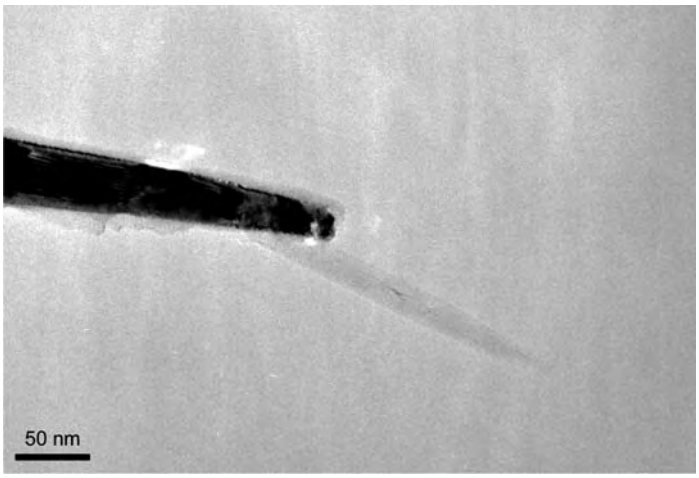

Figure 7.9 Mounted CNT tip (after N. de Jonge).

the largest electron microscope market. The lateral resolution is limited by the chromatic aberration, so an electron gun with a small energy spread is desired. This application requires the highest emission current for a single CNT. The figure of merit for such an electron gun is its normalized or "reduced" brightness *B*. The brightness is the emission current density per unit solid angle per electronvolt energy width [37–40].

Existing SEMs use thermionic emitters, Schottky emitters consisting of ZrO_2-coated tungsten operating at 1800 K or tungsten cold field emission tips. A thermionic cathode emits electrons from a hot solid of low work function. This has limited brightness and a rather wide energy width. The Schottky emitter has a higher brightness, but it still has a rather large energy spread of 0.7 eV (Table 7.2, Fig. 7.10). The W field emission tip has a similar purpose to the CNT field emission tip. However, the CNT can be much sharper than the W tip, so it shows a higher performance.

The CNT field emitter for SEM consists of a single MWNT mounted on a tungsten support (Figure 7.9). An MWNT is used in preference to an SWNT because it is mechanically stiffer. The CNT field emitter has the highest brightness, because

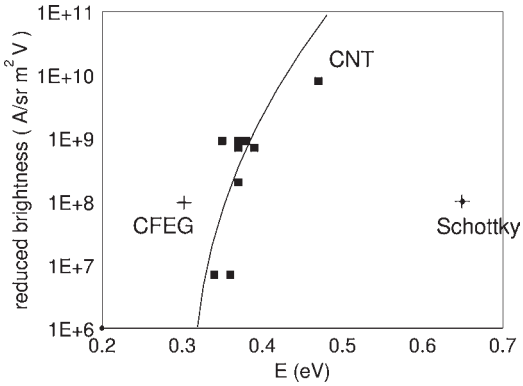

Figure 7.10 Reduced brightness versus energy spread (*E*) for different electron sources, CNT field emission, cold field emission (tungsten tips) and Schottky emitters (N. de Jonge, personal communication).

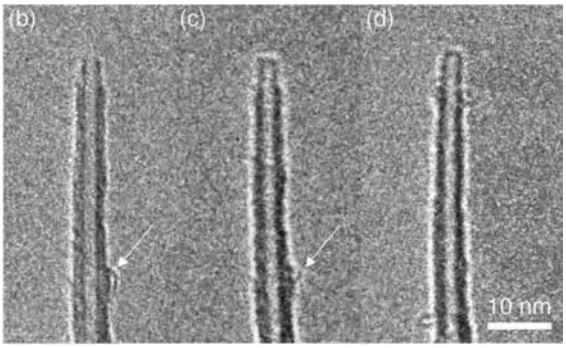

Figure 7.11 Closing the cap of a CNT by annealing [41].

its effective source size is so small. Continuing the electron "rays" backwards, the effective source diameter is 2 nm. The energy width of the field emitter is the lowest, about 0.35 eV, because it is a cold emitter [40]. The energy width is found by applying the Fowler–Nordheim equation for each electron energy.

A number of developments were required to bring this technology to a successful point. First, it was necessary to show that the emission had high stability and low noise. The stability is related to the atomic structure of the tip. This must not change during its lifetime, so it is useful to anneal the graphitic wall structure of the nanotube tip into a stable state, by self-heating it with a large emission current [41], Fig. 7.11.

The emission current also depends on any adsorbed gas molecules. Dean and coworkers showed that adsorbed molecules lower the emission barrier by allowing resonant tunneling. However, adsorbed molecules do not give rise to stable

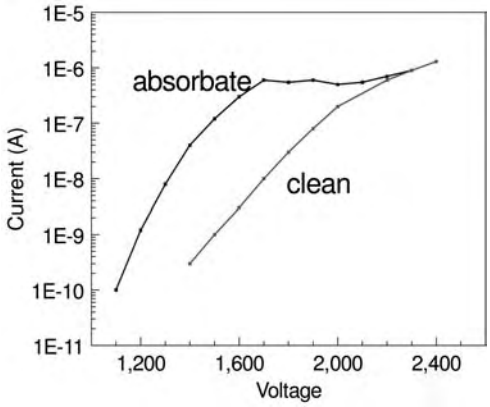

Figure 7.12 Emission current in the two regimes, clean tip and with adsorbed molecule on tip.

emission [42–45]. They can move about or be annealed off under a large current, leading to undesirable jumps in the emission current. Hence it is much more preferable to have no adsorbed molecules on the tip, in order to ensure continuous, stable operation. High current emission desorbs the molecules and this desorption is evident by a drop in the emission current [45], as seen in Figure 7.12. Evidence of desorption is also seen in the change of the emission pattern (Figure 7.13). The emission pattern can be seen in an emission microscope. The pattern shows the 6- or 5-fold patterns of the tip atoms for a clean tip, whereas an adsorbate will give rise to a lower symmetry pattern [43].

Another advantage of FE tips is low noise. The emission from untreated tips consists of a number of steps and peaks. However, after running at elevated current to desorb adsorbates and anneal the tip, the emission moves into a low-noise state. The emission noise is in fact lower than for a thermionic cathode. The main noise component is $1/f$ noise [46].

As the SEM application involves high emission currents, there have been studies of the failure mechanism at high currents [47]. The tip was imaged under normal emission and was found to be highly stable. Note that previously high currents were used to anneal the tip end and close the cap structure, to improve emission. At the highest currents, some atomic rearrangement occurs and, ultimately, some of the tip breaks off.

The next requirement is a manufacturing route. The first emitters were "hand made" by dipping a W tip into a mat of CNTs and attaching one nanotube, which was then broken off [48]. More recently, it has been possible to deposit catalyst on the W support and grow a CNT directly on the support to make the emitters [3, 48]. This opens up the possibility of a changeable emitter gun, without bringing the SEM up to air. FEI, once part of Philips, is a leading company in this area. This market is likely to succeed.

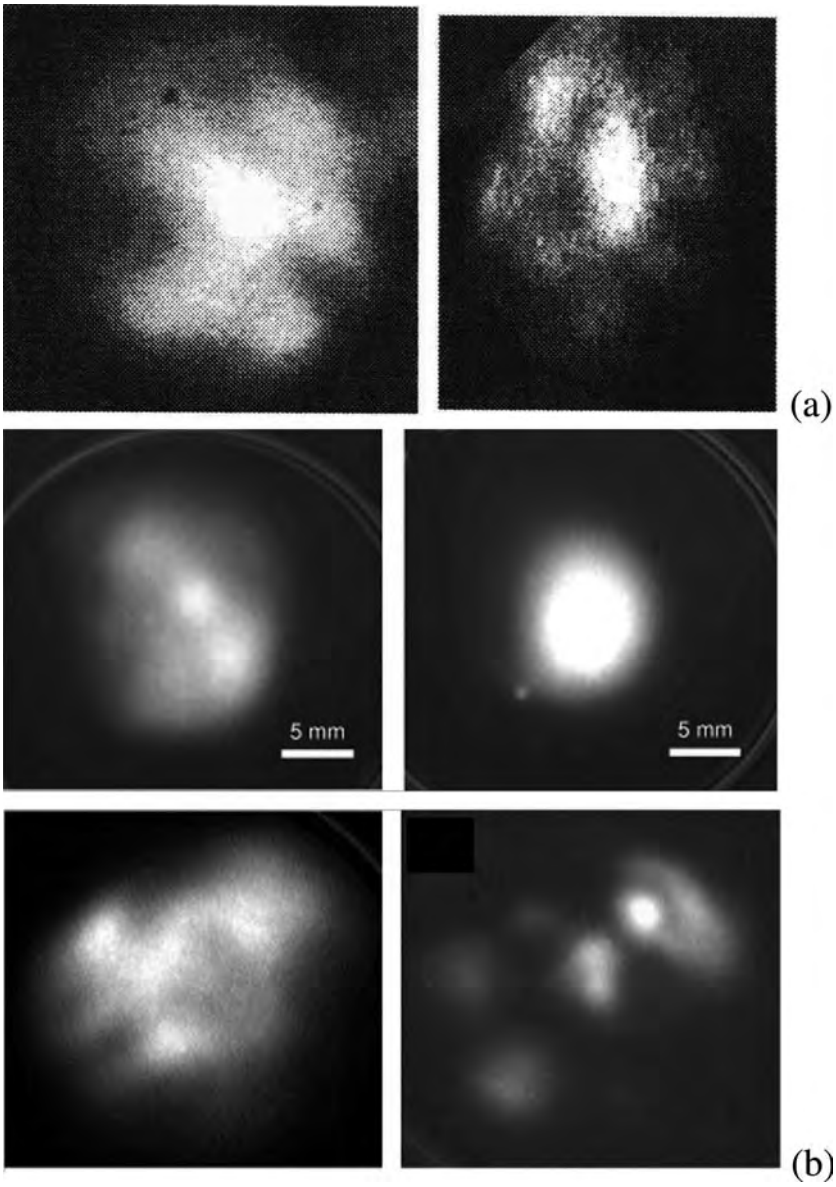

Figure 7.13 Field emission images of (a) clean CNT tips and (b) CNT tips with adsorbed molecules on them [43].

7.4.3
Microwave Amplifiers

The need for higher bandwidth and more channels has led to a need to use the frequency range of 30 GHz and above. The power requirements (10 W) and high frequency mean that traveling wave tubes are used. They are often in satellites where weight should be minimized.

In most areas, semiconductor electronics has largely taken over from vacuum microelectronics. There is one area where vacuum microelectronics can still compete, namely in high-power, high-frequency devices (Figure 7.14). This is because electron speeds in semiconductors are rather low compared with those in a vacuum and it is difficult to make small, high-power devices which can dissipate the heat. Thus traveling wave tube (TWT) amplifiers are still used for microwaves.

In a conventional TWT, an electron beam passes through an input helical coil which velocity modulates the RF on to the beam to form a series of electron bunches. The beam then passes through a multi-stage collector coil which extracts the amplified RF.

The conventional traveling wave tube amplifier will inject the RF voltage on to a grid above a thermionic cathode. This will modulate an electron beam, which provides the power amplification (Figure 7.15).

A modified design is to modulate the electron beam directly by introducing the RF signal on to a grid above the thermionic cathode. However, it is difficult to design an appropriate cathode–grid spacing in this case. The cathode–grid separation should be as small as possible to achieve high frequencies. However, this means that the grid must withstand the radiant heat. A cold cathode is preferable [49–52].

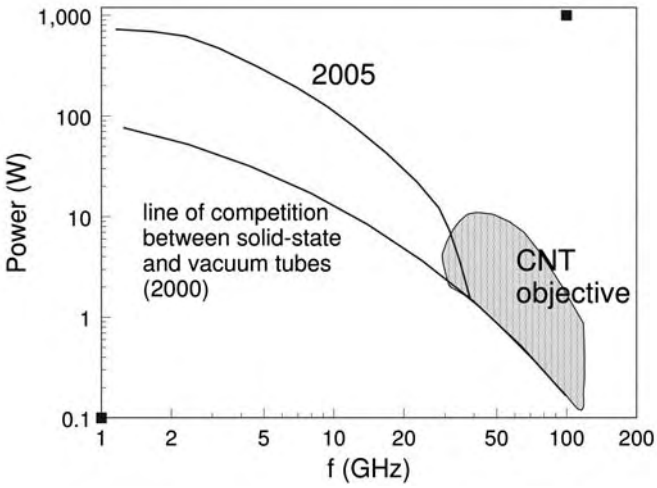

Figure 7.14 Operating regime of CNT-based traveling wave tubes versus solid-state devices.

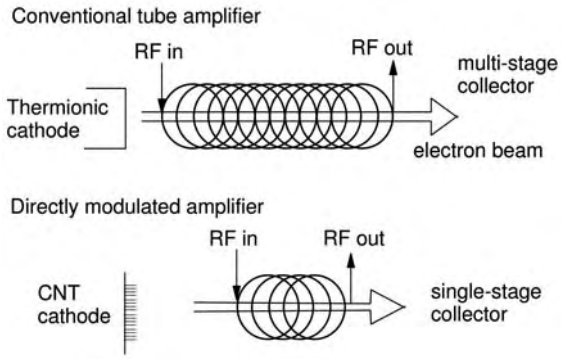

Figure 7.15 Schematic of operating principle of traveling wave tube (P. Leganeux, personal communication).

This application requires the highest emission current densities. This requires an emitting array, not a single nanotube, and that the maximum fraction of the tubes emit. A ballast resistor cannot be used to share current, because this limits the current. A technology has been developed to make such arrays. The cost is not initially a limiting factor. Electron beam lithography is used to pattern an array of catalyst dots from which the array of MWNTs is grown by PECVD [53]. It is known that if the dot size is kept below 100 nm, then only a single nanotube grows from each dot [54]. Following Nilsson et al. [21], the array is designed such that the spacing equals twice the nanotube height. Great care is taken over the uniformity of the nanotubes in terms of their height, diameter, spacing and tip uniformity [53] (Figure 7.16). This is essential to ensure a uniform emission from many tubes. Otherwise, there is a distribution of aspect ratios and field enhancement factors, which leads to emission from only a small fraction of the tubes and a low current density.

To increase the emission current density further, the array is scaled down in size, to smaller diameters, smaller spacing and smaller heights. Current densities of the order of $10\,A\,cm^{-2}$ are possible.

7.4.4
X-Ray Imaging Tubes

Field emission arrays can also be used for X-ray imaging tubes [55, 56]. In a conventional X-ray tube, a thermionic cathode generates an electron beam which is then focused on a metallic target, which emits the X-rays. The X-ray intensity is limited by the focusing of the beam and the heat dissipation from the target. X-rays are increasingly used in tomography to provide three-dimensional images of the body. Time resolution is useful if an image of moving parts such as the heart, lungs or circulation is required. A light-weight source is an advantage for such tomography.

Thermionic emission has a slow response time and is not so suitable for time-resolved imaging. In this case, a field emission source is a particular advantage.

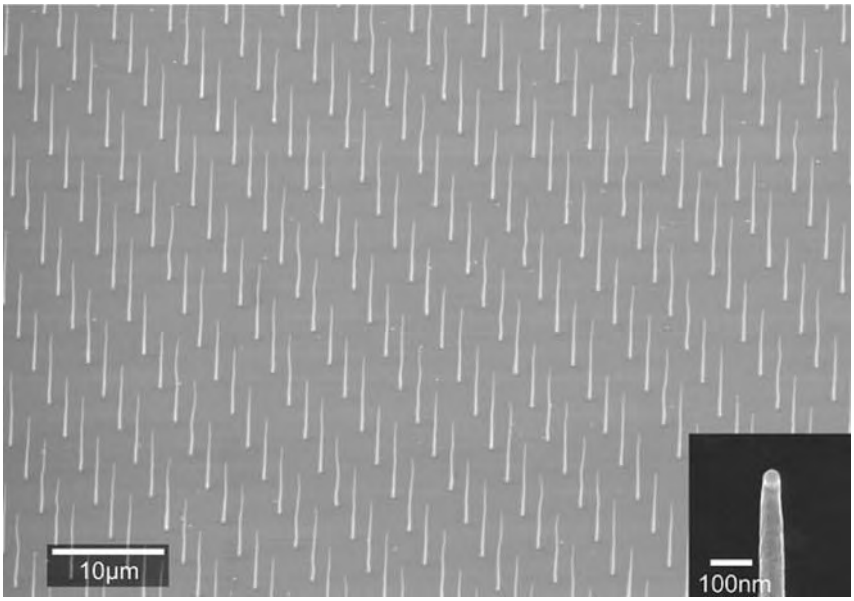

Figure 7.16 Illustration of the possible quality of PECVD grown vertically aligned MWNT arrays, as used in cathodes for microwave amplifiers (W. Milne, personal communication).

Again, the requirement is for a high emission current density and stability of current. Xinik [56] and some other firms are involved in this type of development. Oxford Instruments have developed a portable X-ray imager for studying line breaks on circuit boards, etc. Figure 7.17 shows an X-ray image of a mouse taken by the Xinik system.

7.4.5 Lamps

One of the first applications of field emission was to high-intensity lamps for large-scale projection displays, for sports stadiums [57]. This then developed into back lights for LCDs. Bonard et al. [58] proposed CNT field emission-driven fluorescence lamps. However, the economics of this will not work.

There are numerous other possible applications such as ionizers in gas detectors and mass spectrometers, which are still being developed [59, 60].

7.5 Conclusion

Field emission is often cited as one of the most promising application areas of carbon nanotubes. It has led to intensive studies of the mechanism so that field

Figure 7.17 X-ray image of a mouse from CNT-based X-ray imager (O. Zhou, personal communication).

emission from CNTs is now well understood. The most promising applications are in SEM electron guns where they do not meet an established market. X-ray imagers are a similar case, but this is less well developed. On the other hand, field emission displays have been strongly developed, but face entrenched successful products, LCDs and OLEDs, and this is proving a difficult application.

7.6 Acknowledgments

The author is grateful to W. Milne, N. de Jonge, O. Groning, P. Legagneux and K. Teo for diagrams and to the EC for funding the projects CARBEN, NANOLITH, CARDECOM and CANAPE in which some of the work described here was carried out.

References

1 P. R. Schwoebel, I. Brodie, *J. Vac. Sci. Technol. B* **13** (1995) 1391.
2 J. M. Bonard, H. Kind, L. Stockli, N. A. Nilsson, *Solid State Electron.* **45** (2001) 893.
3 W. I. Milne, K. Teo, I. Bu, G. Amaratunga, N. de Jonge, M. Allioux, J. T. Oostveen, P. Legagneux, E. Minoux, L. Gangloff, L. Hudanski, J. P. Schnell, L. D. Dieumegard, E. Peauger, T. Wells, M. Elgomati, *Phys. Status Solidi A* **203** (2006) 1058.
4 F. J. Himpsel, J. S. Knapp, J. A. Van Vechten, D. E. Eastman, *Phys. Rev. B* **20** (1979) 624.

5 B. B. Pate, P. M. Stefan, C. Binns, P. J. Jupiter, M. L. Shek, I. Lindau, W. E. Spicer, *J. Vac. Sci. Technol.* **19** (1981) 249.
6 J. Robertson, *J. Vac. Sci. Technol. B* **17** (1999) 659.
7 W. Zhu, G. P. Kochanski, S. Jin, L. Seibles, *J. Appl. Phys.* **78** (1995) 2707.
8 T. Ono, T. Sakai, N. Sakuma, M. Suzuki, H. Yoshida, S. Uchikoga, *Diamond Relat. Mater.* **15** (2006) 1998.
9 Y. M. Wong, W. P. Kang, J. L. Davidson, B. K. Choi, W. Hofmeister, J. H. Huang, *Diamond Relat. Mater.* **14** (2005) 2069.
10 G. A. J. Amaratunga, S. R. P. Silva, *Appl. Phys. Lett.* **68** (1996) 2529.
11 A. A. Talin, T. E. Felter, T. A. Friedmann, J. P. Sullivan, M. P. Siegal, *J. Vac. Sci. Technol. A* **14** (1996) 1719.
12 B. S. Satyanarayana, A. Hart, W.I. Milne, J. Robertson, *Appl. Phys. Lett.* **71** (1997) 1430.
13 L. K. Cheah, X. Shi, E. Liu, B. K. Tay, *J. Appl. Phys.* **85** (1999) 6816.
14 N. Missert, T. A. Friedmann, J. P. Sullivan, R. G. Copeland, *Appl. Phys. Lett.* **70** (1997) 1995.
15 T. W. Mercer, N. J. DiNardo, J. B. Rothman, M. P. Siegal, T. A. Friedmann, L. Martinez-Miranda, *Appl. Phys. Lett.* **72** (1998) 2244.
16 J. Robertson, *Mater. Sci. Eng. Revs.* **37** (2002) 129.
17 W. A. de Heer, A. Chatelain, D. Ugarte, *Science* **270** (1995) 1179.
18 A. G. Rinzler, J. H. Hafner, P. Nikolaev, L. Lou, S. G. Kim, D. Tomanek, P. Nordlander, D. T. Colbert, R. E. Smalley, *Science* **269** (1995) 1550.
19 O. Groning, O. M. Kuttel, C. Emmenegger, P. Groning, L. Schlapbach, *J. Vac. Sci. Technol. B* **18** (2000) 665.
20 S. T. Purcell, P. Vincent, C. Journet, V. T. Binh, *Phys. Rev. Lett.* **88** (2002) 105502.
21 L. Nilsson, O. Groning, C. Emmenegger, O. Kuttel, E. Schaller, L. Schlapbach, H. Kind, J. M. Bonard, K. Kern, *Appl. Phys. Lett.* **76** (2000) 2071.
22 V. Semet, V. T. Binh, P. Vincent, D. Guillot, K. Teo, M. Chhowalla, G. Amaratunga, W. I. Milne, P. Legagneux, D. Pribat, *Appl. Phys. Lett.* **81** (2002) 343.
23 L. Nilsson, O. Grnonig, P. Gronoing, O. Kuttel, L. Schlapbach, *J. Appl. Phys.* **90** (2001) 768.
24 Y. Saito, K. Hamaguchi, K. Hata, K. Uchida, Y. Tasaka, F. Ikazaki, Y. Nishina, *Nature* **389** (1997) 554.
25 J. D. Levine, R. Meyer, R. Baptist, T. E. Felter, A. A. Talin, *J. Vac. Sci. Technol. B* **13** (1995) 474.
26 W. B. Choi, D. S. Chung, J. H. Kang, H. Y. Kim, Y. W. Jin, I. T. Han, Y. H. Lee, J. E. Jung, N. S. Lee, G. S. Park, J. M. Kim, *Appl. Phys. Lett.* **75** (1999) 3129.
27 W. I. Milne, K. B. K. Teo, G. A. J. Amaratunga, P. Legagneux, L. Gangloff, J. P. Schnell, V. Semet, V. T. Binh, O. Gronning, *J. Mater. Chem.* **14** (2004) 933.
28 W. B. Choi, D. S. Chung, J. H. Kang, H. Y. Kim, J. W. Jin, J. M. Kim, *Appl. Phys. Lett.* **78** (2001) 1547.
29 D. S. Chung, S. H. Park, H. W. Lee, J. H. Choi, S. N. Cha, J. M. Kim, *Appl. Phys. Lett.* **80** (2002) 4045.
30 S. G. Yu, W. Yi, J. Lee, T. Jeong, J. Heo, J. H. Kang, C. S. Lee, *Appl. Phys. Lett.* **80** (2002) 4036.
31 J. H. Choi, A. R. Zoulkarneev, Y. W. Jin, Y. J. Park, D. S. Chung, J. M. Kim, *Appl. Phys. Lett.* **84** (2004) 1022.
32 W. S. Kim, J. Lee, T. W. Jeong, J. N. Heo, B. Y. Kong, Y. Wan, J. M. Kim, *Appl. Phys. Lett.* **87** (2005) 163112.
33 J. H. Lee, S. H. Lee, H. J. Lee, J. N. Heo, T. W. Jeong, C. W. Baik, S. H. Park, S. G. Yu, J. M. Kim, *Appl. Phys. Lett.* **89** (2006) 253115.
34 B. F. Coll, K. A. Dean, E. Howard, J. E. Jaskie, *J. Soc. Inf. Display* **14** (2006) 477.
35 J. Dijon, et al., *AIP Conf. Proc.* **685** (2003) 592.
36 S. Uchikoga, in *Proceedings of the 18th International Symposium on Power Semiconductor ICs*, IEEE, 2006.
37 N. de Jonge, Y. Lamy, K. Achoots, T. H. Oosterkamp, *Nature* **420** (2002) 393.
38 N. de Jonge, *J. Appl. Phys.* **95** (2004) 673.
39 N. de Jonge, M. Allioux, M. Doytcheva, M. Kaiser, *Appl. Phys. Lett.* **85** (2004) 1607.
40 N. de Jonge, M. Allioux, J. L. Oostveen, K. B. K. Teo, W. I. Milne, *Phys. Rev. Lett.* **94** (2005) 186807.

41 N. de Jonge, M. Doytcheva, M. Allioux, M. Kaiser, S. A. M. Mentink, K. Teo, R. Lacerda, W. I. Milne, *Adv. Mater.* **17** (2005) 451.
42 K. A. Dean, B. R. Chalamala, *Appl. Phys. Lett.* **75** (1999) 3017.
43 K. A. Dean, B. R. Chalamala, *J. Appl. Phys.* **85** (1999) 3832.
44 K. A. Dean, B. R. Chalamala, *Appl. Phys. Lett.* **76** (2000) 375.
45 K. A. Dean, P. von Allmen, B. R. Chamamala, *J. Vac. Sci. Technol. B* **17** (1999) 1959.
46 N. de Jonge, M. Allioux, J. T. Oostveen, K. B. K. Teo, W. I. Milne, *Appl. Phys. Lett.* **87** (2005) 133118.
47 M. Doytocheva, M. Kaiser, N. de Jonge, *Nanotechnology* **17** (2006) 3226.
48 N. de Jonge, Y. Lamy, M. Kaiser, *Nano Lett.* **3** (2003) 1621.
49 L. Gangloff, et al., *Nano Lett.* **4** (2004) 1575.
50 W. I. Milne, et al., *Curr. Appl. Phys.* **4** (2004) 513.
51 K. B. K. Teo, E. Minoux, L. Hudanski, F. Peauger, J. P. Schnell, L. Gangloff, P. Legagneux, D. Dieumegard, G. Amaratunga, W. Milne, *Nature* **437** (2005) 968.
52 E. Minoux, O. Groning, K. Teo, S. H. Dalal, L. Gagloff, J. P. Schnell, L. Hudanski, I. Bu, P. Vincent, P. Legagneux, G. Amaratunga, W. Milne, *Nano Lett.* **5** (2005) 2135.
53 K. B. K. Teo, S. B. Lee, M. Chhowalla, V. Semet, Y. T. Binh, O. Grnoning, M. Catignolles, A. Loiseau, G. Pirio, P. Legagneux, D. Pribat, D. G. Hasko, H. Ahmed, G. Amaratunga, W. I. Milne, *Nanotechonlogy* **14** (2003) 204.
54 V. I. Merkulov, D. H. Lowndes, Y. Y. Wei, G. Eres. E. Voelkl, *Appl. Phys. Lett.* **76** (2000) 3555.
55 G. Z. Yue, Q. Qiu, B. Gao, Y. Cheng, J. Zhang, H. Shimoda, S. Chang, J. P. Lu, O. Zhou, *Appl. Phys. Lett.* **81** (2000) 355.
56 C. Bower, O. Zhou, W. Zhu, D. J. Werder, S. Jin, *Appl. Phys. Lett.* **77** (2000) 2767.
57 Y. Saito, S. Uemura, *Carbon* **38** (2000) 169.
58 J. M. Bonard, et al., *Appl. Phys. Lett.* **78** (2001) 2775.
59 A. Modi, P. M. Ajayan, *Nature* **424** (2003) 171.
60 D. J. Riley, M. Mann, W. I. Milne, *Nano Lett.* **3** (2003) 1455.

8
Carbon Nanotube Gas Sensors

John T. W. Yeow, Department of Systems Design Engineering, University of Waterloo, Ontario, Canada

8.1
Introduction

The development of nanotechnology has been very intense for the past decade. Our ability to fabricate nanomaterials and construct nanostructures has allowed us to invent novel devices for new applications. By exploiting the inherent physical, electrical and mechanical properties of nanomaterials, it is possible to enhance of the performance of conventional devices by increasing their portability, selectivity, sensitivity and power efficiency. Particularly, the unique properties of nanomaterials such as carbon nanotubes (CNTs) are well suited for sensor applications. The

Advanced Micro & Nanosystems Vol. 8. Carbon Nanotube Devices.
Edited by Christofer Hierold

ISBN: 978-3-527-31720-2

cylindrical shape and high aspect ratio of CNTs allow large surface-to-volume structure that is ideal for gas or chemical adsorption.

8.2 Fabrication of Carbon Nanotube Gas Sensors

Carbon nanotube gas sensors are based on many sensing principles such as change in resistance, capacitance, electrical breakdown in a medium and conductance that are induced within the CNTs or by the CNTs. Therefore, the preparation of CNTs and the integration of CNTs within a sensor are extremely important. It is obvious that the sensor should be designed such that the sensing material, CNTs, receives maximum exposure to the medium. To improve the sensitivities and selectivities of CNT gas sensors, there has been intensive research into processing, purifying and configuring CNTs. This section describes various techniques for preparing CNTs for sensing applications.

One of the most important components of a sensor is the transducing material. The quality and quantity of the material will ultimately affect the performance of the sensor. The ability to produce sensing materials with consistent quality is crucial to providing repeatable and uniform performance of not just one but a batch of sensors.

Iijima discovered multi-walled CNTs (MWNTs) in 1991 by using carbon arc-discharge techniques [1]. Subsequently, single-walled CNTs (SWNTs) were grown by Iijima and Ichihashi [2] and Bethune et al. [3] using an arc-discharge method with a metal catalyst. Currently, three popular techniques are used to produce CNTs: carbon arc discharge, laser ablation and chemical vapor deposition (CVD).

8.2.1 Arc-Discharge Method

The arc-discharge method was the first technique to be used to produce CNTs. The method was initially used to mass produce fullerenes [4]. Graphite rods in contact were evaporated by applying AC voltages in the presence of an inert gas to produce fullerenes. Similar experiments were carried out using two separate graphite rods – one as the anode and the other as the cathode. A sufficiently high DC voltage was applied to generate an electric arc between the two rods as they are brought closer to one another. The evaporated anode generates fullerenes in the form of soot in the chamber. Within the deposit on the cathode, CNTs were discovered by Iijima. The production of fullerenes and growth of CNTs are carried within a vacuum chamber filled with inert gas. The role of the inert gas is to increase the speed at which carbon is deposited. When pure graphite rods are used, MWNTs are produced by controlling the inert gas pressure and arcing current. Large-scale synthesis of MWNTs has been achieved [5, 6] in He gas. When a graphite rod containing metal catalysts and a pure graphite rod are used as the anode and cathode, respectively, SWNTs can be produced. The arc-discharge method has been shown to produce high-quality CNTs. The two most important

parameters to take into account by this method are control of the arcing current and the optimal selection of the inert gas pressure in the chamber [7].

Various metal catalysts (Ni, Co, Fe, Pt, Pd) and inert gases (He, Ar, CH_4) have been used to grow CNTs. Bethune et al. [3] used Co, Ni and Fe to synthesize the first SWNTs. Currents between 95 and 105 A and He gas pressures between 100 and 500 Torr were used to produce 1.2 ± 0.1 nm SWNTs with Co as catalyst. Journet et al. [8] were able to optimize SWNT growth and achieved mass production by using a mixture of bimetallic catalysts (Ni–Co, Co–Y or Ni–Y) in He gas. Another method of note is the work of Zhao et al. [9], who used Fe as catalyst and H_2–Ar gas mixture as inert gas to produce a partially aligned 30-cm long macroscopic network of SWNTs. The Fe nanoparticles can be easily purified by heating in air at 420 °C and then rinsing in dilute HCl.

8.2.2
Laser Ablation

The laser ablation method was used to produce fullerenes by Smalley's group in 1992 [10]. The group used pulsed laser ablation of a graphite composite that was doped with metallic catalysts under a constant inert gas pressure and flow rates [11] to produce SWNTs. Typically, a YAG or CO_2 laser is used to ablate and vaporize a carbon target in the presence of high-temperature Ar gas to form SWNTs. The focal point of the laser is scanned across the target so that fresh carbon sources are vaporized constantly. This method has been shown to produce ropes of SWNTs that are 5–20 nm in diameter and 10–100 μm long. Interestingly, it was suggested by Scott et al. [12] that the carbon of the nanotubes is contributed by both direct laser ablation of the carbon target and carbon particles suspended in the reaction zone. High-quality SWNTs can be synthesized when the nanotubes are formed within the reaction zone of the laser beam because the nanotubes can be purified and annealed during the high-temperature ablation process.

The laser ablation method has been shown to produce SWNTs of varying diameters with a high degree of controllability. The control parameters include chamber temperature, types of metallic catalysts and flow rate of the inert gas [13–15]. A higher chamber temperature or the use of a Ni–Y catalyst increases the SWNT diameter. On the other hand, using Rh–Pd catalyst will decrease the diameter of SWNTs [15, 16]. The flow rate of the inert gas has to be carefully controlled because it affects the distribution of the nanotube diameter. This suggests that in contrast to the vaporization process that occurs on the nanosecond scale, the rate of the growth process is on the order of seconds [14]. The amount of CNTs produced was affected by the following parameters: (i) amount and type of catalysts; (ii) laser power and wavelength; (iii) temperature; (iv) pressure; (v) type of inert gas; and (vi) the fluid dynamics near the carbon target [17, 19].

8.2.3
Chemical Vapor Deposition

Chemical vapor deposition (CVD) for synthesizing CNTs is a technique by which hydrocarbon gas is decomposed into reactive radical species in the presence of

metallic catalysts at high temperature. The radical species allow CNTs to form on a layer of catalyst that coats the substrate. The CVD method is a popular choice for producing CNTs because it is simple and economical. CNTs can be produce at low temperature and under ambient pressure. The resources for hydrocarbon are plentiful in any state – solid, liquid or gas. As a result, a wide selection of materials can be used as substrates to allow the growth of CNTs in any form and morphology. Commonly used hydrocarbon sources are methane, ethylene and acetylene.

Using this technique, Yacaman et al. [20] produced CNTs with a length of 50 μm by using acetylene as hydrocarbon source and Fe nanoparticles as catalysts at 700 °C. With the same catalyst nanoparticles, Endo et al. [21] produced CNTs from pyrolysis of benzene at 1100 °C. Subsequently, Dai et al. [22] used a combination of CO and Mo particles to produce the first CVD-synthesized SWNTs at 1200 °C. It is worth noting that Smalley's group [23] invented the HiPco process for the mass production (10 g day^{-1}) of high-purity SWNTs, which is based on the hydrocarbon gas CVD technique. The process involves using Fe as catalyst from $Fe(CO)_5$ under high pressure (30–50 atm) and high temperature (900–1000 °C) conditions. It is reported that SWNTs of 97 mol% purity can be produced at a rate of 450 mg h^{-1}.

The key parameters to control in a CVD process are the types of hydrocarbons, catalysts and the growth temperature. Chaisitsak et al. [24] reported that both SWNTs and MWNTs can be synthesized by varying the growth conditions. In general, an elevated growth temperature increases the density and growth rate of CNTs. The CNTs tend to be vertically aligned as the temperature increases. It is also observed that the temperature affects the types of CNTs produced. A low-temperature (600–900 °C) CVD process is likely to produce MWNTs, whereas a higher temperature (900–1200 °C) produces SWNTs. However, the MWNTs grown under low temperature have shown high defect densities because of the lack of sufficient thermal energy to anneal the CNTs during the fabrication process [18].

Each of the above-mentioned techniques has its own advantages and disadvantages. The arc-discharge and laser ablation techniques are able to produce high yields (>70%) of SWNTs. However, the CNTs are produced in the form of tangled network of nanotubes, which makes purification and utilization challenging. In addition, these two techniques rely on extremely high temperature (>3000 °C) to evaporate the carbon target [25]. The CVD technique, on the other hand, is able to produce aligned and ordered CNTs on a large scale. For example, Wang et al. [26] used a combination of ethylene gas and Fe–alumina catalyst at 700 °C to produce a few kilograms of high-purity (>70%) MWNTs per hour.

8.2.4
Carbon Nanotube Purification

The unique properties of CNTs are well characterized. The development of CNT-based sensors is based on exploiting the fascinating transduction capability of CNTs. There are numerous challenges on the way to realizing CNT-based sensors. The challenge begins at the synthesis stage, where high-purity CNTs are desired.

The growth of CNTs is induced by a graphite target or a hydrocarbon source coated with various metallic catalysts in the presence of inert buffer gases at elevated temperature. It is inevitable that the resulting product is mixed with a number of impurities. These impurities are made up of a combination of carbonaceous materials and metal nanoparticles. The purity of CNTs can be evaluated qualitatively using Raman spectroscopy [27], whereas near-infrared spectroscopy is used for the quantitative assessment [28].

When the arc-discharge technique is used, the impurities can be reduced by the oxidation process. However, 95% of the original materials are oxidized to leave only 10–20% of the remaining material for synthesizing pure nanotubes [29]. Generally, there are two methods to purify CNTs by oxidation: gas-phase purification [29, 30] and liquid-phase purification [31, 33]. Ebbesen et al. [29] reported using a gas-phase oxidation method, but met with limited success in terms of yield rate. Liquid-phase oxidation was demonstrated to produce more homogeneous oxidation by Hiura et al. [31]. Kim et al. [33] performed purification with oxidants such as nitric acid, sulfuric acid and their mixture. Scanning electron microscopy (SEM) showed that this technique yielded purified SWNTs with a length of 2 μm. Scanning tunneling electron microscopy (STM) confirmed that the integrity of the surface of the purified SWNTs was preserved and metal catalysts were effectively removed. Bandow et al. [34] demonstrated the purification of SWNTs by the pulsed laser ablation technique. Coexisting impurities are first separated by the laser pulses and then suspended in nonaqueous solution using a cationic surfactant before the SWNTs are trapped by a membrane filter. The limitation of this technique is that it is incapable of large-scale industrial purification of CNTs. To address this deficiency, Rinzler et al. [35] proposed a technique by which SWNTs are refluxed in concentrated nitric acid before repetitive washing, centrifugation and filtration cycles. Xu et al. [36] purified SWNTs synthesized by a carbon monoxide-based CVD technique by a combination of sonification, oxidation and acid washing stages. MWNTs grown by the CVD technique are treated by wet and dry oxidation procedures to remove impurities [37].

Other methods of purification invariably include a sequence of acid treatment, microfiltration and heating processes [38–41]. The effectiveness of a purification process is characterized by its ability to achieve high-purity CNTs while at the same time maintaining or enhancing the structural, mechanical and electrical properties of the CNTs.

8.3 Design of Carbon Nanotube Gas Sensors

The preparation of the sensing material is very critical to any sensor. The performance of a sensor is highly dependent on the configuration, morphology, thickness and the composite ratio of the sensing materials. This is especially true in the case of CNT-based sensors. A good sensor has to provide a uniform, linear, repeatable and sensitive response. Noise rejection capability and selectivity are also

important criteria that a sensor needs to satisfy. Many research groups have been successful in demonstrating functional CNT-based sensors. This section describes the design and fabrication processes that have been developed to realize CNT-based gas sensors.

8.3.1
CNT Composite Sensing Materials for Gas Sensing

Santhanam et al. [42] developed a vapor-phase chemical sensor for the detection of different chloromethanes, using a novel nanocomposite material that is based on MWNTs and poly(3-methylthiophene). The MWNTs were first functionalized such that the carboxyl group is attached to the nanotube to facilitate stronger interaction between MWNTs and poly(3-methylthiophene). The nanocomposite was synthesized from two solutions, one with 980 μL of the monomer in 10 mL of chloroform and the other with a weighed amount of MWNTs (45 mg) and 0.16 g of $FeCl_3$ in 10 mL of chloroform. The two solutions were warmed for 15 min before being mixed and stirred for 24 h. The final composite was precipitated by adding 150–200 mL of methanol to the solution mixture before being dried in an oven at 100 °C. The nanocomposite was mixed with poly(ethylene oxide) in a 7 : 3 ratio. Acetonitrile was added to the mixture to form a paste. The nanocomposite paste was deposited between two palladium electrodes on a polymer substrate. Wire leads were soldered on to the electrodes to connect the sensor to a resistance measuring circuit.

The processability and controllability of the nanocomposites can be a challenge. The Langmuir–Blodgett (LB) molecular engineering technique based on a highly controlled layer-by-layer deposition is used as a nanomaterial processing method to achieve greater structural uniformity. Penza et al. [43] fabricated an SWNT–cadmium arachidate (CdA) amphiphilic matrix by using the LB technique to realize a surface acoustic wave (SAW) highly sensitive organic vapor sensor with a sub-ppm limit of detection. The CdA host matrix consists of two monovalent anionic fatty acids of deprotonated arachidic acid complexed with single divalent cationic cadmium for electrical charge neutralization. This organic matrix is suitable for covering SWNTs in the LB nanocomposite. In this process, arachidic acid ($0.734\,mg\,mL^{-1}$) in chloroform and a solution of SWNT ($0.202\,mg\,mL^{-1}$) in chloroform were prepared. A third solution was created by mixing equal proportions of both solutions. The mixed solution was ultrasonicated for 1 h before being spread on a subphase constituted of deionized water (18 MΩ) with 10^{-4} M $CdCl_2$. The monolayer of nanocomposite layer was mechanically compressed at a rate of $15\,mm\,min^{-1}$ up to a surface pressure of $27\,mN\,m^{-2}$. The nanocomposite was deposited on a sensor and allowed to dry for 12 h. A schematic of the nanocomposite SAW sensor is shown in Figure 8.1. Figure 8.2 presents SEM images of the nanocomposite and SWNTs. This nanocomposite gas sensor has been demonstrated to be very sensitive to polar and nonpolar organic molecules such as ethanol, ethyl acetate and toluene. More in-depth discussions on the sensor's performance are presented in Section 8.5.3.

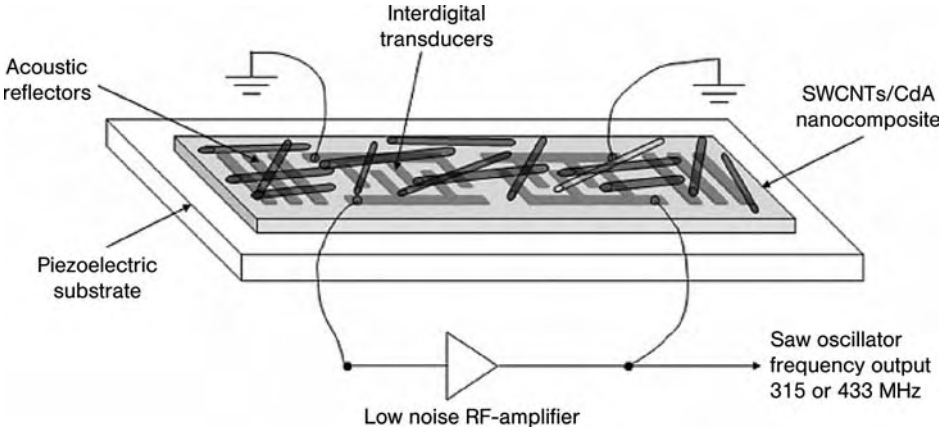

Figure 8.1 Microacoustic two-port SAW sensor coated with SWNT 27.5 wt.% nanocomposite film [43].

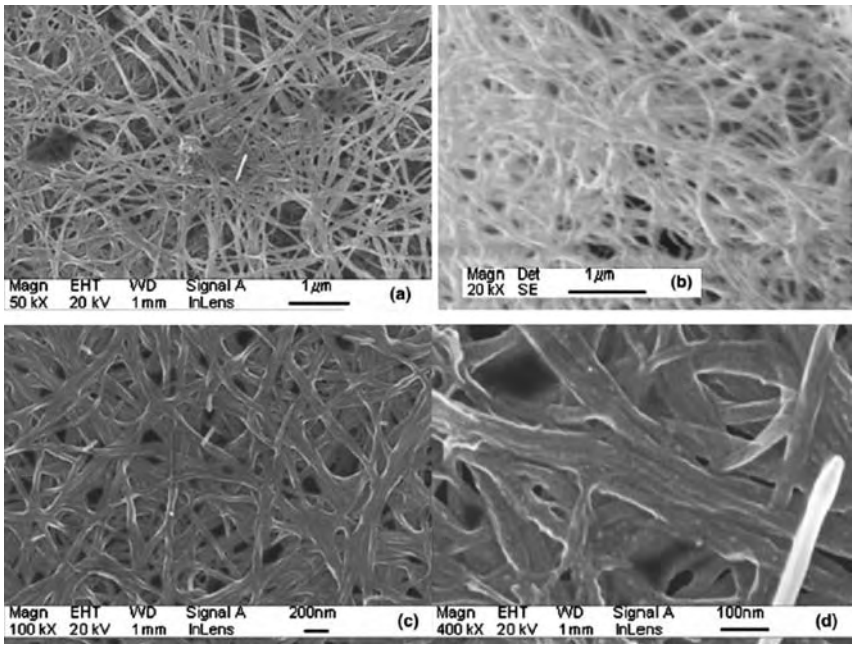

Figure 8.2 SEM images of (a) SWNT–CdA 27.5 wt.% nanocomposite at 50 000×; (b) SWNT thin film; (c) SWNT–CdA 27.5 wt.% nanocomposite at 100 000×; (d) SWNT–CdA 27.5 wt.% nanocomposite at 400 000× [43].

Varghese et al. [44] used an MWNT–SiO_2 composite as the capacitive sensing material for detecting CO_2, CO, humidity and ammonia. The sensor design is shown in Figure 8.3. Copper interdigital electrodes were fabricated by photolithography on a printed circuit board (PCB). A thin layer of SiO_2 was deposited on the PCB to provide insulation between electrodes. MWNTs were prepared by suspension in a toluene ultrasonic bath. The nanotubes were subsequently rinsed with 2-propanol and allowed to dry. The nanocomposite was produced by mixing the nanotubes with an SiO_2 solution (20% SiO_2 nanoparticles dispersed in water) with a dry-weight ratio of 2 : 3. The solution was then spin-coated on to the insulating SiO_2 layer to create the capacitive gas sensor. This gas sensor demonstrated reversible responses to humidity, CO and CO_2.

Philip et al. [45] reported the use of MWNTs and poly(methyl methacrylate) (PMMA) nanocomposite thin film for organic vapor detection. The MWNTs were grown by the chemical vapor deposition technique. A hydrocarbon source, acetylene gas, was decomposed by microwave irradiation at 600 °C in the presence of as a catalyst, iron(III) nitrate. Purity in the range 60–80% was obtained by this method. Potassium permanganate and a phase transfer catalyst were used as oxidants to functionalize the nanotubes [46]. Subsequently, the purified nanotubes (0.12 g) and dichloromethane (25 mL) were added and the solution mixture was ultrasonicated for 30 min. The nanotubes were mixed with a combination of a phase transfer agent, potassium permanganate and acetic acid. The nanocompos-

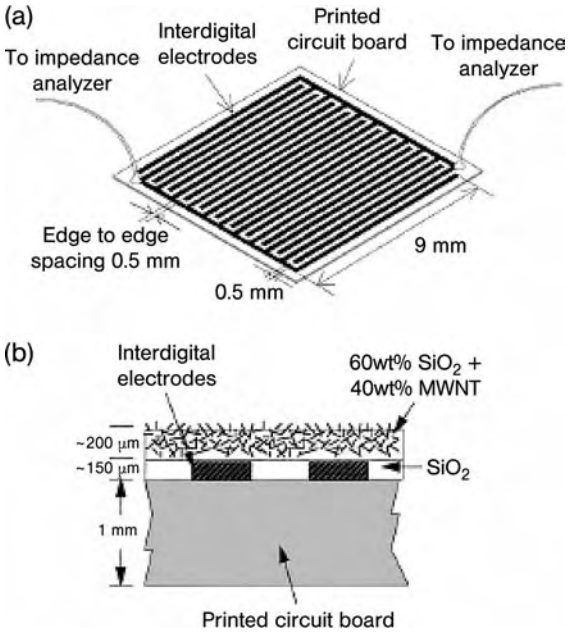

Figure 8.3 (a) Top view of the layout of the gas sensor; (b) cross-sectional view that show the insulation and sensing layer of the sensor [44].

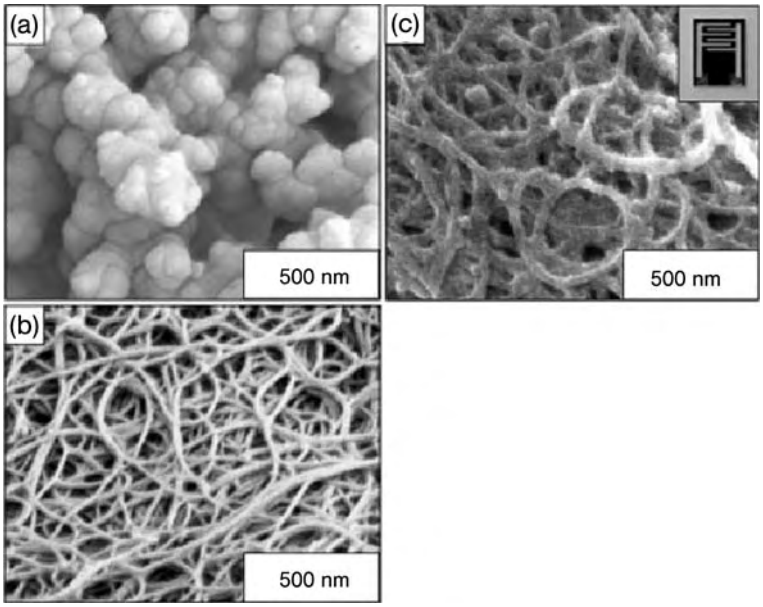

Figure 8.4 SEM images of (a) polypyrrole granules, (b) purified SWNTs and (c) SWNT–Ppy nanocomposite formed by *in situ* chemical polymerization [45].

ite was created by ultrasonication of nanotubes and PMMA in dichloromethane. A PCB with parallel conducting electrodes was coated with the nanocomposites to form the sensing medium. Other polymer has also been used to form nanocomposites from nanotubes. Organic vapors such as dichloromethane, chloroform and acetone have been shown to respond to the gas sensor. An et al. [47] fabricated a gas sensor based on a nanocomposite by polymerizing pyrrole monomer with SWNTs. Polypyrrole (Ppy) was prepared by chemical polymerization of pyrrole mixed with SWNTs. As a result, Ppy was uniformly coated on to the large surface area of the nanotubes to increase the active sites for gas adsorption. Figure 8.4 illustrates an SEM image of Ppy, SWNTs and SWNT–Ppy composites. The SWNT–Ppy nanocomposite was then coated on to patterned electrodes to provide electrical connection. The SWNT–Ppy composite was used to sense the presence of NO_2. More in-depth discussions on the performance of the sensor are presented in Section 8.5.2.

A nanocomposite containing SWNT–silicone-containing polyelectrolyte (Si-PE) for humidity sensing has been demonstrated by Li et al. [48].

8.3.2
Raw CNT Matrix

The use of nanotube thin films directly as a mechanism for gas sensors has been demonstrated. Modi et al. [49] fabricated a miniature ionization gas sensor for the

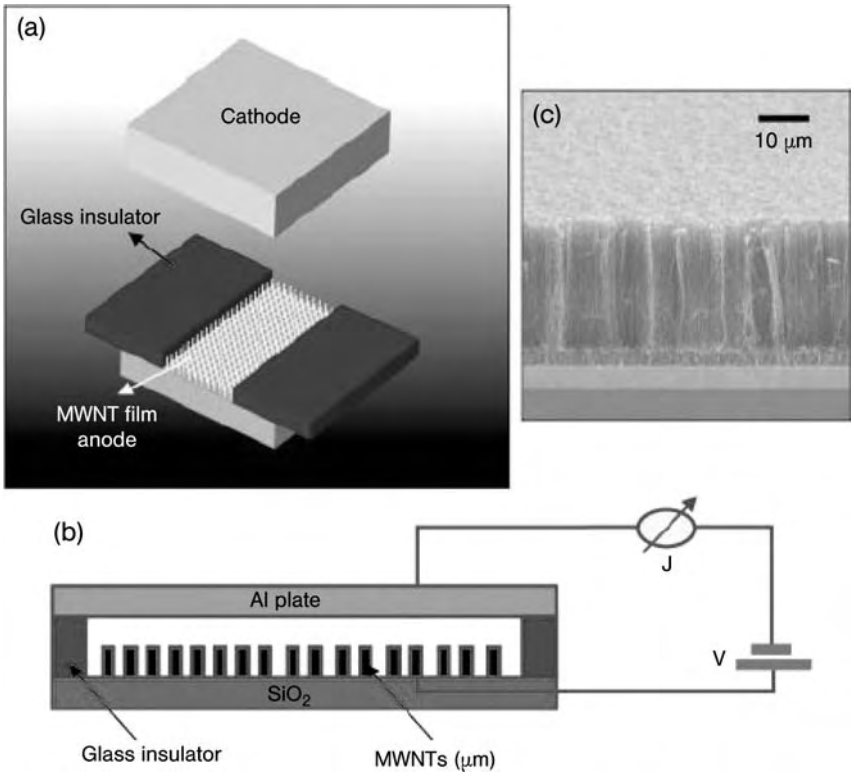

Figure 8.5 (a) Device components of miniature ionization sensor; (b) schematic of ionization sensor device; (c) SEM image of vertically aligned CNTs that are grown on an SiO_2 thin film [49].

detection of various gases by measuring their ionization signatures. MWNTs were grown on a layer of SiO_2 by the CVD method to form an anode. Two glass insulators were used as spacers. An Al plate was placed on top of the glass insulators to act as the cathode. Figure 8.5a, b and c show the integration of anode and cathode of the CNT device, device design and SEM view of nanotubes, respectively. The ionization gas sensor has been shown to detect a wide variety of gases such as Ar, O_2, CO_2, N_2, He, NH_3 and air.

A similar device was also demonstrated by Kim [50] to detect inert air. In this device, a layer of Ti was deposited on a silicon substrate. The Ti acts as an adhesion layer and also prevents reaction between Fe metal catalysts with the substrate. CNTs are grown using the thermal CVD method with C_2H_2 as a precursor gas. A flat Pyrex glass of 500 μm thickness was anodically bonded to the p-type silicon anode on the top and the n-type silicon substrate on the bottom. V-grooves were etched on the Pyrex glass to provide openings for the nanotube sensor and at the same time facilitate the flow of gas. Kim's gas sensor is shown in Figure 8.6. More

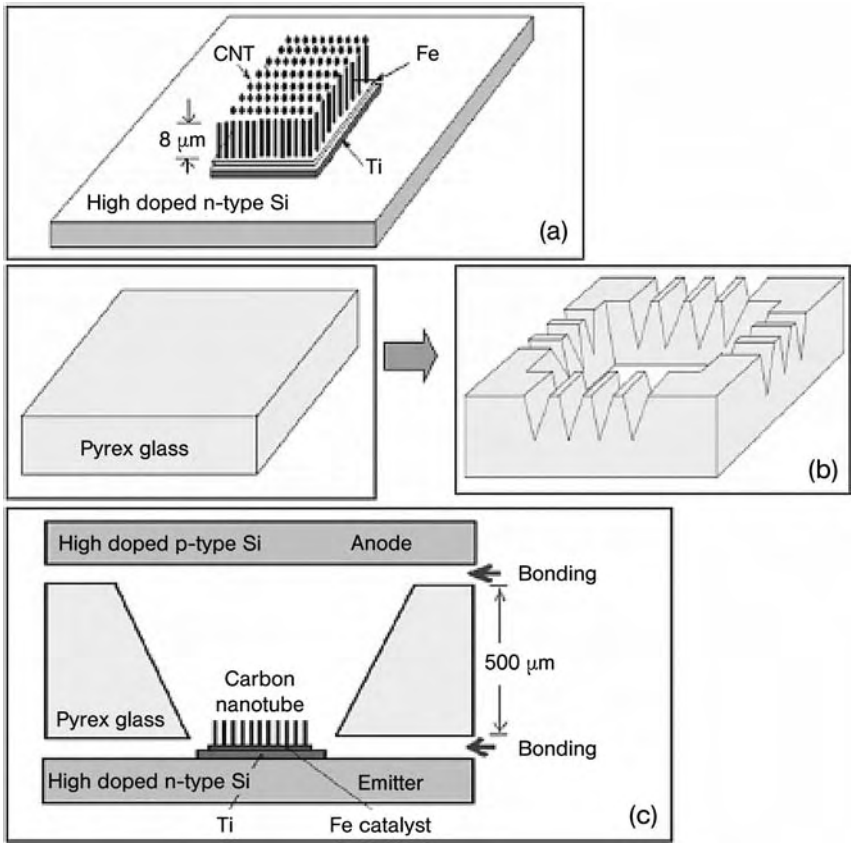

Figure 8.6 (a) Aligned nanotubes are grown by the CVD method on the Ti layer by using Fe as catalyst; (b) V-grooves are etched on Pyrex glass to provide air opening; (c) complete schematic of the ionization sensor [50].

in-depth discussions on the Modi and Kim devices are presented in Section 8.5.1.

Valentini et al. [51] fabricated a nanotube gas sensor that is based on detecting the change in resistance of SWNTs between neighboring electrodes. A silicon substrate is deposited with interdigitated patterns of Si_3N_4 and platinum thin films. A 5-nm Ni catalyst is deposited on the Si_3N_4 thin film and baked at 650 °C in vacuum for 45 min. Growth of SWNTs is induced by a radiofrequency (RF) plasma-enhanced CVD (PECVD) process at 850 °C. The final pulsed PECVD deposition process requires an RF power peak of 100 W operating at 50% duty cycle with 0.2 s period at a fixed pressure and temperature of 1 Torr and 650 °C, respectively. A CH_4 gas flow at a rate of 84 sccm is used as a hydrocarbon source in the process. The technique is able to produce a patterned SWNT that runs between Pt electrodes as shown in Figure 8.7. The sensor was used to detect gases such as NO_2,

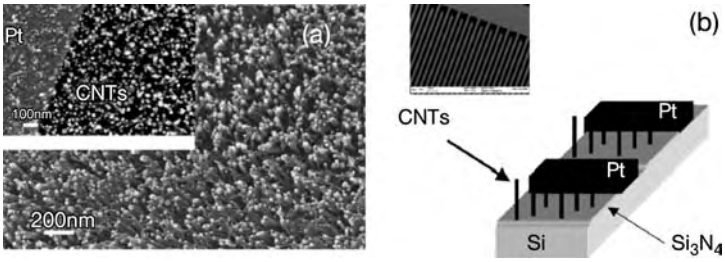

Figure 8.7 (a) SEM image of the SWNTs grown on Si_3N_4 with (inset) the patterned Pt electrode; (b) design layout of serpentine SWNTs with SWNTs synthesized on Si_3N_4 [51].

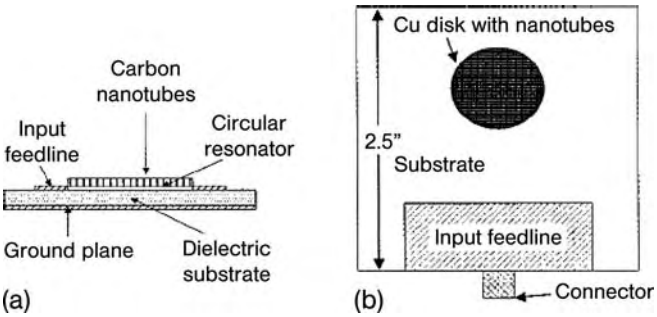

Figure 8.8 (a) A resonator plate incorporating SWNTs; (b) top view of the resonator with micro input feedline and patterned SWNTs [52].

CO, NH_3, H_2O and C_2H_5OH. More in-depth discussions on the performance of the sensor are presented in Section 8.5.2.

A circular resonator made from a Duroid board (Rogers RO4003) was fabricated such that it has a resonant frequency of 4 GHz. The configuration of the resonator is governed by the equation [52]

$$f_0 = \frac{1.841c}{2\pi a\sqrt{\varepsilon_r}} \tag{1}$$

where f_0 is the resonant frequency of the resonator, c is the speed of light, a is the radius of the disk and ε_r is the relative dielectric constant of the substrate.

Chopra et al. [52] synthesized SWNTs by the arc-discharge method and coated them on top of the Cu disk using a conductive epoxy (Circuit Works 2400). An input feedline also serves as an output port to a network analyzer. Figure 8.8a shows a cross-sectional view of the resonator. The top view of the device with circular resonator coated with SWNTs and the input/output feedline is presented in Figure 8.8b. The resonant frequency was determined through the return loss spectrum of the device. The effective dielectric constant of the device is a function

of the dielectric constant of the substrate, the conductive epoxy, the nanotubes and the gas media. This method proved to be effective in detecting both polar (NH_3 and CO) and nonpolar gases (He, Ar, N_2 and O_2). More in-depth discussions on the detection principle are presented in Section 8.5.3.

8.3.3
CNT FET Devices

The use of semiconducting SWNTs in field-effect transistors (FETs) has attracted immense attention. The unique electrical properties of CNTs have the potential to play an important role in the next generation of transistors. The recent report on gas sensing by CNT–FETs is interesting. Kong et al. [53] demonstrated that nanotube transistors can be used to detect NO_2 and NH_3. Someya el al. [54] reported that SWNT-FETs are sensitive to a wide range of alcoholic vapors. The response of nanotube FETs is repeatable and reversible. A cross-sectional view and SEM image of the SWNT-FET are shown in Figure 8.9. The SWNTs are grown in the presence of Fe–Mo catalysts on 100-nm thick SiO_2 by the CVD technique. The CVD growth is performed at 850 °C for 4 min under the flow of a mixture of gases (500 mL min^{-1} of argon, 50 mL min^{-1} of hydrogen and 500 mL min^{-1} of methane). Subsequently, the substrate with nanotubes is loaded into a metal thin film evaporator. A 5-nm Cr adhesion layer and a 25-nm Au contact are patterned and deposited to form the source (S) and drain (D) of the FET. The gap between the S and D electrodes is 2.5 or 5 μm. The elimination of resist in the patterning process allows good contact resistance without annealing of the thin films.

Jang et al. [55] proposed using laterally grown MWNTs between two electrodes as the sensing element to detect NH_3 even at room temperature. Figure 8.10 presents the MWNT resistive gas sensor. The fabrication process is a combination of conventional silicon processing techniques and nanotube growth process. A

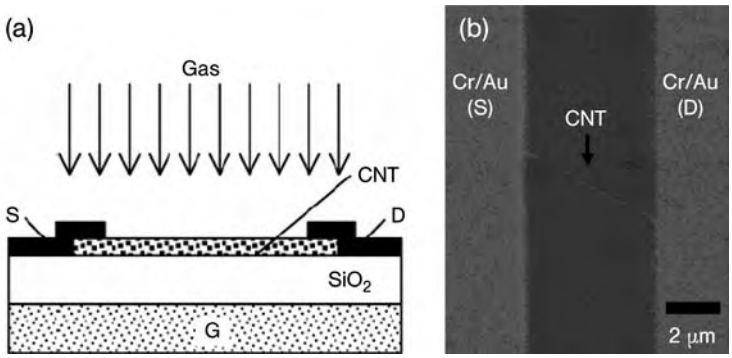

Figure 8.9 (a) Cross-section schematic of the SWNT–FET; (b) SEM image of the actual gas sensor. A strand of CNT acts as a conducting bridge between the source and the drain of the FET [54].

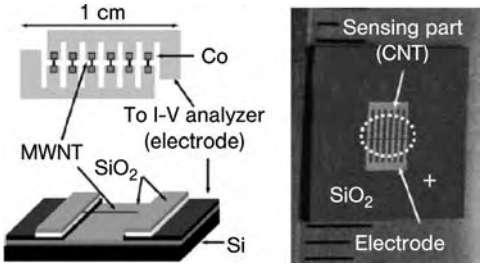

Figure 8.10 Schematic of the design and photograph of the actual sensor [55].

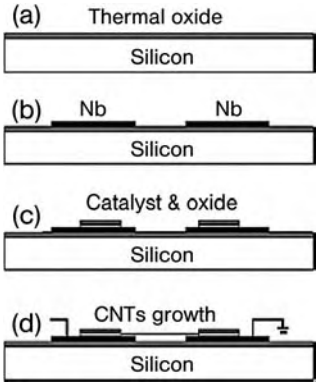

Figure 8.11 Cross-sectional fabrication process of a resistive sensor based on laterally grown MWNT [55].

thin layer of oxide was deposited on an n-type Si wafer by a thermal deposition process at 1100 °C (Figure 8.11a). The 100-nm thick Nb layer is deposited and patterned by photolithography and dry etching to form the electrodes (Figure 8.11b). Consecutive layers of Co and oxide were deposited at defined locations on the electrodes and patterning was achieved through a lift-off process in acetone (Figure 8.11c). The 100-nm thick top oxide layer inhibits any vertical nanotube growth and minimizes exposure to target gases. Subsequently, MWNTs were synthesized by the CVD technique with C_2H_2 as hydrocarbon source (Figure 8.11d). A 3 V bias was applied across the Nb electrodes to induce growth in the lateral direction [56–58]. The sensor's performance is discussed in Section 8.5.2.

Adsorption is one of the most popular techniques for implementing nanotube gas sensors. Since adsorption requires active sites for physical attachment of gas molecules, the large surface area of CNTs is ideal for chemisorption and physisorption. The adsorption of molecules creates a measurable change in the electrical conductance of the CNTs. The selectivity and sensing resolution of an adsorption-based sensor are highly dependent on the adsorption energies and charge transfer capability of the gas species. Therefore, functionalized CNTs or nanocomposites are often used to improve sensing performance. It has been

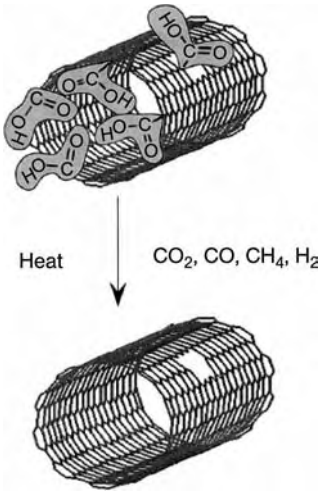

Figure 8.12 The open-ended SWNT is blocked by carboxylic acid groups at the entry port and defect port to the nanotubes. These functional groups are removed by thermal treatment (>600 K) leading to enhanced adsorption of gas molecules on the inner wall of the nanotube [66].

determined that the interior walls of SWNT nanotubes exhibit stronger binding energies for gas species than the outer walls. It is well known for the case of molecules that are in close proximity to the curved internal surface of the nanotube [59–61]. Nanotubes are grown with their ends closed. They undergo a chemical process to open the capped ends [62–65]. Unfortunately, infrared (IR) spectroscopy shows that the chemical cutting process leaves behind functional groups that block entry to the nanotubes. Kuznetsova et al. [66] reported that thermal decomposition of the functional blocks opens the nanotubes for Xe adsorption on the inner surfaces of the nanotubes. Thermally treated open-ended SWNTs have been shown to adsorb 280 times as much Xe as a closed SWNT. Figure 8.12 illustrates that heating the blocked SWNTs in vacuum to about 600 K will remove the carboxylic acid groups that block the entry ports to the nanotubes.

8.4
Simulation Studies of Nanotube-Based Gas Sensing

The recent advances in the development of nanotube-based gas sensors have also stimulated simulations and theoretical studies on the gas detection performance of CNTs. Although the realization of a functioning prototype is required to demonstrate the feasibility and to characterize the performance of a device, simulations are often used to gain insight into the functioning of the device before initiating an expensive and time-consuming device fabrication process. Several groups have

studied the gas sensing mechanisms of CNTs through theoretical models and simulations.

Zhao et al. [67] performed extensive studies on gas molecule adsorption in CNTs and CNT bundles by using first principle methods. They reported the adsorption mechanisms of various gases such as NO_2, O_2, NH_3, N_2, H_2O, Ar and H_2. Zhao et al. performed self-consistent field (SCF) electronic structure calculations based on density functional theory (DFT) with either localized basis (DMol) or plane-wave basis. The equilibrium geometry, adsorption energy and charge transfer are calculated by using the DMol program [68]. They used a double numerical basis such as the d-polarization function (DND) in all the DMol electron SCF calculations. The density functional is treated by a local density approximation (LDA) with exchange-correlation potential parameterized by Perdew et al. [69]. Geometry optimizations are performed with the Broyden–Fletcher–Goldfarb–Shanno (BFGS) algorithm with convergence criterion of 10^{-3} au on the gradient and displacement and 10^{-5} au on the total energy and electron density. The SCF plane-wave pseudopotential technique can provide more accurate electronic band structure and electron density [70]. The Troullier–Martin norm-conserving nonlocal pseudopotential model is used to describe the ion–electron interaction [71]. The energy cutoff of the plane wave basis is chosen up to 760 eV. The first principles theoretical derivation compared well with gas molecule adsorption experiments on a graphene sheet.

It is determined from Table 8.1 that the computed LDA values correspond well with the "best estimated" experimental data [72]. The computed results showed that all the gas molecules are weakly bound to the nanotube and the tube–molecule interaction can be identified as physisorption. The tube–molecule interactions can be characterized as van der Waals-like interactions between the gas molecules and graphite surface. Through computation techniques, it was determined that gas adsorption is not dependent on the tube size and chirality. In the case of nanotube bundles, there are four possible sites for gas adsorption, as shown in Figure 8.13. Simulation results confirm that the adsorption energy and charge transfer of gas molecules such as H_2 are significantly larger in the interstitial and groove sites of

Table 8.1 Equilibrium height (h, defined by the distance between molecule mass center and the center of six-membered carbon ring on graphite), adsorption energy (E_a) of various molecules on the graphene sheet.

Parameter[a]	CO_2	CH_4	N_2	H_2	*Ar*
h^{LDA} (Å)	3.11	3.34	3.31	2.92	3.31
E_a^{LDA} (meV)	151	154	110	92	97
h^{exp} (Å)	3.2	3.45	3.34	2.87	3.1
E_a^{exp} (meV)	178	126	104	42	99

a LDA denotes LDA calculation and exp represents the "best estimated" experimental data [72].

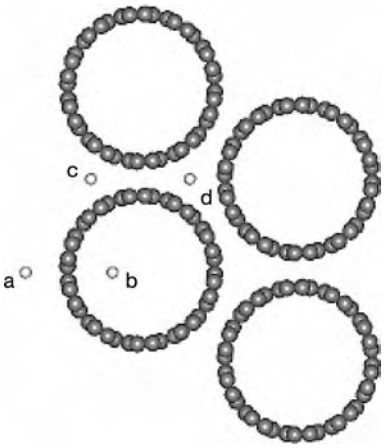

Figure 8.13 Four possible sites for gas adsorption in nanotube bundle: (a) surface; (b) pore; (c) groove; and (d) interstitial [67].

Table 8.2 Equilibrium tube–molecule distance (*d*), adsorption energy (E_a) and charge transfer (*Q*) of the H_2 molecule on four adsorption sites in the (10,10) SWNT bundle [67].

Site	d *(Å)*	E_a *(meV)*	Q *(e)*
Surface	3.01	94	0.014
Pore	2.83	111	0.012
Groove	3.33	114	0.026
Interstitial	3.33	174	0.035

the nanotube bundle than those on the surface site. Table 8.2 shows the calculated tube–molecule distance (*d*), adsorption energy (E_a) and charge transfer (*Q*) of the H_2 molecule at different sites in the CNT bundles.

Although gas sensors based on CNTs have shown high sensitivity to the presence of small concentrations of molecules, they can only be applied to detect gases molecules that will bind to the wall of the CNTs. Peng et al. [73] proposed a new type of gas sensor that is based on substitutional doping of impurity atoms into intrinsic SWNTs or by using composite $B_xC_yN_z$ nanotubes. The feasibility of such sensors is demonstrated through first-principles calculations. Similarly to Zhao et al. [67], DFT and LDA with ultrasoft pseudopotential, plane-wave basis sets and periodic boundary conditions were used to model the response of doped CNT sensors. The use of CNTs doped with boron and nitrogen atoms and an intrinsic BC_3 nanotube [74, 75] is determined to be very responsive to CO due to strong binding between the gas molecules and the nanotubes. Charges are transferred between adsorbed gas molecules and nanotubes. The total charge transferred is

Table 8.3 Computed data for adsorption energy, tube–molecule distance and charge transfer of CO on doped CNTs or $B_xC_yN_z$ nanotubes [73].

	E_z *(eV)*[c]	*Configuration*	E_b *(eV)*	d *(Å)*	E_T *(e)*[d]
CNT	0.56	CO[e]	No binding		
		OC[f]	No binding		
B–CNT[a]	0.44	CO	–0.85	1.52	0.59
		OC	–0.27	2.83	0.02
N–CNT[b]	0.43	CO	–0.22	2.99	0.05
		OC	–0.18	2.82	0.08
BC_3	0.61	CO	–1.72	1.50	0.50
		OC	–0.28	2.53	0.04

a Intrinsic nanotube doped with boron atom in two-unit cell.
b Intrinsic nanotube doped with nitrogen atom in two-unit cell.
c HOMO–LUMO band gap.
d Electron charge transfer from nanotube to molecules.
e CO molecule binds to the nanotube with the carbon atom close to the tube.
f CO molecule binds to the nanotube with the oxygen atom close to the tube.

calculated by considering the charge difference between the molecule adsorbed on the nanotube and an individual gas molecule [76]. Table 8.3 shows the adsorption energies and charge transfer between CO molecule and nanotubes.

Figure 8.14 illustrates the different configurations of adsorption of CO molecules on boron- and nitrogen-doped CNTs and BC_3 nanotubes. It is determined that the doped and BC_3 nanotubes CNTs experience significant changes in electrical properties when exposed to CO and water molecules. The change in electrical properties is induced by an increase in local chemical reactivity that promotes binding between target molecules and nanotubes.

Similar computations performed on the adsorption of H_2O molecules show that the large electron charge transfer changes the conductance of the nanotubes. The measured voltage change due to the charge transfer is related to the gate capacitance of the device [73]:

$$\Delta Q = C_g \Delta V_g = \delta\theta\left(\frac{\pi d l}{\sigma}\right) \tag{2}$$

where C_g is the capacitance of the nanotubes, ΔV_g the voltage change measured in the experiments, d the nanotube diameter, l the nanotube length, σ the molecule cross-sectional area and θ the molecule coverage on the nanotube surface.

It is determined that the binding of CO and H_2O molecules with boron-doped CNTs is through chemical adsorption and the adsorption between CO and H_2O molecules with nitrogen-doped CNTs is by physical adsorption. Desorption of the target molecules can be realized by exposing the CNTs to UV light [77]. Table 8.4 shows the adsorption energy, tube–molecule distance and charge transfer on doped CNTs or $B_xC_yN_z$ nanotubes. The stronger binding energies and shorter

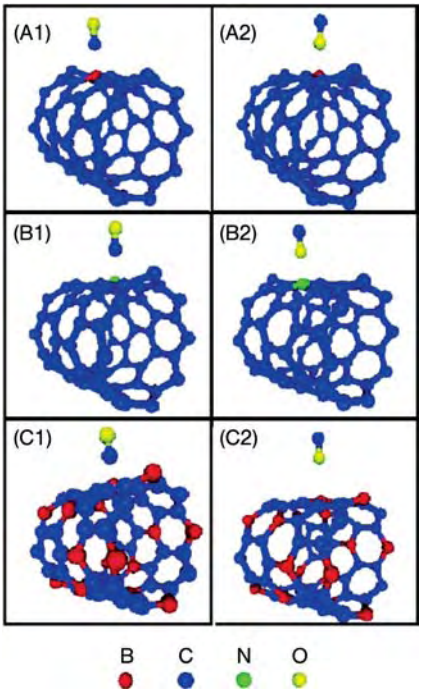

Figure 8.14 Semiconducting (8,0) CNT with one boron atom substituted in an intrinsic CNT. (A1) Boron atom is close to the carbon atom of a CO molecule; (A2) boron atom is close to the oxygen atom of a CO molecule; semiconducting (8,0) CNT with one nitrogen atom substituted in an intrinsic CNT; (B1) nitrogen atom is close to the carbon atom of a CO molecule; (B2) nitrogen atom is close to the oxygen atom of a CO molecule; semiconducting (8,0) BC_3 nanotube that binds to CO molecule; (C1) boron atom is close to the carbon atom of a CO molecule; (C2) boron atom is close to the oxygen atom of a CO molecule [73].

distances between both CO and H_2O and boron-doped CNTs suggest that the binding is ionic in nature.

The grand canonical Monte Carlo (GCMC) method [78] was used to simulate the physisorption of H_2 in parallel SWNTs by Williams and Eklund [79]. From their study, it was determined that small-diameter ropes of SWNTs are preferred to increase H_2 adsorption on nanotubes. Ayappa [80] reported using GCMC to investigate the adsorption of gas mixtures on SWNTs. At high temperatures, energetically favored species are adsorbed whereas smaller species are able to eliminate larger species from the nanotubes with intermediate CNT diameters at low temperatures.

It is well known that CNTs are highly hydrophobic, and therefore the water–tube interaction is weak. It has been proposed that hydrophobic structures such as CNTs can have significant water occupancy. Water molecules inside CNTs are undisturbed by external forces, allowing strong and lasting hydrogen bonds to

Table 8.4 Computed data for adsorption energy, tube–molecule distance and charge transfer of H_2O on doped CNTs or $B_xC_yN_z$ nanotubes [73].

	E_2 *(eV)*[f]	*Configuration*	E_b *(eV)*	d *(Å)*	E_T *(e)*[g]
CNT	0.56	H_2O	No binding		
B–CNT[a]	0.44	B–H_2O[h]	–0.56	1.70	–0.12
N–CNT[b]	0.43	N–H_2O[i]	–0.23	3.12	–0.02
BN–CNT[c]	0.48	B–H_2O	–0.48	1.72	–0.2
		N–H_2O	–0.24	3.14	–0.02
B2N–CNT[d]	0.44	N–H_2O	–0.64	3.15	–0.28
BN2–CNT[e]	0.42	B–H_2O	–0.53	1.51	–0.08
BC_3N–type 2	0.93	B–H_2O	–0.48	1.72	–0.21
		N–H_2O	–0.18	3.14	–0.05

a Intrinsic nanotube doped with boron atom in two-unit cell.
b Intrinsic nanotube doped with nitrogen atom in two-unit cell.
c Intrinsic nanotube doped with boron–nitrogen atom pair in two-unit cell.
d Intrinsic nanotube doped with boron–nitrogen–boron atom pair in two-unit cell.
e Intrinsic nanotube doped with nitrogen–boron–nitrogen atom pair in two-unit cell.
f HOMO–LUMO band gap.
g Electron charge transfer from the nanotube to molecules.
h H_2O molecule binds to the nanotube with the oxygen atom close to the boron atom.
i H_2O molecule binds to the nanotube with the oxygen atom close to the nitrogen atom.

form [81]. Similar reasoning could be applied in the case of the porous structures formed between the inter-tube spacings among neighboring CNTs. Capillary condensation can be induced in the minuscule pores at low relative humidity and temperature. The applications of capillary condensation by exploiting the morphology of CNTs have been demonstrated. This sensing principle will be discussed in later sections.

The iterative design, fabrication and verification process of nanotechnology-based sensors are extremely time consuming and expensive. As simulation models and techniques to describe the behaviors of nanocomposites and nano-domain phenomena become more mature and widely accepted, it is expected that the design cycle will shorten significantly and the viability of sensor designs can be determined before costly investments are committed.

8.5 Sensing Mechanisms

Carbon nanotubes offer many unique properties that are being exploited for sensing gas molecules. The large surface-to-volume ratio of CNTs provides many adsorption sites for gas molecules. The high aspect ratio of CNTs provides high concentration of electrical field that is dependent on the presence of gas species. The change in electrical properties is used to detect target gases. The morphology of CNTs bundles may amplify and induce a change of gas phases to increase sen-

sitivity of the sensors. This section describes the sensing mechanisms that exploit the various properties of CNTs for gas sensing applications.

8.5.1
Electron Emitter

The detection principle of ionization gas sensors is based on the signature ionization characteristics of target gases. Traditional ionization sensors are large in size, heavy, require high power to operate and generate large breakdown voltages. Modi et al. [49] demonstrated an ionization gas sensor that incorporates CNTs (the fabrication process is discussed in Section 8.3.2). The extremely sharp tips of the CNTs serve to concentrate very high electric fields at relatively low voltages. As a result, the breakdown voltages are lowered significantly in comparison with traditional sensors. The lower breakdown voltages enable a miniature ionization sensor to be obtained that is safer to operate and requires lower operating power.

The MWNTs are grown on an SiO_2 thin film to form an anode (Figure 8.5). An aluminum plate is used as the cathode to provide a difference in potential to create an electric field between the capacitor. The nanometer tip diameter of MWNTs creates very intense nonlinear electric fields around the tips [82, 85]. The intense electric field creates highly ionized gas around the tips to induce the breakdown process. As a result, a power electron avalanche occurs between the two electrodes at relatively low voltages. This technique offers several advantages over CNT sensors that are based on gas–nanotube adsorption. The sensing mechanism does not depend on the adsorption energy or charge transfer characteristics of gases. Therefore, inert gases which have low chemical reactivity and weak physisorption can be detected. The ionization technique is able to distinguish between gases or gas mixtures by measuring the distinct breakdown voltages of the gas media [86, 87]. In addition to providing high selectivity, the amount of current discharge can be used to provide concentration information. Figure 8.15 illustrates the distinct breakdown voltage for each target gas. Figure 8.16 shows that the breakdown voltage is relatively unchanged and unaffected by the gas concentration. The discharge current is shown to be related to the gas concentration in Figure 8.17. It can be concluded that through a combination of breakdown voltage and discharge information, the concentration of a particular gas can be determined. Since no adsorption and desorption is involved in the sensing process, the sensor provides fast response times. More importantly, consideration of sensing hysteresis is not necessary. A similar CNT ionization gas sensor was tested by Kim for 24 h under a 1 kV static voltage [50]. As shown in Figure 8.18, the performance of the sensor is not degraded over time.

8.5.2
Resistivity Change

The detection and monitoring of gases through a change in the electrical properties of the sensing material have been developed for a wide range of applications

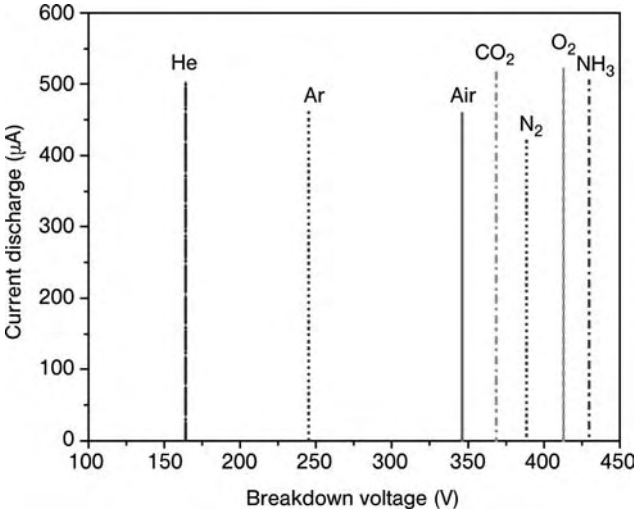

Figure 8.15 The I–V characteristics of the ionization sensor. The breakdown voltages are clearly shown for He, Ar, Air, CO_2, N_2, O_2 and NH_2 [49].

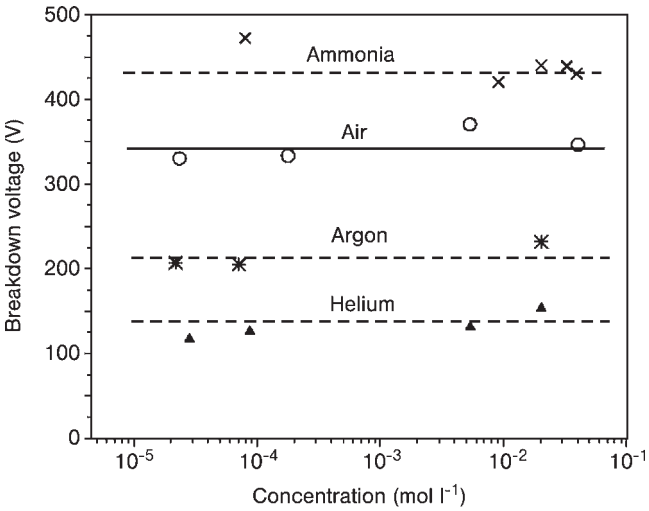

Figure 8.16 Breakdown voltages are shown to be independent of gas concentration [49].

[88, 91]. Sensing materials such as conducting polymers are responsive to many gases and gas mixtures, but their selectivity is poor. There are also challenges regarding the environmental stability of polymers. Oxide-based sensors are environmentally stable, but they operate at elevated temperatures of >300 °C and fail to respond at ambient temperature. The use of nanotubes or a nanocomposite that contain nanotubes has shown potential to deliver miniaturization, performance

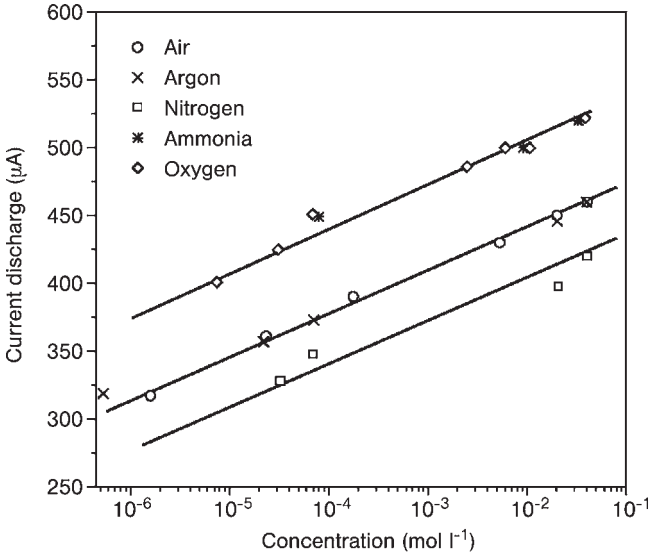

Figure 8.17 The current discharge increases logarithmically with gas concentration [49].

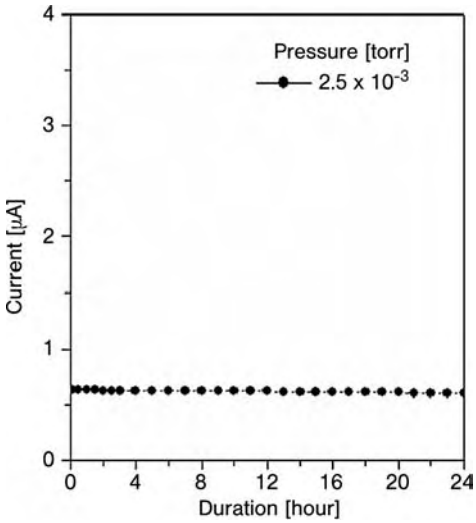

Figure 8.18 Durability test of the sensor at 1 kV [50].

stability, detection selectivity and sensitivity. Adsorption of target gas molecules on the wall of the nanotubes will change the electrical properties through charge transfer and chemical reactivity processes. The measurable change is then correlated with the presence of the gas or the concentration of a specific gas.

MWNTs and 3-methylthiophene nanocomposite is shown to display changes in electrical resistance when exposed to different chloromethanes. The use of

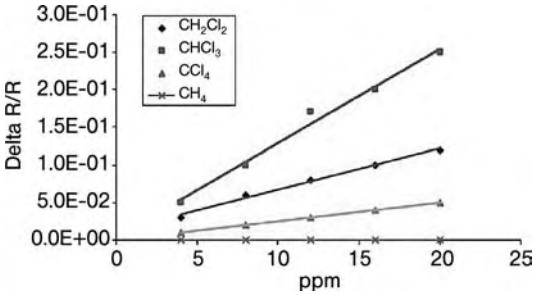

Figure 8.19 The sensitivity as a function of concentration of the MWNT–poly (3-methylthiophene) nanocomposite for different chloromethanes [42].

3-methylthiophene alone was shown to be unresponsive to chloroform [92]. Santhanam et al. [42] demonstrated that the new nanocomposite shows strong interactions with a variety of chloromethanes. Figure 8.19 shows that the nanocomposite sensor has a linear response to the concentration of chloromethanes.

An MWNT–PMMA nanocomposite sensor fabricated by Philip et al. [45] shows a large resistance response on the order of 10^2–10^3 when exposed to organic vapors such as dichloromethane, chloroform and acetone. The fabrication process of the sensor is presented in Section 8.3.1. The underlying sensing principle is based on the increase in resistance experienced by neighboring nanotubes when the analytes are adsorbed within the polymer matrix. Within the nanocomposites, electron hopping occurs in the network of closely laid nanotubes by quantum mechanical tunneling effects [93–96]. The contact resistance between nanotubes provides the baseline resistance of the nanocomposites. The polymer matrix swells when the organic vapors are adsorbed. The increased material volume increases the distance between neighboring nanotubes and thereby increasing the contact resistance of the sensing thin film. The oxidation of nanotubes produces COOH and OH groups along the walls of the MWNTs [97].These functional groups create hydrogen bonds to improve the dispersion and adhesion of nanotubes within the polymer matrix. Since the number of conducting paths within the nanocomposite is large, any slight change in film volume will induce a large increase in resistance. The responses of the gas sensor to dichloromethane, chloroform and acetone are shown in Figure 8.20a. Figure 8.20b presents the repeatability and reversibility of the sensor during periodic exposure of dichloromethane.

In addition to changing the electrical properties of nanotubes, An et al. [47] used SWNTs as structural materials to increase the surface of sensing material. *In situ* chemically polymerized polypyrrole (Ppy) was mixed with SWNTs to form the sensing nanocomposite. A conducting path is created by spin-coating the nanocomposite on to prepatterned electrodes. The overall resistivity of SWNT–Ppy is greatly reduced by the presence of the conducting SWNTs. In addition, the Ppy surface area on which gas adsorption can occur is increased threefold. Figure 8.21 presents the response of the annealed nanocomposite over time. As shown in

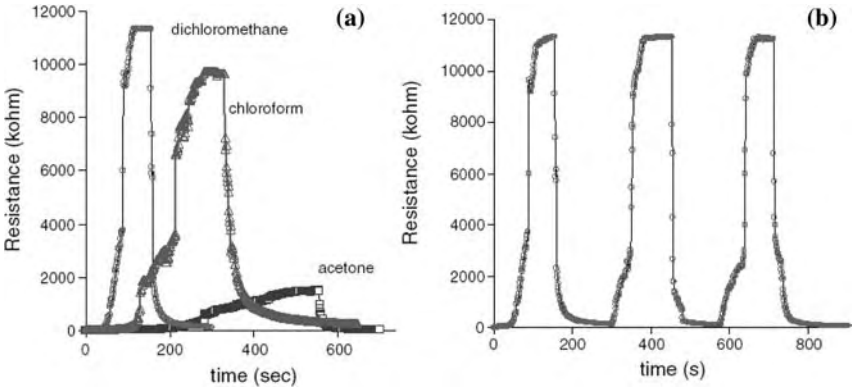

Figure 8.20 (a) Response of CNT and PMMA nanocomposites to different organic gases; (b) reversibility and repeatability test on the nanocomposite to dichloromethane [45].

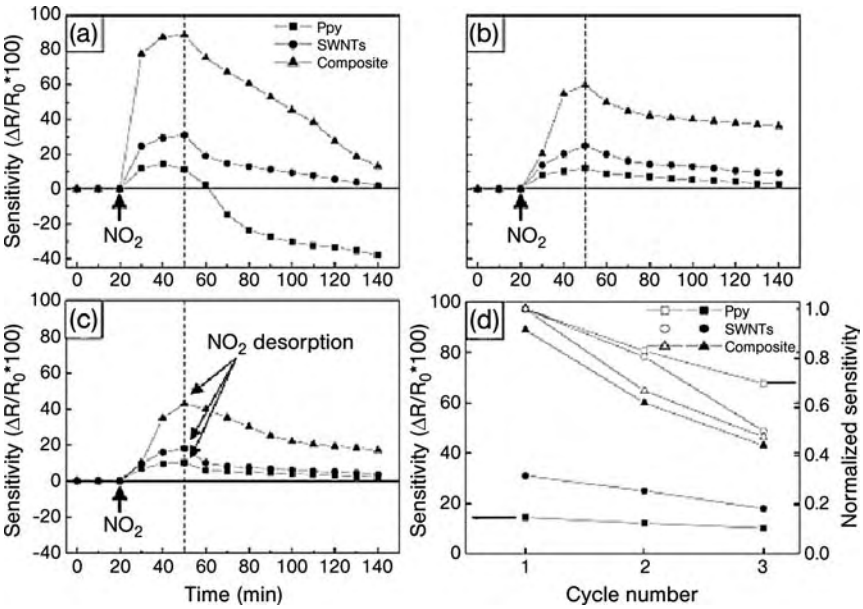

Figure 8.21 The response of SWNT–Ppy nanocomposite to NO_2 with a concentration of 3000 ppm over time. (a) First cycle of gas exposure with arrow indicating NO_2 injection and dotted line indicating NO_2 desorption; (b) second cycle after 24 h; (c) third cycle after 48 h; (d) the change in sensitivity over the number of cycles [47].

Figure 8.21a, the resistance of all three materials increases during the 30 min of NO_2 exposure. This is particularly true for the case of the nanocomposite. When the gas supply was turned off, the resistance was slowly reduced to the baseline value. It is interesting to note that the resistance of Ppy decreases to a level that is much lower than its initial value. It is suggested that the contact resistance of Ppy is further decrease by Joule heating during the operation of the sensor. Although the resistance of the SWNT and the nanocomposite is fully recovered after 1.5 h in the first cycle, the final baseline resistance for the second and third cycles proves that NO_2 molecules are still adsorbed on the materials. This effect may be caused by the presence of remnant gas species through chemisorption. The large surface area facilitates active sites for both physisorption and chemisorption. Molecules held by weak physisorption can be released easily over time; however, the more strongly chemisorbed gas molecules can be effectively desorbed by providing a constant voltage bias to create Joule heating. The higher final resistance of the SWNT and the nanocomposite is shown in Figure 8.21b and c. Figure 8.21b shows the change in sensitivity for all three materials over three cycles. It is apparent that the nanocomposite is more adversely affected by chemisorption than the other two materials.

Valentini et al. [51] reported the use of nanotube thin films to detect NO_2, CO, NH_3, H_2O and C_2H_5OH. The fabrication process of the sensor is discussed in Section 8.3.2. The response of the resistive sensor to the presence of NO_2 at various temperatures is shown in Figure 8.22a. It is observed that the sensor remained responsive to NO_2 at room temperature. The baseline resistance of the SWNT thin film decreased with increase in operating temperature. An optimal tradeoff between sensitivity and fast adsorption and desorption is determined to occur at a temperature of 165 °C. Figure 8.22b presents the response of the sensor from a concentration of 10 to 100 ppb. The overall resistance of the SWNT network is contributed by the resistance of the individual nanotube, junctions between neighboring nanotubes and quantum mechanical tunneling between closely spaced nanotubes. It is suggested that higher temperature facilitates the decomposition of NO_2 to O_2 molecules that are adsorbed at the defective sites of SWNTs, thereby producing volatile species such as CO and CO_2 that consume the defective sites. As a result, the number of metallic-like (Fermi) junctions is decreased because of fewer impurities. In contrast, as shown in Figure 8.22c, an increase in resistance was experienced for H_2O, C_6H_6 and ethanol. However, Figure 8.22d reveals that that the sensor is unresponsive to CO. The electron transport phenomenon has been described [98].

Another study of resistive gas sensors was reported by Jang et al. [55]. The sensing device and fabrication process are shown in Figures 8.10 and 8.11, respectively. The fabrication process is discussed in Section 8.3.3 The laterally grown MWNTs are shown to be responsive to the presence of NH_3 even at room temperature. The dynamic response of the sensor is presented in Figure 8.23a. The increase in the resistance of the MWNTs can be explained by conventional p-type semiconductor theory. When the sensor is exposed to an electron donor, electron charge transfer occurs from the electron donor to the p-type semiconducting

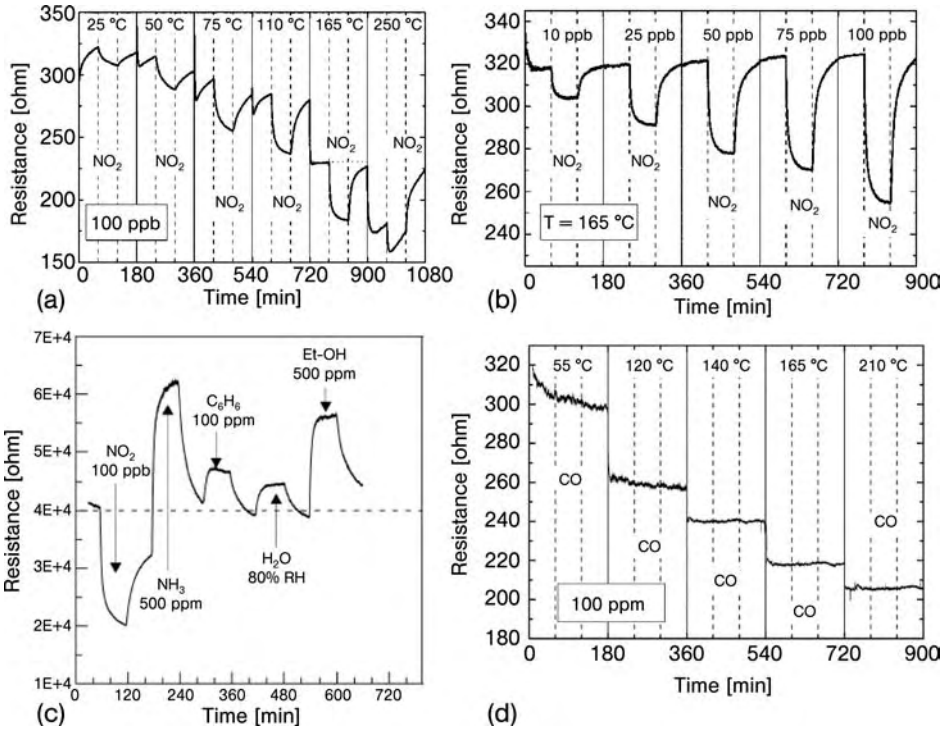

Figure 8.22 Experiments characterizing the performance of the resistive sensor. (a) Response of sensor to NO_2 at different operating temperatures; (b) response of sensor to different concentration of NO_2 at a constant operating temperature of 165°C; (c) response of sensor to different gases; (d) response of sensor to CO at different operating temperatures [51].

nanotubes. An electron donor gas such as NH_3 will shift the valence band of the nanotubes away from the Fermi level, thus depleting holes and increasing resistance. The response time of the sensor to NH_3 in the presence of Ar is shown in the inset of Figure 8.23a. The sensing response changes linearly with temperature. This linear relationship is important to calibrate the sensor during operating temperatures. The change in resistance to temperature increase for an NH_3 flow rate of 500 sccm is presented in Figure 8.23b.

A gas sensor with a simple fabrication process was developed by Li et al. [99]. SWNTs are cast on interdigitated electrodes to provide conducting paths. The performance of the sensing device at four different concentrations is shown in Figure 8.24. It is observed that the recovery time is on the order of 10 h because of the higher adsorption energy between NO_2 and the nanotubes. This is typical for nanotube-based sensors for NO_2 [53]. It was demonstrated that UV illumination hastens the recovery process by decreasing the desorption energy barrier [77].

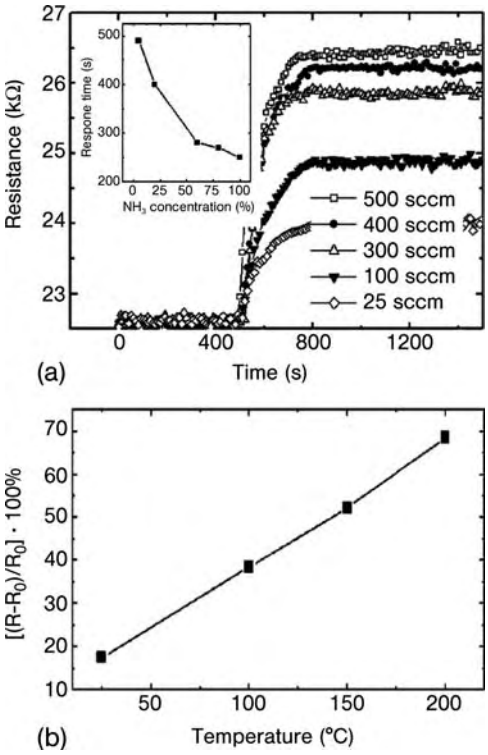

Figure 8.23 (a) Dynamic response of sensor to different NH_3 flow rates; inset, response time of sensor to concentration of NH_3 in Ar gas; (b) linear change in resistance with temperature change [55].

Figure 8.24a shows the adsorption and desorption processes without UV treatment. Figure 8.24b presents the same process with UV illumination to aid the desorption process.

8.5.3
Frequency Shift

Penza et al. [43] demonstrated a highly sensitive acoustic vapor sensor based on a SAW two-port quartz resonator operating at 315 and 433 MHz. The fabrication process of the sensor is presented in Section 8.3.1. The sensing device and SEM images of SWNT–CdA are shown in Figures 8.1 and 8.2, respectively. The response of the SAW 433 MHz acoustic sensor with SWNT–CdA 27.5 wt.% nanocomposite and pure CdA matrix is presented in Figure 8.25a. The pure CdA matrix served as a control to compare the performance of the nanocomposite. Eight cycles of decreasing ethanol concentration over a 5-min time span were used. It is clearly shown that the resonant frequency of both devices decreases as they were exposed

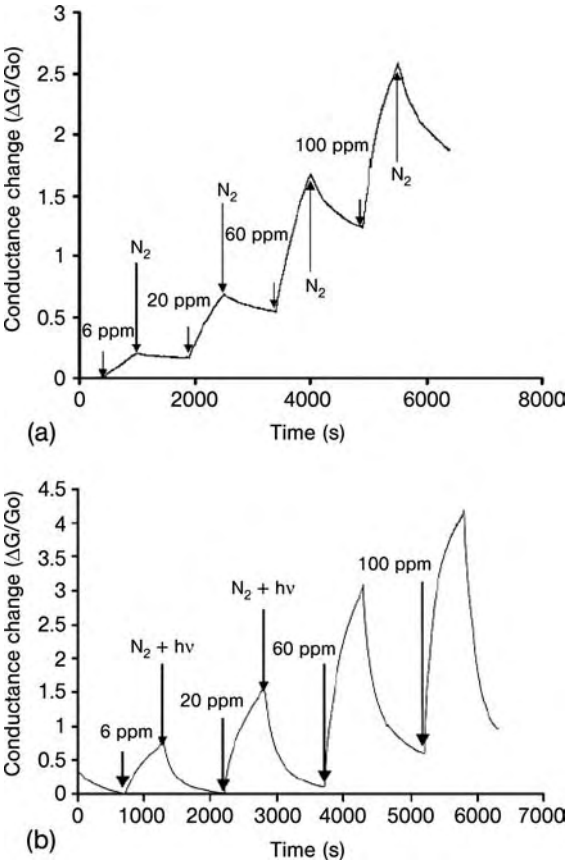

Figure 8.24 (a) Change in conductance of the sensor when exposed NO_2 without UV illumination; the N_2 gas is used to dilute or purge the test chamber; (b) change in conductance of the sensor when exposed NO_2 with UV illumination [99].

to the analyte. As expected, the nanocomposite demonstrated higher sensitivity over the control device. The SWNTs served to increase the surface area for adsorption and enhanced the overall chemical reactivity of the sensing thin film. The greater amount of adsorbed molecules caused a larger shift in frequency response of the SWNT–CdA sensor. Figure 8.25b shows the frequency shift of both acoustic sensors as a function of ethanol concentration. The sensitivity of a pure CdA sensor had a sensitivity of 20.05 Hz ppm^{-1}. With the incorporation of SWNT, the sensitivity of a CdA-based acoustic sensor was increased by a factor of two to 39.0 Hz ppm^{-1}. It has also been determined that the limit of detection for a SAW 433 MHz SWNT–CdA sensor is 0.7, 0.9 and 0.7 ppm for ethanol, ethyl acetate and toluene, respectively. The proposed acoustic sensor based on SWNT–CdA nanocomposite showed excellent response in terms of linearity, repeatability, sensitivity and limit of detection.

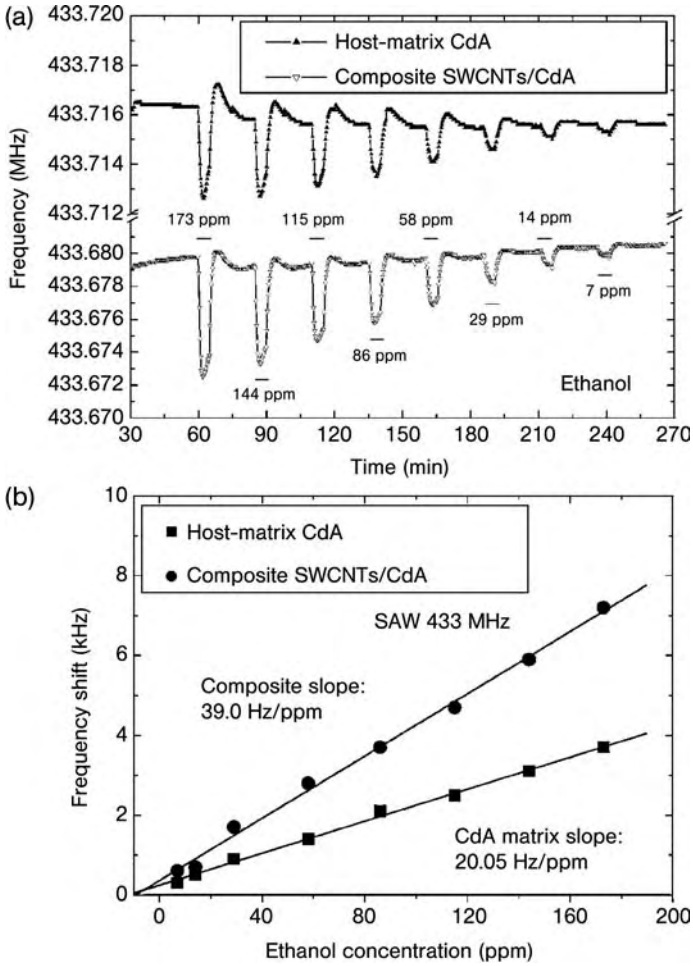

Figure 8.25 (a) Frequency shift responses of pure CdA matrix and SWNT–CdA nanocomposite when subjected to eight pulses of ethanol injection; (b) frequency shift as a function of concentration of ethanol [43].

Another sensing device that utilized a shift in resonant frequency was presented by Chopra et al. [52]. The fabrication process of the sensor is discussed in Section 8.3.2. The sensing principle is based on a change in dielectric constant of the sensing material in the presence of certain gases. This method proved to be effective in detecting both polar (NH_3 and CO) and nonpolar gases (He, Ar, N_2 and O_2). First, the sensor is place within a chamber with a pressure of ~10^{-5} Torr in order to remove gas molecules already adsorbed on the nanotubes (degassing). Second, gases are injected within the chamber to characterize the sensor's performance. It is shown that the sensor is responsive even to inert gases such as He. The resonance frequency is shifted to 3.8885 GHz from the degassed baseline value. The

effective dielectric constant is recovered upon the removal of He. This suggests that inert gases can be detected through electrical transport mechanisms induced by molecular collisions with the walls of nanotubes [100]. As shown in Figure 8.26a, similar responses to O_2 and NH_3 are experienced. It is well understood that a change in dielectric constant of the material will change its resonant frequency. Therefore, a change in resonant frequency (f_0) implies the change (Δf_{gas}) is directly related to the dielectric constant of gas and the gas–nanotube interaction. The dielectric constant of a gas is governed by the Debye equation [101]:

$$\varepsilon = 1 + 4\pi N_1\left(\alpha_0 + \frac{\mu^2}{3kT}\right) \tag{3}$$

where ε is the dielectric constant, N_1 is the number of molecules per cm^3, α_0 is the polarizability per molecule, μ is the dipole moment, k is Boltzmann's constant and T is the absolute temperature.

Figure 8.26b shows the frequency shift from the initial degassed resonant frequency when the sensor is exposed to a variety of gases. It is noted that the response to polar gases is much greater than that to nonpolar gases. From Equation (3), this is expected because $\mu = 0$ for nonpolar gases and $\mu \neq 0$ for polar gases. Therefore, polar gases have a larger dielectric constant than nonpolar gases. For the polar gases, it is shown that a larger dielectric constant will result in a larger shift in frequency.

8.5.4
Capacitive

Yeow and She [102] demonstrated the use of a matrix of randomly aligned CNT sensors for capacitive sensing of humidity. The design of the parallel plate capacitor sensor is shown in Figure 8.27. The presence of MWNTs increases the sensing surface area and therefore increases the capacitance of the sensor. More importantly, the random entanglement and alignment of nanotubes form nanopores and interstitial gaps that will induce capillary condensation of water vapor. The interconnected capillary voids increase the surface areas for adsorption of vapor molecules. The tiny compartments facilitate adhesion of molecules to the walls of the nanotubes to subsequently form mono-/multilayers of molecules around the perimeter of the pores. The congregation of molecules allows fewer molecules at a lower relative humidity to condense into water with the pores and interstitial gaps. The condensation of vapor molecules is believed to start at the junction of neighboring nanotubes before saturating the pores around the perimeter. This action of capillary condensation by which vapor molecules experience a phase change to a liquid phase at lower relative humidity is exploited to increase the sensitivity of the sensor. The presence of water causes a large change in the effective dielectric due to the higher dielectric constant of water of 80. Capillary condensation within a pore with a radius of r_K at a particular relative humidity and temperature is described by Kelvin's relation:

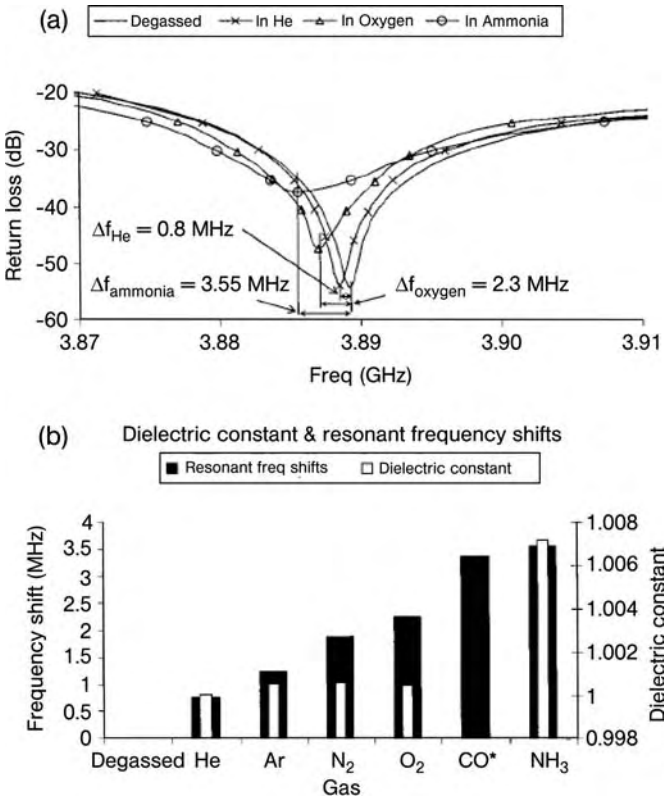

Figure 8.26 (a) Return loss spectrum of sensor when exposed to various gases; (b) frequency shift from initial f_0 of polar and nonpolar gases [52].

$$r_K = \frac{2M\gamma\cos\theta}{R\rho T\ln\left(\frac{P_s}{P_0}\right)} \tag{4}$$

where P_0 is the water vapor pressure, P_s is the water vapor pressure at saturation, γ is the surface tension, R is the universal gas constant, T is the absolute temperature, ρ is the density of water, M is the molecular weight of water and θ is the contact angle.

The unique morphology of the nanostructures induces capillary condensation that increases the capacitance response to a smaller change in relative humidity. In essence, a high-sensitivity humidity sensor can be achieved. A reference sensor, a Honeywell sensor (HIH-3610-001) that is based on a thermoset polymer capacitive sensing element, is used to characterize the performance of the nanotube sensor. Figure 8.28 shows the overall sensing response of the nanotube and the Honeywell sensors. The relative humidity is increased from 65 to 80% at $t = 150$ s during the experiment. Desorption or a falling response is comparable to that of

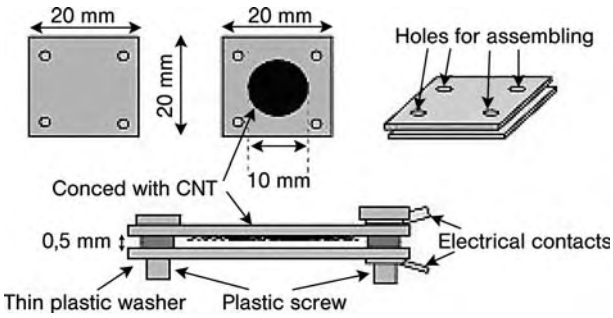

Figure 8.27 Parallel plate capacitive humidity sensor with MWNTs deposited on one plate [102].

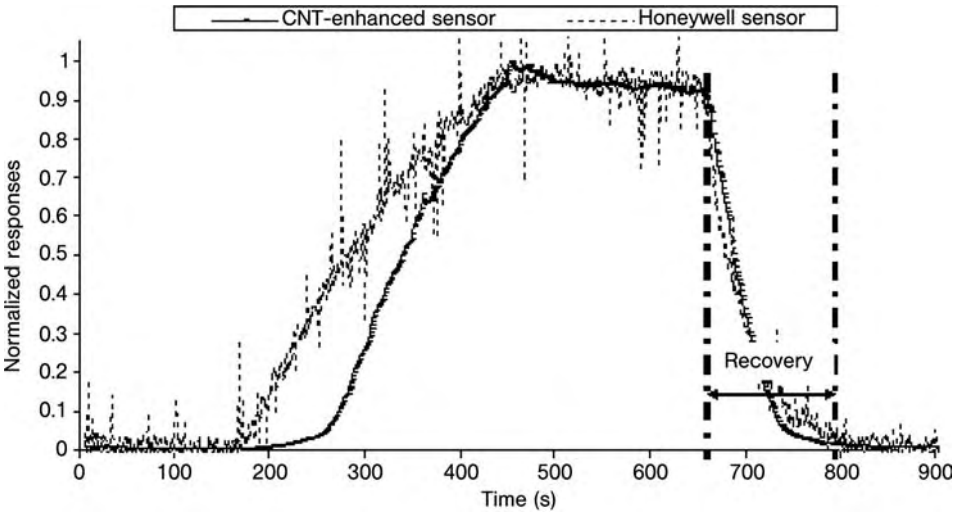

Figure 8.28 The normalized response of the nanotube and the Honeywell sensors [102].

the commercially available humidity sensor. The adsorption and subsequent capillary condensation process is nonlinear. The capacitive response of the nanotube sensor is categorized into two regimes: (i) initial nonlinear capillary condensation and (ii) linear saturated capillary condensation. Figure 8.29 shows the response of the sensors to a change in relative humidity from 65 to 80%. The noisy response of the Honeywell sensor is caused by the fast-moving and turbulent airflow caused by the humidifier during its attempts to maintain constant relative humidity within the test chamber. Response 1 in Figure 8.29a shows the response time when capillary condensation starts to manifest itself. Figure 8.29b illustrates the linear response time when the capillary condensation effect is saturated.

A chemicapacitor based on SWNTs has been proposed by Yeow and She [102] and Snow et al. [103] to detect a wide variety of gases. A network of SWNTs is grown on a 250-nm thermal oxide between electrodes to serve as one plate of the

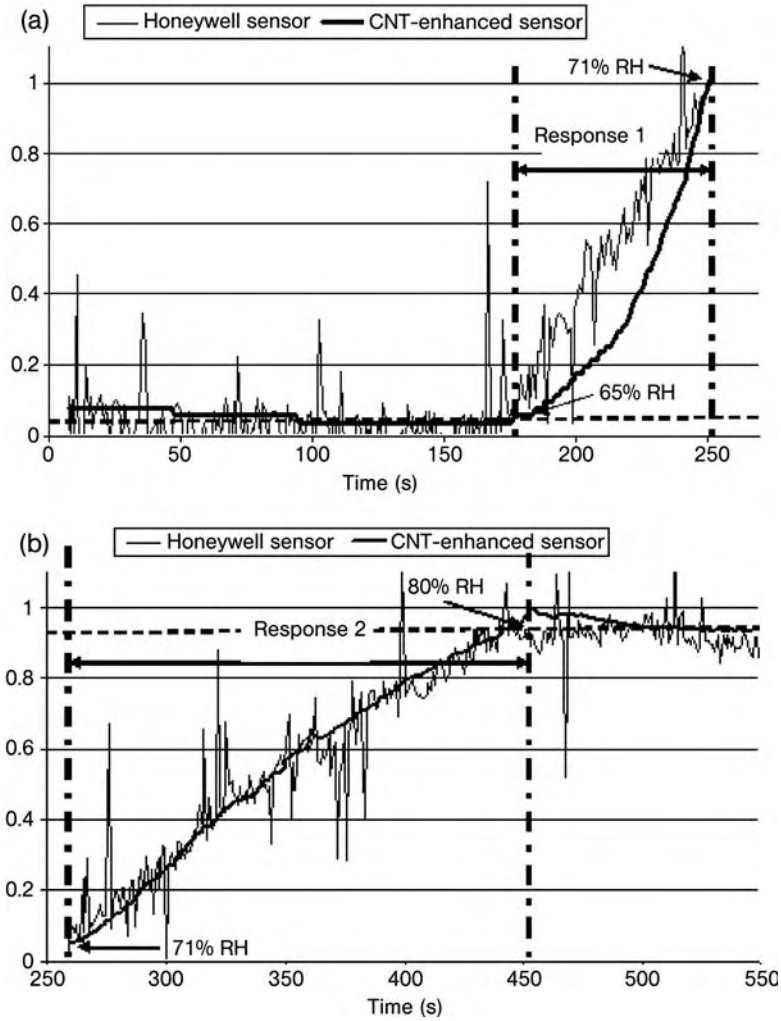

Figure 8.29 Rising time response of the nanotube and Honeywell sensors in (a) nonlinear capillary condensation onset regime and (b) linear saturation regime [102].

capacitor. The other plate is made of heavily doped Si substrate. A 30 kHz, 0.1 V AC voltage is used between the SWNTs and the substrate as excitation voltage to measure the capacitance. The high aspect ratio of SWNTs creates a large concentration of electric fields (~10^5–10^6 V cm^{-1} for a 0.1 V bias) around the tips. The strong fields produce a net polarization of the adsorbed species that induce an increase in measured capacitance. The capacitance response of the sensor to various chemical vapors is shown in Table 8.5.

Table 8.5 Capacitance response of the sensor to a number of chemical vapors. The parameters listed are equilibrium vapor pressure P_0, at 25 °C, vapor concentration, P, in ppm and the measured values of $\Delta C/C$ corresponding to $P/P_0 = 1\%$ [103].

Chemical vapor	P_0 *(mbar) at* 25 °C	P *(ppm) at* 1% P/P_0	μ *(D)*	$\Delta C/C \times 10^{-3}$ *at* 1% P/P_0
Benzene	127	1290	0	0.3 ± 0.1
Hexane	200	2030	0	0.4
Heptane	61	618	0	0.2
Toluene	38	385	0.38	0.5
Trichloroethylene	91	922	0.8	0.6
Chloroform	257	2600	1.04	0.8
Trichloroethane	38	385	1.4	0.8
2-Propanol	108	1093	1.58	3.8
Ethanol	78	792	1.69	3.0
Chlorobenzene	16	162	1.69	0.4
Methanol	168	1702	1.7	2.7
Tetrahydrofuran	215	2180	1.75	5.9
Ethyl acetate	127	1290	1.78	3.1
Water	32	324	1.85	0.5
Dichlorobezene	2	20.3	2.5	0.4
Acetone	304	3080	2.88	6.1
Dimethyl methylphosphonate	1.6	16.2	3.62	10.2
N,N-Dimethylformamide	5	50.7	3.82	9.3
Dinitrotoluene	0.0028	0.028	4.39	0.5

8.6 Applications of CNT Sensors

Gas sensing systems are attracting much interest because of increasing concern about monitoring and controlling the ambient environment. Gas sensors have a wide range of applications that extend through the automotive, biomedical, pharmaceutical and consumer electronics industries. A recent and important use of gas sensors is that of homeland security. Real-time monitoring of the environment, especially for monitoring toxic or pathogenic gases, is attracting widespread attention. The intense development of nanotechnology has created the potential to build low-cost, highly sensitive and portable sensors with low power consumption. Gradually, nanotube-based gas sensors will find their niche in the commercial markets.

The effect of global warming is of great current concern. The general public is well aware of the adverse effects of combustion gases from automobiles and harmful greenhouse gases from industries. There is a definite need for more efficient and effective gas sensors for real-time minimally obtrusive monitoring. CNT-based sensors have the potential to provide significant improvements over conventional solid-state sensor technologies. In contrast to conventional

technologies where high temperature is often required for operation, CNT-based sensors have been shown to offer superior sensing performance at room temperature [104]. Exposure to clear and colorless toxic gases such as chloromethane can cause serious damage to the nervous system. The release of CO_2 into the atmosphere causes global warming. The presence of CO above a safe limit can be fatal. The emission of NO_2 from diesel engines is poisonous. CNT-based sensors have already been reported to sense chloromethane [42, 49], CO_2 [105], CO [44, 106–108], NO_2 [51, 53, 99, 109–112] and many others [43, 103, 113–116].

CNT-based sensors also find applications in the medical and pharmaceutical industries. The availability of CNT-based humidity sensors [102, 107] could be used for testing and verification of the effectiveness of certain drugs. The population of bacteria can be correlated with the humidity content that is dictated by the respiration of microbials. A highly sensitive humidity sensor will be able to characterize the performance of a drug by inferring the change in population of the bacteria by measuring the corresponding change in humidity. A CNT-based hydrogen gas sensor can be used in hydrogen monitoring and control for petroleum transformation, welding, rocket engines and fuel cells. Recent research shows that raw SWNTs and palladium-modified SWNT thin films are good sensing materials for hydrogen sensing [117]. It has been demonstrated that CNT-based sensors provide high sensitivity to hydrogen over a wide temperature range (from room temperature to 170 °C) [118].

8.7 Conclusions

The exploitation of the unique inherent material properties of CNTs and the formation of complex morphologies and structures by the CNT matrix have allowed the realization of highly sensitive and selective gas sensors. Polar (NH_3 and CO) and nonpolar gases (He, Ar, N_2 and O_2) can be detected with high sensitivity through changes in the dielectric constant of the CNT nanocomposite. The change in dielectric constant is proportional to a measured change in the resonant frequency of the sensing material. The incorporation of CNTs has not only enabled the formulation of new sensing materials, it has also enhanced existing gas-sensing materials by increasing their sensitivity to minute quantities of gas molecules. For example, with the incorporation of SWNTs, the sensitivity of a CdA-based acoustic sensor was increased by a factor of two to 39.0 Hz ppm^{-1}. The limit of detection for a SAW 433 MHz SWNT–CdA sensor has been determined as 0.7, 0.9 pm and 0.7 ppm for ethanol, ethyl acetate and toluene, respectively. When exposed to organic vapors such as dichloromethane, chloroform and acetone, a CNT-based sensor has a resistance response on the order of 10^2–10^3. Furthermore, a highly sensitive nanotube gas sensor has been reported to respond to NO_2 concentration that ranges from 10 to 100 ppb. Techniques to address issues such as drift and repeatability of the sensing device have been proposed. Heating of the nanotubes to provide Joule heating seems to be a promising and effective method to induce

faster desorption of gas molecules. For inert gases which have low chemical reactivity and weak physisorption, an ionization technique has been proposed. Sensors based on the ionization technique are able to distinguish between gases or gas mixtures by measuring the distinct breakdown voltages of the gas media. In addition to providing high selectivity, the amount of current discharge can be used to provide concentration information. Although CNTs are promising materials to enable the next generation of highly sensitive and selective gas sensors to be developed, there remain challenges to be addressed by researchers in all stages of sensor design. Challenges include improving our ability to synthesize identical and reproducible CNTs with consistent properties and the subsequent steps of integrating the sensing materials into a functioning device.

References

1 S. Iijima, *Nature* **354** (1991) 56.
2 S. Iijima, T. Ichihashi, *Nature* **262** (1993) 603.
3 D. S. Bethune, C.-H. Kiang, M. de Vries, G. Gorman, R. Savoy, J. Vazquez, R. Beyers, *Nature* **363** (1993) 605.
4 W. Kratschmer, et al., *Nature* **347** (1990) 354.
5 T. W. Ebbesen, P. M. Ajayan, *Nature* **358** (1992) 220.
6 D. T. Colbert, et al., *Science* **266** (1994) 1218.
7 T. W. Ebbesen (ed.), *Carbon Nanotubes – Preparation and Properties*, CRC Press, Boca Raton, FL, 1997, p. 139.
8 C. Journet, et al., *Nature* 388 (1997) 756.
9 X. Zhao, et al., *Chem. Phys. Lett.* **373** (2003) 266.
10 T. Guo, T., et al., *Science* **257** (1992) 1661.
11 A. Thess, et al., *Science* **273** (1996) 483.
12 C. D. Scott, et al., *Appl. Phys. A* **72** (2001) 573.
13 S. Bandow, et al., *Phys. Rev. Lett.* **80** (1998) 3779.
14 R. Sen, et al., *Chem. Phys. Lett.* **332** (2000) 467.
15 H. Kataura, et al., *Carbon* **38** (2000) 1691.
16 H. Kataura, et al., *Jpn. J. Appl. Phys* **37** (1998) L616.
17 S. Farhat, et al., *J. Nanosci. Nanotechnol.* **4** (2004) 377.
18 H. Dai, in *Carbon Nanotubes*, M. S. Dresselhaus, G. Dresselhaus, P. Avouris, (eds.), Springer, New York, Vol. 80, 2001, p. 29.
19 S. Arepalli, et al., *J. Nanosci. Nanotechnol.* **4** (2004) 762.
20 M. J. Yacaman, et al., *Appl. Phys. Lett.* **62** (1993) 202.
21 M. Endo, et al., *J. Phys. Chem. Solids* **54** (1993) 1841.
22 H. Dai, et al., *Chem. Phys. Lett.* **260** (1996) 471.
23 M. J. Bronikowski, et al., *J. Vac. Sci. Technol. A* **19** (2001) 1800.
24 S. Chaisitsak, et al., *Diamonds Relat. Mater.* **13** (2004) 438.
25 V. N. Popov, *Mater. Sci. Eng. R.* **43** (2004) 61.
26 Y. Wang, et al., *Chem. Phys. Lett.* **364** (2002) 568.
27 A. C. Dillon, et al., *J. Nanosci. Nanotechnol.* **4** (2004) 691.
28 B. Zhao, et al., *J. Nanosci. Nanotechnol.* **4** (2004) 995.
29 T. W. Ebbesen, et al., *Nature* **367** (1994) 519.
30 S. Gajewski, et al., *Diam. Rel. Mater.* **12** (2003) 816.
31 H. Hiura, et al., *Adv. Mater.* **7** (1995) 275.
32 L. Vaccarini, et al., *Synth. Met.* **103** (1999) 2492.
33 H. Y. Kim, et al., *Proc. Mater. Res. Soc. Symp.* (2000) 593.
34 S. Bandow, et al., *J. Phys. Chem. B* **101** (1997) 8839.
35 A. G. Rinzler, et al., *Appl. Phys. A* **67** (1998) 29.

36 C. Xu, et al., *Chem. Res. Chin. Univ.* **18** (2002) 130.
37 L. P. Biro, et al., *Mater. Sci. Eng. C* **19** (2002) 9.
38 E. Dujardin, et al., *Adv. Mater.* **10** (1998) 611.
39 K. B. Shelimov, et al., *Chem. Phys. Lett.* **282** (1998) 429.
40 A. R. Harutyunyan, et al., *J. Phys. Chem. B* **106** (2002) 8671.
41 C. J. Ko, et al., *Microelectron. Eng.* **73–74** (2004) 570.
42 K. S. V. Santhanam, et al., *Sens. Actuators B* **106** (2005) 766.
43 M. Penza, et al., *Chem. Phys. Lett.* **409** (2005) 349.
44 O. K. Varghese, et al., *Sens. Actuators B* **81** (2001) 32.
45 B. Philip, et al., *Smart Mater. Struct.* **12** (2003) 935.
46 L. Valentinia, et al., *Smart Mater. Struct.* **11** (2002) 962.
47 K. H. An, et al., *Adv. Mater.* **16** (2004) 1005.
48 T. Li, et al., *J. Mater. Sci.* **40** (2005) 245.
49 A. Modi, et al., *Nature* **424** (2003) 171.
50 S. J. Kim, *J. Phys. D: Appl. Phys.* **39** (2006) 3026.
51 L. Valentini, et al., *Diamonds Relat. Mater.* **13** (2004) 1301.
52 S. Chopra, et al., *Appl. Phys. Lett.* **80** (2002) 4632.
53 J. Kong, et al., *Science* **287** (2000) 622.
54 T. Someya, et al., *Nano Lett.* **3** (2003) 877.
55 Y. T. Jang, et al., *Sens. Actuators B* **99** (2004) 118.
56 Y.-H. Lee, et al., *Adv. Mater.* **13** (2001) 1371.
57 S. Santucci, *Appl. Phys. Lett.* **82** (2003) 961.
58 Y.-T. Jang, et al., *Solid State Commun.* **126** (2003) 305.
59 M. W. Maddox, K. E. Gubbins, *J. Chem. Phys.* **107** (1997) 9659.
60 G. Stan, M. W. Cole, *J. Low. Temp. Phys.* **110** (1998) 539.
61 G. Stan, M. W. Cole, *Surf. Sci.* **395** (1998) 280.
62 M. Dresselhaus, et al., *Science of Fullerenes and Carbon Nanotubes*, Academic Press, San Diego, CA, 1996.
63 J. Liu, et al., *Science* **280** (1998) 1253.
64 S. C. Tsang, et al., *Nature* **362** (1993) 520.
65 P. M. Ajayan, et al., *Nature* **362** (1993) 522.
66 A. Kuznetsova, et al., *J. Chem. Phys* **321** (2000) 292.
67 J. Zhao, et al., *Nanotechnology* **13** (2002) 195.
68 B. Delley, *J. Chem. Phys.* **92** (1990) 508.
69 J. P. Perdew, et al., *Phys. Rev. B* **45** (1992) 13244.
70 M. C. Payne, et al., *Rev. Mod. Phys.* **64** (1992) 1045.
71 N. Troullier, et al., *Phys. Rev. B* **43** (1991) 1993.
72 G. Vidali, et al., *Surf. Sci. Rep.* **12** (1991) 133.
73 S. Peng, et al., *Nano Lett.* **3** (2003) 513.
74 Z. Weng-Sieh, et al., *Phys. Rev. B* **51** (1995) 11229.
75 E. Hernandez, et al., *Phys. Rev. Lett.* **80** (1998) 4502.
76 P. G. Collins, et al., *Science* **287** (2000) 1801.
77 R. Chen, et al., *Appl. Phys. Lett.* **79** (2001) 2258.
78 J. D. Adams, *Mol. Phys.* **29** (1975) 307.
79 K. A. Williams, P. C. Eklund, *J. Chem. Phys.* **320** (2000) 352.
80 K. G. Ayappa, *Langmuir* **14** (1998) 880.
81 G. Hummer, et al., *Nature* **414** (2001) 188.
82 W. A. de Heer, et al., *Science* **270** (1995) 1179.
83 N. de Jonge, et al., *Nature* **420** (2002) 393.
84 R. G. Forbes, et al., *Ultramicroscopy* **95** (2003) 57.
85 C. Edgcombe, J. Valdré, *Microscopy* **203** (2001) 188.
86 J. Meek, J. Craggs, *Electrical Breakdown of Gases*, Wiley, New York, 1978, p. 129.
87 M. Abdel-Salam, et al., *High-Voltage Engineering – Theory and Practice*, Marcel Dekker, New York, 2000.
88 M. C. Gallazzi, et al., *Sens. Actuators B* **88** (2003) 178.
89 P. N. Bartlett, S. K. Ling-Chung, *Sens. Actuators B* **20** (1989) 287.
90 Y. Sakurai, et al., *Sens. Actuators B* **83** (2002) 270.
91 J. P. Blanc, et al., *Sens. Actuators B* **1** (1990).
92 Y. Sakurai, et al., *Sens. Actuators B* **83** (2002) 270.

93 L. Valentinia L, et al., *Compos. Sci. Technol.* **63** (2003) 1149.
94 B. Safadi, et al., *J. Appl. Polym. Sci.* **84** (2002) 2660.
95 H. W. Goh, et al., *Chem. Phys. Lett.* **373** (2003) 277.
96 A. Allaouia, et al., *Compos. Sci. Technol.* **62** (2002) 1993.
97 Y. Fan, et al., *Adv. Mater.* **14** (2002) 130.
98 D. J. Bae, et al., *Phys. Rev. B* **64** (2001) 233.
99 J. Li, et al., *Nano Lett.* **3** (2003) 929.
100 G. U. Sumanasekera, et al., *Phys. Rev. Lett.* **85** (2000) 1096.
101 N. E. Hill, V. N. Reinhold, *Dielectric Properties and Molecular Behavior*, Van Nostrand Reinhold, New York, 1969.
102 J. T. W. Yeow, J. P. M. She, *Nanotechnology* **17** (2006) 5441.
103 E. S. Snow, et al., *Science*, **307** (2005) 1942.
104 P. H. Zhang, et al., *Phys. Rev. Lett.* **81** (1998) 5346.
105 K. G. Ong, et al., *IEEE Sens. J.* **2** (2002) 82.
106 F. Picaud, et al., *J. Appl. Phys.* **97** (2005) 114316.
107 L. B. da Silva, et al., *Nano Lett.* **4** (2004) 65.
108 S. Chopra, et al., *Appl. Phys. Lett.* **83** (2003) 2280.
109 P. Young, et al., *J. Nanosci. Nanotechnol.* **5** (2005) 1509.
110 P. Qi, et al., *Nano Lett.* **3** (2003) 347.
111 J. Suehiro, et al., *Sens. Actuators B* **108** (2005) 398.
112 Y. X. Liang, et al., *Appl. Phys. Lett.* **85** (2004) 666.
113 Q. Zhao, et al., *Polym. Adv. Technol.* **13** (2002) 759.
114 M. Penza, et al., *Thin Solid Films* **472** (2005) 246.
115 M. Penza, et al., *Sens. Actuators B* **111–112** (2005) 171.
116 Y. Zhang, et al., *Sens. Actuators A* **120** (2005) 142.
117 S. Sotiropoulou, N. A. Chaniotakis, *Anal. Bioanal. Chem.* **375** (2003) 103.
118 J. Wang, et al., *J. Am. Chem. Soc.* **125** (2003) 2408.

Index

Advanced Micro & Nanosystems Vol. 8. Carbon Nanotube Devices.
Edited by Christofer Hierold

ISBN: 978-3-527-31720-2

d

t